CAVE DEPOSITS: PROCESSES, APPROACHES AND ENVIRONMENTAL SIGNIFICANCE

EDITED BY: Leonardo Piccini, Eleonora Regattieri, Andrea Zerboni and Aurel Perșoiu

PUBLISHED IN: Frontiers in Earth Science

frontiers Research Topics

ISSN 1664-8714
ISBN 978-2-88974-807-5
DOI 10.3389/978-2-88974-807-5

About Frontiers

Frontiers is more than just an open-access publisher of scholarly articles: it is a pioneering approach to the world of academia, radically improving the way scholarly research is managed. The grand vision of Frontiers is a world where all people have an equal opportunity to seek, share and generate knowledge. Frontiers provides immediate and permanent online open access to all its publications, but this alone is not enough to realize our grand goals.

Frontiers Journal Series

The Frontiers Journal Series is a multi-tier and interdisciplinary set of open-access, online journals, promising a paradigm shift from the current review, selection and dissemination processes in academic publishing. All Frontiers journals are driven by researchers for researchers; therefore, they constitute a service to the scholarly community. At the same time, the Frontiers Journal Series operates on a revolutionary invention, the tiered publishing system, initially addressing specific communities of scholars, and gradually climbing up to broader public understanding, thus serving the interests of the lay society, too.

Dedication to Quality

Each Frontiers article is a landmark of the highest quality, thanks to genuinely collaborative interactions between authors and review editors, who include some of the world's best academicians. Research must be certified by peers before entering a stream of knowledge that may eventually reach the public - and shape society; therefore, Frontiers only applies the most rigorous and unbiased reviews.
Frontiers revolutionizes research publishing by freely delivering the most outstanding research, evaluated with no bias from both the academic and social point of view. By applying the most advanced information technologies, Frontiers is catapulting scholarly publishing into a new generation.

What are Frontiers Research Topics?

Frontiers Research Topics are very popular trademarks of the Frontiers Journals Series: they are collections of at least ten articles, all centered on a particular subject. With their unique mix of varied contributions from Original Research to Review Articles, Frontiers Research Topics unify the most influential researchers, the latest key findings and historical advances in a hot research area! Find out more on how to host your own Frontiers Research Topic or contribute to one as an author by contacting the Frontiers Editorial Office: frontiersin.org/about/contact

CAVE DEPOSITS: PROCESSES, APPROACHES AND ENVIRONMENTAL SIGNIFICANCE

Topic Editors:
Leonardo Piccini, University of Florence, Italy
Eleonora Regattieri, Pisa Research Area, Italian National Research Council, Italy
Andrea Zerboni, University of Milan, Italy
Aurel Perșoiu, Emil Racovita Institute of Speleology, Romanian Academy, Romania

Citation: Piccini, L., Regattieri, E., Zerboni, A., Perșoiu, A., eds. (2022). Cave Deposits: Processes, Approaches and Environmental Significance. Lausanne: Frontiers Media SA. doi: 10.3389/978-2-88974-807-5

Table of Contents

frontiers in Earth Science

EDITORIAL
published: 10 March 2022
doi: 10.3389/feart.2022.858704

Editorial: Cave Deposits: Processes, Approaches and Environmental Significance

Leonardo Piccini[1]*, *Eleonora Regattieri*[2], *Andrea Zerboni*[3] and *Aurel Perşoiu*[4,5]

[1]Department of Earth Science, Università degli Studi di Firenze, Florence, Italy, [2]Institute of Earth Science and Georesources, Italian National Research Council, Pisa, Italy, [3]Dipartimento di Scienze della Terra "A. Desio", Università degli Studi di Milano, Milan, Italy, [4]Emil Racoviță Institute of Speleology, Romanian Academy, Cluj-Napoca, Romania, [5]Stable Isotope Laboratory, Ștefan cel Mare University, Suceava, Romania

Keywords: cave deposits/sediments, speleothem, anthropogenic deposit, paleohydrology, environmental proxies

Editorial on the Research Topic

Cave Deposits: Processes, Approaches and Environmental Significance

Caves are natural cavities accessible to humans mainly formed by the dissolution of carbonate and evaporitic rocks and, occasionally, by subsurface weathering in quartz-bearing rocks (Ford and Williams, 2007). While the different morphogenetic processes can quickly shape and dissolve landforms at the Earth's surface, caves can remain intact for several millions of years, thus surviving the landscapes in which they were formed (Granger et al., 2001). Water flowing through caves carries chemical and physical signals in the form of dissolved ions and clastic sediments that, accumulating within them, can form detailed archives of environmental and climatic change occurring at the Earth's surface (White, 2007). These deposits are among the most important continental paleo-environmental archives, offering a wide array of physical, geochemical, and biological proxies concerning climatology, hydrology, tectonics, ecology, and biology; at very different timescales (from sub-annual to orbital) and going back millions of years. Additionally, caves have been inhabited since prehistory and preserve anthropogenic sediments crucial to the understanding of human evolution, adaptation, and behavior. In the last decades, cave deposits have been targeted by numerous studies, and the progressive improvement of analytical methods now allows obtaining detailed, high resolution and well-dated records of present and past climate and environmental changes (Fairchild and Baker, 2012). Because speleothems have been preferentially the subject of these studies, the aim of this Research Topic is to present recent results and implications concerning the study of other types of cave infillings and sediments: precipitation and alteration minerals, water transported sediments, wall-weathering materials, biogenic (including anthropogenic) formations, cave ice and gravitative debris. The purpose is to furnish a state-of-the-art on methodological approaches, analytical procedures and dating methods, thus offering a novel and comprehensive view on cave deposits.

Four articles of this Research Topic collection concern cave clastic sediments, which, despite being volumetrically the most common deposits in caves, are much less studied than speleothems due to the difficulties of dating and determining their source and depositional mechanisms (Springer, 2005).

Kurečić et al. investigated an allogenic sedimentary sequence in Cerovačka Cave (Croatia), accumulated as a complex combination of breakdown, diamicton, and slackwater deposits. This study highlights how differences in facies formation in caves can lead to the understanding of the complex interplay between geomorphologic, tectonic, and climatic processes over the past tens of thousands of years, which would otherwise leave no trace at the surface. By firmly anchoring the chronology of the deposit with luminescence and radiocarbon dating, the authors prepare the scene

OPEN ACCESS

Edited by:
Nadia Solovieva,
University College London,
United Kingdom

Reviewed by:
Bogdan Ridush,
Yuriy Fedkovych Chernivtsi National University, Ukraine

***Correspondence:**
Leonardo Piccini
leonardo.piccini@unifi.it

Specialty section:
This article was submitted to Quaternary Science, Geomorphology and Paleoenvironment, a section of the journal Frontiers in Earth Science

Received: *20 January 2022*
Accepted: *18 February 2022*
Published: *10 March 2022*

Citation:
Piccini L, Regattieri E, Zerboni A and Perşoiu A (2022) Editorial: Cave Deposits: Processes, Approaches and Environmental Significance. Front. Earth Sci. 10:858704. doi: 10.3389/feart.2022.858704

for future, detailed investigation that could reveal centennial to millennial environmental variability and dynamics of human societies as recorded by the various proxies harbored in the investigated sedimentary sequence.

Sauro et al. report on the potential of clastic sediments for reconstructing the paleogeographic evolution of a karst system at high altitude in the Dolomites (southern Italian Alps). In their reconstruction, authors identified the source of the clastic infilling of the Raponzolo Cave and applied cosmogenic isotopes and U-Pb dating to constrain the burial time. Such multi-dating approach allowed them to reconstruct the evolution of the karst system, concluding that speleogenesis occurred since the Late Miocene because of the interplay between climatic triggers and tectonics. This contribution confirms the high potentiality of cave clastic sediments as tool to reconstruct ancestral evolution phases of the karst system and its response to multiple forcing.

Nannoni et al. describe a particular type of recent cave deposits where a significant portion of the detrital material is produced by the numerous marble quarries that impact the karst area of the Apuan Alps (Northern Italy). Mineralogical composition of sediments collected along karst waterways and springs shows variable proportions of calcite associated with dolomite and silicates. Cave deposits of natural origin have usually a fine-sand grain size whereas present spring sediments have a more variable grain-size distribution. Through innovative techniques of morphometric and chemical-physical analysis of sediments, it was possible to distinguish, although qualitatively, the particles of natural origin from the anthropogenic ones.

Patania et al. introduce the topic of preservation of archaeological sediments in cave-entrance/rockshelter environments. They explore the archaeological sequence of the Kisese II Rockshelter (Tanzania) highlighting that natural and anthropogenic processes promoting soil instability and erosion, also contribute to the loss of archaeological sediments, thus hampering our ability to reconstruct human adaptive strategies. Their geoarchaeological approach consider several variables (soil, vegetation, fauna, and anthropogenic features) in charge of enhancing surface processes, thus offering innovative tools to support archaeologists and heritage specialists. This multi-scalar approach seems essential for the construction of appropriate mitigation strategies for the preservation of archaeological cultural heritage.

Three papers deal with peculiar wall formations of chemical or biochemical origin.

Bernardini et al. describe a unique stromatolite-like manganese-rich deposit on cave walls in Grotta del Cervo (Central-southern Italy), and using a multidisciplinary investigation show that patina records the dynamics of the palaeofloods during which it was deposited. Combining geochemical and microbiological analyses, the authors make a compelling case for the possibility of using the internal microstratigraphy of the deposit as an archive of the succession of both flood events and processes within single-flooding events, opening a window into a novel proxy for past climatic reconstructions.

Jurado et al. investigated a common but still puzzling type of parietal deposit: vermiculations. The study concerns an alpine cave subjected to extreme climate conditions, located in Central Italian Alps and recently discovered thanks to the local glaciers retreat. The authors present a detailed geomicrobiological study revealing microbial communities dominated by 13 main phyla of *Bacteria* and contained a negligible percentage (<1%) of *Archaea*. The two major bacterial classes were *Gammaproteobacteria* and *Betaproteobacteria*, whose metabolic traits are associated to the nitrogen cycle. In addition, psychrophilic and methanotrophic bacterial groups were identified. Many uncultured members indicate the presence of still unexplored microbial taxa.

Piccini et al. presents a preliminary investigation on a very peculiar type of crusts or nodules covering the rock walls of inactive conduits in the Monte Corchia Cave (Apuan Alps, Northern Italy). Samples were analyzed by diffractometry and SEM-EDS revealing the occurrence of hydroxyapatite or fluorapatite mixed with Fe/Mn incrustations and allogenic clastic particles. Crusts are interpreted as related to precipitation during a waterfilled phase. Phosphate nodules are almost entirely composed by hydroxyapatite or fluoroapatite and could be the result of long-term chemical (or bio-chemical) precipitation in air-filled environments.

Despite speleothems are the most studied cave deposit, only one paper deals with them, demonstrating that caves offer a wide variety of secondary formations, the analysis of which is just in the initial phase. Weber et al. investigate four Holocene stalagmites from Hüttenbläserschachthöhle cave (Germany) by applying a detailed multiproxy approach (stable C and O isotopes, trace elements composition and Sr isotopes). They evaluate the proxy data consistency by comparing the different stalagmites and found coherent variations over overlapping periods. They also evaluate the robustness of the inferred climatic variations by comparing with a coeval record obtained from the nearby, well-studied Bunker Cave. Overall, the study highlights the importance of a multi-proxy approach, and the need to replicate speleothem records within a cave system, and ideally using several caves from the same region.

Finally, a paper concerns with the most ephemeral deposit occurring in caves: ice. Kern and Perşoiu review past achievements in reconstructing past environmental changes based on the study of multiple proxies harbored by cave glaciers and, based on their (and collaborators) 20 + years-long expertise, propose a *Cave Ice Sedimentary Architecture and Deposition (CISAD)* approach for further similar studies. CISAD would (in the author's vision) put mechanisms behind ice accumulation and those responsible for climate-proxy relationships first, and once these are understood, subsequent studies should proceed to reconstruct past climate and environmental variability.

As a whole, this collection shows a wide, well-differentiated panorama of conventional and unconventional cave materials that can be investigated and analyzed, offering efficient reconstruction of past environmental changes. By highlighting *other-than-speleothems* deposits we wish to draw attention

especially on these as archives of past natural and anthropic environmental histories.

AUTHOR CONTRIBUTIONS

All the authors made a substantial direct and intellectual contribution to the work and approved it for publication.

REFERENCES

Fairchild, I. J., and Baker, A. (2012). *Speleothem Science*. John Wiley & Sons. doi:10.1002/9781444361094

Ford, D., and Williams, P. D. (2007). *Karst Hydrogeology and Geomorphology*. Chichester, UK: Wiley, 562.

Granger, D. E., Fabel, D., and Palmer, A. N. (2001). Pliocene–Pleistocene Incision of the Green River, Kentucky, Determined from Radioactive Decay of Cosmogenic 26Al and 10Be in Mammoth Cave Sediments. *Geol. Soc. Am. Bull.* 113, 825–836. doi:10.1130/0016-7606(2001)113<0825:ppiotg>2.0.co;2

Springer, G. S. (2005). "Clastic Sediments in Caves," in *Encyclopedia of Caves*. Editors D. Culver and W. White (MA, USA: Elsevier), 102–108.

White, W. B. (2007). Cave Sediments and Paleoclimate. *J. Cave Karst Stud.* 69, 76–93.

ACKNOWLEDGMENTS

We thank all the authors for their valuable contributions to this Research Topic, the reviewers who shared their valuable time to improve the manuscripts, and the members of Frontiers Team and the Editor in Chief for their help at different stages of preparing this collection.

Conflict of Interest: The authors declare that the research was conducted in the absence of any commercial or financial relationships that could be construed as a potential conflict of interest.

Publisher's Note: All claims expressed in this article are solely those of the authors and do not necessarily represent those of their affiliated organizations, or those of the publisher, the editors and the reviewers. Any product that may be evaluated in this article, or claim that may be made by its manufacturer, is not guaranteed or endorsed by the publisher.

frontiers in Earth Science

ORIGINAL RESEARCH
published: 16 December 2020
doi: 10.3389/feart.2020.586248

Microbial Communities in Vermiculation Deposits from an Alpine Cave

*Valme Jurado[1], Jose Luis Gonzalez-Pimentel[1], Ana Zelia Miller[1,2], Bernardo Hermosin[1], Ilenia M. D'Angeli[3], Paola Tognini[4], Jo De Waele[3] and Cesareo Saiz-Jimenez[1]**

[1] Instituto de Recursos Naturales y Agrobiologia, IRNAS-CSIC, Sevilla, Spain, [2] Laboratorio HERCULES, Universidade de Evora, Evora, Portugal, [3] Department of Biological, Geological and Environmental Sciences, Italian Institute of Speleology, Bologna University, Bologna, Italy, [4] Gruppo Grotte Milano CAI-SEM, Federazione Speleologica Lombarda, Milano, Italy

Morgana Cave is located in *Val di Scerscen*, Central Italian Alps. The cave opens at an altitude of 2,600 m a.s.l. close to the retreating glacier *Vedretto di Scerscen*, and its entrance was discovered 30 years ago hidden underneath the glacier. A characteristic of this cave is the occurrence of vermiculation deposits on the walls and ceiling. In general, the composition of the microbial communities in cave vermiculations is relatively unknown and rarely investigated. Here we present the data of a geomicrobiological study of vermiculations from an Alpine cave subjected to extreme climate conditions. The microbial communities were dominated by 13 main phyla of *Bacteria*, and contained a negligible percentage (<1%) of *Archaea*. The two major bacterial classes were *Gammaproteobacteria* and *Betaproteobacteria*, whose metabolic traits were mainly associated with the nitrogen cycle. In addition, psychrophilic and methanotrophic bacterial groups were identified. The occurrence of a large number of uncultured members, at the lowest taxonomic ranks, indicated the presence of still unexplored microbial taxa in the vermiculations.

Keywords: vermiculation deposits, bacteria, archaea, nitrogen cycle, alpine cave

OPEN ACCESS

Edited by:
Aurel Perşoiu, Romanian Academy, Romania

Reviewed by:
Cristina Purcarea, Institute of Biology Bucharest of the Romanian Academy, Romania
Diana Eleanor Northup, University of New Mexico, United States

****Correspondence:***
Cesareo Saiz-Jimenez
saiz@irnase.csic.es

Specialty section:
This article was submitted to Quaternary Science, Geomorphology and Paleoenvironment, a section of the journal Frontiers in Earth Science

Received: *22 July 2020*
Accepted: *19 November 2020*
Published: *16 December 2020*

Citation:
Jurado V, Gonzalez-Pimentel JL, Miller AZ, Hermosin B, D'Angeli IM, Tognini P, De Waele J and Saiz-Jimenez C (2020) Microbial Communities in Vermiculation Deposits from an Alpine Cave. Front. Earth Sci. 8:586248. doi: 10.3389/feart.2020.586248

INTRODUCTION

Global warming is causing a rapid glacial retreat. The total glacier-covered surface area in the Alps decreased from an estimated 4,500 km^2 around 1850 to around 2,200 km^2 in 2001, 1,800 km^2 in 2010 (Haeberli et al., 2013) and 1,650 km^2 in 2015 (Sommer et al., 2020).

The glacier *Vedretta di Scerscen* is located in *Val di Scerscen*, Central Italian Alps (Northern Lombardy), in the scenic setting of *Valmalenco* (**Figures 1A,G**). The glacier retreat has uncovered a few caves, the most important of which, opening at about 2,600 m a.s.l., are: Veronica Cave (638 m long), Morgana Cave (770 m), and *Tana dei Marsooi* (77 m). These caves represent very interesting systems from both pure geological-geomorphological and microbiological standpoints (De Waele et al., 2014).

Morgana Cave was hidden underneath the rapidly retreating glacier until the end of the last century (**Figure 1B**). In the Morgana Cave area, snow and ice remain until the beginning of June. At the sampling time (July 17th, 2017) the entrance of the cave was open, but there was still snow around and above the cave. The cave had very low temperatures, slightly above 0°C, with freezing occurring close to the entrance, and rather stable conditions occurring deeper into the cave (reaching 2°C 50 m inward).

FIGURE 1 | Morgana Cave. **(A)** Panoramic view of the caves location; **(B)** Entrance partially covered by snow; **(C)** Phreatic morphologies; **(D)** Phreatic and vadose morphologies (sampling site M1); **(E)** Glacial sediments; **(F)** Phreatic and condensation-corrosion features; **(G)** Planimetry and cross-section of the cave. The six sampling sites from the innermost M1 to the outermost zone M5-M6 have been indicated on the map. Photos **(A)** and **(B)** by A. Granati, photos **(C–F)** by M. Inglese. Planimetry from Gruppo Grotte Milano.

Morgana Cave is characterized by phreatic morphologies (**Figures 1C,D**) and contains glacial sediments (**Figure 1E**). The cave probably formed before the last ice age. The entrance area of Morgana cave and many smaller nearby caves were all apparently cut both by valley slope retreat and ice scouring. The caves are characterized by shallow vadose entrenchments (**Figure 1D**) which record a later phase of free-running meltwaters in the cave passages. Air circulation triggered by the temperature difference between the cave interior and exterior induces condensation-corrosion processes, which are actually shaping the cave wall and ceiling morphologies (**Figure 1F**), with smooth reliefs, notches and cupola (D'Angeli et al., 2018).

Vermiculation deposits are among the most characteristic features of Morgana Cave. Vermiculation patterns developing on wall surfaces have been found in many caves around the world (Hose and Macalady, 2006; Merino et al., 2014; Bojar et al., 2015; Faucher and Lauriol, 2016; D'Angeli et al., 2017, 2019a, 2019b; Addesso et al., 2020).

Cave vermiculations are thin, irregular and discontinuous deposits of incoherent particles. Generally, they exhibit several kinds of morphologies (i.e. dots, dendritic, hieroglyphic), colors (red, brown, grey or white) and dimensions (De Waele et al., 2014; Addesso et al., 2020). According to Bini et al. (1978) vermiculations are mainly composed of clays and are the

consequence of climatic and environmental conditions, including condensation-evaporation processes. However, other authors reported a different type of vermiculations, the so-called biovermiculations with complex geometric forms resembling clay vermiculations, but lacking significant clay content. These vermiculations are typical of sulfuric acid cave systems in the United States, Mexico, and Italy (Hose et al., 2000; Hose and Macalady, 2006; D'Angeli et al., 2017; D'Angeli et al., 2019a).

According to Bojar et al. (2015) the formation of vermiculation patterns is driven by evaporation and water film rupture of particle aggregates. The rheology of the clayey sediments of vermiculations and the chemistry of the fluids soaking the deposits appear to be important drivers in the formation of the patterns (Freydier et al., 2019). Boston (2016) recognized biovermiculation patterns, observed in limestone caves, lava tubes, mines, etc., as universal signatures of extant and extinct life in which the mathematical similarity of the patterns are the morphological expression of behavior in response to ecological drivers.

Three papers dealing with the microbiological characterization of vermiculations are worth mentioning. In the first one, Jones et al. (2008) investigated the biovermiculations from the Frasassi Cave system, Italy, and reported that the community was diverse with at least 15 major bacterial lineages, mainly *Betaproteobacteria*, *Gammaproteobacteria*, *Acidobacteria*, *Nitrospirae*, and *Planctomycetes*. These authors identified potential sulfur- and nitrite-oxidizing bacteria, in addition to auto- and heterotrophic microorganisms in the biovermiculations.

D'Angeli et al. (2019b) carried out an extensive geomicrobiological study on the vermiculations from Fetida Cave, Santa Cesarea Terme, Italy, an active sulfuric acid cave influenced by seawater. These vermiculations contained 18 phyla, including autotrophic taxa associated with sulfur and nitrogen cycles and biomineralization processes. The bacterial community was composed of *Proteobacteria* (including *Alpha-*, *Beta-*, *Gamma-*, *Delta-*, *Epsilonproteobacteria*), *Planctomycetes*, *Acidobacteria*, *Chloroflexi*, *Bacteroidetes*, *Actinobacteria*, and *Nitrospirae* in decreasing order of abundance. *Archaea* constituted <4.3% of the total community and were dominated by members of the phylum *Thaumarchaeota*.

Adesso et al. (2020) found that the most abundant phylum in vermiculations from the Italian Pertosa-Auletta Cave was *Proteobacteria*, followed by *Acidobacteria, Actinobacteria, Nitrospirae, Firmicutes, Planctomycetes, Chloroflexi, Gemmatimonadetes, Bacteroidetes and Latescibacteria.* Less-represented taxonomic groups (<1%), as well as unclassified ones, were also detected.

Recently uncovered caves located close to retreating glaciers are ideal places to study microbial life in cold ecosystems. The geomicrobiology of Alpine caves and their vermiculations remains largely understudied due to the remoteness and difficult access to the caves, as most of them are far away from mountain paths. In addition, sampling in high mountain caves is not an easy task due to severe working conditions. Opportunities to obtain samples are rare, and the samples are small and hard to collect due to their mineral composition. The small sample size sometimes makes it difficult to perform a complete microbiological analysis.

Vermiculations, being aggregates of weathered minerals and clays, represent an interesting and suitable niche for microorganisms. In addition, organic compounds are largely adsorbed onto the clays. Clays also increase water retention with respect to the host rock, facilitating colonization and thriving of microorganisms. Therefore, vermiculation deposits are ideal sites for studying the diversity of cold-adapted microbial communities in Morgana Cave.

Here we report the microbial community of different vermiculation deposits (**Figure 2**) collected on the walls of Morgana Cave, in an attempt to expand the understanding on the geomicrobiology of Alpine caves.

MATERIALS AND METHODS

Sampling

Morgana Cave (44° 08′ 46.6″ N, 8° 09′ 31.7″ E, WGS84), was visited on the July 17–18th 2017. Six samples of vermiculations were collected in different passages of the cave (from the innermost part M1 towards the outermost zone of the cave in M5-6, as shown in **Figure 1**), using sterilized scalpels.

Sample M1 was composed of whitish-grey vermiculations close to a flowing water body, M2 of whitish vermiculations (small dots), M3 of dense grey vermiculations, M4 of whitish vermiculations (dots), M5 of dense brown vermiculations and M6 of white vermiculations (elongated) (**Figure 2**).

The samples, stored in sterile containers, were maintained at 5°C until laboratory arrival and those used for field emission scanning electron microscopy (FESEM) were fixed *in situ*. The samples for molecular biology were preserved in RNAlater and then conserved at −80°C in the laboratory.

Vermiculations showed different colors (whitish, greyish, brownish); the whitish are dominated by dolomite clasts, whereas clay minerals have been solely observed in the greyish and brownish deposits.

Field Emission Scanning Electron Microscopy

The morphology of the different vermiculations was studied by field emission scanning electron microscopy (FESEM) combined with energy dispersive X-ray spectroscopy (EDS). Previously, samples were dried at 50°C for 24 h and directly mounted on sample stubs, sputter coated with gold, and subsequently examined in a FEI Teneo FESEM equipped with an EDS detector. FESEM examinations were operated using the secondary electron (SE) detection mode (Everhart-Thomley) with an acceleration voltage of 5 kV for ultra-high resolution images and 10 kV for elemental microanalysis.

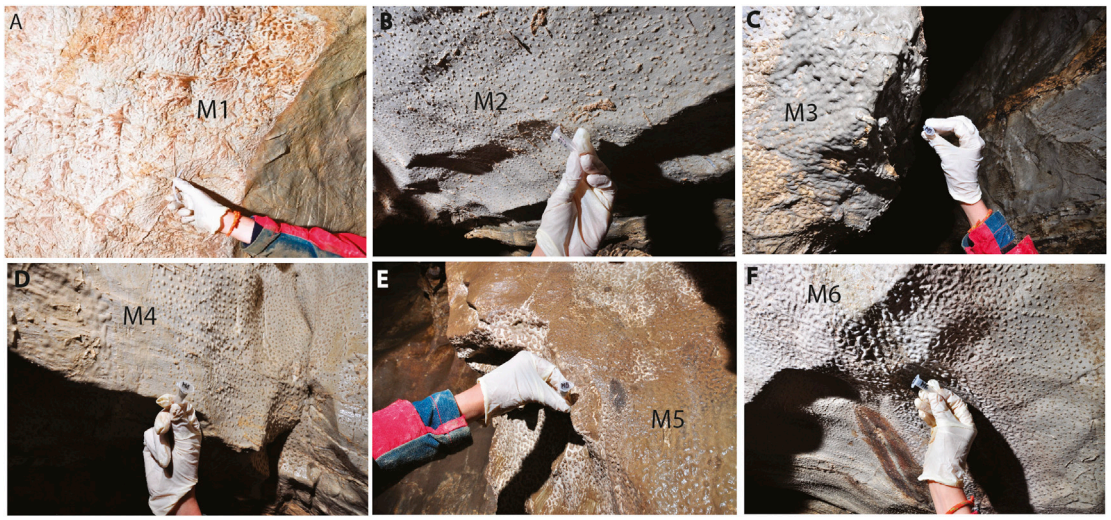

FIGURE 2 | (A-F) Vermiculation deposits (from M1 to M6) collected from the walls of Morgana Cave. They present different shapes and colors such as whitish, brown, and greyish (photos by M. Inglese).

Nucleic Acid Extraction

Genomic DNA and RNA were extracted from 300 mg of samples using the DNeasy PowerBiofilm DNA and RNA isolation kits according to manufacturer's protocols (Qiagen) and quantified using a Qubit 2.0 fluorometer (Invitrogen). DNA and RNA were stored at −80°C until their use.

Genomic DNA and RNA were extracted from all samples. Only DNA from samples M2, M3, M4, M5, and M6 reached sufficient concentration (>10 ng/μl) for next generation sequencing. RNA concentrations were very low, <0.2 ng/μl, insufficient for sequencing.

Next-Generation Sequencing and Data Analysis

The extracted DNA of all samples (except M1) was analyzed by next generation sequencing (NGS). We investigated the bacterial V3 and V4 regions of the 16S SSU rRNA gene using Illumina MiSeq and 2 × 250 paired end sequencing, according to the Illumina 16S metagenomic library preparation protocol used by Macrogen (Seoul, Korea).

The primer sequences used in this study were 341F (CCTACGGGNGGCWGCAG) and 805R (GACTACHVGGGTATCTAATCC).Takahashi et al. (2014) showed that this prokaryotic universal primer for simultaneous analysis had a coverage rate of 98% for *Bacteria* and 94.6% for *Archaea*. Raw data were processed in QIIME 1.9.1 (Caporaso et al., 2010). Quality control and trimming were performed using FASTQC (http://www.bioinformatics.babraham.ac.uk/projects/fastqc/) and Trimmomatic (0.36 version), respectively. Paired end reads were assembled using PEAR (Zhang et al., 2014). Primers removal was carried out using a PERL script developed by the Environmental Microbiology group (IRNAS-CSIC). Operational Taxonomic Units (OTUs) were clustered at 97% cutoff using UCLUST (Edgar, 2010). The SILVA database (version 132) was used to assign the taxonomic classification of each 16S rRNA gene sequence with a threshold of 80% (Quast et al., 2013). The alpha_diversity.py command was employed for alpha diversity measurements.

Amplification of Functional Genes and Clone Library Construction

Amplification of functional genes from genomic DNA, *nifH* (as a measure of N-fixing bacteria) and *amoA* (as a measure of ammonia-oxidizing archaea and bacteria) were previously described by Mao et al. (2011). We used primers PolF (5′-TGC GAY CCS AAR GCB GAC TC-3′) and PolR (5′-ATS GCC ATC ATY TCR CCG GA -3′) for detecting *nifH* gene (Poly et al., 2001); Arch-amoAF (5′-STA ATG GTC TGG CTT AGA CG-3′) and Arch-amoAR (5′-GCG GCC ATC CAT CTG TAT CT-3′) for archaeal *amoA* gene (Francis et al., 2005); and amoA-1F (5′-GGG GTT TCT ACT GGT GGT-3′) and amoA-2R (5′-CCC CTC KGS AAA GCC TTC TTC-3′) for bacterial *amoA* gene (Rotthauwe et al., 1997). Clone libraries protocol was detailed by Gonzalez-Pimentel et al. (2018). Plasmids were sequenced by Secugen Sequencing Services (CSIC, Madrid, Spain). Sequences were checked for chimera by chimera.slayer as implemented in the software package mothur (Schloss et al., 2009). Sequences were aligned using mothur. After this analysis, all sequences were compared to the nonredundant database of sequences deposited at the National Center for Biotechnology (NCBI; http://www.ncbi.nlm.nih.org/blast/) using BLASTN algorithm. Statistical data (Chao1, Shannon and Simpson indices) were calculated as described by Riquelme et al. (2017).

Phylogenetic trees were constructed using the maximum-likelihood (Felsenstein, 1981) method in MEGA X (Kumar et al., 2018). A bootstrap analysis of 1000 re-samplings was used to evaluate the trees' robustness.

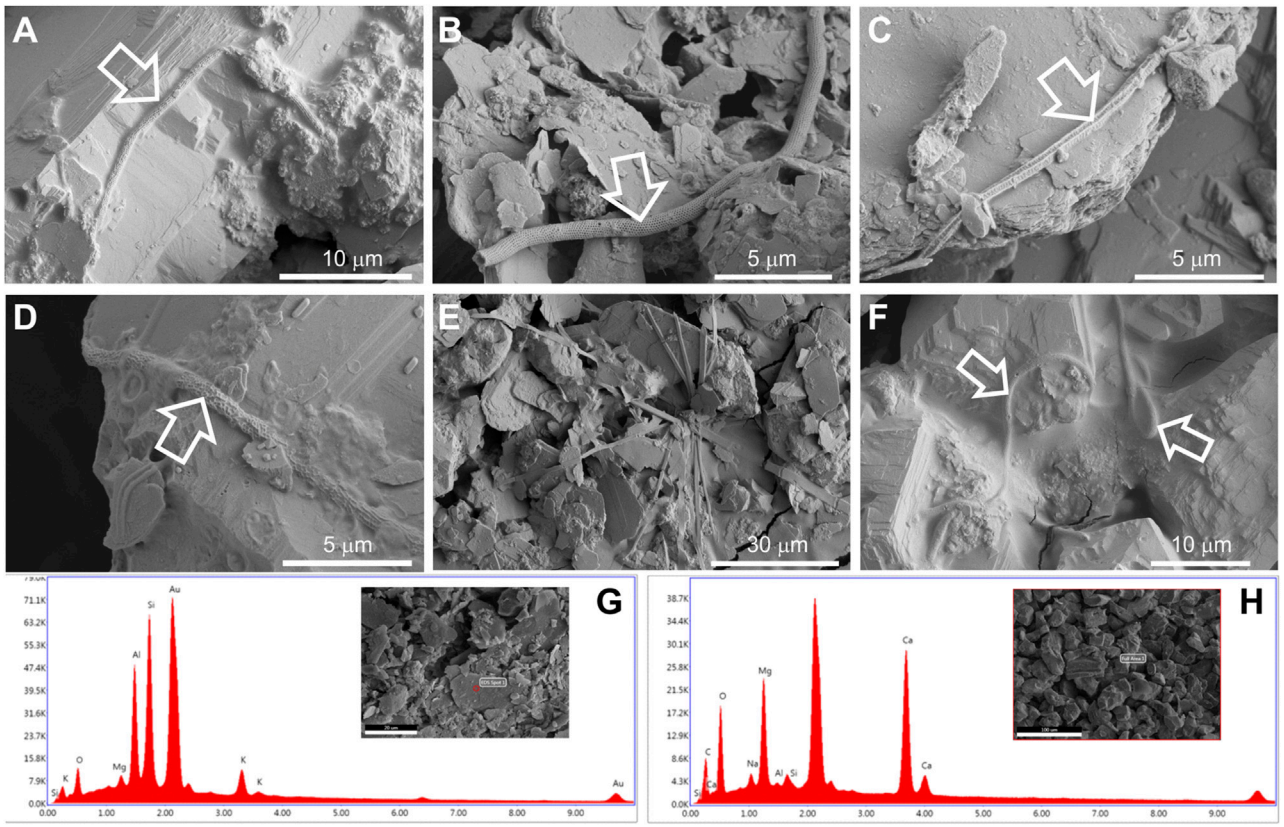

FIGURE 3 | FESEM images from samples M1 **(A)**, M3 **(B,C)**, M4 **(D)**, M5 **(E)**, and M6 **(F)** depicting microbial structures associated with vermiculations. FESEM with corresponding EDS spectra from sample M5 **(G)** denotes the presence of clay minerals, due to the abundance of Al and Si, and sample M6 **(H)**, rich in Ca and Mg, of dolomite.

Deposit of Sequences

Raw sequences were deposited in the NCBI SRA database under accession numbers ERS3506978-ERS3506982. Clone sequences (≈360 bp for *nifH* gene, 650 bp form archaeal *amoA* gene and 490 bp for bacterial *amoA* gene) were deposited at GenBank under the accession numbers LR596555-LR5965594, LR596553, and LR778119-LR778132.

RESULTS

Field Emission Scanning Electron Microscopy

The study of the samples by field emission scanning electron microscopy (FESEM) revealed the presence of filamentous microorganisms in the vermiculations of Morgana Cave (**Figure 3**). Most of the microbial features observed in samples M1, M3, M4, M5, and M6 resemble the enigmatic reticulated filaments reported in caves worldwide (Melim et al., 2008; Miller et al., 2012), which are long tubular filaments with peculiar surface ornamentation (Miller et al., 2012; Melim et al., 2015).

In general, these long filaments (<100 μm) were found embedded in a slimy matrix of extracellular polymeric substances (**Figures 3A,D,F**). These filaments depict mineralized empty sheaths (**Figure 3B**), which can be attributed to the lysis of the cells and disappearance of living microorganisms.

The reticulated quadrangular-shaped filament depicted in **Figure 3C** is another type of intriguing structure, which, to our knowledge, has not been observed in other caves. In addition, flat filaments were found, which are probably mineral based on their morphology (**Figure 3E**).

The analysis of all the samples with energy dispersive X-ray spectroscopy (EDS) revealed that the bulk samples M1, M2, M4, and M6 contain high amounts of Ca and Mg (**Supplementary Figure S1**), suggesting the presence of dolomite derived from the host rock of Morgana Cave. Samples M3 and M5 showed the presence of Al and Si, indicating clay minerals (**Supplementary Figure S1**), consistent with the morphology of the mineral grains. EDS microanalysis of the mineral grains from samples M5 (clay minerals) and M6 (dolomite) are depicted in **Figures 3G,H**.

Microbial Diversity

The amplicons for Illumina MiSeq analysis ranged from 839,691 to1,064,792 reads across the five vermiculation deposits, corresponding to 65,118–86,338 OTUs (**Table 1**).

Chao1, Shannon and Simpson indices were calculated to estimate alpha diversity (**Table 1**). Regardless of variation in

TABLE 1 | Estimation of alpha-diversity indices in vermiculation deposits from Morgana Cave.

Samples	Colors	Total reads	Total OTUs	Chao1	Shannon index	Simpson index
M2	Whitish	1,064,792	77,719	87,670.74	12.00	0.9912
M3	Greyish	839,691	65,118	74,441.90	12.38	0.9965
M4	Whitish	993,049	81,864	94,318.76	12.61	0.9968
M5	Brown	1,041,703	86,338	94,095.83	12.87	0.9968
M6	White	1,064,637	66,018	73,246.60	11.61	0.9934

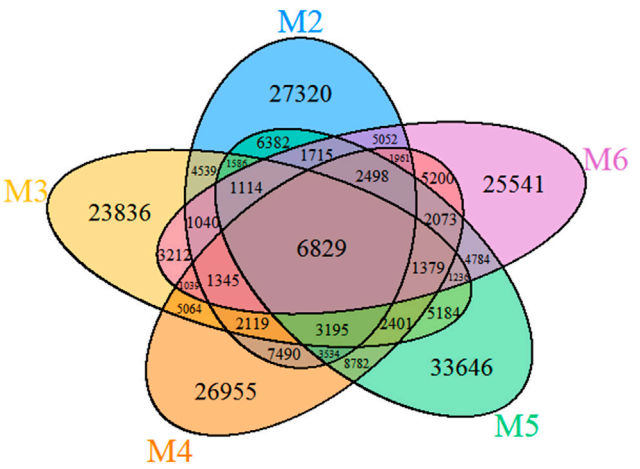

FIGURE 4 | Venn diagram of the five vermiculation deposits from Morgana Cave.

community composition, Shannon and Simpson indices were similar across samples. The species richness and evenness in M4 and M5 were higher than in M2, M3, and M6.

The VENN diagram of the OTUs distribution in the five vermiculations (**Figure 4**) revealed the presence of 137,298 OTUs that are unique to vermiculation deposits. Most of these unique taxa were found in sample M5 (33,646), followed by M3 (23,836) and M2 (27,320). The common microbial core comprised 6,829 distinct OTUs. The largest OTUs number (30,691) was shared between M4 and M5 with the highest bacterial diversity, whilst the lowest common prokaryotic OTUs were found between M2 and M3 (21,767) and M5 and M6 (21,628).

Table 2 shows that the microbial communities of the samples from Morgana Cave were almost totally composed of *Bacteria*, ranging from 99.33 (in M2) up to 99.79% (in M5). *Archaea* exhibited a low percentage ranging from 0.65 (in M2) to 0.19% (in M5). Unclassified members at domain level ranged from 0.05 to 0.02%. This distribution of taxa is similar to those reported by Itcus et al. (2018) from a perennial ice cave, where the range was 94.90–99.03% for *Bacteria* and 0–1.03% for *Archaea*.

Archaeal Phyla

Four *Archaea* phyla were found in the vermiculations of Morgana Cave, *Diapherotrites*, *Euryarchaeota*, *Nanoarchaeota* and *Thaumarchaeota* (**Figure 5**), although with very low relative

TABLE 2 | Domains distribution in vermiculation deposits from Morgana Cave.

Domains	M2 (%)	M3 (%)	M4 (%)	M5 (%)	M6 (%)
Archaea	0.65	0.33	0.48	0.19	0.31
Bacteria	99.33	99.64	99.48	99.79	99.66
Unclassified	0.03	0.03	0.05	0.02	0.03

abundances of OTUs. The class *Thermoplasmata* (*Euryarchaeota* phylum) ranged between 0.17 and 0.04%, *Woesearchaeia* (*Nanoarchaeota* phylum) between 0.37 and 0.08%, and *Nitrososphaeria* (*Thaumarchaeota* phylum) between 0.16 and 0.06%. The class *Thermoplasmata* was mainly present in M2, M3, and M6, and includes the order *Methanomassiliicoccales* with methanogenic archaea which accounted for 9.7% of all the *Archaea* present in the vermiculations. In addition, we observed an uncultured order of *Thermoplasmata* accounting for 17.3%.

The class *Woesearchaeia* was the most abundant (50%), considering all *Archaea* classes, particularly in M2 and M4. The class *Nitrososphaeria* was mainly present in M2, with the order *Nitrosopumilales*, accounting for 17.4% of all the *Archaea*. This last order includes *Nitrosopumilus maritimus*, an ammonia-oxidizing archaea (Pester et al., 2011).

Bacterial Phyla

Thirteen major phyla (>1% relative abundance) were found in the vermiculations from Morgana Cave, but predominant phyla were *Proteobacteria, Actinobacteria*, *Acidobacteria*, *Chloroflexi*, *Planctomycetes*, and *Bacteroidetes* (**Table 3**). Less abundant phyla were *Nitrospirae*, *Rokubacteria*, *Gemmatimonadetes*, *Latescibacteria*, *Patescibacteria*, *Verrucomicrobia*, and *Zixibacteria*. In addition to the 13 major phyla, another 35 phyla were retrieved with relative abundances <1%. They encompass *Armatimonadetes*, *Chlamydiae*, *Dependentiae*, GAL15, and *Omnitrophicaeota* with abundances between 0.8 and 0.5%; and *Cyanobacteria*, *Elusimicrobia* and WS2 with abundances of 0.1%. The rest of phyla: *Acetothermia*, *Atribacteria*, *Calditrichaeota*, *Coprothermobacteraeota*, *Dadabacteria*, *Entotheonellaeota*, *Epsilonbacteraeota*, *Fibrobacteres*, *Firmicutes*, *Hydrogenedentes*, *Kiritimatiellaeota*, *Lentisphaerae*, *Margulisbacteria*, *Nitrospinae*, *Poribacteria*, *Spirochaetes*, *Synergistetes*, *Tenericutes*, Anck6, BRC1, FBP, FCPU426, LCP-89, WPS-2, TA06, and PAUC34f were present in abundances below 0.1%.

Figure 6 displays the bacterial classes with a relative abundance >1% in at least one of the samples retrieved from Morgana Cave

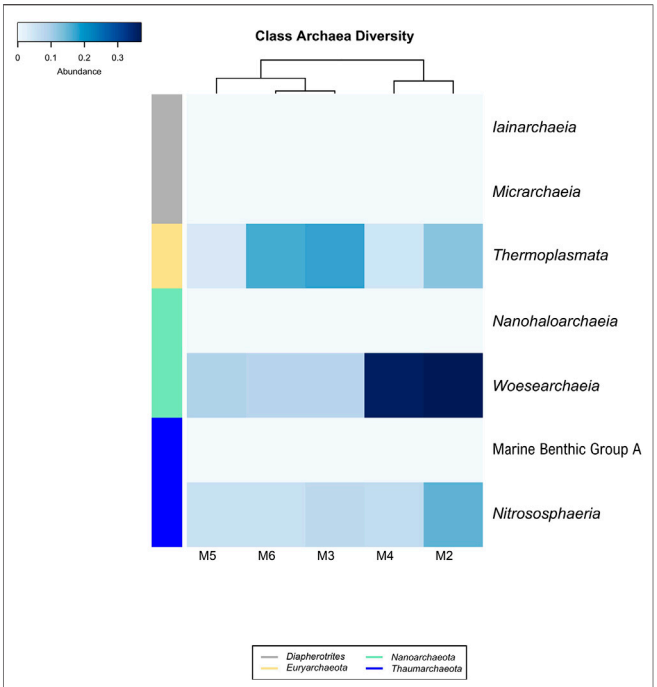

FIGURE 5 | Heat-map analysis of Morgana Cave archaeal community relative abundance at class level. The identified groups are presented in the right column and their phylum level indicated in left-colors column.

vermiculations. The most abundant classes were largely represented by *Gamma-* and *Betaproteobacteria*, followed by *Planctomycetacia*, *Acidimicrobiia*, *Rubrobacteria*, *Ignavibacteria*, NC10 from the phylum *Rokubacteria*, and *Blastocatellia*, with percentages above 5% in at least one of the vermiculations.

Gammaproteobacteria were represented by the orders *Methylococcales*, wb1-P19, and PLTA13 (**Figure 7**; **Table 4**; **Supplementary Table S1**). The most abundant uncultured lineage was wb1-P19, seconded by PLTA13. The third and least abundant order was represented by the methanotrophic *Methylococcales*.

The class *Betaproteobacteria* was composed of sequences of uncultured members of families from which only *Nitrosomonadaceae* and *Burkholderiaceae* were identified (**Figure 7**; **Table 4**; **Supplementary Table S1**).

In Morgana Cave *Planctomycetacia* members were affiliated with the family *Gemmataceae* and other uncultured families and genera, with relatively low relative abundances (**Supplementary Table S1**).

Actinobacteria were mainly composed by the classes *Acidimicrobiia* and *Rubrobacteria* (**Figure 6**). In the class *Acidimicrobiia* we observed sequences of the uncultured actinobacterium IMCC26256 (**Figure 7**), clearly separated from other *Acidimicrobiia* species (Hu et al., 2018). The class *Rubrobacteria* with the genus *Gaiella* is well represented in the different vermiculations (**Supplementary Table S1**).

Ignavibacteria is a recently established class of *Bacteroidetes* and was denoted by clone BVS26 in the vermiculations of Morgana Cave (mainly in M2 and M4).

TABLE 3 | Major bacterial phyla in vermiculation deposits from Morgana Cave[a].

Phylum	M2	M3	M4	M5	M6
Proteobacteria	46.06	39.16	38.48	43.21	36.49
Actinobacteria	8.77	10.15	11.24	4.34	11.37
Acidobacteria	6.84	10.44	6.64	11.07	8.98
Chloroflexi	6.11	9.44	9.57	6.95	10.11
Planctomycetes	6.42	6.53	7.89	8.63	9.18
Bacteroidetes	8.19	3.31	9.23	9.43	6.21
Nitrospirae	4.07	4.68	2.56	3.25	2.82
Rokubacteria	2.27	5.08	2.58	1.95	3.29
Gemmatimonadetes	1.72	3.61	2.16	2.42	1.87
Latescibacteria	1.97	2.51	1.97	1.41	1.38
Patescibacteria	2.14	0.93	1.39	1.24	1.69
Verrucomicrobia	0.95	0.82	0.99	2.05	1.61
Zixibacteria	1.04	0.63	1.37	1.41	0.40

[a]*Relative abundance >1% in at least one of the samples.*

The class NC10 of the *Rokubacteria* phylum was most abundant in M3 (**Figure 6**), with a slightly higher relative abundance of the order MIZ17 over *Rokubacteriales*, whereas in other vermiculations (M2, M4, M5, and M6) *Rokubacteriales* dominated over MIZ17 (**Supplementary Table S1**).

Of the 26 existing subdivisions in the phylum *Acidobacteria* only five were found in Morgana Cave (**Figure 6**): *Acidobacteriia*, *Blastocatellia*, *Holophagae* and subdivisions 17 and 6. Within the *Blastocatellales* the families *Blastocatellaceae* and *Pyrinomonadaceae* contained the uncultured genera JGI and RB41, respectively (**Supplementary Table S1**). In general, the relative abundances of the different subdivisions were low, and in most cases rarely exceeded 1%.

Regarding the distribution in classes in the different vermiculations (**Figure 6**; **Supplementary Table S1**) vermiculation M2 presented the highest relative abundances in *Beta-* and *Gammaproteobacteria*. M3 showed a high diversity with the majority of relative abundances in 12 different classes, corresponding to eight phyla. In this vermiculation, *Beta-* and *Gammaproteobacteria* were also highly significant.

Vermiculation M4 revealed high relative abundances with respect to other vermiculations only in two classes of *Chloroflexi* and one of *Bacteroidetes*. M5 showed high relative abundances in 2 classes of *Bacteroidetes*, and one each of *Acidobacteria, Planctomycetes, Zixibacteria* and *Verrucomicrobia*. M6 presented high relative abundances in two classes of *Chloroflexi*, and one of *Planctomycetes* and *Actinobacteria*.

Functional Genes

To determine the involvement of the vermiculation communities in the nitrogen cycle, we surveyed the presence of functional genes involved in nitrogen fixation (*nifH*) and ammonia oxidation to nitrite (*amoA*). We observed *nifH* presence in the vermiculations M1, M2, M5, and M6. The phylogenetic analysis placed the sequences among nitrogen-fixing species (**Supplementary Figure S2**).

In addition, we detected the presence of functional genes involved in ammonia oxidation (*amoA*) in M1, M2, and M6 corresponding to *Archaea*. Regarding the bacteria, we identified genes related to *Nitrosospira* in M2 and M3. Phylogenetic

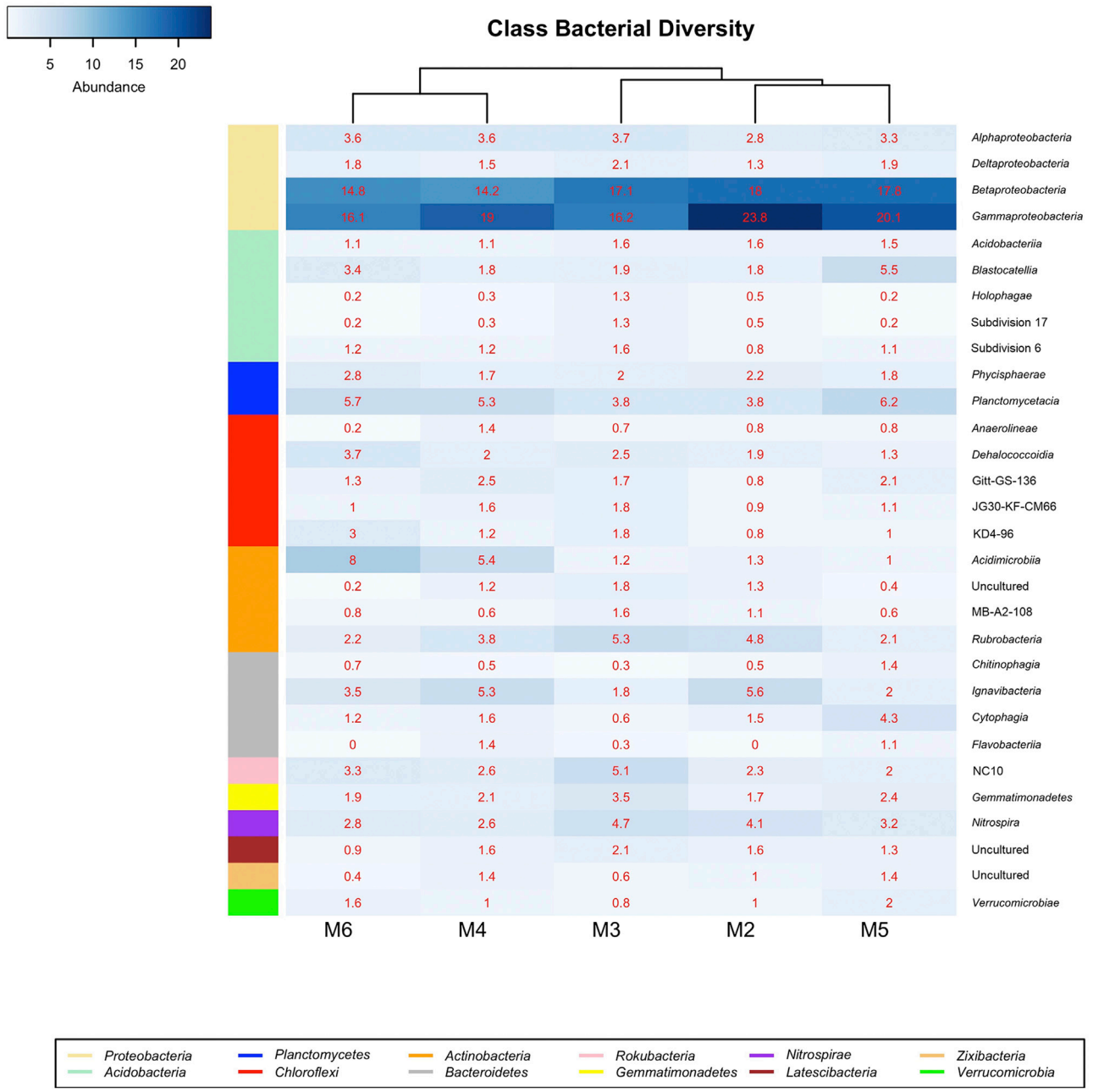

FIGURE 6 | Heat-map analysis of Morgana Cave bacterial community relative abundance at class level. The identified groups are presented in the right column and their phylum level indicated in left-colors column.

analyses (**Supplementary Figure S3A**) indicated that the closest relatives of bacterial *amoA* gene sequences was the genus *Nitrosospira*, while the genus *Nitrosopumilus* was the closest to archaeal sequences (**Supplementary Figure S3B**).

DISCUSSION

Microbial communities typically show a few dominant phyla and simultaneously a high number of phyla with a quite low abundance, in most cases <0.1%. Sogin et al. (2006) referred to this as the "rare biosphere", microorganisms that cannot be identified without deep-sequencing NGS approaches. Only one third of the 35 less abundant phyla retrieved from the vermiculations of Morgana Cave have been also found in other caves (Ortiz et al., 2013; De Mandal et al., 2016; Hershey and Barton, 2018). For Pascoal et al. (2020) the rare biosphere constitutes an important "genomic reservoir" or "pool of diversity" and likely plays fundamental roles in ecosystem functioning.

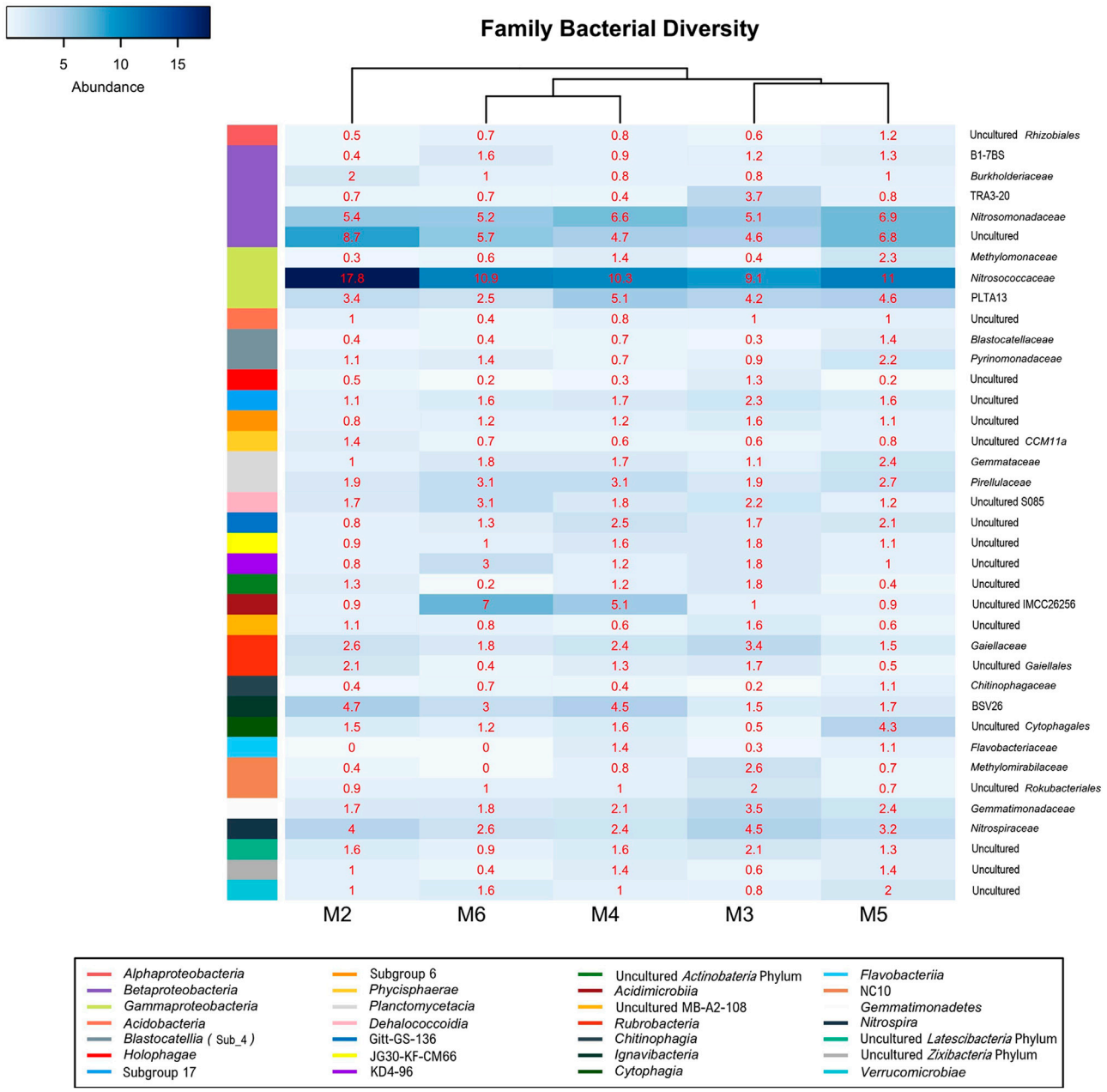

FIGURE 7 | Heat-map analysis of Morgana Cave bacterial community relative abundance at family level. The identified groups are presented in the right column and their class level indicated in left-colors column.

Vermiculations form an ecological niche suitable for microorganisms due to the presence of different mineral particles and water retention. Samples from vermiculations M3 and M5 were mainly composed of clay minerals (**Figure 3**; **Supplementary Figure S1**), and M5 showed greater diversity than dolomite-rich vermiculations. Organic compounds and bacteria are generally adsorbed onto clay minerals (Bingham and Cotrufo, 2015; Cuadros, 2017), which might explain the abundance of taxa in the clay-containing vermiculations with respect to dolomite-rich vermiculations. In both types of vermiculations, EPS and reticulated filaments were evident. These enigmatic filaments have been found in microbial mats from caves worldwide, such as limestone caves and basaltic lava tubes (Melim et al., 2008; Jones, 2009, 2010, 2011; Miller et al., 2014; Riquelme et al., 2015a), as well as in a granite spring water tunnel in Portugal (Miller et al., 2012). They were characterized as long microbial filaments with hexagonal and diamond-shaped chambers resembling honeycombed structures, but attempts to decipher their taxonomic affiliation have failed thus far.

TABLE 4 | Taxonomic affiliation of the sequences of *Betaproteobacteria* and *Gammaproteobacteria*, based on 16S rRNA amplicon sequence reads.

Class *Betaproteobacteria*

Order	Family	Genus	Relevant BLAST hits	Accession number	Identity (%)
B1-7BS	Uncultured	Uncultured	Uncultured bacterium from lava cave in La Palma, Canary Islands, Spain	LR130620	98.71
			Denitratisoma oestradiolicum	KF810120	94.86
			Azoarcus olearius	LT853755	93.98
Burkholderiales	*Burkholderiaceae*	Uncultured	Uncultured bacterium from lava cave in Terceira Island, Azores, Portugal	JF266494	99.14
			Piscinibacter aquaticus	LC430085	93.62
			Piscinibacterium candidicorallinum	MN598642	93.15
			Methylibium sp.	LC040878	93.36
			Rhizobacter sp.	KC248052	92.72
TRA3-20	Uncultured	Uncultured	Uncultured bacterium from subsurface sediment in Richland, WA, USA	HM186413	98.92
			Uncultured bacterium from Alpine cave in Austria	KF964441	98.28
			Nitrosovibrio tenuis	FR828474	92.72
Nitrosomonadales	*Nitrosomonadaceae*	IS-44	Uncultured bacterium from lava cave in Terceira Island, Azores, Portugal	JN672428	99.14
			Nitrosospira lacus	CP021106	94.62
	Nitrosomonadaceae	MND1	Uncultured bacterium from lava cave in Terceira Island, Azores, Portugal	JF265837	97.20
			Thiobacter subterraneus	NR024834	92.04
			Cupriavidus sp.	MK509787	91.83
Uncultured	Uncultured	Uncultured	Uncultured bacterium from lava cave in La Palma, Canary Islands, Spain	LR130616	99.35
			Nitrosospira sp.	EF015571	93.12

Class *Gammaproteobacteria*

Order	Family	Genus	Relevant BLAST hits	Accession number	Identity (%)
Methylococcales	*Methylococcaceae*	IheB2-23	Uncultured bacterium from lava cave Terceira Island, Azores, Portugal	JN850279	98.71
			Methylococcus mobilis	NR_104922	92.04
			Methylosarcina fibrata	NR_025039	91.83
wb1-P19	Uncultured	Uncultured	Uncultured bacterium from lava cave in La Palma, Canary Islands, Spain	LR130706	99.35
			Thioprofundum hispidum	NR_112620	94.62
PLTA13	Uncultured	Uncultured	Uncultured bacterium from lava cave in Terceira Island, Azores, Portugal	JN850147	99.35
			Halochromatium sp.	FN293083	89.25
			Lamprobacter modestohalophilus	EF153292	89.03
			Thiocapsa sp.	FN293065	88.82
			Steroidobacter sp.	KF595153	88.39

Identities were based on nucleotide sequence similarities with their closest relatives in NCBI databases using BLAST hits.

Melim et al. (2008) reported long reticulated filaments (up to 75 μm long and 0.5 μm in diameter) in calcite speleothems from limestone caves in New Mexico, and in lava tubes from Cape Verde Islands. (Jones 2009, 2010, 2011) described the occurrence of reticulated filaments in caves from the British West Indies, and suggested they are calcified filaments. Contrasting with those filaments described by Melim et al. (2008) and (Jones 2009, 2010), rich in carbon and calcium, respectively, Miller et al. (2012) found reticulated filaments rich in Mn oxides. These filaments were composed of an inner cellular structure coated by an exterior sheath of manganese oxides (Miller et al., 2012). Melim et al. (2015) reported living reticulated filaments associated with clay minerals in a limestone cave in Germany. They were rich in carbon, without mineralized sheaths. Most of these filaments were coated with clays, obscuring wall ornamentation, as also observed in samples from Morgana Cave. In fact, this association with clays could explain their presence in the vermiculations M3 and M5. Shedding light on the origin and nature of these intricate reticulated filaments is a still a challenge for geomicrobiologists.

Archaea are ubiquitous in terrestrial and marine ecosystems (Eme et al., 2017), but the richness of this domain in the vermiculations of Morgana Cave was scarce. Tebo et al. (2015) did not find any archaeal rRNA gene sequences in the volcanic ice caves of Mt. Erebus, Antarctica. Itcus et al. (2018) reported the lack of *Archaea* in surface ice blocks from a perennial ice cave and negligible percentages in ice cores. In addition, Icelandic and Antarctic lakes were dominated by *Bacteria* with no detectable or few archaeal members (Achberger et al., 2017).

In Morgana Cave a few groups of microorganisms could be involved in the nitrogen cycle. Ward et al. (2019) recognized four clades of ammonia oxidizers, which included members of the *Thaumarchaeota* (*Archaea*), the *Nitrococcaceae* family (*Gammaproteobacteria*), the *Nitrosomonadaceae* family (*Betaproteobacteria*) and some members of *Nitrospirae*.

The order *Nitrosopumilales* (*Thaumarchaeota*) contains the families *Nitrosopumilaceae* and *Candidatus* Nitrosotenuaceae, which includes *Nitrosopumilus maritimus* and *Candidatus* Nitrosotenuis cloacae, respectively (Qin et al., 2017). Ammonia-oxidizing archaea were detected in the vermiculations through the identification of the gene encoding monooxygenae subunit A (*amoA*), however the relative abundance is very low as shown in **Table 2**. Among the bacteria, *amoA* genes related to *Nitrosospira* (*Betaproteobacteria*) were also found.

The high proportion of bacteria over archaea found in the vermiculations is consistent with previous reports indicating that in terrestrial ecosystems nitrate stimulates the activity of ammonia-oxidizing bacteria, but not that of archaea (Meinhardt et al., 2018). In addition, Zhang et al. (2019a) reported that bacterial *amoA* gene abundance was significantly higher than that of archaea due to the activity of cold adapted *Nitrosospira* in rivers from the Qinghai-Tibet Plateau. In this context, Zhang et al. (2019b) showed that soil microbial communities were adapted to high nitrogen levels, strengthening the function of ammonia oxidation in order to deplete the excess of nitrogen.

Among *Bacteria*, the phylum *Proteobacteria* and the classes *Gammaproteobacteria* and *Betaproteobacteria* were the majority in the vermiculations, with percentages in all the samples exceeding 14%.

The gammaproteobacterial order wb1-P19 was the most abundant group in the vermiculations. Holmes et al. (2001) proposed that wb1-P19 clustered phylogenetically with sulfur or nitrite-oxidizing autotrophic bacteria. Unfortunately, records on this lineage were very scarce, with only three references in the literature (Holmes et al., 2001; Schabereiter-Gurtner et al., 2002; Zhu et al., 2019). These three papers reported this order in caves. Remarkably, Zhu et al. (2019) found that in Chinese caves, in addition to wb1-P19, uncultured *Rokubacteriales* and *Gaiellales* were also present, similar to our results in the vermiculations.

Table 4 shows the taxonomic affiliation of the representative sequences of OTUs classified as *Gammaproteobacteria*. In this case, the closest related sequences corresponded to uncultured bacteria from volcanic caves in the Terceira and La Palma islands, located in the Macaronesia region (Riquelme et al., 2015b; Gonzalez-Pimentel et al., 2018). This is striking due to the different environmental and climate (subtropical) conditions of the region and the mineral composition of the volcanic rocks (basalts) (Morgana is an Alpine cave developed on dolomitic marble).

Unfortunately, little information on metabolic traits has been reported for these uncultured volcanic cave bacteria. Gonzalez-Pimentel et al. (2018) stated that sulfur and nitrogen were associated with the chemical composition of basaltic rocks in lava tubes, and sulfur and nitrate oxidizers or reducers, such as bacteria from the *Proteobacteria* phylum, were very abundant in La Palma cave. Also, this phylum has similar abundances in Terceira cave (Riquelme et al., 2015b). Interestingly, Hathaway et al. (2014a) studied the diversity of ammonia oxidation (*amoA*) and nitrogen fixation (*nifH*) genes in lava caves from the Azores. They found that *Nitrosospira*-like sequences dominated the ammonia-oxidizing bacteria community, and the nitrogen fixation community was dominated by *Klebsiella pneumoniae*-like sequences. Note that *Nitrosospira* sequences were also present in vermiculations from Morgana Cave.

Apart from the close relationship between analyzed representative sequences and uncultured bacteria from the lava caves, secondary affiliations are indicated in **Table 4**. Some sequences from Morgana Cave were closely related to the gammaproteobacterial genera *Methylococcus*, *Methylosarcina*, *Thioprofundum*, *Halochromatium*, *Lamprobacter*, *Thiocapsa*, and *Steroidobacter*, with identity percentages ranging between 88.39 and 94.62%. According to Yarza et al. (2014), who established taxonomic boundaries for higher taxonomic levels for taxa of bacteria, the Morgana Cave uncultured bacterium close to *Methylococcus* and *Methylosarcina* must be included in the family *Methylococcaceae*. This family comprises methane-oxidizing bacteria that carry out the first step of nitrification, the oxidation of ammonia to nitrite, through the intermediate hydroxylamine (Hazeu et al., 1980; Wise et al., 2001; Sutka et al., 2003; Poret-Peterson et al., 2008).

The uncultured bacterium close to *Thioprofundum* must be placed within this genus. *Thioprofundum hispidum* is an

obligately chemolithoautotrophic sulfur-oxidizing bacterium that bases its metabolism on sulfur oxidation and carbon dioxide fixation (Mori and Suzuki, 2014).

The uncultured bacteria related to *Halochromatium, Lamprobacter*, and *Thiocapsa* should be included in the *Chromatiaceae*, a family of phototrophic purple sulfur bacteria growing under anoxic conditions using sulfide as photosynthetic electron donor, which is oxidized to sulfate via intermediate accumulation of globules of elemental sulfur (Imhoff, 2014).

The uncultured bacterium related to *Steroidobacter*, a genus classified under *incertae sedis*, is close to the family *Solimonadaceae*. *Steroidobacter* anaerobically metabolizes steroids with nitrate reduction to dinitrogen monoxide, and further to dinitrogen (Fahrbach et al., 2008) A *Steroidobacter* OTU was also found in Californian lava caves (Lavoie et al., 2017).

The class *Betaproteobacteria* was placed with lower relative abundance, represented by *Nitrosomonadales* and some uncultured members. The order *Nitrosomonadales* is composed of the genera IS-44 and MND1 of the family *Nitrosomonadaceae*. All the cultivated representatives of this family are lithoautotrophic ammonia oxidizers (Prosser et al., 2014). IS-44 is rarely cited in the literature and, among the scarce reports, was found to be a member of the microbial community of composts (Neher et al., 2013). MND1 was found in ferromanganese nodules, soils and caves and may be diverse in functions in a wide range of environmental conditions (Jones et al., 2008; Spain et al., 2009).

Table 4 shows the complete taxonomic affiliation of the representative sequences of OTUs classified as *Betaproteobacteria*. In this class, also OTUs from Morgana Cave were closely related (97–99%) with uncultured bacteria from the volcanic caves. In addition, OTUs affiliated to the order TRA3-20 were closely related to uncultured bacteria from a United States subsurface basaltic site (Lin et al., 2012) and from an Alpine cave in Austria (Reitschuler et al., 2015). However, other more distant affiliations, within the family *Nitrosomonadaceae*, were *Nitrosospira lacus*, a psychrotolerant ammonia-oxidizing bacterium (Urakawa et al., 2015). The finding of bacterial ammonia oxidizer communities at elevated altitude on Mt. Everest suggests that this group is sufficiently adapted to survive in Alpine areas (Zhang et al., 2009). *Nitrosospira* sp. and *Nitrosovibrio tenuis* are also ammonia-oxidizing bacteria (Prosser et al., 2014).

Other uncultured bacteria included in the betaproteobacterial order B1-7BS are related to the denitrifying *Denitratisoma oestradiolicum* (Fahrbach et al., 2008) and the nitrogen-fixing *Azoarcus olearius* (Chen et al., 2013).

An uncultured bacterium within the family *Burkholderiaceae* is related to sequences of *Piscinibacter aquaticus*, *Piscinibacterium candidicorallinum*, *Rhizobacter* sp. and *Methylibium* sp., genera of uncertain position placed as unclassified *Burkholderiales*. Most strains from these genera are able to perform nitrate reduction (Sheu et al., 2016).

Within the genus MND1, family *Nitrosomonadaceae*, an uncultured bacterium closely related to another from Terceira lava cave, and more distant from *Thiobacter subterraneus*, a thermophilic, sulfur-oxidizing bacterium (Hirayama et al., 2005) and *Cupriavidus* sp., a genus including nitrate reducing strains (Vandamme and Coenye, 2004) was included.

Therefore, the scope of the metabolic diversity within the two main *Proteobacteria* classes, *Gamma-* and *Betaproteobacteria*, in the Morgana Cave vermiculations remains largely unknown, although there is great evidence of possible participations in the carbon, nitrogen and sulfur cycles.

In a lower level of abundance, two orders were found in the vermiculations: the actinobacterial *Gaiellales*, and *Nitrospirales*. *Gaiellales* comprises the genus *Gaiella* with only one known species: *G. occulta*, isolated from a deep aquifer with poorly mineralized waters. Distinctive characteristics are the presence of internally branched iso-fatty acids found in no other bacterium and the utilization of organic compounds (Albuquerque et al., 2011). The genome was studied by Severino et al. (2019) identifying genes of nitrate reduction. This genus was also found in volcanic caves (Riquelme et al., 2015a; Gonzalez-Pimentel et al., 2018).

The genus *Nitrospira* comprises ammonia-oxidizing bacteria which are relatively common in caves (Saiz-Jimenez, 2015). Its metabolic versatility, including the participation in different nitrogen cycling processes, is a key factor for the ubiquity and the high diversity of *Nitrospira* in caves (Tomczyk-Żak and Zielenkiewicz, 2016). *Nitrospira* was previously found in volcanic caves from the Azores, New Mexico, Hawai'i, and California (Northup et al., 2011; Riquelme et al., 2015b; Lavoie et al., 2017).

The phyla *Rokubacteria*, *Gemmatimonadetes*, *Latescibacteria*, *Patescibacteria*, *Verrucomicrobia*, and *Zixibacteria* had the lowest abundances in the vermiculations. They are commonly represented by uncultured bacteria that can only be identified in deep-sequencing NGS (Sogin et al., 2006). Most of these phyla are part of a rare cave biosphere formed by uncultured bacteria present in low numbers (Hershey and Barton, 2018).

Nitrogen fixation (*nifH*) genes have been found in Azorean and Brazilian caves (Hathaway et al., 2014a; Marques et al., 2018), suggesting this metabolic trait is widespread in the subsurface environment. Nearly all known diazotrophs contain a minimum of six conserved genes: *nifH*, *nifD*, *nifK*, *nifE*, *nifN*, and *nifB*, but for practical reasons in environmental studies only the *nifH* gene is commonly used as an indicator of nitrogen fixation activity. Although Dos Santos et al. (2012) stated that false positives can be obtained if only *nifH* is used, the data here reported and the phylogenetic tree of **Supplementary Figure S2** place the sequences retrieved from the vermiculations among well-known nitrogen-fixing species, thus suggesting that potential nitrogen-fixing bacteria are present in the cave.

In addition, **Table 4** shows that some sequences from the vermiculations were related to the betaproteobacterial nitrogen-fixing *Azoarcus,* and the gammaproteobacterial *Thiocapsa*. Furthermore, the sequence similarities of *nifH* genes with the genera *Thiocystis*, *Chlorobium*, and *Aquaspirillum* support the belief that uncultured bacteria have metabolic traits related to nitrogen-fixation in the vermiculations. Uncultured members of the *Rhizobiales*, *Bulkholderiales*, *Methylococcales*, *Dehalococcoidia*, and *Euryarchaeota* were also observed in the

vermiculations and many species of these groups were reported as diazotrophs by Dos Santos et al. (2012).

In Alpine caves it is important to investigate how microbes acquire energy and obtain organic carbon. In this context, one of the major impacts on oligotrophic caves is organic carbon, which enriches the ecosystem, brought into the cave from outside.

Atmospheric transport and deposition of carbon and nitrogen is an important dispersal process on the earth's surface. Several papers have reported the presence of organic carbon in the ice and snow of the Alps (Gröllert et al., 1997; Legrand et al., 2007; Preunkert and Legrand, 2013). This organic carbon derives from anthropogenic and biogenic sources, and is mainly composed of mono- and dicarboxylic acids, aliphatic alcohols, monoterpenes, phenols and humic-like substances (Guilhermet et al., 2013; Legrand et al., 2013; Müller-Tautges et al., 2016; Materic et al., 2019). These compounds constitute suitable carbon sources for microorganisms.

In addition, the Alpine region is characterized by nitrogen deposition with a rate of 10.5 kg ha^{-1} yr^{-1} at elevations around 1,200 m a.s.l. (Balestrini et al., 2013), and 0.5–3 kg N ha^{-1} yr^{-1} at elevations above 2,000 m a.s.l. (Filippa et al., 2010). Colombo et al. (2019) studied the nitrogen forms in meltwater samples collected in the period 2012–2015 from the Indren Glacier (ca. 4,000 m a.s.l., Mt. Rosa, NW Italian Alps), 150 km west of *Val di Scerscen*. Among the nitrogen forms, they found abundant NO_3^-, NH_4^+, and organic nitrogen. Similar results for nitrogen and sulfur deposition in the Alps were reported by Rogora et al. (2006), Balestrini et al. (2013), and Muri (2013).

The presence of organic carbon, nitrogen and sulfur in the Alps suggests that its content in the meltwaters from the glacier *Vedretto di Scerscen* has likely enhanced the activity of cave microorganisms involved in the geochemical cycles, and particularly of the most copiotrophic groups, such as *Betaproteobacteria* and *Gammaproteobacteria* involved in the nitrogen cycle (**Figure 6**; **Table 4**).

Chemolithoautotrophic bacteria provide a way to evaluate whether microbes are capable of producing their own energy and organic carbon to sustain an ecosystem. A possible metabolic pathway in vermiculations, in addition to nitrogen and sulfur, is methanotrophy. This is supported by the presence of the *Rokubacteria* class NC10, able of anaerobic oxidation of methane coupled to denitrification, as well as members of the *Methanomassiliicoccales* order which includes methanogenic archaea (Borrel et al., 2014). Uncultured members of the *Methylococcales* were present in the vermiculations suggesting that gammaproteobacterial methanotrophs may occur in this cave. *Rokubacteria* abundance ranged from 2 to 5%, *Methylococcales* from 0.3 to 2.3%, while *Methanomassiliicoccales* abundance was lower than 0.1% in all the vermiculations. These data indicate that bacteria metabolizing organic matter brought into the cave from external sources probably contribute more to the ecosystem than methanotrophic bacteria.

On the other hand, Alpine ecosystems are covered by snow and ice for most of the year, and ice and glacier caves are characterized by low temperatures below 0°C and inhabited by extremophiles. In these ecosystems, cave microorganisms have to cope with severe environmental constraints.

Bowman (2017) studied the genomes of 257 bacterial and archaeal genera related to cold ecosystems, from which 59 genera could be considered highly cold adapted and 137 genera included psychrotolerant species. From the list only *Flavobacterium* was present in the vermiculations analyzed in this work. Members of the *Flavobacteria* group colonized cold springs in the Qinghai-Tibetan Plateau (Li et al., 2012) and represented 12% of the isolates from high-altitude ice cores in the Tibetan Plateau (Liu et al., 2019).

Flavobacterium, *Cytophaga* species and *Ignavibacteria* contain antifreeze DUF3494-type proteins, which are present only in cold-adapted taxa (Bowman, 2017). The finding in the vermiculations of uncultured members of the classes *Cytophagia* and *Ignavibacteria*, in addition to the genus *Terrimonas*, from which novel species were isolated from Arctic environments (Kim et al., 2017), suggests that psychrophilic bacteria may be present in the vermiculations. Psychrophilic ammonia-oxidizing bacteria were also reported in cold environments (Zhang et al., 2009; Urakawa et al., 2015).

In spite of the extensive investigations on the microbiology of several glacial environments, very little is known on the diversity, activity and environmental role of microorganisms colonizing Alpine caves. In previous studies of ice caves, the presence of unclassified bacteria was common (Itcus et al., 2018; Purcarea, 2018). This also occurs in the vermiculations of Morgana Cave, where most of the retrieved phyla contain a large number of uncultured representatives, with unknown metabolic traits. As a matter of fact, many taxa common in subsurface soils are represented by high proportions of novel and undescribed microbial lineages, less amenable to currently known cultivation techniques (Brewer et al., 2019).

It is noteworthy that some of the *Beta-* and *Gammaproteobacteria* OTUs from the Alpine Morgana Cave (**Table 4**) were closely related to sequences from two subtropical volcanic caves in the Macaronesia region (Azores and Canary islands). Hathaway et al. (2014b) suggested that the distribution of lava cave organisms is not cosmopolitan, as they found substantial differences in the microbial diversity of lava caves from the Azores and Hawai'i. In fact, at the OTU level, there was only 5% overlap between the two archipelagoes. Nevertheless, the similarities of OTUs between our high Alpine and two subtropical volcanic caves are remarkable. Porca et al. (2012) studied microbial communities from geographically distinct limestone caves and reported the existence of a common core of microorganisms that were morphologically similar and related in phylogeny. These authors suggested that, in nutrient-limited environments, in order to efficiently exploit nutrients, cave microorganisms could develop complex cooperative and mutualistic associations which could explain the broad distribution of bacterial phyla in caves.

Conversely, it was clear that the comparison of the microbial communities from Morgana Cave vermiculations with those of the Frasassi and Fetida sulfuric acid caves revealed striking differences, due to the extremely different environments (alkaline in Morgana and highly acid in sulfuric caves). In fact, Fetida Cave vermiculations showed high abundance of unclassified *Betaproteobacteria* and sulfur-oxidizing *Hydrogenophilales* (including *Sulfuriferula*), *Acidiferrobacterales* (including *Sulfurifustis*), sulfur-reducing *Desulfurellales*, and ammonia-oxidizing *Planctomycetes* and *Nitrospirae* (D'Angeli et al., 2019b).

The Frasassi Cave vermiculation community was diverse, including as major lineages *Betaproteobacteria* (composed of

unclassified bacteria, some related to sulfur-oxidizing bacteria), *Gammaproteobacteria* (composed of relatives of *Piscirickettsiaceae*, *Nevskiaceae*, *Acidothiobacillaceae*, and unclassified bacteria), *Acidobacteria*, *Nitrospirae*, and *Planctomycetes* (Jones et al., 2008). The data from Frasassi and Fetida sulfuric acid caves suggests that pH and sulfur are important drivers in the composition of their vermiculation microbial communities. On the contrary, vermiculations from the carbonate Morgana Cave have different communities, indicating that the microbial composition of vermiculations largely depends on environmental conditions and other factors. To summarize, the microbial groups identified in the vermiculations of this Alpine cave differed significantly from those retrieved from sulfuric acid caves, suggesting that mineral composition and pH play a major role in the colonization and establishment of communities.

This study provides new insights into vermiculation microbial communities from Morgana Cave which are composed of cosmopolitan bacteria in addition to a few niche-specific members. It is remarkable that this Alpine cave, supposed to be oligotrophic in nature due to the altitude and its remoteness, revealed that the 2 major bacterial classes *Gammaproteobacteria* and *Betaproteobacteria*, are composed of copiotrophic members whose metabolic traits are mainly associated with the nitrogen cycle. Evidences of the presence of methane- and sulfur-oxidizing bacteria are also found. This highlights the importance of atmospheric transport and deposition of anthropogenic pollutants which enhance the colonization and activity of microorganisms in pristine environments.

CONCLUSION

The microbial communities from Morgana Cave vermiculations were composed of different major evolutionary lineages. The vermiculations were dominated by the phyla *Proteobacteria*, *Actinobacteria*, *Acidobacteria*, *Chloroflexi*, *Planctomycetes*, and *Bacteroidetes*. The most abundant classes were *Gamma-* and *Betaproteobacteria*, followed by *Planctomycetacia*, *Acidimicrobiia*, *Rubrobacteria*, *Ignavibacteria*, NC10 from the phylum *Rokubacteria*, and *Blastocatellia*. The microorganisms linked to the nitrogen cycle are noteworthy, and their abundance must be related to atmospheric deposition of different forms of nitrogen coming from glacier meltwaters and rain/snow melt infiltrating into the cave. In addition, psychrophilic and methanotrophic bacterial groups were identified. The high number of phyla and candidate phyla (48) found in this oligotrophic high mountain cave is remarkable. The high percentage of uncultured bacteria present in the vermiculations, particularly at the lowest taxonomic ranks (only four genera were identified) indicates that the microbial diversity of Alpine caves deserves further research.

DATA AVAILABILITY STATEMENT

The datasets presented in this study can be found in online repositories. The names of the repository/repositories and accession number(s) can be found in the article/**Supplementary Material**.

ETHICS STATEMENT

Written informed consent was obtained from the individual(s) for the publication of any potentially identifiable images or data included in this article.

AUTHOR CONTRIBUTIONS

VJ performed the molecular biology, VJ, BH, and JG-P contributed to bioinformatics and statistical data analyses and AM to FESEM. ID'A and PT participated to cave sampling and described the sampling locations and the caves. JDW and CS-J led the research. JDW participated in discussions and corrected the manuscript. CS-J wrote the manuscript. All of the authors reviewed the manuscript and approved the final version.

FUNDING

Funding was provided by the Spanish project MINECO CGL2016-75590-P with ERDF funds. The Rotary Club in Sondrio (Italy) also provided funds for sample analysis thanks to C. Mazza, M. Boccardi, and P. Nana, with the Municipality of Lanzada (S. Bardea) and the Istituto Mineralogico Valtellinese (I. Foianini) supporting the cave research project.

ACKNOWLEDGMENTS

We acknowledge support of the publication fee by the CSIC Open Access Publication Support Initiative through its Unit of Information Resources for Research (URICI). Thanks to Mauro Inglese and Angelo Granati for the pictures in **Figures 1**, **2**. We gratefully acknowledge the valuable comments of Cristina Purcarea and Diana E. Northup that helped to improve the initial submission of the manuscript.

SUPPLEMENTARY MATERIAL

The Supplementary Material for this article can be found online at: https://www.frontiersin.org/articles/10.3389/feart.2020.586248/full#supplementary-material.

REFERENCES

Achberger, A. M., Michaud, A. B., Vick-Majors, T. J., Christner, B. C., Skidmore, M. L., Priscu, J. C., et al. (2017). "Microbiology of subglacial environments," in *Psychrophiles: from biodiversity to biotechnology*. Editor R. Margesin (Cham: Springer Nature Switzerland), 83–110.

Addesso, R., Gonzalez-Pimentel, J. L., D'Angeli, I. M., De Waele, J., Saiz-Jimenez, C., Jurado, V., et al. (2020). Microbial community characterizing vermiculations from karst caves and its role in their formation. *Microb. Ecol.* 2020. doi:10.1007/s00248-020-01623-5

Albuquerque, L., França, L., Rainey, F. A., Schumann, P., Nobre, M. F., and Da Costa, M. S. (2011). *Gaiella occulta* gen. nov., sp. nov., a novel representative of a deep branching phylogenetic lineage within the class *Actinobacteria* and proposal of *Gaiellaceae* fam. nov. and *Gaiellales* ord. nov. *Syst. Appl. Microbiol.* 34, 595–599. doi:10.1016/j.syapm.2011.07.001

Balestrini, R., Arese, C., Freppaz, M., and Buffagni, A. (2013). Catchment features controlling nitrogen dynamics in running waters above the tree line (central Italian Alps). *Hydrol. Earth Syst. Sci.* 17, 989–1001. doi:10.5194/hess-17-989-2013

Bingham, A. H., and Cotrufo, M. F. (2015). Organic nitrogen storage in mineral soil: implications for policy and management. *Soil Discuss.* 2, 587–618. doi:10.1016/j.scitotenv.2016.02.020

Bini, A., Cavalli Gori, M., and Gori, S. (1978). A critical review of hypotheses on the origin of vermiculations. *Int. J. Speleol.* 10, 11–33. doi:10.5038/1827-806X.10.1.2

Bojar, A-V., Guja, O., and Stefanescu, D. (2015). Vermiculation patterns in Coiba Mare Cave, Bihor Mountains, Romania. *Quater. Int.* 357, 212–219. doi:10.1016/j.quaint.2014.07.028

Borrel, G., Parisot, N., Harris, H. M. B., Peyretaillade, E., Gaci, N., Tottey, W., et al. (2014). Comparative genomics highlights the unique biology of Methanomassiliicoccales, a Thermoplasmatales-related seventh order of methanogenic archaea that encodes pyrrolysine. *BMC Genom.* 15, 679. doi:10.1186/1471-2164-15-679

Boston, P. J. (2016). Biovermiculation biopatterns as universal signatures of extant and extinct life. *Geol. Soc. America Abstr. Prog.* 48, 7, Paper No. 109-8. doi:10.1130/abs/2016AM-286766

Bowman, J. P. (2017). "Genomics of psychrophilic bacteria and archaea," in *Psychrophiles: from biodiversity to biotechnology*. Editor R. Margesin (Cham: Springer Nature Switzerland), 345–387.

Brewer, T. E., Aronson, E. L., Arogyaswamy, K., Billings, S. A., Botthoff, J. K., Campbell, A. N., et al. (2019). Ecological and genomic attributes of novel bacterial taxa that thrive in subsurface soil horizons. *mBio* 10, e01318-19. doi:10.1128/mBio.01318-19

Caporaso, J. G., Kuczynski, J., Stombaugh, J., Bittinger, K., Bushman, F. D., Costello, E. K., et al. (2010). QIIME allows analysis of high-throughput community sequencing data. *Nat. Methods* 7, 335–336. doi:10.1038/nmeth.f.303

Chen, M.-H., Sheu, S.-Y., James, E. K., Young, C.-C., and Chen, W.-M. (2013). *Azoarcus olearius* sp. nov., a nitrogen-fixing bacterium isolated from oil-contaminated soil. *Int. J. Syst. Evol. Microbiol.* 63, 3755–3761. doi:10.1099/ijs.0.050609-0

Colombo, N., Bocchiola, D., Martin, M., Confortola, G., Salerno, F., Godone, D., et al. (2019). High export of nitrogen and dissolved organic carbon from an Alpine glacier (Indren Glacier, NW Italian Alps). *Aquat. Sci.* 81, 74. doi:10.1007/s00027-019-0670-z

Cuadros, J. (2017). Clay minerals interaction with microorganisms: a review. *Clay Miner.* 52, 235–261. doi:10.1180/claymin.2017.052.2.05

D'Angeli, I. M., De Waele, J., Ieva, M. G., Leuko, S., Cappelletti, M., Parise, M., et al. (2017). Next-generation sequencing for microbial characterization of biovermiculation from a sulfuric acid cave in Apulia (Italy)," in *Proceedings 17th international congress of speleology*. Editors K. Moore and S. White (Sydney: Australian Speleological Federation), 377–380.

D'Angeli, I. M., Parise, M., Vattano, M., Madonia, G., Galdenzi, S., and De Waele, J. (2019a). Sulfuric acid caves of Italy: a review. *Geomorphology* 333, 105–122. doi:10.1016/j.geomorph.2019.02.025

D'Angeli, I. M., Santagata, T., Tognini, P., Foianini, I., Audra, P., Cahiol, D. A., et al. (2018). Late stage condensation-corrosion in high mountain marble cave (Val di Scerscen, Bernina Massif, Valtellina, Italy). *Geophys. Res. Abstr.* 20, EGU2018-8296. doi:10.1007/978-3-642-12486-0

D'Angeli, I. M., Ghezzi, D., Leuko, S., Firrincieli, A., Parise, M., Fiorucci, A., et al. (2019b). Geomicrobiology of a seawater-influenced active sulfuric acid cave. *PLoS One* 14, e0220706. doi:10.1371/journal.pone.0220706

De Mandal, S., Zothansanga, Panda, A. K., Bisht, S. S., and Kumar, N. S. (2016). MiSeq HV4 16S rRNA gene analysis of bacterial community composition among the cave sediments of Indo-Burma biodiversity hotspot. *Environ. Sci. Pollut. Res.* 23, 12216–12226. doi:10.1007/s11356-016-6423-9

De Waele, J., Galdenzi, S., Madonia, G., Menichetti, M., Parise, M., Piccini, L., et al. (2014). "A review on hypogene caves in Italy," in *Hypogene cave morphologies*. Editors A. Klimchouk, I. D. Sasowsky, J. Mylroie, S. A. Engel, and A. S. Engel (Leesburg: Karst Waters Institute Special Publication),Vol. 18, 28–30.

Dos Santos, P. C., Fang, Z., Mason, S. W., Setubal, J. C., and Dixon, R. (2012). Distribution of nitrogen fixation and nitrogenase-like sequences amongst microbial genomes. *BMC Genom.* 13, 162. doi:10.1186/1471-2164-13-162

Edgar, R. C. (2010). Search and clustering orders of magnitude faster than BLAST. *Bioinformatics* 26, 2460–2461. doi:10.1093/bioinformatics/btq461

Eme, L., Spang, A., Lombard, J., Stairs, C. W., and Ettema, T. J. G. (2017). Archaea and the origin of eukaryotes. *Nat. Rev. Microbiol.* 15, 711–723. doi:10.1038/nrmicro.2017.133

Fahrbach, M., Kuever, J., Remesch, M., Huber, B. E., Kämpfer, P., Dott, W., et al. (2008). *Steroidobacter denitrificans* gen. nov., sp. nov., a steroidal hormone-degrading gammaproteobacterium. *Int. J. Syst. Evol. Microbiol.* 58, 2215–2223. doi:10.1099/ijs.0.65342-0

Faucher, B., and Lauriol, B. (2016). Les vermiculations de la grotte Wilson (Lac la Pêche, Québec, Canada). Contexte morphoclimatique, analyses sédimentologiques et distribution spatiale. *Géomorphologie* 22, 95–103. doi:10.4000/geomorphologie.11280

Felsenstein, J. (1981). Evolutionary trees from DNA sequences: a maximum likelihood approach. *J. Mol. Evol.* 17, 368–376. doi:10.1007/BF01734359

Filippa, G., Freppaz, M., Williams, M. W., and Zanini, E. (2010). Major element chemistry in inner alpine snowpacks (Aosta Valley Region, NW Italy). *Cold Reg. Sci. Technol.* 64, 158–166. doi:10.1016/j.coldregions.2010.07.005

Francis, C. A., Roberts, K. J., Beman, J. M., Santoro, A. E., and Oakley, B. B. (2005). Ubiquity and diversity of ammonia-oxidizing archaea in water columns and sediments of the ocean. *Proc. Natl. Acad. Sci. U.S.A.* 102, 14683–14688. doi:10.1073/pnas.0506625102

Freydier, P., Martin, J., Guerrier, B., Jeannin, P. Y., and Doumenc, F. (2019). Rheology of cave sediments: application to vermiculation. *Rheol. Acta* 58, 675–685. doi:10.1007/s00397-019-01167-7

Gonzalez-Pimentel, J. L., Miller, A. Z., Jurado, V., Laiz, L., Pereira, M. F. C., and Saiz-Jimenez, C. (2018). Yellow colored mats from lava tube of La Palma (Canary Islands, Spain) are dominated by metabolically active Actinobacteria. *Sci. Rep.* 8, 1944. doi:10.1038/s41598-018-20393-2

Gröllert, C., Kasper, A., and Puxbaum, H. (1997). Organic compounds in high alpine snow. *Int. J. Environ. Anal. Chem.* 67, 213–222. doi:10.1080/03067319708031405

Guilhermet, J., Preunkert, S., Voisin, D., Baduel, C., and Legrand, M. (2013). Major 20th century changes of water-soluble humic-like substances (HULISWS) aerosol over Europe inferred from Alpine ice cores. *J. Geophys. Res. Atmos.* 11, 3869–3878. doi:10.1002/jgrd.50201

Haeberli, W., Paul, F., and Zemp, M. (2013). "Vanishing glaciers in the European Alps," in *Fate of mountain glaciers in the anthropocene*. Editors P. J. Crutzen, L. Bengtsson, and V. Ramanathan (Vatican city: Pontifical Academy of Sciences, Scripta Varia), Vol. 118.

Hathaway, J. J. M., Garcia, M. G., Moya Balasch, M., Spilde, M. N., Stone, F. D., Dapkevicius, M. L. N. E., et al. (2014b). Comparison of bacterial diversity in Azorean and Hawai'ian lava cave microbial mats. *Geomicrobiol. J.* 31, 205–220. doi:10.1080/01490451.2013.777491

Hathaway, J. J. M., Sinsabaugh, R. L., Dapkevicius, M. L. N. E., and Northup, D. E. (2014a). Diversity of ammonia oxidation (*amoA*) and nitrogen fixation (*nifH*) genes in lava caves of Terceira, Azores, Portugal. *Geomicrobiol. J.* 31, 221–235. doi:10.1080/01490451.2012.752424

Hazeu, W., Batenburg-van der Vegte, W. H., and de Bruyn, J. C. (1980). Some characteristics of *Methylococcus mobilis* sp. nov. *Arch. Microbiol.* 124, 211–220. doi:10.1007/BF00427729

Hershey, O. S., and Barton, H. A. (2018). "The microbial diversity of caves," in *Cave ecology*. Editors O. T. Moldovan, L. Kovác, and S. Halse (Cham: Springer Nature Switzerland), 69–90.

Hirayama, H., Takai, K., Inagaki, F., Nealson, K. H., and Horikoshi, K. (2005). *Thiobacter subterraneus* gen. nov., sp. nov., an obligately chemolithoautotrophic, thermophilic, sulfur-oxidizing bacterium from a subsurface hot aquifer. *Int. J. Syst. Evol. Microbiol.* 55, 467–472. doi:10.1099/ijs.0.63389-0

Holmes, A. J., Tujula, N. A., Holley, M., Contos, A., James, J. M., Rogers, P., et al. (2001). Phylogenetic structure of unusual aquatic microbial formations in Nullarbor caves, Australia. *Environ. Microbiol.* 3, 256–264. doi:10.1046/j.1462-2920.2001.00187.x

Hose, L. D., and Macalady, J. L. (2006). "Observations from active sulfuric karst systems: is the present the key to understanding Guadalupe Mountain speleogenesis?," in *Caves and karst of Southeastern New Mexico*. Editors L. Land, L. V. W. Lueth, W. Raatz, P. Boston, and D. L. Love (Socorro: New Mexico Geological Society), 185–194.

Hose, L. D., Palmer, A. N., Palmer, M. V., Northup, D. E., Boston, P. J., and DuChene, H. R. (2000). Microbiology and geochemistry in a hydrogen-sulphide-rich karst environment. *Chem. Geol.* 169, 399–423. doi:10.1016/50009-2541(00)00217-5

Hu, D., Cha, G., and Gao, B. (2018). A phylogenomic and molecular markers based analysis of the class *Acidimicrobiia*. *Front. Microbiol.* 9, 987. doi:10.3389/fmicb.2018.00987

Imhoff, J. F. (2014). "The family Chromatiaceae" in *The prokaryotes. Gammaproteobacteria* Editors E. Rosenberg, E. F. DeLong, S. Lory, E. Stackebrandt, and F. Thompson (Berlin: Springer-Verlag), 151–178.

Itcus, C., Pascu, M. D., Lavin, P., Persoiu, A., Iancu, L., and Purcarea, C. (2018). Bacterial and archaeal community structures in perennial cave ice. *Sci. Rep.* 8, 15671. doi:10.1038/s41598-018-34106-2

Jones, B. (2009). Cave Pearls—the integrated product of abiogenic and biogenic processes. *J. Sediment. Res.* 79, 689–710. doi:10.2110/jsr.2009.071

Jones, B. (2010). Speleothems in a wave-cut notch, Cayman Brac, British West Indies: the integrated product of subaerial precipitation, dissolution, and microbes. *Sediment. Geol.* 232, 15–34. doi:10.1016/j.sedgeo.2010.09.003

Jones, B. (2011). Biogenicity of terrestrial oncoids formed in soil pockets, Cayman Brac, British West Indies. *Sediment. Geol.* 236, 95–108. doi:10.1016/j.sedgeo.2010.12.009

Jones, D. S., Lyon, E. H., and Macalady, J. L. (2008). Geomicrobiology of biovermiculations from the Frasassi cave system. *J. Cave Karst Stud.* 70, 78–93. https://caves.org/pub/journal/PDF/v70/cave-70-02-78.pdf.

Kim, M. C., Kang, O. C., Kim, C. M., Zhang, Y., Liu, Z., Wei, Z., et al. (2017). *Terrimonas crocea* sp. nov., isolated from the till of a high Arctic glacier. *Int. J. Syst. Evol. Microbiol.* 67, 868–874. doi:10.1099/ijsem.0.001689

Kumar, S., Stecher, G., Li, M., Knyaz, C., and Tamura, K. (2018). MEGA X: molecular evolutionary genetics analysis across computing platforms. *Mol. Biol. Evol.* 35, 1547–1549. doi:10.1093/molbev/msy096

Lavoie, K. H., Winter, A. S., Read, K. J. H., Hughes, E. M., Spilde, M. N., and Northup, D. E. (2017). Comparison of bacterial communities from lava cave microbial mats to overlying surface soils from Lava Beds National Monument, USA. *PloS One* 12, e0169339. doi:10.1371/journal.pone.0169339

Legrand, M., Preunkert, S., Jourdain, B., Guilhermet, J., Faïn, X., Alekhina, I., et al. (2013). Water-soluble organic carbon in snow and ice deposited at Alpine, Greenland, and Antarctic sites: a critical review of available data and their atmospheric relevance. *Clim. Past* 9, 2195–2211. doi:10.5194/cp-9-2195-2013

Legrand, M., Preunkert, S., Schock, M., Cerqueira, M., Kasper-Giebl, A., Afonso, J., et al. (2007). Major 20th century changes of carbonaceous aerosol components (EC, WinOC, DOC, HULIS, carboxylic acids, and cellulose) derived from Alpine ice cores, *J. Geophys. Res.* 112, D23S11. doi:10.1029/2006JD008080

Li, G., Jiang, H., Hou, W., Wang, S., Huang, L., Ren, H., et al. (2012). Microbial diversity in two cold springs on the Qinghai-Tibetan Plateau. *Geosci. Front.* 3, 317–325. doi:10.1016/j.gsf.2011.12.004

Lin, X., Kennedy, D., Fredrickson, J., Bjornstad, B., and Konopka, A. (2012). Vertical stratification of subsurface microbial community composition across geological formations at the Hanford Site. *Environ. Microbiol.* 14, 414–425. doi:10.1111/j.1462-2920.2011.02659.x

Liu, Y., Priscu, J. C., Yao, T., Vick-Majors, T. J., Michaud, A. B., and Sheng, L. (2019). Culturable bacteria isolated from seven high-altitude ice cores on the Tibetan Plateau. *J. Glaciol.* 65, 29–38. doi:10.1017/jog.2018.86

Mao, Y., Yannarell, A. C., and Mackie, R. I. (2011). Changes in N-transforming archaea and bacteria in soil during the establishment of bioenergy crops. *PloS One* 6, e24750. doi:10.1371/journal.pone.0024750

Marques, E. L. S., Gross, E., Dias, J. C. T., Pirovani, C. P., and Rezende, R. P. (2018). Ammonia oxidation (*amoA*) and nitrogen fixation (*nifH*) genes along metasandstone and limestone caves of Brazil. *Geomicrobiol. J.* 35, 869–878. doi:10.1080/01490451.2018.1482386

Materic, D., Ludewig, E., Xu, K., Röckmann, T., and Holzinger, R. (2019). Brief communication: analysis of organic matter in surface snow by PTR-MS-implications for dry deposition dynamics in the Alps. *Cryosphere* 13, 297–307. doi:10.5194/tc-13-297-2019

Meinhardt, K. A., Stopnisek, N., Pannu, M. W., Strand, S. E., Fransen, S. C., Casciotti, K. L., et al. (2018). Ammonia-oxidizing bacteria are the primary N_2O producers in an ammonia-oxidizing archaea dominated alkaline agricultural soil. *Environ. Microbiol.* 20, 2195–2206. doi:10.1111/1462-2920.14246

Melim, L. A., Northup, D. E., Spilde, M. N., Jones, B., Boston, P. J., and Bixby, R. J. (2008). Reticulated filaments in cave pool speleothems: microbe or mineral? *J. Cave Karst Stud.* 70, 135–141. doi:10.7939/R3J38KZ7V

Melim, L. A., Northup, D. E., Spilde, M. N., and Boston, P. J. (2015). Update: living reticulated filaments from Herbslabyrinth-Adventhöhle Cave system, Germany. *J. Cave Karst Stud.* 77, 87–90. doi:10.4311/2015MB0112

Merino, A., Ginés, J., Tuccimei, P., Soligo, M., and Fornós, J. J. (2014). Speleothems in Cova des Pas de Vallgornera: their distribution and characteristics within an extensive coastal cave from the eogenetic karst of southern Mallorca (Western Mediterranean). *Int. J. Speleol.* 43, 125–142. doi:10.5038/1827-806X.43.2.3

Miller, A. Z., Hernández-Mariné, M., Jurado, V., Dionísio, A., Barquinha, P., Fortunato, E., et al. (2012). Enigmatic reticulated filaments in subsurface granite. *Environ. Microbiol. Rep.* 4, 596–603. doi:10.1111/j.1758-2229.2012.00375.x

Miller, A. Z., Pereira, M. F. C., Calaforra, J. M., Forti, P., Dionísio, A., and Saiz-Jimenez, C. (2014). Siliceous speleothems and associated microbe- mineral interactions from Ana Heva Lava Tube in Easter Island (Chile). *Geomicrobiol. J.* 31, 236–245. doi:10.1080/01490451.2013.827762

Mori, K., and Suzuki, K. -I. (2014). "The family *Thioalkalispiraceae*", in *The Prokaryotes. Gammaproteobacteria*. Editors E. Rosenberg, E. F. DeLong, S. Lory, E. Stackebrandt, and F. Thompson (Berlin: Springer-Verlag), 653–658.

Müller-Tautges, C., Eichler, A., Schwikowski, M., Pezzatti, G. B., Conedera, M., and Hoffmann, T. (2016). Historic records of organic compounds from a high Alpine glacier: influences of biomass burning, anthropogenic emissions, and dust transport. *Atmos. Chem. Phys.* 16, 1029–1043. doi:10.5194/acp-16-1029-2016

Muri, G. (2013). Atmospheric deposition chemistry in a subalpine area of the Julian Alps, North-West Slovenia. *J. Limnol.* 72, 291–300. doi:10.4081/jlimnol.2013.e23

Neher, D. A., Weicht, T. R., Bates, S. T., Leff, J. W., and Fierer, N. (2013). Changes in bacterial and fungal communities across compost recipes, preparation methods, and composting times. *PloS One* 8, e79512. doi:10.1371/journal.pone.0079512

Northup, D. E., Melim, L. A., Spilde, M. N., Hathaway, J. J. M., Garcia, M. G., Moya, M., et al. (2011). Lava cave microbial communities within mats and secondary mineral deposits: implications for life detection on other planets. *Astrobiology* 11, 601–618. doi:10.1089/ast.2010.0562

Ortiz, M., Neilson, J. W., Nelson, W. M., Legatzki, A., Byrne, A., Yu, Y., et al. (2013). Profiling bacterial diversity and taxonomic composition on speleothem surfaces in Kartchner Caverns, AZ. *Microb. Ecol.* 65, 371–383. doi:10.1007/s00248-012-0143-6

Pascoal, F., Magalhães, C., and Costa, R. (2020). The link between the ecology of the prokaryotic rare biosphere and its biotechnological potential. *Front. Microbiol.* 11, 231. doi:10.3389/fmicb.2020.00231

Pester, M., Schleper, C., and Wagner, M. (2011). The Thaumarchaeota: an emerging view of their phylogeny and ecophysiology. *Curr. Op. Microbiol.* 14, 300–306. doi:10.1016/j.mib.2011.04.007

Poly, F., Ranjard, L., Nazaret, S., Gourbiere, F., and Monrozier, L. J. (2001). Comparison of *nifH* gene pools in soils and soil microenvironments with contrasting properties. *App. Environ. Microbiol.* 67, 2255–2262. doi:10.1128/AEM.67.5.2255-2262.2001

Porca, E., Jurado, V., Zgur-Bertok, D., Saiz-Jimenez, C., and Pasic, L. (2012). Comparative analysis of yellow microbial communities growing on the walls of geographically distinct caves indicates a common core of microorganisms involved in their formation. *FEMS Microbiol. Ecol.* 81, 255–266. doi:10.1111/j.1574-6941.2012.01383.x

Poret-Peterson, A. T., Graham, J. E., Gulledge, J., and Klotz, M. G. (2008). Transcription of nitrification genes by the methane-oxidizing bacterium, *Methylococcus capsulatus* strain Bath. *ISME J.* 2, 1213–1220. doi:10.1038/ismej.2008.71

Preunkert, S., and Legrand, M. (2013). Towards a quasi-complete reconstruction of past atmospheric aerosol load and composition (organic and inorganic) over Europe since 1920 inferred from Alpine ice cores. *Clim. Past* 9, 1403–1416. doi:10.5194/cp-9-1403-2013

Prosser, J. I., Head, I. M., and Stein, L. Y. (2014). "The family *Nitrosomonadaceae*," in *The Prokaryotes. Alphaproteobacteria and Betaproteobacteria*. Editors E. Rosenberg, E. F. DeLong, S. Lory, E. Stackebrandt, and F. Thompson (Berlin: Springer-Verlag), 901–918.

Purcarea, C. (2018). "Microbial life in ice caves," in *Ice caves*. Editors A. Persoiu and A. S. E. Lauritzen (Amsterdam: Elsevier), 173–187.

Qin, W., Heal, K. R., Ramdasi, R., Kobelt, J. N., Martens-Habbena, W., Bertagnolli, A. D., et al. (2017). *Nitrosopumilus maritimus* gen. nov., sp. nov., *Nitrosopumilus cobalaminigenes* sp. nov., *Nitrosopumilus oxyclinae* sp. nov., and *Nitrosopumilus ureiphilus* sp. nov., four marine ammonia-oxidizing archaea of the phylum *Thaumarchaeota*. *Int. J. Syst. Evol. Microbiol.* 67, 5067–5079. doi:10.1099/ijsem.0.002416

Quast, C., Pruesse, E., Yilmaz, P., Gerken, J., Schweer, T., Yarza, P., et al. (2013). The SILVA ribosomal RNA gene database project: improved data processing and web-based tools. *Nucleic Acid. Res.* 41, D590–D596. doi:10.1093/nar/gks1219

Reitschuler, C., Lins, P., Schwarzenauer, T., Spötl, C., Wagner, A. O., and Illmer, P. (2015). New undescribed lineages of non-extremophilic Archaea form a constant and dominant element within alpine moonmilk microbiomes. *Geomicrobiol. J.* 32, 890–902. doi:10.1080/01490451.2015.1025317

Riquelme, C., Hathaway, J. J. M., Dapkevicius, M. L. N. E., Miller, A. Z., Kooser, A., Northup, D. E., et al. (2015a). Actinobacterial diversity in volcanic caves and associated geomicrobiological interactions. *Front. Microbiol.* 6, 1342. doi:10.3389/fmicb.2015.01342

Riquelme, C., Rigal, F., Hathaway, J. J. M., Northup, D. E., Spilde, M. N., Borges, P. A. V., et al. (2015b). Cave microbial community composition in oceanic islands: disentangling the effect of different colored mats in diversity patterns of Azorean lava caves. *FEMS Microbiol. Ecol.* 91, fiv141. doi:10.1093/femsec/fiv141

Riquelme, C., Dapkevicius, M. L. E., Miller, A. Z., Charlop-Powers, Z., Brady, S., Mason, C., et al. (2017). Biotechnological potential of Actinobacteria from Canadian and Azorean volcanic caves. *Appl. Microbiol. Biotechnol.* 101, 843–857. doi:10.1007/s00253-016-7932-7

Rogora, M., Mosello, R., Arisci, S., Brizzio, M. C., Barbieri, A., Balestrini, R., et al. (2006). An overview of atmospheric deposition chemistry over the Alps: present status and long-term trends. *Hydrobiologia* 562, 17–40. doi:10.1007/s10750-005-1803-z

Rotthauwe, J. H., Witzel, K. P., and Liesack, W. (1997). The ammonia monooxygenase structural gene amoA as a functional marker: molecular fine-scale analysis of natural ammonia-oxidizing populations. *Appl. Environ. Microbiol.* 63, 4704–4712. doi:10.1128/AEM.63.12.4704-4712.1997

Saiz-Jimenez, C. (2015). "The microbiology of show caves, mines tunnels and tombs: implications for management and conservation," in *Microbial life of cave systems*. Editor A. S. Engel (Berlin: DeGruiter), 231–261.

Schabereiter-Gurtner, C., Saiz-Jimenez, C., Piñar, G., Lubitz, W., and Rölleke, S. (2002). Phylogenetic 16S rRNA analysis reveals the presence of complex and partly unknown bacterial communities in Tito Bustillo cave, Spain, and on its Paleolithic paintings. *Environ. Microbiol.* 4, 392–400. doi:10.1046/j.1462-2920.2002.00303.x

Schloss, P. D., Westcott, S. L., Ryabin, T., Hall, J. R., Hartmann, M., Hollister, E. B., et al. (2009). Introducing mothur: open-source, platform-independent, community-supported software for describirng and comparing microbial communities. *Appl. Environ. Microbiol.* 75, 7537–7541. doi:10.1128/AEM.01541-09

Severino, R., Froufe, H. J. C., Barroso, C., Albuquerque, L., Lobo-da-Cunha, A., da Costa, M. S., et al. (2019). High-quality draft genome sequence of *Gaiella occulta* isolated from a 150 meter deep mineral water borehole and comparison with the genome sequences of other deep-branching lineages of the phylum *Actinobacteria*. *Microbiol. Open* 8, e00840. doi:10.1002/mbo3.8407

Sheu, S.-Y., Li, Y.-S., and Chen, W.-M. (2016). *Piscinibacterium candidicorallinum* gen. nov., sp. nov., a member of the order *Burkholderiales* isolated from a fish pond. *Int. J. Syst. Evol. Microbiol.* 66, 5260–5267. doi:10.1099/ijsem.0.001505

Sogin, M. L., Morrison, H. G., Huber, J. A., Welch, D. M., Huse, S. M., Neal, P. R., et al. (2006). Microbial diversity in the deep sea and the underexplored "rare biosphere". *Proc. Natl. Acad. Sci. U.S.A.* 103, 12115–12120. doi:10.1073/pnas.0605127103

Sommer, C., Malz, P., Seehaus, T. C., Lippl, S., Zemp, M., and Braun, M. H. (2020). Rapid glacier retreat and downwasting throughout the European Alps in the early 21st century. *Nat. Comm.* 11, 3209. doi:10.1038/s41467-020-16818-0

Spain, A. M., Krumholz, L. R., and Elshahed, M. S. (2009). Abundance, composition, diversity and novelty of soil Proteobacteria. *ISME J.* 3, 992–1000. doi:10.1038/ismej.2009.43

Sutka, R. L., Ostrom, N. E., Ostrom, P. H., Gandhi, H., and Breznak, J. A. (2003). Nitrogen isotopomer site preference of N_2O produced by *Nitrosomonas europaea* and *Methylococcus capsulatus* Bath. *Rapid Commun. Mass. Spectrom.* 17, 738–745. doi:10.1002/rcm.968

Takahashi, S., Tomita, J., Nishioka, K., Hisada, T., and Nishijima, M. (2014). Development of a prokaryotic universal primer for simultaneous analysis of *Bacteria* and *Archaea* using next-generation sequencing. *PloS One* 9, e105592. doi:10.1371/journal.pone.0105592

Tebo, B. M., Davis, R. E., Anitori, R. P., Connell, L. B., Schiffman, P., and Staudigel, H. (2015). Microbial communities in dark oligotrophic volcanic ice cave ecosystems of Mt. Erebus, Antarctica. *Front. Microbiol.* 6, 179–192. doi:10.3389/fmicb.2015.00179

Tomczyk-Żak, K., and Zielenkiewicz, U. (2016). Microbial diversity in caves. *Geomicrobiol. J.* 33, 20–38. doi:10.1080/01490451.2014.1003341

Urakawa, H., Garcia, J. C., Nielsen, J. L., Le, V. Q., Kozlowski, J. A., Stein, L. Y., et al. (2015). *Nitrosospira lacus* sp. nov., a psychrotolerant, ammonia-oxidizing bacterium from sandy lake sediment. *Int. J. Syst. Evol. Microbiol.* 65, 242–250. doi:10.1099/ijs.0.070789-0

Vandamme, P., and Coenye, T. (2004). Taxonomy of the genus *Cupriavidus*: a tale of lost and found. *Int. J. Syst. Evol. Microbiol.* 54, 2285–2289. doi:10.1099/ijs.0.63247-0

Ward, L. M., Johnston, D. T., and Shih, P. M. (2019). Phanerozoic radiation of ammonia oxidizing bacteria. BioRxiv [preprint]. doi:10.1101/655399

Wise, M. G., McArthur, J. V., and Shimkets, L. J. (2001). *Methylosarcina fibrata* gen. nov., sp. nov. and *Methylosarcina quisquiliarum* sp. nov., novel type I methanotrophs. *Int. J. Syst. Evol. Microbiol.* 51, 611–621. doi:10.1099/00207713-51-2-611

Yarza, P., Yilmaz, P., Pruesse, E., Glöckner, F. O., Ludwig, W., Schleifer, K. -H., et al. (2014). Uniting the classification of cultured and uncultured bacteria and archaea using 16S rRNA gene sequences. *Nat. Rev. Microbiol.* 12, 635–645. doi:10.1038/nrmicro3330

Zhang, J., Kobert, K., Flouri, T., and Stamatakis, A. (2014). PEAR: a fast and accurate Illumina Paired-End reAd mergeR. *Bioinformatics* 30, 614–620. doi:10.1093/bioinformatics/btt593

Zhang, L-M., Wang, M., Prosser, J. I., Zheng, Y. -M., and He, J. -Z. (2009). Altitude ammonia-oxidizing bacteria and archaea in soils of Mount Everest. *FEMS Microbiol. Ecol.* 70, 208–217. doi:10.1111/j.1574-6941.2009.00775.x

Zhang, S., Xia, X., Li, S., Zhang, L., Wang, G., Li, M., et al. (2019a). Ammonia oxidizers in high-elevation rivers of the Qinghai-Tibet Plateau display distinctive distribution patterns. *Appl. Environ. Microbiol.* 85, e01701-19. doi:10.1128/AEM.01701-19

Zhang, X., Johnston, E. R., Wang, Y., Yu, Q., Tian, D., Wang, Z., et al. (2019b). Distinct drivers of core and accessory components of soil microbial community functional diversity under environmental changes. *mSystems* 4, e00374-19. doi:10.1128/mSystems.00374-19

Zhu, H. -Z., Zhang, Z. F., Zhou, N., Jiang, C. Y., Wang, B. J., Cai, L., et al. (2019). Diversity, distribution and co-occurrence patterns of bacterial communities in a karst cave system. *Front. Microbiol.* 10, 1726. doi:10.3389/fmicb.2019.01726

Conflict of Interest: The authors declare that the research was conducted in the absence of any commercial or financial relationships that could be construed as a potential conflict of interest.

frontiers in Earth Science

ORIGINAL RESEARCH
published: 12 March 2021
doi: 10.3389/feart.2021.642651

Opposite Trends in Holocene Speleothem Proxy Records From Two Neighboring Caves in Germany: A Multi-Proxy Evaluation

Michael Weber[1,2], Yvonne Hinz[1], Bernd R. Schöne[1], Klaus Peter Jochum[2], Dirk Hoffmann[3], Christoph Spötl[4], Dana F. C. Riechelmann[1] and Denis Scholz[1]*

[1] Institute for Geosciences, Johannes Gutenberg University Mainz, Mainz, Germany, [2] Climate Geochemistry Department, Max Planck Institute for Chemistry (Otto Hahn Institute), Mainz, Germany, [3] Isotope Geology Department, Georg-August-University Göttingen, Göttingen, Germany, [4] Institute of Geology, University of Innsbruck, Innsbruck, Austria

OPEN ACCESS

Edited by:
Eleonora Regattieri, Pisa Research Area, Italian National Research Council, Italy

Reviewed by:
Maša Surić, University of Zadar, Croatia
Silvia Frisia, University of New South Wales, Australia

***Correspondence:**
Michael Weber
michael.weber@uni-mainz.de

Specialty section:
This article was submitted to Quaternary Science, Geomorphology, and Paleoenvironment, a section of the journal Frontiers in Earth Science

Received: 16 December 2020
Accepted: 22 February 2021
Published: 12 March 2021

Citation:
Weber M, Hinz Y, Schöne BR, Jochum KP, Hoffmann D, Spötl C, Riechelmann DFC and Scholz D (2021) Opposite Trends in Holocene Speleothem Proxy Records From Two Neighboring Caves in Germany: A Multi-Proxy Evaluation. Front. Earth Sci. 9:642651. doi: 10.3389/feart.2021.642651

Holocene climate in Central Europe was characterized by variations on millennial to decadal time scales. Speleothems provide the opportunity to study such palaeoclimate variability using high temporal resolution proxy records, and offer precise age models by U-series dating. However, the significance of proxy records from an individual speleothem is still a matter of debate, and limited sample availability often hampers the possibility to reproduce proxy records or to resolve spatial climate patterns. Here we present a palaeoclimate record based on four stalagmites from the Hüttenbläserschachthöhle (HBSH), western Germany. Two specimens cover almost the entire Holocene, with a short hiatus in between. A third stalagmite grew between 6.1 ± 0.6 ka and 0.6 ± 0.1 ka and a fourth one covers 11.0 ± 0.4 ka to 8.2 ± 0.2 ka. Trace element and stable isotope data allow to compare coeval stalagmites and to reconstruct potential climate patterns in the Holocene. In addition, Sr isotopes reveal soil processes and recharge of the aquifer. The aim of this study was to evaluate the consistency of the proxy data recorded by the individual stalagmites and to validate the results using a multi-proxy approach. Due to the close proximity of HBSH (<1 km) to the intensively investigated Bunker Cave system, this dataset also provides the unique opportunity to compare this record with a time-series from another cave system in the same climate region. While the initial growth phase at the onset of the Holocene shows similar patterns in both caves, the data show an opposing trend in the past 6 ka, most likely induced by the effect of disequilibrium isotope fractionation, resulting in a strong increase in $\delta^{13}C$ and $\delta^{18}O$ values. The stable isotope data from Bunker Cave do not show this pattern. Trace element data support the interpretation of the HBSH stable isotope data, highlighting the importance of a multi-proxy approach, and the need to replicate speleothem records both within a cave system and ideally using other caves in the region.

Keywords: stalagmite, PCP, Sr isotopes, Central Europe, stable isotopes, disequilibrium isotope effects, trace elements

INTRODUCTION

Speleothems are well established terrestrial palaeoclimate archives and widely used for the reconstruction of past climate and environmental variability on different time scales (e.g., Genty et al., 2003; Fohlmeister et al., 2012; Moseley et al., 2014; Luetscher et al., 2015; Wassenburg et al., 2016a; Mischel et al., 2017a; Lechleitner et al., 2018; Weber et al., 2018a; Budsky et al., 2019). One of their key features is the possibility to obtain independent, precise and accurate ages, using the U-series disequilibrium method (Scholz and Hoffmann, 2008; Cheng et al., 2013) and the construction of a robust age-depth model, provided that post-depositional alteration did not affect U-mobilization (Scholz et al., 2014; Bajo et al., 2016). The most commonly used climate proxies in speleothem science are the stable oxygen ($\delta^{18}O$) and carbon ($\delta^{13}C$) isotopes as well as trace elements (McDermott, 2004; Fairchild et al., 2006; Fairchild and Treble, 2009; Lachniet, 2009). Both can be measured at high spatial resolution in the sub-100 μm-range and converted into a temporally aligned dataset using an age-depth model (e.g., Scholz and Hoffmann, 2011; Breitenbach et al., 2012). Trace elements can be analyzed at similar or even higher resolution and have been extensively used in speleothem science to further constrain environmental and climate reconstructions (e.g., Fairchild et al., 2000; Treble et al., 2003; Fairchild and Treble, 2009; Sinclair et al., 2012). Furthermore, additional proxies have been established for speleothems, such as Sr isotopes to reconstruct changes in aeolian dust transport, weathering conditions, precipitation amount, and water pathways in the karst aquifer (e.g., Banner et al., 1994, 1996; Li et al., 2005; Hori et al., 2013; Belli et al., 2017; Weber et al., 2017, 2018a).

Although all these proxies – and in particular stable oxygen and carbon isotopes – have been intensively studied, the reconstruction of past climate variability can be hampered by several processes. Besides the natural variability of $\delta^{18}O$ and $\delta^{13}C$ values reflecting climatic and environmental changes, karst and in-cave processes can also significantly alter the resulting proxy signal captured by the speleothem (e.g., Mickler et al., 2006; Lachniet, 2009; Deininger et al., 2012; Riechelmann et al., 2013; Hansen et al., 2017, 2019). Therefore, it is important to evaluate the significance of a stable isotope record obtained from a single speleothem, either by using a multi-proxy approach to validate the stable isotope data, or, if available, by analyzing several speleothems from the same time interval and cave system. This is especially crucial for time intervals of sparse speleothem growth, e.g., during Marine Isotope Stage 3 in Central Europe (McDermott, 2004; Fankhauser et al., 2016; Weber et al., 2018a), and when additional samples are not available. In contrast to time intervals with a low number of speleothem records, the favorable climatic conditions during the Holocene resulted in intensive speleothem growth (e.g., McDermott et al., 1999; Mangini et al., 2007; Fohlmeister et al., 2012, 2013; Warken et al., 2018; Comas-Bru et al., 2020), providing the largest possible cross-continental dataset to evaluate the significance of speleothem proxy records.

Although Holocene climate variability is much smaller compared to glacial-interglacial timescales (Mayewski et al., 2004; McDermott, 2004; Wanner et al., 2008), significant changes and trends in precipitation and temperature also occurred during the Holocene. Here, speleothem proxy data from Hüttenbläserschachthöhle (HBSH), western Germany, covering almost the entire Holocene is presented. In total, four stalagmites were investigated and their $\delta^{18}O$ and $\delta^{13}C$ values analyzed. These records were stacked and their significance evaluated by comparing them with published data from the nearby Bunker cave (<1 km distance to Hüttenbläserschachthöhle). To further evaluate the stable isotope data, a multi-proxy approach including trace element and Sr isotope data was used.

SITE AND SAMPLE DESCRIPTION

Hüttenbläserschachthöhle (HBSH)

Hüttenbläserschachthöhle (HBSH in the following) is located within upper Middle Devonian limestones (Givetian stage) of the northern Rhenish Slate Mountains (Iserlohn-Letmathe, NW Germany, **Figure 1A** (Burchette, 1981). Ridges and valleys in the area of Iserlohn-Letmathe generally follow the WSW-ENE strike of the rock formation (von Kamp and Ribbert, 2005). The approximately 700 m thick limestone was deposited in a shallow shelf (Paeckelmann, 1922; Krebs, 1974). At the transition between the Givetian and the Frasnian, basin subsidence and sea-level rise exceeded carbonate sedimentation, giving rise to siliciclastic depositions in deeper water depths (Hammerschmidt et al., 1995).

Hüttenbläserschachthöhle was discovered in 1993 and is one of the largest and speleothem-richest caves in Iserlohn-Letmathe (Hammerschmidt et al., 1995; Richter et al., 2015). The cave has a total length of 4.8 km with a vertical extent of 46 m (Grebe, 1994) and consists of three levels. On each level, a main corridor exists, which probably represents the former phreatic karst water collector. The cave levels can be correlated to river terraces in the Rhenish Slate Mountains (Niggemann et al., 2003). The area above HBSH and the nearby Bunker Cave is covered by similar vegetation consisting of C3-plants such as ash, beech trees and shrubs. The mean annual precipitation is 972 ± 173 mm (1 SD, 1978–2020) and the mean annual temperature in the area is 8.9 ± 0.7°C (1 SD; 1994–2020, DWD weather station Lüdenscheid, approximately 15 km south of HBSH). The $\delta^{18}O$ values of precipitation range from −5 ‰ in summer to −13 ‰ in winter and averages −8.0 ‰ between 2006 and 2013 (Riechelmann et al., 2017).

Speleothem Samples

The four stalagmites covering the Holocene (HSBH-1, HBSH-3, HBSH-4, and HBSH-5, **Figure 2**) were collected from deep parts of HBSH. HBSH-1 is a ca. 55 cm-long stalagmite with clearly visible macroscopic banding. X-ray diffraction revealed that most of the sample consist of aragonite, with very few and short calcite sections (Jochum et al., 2012; Yang et al., 2015; Lin et al., 2017). This study focuses on an approximately 5 cm-long section from the top of the stalagmite. In contrast to HBSH-1, all other stalagmites of this study consist of calcite. HBSH-3 is approximately 22 cm long, banded and bright beige colored with some interspersed darker areas. HBSH-4 also

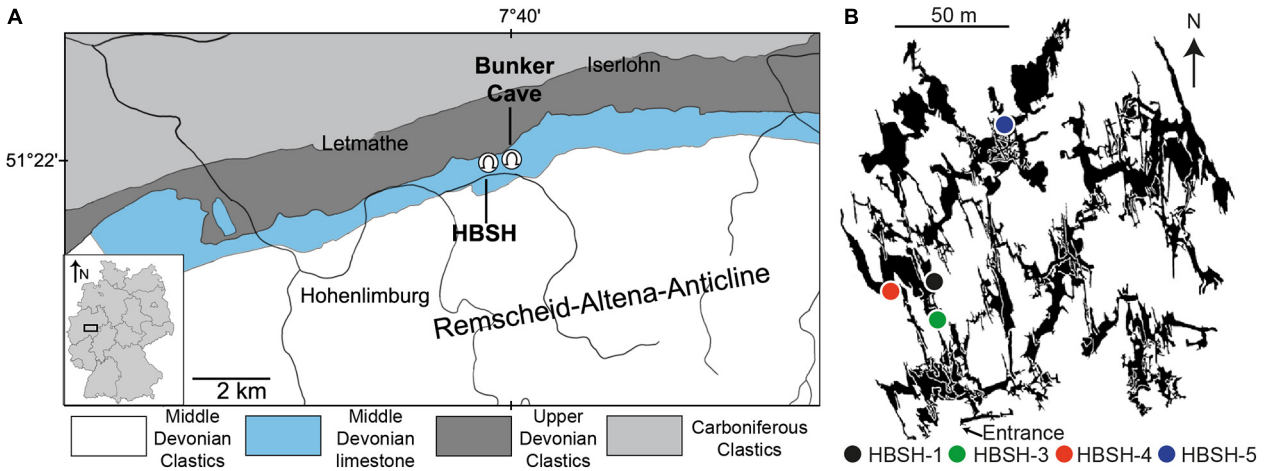

FIGURE 1 | (A) Geological map of the cave area with the locations of Hüttenbläserschachthöhle (HBSH) and Bunker Cave. Modified after Riechelmann et al. (2011). **(B)** Cave map of HBSH with the location of the stalagmite sampling sites. Modified after Grebe (1994).

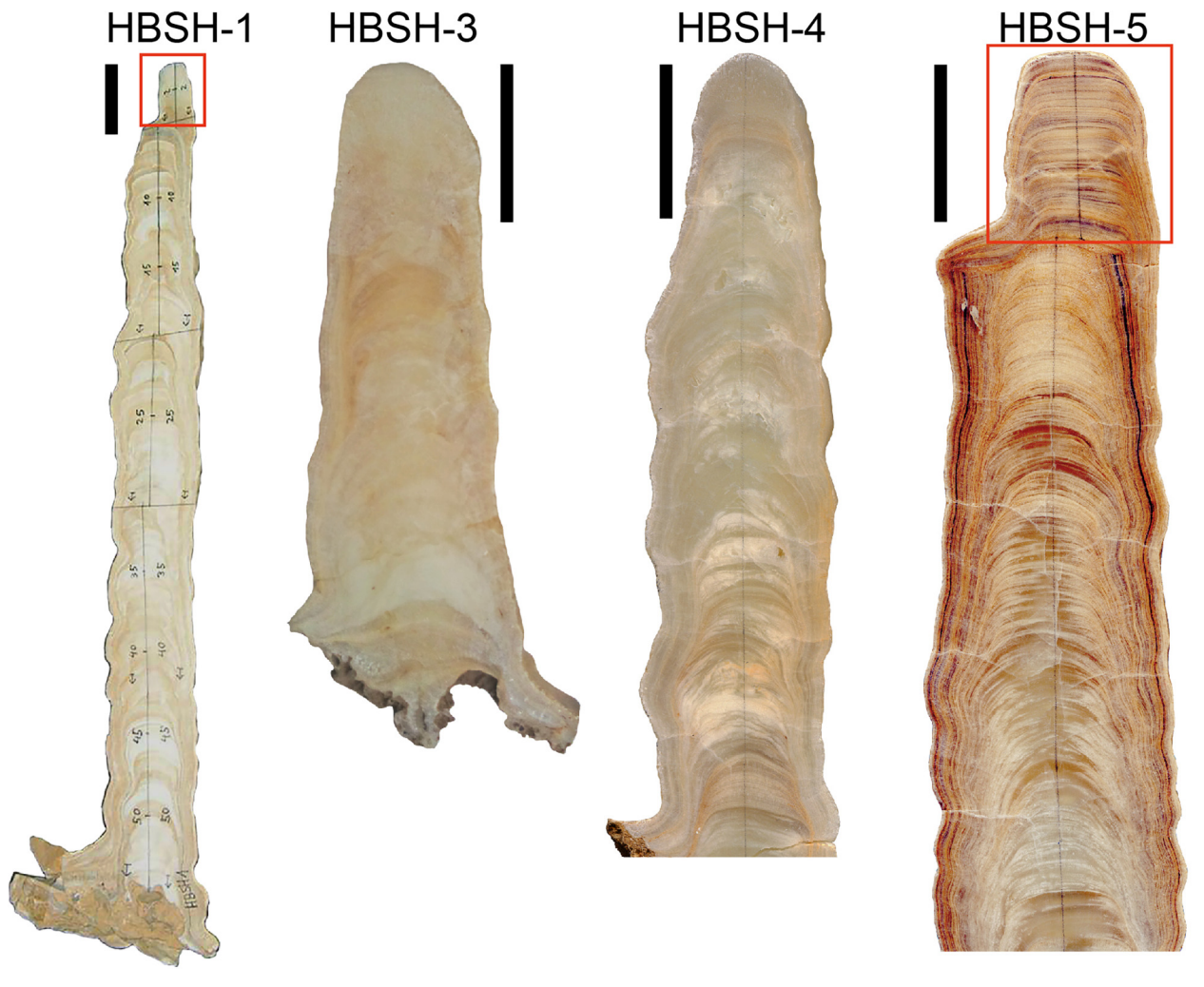

FIGURE 2 | Pictures of the HBSH stalagmites. For HBSH-1 and HBSH-5, only the upper parts covering the Holocene (highlighted by the red box) were investigated. For HBSH-3 and HBSH-4, the major parts grew during the Holocene. All scale bars are 5 cm.

shows banding throughout the whole stalagmite, which measures 30 cm in length, with a bright beige to gray colur. HBSH-5 has a total length of 33 cm, showing macroscopic banding and a generally darker color than the other HBSH stalagmites. While stalagmites HBSH-1, -3, and -4 grew in close proximity in the western part of HBSH, HBSH-5 was sampled in the norther part of HBSH (**Figure 1B**). This area is only sparsely decorated with speleothem deposits, potentially related to limited fractures in the overlying host rock (Hammerschmidt et al., 1995). The top section of HBSH-5 covering approximately 6 cm was investigated in this study.

ANALYTICAL METHODS

^{230}Th/U-Dating

Stalagmite samples were dated using the ^{230}Th/U dating method and analyzed by multi-collector inductively coupled plasma mass spectrometry (MC-ICP-MS) at the Max Planck Institute for Chemistry (MPIC), Mainz, the Institute for Geosciences, Mainz, and the Bristol Isotope Group (BIG), Bristol (HBSH-1). Samples were cut along the growth axes using a diamond wire saw. In total, 47 samples were analyzed at MPIC, seven samples at the Institute for Geosciences, Mainz, and five samples at BIG (**Table 1**). For sample HBSH-3, HBSH-4, and HBSH-5, sample amounts of approximately 300 mg were used, and chemical separation of U and Th prior to analysis was performed at the MPIC and the Institute for Geosciences following the methods described in Hoffmann (2008) and Yang et al. (2015). Chemical separation for HBSH-1 was performed at BIG as described by Hoffmann et al. (2007). At MPIC, a Nu Plasma MC-ICP-MS was used to analyze U and Th in separated sessions following the protocol described in Obert et al. (2016). Details of the calibration of the U-Th-spike are presented by Gibert et al. (2016). Introduction of the samples dissolved in 0.8 mol/L HNO_3 was performed using a CETAC Aridus II desolvating nebulizer system. A daily tuning protocol was used to achieve highest signal intensities and optimized peak shapes. At the Institute for Geosciences, a Neptune Plus MC-ICP-MS was coupled to a CETAC Aridus 3 desolvating nebulizer system, performing the same protocol as described for the Nu Plasma at MPIC. Measurements at BIG were performed using a Neptune MC-ICP-MS coupled to a CETAC Aridus desolvating system, following the methods described in Hoffmann et al. (2007). Age-depth models (**Figure 3**) were calculated using the algorithm StalAge (Scholz and Hoffmann, 2011).

Stable Isotope Analysis

Stable carbon and oxygen isotope values (δ^{13}C and δ^{18}O) for HBSH-3, HBSH-4, and HBSH-5 were determined at the Institute for Geosciences, Johannes Gutenberg University Mainz. Samples were obtained with a semi-automated drilling device at a spatial resolution of 500 µm. In total, 1350 samples were analyzed using a Thermo Fisher Scientific MAT 253 continuous-flow isotope ratio mass spectrometer equipped with a Gasbench II. Stable carbon and oxygen isotope values for HBSH-1 were obtained at the Institute of Geology, University of Innsbruck, using a Merchantek video-controlled Micromill device (Dettman and Lohmann, 1995) at a spatial resolution of 150 µm, resulting in a total number of 301 samples. Analyses were performed using a Thermo Fisher Scientific Delta^{plus}XL isotope ratio mass spectrometer linked to a Gasbench II. Analytical precision and accuracy at the 1 σ-level was better than 0.08 ‰ for δ^{13}C and δ^{18}O. All values are reported relative to V-PDB.

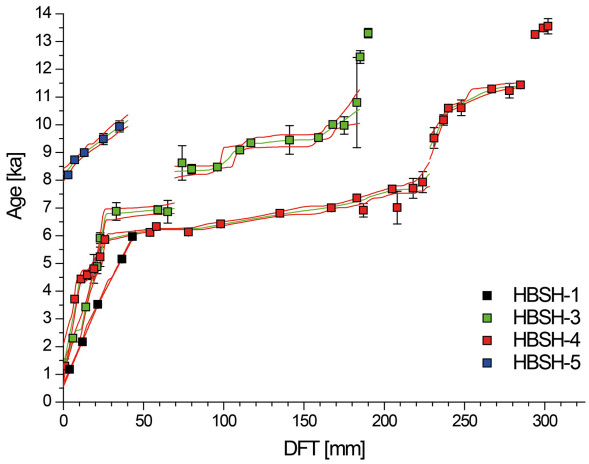

FIGURE 3 | Age-depth relationships for stalagmites HBSH-1 (black), HBSH-3 (green), HBSH-4 (red), and HBSH-5 (blue). The colored squares represent the individual ^{230}Th/U-ages with their respective 2 SE uncertainties. Note that some of the error bars are smaller than the symbols. Detailed uncertainties are given in **Table 1**. The green lines represent the age models calculated by StalAge (Scholz and Hoffmann, 2011) with the red lines representing the corresponding age uncertainties at the 95% confidence level for each sample. For the sections corresponding to the periods prior to the onset of the Holocene in stalagmites HBSH-3 and HBSH-4, no age model was calculated.

Trace Element Analyses

Laser ablation inductively coupled plasma mass spectrometry (LA-ICP-MS) was used to determine trace element concentrations in HBSH-1, HBSH-3, and HBSH-5. A Thermo Fisher Scientific Element 2 SF-ICP-MS was coupled to a New Wave UP-213 laser ablation system at the MPIC. For all samples, the following laser parameters were applied: spot analyses with a spot size of 100 µm, a repetition rate of 10 Hz and an energy output of 60%, resulting in a fluence of ≈5 J/cm^2. Background signals were collected for 14 s prior to ablation and subtracted from the sample signal, followed by a wash-out time of 20 s. The following analytes were measured during the session: ^{25}Mg, ^{31}P, ^{88}Sr, and ^{137}Ba. NIST SRM 612 was analyzed for calibration purposes at the beginning, between each set and at the end of the routine. ^{43}Calcium was used as internal reference to calculate trace element concentrations. Data evaluation was performed offline, following the calculations presented in Mischel et al. (2017b).

Data Processing and Statistics

All speleothems show a high variability in growth rate, both within individual stalagmites and between coeval stalagmites

TABLE 1 | Uranium and Th concentrations, activity ratios and ^{230}Th/U-ages for the Holocene stalagmites from HBSH. All uncertainties are quoted as 2 SE. All activity ratios and ages were corrected for detrital contamination assuming a ^{232}Th/^{238}U mass ratio of 3.8 ± 1.9, calculated from the average Th and U concentrations of tonalities which are believed to be representative for the bulk continental crust (Wedepohl, 1995). ^{230}Th, ^{234}U, and ^{238}U were assumed to be in secular equilibrium for the detritus. Activity ratios were calculated using the half-lives from Cheng et al. (2000). All measurements highlighted with an asterisk were measured at the Institute for Geosciences with a Neptune Plus MC-ICP-MS. Sample HBSH-1 was analyzed at the BIG. BDL = below detection limit; NA = not available due to ^{232}Th concentration below detection limit. All ages are given relative to the year AD 2000.

Sample	DFT [mm]	^{232}Th [ng/g]	Uncertainty	^{238}U [ng/g]	Uncertainty	(^{234}U /^{238}U)	Uncertainty	(^{230}Th /^{238}U)	Uncertainty	(/^{232}Th /^{232}Th)	Uncertainty	Uncorrected age [ka]	Uncertainty [ka]	Corrected Age [ka]	Uncertainty [ka]
HBSH-1-0.4	4.0	2.167	0.284	2727.52	364.02	1.965	0.003	0.0211	0.0002	81.9	0.5	1.18	0.01	1.17	0.01
HBSH-1-1.2	12.0	2.543	0.290	3427.39	392.00	2.142	0.003	0.0421	0.0002	174.3	0.9	2.17	0.01	2.16	0.01
HBSH-1-2.2	21.5	0.690	0.086	6186.75	773.74	1.891	0.003	0.0601	0.0003	1647.7	12.0	3.51	0.02	3.51	0.02
HBSH-1-3.7	36.5	4.109	0.320	4876.50	372.62	1.932	0.003	0.0895	0.0004	325.2	2.1	5.16	0.03	5.15	0.03
HBSH-1-4.3	43.0	34.837	2.624	4219.61	315.69	1.838	0.003	0.0981	0.0011	37.1	0.1	6.09	0.03	5.96	0.07
HBSH-3-0.2	2.0	0.906	0.055	38.54	0.48	1.228	0.014	0.0411	0.0145	6.1	1.9	4.26	1.33	3.70	1.34
HBSH-3-0.6	6.0	0.453	0.005	72.30	0.43	1.211	0.002	0.0253	0.0011	13.1	0.4	2.44	0.07	2.29	0.10
HBSH-3-1.4	14.0	0.066	0.001	38.05	0.25	1.208	0.002	0.0373	0.0011	66.6	2.1	3.46	0.10	3.41	0.11
HBSH-3-2.1	21.0	1.540	0.015	80.34	0.49	1.204	0.003	0.0527	0.0026	9.2	0.2	5.32	0.09	4.87	0.25
HBSH-3-2.3	23.0	0.789	0.014	99.27	0.79	1.208	0.008	0.0638	0.0021	25.3	0.8	6.09	0.18	5.90	0.20
HBSH-3-3.3	33.0	0.864	0.009	43.21	0.29	1.205	0.002	0.0737	0.0033	12.0	0.4	7.34	0.22	6.86	0.32
HBSH-3-5.9	59.0	0.413	0.005	45.97	0.31	1.212	0.002	0.0746	0.0016	26.1	0.5	7.12	0.12	6.91	0.16
HBSH-3-6.5*	65.0	6.530	0.043	87.64	0.52	1.226	0.002	0.0748	0.0044	3.8	0.1	8.60	0.15	6.85	0.41
HBSH-3-7.4	74.0	2.670	0.029	91.33	0.55	1.249	0.003	0.0951	0.0067	11.4	0.2	9.96	0.21	8.61	0.62
HBSH-3-8.0	80.0	0.096	0.001	51.95	0.35	1.249	0.002	0.0926	0.0018	153.8	3.4	8.42	0.17	8.38	0.17
HBSH-3-9.6	96.0	0.030	0.000	63.08	0.42	1.252	0.002	0.0937	0.0008	603.0	9.6	8.48	0.08	8.46	0.08
HBSH-3-11.0	110.0	0.432	0.005	109.01	0.85	1.259	0.007	0.1008	0.0013	78.5	1.1	9.17	0.13	9.08	0.13
HBSH-3-11.7	117.0	0.299	0.004	121.87	0.72	1.266	0.002	0.1041	0.0014	130.7	2.2	9.39	0.13	9.34	0.14
HBSH-3-14.1	141.0	0.111	0.005	93.56	1.96	1.278	0.026	0.1062	0.0051	273.8	17.1	9.47	0.51	9.44	0.52
HBSH-3-15.9	159.0	0.056	0.001	67.35	0.45	1.266	0.002	0.1061	0.0012	394.0	6.3	9.54	0.11	9.52	0.11
HBSH-3-16.8	168.0	0.007	0.000	52.59	0.36	1.263	0.002	0.1109	0.0012	2597.0	77.8	10.00	0.11	9.99	0.11
HBSH-3-17.5*	175.0	3.980	0.030	68.82	0.45	1.318	0.002	0.1155	0.0035	6.8	0.1	11.22	0.15	9.96	0.31
HBSH-3-18.3	183.0	13.302	0.132	88.41	0.69	1.343	0.011	0.1270	0.0182	3.3	0.1	14.06	0.26	10.79	1.63
HBSH-3-18.5*	185.0	6.838	0.048	156.76	0.99	1.369	0.001	0.1481	0.0025	11.1	0.1	13.34	0.11	12.42	0.23
HBSH-3-19.0	190.0	1.162	0.014	87.29	0.63	1.382	0.002	0.1593	0.0019	37.3	0.4	13.56	0.11	13.29	0.17
HBSH-4-0.1	1.0	1.859	0.019	91.22	0.52	1.209	0.002	0.0143	0.0028	2.9	0.1	1.77	0.07	1.29	0.26
HBSH-4-0.7	7.0	1.198	0.012	158.11	1.07	1.208	0.005	0.0404	0.0012	17.1	0.3	3.88	0.08	3.70	0.12
HBSH-4-1.1	11.0	1.117	0.012	192.76	1.18	1.179	0.002	0.0469	0.0009	25.5	0.3	4.56	0.05	4.42	0.08
HBSH-4-1.5	15.0	0.205	0.004	243.41	1.47	1.180	0.002	0.0486	0.0018	177.4	7.2	4.59	0.17	4.57	0.17

(Continued)

TABLE 1 | Continued

Sample	DFT [mm]	^{232}Th [ng/g]	Uncertainty	^{238}U [ng/g]	Uncertainty	(^{234}U /^{238}U)	Uncertainty	(^{230}Th /^{238}U)	Uncertainty	(/^{232}Th /^{232}Th)	Uncertainty	Uncorrected age [ka]	Uncertainty [ka]	Corrected Age [ka]	Uncertainty [ka]
HBSH-4-1.9	19.0	7.369	0.073	173.13	0.98	1.181	0.002	0.0509	0.0054	4.4	0.1	5.83	0.07	4.79	0.52
HBSH-4-2.3*	23.0	8.998	0.064	143.71	0.91	1.185	0.001	0.0556	0.0037	3.5	0.0	6.75	0.09	5.22	0.35
HBSH-4-2.6	26.0	0.400	0.004	236.87	1.45	1.171	0.002	0.0612	0.0007	111.7	1.5	5.89	0.06	5.85	0.07
HBSH-4-5.4	54.0	0.131	0.002	268.41	1.57	1.132	0.002	0.0618	0.0010	386.8	7.6	6.12	0.10	6.11	0.10
HBSH-4-5.8	58.0	0.205	0.003	262.36	1.62	1.129	0.002	0.0636	0.0008	250.1	4.1	6.33	0.08	6.31	0.08
HBSH-4-7.8	78.0	0.231	0.003	288.26	1.72	1.160	0.002	0.0643	0.0010	246.3	4.8	6.22	0.10	6.12	0.10
HBSH-4-9.8	98.0	0.163	0.002	276.67	1.70	1.160	0.002	0.0664	0.0008	346.1	5.7	6.43	0.08	6.41	0.08
HBSH-4-13.5	135.0	0.093	0.001	328.15	1.89	1.157	0.002	0.0700	0.0007	758.0	10.2	6.81	0.07	6.80	0.07
HBSH-4-16.7	167.0	0.000	0.001	303.52	1.84	1.159	0.002	0.0721	0.0008	173071.5	472258.2	6.99	0.08	6.99	0.08
HBSH-4-18.3	183.0	1.506	0.015	302.81	1.75	1.138	0.002	0.0742	0.0008	46.4	0.5	7.47	0.06	7.34	0.08
HBSH-4-18.7	187.0	3.763	0.050	281.12	1.60	1.134	0.002	0.0697	0.0024	16.7	0.4	7.24	0.17	6.90	0.24
HBSH-4-20.5	205.0	1.045	0.011	296.24	2.11	1.155	0.005	0.0785	0.0009	68.8	0.9	7.75	0.09	7.67	0.10
HBSH-4-20.8	208.0	13.369	0.132	281.26	1.61	1.156	0.002	0.0720	0.0060	5.4	0.1	8.19	0.10	7.00	0.59
HBSH-4-21.8	218.0	5.615	0.055	200.84	1.14	1.155	0.002	0.0788	0.0035	9.4	0.1	8.39	0.08	7.70	0.36
HBSH-4-22.4*	224.0	12.987	0.089	191.34	1.20	1.187	0.001	0.0833	0.0038	4.5	0.0	9.57	0.08	7.91	0.38
HBSH-4-23.1	231.0	7.632	0.076	245.08	1.41	1.182	0.002	0.0989	0.0038	10.4	0.1	10.27	0.08	9.51	0.37
HBSH-4-23.7	237.0	3.146	0.032	242.88	1.47	1.155	0.003	0.1029	0.0017	25.0	0.3	10.48	0.09	10.16	0.19
HBSH-4-24.0	240.0	1.048	0.011	307.01	1.85	1.177	0.002	0.1091	0.0009	98.4	1.1	10.66	0.09	10.58	0.09
HBSH-4-24.8*	248.0	BDL	BDL	281.40	1.79	1.180	0.001	0.1096	0.0028	NA	NA	10.59	0.28	10.59	0.28
HBSH-4-26.7	267.0	2.244	0.023	306.56	1.89	1.206	0.002	0.1187	0.0012	50.3	0.5	11.45	0.09	11.27	0.12
HBSH-4-27.8	278.0	0.356	0.010	298.43	1.84	1.204	0.002	0.1180	0.0025	303.4	10.7	11.27	0.26	11.22	0.26
HBSH-4-28.5*	285.0	0.613	0.005	292.35	1.84	1.208	0.001	0.1205	0.0008	176.2	1.4	11.47	0.07	11.42	0.08
HBSH-4-29.4	294.0	0.918	0.010	291.94	1.92	1.217	0.004	0.1395	0.0011	136.4	1.5	13.31	0.11	13.24	0.12
HBSH-4-29.9	299.0	1.340	0.013	318.18	1.85	1.222	0.002	0.1425	0.0010	104.2	1.0	13.57	0.09	13.48	0.10
HBSH-4-30.2	302.0	7.717	0.076	359.05	2.08	1.228	0.002	0.1438	0.0027	21.2	0.2	14.04	0.13	13.54	0.28
HBSH-5-0.3	3.0	2.162	0.021	172.21	1.18	3.042	0.013	0.2216	0.0021	54.6	0.5	8.30	0.07	8.18	0.09
HBSH-5-0.7	7.0	5.670	0.057	205.14	1.20	3.283	0.009	0.2544	0.0032	28.7	0.3	8.96	0.06	8.72	0.12
HBSH-5-1.3	13.0	1.708	0.023	68.17	0.45	3.324	0.009	0.2650	0.0037	32.9	0.5	9.19	0.10	8.98	0.13
HBSH-5-2.5	25.0	7.054	0.114	211.18	1.30	3.320	0.014	0.2788	0.0056	26.1	0.6	9.76	0.16	9.47	0.21
HBSH-5-3.5	35.0	32.228	0.559	2196.37	16.80	3.342	0.015	0.2936	0.0055	61.8	1.5	10.05	0.19	9.89	0.25

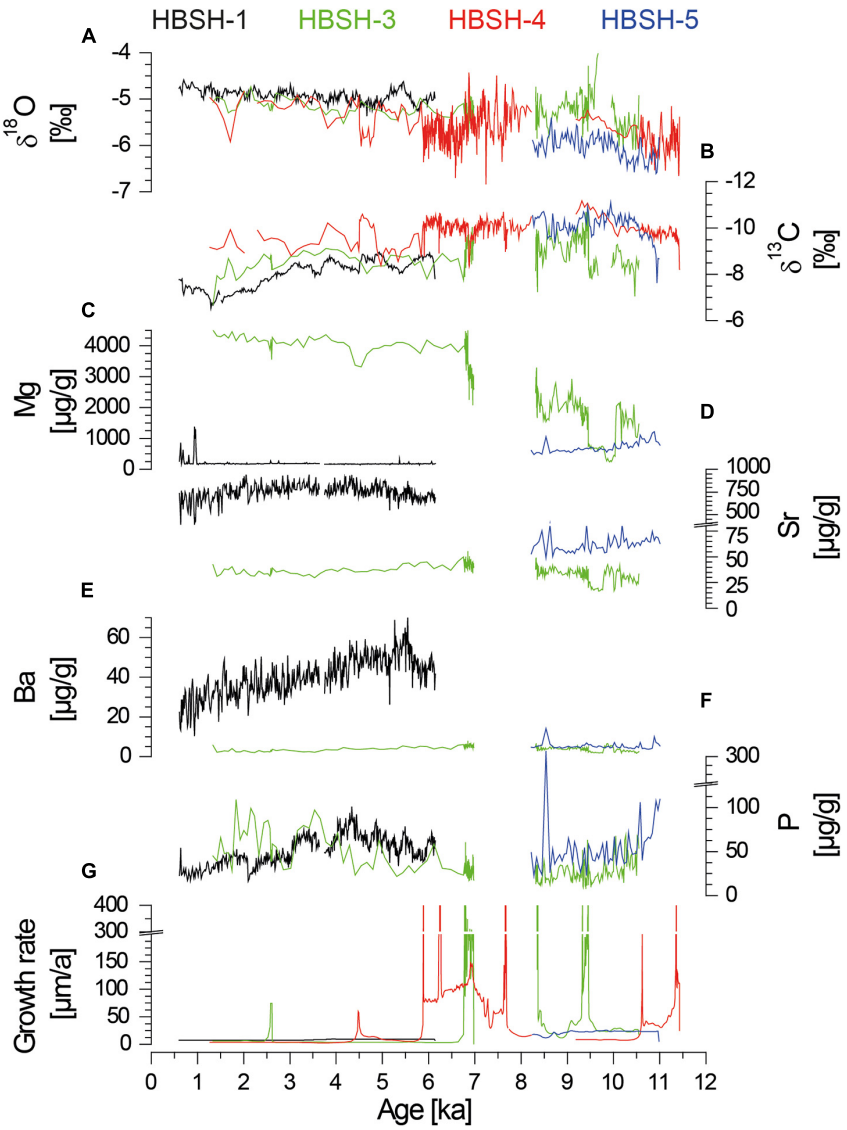

FIGURE 4 | Proxy data for stalagmites HBSH-1 (black), HBSH-3 (green), HBSH-4 (red) and HBSH-5 (blue) based on the age-depth model. **(A)** $\delta^{18}O$ and **(B)** $\delta^{13}C$ values. **(C)** Mg, **(D)** Sr, **(E)** Ba, and **(F)** P concentrations. **(G)** Growth rate. Note the inverted axis for $\delta^{13}C$ and the breaks in the *y*-axis for Sr, P, and growth rate.

(**Figure 4** and **Supplementary Figure A4**). Therefore, the stable isotope and trace element data shows high variability in temporal resolution. The aim of this study is to identify common long-term trends in the proxy records of the different samples, independent of the absolute $\delta^{13}C$ and $\delta^{18}O$ values, as well as trace element concentrations. To overcome potential biases due to differences in age resolution, centennial means for the stable isotope and trace element data were calculated. This is also a basic requirement for regression analysis (see sections "Within-cave correlation of speleothem records from HBSH and Bunker Cave" and "Inter-cave correlation of speleothem records from HBSH and Bunker Cave"), which was performed with the centennial stable isotope data using the statistical software R (R Core Team, 2020). The stalagmite samples differ in their mineralogy (i.e., aragonite and calcite) as well as growth rate and absolute $\delta^{13}C$ and $\delta^{18}O$ values. These differences can cause steps in the stacked isotope time series, which is particularly important for intervals of low replication, and if only a single stalagmite is available for a specific time interval. To avoid steps in the final dataset (**Figures 4**, **5**), a composite stack for HBSH (**Figure 5**) was constructed using scaled stable isotope data of each speleothem. Scaling was performed using the "scale()" function of the statistical software R (R Core Team, 2020) and refers to subtraction of the mean and division by the standard deviation for each time series. Due to the scaling, differences in absolute $\delta^{13}C$ and $\delta^{18}O$ values can be neglected. After calculating the scaled stable isotope data for each stalagmite, a composite stack was constructed using the previously calculated centennial means of all HBSH stalagmites. The number of individual analyses, which were arithmetically averaged for each mean value (replication), are also provided. These calculations were not only performed for HBSH, but also for the stable isotope values from

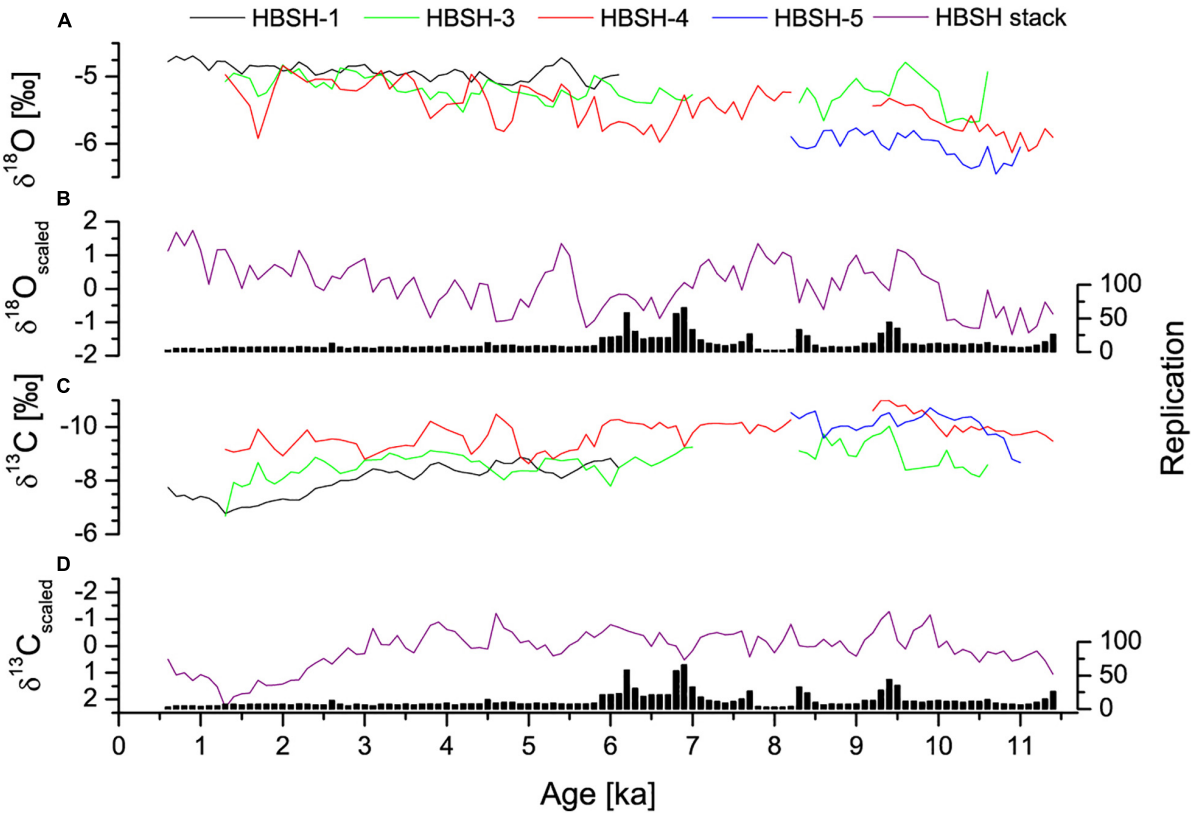

FIGURE 5 | (A) $\delta^{18}O$ and **(C)** $\delta^{13}C$ values averaged by a centennial mean for stalagmites HBSH-1 (black), HBSH-3 (green), HBSH-4 (red), and HBSH-5 (blue). Scaled stable isotope time series for $\delta^{18}O$ values **(B)** and $\delta^{13}C$ values **(D)**. For all records, the replication indicates the number of stable isotope measurements averaged for the centennial mean for the specific time interval. Note the inverted axis for $\delta^{13}C$.

stalagmites from Bunker Cave covering the same time interval (Fohlmeister et al., 2012). Principal component analysis (PCA) was performed with the centennial means for stable isotope and trace elements and the "fviz_pca_biplot()" function of the statistical software R (R Core Team, 2020) and centennial means were calculated for stable isotopes and trace elements. To test the suitability of our dataset for PCAs and justify this approach, the Kaiser-Meyer-Olkin test for sampling adequacy (>0.5; Kaiser, 1970; Kaiser and Rice, 1974) and Bartlett's test of sphericity (<0.05; Bartlett, 1937) were employed. Sample HBSH-5 did not pass the Kaiser-Meyer-Olkin test. Only principal components (PCs) with a standard deviation > 1.0 were considered and a cut-off value of 0.4 was chosen to describe the most important parameters of the PCA (Budaev, 2010). Detailed results including eigenvalues and factor loadings are presented in **Supplementary Table A1**. To evaluate the relationship between trace element and stable isotope data, a correlation analysis was performed using the statistical software R (R Core Team, 2020).

Strontium Isotope Analyses

Strontium isotope ratios ($^{87}Sr/^{86}Sr$) were determined for speleothem samples HBSH-3 (n = 9), HBSH-4 (n = 9), and HBSH-5 (n = 3). The samples (2 – 7 mg) were processed at the Institute for Geosciences, using a laminar flow hood in a clean laboratory, following the methods described by Lugli et al. (2017) and Weber et al. (2018b) for dissolution and separation of Sr using Sr-spec resin. $^{87}Sr/^{86}Sr$ ratios were determined at the MPIC using a Nu Plasma MC-ICP-MS coupled to a CETAC Aridus II desolvating nebulizing system following the methods described by Weber et al. (2017). Ion beams were simultaneously collected using seven Faraday cups covering the m/z range of 82 – 88, representing the following isotopes: ^{82}Kr, ^{83}Kr, ^{84}Sr, ^{85}Rb, ^{86}Sr, ^{87}Sr, and ^{88}Sr. Strontium solutions were diluted to approximately 50 µg/mL and measured in a standard-bracketing sequence, correcting for a NIST SRM 987 $^{87}Sr/^{86}Sr$ ratio of 0.710248 (McArthur et al., 2001). Correction for instrumental mass bias was performed using an exponential law, using a $^{88}Sr/^{86}Sr$ ratio of 8.375209 (Steiger and Jäger, 1977).

RESULTS

$^{230}Th/U$-Dating

Results of the $^{230}Th/U$-dating are presented in **Table 1**. Resulting age-depth models of all speleothem samples are presented in **Figure 3**, and all following ages refer to the age models resulting from StalAge (Scholz and Hoffmann, 2011). The studied section of speleothem HBSH-1 shows slow continuous growth between

6.1 ± 0.6 ka and 0.60 ± 0.06 ka with a stable growth rate of 8 μm/a (calculated based on the age-depth model). Sample HBSH-3 shows a more complex growth history. Two measurements yielded ages of 13.3 ± 0.2 ka and 12.4 ± 0.2 ka corresponding to the Bølling-Allerød. These ages were not included in the age model. Growth during the Holocene started at 10.8 ± 1.6 ka and continued at least until 8.3 ± 0.2 ka with the fastest growth rate (>100 μm/a) between 9.5 and 9.0 ka. A growth stop between 8.3 ± 0.2 ka and 7.0 ± 0.2 ka is indicated by the age-depth model and is followed by a phase of slow growth (6 μm/a) until the final stop at 1.3 ± 0.2 ka. The growth history of speleothem HBSH-4 is similar to HBSH-3 with an initial growth phase during the Bølling-Allerød between 13.6 ± 0.3 ka and 13.2 ± 0.1 ka, followed by a growth stop until 11.4 ± 0.1 ka, representing a growth inception shortly after the onset of the Holocene at 11.7 ± 0.1 ka. The initial growth phase for HBSH-4 lasted until 9.2 ± 0.4 ka and shows a deceleration from >30 μm/a to <10 μm/a toward a hiatus. Growth resumed around 8.2 ± 0.4 ka, and fast continuous growth (60 – 100 μm/a) is observed until 5.8 ± 0.1 ka, where a distinct growth deceleration (<10 μm/a) occurred, lasting until at least 3.7 ± 0.1 ka. The youngest age obtained from HBSH-4 is 1.3 ± 0.3 ka, and a continuous growth of approximately 3 μm/a until then is assumed. Speleothem HBSH-5 shows continuous growth between 9.9 ± 0.3 ka and 8.2 ± 0.1 ka and a rather constant growth rate of ≈20 μm/a for most of the studied part of the specimen. Only the youngest part shows a decelerating growth rate down to ≈10 μm/a between 8.7 ± 0.1 ka and 8.2 ± 0.1 ka.

Trace Elements

Trace element records of HBSH-1, -3, and -5 of Mg, P, Sr and Ba are presented in **Figure 4** and **Supplementary Figures A1–A3**.

Since HBSH-1 consists of aragonite (in contrast to the calcite speleothems HBSH-3 and HBSH-5), its trace element concentrations differ significantly from those of the other stalagmites (c.p., Wassenburg et al., 2016b). Magnesium in HBSH-1 is low (≈180 μg/g) for major parts of the sample except for some spikes, during the most recent 1000 years. For the whole growth phase, no general increasing or decreasing trend in Mg is visible. The Sr concentration is relatively high in comparison to the calcite speleothems, increasing from 500 to 800 μg/g towards more recent ages until 3.5 ± 0.1 ka. Afterward, this trend is reversed. The same pattern is visible in P, while Ba decreases on a longer time scale toward younger ages.

HBSH-3 has a much higher Mg concentration (1000 and 4500 μg/g). In general, Mg increases toward younger ages, especially in the second growth phase between 7.0 ± 0.2 ka and 1.3 ± 0.2 ka. Strontium and Ba show a similar trend with increasing concentrations until the growth stop and decreasing concentrations after growth resumed at 7.0 ± 0.2 ka. The opposite trend is true for P. A prominent feature is the decrease in concentration for Mg, Sr and Ba around 9.5 ± 0.2 ka.

HBSH-5 does not show large trace element variations besides an increase in Mg, Ba, and P around 8.5 ± 0.2 ka, which is contemporaneous with a decrease in Sr concentration. In general, all four observed trace element concentrations decrease toward the growth stop around 8.2 ± 0.1 ka.

Stable Isotopes

The $\delta^{13}C$ values are presented in **Figure 4B**. Since the four speleothems show different growth rates, a centennial mean based on the age-depth model for each speleothem sample (**Figure 5C**) was calculated to focus on longer-term trends. Stalagmites HBSH-3 and HBSH-4 started to grow at the beginning of the Holocene, or shortly after, while growth of HBSH-5 re-initiated at that time. The three stalagmites start with similar $\delta^{13}C$ values (between −8 and −9 ‰) and then rapidly tend toward more negative values until reaching their most negative values around 9.5 ka. HBSH-3 and HBSH-4 also reached their most negative $\delta^{13}C$ values almost simultaneously around 9.4 ± 0.1 ka, when HBSH-5 also shows a negative peak in $\delta^{13}C$. Shortly afterward, HBSH-4 stopped growing, while HBSH-3 and HBSH-5 continued to grow until 8.3 ± 0.2 ka and 8.2 ± 0.1 ka, respectively, and show again less negative $\delta^{13}C$ values. HBSH-4 started growing again around 8.2 ± 0.4 ka with $\delta^{13}C$ values fluctuating between −10 and −9 ‰ with two negative peaks around 4.6 ± 0.2 ka and 3.8 (+0.6, −0.2) ka. HBSH-3 started to grow again at 7.0 ± 0.2 ka with a trend toward less negative $\delta^{13}C$ values, which was further intensified after 3.0 ± 0.3 ka, reaching a peak $\delta^{13}C$ value of −6.7 ‰ at 1.3 ± 0.2 ka, coherent with the final growth stop. The Holocene growth phase of the aragonitic speleothem HBSH-1 commenced at 6.1 ± 0.6 ka with an initial decrease in $\delta^{13}C$ values, followed by a long-term trend toward more negative values, similar to HBSH-3. Negative $\delta^{13}C$ peaks occur in HBSH-1 at 6.0 ± 0.1 ka, 4.6 ± 0.1 ka and 3.9 ± 0.1 ka, all coherent with peaks in $\delta^{13}C$ values in HBSH-4. When HBSH-1 reached its most positive $\delta^{13}C$ value of −6.5 ‰ at 1.3 ± 0.2 ka, HBSH-3 and HBSH-4 stopped growing, while HBSH-1 continued to grow with decreasing $\delta^{13}C$ values until the final growth stop at 0.6 ± 0.1 ka.

Oxygen isotope results of all the HBSH speleothems show a general trend toward less negative $\delta^{18}O$ values during the Holocene. As the $\delta^{13}C$ values, the $\delta^{18}O$ values (**Figure 4A**) show more variable values on annual to decadal time scales. To focus on the long-term trends, centennial means of the $\delta^{18}O$ values (**Figure 5A**) were computed. In contrast to the $\delta^{13}C$ values, the $\delta^{18}O$ values show a more coherent trend in all speleothems. After an initial decrease shortly after growth inception in HBSH-3, HBSH-4 and HBSH-5, these three speleothems show a trend toward less negative $\delta^{18}O$ values until their growth stops at 9.2 ± 0.4 ka (HBSH-4), 8.3 ± 0.2 ka (HBSH-3) and 8.2 ± 0.1 ka (HBSH-5). The least negative $\delta^{18}O$ value of all speleothems is observed in HBSH-3 around 9.6 ± 0.1 ka (−4.6 ‰) and is in agreement with less negative values in HBSH-4 and HBSH-5. Subsequent to the growth stops in HBSH-3 and HBSH-4, both speleothem samples show less negative $\delta^{18}O$ values, although HBSH-4 shows a decrease between 6.7 ± 0.3 ka and 5.8 ± 0.4 ka. Growth in the Holocene part of HBSH-1 started at 6.1 ± 0.6 ka and also tends to less negative $\delta^{18}O$ values throughout the Holocene. The most prominent positive peak in $\delta^{18}O$ values in HBSH-1 occurred around 5.4 ± 0.1 ka. HBSH-4 shows a coherent increase in $\delta^{18}O$ values during that time. HBSH-1 does not show any further prominent $\delta^{18}O$ peaks until its growth stopped around 0.6 ± 0.1 ka. However, HBSH-3 and HBSH-4 show a further trend toward

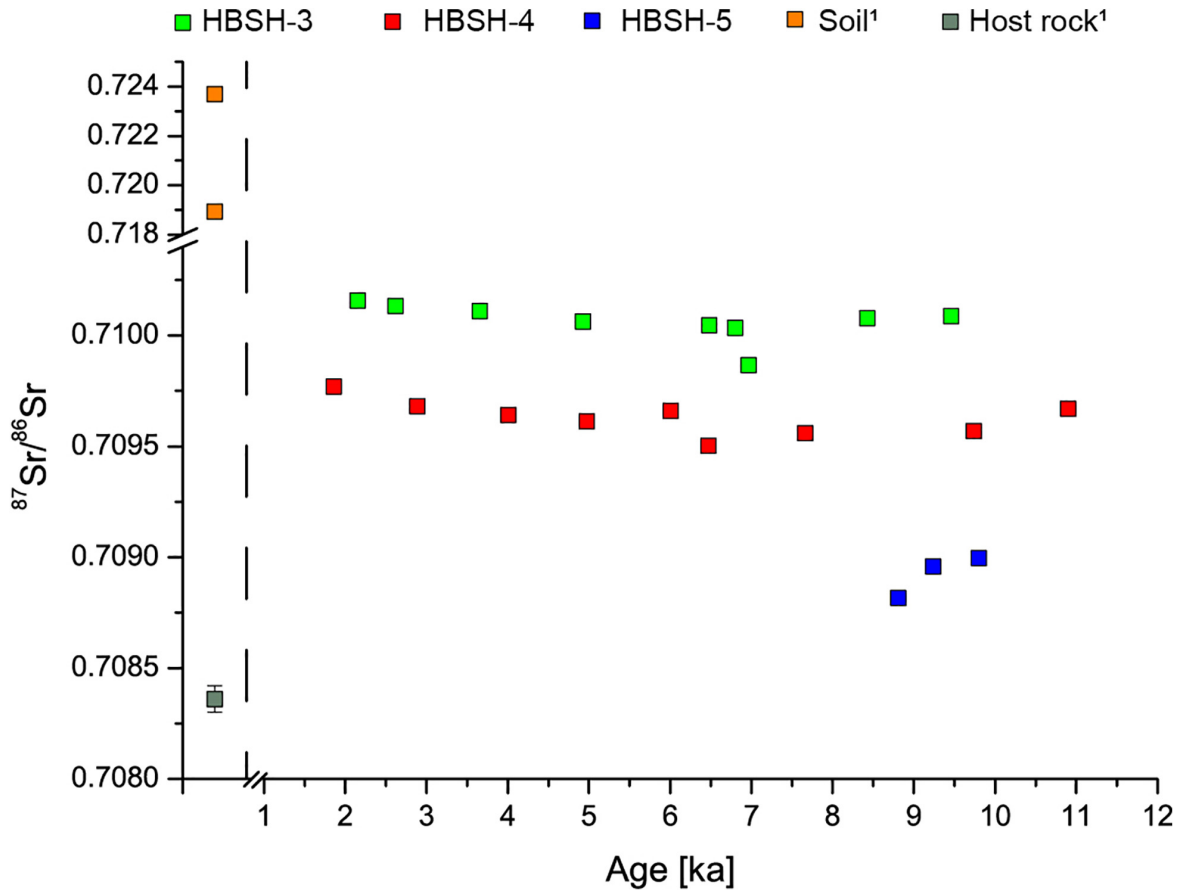

FIGURE 6 | Strontium isotope results for HBSH-3 (green), HBSH-4 (red), and HBSH-5 (blue). ^{1}Sr isotope values from the host rock and overlying soil at the nearby Bunker Cave (Weber et al., 2018a). Note that analytical uncertainties are usually smaller than the plot symbols.

less negative $\delta^{18}O$ values around 1.7 ± 0.5 ka, which is not reflected in HBSH-1.

Strontium Isotopes

HBSH-5 shows the least radiogenic $^{87}Sr/^{86}Sr$ ratios of 0.70899 ± 0.00002 at 9.8 ± 0.2 ka and 0.70882 ± 0.00002 at 8.8 ± 0.1 ka, followed by a strongly decreasing trend toward modern time (**Figure 6**). HBSH-4 shows the same trend in the older growth section toward lower Sr isotope ratios. However, the $^{87}Sr/^{86}Sr$ ratios of HBSH-4 are overall higher with values between 0.70950 ± 0.00002 and 0.70977 ± 0.00002. The lowest value of 0.70950 ± 0.00002 is observed at 6.5 ± 0.1 ka, followed by an increase toward 0.70966 ± 0.00002 at 6.0 ± 0.1 ka. Toward the final growth stop of HBSH-4 at 1.3 ± 0.2 ka, the $^{87}Sr/^{86}Sr$ ratio becomes progressively higher. HBSH-3 shows the highest Sr isotope ratios, with all $^{87}Sr/^{86}Sr$ values above 0.70987 ± 0.00002. While the first growth phase shows identical $^{87}Sr/^{86}Sr$ within uncertainties (0.71009 ± 0.00002 and 0.71008 ± 0.00002), the second growth phase shows the lowest $^{87}Sr/^{86}Sr$ of 0.70987 ± 0.00002 at 7.0 ± 0.2 ka. Afterward, the values increase toward 0.71003 ± 0.00002 at 6.8 ± 0.2 ka and progressively become higher toward younger ages with a maximum $^{87}Sr/^{86}Sr$ ratio of 0.71016 ± 0.00002 at 2.2 ± 0.2 ka.

DISCUSSION

Growth Phases

The four HBSH speleothem samples cover almost the entire Holocene, except the most recent 600 years. Earlier growth phases were identified between 13.6 ± 0.3 ka and 13.3 ± 0.1 ka for HBSH-4 and between 13.3 ± 0.2 ka and 12.4 ± 0.2 ka for HBSH-3 (**Table 1**). These initial growth phases correspond to the Bølling-Allerød interstadial (Köhler et al., 2011).

Based on the age-depth model of HBSH-4, growth during the Holocene commenced at 11.4 ± 0.1 ka. Growth of HBSH-5 re-initiated shortly afterward at 11.0 ± 0.4 ka. Based on the age model, a simultaneous growth start is possible, but this cannot be resolved. The onset of growth in HBSH-3 occurred around 10.6 ± 0.6 ka, which is shortly after HBSH-4 and HBSH-5. Therefore, it is presumed that the climate amelioration at the onset of the Holocene triggered speleothem growth in

HBSH between about 11.4 and 10.6 ka. Between 10.6 and 9.2 ka, the three speleothems grew simultaneously until HBSH-4 stopped at 9.2 ± 0.4 ka. Interestingly, when growth of HBSH-3 and HBSH-5 had stopped (8.3 ± 0.2 ka), HBSH-4 started to grow again at 8.2 ± 0.4 ka with a growth rate rapidly increasing from <10 μm/a to up to >100 μm/a (**Figure 4G** and **Supplementary Figure A4**). HBSH-4 growth rate declined after 6.0 ± 0.1 ka to <10 μm/a. The growth rate of HBSH-3 declined around 6.5 ± 0.4 ka with values <10 μm/a in the same range as observed for HBSH-4 (**Figure 4G** and **Supplementary Figure A4**). Growth of HBSH-1 between 6.1 ± 0.6 ka and 0.6 ± 0.1 ka was continuous for the whole growth period, but the growth rate was very small (< 10 μm/a) and agrees with the rates observed in HBSH-3 and HBSH-4, although those are more variable (**Figure 4G** and **Supplementary Figure A4**). In general, the older growth phase during the first half of the Holocene was characterized by higher growth rates than the younger phase. The transition between these two phases in HBSH occurred between 7 and 6 ka and was marked by a reduction in growth rate. This is evident from all four speleothems from HBSH: the two speleothems covering this transition (HBSH-3 and HBSH-4) as well as the two stalagmites that only grew during one of these phases (HBSH-5 in the older phase and HBSH-1 in the younger phase).

Stable Isotopes

The $\delta^{18}O$ values of all Holocene HBSH speleothems show the same increasing trend on the long time-scale (**Figures 4A**, **5A**). At the onset of the Holocene, $\delta^{18}O$ values are lowest in the three coeval specimens HBSH-3, HBSH-4, and HBSH-5, although their absolute values differ. A first peak in $\delta^{18}O$ values is reached around 9.4 ka, with maximum values in HBSH-3 and HBSH-4. HBSH-5 reached a stable value of ca. −5.5 ‰ at that time and remained at that level until the final growth stop at 8.2 ± 0.1 ka. In HBSH-3, the $\delta^{18}O$ values slightly decrease until the growth stop at 8.3 ± 0.2 ka. Simultaneously, HBSH-4 started to grow again with less negative values than prior to the growth stop and remained at that level (ca. −5 ‰) until 7.0 ± 0.1 ka. At that time, $\delta^{18}O$ values decrease by around 1 ‰ and HBSH-3 started to grow again. From that on, the $\delta^{18}O$ values increase progressively until growth finally stopped. When HBSH-1 started to grow at 6.1 ± 0.6 ka, the $\delta^{18}O$ values also progressively increased until the least negative $\delta^{18}O$ value of −4.7 ‰ at 0.6 ± 0.1 ka. After 5 ka, the three coeval speleothems show comparable $\delta^{18}O$ values.

For speleothem $\delta^{18}O$ values, the major influencing factors are the cave temperature and the $\delta^{18}O$ value of precipitation above the cave. The $\delta^{18}O$ value of modern precipitation in the cave region varies between −5 ‰ in summer and −13 ‰ in winter, resulting in an infiltration-weighted $\delta^{18}O$ value of −8.1 ‰ (Riechelmann et al., 2017). In comparison to the nearby Bunker Cave, the $\delta^{18}O$ values in the younger parts of the HBSH samples are less negative. Recent calcite precipitates from Bunker Cave show a relationship between $\delta^{18}O$ values and drip rate. The calcite $\delta^{18}O$ values for a fast-dripping site are −6.3 ± 0.3 ‰ and −5.6 ± 0.2 ‰ for a slow dripping site (Riechelmann et al., 2013). Hence, it is reasonable to assume that the high $\delta^{18}O$ values of the HBSH stalagmites indicate very slow drip rates. However, considering that the $\delta^{18}O$ values of the HBSH stalagmites are generally higher than those of the Bunker Cave stalagmites, they were probably also influenced by additional factors. In Bunker Cave, Holocene $\delta^{18}O$ variability has been mainly attributed to changes in winter precipitation and temperature (Fohlmeister et al., 2012). In that study, less negative speleothem $\delta^{18}O$ values were interpreted to reflect cold and dry winters and vice versa. In HBSH, this interpretation would indicate a trend toward colder and dryer winters during the course of the Holocene. Besides climatic factors, disequilibrium isotope fractionation can influence the $\delta^{18}O$ values of speleothems (Lachniet, 2009; Mühlinghaus et al., 2009; Deininger et al., 2012; Hansen et al., 2019). Since a trend toward slower growth rates with time in the HBSH speleothems is observed, these disequilibrium effects may have altered the $\delta^{18}O$ values due to increasing drip intervals (Hendy, 1971; Lachniet, 2009; Riechelmann et al., 2013; Dreybrodt et al., 2016; Hansen et al., 2019), causing $\delta^{18}O$ values to increase. In addition, prior calcite precipitation (PCP) is another factor potentially influencing the stable isotope signals.

The HBSH speleothems show generally different $\delta^{13}C$ values during the first and the second part of the Holocene, starting around 7 – 6 ka (**Figures 4B**, **5C**). After growth inception, the $\delta^{13}C$ values tend toward more negative values in HBSH-4 and HBSH-5, which is most likely related to the climate amelioration at the onset of the Holocene. Increased biological activity and vegetation development in the newly formed soil results in more negative $\delta^{13}C$ values, due to the biological fractionation of carbon in the soil with increased biological activity (McDermott, 2004). This trend is less clear for HBSH-3. However, this might be related to a later onset of growth of this speleothem, where the overlying soil and vegetation was already established. The most negative peak in $\delta^{13}C$ is reached around 9.4 ka in HBSH-3 and HBSH-4, with HBSH-5 showing a negative peak as well. This is coherent with a maximum in $\delta^{18}O$ of these three speleothems (**Figures 4**, **5**). In general, this older phase seems to be characterized by increased soil biological activity and root respiration, indicating relatively warm and humid climate conditions during the early Holocene at HBSH. Interestingly, HBSH-4 stopped growing shortly after reaching its most negative $\delta^{13}C$ values, while HBSH-5 remains at that $\delta^{13}C$ level and HBSH-3 shows a slight trend toward less negative values until these stalagmites stopped to grow at 8.3 ± 0.2 ka and 8.2 ± 0.1 ka, respectively. At the same time, HBSH-4 resumed growth with $\delta^{13}C$ values around −10 ‰ and the highest growth rate of the entire stalagmite. The negative $\delta^{13}C$ values and the high growth rate suggest favorable climate conditions at that time, consistent with the Holocene climate optimum (Mayewski et al., 2004). HBSH-3 started to grow again at 7.0 ± 0.2 ka with a high growth rate and $\delta^{13}C$ values around -9.5 ‰. However, growth rate in HBSH-3 rapidly declined after re-inception of growth and the $\delta^{13}C$ values increase toward −8 to −8.5 ‰. This pattern is also visible in HBSH-4 around 6 ka, where the $\delta^{13}C$ values increase by more than 1 ‰ and

growth rate declined to less than 10 μm/a. This coherent pattern indicates reduced water availability in the karst system, which can either be related to a climatic deterioration or hydrological changes in the epikarst and the vadose zoneresulting in reduced water availability in the cave. Due to the observed time lag of approximately 1,000 years between the two samples, this can potentially be caused by delayed changes in the water circulation routes in the overlying karst aquifer. Shortly before the transition toward less negative $\delta^{13}C$ values and slower growth rates in HBSH-4, stalagmite HBSH-1 recommenced growing at 6.1 ± 0.6 ka. The initial $\delta^{13}C$ values changed rapidly toward more negative values, before reaching a minimum at 6.0 ± 0.1 ka. Further on, $\delta^{13}C$ values of HBSH-1 progressively increased. The same trend is visible in HBSH-3, while the low growth rate of HBSH-4 resulted in smoothed signals. However, some coherent patterns can be identified. At 5 ka, HBSH-1 and HBSH-4 show a simultaneous decrease in $\delta^{13}C$ until 4.5 ka, where $\delta^{13}C$ values increase in both stalagmites. A second $\delta^{13}C$ minimum is observed in all three speleothems at 4 ka. However, the general trend of $\delta^{13}C$ values is still toward higher values, reaching their maximum at 1.3 ± 0.2 ka, when HBSH-3 and HBSH-4 finally stopped growing. In contrast, HBSH-1 continued to grow with a constant growth rate and decreasing $\delta^{13}C$ values (−7.8 ‰ at 0.6 ± 0.1 ka).

Changes in $\delta^{13}C$ values of speleothems have often been related to environmental and climatic factors, such as vegetation cover and soil biological activity. However, due to changes in the stalagmite growth rates, (disequilibrium) isotope fractionation during speleothem deposition may introduce substantial biases. For instance, an increase in $\delta^{13}C$ values may not only reflect decreasing availability of soil CO_2, but also a decrease in drip rate, i.e., a longer residence time of the drip water on the speleothem surface, enhancing disequilibrium isotope fractionation (Mühlinghaus et al., 2009; Scholz et al., 2009; Deininger et al., 2012; Riechelmann et al., 2013). Since growth rate remarkably dropped in all speleothems around 7 – 6 ka, it is likely that the average drip interval in HBSH increased. This is a potential cause for the progressive increase in $\delta^{13}C$ values of HBSH-1, HBSH-3, and HBSH-4 during the second half of the Holocene, because their growth rates are below <10 μm/a during that time interval. In contrast, the first part of the Holocene was characterized by a faster growth rate and decreasing $\delta^{13}C$ values in HBSH. During this time interval, isotope disequilibrium effects on the speleothem surface played a minor role and the decreasing trend likely reflects increasing vegetation density, soil cover and biological activity.

Trace Elements

Trace elements in HBSH-5 show a decreasing trend toward the growth stop (**Figure 4** and **Supplementary Figure A3**). At 8.5 ± 0.2 ka, Mg, P, and Ba increases, while Sr decreases. This timing is coherent with the negative peaks in $\delta^{13}C$ and $\delta^{18}O$. In general, the correlation between the four investigated trace elements is positive, with Ba and P showing the highest correlation of $R = 0.70$ (**Supplementary Figure A5**, $p < 4 \times 10^{-4}$). In addition, there is a positive correlation of $R = 0.49$ between $\delta^{13}C$ and Mg ($p < 7 \times 10^{-3}$), indicating PCP. Since the decrease in $\delta^{13}C$ values is attributed to soil formation and increasing biological activity, the decrease in Mg seems to be also related to these processes, i.e., enhanced soil bioproductivity and wet conditions causing lower Mg concentrations (Riechelmann et al., 2012; Wassenburg et al., 2016b; Weber et al., 2018a). Furthermore, the decrease in Mg is similar as during the initial Holocene phase in Bunker Cave (Fohlmeister et al., 2012). The authors attributed this pattern to the deposition of Mg-bearing loess during the previous glacial period and the progressive leaching of carbonate from the loess in the early Holocene. Due to the close proximity (<1 km) to Bunker Cave, the same should be true for HBSH and is an additional explanation for the Mg trend observed in HBSH-5. Since HBSH-5 only covers the early part of the Holocene, the transition observed in the growth rate and stable isotopes is not captured by this speleothem. However, HBSH-3 covers most parts of the Holocene besides the hiatus between 8.3 ± 0.2 ka and 7.0 ± 0.2 ka. Therefore, changes between the two different phases in HBSH-3 are expected. The first growth phase of HBSH-3 shows lower Mg concentrations than the second one. This transition is visible in the results of the PCA (**Figure 7B**), where Mg separates the early (11.5 – 8.1 ka) and late (7.0 – 1.1 ka) growth phases along PC2. In addition, $\delta^{13}C$ values are lower in the first growth phase. For the $\delta^{13}C$ values, the PCA especially separates the growth phases between 9.3 – 8.1 ka and 4.0 – 1.1 ka along PC1. Based on the assumption proposed for HBSH-5, the first phase is expected to have been wetter and more strongly influenced by soil formation and biological activity. Due to the increase of Mg over time, the Mg concentration is positively correlated with the $\delta^{18}O$ values ($R = 0.51$, $p < 7 \times 10^{-3}$, **Supplementary Figure A6**). Similar or even higher correlations exist between Mg and Sr ($R = 0.51$, $p < 6 \times 10^{-6}$) and Ba and Sr ($R = 0.78$, $p < 2 \times 10^{-14}$), indicating the same source for Ba and Sr, most likely the host rock. However, the correlation between Sr and Mg is mainly based on the first growth phase, where Ba, Sr, and Mg increase. This is clearly visible in the correlation matrix in **Figure 8A**, where only data from the first growth phase (10.6 ± 0.6 to 8.3 ± 0.2 ka) are shown. Strontium and Ba show a strongly positive correlation ($R = 0.92$, $p < 1 \times 10^{-16}$), as well as Sr and Mg ($R = 0.72$, $p < 1 \times 10^{-16}$) and Ba and Mg ($R = 0.53$, $p < 1 \times 10^{-16}$). Magnesium, however, is slightly negatively correlated with $\delta^{13}C$ ($R = -0.19$, $p < 0.04$) and $\delta^{18}O$ ($R = -0.24$, $p < 0.005$). In the second growth phase (7.0 ± 0.2 ka to 1.3 ± 0.2 ka), Mg further increases, while Ba and Sr decrease. The correlation matrix for the younger part (**Figure 8B**) shows, that Mg is positively correlated with both stable isotopes during this time span ($\delta^{13}C$ $R = 0.41$, $p < 5 \times 10^{-6}$, $\delta^{18}O$ $R = 0.23$, $p < 0.02$). Furthermore, Mg is slightly negatively correlated with Ba ($R = -0.39$, $p < 3 \times 10^{-6}$), while Sr and Ba still show a strong positive correlation ($R = 0.92$, $p < 1 \times 10^{-16}$). This indicates an additional process during the younger part of the Holocene, which overprints the host rock signal for the trace elements and disrupts the relationship between Sr, Ba, and Mg, e.g., growth mechanisms of the speleothems (e.g., Paquette and Reeder, 1995;

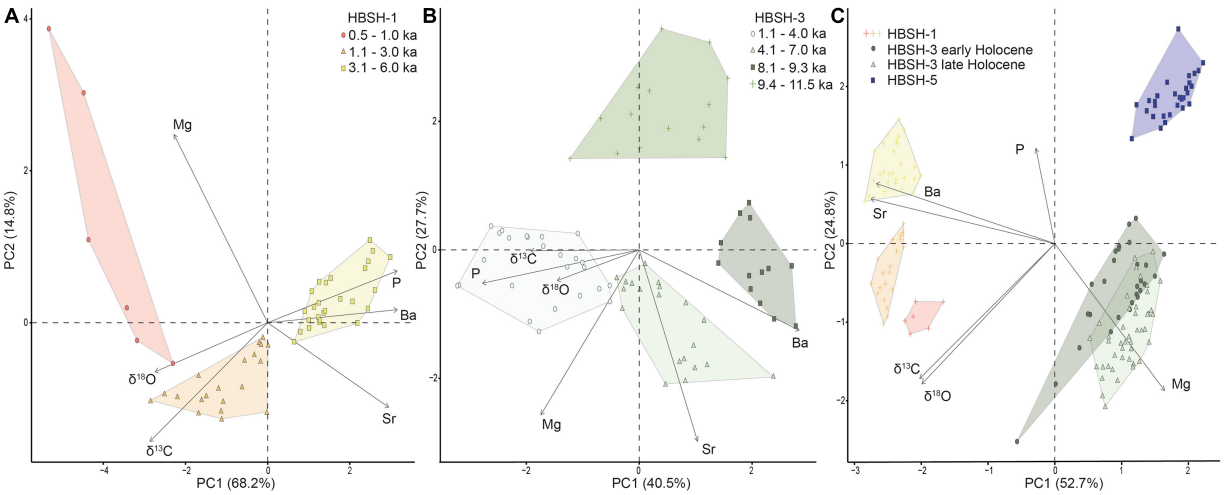

FIGURE 7 | Principal components (PCs) for stalagmites **(A)** HBSH-1, **(B)** HBSH-3, and **(C)** HBSH-1, HBSH-3 and HBSH-5. Since HBSH-5 did not pass the Kaiser-Meyer-Olkin test, only individual PCs for HBSH-1 and HBSH-3 are shown. Data points which are clearly separated from each other are grouped together with the same color.

Fairchild et al., 2000; Treble et al., 2005; Mattey et al., 2010). The increase in Mg concentration may not only be attributed to changes in pathways in the vadose zone, but also to changes in the residence time of the percolating water. PCP (Fairchild et al., 2000; Riechelmann et al., 2011) can influence the Mg concentration, with increasing PCP leading to an increase in Mg in the speleothem (Tooth and Fairchild, 2003). This could explain increasing Mg concentrations in the younger part and supports the assumption of a drier climate. In addition, differences in dissolution characteristics of calcite and dolomite (Fairchild and Treble, 2009) can cause differences in the Mg concentration. The host rock of HBSH is similar to the host rock above Bunker Cave, where dolomite is present (Grebe, 1993). During drier conditions, the contribution of dolomite to the drip water will increase and result in increased Mg concentrations in the speleothems.

HBSH-1 shows some obvious differences in the trace element concentrations in comparison to HBSH-3 and HBSH-5 since it consists of aragonite. The Mg concentration is much lower (approximately 200 μg/g) and does not change within the stalagmite apart from some peaks in the last 1 ka. In contrast, Sr values are elevated (500 – 800 μg/g) and show minima in the youngest part, while Mg shows the opposite trend. This is related to thin layers of calcite (Jochum et al., 2012). The PCA (**Figure 7A**) also confirms this observation, since Mg and Sr vectors show opposite directions. This is mainly attributed to the section < 1.0 ka, where also the trace element data (**Figure 4**) hint toward thin layers of calcite. In general, Ba, Sr, and P show a decreasing trend toward younger ages and are positively correlated (**Supplementary Figure A7**). As observed in the younger part of HBSH-3, Mg is negatively correlated with Ba ($R = -0.58$, $p < 5 \times 10^{-6}$) and Sr ($R = -0.62$, $p < 5 \times 10^{-7}$). This indicates that the younger part is influenced by an additional process as described for HBSH-3. By comparing the trace element distribution between HBSH-1 and HBSH-5, which represent only the younger and older part, respectively, the transition described for HBSH-3 is also visible. HBSH-5 shows a weak positive correlation between Mg and Ba and Sr. In contrast, the younger HBSH-1 stalagmite shows a negative correlation between Mg and Ba ($R = -0.58$, $p < 5 \times 10^{-6}$) and Sr ($R = -0.62$, $p < 5 \times 10^{-7}$).

Sr Isotopes

Strontium isotopes in speleothems have been successfully applied to assess water availability in the karst system and differences in the relative contributions of host rock and overlying soil due to changes in atmospheric deposition and weathering behavior of soils (e.g., Banner et al., 1994; Zhou et al., 2009; Belli et al., 2017; Weber et al., 2018a). Since HBSH is in close proximity to Bunker Cave and formed within the same limestone (Grebe, 1993, 1994), the host rock is expected to show the same Sr isotope signature. Therefore, the Sr isotope ratios for host rock and overlying soil reported in Weber et al. (2018a) for Bunker Cave with values of $^{87}Sr/^{86}Sr = 0.70836 \pm 0.00006$ for the host rock, 0.71893 ± 0.00001 for soil horizon C and 0.7237 ± 0.0003 for soil horizon A are used. All $^{87}Sr/^{86}Sr$ ratios of the speleothem samples lie between these end members (**Figure 6**), and changes in the Sr isotope composition are likely related to changes within this binary mixing system.

Similar to the changes observed for the trace elements, the Sr isotopes show a change in their trend between the early and the later growth phase. While the three studied speleothems show a trend toward less radiogenic Sr isotopes ratios in the first growth phase, shifts are observed for HBSH-3 and HBSH-4. In HBSH-3, the lowest $^{87}Sr/^{86}Sr$ is observed at 6.7 ± 0.3 ka, shortly after the onset of the second growth phase. This trend toward lower $^{87}Sr/^{86}Sr$, i.e., the value of the host rock, can be related to a longer residence time of the percolating water in the host rock after the hiatus. Therefore, the influence of the host rock Sr isotope signature increasingly affected the $^{87}Sr/^{86}Sr$ ratio of the speleothem. At 6.8 ± 0.3 ka, $^{87}Sr/^{86}Sr$ strongly increases

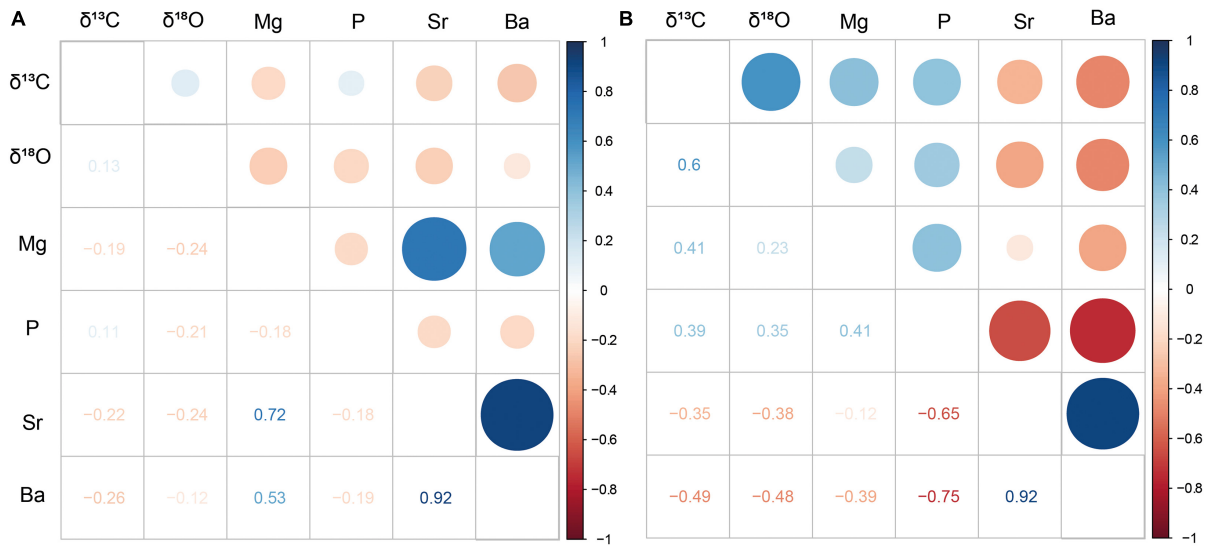

FIGURE 8 | Correlation matrix of centennial means for stable carbon and oxygen isotopes and trace elements of stalagmite HBSH-3 during the early **(A)** and late **(B)** phase of the Holocene. The size of the circles increases with increasing positive/negative correlation.

toward the growth stop. The same is true for HBSH-4, where a strong increase in $^{87}Sr/^{86}Sr$ between 6.5 and 6.0 ka is visible, coherent with a change in growth rate. Again, $^{87}Sr/^{86}Sr$ gets more radiogenic toward younger ages. The increasing $^{87}Sr/^{86}Sr$ ratios are consistent with the reduced growth rate, as well as the trend toward less negative $\delta^{13}C$ and $\delta^{18}O$ values and the increase in Mg concentration. Therefore, these factors are likely influenced by the same process, i.e., a decrease in water availability. However, this drying trend is not consistent with the Sr isotope evolution observed in Bunker Cave during the early MIS 3 (Weber et al., 2018a). In this study, two growth phases during early MIS 3 show different environmental conditions. While the early phase is believed to have been warm and humid with enhanced soil formation and a high weathering rate, the second phase was characterized by dry conditions resulting in increased $\delta^{13}C$ values and Mg concentrations. Strontium isotopes, however, tend toward less radiogenic values.

There are several different processes potentially explaining these differences. Although both cave systems lie in close proximity, the processes in the vadose zone can be highly variably and complex. In addition, environmental conditions during MIS 3 were likely different than during the Holocene. Therefore, changes in the karst system do not necessarily affect two different caves in the same way. While for Bunker Cave increased rainfall is considered to cause an overflow system in the karst reducing the influence of the host rock on the Sr isotope signature and vice versa (Riechelmann et al., 2011; Weber et al., 2018a), this is not necessarily true for HBSH. The $^{87}Sr/^{86}Sr$ ratios of the younger speleothem generation in HBSH, which suggests apparently drier conditions, may have been influenced in different ways, for instance due to changes in the relative portion of host-rock and soil-derived Sr. Thus, although the drip sites in HBSH might have been influenced by less recharge, this may not be related to drier conditions in the catchment. In Bunker Cave, no drying trend during the Holocene was observed (Fohlmeister et al., 2012). Therefore, it is unlikely that changes in precipitation amount are responsible for the drying observed in HBSH. In contrast, changes in hydrological pathways might have caused this trend in the younger part. Consequently, the climatic conditions were still favorable and were potentially decoupled from the cave conditions.

Within-Cave Correlation of Speleothem Records From HBSH and Bunker Cave

To evaluate the significance of a single speleothem stable isotope record within HBSH, the centennial means are used to calculate correlations between the four samples, the PCA, as well as the two $\delta^{13}C$ and $\delta^{18}O$ time series (**Figures 5**, **7**, **9**, **10A**). In general, the stable isotope records of the individual speleothems are highly positive correlated with the respective stack. This proves that the stack still captures the trends observed in the stalagmites. In addition, the $\delta^{18}O$ values of all four stalagmites are positively correlated with each other, suggesting a common forcing. The same is true for the $\delta^{13}C$ values. However, differences are observed when comparing the $\delta^{13}C$ and $\delta^{18}O$ values within HBSH. While the $\delta^{18}O$ record of HBSH-5 is positively correlated with the $\delta^{13}C$ records of the other speleothems, the $\delta^{13}C$ record of HBSH-5 is negatively correlated with all $\delta^{18}O$ records, as well as the $\delta^{18}O$ HBSH stack. This observation further supports the transition within the Holocene, as described in the previous sections. HBSH-5 only grew during the early phase and shows the initial decrease in $\delta^{13}C$ at the onset of the Holocene. Thus, this specimen does not record the transition. The $\delta^{13}C$ and $\delta^{18}O$ stacks are weakly positively correlated ($R = 0.33$, $p < 5 \times 10^{-4}$). However, this correlation is mainly caused

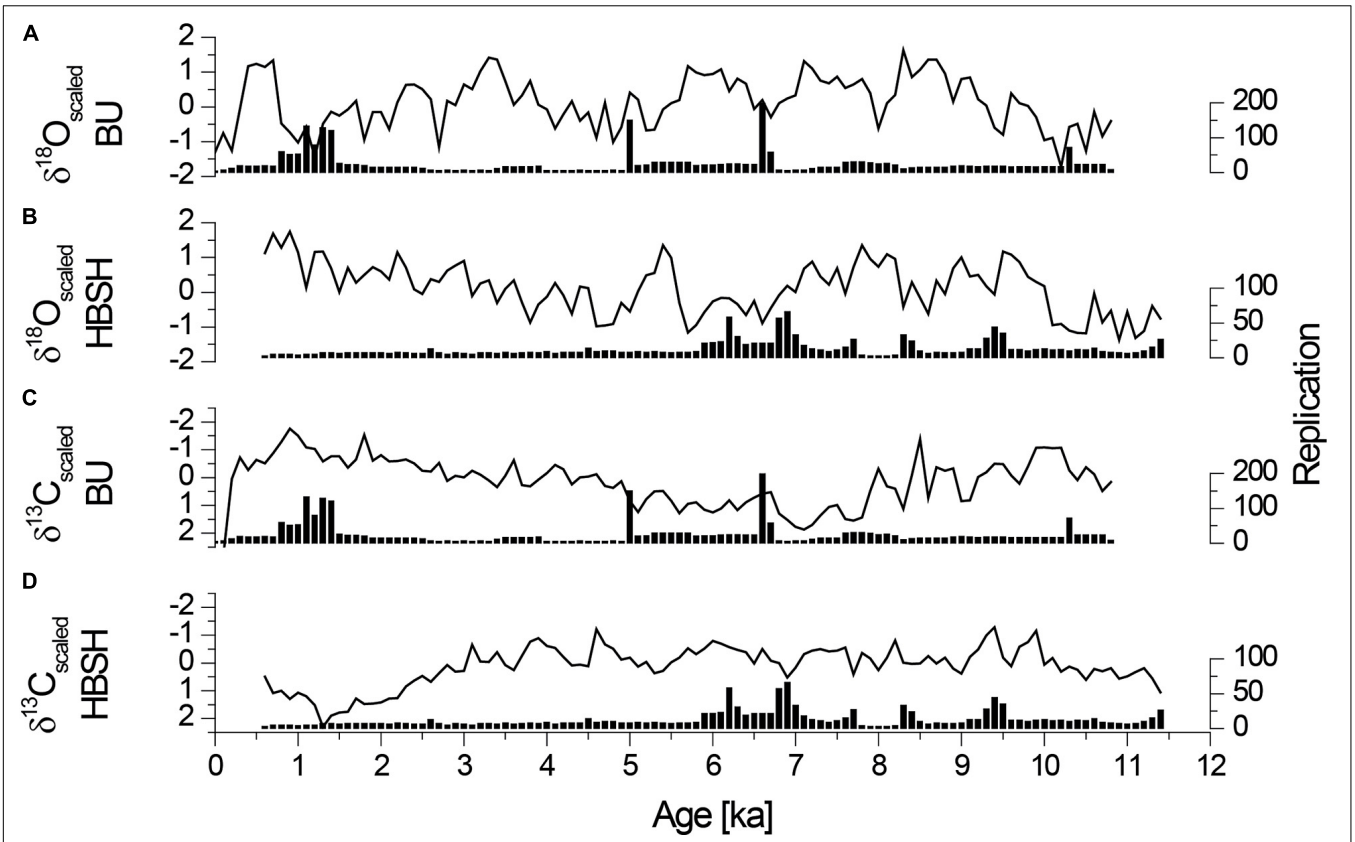

FIGURE 9 | Scaled stable isotope stacks for **(A)** $\delta^{18}O$ values from Bunker Cave, **(B)** $\delta^{18}O$ values from HBSH, **(C)** $\delta^{13}C$ values from Bunker Cave, and **(D)** $\delta^{13}C$ values from HBSH. For all stacks, the replication indicates the number of stable isotope measurements averaged for the centennial mean for the specific time interval. Note that the axes for $\delta^{13}C$ are inverted to match the plots shown in **Figures 4**, **5**.

by the same trend in the youngest section, which is strongly expressed by the positive correlation between the $\delta^{13}C$ stack and the $\delta^{18}O$ record of HBSH-1 ($R = 0.65$, $p < 8 \times 10^{-8}$) and the $\delta^{18}O$ stack and the $\delta^{13}C$ record of HBSH-1 ($R = 0.69$, $p < 4 \times 10^{-9}$).

The PCA including HBSH-1, HBSH-3, and HBSH-5 (**Figure 7C**) shows a clear separation between the three stalagmites, without any overlap. In addition, a further separation within HBSH-1 and in HBSH-3 is visible. In principle, both stable isotope values separate HBSH-1 and HBSH-5 from each other and show a strong anti-correlation. While HBSH-5 groups together, HBSH-1 is separated in three different clusters (**Figures 7A,C**). HBSH-3 is the only stalagmite in the PCA which covers almost the whole Holocene and where differences between the early and late growth phase (**Figure 8**) are expected. The PCA confirms that Mg, Sr and Ba are the main separators for this sample and that $\delta^{13}C$ and $\delta^{18}O$ start to diverge during the late Holocene (**Figure 7B**). The overall separation between the three stalagmites shows that each is dependent of other processes, i.e., the difference between aragonite and calcite, as well as the time of formation.

In contrast to HBSH, the correlation matrix for Bunker Cave (**Figure 10B**) shows positive correlations between all stalagmites and isotope curves, covering the same time interval. This indicates that these two isotope systems were influenced by similar processes, as all individual samples show a positive correlation with the $\delta^{13}C$ and $\delta^{18}O$ stacks, for the same as well as for the other isotope.

Inter-Cave Correlation of Speleothem Records From HBSH and Bunker Cave

The two $\delta^{18}O$ stacks for HBSH and Bunker Cave are not significantly correlated (**Figures 9**, **11A**).This is largely related to differences in the correlations of individual speleothems. While Bu2 and Bu6 show positive but insignificant correlations with all HBSH stalagmites covering the same time span, Bu4 does not show any correlation with HBSH specimens. Bu1 even shows negative correlations with the HBSH $\delta^{18}O$ records. This indicates, that the Bu speleothems do not show an overall common $\delta^{18}O$ trend as described for HBSH. However, the Bunker Cave speleothems do not overlap as much as the HBSH speleothems in their growth history. Thus, the resulting Bunker Cave stack is largely influenced by stalagmite Bu4, which grew from 8 ka until recent times. Since Bu4 does not show any correlation with the HBSH speleothems, the lack of correlation between the HBSH and the Bunker Cave stacks is reasonable. These

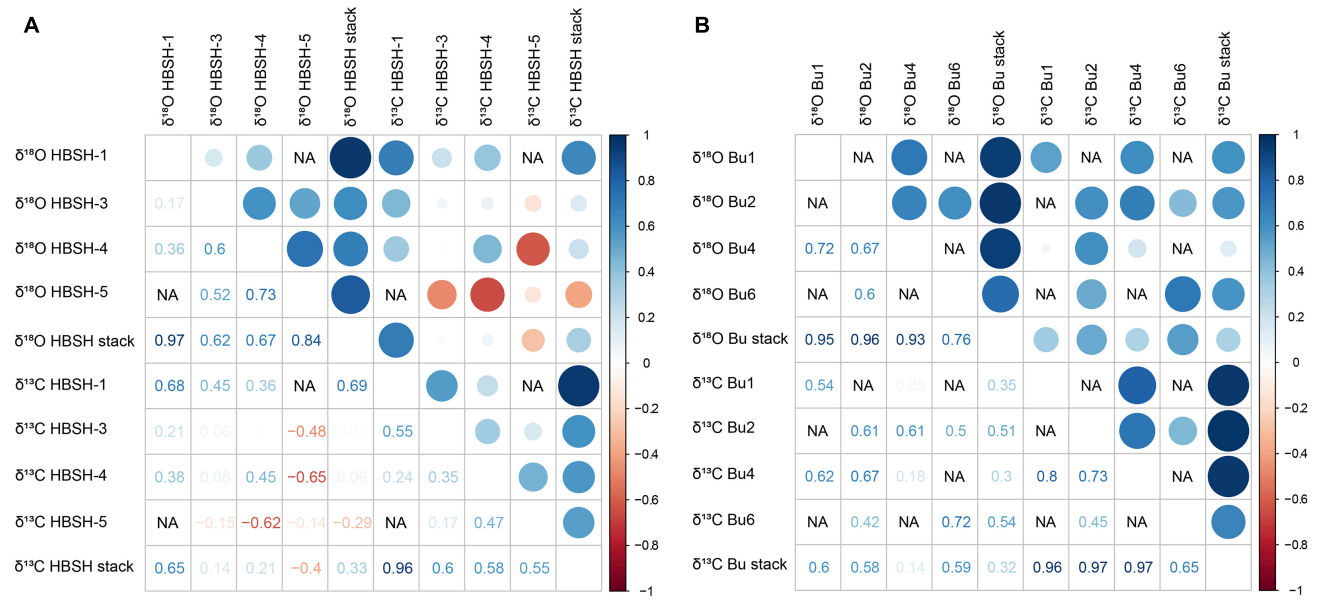

FIGURE 10 | $\delta^{18}O$ and $\delta^{13}C$ correlation matrix for centennial means of **(A)** the four HBSH stalagmites, as well as the two HBSH stacks and **(B)** the four Holocene stalagmites (Fohlmeister et al., 2012) and two stacks from Bunker Cave (Bu). The size of the circles increases with increasing positive/negative correlation.

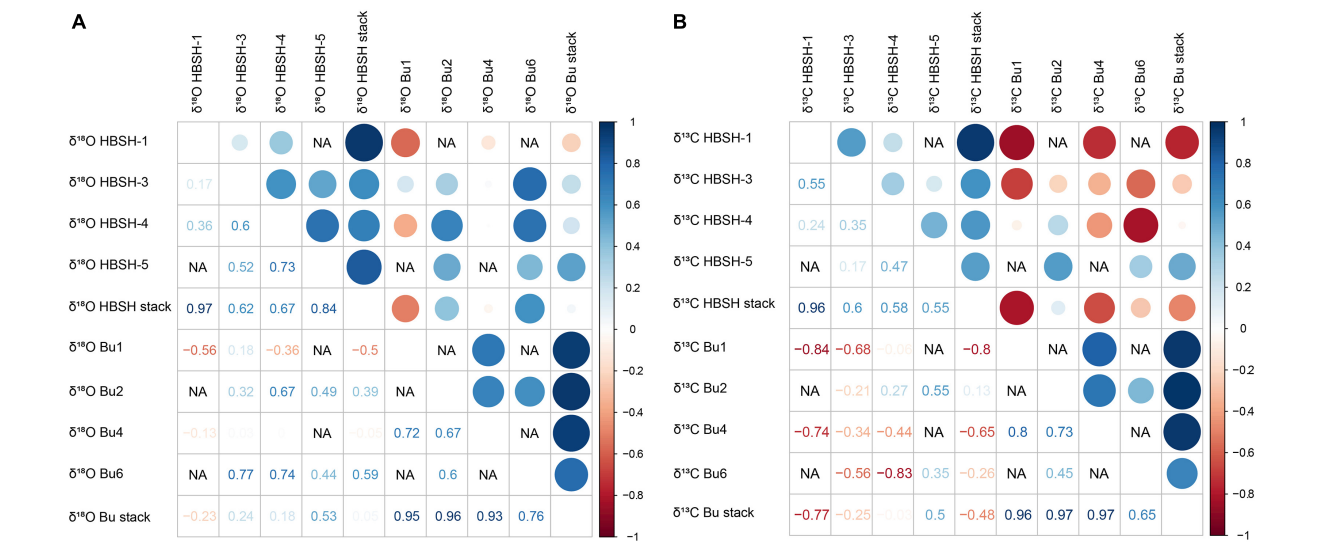

FIGURE 11 | (A) Correlation matrix of centennial means for $\delta^{18}O$ of the four Bu (Fohlmeister et al., 2012) and HBSH stalagmites, as well as the two HBSH and Bu stacks. **(B)** As for **(A)** for the $\delta^{13}C$ values. The size of the circles increases with increasing positive/negative correlation.

findings further support the strong transition in the HBSH records during the middle Holocene. The positive correlation of Bu2 and Bu6 during the early Holocene shows that during that time the records from both caves capture a common signal. However, since Bu4 and Bu1 started to grow around 8 and 6 ka, respectively, both stalagmites mainly cover periods when HBSH is expected to be already influenced by cave-specific processes.

For the $\delta^{13}C$ records (**Figure 11B**), the comparison between the two cave systems yielded significantly negative correlations. This is especially true for HBSH-1 and the coeval stalagmites Bu1 ($R = -0.56$, $p < 2 \times 10^{-7}$) and Bu4 ($R = -0.74$, $p < 2 \times 10^{-10}$), which grew during the late Holocene. In addition, HBSH-3 shows negative correlations with all Bunker Cave stalagmites, although covering large parts of the Holocene. A different pattern in visible for HBSH-4, which indicates a weak positive correlation with Bu2, which grew during the early Holocene until approximately 8 ka. In contrast, the comparison with Bu4 yielded a negative correlation ($R = -0.44$, $p < 3 \times 10^{-4}$). Interestingly, the $\delta^{13}C$ values of HBSH-5 show a positive correlation with the coeval Bu2

($R = 0.55$, $p < 3 \times 10^{-3}$) stalagmite, which grew during the early Holocene. This indicates, that the early Holocene $\delta^{13}C$ signal is consistently registered in both HBSH and Bunker Cave, while later on, the $\delta^{13}C$ trends become dispersed and yield negative correlations. This observation is in agreement with the previously observed transition in the stable isotope, trace element and Sr isotope records.

The comparison of the stable isotope stacks from the two caves (**Figure 9**) underscores the results of the correlation analysis. For the $\delta^{18}O$ values, the first part of the Holocene shows some common features between HBSH and Bunker Cave speleothems, such as a peak around 9.6 ka and a general trend toward less negative values. However, this pattern disappears or even reverses in the late Holocene, especially for the youngest 3 – 4 ka, where the trends are opposite. Similar patterns can be observed in the $\delta^{13}C$ stack, with a trend toward more negative $\delta^{13}C$ values in the first part until ca. 9.5 ka, recorded in both caves. This represents the onset of the Holocene with increased vegetation and soil formation. However, from 7 – 6 ka onward, a pronounced trend of divergence is observed. At 6.5 ka, the $\delta^{13}C$ values in Bunker Cave become progressively more negative, while the $\delta^{13}C$ values in HBSH tend toward less negative values after 6 ka, resulting in a strongly negative correlation.

Implications for Speleothem-Based Palaeoclimate Reconstructions

Our results show that the use of stable isotopes for palaeoclimate reconstructions using speleothems may be strongly biased by non-climatic/non-environmental factors. Although HBSH and Bunker Cave are less than 1 km apart, the stable isotope records of stalagmites from these caves lack a consistent pattern for large parts of the Holocene. The speleothems from HBSH show a trend toward less negative $\delta^{13}C$ values during the last 6 ka. This could be interpreted as a general trend toward drier conditions, less vegetation cover and reduced soil biological activity, associated with a less humid climate. However, by comparing these results with the much more intensively studied Bunker Cave dataset (including both cave monitoring and palaeoclimate studies, e.g., Riechelmann et al., 2011, 2017; Fohlmeister et al., 2012; Weber et al., 2018a) and other well-established climate archives for the same time interval (e.g., Wanner et al., 2008; Fohlmeister et al., 2013; Sirocko et al., 2016), this interpretation is unlikely. Growth rate and the trace element composition of the speleothems suggest that the increase in the $\delta^{13}C$ values, and probably also the $\delta^{18}O$ values, mainly results from disequilibrium isotope fractionation on the speleothem surface due to increased drip intervals and/or PCP. Besides these general differences between the two cave systems, there are also differences between individual speleothem records from the same cave. While the aragonitic HBSH-1 stalagmite shows a strong positive correlation between the two isotopes, the calcitic HBSH-5 stalagmite yields a slightly negative correlation. Not all speleothems from the same cave grew simultaneously. Monitoring studies of cave systems have shown that not necessarily all drip sites within a cave yielded a geochemically consistent picture. For instance, Musgrove and Banner (2004) showed that the hydro-geochemistry ($^{87}Sr/^{86}Sr$, Sr/Ca, and Mg/Ca) of different drip sites in a cave in central Texas is temporally and spatially variable. Other studies showed that also the drip rate of drip sites within the same cave (Ciur-Izbuc Cave, Romania) can be significantly different and decoupled from rainfall (Moldovan et al., 2018). This is further supported by a study identified a chaotic discharge behavior in Cathedral Cave (Australia), which especially influences growth-rate dependent climate proxies (Mariethoz et al., 2012). This highlights the complex interplay between processes in the karst system and the growth dynamics of speleothems. Therefore, reconstructions based on single speleothems should be viewed with caution and replication, as well as a multi-proxy approach together with statistical approaches should be applied to disentangle potential site-specific cave effects from environmental signals.

CONCLUSION

By comparing stable isotope records from HBSH and the nearby Bunker Cave, both differences between the two caves and within the individual stalagmites from HBSH were identified. While the proxy records show similar trends in both caves for the early Holocene, a diverging pattern, especially in the $\delta^{13}C$ values was observed during the late Holocene. By using a multi-proxy approach of stable isotopes, trace elements and Sr isotopes, it is possible to show that the younger part in HBSH was largely influenced by a drying of the karst system, causing an increase in $\delta^{13}C$ and $\delta^{18}O$ values due to disequilibrium fractionation and PCP. This shows that individual stalagmites may faithfully capture climatic and environmental signals, while stalagmites from other parts of the same cave may be strongly influenced by highly localized cave-internal processes. Replicating stalagmite records and applying several proxies is therefore essential to obtain robust palaeoclimate information.

DATA AVAILABILITY STATEMENT

The original contributions presented in the study are included in the article and **Supplementary Material**, further inquiries can be directed to the corresponding author.

AUTHOR CONTRIBUTIONS

MW, DS, and YH designed the study. MW, YH, DS, BS, and CS performed the stable isotope analysis and interpretation. MW, YH, DS, DH, and KJ was performed dating of the samples. YH, KJ, and DS performed Trace element analysis and data evaluation. MW performed Strontium isotope analysis and the regression analysis, and wrote the manuscript, DS, BS, CS, DR, and KJ improved the manuscript. All authors discussed the results and commented on the manuscript.

FUNDING

MW, KJ, and DS are grateful to the Max Planck Graduate Center and the German Research Foundation (DFG SCHO 1274/9-1 and SCHO 1274/11-1) for funding.

ACKNOWLEDGMENTS

We thank B. Schwager, B. Stoll, U. Weis, M. Wimmer, M. Maus, and M. Großkopf for assistance in the laboratory and K. Weber for discussion of the PCA. Detailed and constructive comments and suggestions of two reviewers and the editor are greatly acknowledged.

SUPPLEMENTARY MATERIAL

The Supplementary Material for this article can be found online at: https://www.frontiersin.org/articles/10.3389/feart.2021.642651/full#supplementary-material

REFERENCES

Bajo, P., Hellstrom, J., Frisia, S., Drysdale, R., Black, J., Woodhead, J., et al. (2016). "Cryptic" diagenesis and its implications for speleothem geochronologies. *Quat. Sci. Rev.* 148, 17–28. doi: 10.1016/j.quascirev.2016.06.020

Banner, J. L., Musgrove, M., and Capo, R. C. (1994). Tracing ground-water evolution in a limestone aquifer using Sr isotopes: effects of multiple sources of dissolved ions and mineral-solution reactions. *Geology* 22, 687–690. doi: 10.1130/0091-7613(1994)022<0687:TGWEIA>2.3.CO;2

Banner, J. L., Musgrove, M. L., Asmerom, Y., Edwards, R. L., and Hoff, J. A. (1996). High-resolution temporal record of holocene ground-water chemistry: tracing links between climate and hydrology. *Geology* 24, 1049–1053. doi: 10.1130/0091-7613(1996)024<1049:HRTROH>2.3.CO;2

Bartlett, M. S. (1937). Properties of sufficiency and statistical tests. *Proc. R. Soc. Lond. Ser. A Math. Phys. Sci.* 160, 268–282. doi: 10.1098/rspa.1937.0109

Belli, R., Borsato, A., Frisia, S., Drysdale, R., Maas, R., and Greig, A. (2017). Investigating the hydrological significance of stalagmite geochemistry (Mg, Sr) using Sr isotope and particulate element records across the Late Glacial-to-Holocene transition. *Geochim. Cosmochim. Acta* 199, 247–263. doi: 10.1016/j.gca.2016.10.024

Breitenbach, S. F. M., Rehfeld, K., Goswami, B., Baldini, J. U. L., Ridley, H. E., Kennett, D., et al. (2012). COnstructing proxy-record age models (COPRA). *Clim. Past* 8, 1765–1779. doi: 10.5194/cp-8-1765-2012

Budaev, S. V. (2010). Using principal components and factor analysis in animal behaviour research: caveats and guidelines. *Ethology* 116, 472–480. doi: 10.1111/j.1439-0310.2010.01758.x

Budsky, A., Scholz, D., Wassenburg, J. A., Mertz-Kraus, R., Spötl, C., Riechelmann, D. F. C., et al. (2019). Speleothem $\delta^{13}C$ record suggests enhanced spring/summer drought in south-eastern Spain between 9.7 and 7.8 ka–A circum-Western Mediterranean anomaly? *Holocene* 29, 1113–1133. doi: 10.1177/0959683619838021

Burchette, T. P. (1981). European devonian reefs: a review of current concepts and models. *SEPM Special Publ.* 30, 85–142. doi: 10.2110/pec.81.30.0085

Cheng, H., Edwards, R. L., Hoff, J., Gallup, C. D., Richards, D. A., and Asmerom, Y. (2000). The half-lives of uranium-234 and thorium-230. *Chem. Geol.* 169, 17–33. doi: 10.1016/S0009-2541(99)00157-6

Cheng, H., Lawrence Edwards, R., Shen, C.-C., Polyak, V. J., Asmerom, Y., Woodhead, J., et al. (2013). Improvements in ^{230}Th dating, ^{230}Th and ^{234}U half-life values, and U–Th isotopic measurements by multi-collector inductively coupled plasma mass spectrometry. *Earth Planet. Sci. Lett.* 371–372, 82–91. doi: 10.1016/j.epsl.2013.04.006

Comas-Bru, L., Rehfeld, K., Roesch, C., Amirnezhad-Mozhdehi, S., Harrison, S. P., Atsawawaranunt, K., et al. (2020). SISALv2: a comprehensive speleothem isotope database with multiple age–depth models. *Earth Syst. Sci. Data* 12, 2579–2606. doi: 10.5194/essd-12-2579-2020

Deininger, M., Fohlmeister, J., Scholz, D., and Mangini, A. (2012). Isotope disequilibrium effects: the influence of evaporation and ventilation effects on the carbon and oxygen isotope composition of speleothems – A model approach. *Geochim. Cosmochim. Acta* 96, 57–79. doi: 10.1016/j.gca.2012.08.013

Dettman, D. L., and Lohmann, K. C. (1995). Microsampling carbonates for stable isotope and minor element analysis; physical separation of samples on a 20 micrometer scale. *J. Sediment. Res.* 65, 566–569. doi: 10.1306/D426813F-2B26-11D7-8648000102C1865D

Dreybrodt, W., Hansen, M., and Scholz, D. (2016). Processes affecting the stable isotope composition of calcite during precipitation on the surface of stalagmites: laboratory experiments investigating the isotope exchange between DIC in the solution layer on top of a speleothem and the CO_2 of the cave atmosphere. *Geochim. Cosmochim. Acta* 174, 247–262. doi: 10.1016/j.gca.2015.11.012

Fairchild, I. J., Borsato, A., Tooth, A. F., Frisia, S., Hawkesworth, C. J., Huang, Y., et al. (2000). Controls on trace element (Sr–Mg) compositions of carbonate cave waters: implications for speleothem climatic records. *Chemi. Geol.* 166, 255–269. doi: 10.1016/S0009-2541(99)00216-8

Fairchild, I. J., Smith, C. L., Baker, A., Fuller, L., Spotl, C., Mattey, D., et al. (2006). Modification and preservation of environmental signals in speleothems. *Earth Sci. Rev.* 75, 105–153. doi: 10.1016/j.earscirev.2005.08.003

Fairchild, I. J., and Treble, P. C. (2009). Trace elements in speleothems as recorders of environmental change. *Quat. Sci. Rev.* 28, 449–468. doi: 10.1016/j.quascirev.2008.11.007

Fankhauser, A., Mcdermott, F., and Fleitmann, D. (2016). Episodic speleothem deposition tracks the terrestrial impact of millennial-scale last glacial climate variability in SW Ireland. *Quat. Sci. Rev.* 152, 104–117. doi: 10.1016/j.quascirev.2016.09.019

Fohlmeister, J., Schröder-Ritzrau, A., Scholz, D., Spötl, C., Riechelmann, D. F. C., Mudelsee, M., et al. (2012). Bunker Cave stalagmites: an archive for central European Holocene climate variability. *Clim. Past* 8, 1751–1764. doi: 10.5194/cp-8-1751-2012

Fohlmeister, J., Vollweiler, N., Spötl, C., and Mangini, A. (2013). COMNISPA II: update of a mid-European isotope climate record, 11 ka to present. *Holocene* 23, 749–754. doi: 10.1177/0959683612465446

Genty, D., Blamart, D., Ouahdi, R., Gilmour, M., Baker, A., Jouzel, J., et al. (2003). Precise dating of dansgaard-oeschger climate oscillations in western Europe from stalagmite data. *Nature* 421, 833–837. doi: 10.1038/nature01391

Gibert, L., Scott, G. R., Scholz, D., Budsky, A., Ferràndez, C., Ribot, F., et al. (2016). Chronology for the Cueva Victoria fossil site (SE Spain): evidence for Early Pleistocene Afro-Iberian dispersals. *J. Hum. Evol.* 90, 183–197. doi: 10.1016/j.jhevol.2015.08.002

Grebe, W. (1993). Die bunkerhöhle in iserlohn-letmathe (Sauerland). *Mitteilung des Verbands der deutschen Höhlen-und Karstforscher, München* 39, 22–23.

Grebe, W. (1994). Die Hüttenbläserschachthöhle—eine neu entdeckte Höhle in Iserlohn-Letmathe. *Mitteilungen & Berichte Speläogruppe Letmathe* 10, 49–65.

Hammerschmidt, E., Niggemann, S., Grebe, W., Oelze, R., Brix, M. R., and Richter, D. K. (1995). Höhlen in Iserlohn.–Schriften zur Karst- und Höhlenkunde in Westfahlen Heft 1, Iserlohn, 154.

Hansen, M., Scholz, D., Froeschmann, M.-L., Schöne, B. R., and Spötl, C. (2017). Carbon isotope exchange between gaseous CO_2 and thin solution films: artificial cave experiments and a complete diffusion-reaction model. *Geochim. Cosmochim. Acta* 211, 28–47. doi: 10.1016/j.gca.2017.05.005

Hansen, M., Scholz, D., Schöne, B. R., and Spötl, C. (2019). Simulating speleothem growth in the laboratory: determination of the stable isotope fractionation ($\delta^{13}C$ and $\delta^{18}O$) between H_2O. DIC and $CaCO_3$. *Chem. Geol.* 509, 22–44. doi: 10.1016/j.chemgeo.2018.12.012

Hendy, C. H. (1971). The isotopic geochemistry of speleothems—I. The calculation of the effects of different modes of formation on the isotopic composition

of speleothems and their applicability as palaeoclimatic indicators. *Geochim. Cosmochim. Acta* 35, 801–824. doi: 10.1016/0016-7037(71)90127-X

Hoffmann, D. L. (2008). 230Th isotope measurements of femtogram quantities for U-series dating using multi ion counting (MIC) MC-ICPMS. *Int. J. Mass Spectrom.* 275, 75–79. doi: 10.1016/j.ijms.2008.05.033

Hoffmann, D. L., Prytulak, J., Richards, D. A., Elliott, T., Coath, C. D., Smart, P. L., et al. (2007). Procedures for accurate U and Th isotope measurements by high precision MC-ICPMS. *Int. J. Mass Spectrom.* 264, 97–109. doi: 10.1016/j.ijms.2007.03.020

Hori, M., Ishikawa, T., Nagaishi, K., Lin, K., Wang, B.-S., You, C.-F., et al. (2013). Prior calcite precipitation and source mixing process influence Sr/Ca, Ba/Ca and $^{87}Sr/^{86}Sr$ of a stalagmite developed in southwestern Japan during 18.0-4.5 ka. *Chem. Geol.* 347, 190–198. doi: 10.1016/j.chemgeo.2013.03.005

Jochum, K. P., Scholz, D., Stoll, B., Weis, U., Wilson, S. A., Yang, Q. C., et al. (2012). Accurate trace element analysis of speleothems and biogenic calcium carbonates by LA-ICP-MS. *Chem. Geol.* 318, 31–44. doi: 10.1016/j.chemgeo.2012.05.009

Kaiser, H. F. (1970). A second generation little jiffy. *Psychometrika* 35, 401–415. doi: 10.1007/BF02291817

Kaiser, H. F., and Rice, J. (1974). Little jiffy, mark IV. *Educ. Psychol. Meas.* 34, 111–117. doi: 10.1177/001316447403400115

Köhler, P., Knorr, G., Buiron, D., Lourantou, A., and Chappellaz, J. (2011). Abrupt rise in atmospheric CO2 at the onset of the Bølling/Allerød: in-situ ice core data versus true atmospheric signal. *Clim. Past* 7, 473–486. doi: 10.5194/cp-7-473-2011

Krebs, W. (1974). Devonian carbonate complexes of Central Europe. *Soc. Econ. Paleontol. Mineral. Special Publ.* 18, 155–208. doi: 10.2110/pec.74.18.0155

Lachniet, M. S. (2009). Climatic and environmental controls on speleothem oxygen-isotope values. *Quat. Sci. Rev.* 28, 412–432. doi: 10.1016/j.quascirev.2008.10.021

Lechleitner, F. A., Amirnezhad-Mozhdehi, S., Columbu, A., Comas-Bru, L., Labuhn, I., Pérez-Mejías, C., et al. (2018). The potential of speleothems from Western Europe as recorders of regional climate: a critical assessment of the SISAL database. *Quaternary* 1:30. doi: 10.3390/quat1030030

Li, H.-C., Ku, T.-L., You, C.-F., Cheng, H., Edwards, R. L., Ma, Z.-B., et al. (2005). $^{87}Sr/^{86}Sr$ and Sr/Ca in speleothems for paleoclimate reconstruction in Central China between 70 and 280 kyr ago. *Geochim. Cosmochim. Acta* 69, 3933–3947. doi: 10.1016/j.gca.2005.01.009

Lin, Y., Jochum, K. P., Scholz, D., Hoffmann, D. L., Stoll, B., Weis, U., et al. (2017). In-situ high spatial resolution LA-MC-ICPMS 230Th/U dating enables detection of small-scale age inversions in speleothems. *Solid Earth Sci.* 2, 1–9. doi: 10.1016/j.sesci.2016.12.003

Luetscher, M., Boch, R., Sodemann, H., Spotl, C., Cheng, H., Edwards, R. L., et al. (2015). North Atlantic storm track changes during the Last Glacial Maximum recorded by Alpine speleothems. *Nat. Commun.* 6:6344. doi: 10.1038/ncomms7344

Lugli, F., Cipriani, A., Peretto, C., Mazzucchelli, M., and Brunelli, D. (2017). In situ high spatial resolution $^{87}Sr/^{86}Sr$ ratio determination of two Middle Pleistocene (c.a. 580 ka) Stephanorhinus hundsheimensis teeth by LA–MC–ICP–MS. *Int. J. Mass Spectrom.* 412, 38–48. doi: 10.1016/j.ijms.2016.12.012

Mangini, A., Verdes, P., Spötl, C., Scholz, D., Vollweiler, N., and Kromer, B. (2007). Persistent influence of the North Atlantic hydrography on central European winter temperature during the last 9000 years. *Geophys. Res. Lett.* 34:L02704. doi: 10.1029/2006GL028600

Mariethoz, G., Baker, A., Sivakumar, B., Hartland, A., and Graham, P. (2012). Chaos and irregularity in karst percolation. *Geophys. Res. Lett.* 39:L23305. doi: 10.1029/2012GL054270

Mattey, D. P., Fairchild, I. J., Atkinson, T. C., Latin, J.-P., Ainsworth, M., and Durell, R. (2010). Seasonal microclimate control of calcite fabrics, stable isotopes and trace elements in modern speleothem from St Michaels Cave. Gibraltar. *Geol. Soc. Lond. Special Publ.* 336, 323–344. doi: 10.1144/SP336.17

Mayewski, P. A., Rohling, E. E., Curt Stager, J., Karlén, W., Maasch, K. A., David Meeker, L., et al. (2004). Holocene climate variability. *Quat. Res.* 62, 243–255. doi: 10.1016/j.yqres.2004.07.001

McArthur, J. M., Howarth, R. J., and Bailey, T. R. (2001). Strontium isotope stratigraphy: LOWESS Version 3: best fit to the marine Sr-Isotope Curve for 0–509 Ma and accompanying look-up table for deriving numerical age. *J. Geol.* 109, 155–170. doi: 10.1086/319243

McDermott, F. (2004). Palaeo-climate reconstruction from stable isotope variations in speleothems: a review. *Quat. Sci. Rev.* 23, 901–918. doi: 10.1016/j.quascirev.2003.06.021

McDermott, F., Frisia, S., Huang, Y., Longinelli, A., Spiro, B., Heaton, T. H. E., et al. (1999). Holocene climate variability in Europe: evidence from $\delta^{18}O$, textural and extension-rate variations in three speleothems. *Quat. Sci. Rev.* 18, 1021–1038. doi: 10.1016/S0277-3791(98)00107-3

Mickler, P. J., Stern, L. A., and Banner, J. L. (2006). Large kinetic isotope effects in modern speleothems. *Geol. Soc. Am. Bull.* 118, 65–81. doi: 10.1130/B25698.1

Mischel, S. A., Scholz, D., Spötl, C., Jochum, K. P., Schröder-Ritzrau, A., and Fiedler, S. (2017a). Holocene climate variability in Central Germany and a potential link to the polar North Atlantic: a replicated record from three coeval speleothems. *Holocene* 27, 509–525. doi: 10.1177/0959683616670246

Mischel, S. A., Mertz-Kraus, R., Jochum Klaus, P., and Scholz, D. (2017b). TERMITE: an R script for fast reduction of laser ablation inductively coupled plasma mass spectrometry data and its application to trace element measurements. *Rapid Commun. Mass Spectrom.* 31, 1079–1087. doi: 10.1002/rcm.7895

Moldovan, O. T., Constantin, S., and Cheval, S. (2018). Drip heterogeneity and the impact of decreased flow rates on the vadose zone fauna in Ciur-Izbuc Cave. NW Romania. *Ecohydrology* 11:e2028. doi: 10.1002/eco.2028

Moseley, G. E., Spötl, C., Svensson, A., Cheng, H., Brandstätter, S., and Edwards, R. L. (2014). Multi-speleothem record reveals tightly coupled climate between central Europe and Greenland during Marine Isotope Stage 3. *Geology* 42, 1043–1046. doi: 10.1130/G36063.1

Mühlinghaus, C., Scholz, D., and Mangini, A. (2009). Modelling fractionation of stable isotopes in stalagmites. *Geochim. Cosmochim. Acta* 73, 7275–7289. doi: 10.1016/j.gca.2009.09.010

Musgrove, M., and Banner, J. L. (2004). Controls on the spatial and temporal variability of vadose dripwater geochemistry: edwards aquifer, central Texas. *Geochim. Cosmochim. Acta* 68, 1007–1020. doi: 10.1016/j.gca.2003.08.014

Niggemann, S., Mangini, A., Richter, D. K., and Wurth, G. (2003). A paleoclimate record of the last 17,600 years in stalagmites from the B7 cave. Sauerland, Germany. *Quat. Sci. Rev.* 22, 555–567. doi: 10.1016/S0277-3791(02)00143-9

Obert, J. C., Scholz, D., Felis, T., Brocas, W. M., Jochum, K. P., and Andreae, M. O. (2016). $^{230}Th/U$ dating of last interglacial brain corals from bonaire (southern Caribbean) using bulk and theca wall material. *Geochim. Cosmochim. Acta* 178, 20–40. doi: 10.1016/j.gca.2016.01.011

Paeckelmann, W. (1922). Der mitteldevonische massenkalk des bergischen landes. *Abhandlungen der Preußischen Geologischen Landesanstalt* 91, 1–112. doi: 10.5962/bhl.title.134334

Paquette, J., and Reeder, R. J. (1995). Relationship between surface structure, growth mechanism, and trace element incorporation in calcite. *Geochim. Cosmochim. Acta* 59, 735–749. doi: 10.1016/0016-7037(95)00004-J

R Core Team (2020). *R: A Language and Environment for Statistical Computing*. Vienna: R Core Team.

Richter, D. K., Goll, K., Grebe, W., Niedermayr, A., Platte, A., and Scholz, D. (2015). Weichselzeitliche Kryocalcite als Hinweise für Eisseen in der Hüttenbläserschachthöhle (Iserlohn/NRW). *Quat. Sci. J.* 64, 67–81. doi: 10.3285/eg.64.2.02

Riechelmann, D. F. C., Deininger, M., Scholz, D., Riechelmann, S., Schröder-Ritzrau, A., Spötl, C., et al. (2013). Disequilibrium carbon and oxygen isotope fractionation in recent cave calcite: comparison of cave precipitates and model data. *Geochim. Cosmochim. Acta* 103, 232–244. doi: 10.1016/j.gca.2012.11.002

Riechelmann, D. F. C., Schröder-Ritzrau, A., Scholz, D., Fohlmeister, J., Spötl, C., Richter, D. K., et al. (2011). Monitoring bunker cave (NW Germany): a prerequisite to interpret geochemical proxy data of speleothems from this site. *J. Hydrol.* 409, 682–695. doi: 10.1016/j.jhydrol.2011.08.068

Riechelmann, S., Buhl, D., Schröder-Ritzrau, A., Riechelmann, D. F. C., Richter, D. K., Vonhof, H. B., et al. (2012). The magnesium isotope record of cave carbonate archives. *Clim. Past* 8, 1849–1867. doi: 10.5194/cp-8-1849-2012

Riechelmann, S., Schröder-Ritzrau, A., Spötl, C., Riechelmann, D. F. C., Richter, D. K., Mangini, A., et al. (2017). Sensitivity of Bunker Cave to climatic forcings highlighted through multi-annual monitoring of rain-, soil-, and dripwaters. *Chem. Geol.* 449, 194–205. doi: 10.1016/j.chemgeo.2016.12.015

Scholz, D., and Hoffmann, D. (2008). ^{230}Th/U-dating of fossil corals and speleothems. *Quat. Sci. J.* 57, 52–76. doi: 10.3285/eg.57.1-2.3

Scholz, D., and Hoffmann, D. L. (2011). StalAge–An algorithm designed for construction of speleothem age models. *Quat. Geochronol.* 6, 369–382. doi: 10.1016/j.quageo.2011.02.002

Scholz, D., Mühlinghaus, C., and Mangini, A. (2009). Modelling δ^{13}C and δ^{18}O in the solution layer on stalagmite surfaces. *Geochim. Cosmochim. Acta* 73, 2592–2602. doi: 10.1016/j.gca.2009.02.015

Scholz, D., Tolzmann, J., Hoffmann, D. L., Jochum, K. P., Spötl, C., and Riechelmann, D. F. C. (2014). Diagenesis of speleothems and its effect on the accuracy of ^{230}Th/U-ages. *Chem. Geol.* 387, 74–86. doi: 10.1016/j.chemgeo.2014.08.005

Sinclair, D. J., Banner, J. L., Taylor, F. W., Partin, J., Jenson, J., Mylroie, J., et al. (2012). Magnesium and strontium systematics in tropical speleothems from the Western Pacific. *Chem. Geol.* 29, 1–17. doi: 10.1016/j.chemgeo.2011.10.008

Sirocko, F., Knapp, H., Dreher, F., Förster, M. W., Albert, J., Brunck, H., et al. (2016). The ELSA-Vegetation-Stack: reconstruction of landscape evolution zones (LEZ) from laminated eifel maar sediments of the last 60,000 years. *Glob. Planet. Change* 142, 108–135. doi: 10.1016/j.gloplacha.2016.03.005

Steiger, R. H., and Jäger, E. (1977). Subcommission on geochronology: convention on the use of decay constants in geo- and cosmochronology. *Earth Planet. Sci. Lett.* 36, 359–362. doi: 10.1016/0012-821X(77)90060-7

Tooth, A. F., and Fairchild, I. J. (2003). Soil and karst aquifer hydrological controls on the geochemical evolution of speleothem-forming drip waters. Crag Cave, southwest Ireland. *J. Hydrol.* 273, 51–68. doi: 10.1016/S0022-1694(02)00349-9

Treble, P., Shelley, J. M. G., and Chappell, J. (2003). Comparison of high resolution sub-annual records of trace elements in a modern (1911–1992) speleothem with instrumental climate data from southwest Australia. *Earth Planet. Sci. Lett.* 216, 141–153. doi: 10.1016/S0012-821X(03)00504-1

Treble, P. C., Chappell, J., and Shelley, J. M. G. (2005). Complex speleothem growth processes revealed by trace element mapping and scanning electron microscopy of annual layers. *Geochim. Cosmochim. Acta* 69, 4855–4863. doi: 10.1016/j.gca.2005.06.008

von Kamp, H., and Ribbert, K. H. (2005). Erläuterungen zu Blatt 4611 Hagen-Hohenlimburg Geologische Karte von Nordrhein-Westfalen 1: 25.000. Krefeld.

Wanner, H., Beer, J., Bütikofer, J., Crowley, T. J., Cubasch, U., Flückiger, J., et al. (2008). Mid- to Late Holocene climate change: an overview. *Quat. Sci. Rev.* 27, 1791–1828. doi: 10.1016/j.quascirev.2008.06.013

Warken, S. F., Fohlmeister, J., Schröder-Ritzrau, A., Constantin, S., Spötl, C., Gerdes, A., et al. (2018). Reconstruction of late Holocene autumn/winter precipitation variability in SW Romania from a high-resolution speleothem trace element record. *Earth Planet. Sci. Lett.* 499, 122–133. doi: 10.1016/j.epsl.2018.07.027

Wassenburg, J. A., Dietrich, S., Fietzke, J., Fohlmeister, J., Jochum, K. P., Scholz, D., et al. (2016a). Reorganization of the North Atlantic Oscillation during early Holocene deglaciation. *Nat. Geosci.* 9, 602–605. doi: 10.1038/ngeo2767

Wassenburg, J. A., Scholz, D., Jochum, K. P., Cheng, H., Oster, J., Immenhauser, A., et al. (2016b). Determination of aragonite trace element distribution coefficients from speleothem calcite-aragonite transitions. *Geochim. Cosmochim. Acta* 190, 347–367. doi: 10.1016/j.gca.2016.06.036

Weber, M., Lugli, F., Jochum, K. P., Cipriani, A., and Scholz, D. (2018b). Calcium carbonate and phosphate reference materials for monitoring bulk and microanalytical determination of Sr Isotopes. *Geostand. Geoanal. Res.* 42, 77–89. doi: 10.1111/ggr.12191

Weber, M., Scholz, D., Schröder-Ritzrau, A., Deininger, M., Spötl, C., Lugli, F., et al. (2018a). Evidence of warm and humid interstadials in central Europe during early MIS 3 revealed by a multi-proxy speleothem record. *Quat. Sci. Rev.* 200, 276–286. doi: 10.1016/j.quascirev.2018.09.045

Weber, M., Wassenburg, J. A., Jochum, K. P., Breitenbach, S. F. M., Oster, J., and Scholz, D. (2017). Sr-isotope analysis of speleothems by LA-MC-ICP-MS: high temporal resolution and fast data acquisition. *Chem. Geol.* 468, 63–74. doi: 10.1016/j.chemgeo.2017.08.012

Wedepohl, H. K. (1995). The composition of the continental crust. *Geochim. Cosmochim. Acta* 59, 1217–1232. doi: 10.1016/0016-7037(95)00038-2

Yang, Q., Scholz, D., Jochum, K. P., Hoffmann, D. L., Stoll, B., Weis, U., et al. (2015). Lead isotope variability in speleothems—A promising new proxy for hydrological change? First results from a stalagmite from western Germany. *Chem. Geol.* 396, 143–151. doi: 10.1016/j.chemgeo.2014.12.028

Zhou, H., Feng, Y.-X., Zhao, J.-X., Shen, C.-C., You, C.-F., and Lin, Y. (2009). Deglacial variations of Sr and ^{87}Sr/^{86}Sr ratio recorded by a stalagmite from Central China and their association with past climate and environment. *Chem. Geol.* 268, 233–247. doi: 10.1016/j.chemgeo.2009.09.003

Conflict of Interest: The authors declare that the research was conducted in the absence of any commercial or financial relationships that could be construed as a potential conflict of interest.

frontiers in Earth Science

ORIGINAL RESEARCH
published: 29 April 2021
doi: 10.3389/feart.2021.672962

Innovative Approaches for the Sedimentological Characterization of Fine Natural and Anthropogenic Sediments in Karst Systems: The Case of the Apuan Alps (Central Italy)

Alessia Nannoni[1], Leonardo Piccini[1], Pilario Costagliola[1], Nicolò Batistoni[1], Pietro Gabellini[1], Raffaello Cioni[1], Gabriele Pratesi[2] and Silvia Bucci[2]*

[1] Department of Earth Science, Università degli Studi di Firenze, Florence, Italy, [2] Agenzia Regionale per la Protezione Ambientale della Toscana, Florence, Italy

OPEN ACCESS

Edited by:
Davide Tiranti, Agenzia Regionale per la Protezione Ambientale (ARPA), Italy

Reviewed by:
Nadja Zupan Hajna, Research Centre of the Slovenian Academy of Sciences and Arts, Slovenia
William White, Pennsylvania State University (PSU), United States

***Correspondence:**
Alessia Nannoni
alessia.nannoni@unifi.it

Specialty section:
This article was submitted to Quaternary Science, Geomorphology and Paleoenvironment, a section of the journal Frontiers in Earth Science

Received: *26 February 2021*
Accepted: *08 April 2021*
Published: *29 April 2021*

Citation:
Nannoni A, Piccini L, Costagliola P, Batistoni N, Gabellini P, Cioni R, Pratesi G and Bucci S (2021) Innovative Approaches for the Sedimentological Characterization of Fine Natural and Anthropogenic Sediments in Karst Systems: The Case of the Apuan Alps (Central Italy). Front. Earth Sci. 9:672962. doi: 10.3389/feart.2021.672962

The Apuan Alps (NW Tuscany) is an important area of Central Italy characterized by large karst systems mainly fed via direct and diffuse water infiltration (autogenic recharge). These waters usually transport a clastic sediment load, originated by natural, surface and subsurface rock erosion/weathering which, in part, is deposited underground. In the Apuan Alps, during extreme rain event, huge amounts of carbonate powder, produced as a waste resulting from the quarrying operations of the famous "Carrara" marble, mix up with meteoric waters forming a slurry that is transported through the karst openings into the caves, where the carbonate powder may be deposited along with natural sediments. Depending upon karst hydrology and water fluxes, the slurry may eventually reach karst springs heavily reducing water quality. Mineralogical composition of the sediments collected along karst waterways and springs shows variable proportions of calcite associated with dolomite and silicates particles whereas the marble powder samples from quarry areas are mainly composed by calcite grains. Cave deposits of natural origin have usually a fine-sand grain size whereas spring sediments have a more variable grain-size distribution. Marble powder mainly has a silt grain size and produces a sort of "granulometric and morphometric pollution" which influences the transport mechanism of solid load through the karst systems along both vadose and phreatic waterways.

Keywords: karst, cave deposits, groundwater, solid load, Apuan Alps

INTRODUCTION

Caves represent one of the most relevant depositional archives in continental areas. This depends on the possibility that sediments can be preserved for very long times without undergoing significant weathering processes (Sasowsky, 2007). Among the typical cave deposits, those due to carbonate precipitation (speleothems) are by far the most studied because of the possibility to obtain paleoclimatic and paleoenvironmental data with very high temporal resolution (e.g., Fairchild and Baker, 2012 and references there in). Ancient clastic deposits, despite being volumetrically the most

common deposits in caves, are much less studied due to the difficulties of dating (Häuselmann et al., 2020) and of determining their source areas. Recently, an increasing interest has being focused to these deposits because their deposition is strongly related to landscape erosion phases and to extreme flood events, which are correlated with the local climate evolution (Karkanas and Goldberg, 2013). Moreover, transport and depositional dynamics of these sediments have important implications in archeology and paleontology (Martini, 2011).

Cave clastic sediments are usually divided into two categories: allogenic and autogenic sediments (White, 2007). Deposits related to allogenic supply through sinking streams are frequent in both active and relict karst systems (Springer, 2019). The sedimentological investigation of allogenic deposits allows also to get insights on the hydrological functioning of karst aquifers (Bosch and White, 2007; Bella et al., 2020). Autogenic deposits, derived from material coming from the karst system itself, are less common because the weathering processes affecting karst areas are mainly of chemical nature (dissolution) and therefore they do not virtually produce clastic sediments. The autogenic cave deposits are often derived from fragments produced by rock collapses that directly affect the path of the active passages. In this case, the clastic component has variable dimensions and irregular shapes, and a roundness depending on the greater or lesser transport it has undergone. Deposits of this type are generally found only in sectors affected by a consistent high energy flow. Fine carbonate deposits, usually ranging from fine sands to silt grain-size, are also found in caves (e.g., Zupan Hajna, 2002; Zupan Hajna et al., 2008). In this case, carbonate clasts are considered the product of subterranean weathering processes of limestone and dolomite (Zupan Hajna, 2003). Fine autogenic sediments usually occur in the epiphreatic and phreatic portions of karst systems, where they are transported in water-filled conduits. In these conditions transport involves only medium and fine-grained materials (sands, silt, clays) that can run through the entire system up to water outlets (karst springs). Hence, the textural features of these sediments are potentially able to provide us with information on the dynamics and therefore on the structure of the phreatic zones of karst systems (e.g., Winkler et al., 2016). Available literature is mainly focused on the physical and hydraulic properties of these sediments as suspended load during storm events but contributions on the systematic mineralogical, morphological and sedimentological characterization of these deposits are scarce (Drysdale et al., 2001; Herman et al., 2007; Piccini et al., 2019).

The Apuan Alps (AA), in north-western Tuscany, is a very peculiar mountain range in the Mediterranean basin, with many geological and biological features of international interest. This mountain area, whose maximum elevation is 1942 m asl at Pisanino Mount, consists of both metamorphic and non-metamorphic carbonate rocks belonging to three different tectonic units (Carmignani and Kligfield, 1990). The Apuan metamorphic unit is mainly represented by phyllites of the Paleozoic basement (Conti et al., 1993), meta-dolostones, marbles and dolomitic marbles (about 115 km^2 as outcrops) and by cherty limestones (about 20 km^2) (**Figure 1**). Carbonate formations (meta-dolostones and marbles) host well-developed karst landforms and several caves, including some of the largest and deepest of Italy (Piccini, 1998). Karstification developed since late Pliocene following the progressive exhumation of the carbonate sequences. Some major stages of karst development are related to tectonics and paleo-hydrological readjustment of river network (Piccini, 1998; Piccini et al., 2003), whereas climate changes are mainly recorded by cave chemical deposits (e.g., Isola et al., 2019). In the AA, the karst systems frequently host autogenic sediments. They are mainly composed by calcite and dolomite with minor amounts of silicates, thus reflecting the local origin of these sediments, the active role of the natural weathering processes as well as the significant solid load transport effectiveness of the phreatic sectors of karst aquifer.

In the AA, variable amounts of carbonate powder, resulting from the quarrying operations of the worldwide famous "Carrara" marble, are mixed up with meteoric waters during storm events, forming a slurry that is rapidly transported throughout the karst openings into caves (Ekmekci, 1990; Rizzo et al., 2008). There it may be deposited along with natural sediments, modifying their composition. A significant portion of the slurry may reach the numerous springs fed by AA karst systems (Doveri et al., 2019). Consequently, springs may be temporarily affected by huge solid transport phenomena that determine a high turbidity during the flood events (Drysdale et al., 2001; Piccini et al., 2019).

The aim of this pilot study, which uses also unconventional methods and approaches, is to characterize the mineralogical, sedimentological, and morphological features of cave and spring sediments collected in some of the major AA karst systems. The same approach was applied to a few samples of marble powders produced by block sawing in the AA quarrying district. Cave and spring sediments were then compared to the quarry marble powder to investigate how anthropogenic materials can affect clastic sedimentation processes in presently active cave and karst spring environments.

MATERIALS AND METHODS

Twelve sampling sites (**Figure 1**) were selected to study the mineralogical, grain size, and morphological characteristics of cave deposits and to infer their source area and transport dynamic. Two main types of sampling environments were chosen: (1) some of the major AA karst springs, (2) some vadose cave passages, both active and inactive ones. Furthermore, samples were collected also in some quarries, where the marble powder is produced, as examples of the endmember of anthropogenic origin (**Figure 2**).

About 1 dm^3 of sediment was collected in a LDPE bag at each site using a Teflon spoon, reducing the use of metallic tools to avoid contamination. The samples were dried at 45°C, then they were passed through a 2.8 mm sieve to remove impurities such as vegetal material and coarse particles accidentally occurring in the samples. The fraction passing through a 0.250 mm sieve was used for XRD, SEM-EDS and Optical Morphometric (OM) analyses. The sieved fraction to be analyzed was divided one or several

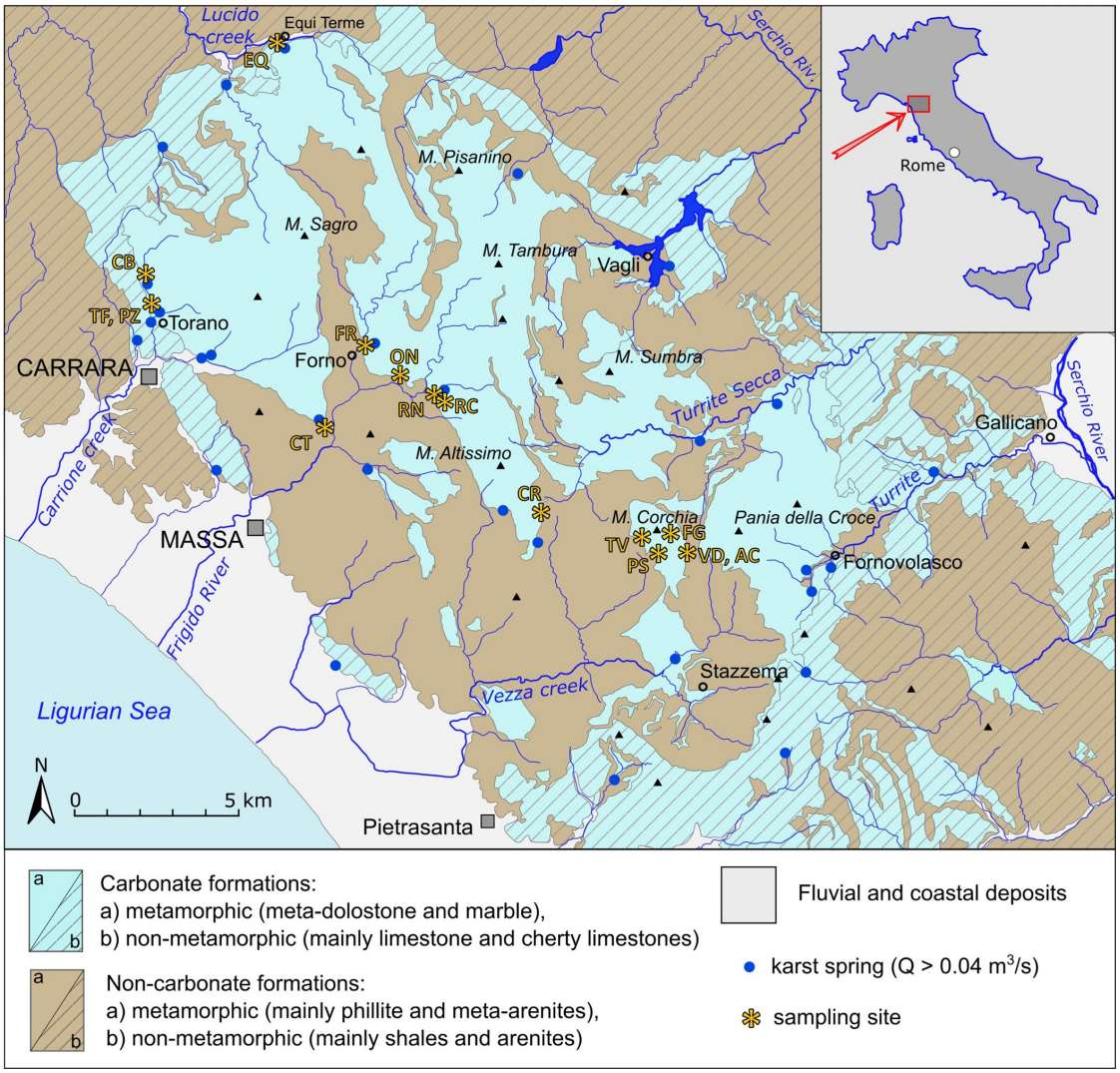

FIGURE 1 | Simplified hydrogeological map of the Apuan Alps (modified after Piccini et al., 2019). Sampling sites are highlighted. More details about the sites are reported in **Table 1**.

times in a sample splitter to obtain small but well-representative quantities (up to a few tens of grams).

Samples Description

The sampled deposits have been grouped as follows (**Table 1**): (1) cave sediments deposited in active vadose passages (active cave sediments), (2) cave sediments deposited in relict vadose passages (relict cave sediments), (3) cave-spring and karst spring deposits transported in phreatic flow condition (spring sediments), and (4) marble powder produced by different sawing techniques (diamond wire and chain sawing). Most of the active and relict cave sediments were collected in the Corchia cave system, one of the largest and complex caves in Italy (Piccini et al., 2008; Piccini, 2011). Relict deposits were also collected in the Buca dell'Onice, an inactive cave in the Frigido River basin containing a thick clastic deposit (Piccini et al., 2003). In the same river basin, active cave deposits were collected into the Buca del Rocciolo e Buca di Renara, two caves that are occasionally inundated during major floods. Three sediment samples were collected in the Buca di Equi, in northern AA, a cave-spring which is partially inundated during floods. Other sediments come from Vauclausian-type springs fed by submerged and inaccessible conduits. Samples that were transported in phreatic conditions and were collected in caves close to the outlet (referred as "cave-spring" in the text) are considered as karst spring deposits.

Analytical Methods

The analyses were performed only on the fraction passing through a sieve with a diameter of 0.250 mm ($\varphi > 2$, i.e., from fine sands to clay grain size) to optimize the adopted instrumental micro-procedures that require a small quantity of sediment (1–3 mm^3). Anyway, almost systematically, the sediment fraction

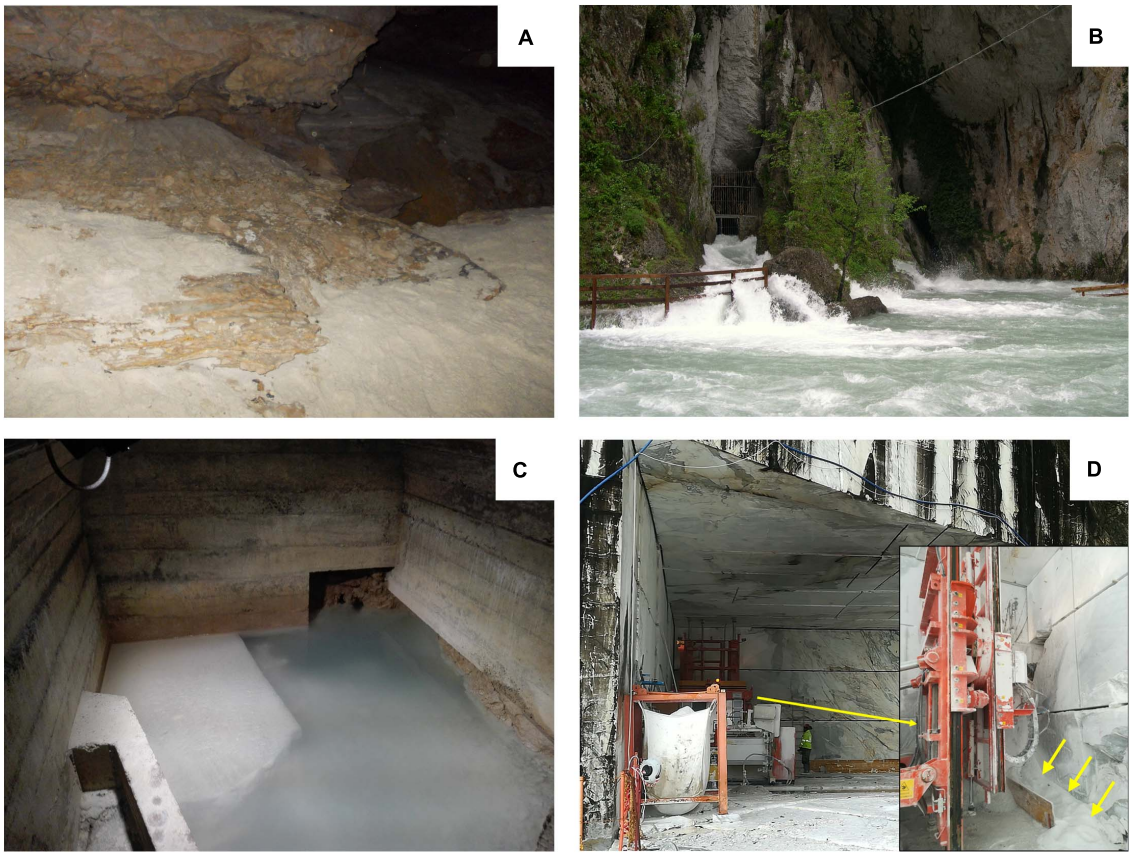

FIGURE 2 | Examples of the chosen sampling sites: **(A)** fine clastic deposit in an occasionally active vadose passage of the Antro del Corchia cave; **(B)** cave-spring outlet (see the text for the terminology) of Buca d'Equi cave during a flood; **(C)** fine whitish deposits in the Tana dei Tufi water gallery, a spring strongly affected by marble slurry pollution; **(D)** quarrying sector where marble powder is produced (yellow arrows point to the powder).

with a diameter exceeding this threshold was negligible (less than 10% of the total volume). Furthermore, the fine components are the most relevant sediment fraction for this study, since they are more easily transported as suspended solid in flowing water and therefore can travel long distances also in phreatic conditions.

XRD measurements were performed at the Centro di Servizi di Cristallografia Strutturale (CRIST) of the Florence University with a Bruker Da Vinci D8 diffractometer operating with a Cu X-ray source, a Theta-Theta goniometer, and a flat Eulero Cradle sample holder, equipped with a Bruker LYNXEYE-XE detector. The filament current of the tube was 40 mA and the acceleration potential 40 kV. Yttrium oxide (Y_2O_3) was used as a reference material.

Samples for microchemical analyses were prepared by means of the sample dispersion unit (SDU) of the image particle analyzer (see below for description): the sediment particles were scattered over a stub (diameter = 12.5 mm) covered with an adhesive graphite tape. This method allowed to properly separate sediment particles and to homogeneously distribute them on the stub. Finally, the samples were carbon-sputtered with a Quorum Q150R ES sample metallizer. Microchemical compositions of the samples were investigated by means of a Scanning Electron Microscope (ZEISS EVO MA15, operating at 15 kV acceleration voltage), coupled with an Energy Dispersive Spectrometer (OXFORD INCA 250 EDS detector and software INCA Feature, Oxford Instruments®) at the Centro di Microscopia Elettronica e Microanalisi (MEMA) of the Florence University. Images were collected using both Secondary Electrons (SE) and Backscattered Electron (BSE) imaging. The software setup was fixed to analyze at least 2000–3500 particles with a circle equivalent diameter larger than 0.0038 mm. Based on EDS micro-chemical analyses, grains were classified in four categories during post processing: calcite, dolomite, silicate, and unclassified particles.

Particles having Ca > 5 wt% (weight percentage) were classified as carbonate grains, then a Ca/Mg ratio of 2 (expressed in moles) was selected as threshold between calcite and dolomite. This value was chosen because of the short acquisition time (4 s) for each particle micro-analysis that often results in a systematic underestimate of the Mg content. Grains that presented Si > 2 wt% were identified as silicate minerals. The particles that did not fall in these three mineral groups were considered "unclassified" and not considered in the dataset analysis. The unclassified group comprises (a) organic matter and metallization residuum (maximum 15% of the analyzed grains), and (b) accessory minerals such as sulfates, oxides/hydroxides, apatite (maximum 2.5% of the analyzed grains).

TABLE 1 | List of the collected samples (the letters of the sample code refer to the sampling site reported in **Figure 1**).

Code	Type	Sampling site	Description
ON.01	Cave, relict	Buca dell'Onice cave, Frigido basin	Terminal chamber, upper deposit
ON.02	Cave, relict	Buca dell'Onice cave, Frigido basin	Terminal chamber, lower deposit
RC.02	Cave, relict	Buca del Rocciolo cave, Frigido basin	Relict epiphreatic passage
FG.01	Cave, relict	Fighiera, Corchia cave, Vezza basin	Relict vadose passage
FG.02	Cave, relict	Fighiera, Corchia cave, Vezza basin	Relict vadose passage
FG.03	Cave, relict	Fighiera, Corchia cave, Vezza basin	Relict vadose passage
AC.01	Cave, relict	Antro del Corchia cave, Vezza basin	Relict vadose passage
VD.05	Cave, relict	Antro del Corchia cave, Vezza basin	Relict vadose passage
VD.01	Cave, active	Antro del Corchia cave, Vezza basin	Active vadose passages
VD.02	Cave, active	Antro del Corchia cave, Vezza basin	Active vadose passages
VD.03	Cave, active	Antro del Corchia cave, Vezza basin	Occasionally inundated chamber
VD.04	Cave, active	Antro del Corchia cave, Vezza basin	Occasionally inundated chamber
VD.06	Cave, active	Antro del Corchia cave, Vezza basin	Active vadose passages
RC.01	Cave, active	Buca del Rocciolo cave, Frigido basin	Epiphreatic passage
CT.01	Karst spring	Cartaro spring, Frigido basin	Spring, settling pool
FR.01	Karst spring	Forno spring, Frigido basin	Spring deposit
FR.02	Karst spring	Forno spring, Frigido basin	Spring deposit
RN.01	Karst spring	Renara spring, Frigido basin	Cave-spring, settled suspended sediment
EQ.01	Karst spring	Buca d'Equi cave, Lucido basin	Cave-spring, close to the cave outlet
EQ.02	Karst spring	Buca d'Equi cave, Lucido basin	Cave-spring, upper passage
EQ.03	Karst spring	Buca d'Equi cave, Lucido basin	Cave-spring, settled suspended sediment
TF.01-t	Karst spring	Tana dei Tufi aqueduct, Carrione basin	Top part of a deposit in an open channel
TF.01-b	Karst spring	Tana dei Tufi aqueduct, Carrione basin	Lower part of a deposit in an open channel
CB.01	Karst spring	Carbonera spring, Carrione basin	Access gallery to the aqueduct
PZ.01	Karst spring	Pizzutello spring, Carrione basin	Main aqueduct, below water surface
CR.01	Quarry	Cervaiole quarry, Altissimo mount	Marble powder, wet chain sawing
CR.02	Quarry	Cervaiole quarry, Altissimo mount	Marble powder, diamond wire
TV.01	Quarry	Tavolini B quarry, Corchia mount	Marble powder, wet chain sawing
TV.02	Quarry	Tavolini B quarry, Corchia mount	Marble powder, diamond wire
PS.03	Quarry	Piastraio quarry, Corchia mount	Marble powder, diamond wire
PS.04	Quarry	Piastraio quarry, Corchia mount	Marble powder, wet chain sawing
PS.05	Quarry	Piastraio quarry, Corchia mount	Marble powder, dry chain sawing

Morphometric and grain-size analyses (MGS) were performed with an automated optical analyzer for particle characterization (Morphologi G3, Malvern Instruments^{TM}). The instrument measures basic parameters (length, width, perimeter, and area) of each particle with diameter ranging from 0.0015 mm up to 3 mm. The software calculates several shape parameters such as circle equivalent diameter (CED), aspect ratio (AR), circularity (C), solidity (S), and convexity (Cv). CED is defined as the diameter of a circle with the same area of the particle 2D-projection. AR, C, S, and Cv are non-dimensional shape parameters defined, respectively, as: the width over the length of the particle, the circle equivalent perimeter over the real particle perimeter, the particle projected area over the particle convex hull area, and the particle convex hull perimeter over the particle perimeter. More details about the instrument and operating protocols can be found in Leibrandt and Le Pennec (2015). The morphometric analysis is presented only for particles falling in the fine to coarse silt size interval (0.0625 – 0.0078 mm, $\varphi = 4 - 7$). This specific grain size interval was selected because it comprises a considerable proportion of particles for all the samples in terms of both volume and number of grains, and because the analysis in narrow size intervals is more helpful for revealing characteristics for these kinds of material (Leibrandt and Le Pennec, 2015; Li et al., 2019). Grain size distributions (GSD) were calculated in volume fractions (V%) and in number of particles (n%) falling in CED intervals of ½ φ (Folk and Ward, 1957; Blott and Pye, 2012). We stress that GSD expressed as number of particles is not a standard sedimentological method, but it is a reliable approach when dealing with grain size data obtained with optical methods instead of sieving, because it allows to distinguish better the grain size differences in the finer portions of sediments (González-Tello et al., 2010).

RESULTS

Grains Mineralogy and Micro-Morphology

XRD analyses showed that the sediments collected in caves and karst springs are mainly composed by calcite, dolomite and secondarily by silicates (**Figure 3**). Calcite and dolomite greatly vary in their relative quantities, as estimated by their diagnostic XRD peak intensities. As expected, quarry samples are made up of calcite only, being marble almost pure metamorphosed limestone (Cantisani et al., 2005).

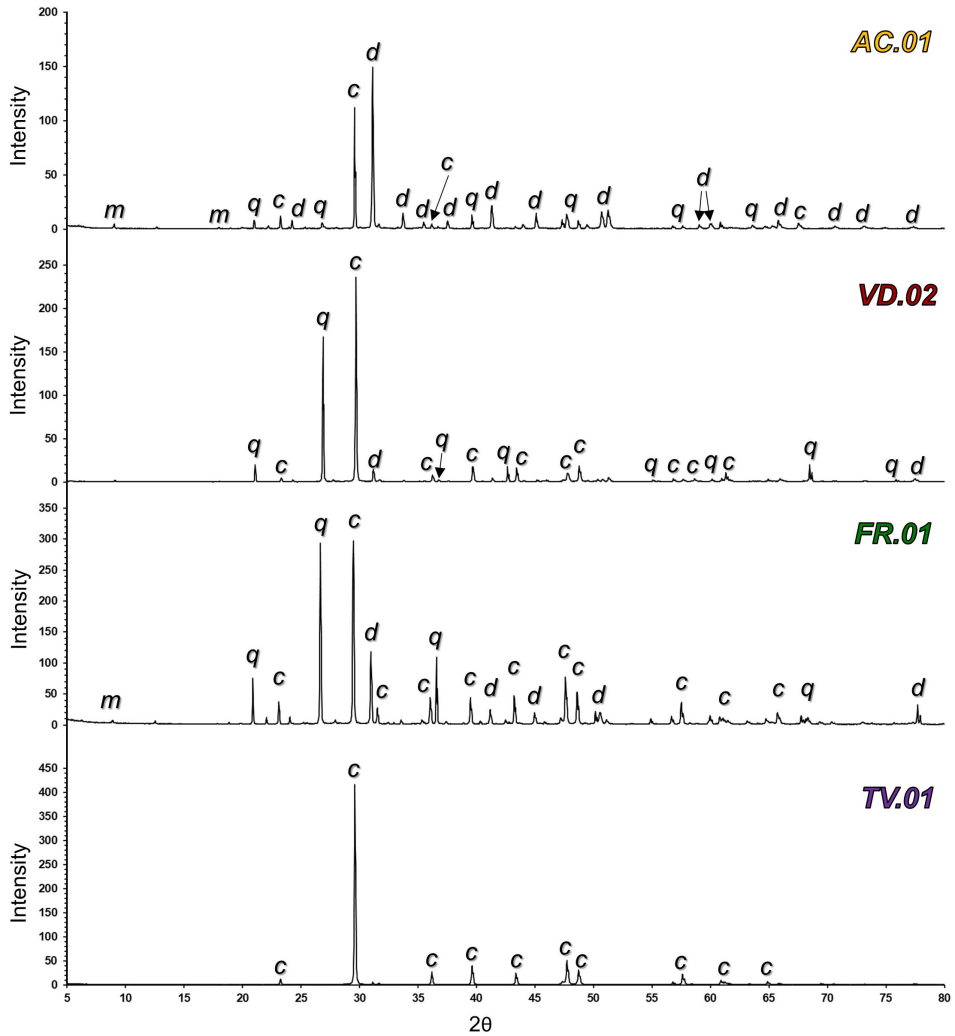

FIGURE 3 | Diffraction patterns of four samples, one for each category of sediments: relict cave sediment (AC.01), active cave sediment (VD.02), cave-spring (FR.01), and marble powder (TV.01). Lowercase letters highlight peaks for specific minerals: c, calcite; d, dolomite; q, quartz; m, muscovite.

SEM-EDS analyses made it possible: to quantify the abundances of the main constituents (calcite, dolomite, and silicates), to observe the shape of the particles, and to get some insights on the grain size of each constituent. Silicate minerals occur with variable proportions in all the studied categories of deposits, but never exceed 50%. The compositional features of the samples are shown in the two ternary diagrams of **Figure 4**. The figure illustrates how the relative proportions of the three main mineralogical constituents can drastically change for many samples if the volume (**Figure 4A**; V%) or the number of particles (**Figure 4B**; n%) is considered. This effect is due to the inhomogeneous size distribution of the three minerals. In the V% diagram, the mineral proportions are indeed heavily influenced by the composition of the coarse fraction, whereas the nature of fine grains determines the position of the samples in the n% diagram, because they are numerically much more abundant than the coarser particles, although volumetrically irrelevant. Ideally, the sample points remaining in the same position in the two diagrams are those having a similar GSD of the three main mineralogical components. Therefore, the grain size of dolomite, quartz and calcite may be highlighted by the relative positions occupied by a sample in the two diagrams.

Samples having a uniform composition, such as quarry materials (CR.01, CR.02, PS.03, PS.04, PS.05, TV.01, and TV.02) and the two cave deposits consisting almost exclusively of dolomite (ON.01 and ON.02) maintain the same location in the two diagrams. Conversely, samples having a variable composition can greatly change their position. For example, sample FR.02 is placed more on the right in the V% diagram respect to the n% diagram, indicating that the silicate and dolomite particles are coarser than the calcite grains. In general, we observe that spring samples have usually more variable proportions of silicates and dolomite but are dominated by fine calcite grains and tend to move toward the calcite corner in the n% diagram. Conversely, most of the cave deposits tend to move toward the dolomite

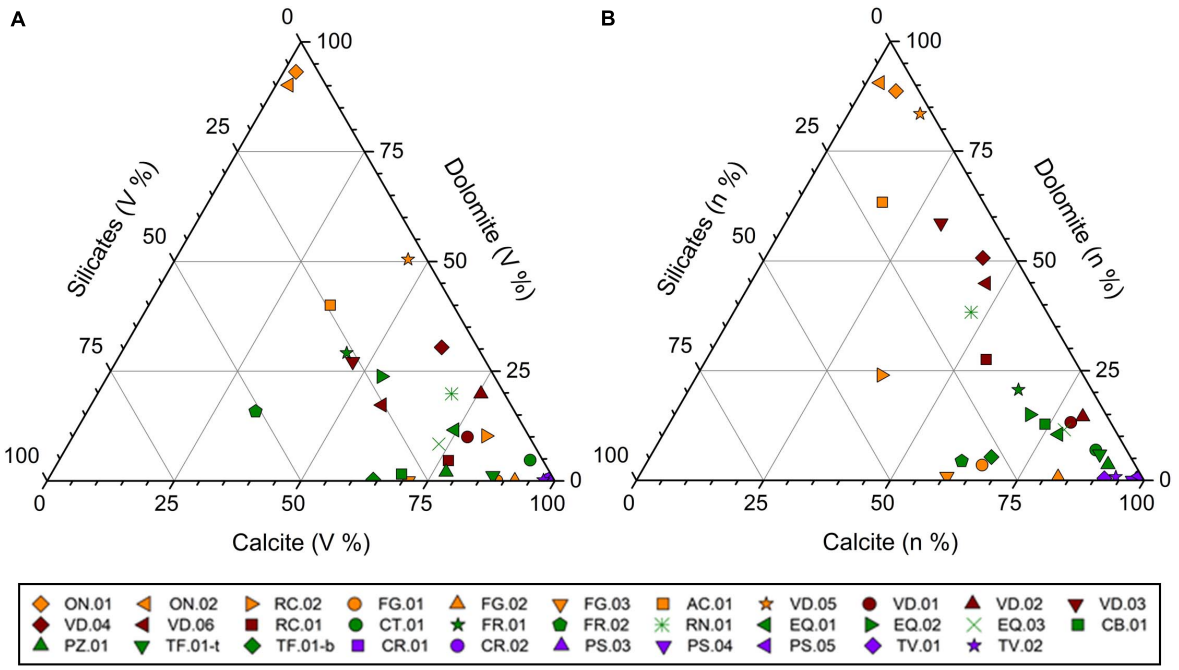

FIGURE 4 | Calcite/dolomite/silicates ternary diagrams expressed as volume percentage **(A)** and number of grain percentage **(B)**. Colors correspond to different types of deposits: orange, ancient cave sediment; dark red, recent cave sediment; green, karst spring and cave-spring; purple, quarry.

vertex, indicating that dolomite particles usually have a finer grain size then calcite ones.

Particles also show distinctive features of the surface. Some carbonate particles show clear traces of dissolution (**Figures 5A,B**), possibly due to natural weathering processes. The surfaces of the clasts of natural origin are always irregular and engraved by small cavities caused by etching such as V-in-V micro-morphologies (**Figure 5A**) frequently observed in calcite and dolomite exposed to chemical aggressive environments (Viles and Moses, 1998). On the contrary, the particles produced by the cutting and squaring of the marble blocks are usually more euhedral with no evidence of dissolution (**Figures 5C,D**). Spring and active cave samples exhibits both micro-morphologies (**Figures 5E,F**). Where present, quartz grains usually show conchoidal fracture surfaces (**Figure 5E**).

Grain Size

Grain size analyses were obtained by means of the optical morphograinsizer because this instrument allows a more statistically robust dataset based on a much greater number of particles respect to SEM-EDS. In the analyzed sediments, GDS obtained by means of SEM-EDS were found to not be reliable even considering the silt-size grains, in contrast to previous findings (Cheetham et al., 2008). The particle size analysis performed on the medium-fine portion (from 0.25 to 0.0015 mm) of the cave, cave-spring sediments and of the cutting-powder collected in quarries, showed quite variable characteristics (**Figure 6**).

Although only the $\varphi > 2$ fraction was analyzed, the GSD expressed as volume percent show substantial differences between the sediment categories. Cave and spring sediments show a high variability of frequency in the $\varphi = 2.0–2.5$ and $\varphi = 2.5–3.0$ grain-size classes, even when considering samples collected in the same site (i.e., FR.01 and FR.02, **Figure 6C**), with values ranging from a few percent to 53%. This larger dispersion in the coarser fraction is possibly influenced by the poor representativeness for some of the analyzed samples for what concerns the coarser particles, due to the small quantity of material used for MGS analysis (1–3 mm^3). The graphs expressed in volume (**Figures 6A,C,E**) are therefore surely significant for all samples when $\varphi > 3$ (CED > 0.125 mm) and mainly in the silt fraction ($\varphi = 4–8$). In this portion of the cave sediments graph (**Figure 6A**) we can distinguish two samples of relict sediments (ON.01 and ON.02) from all the others. The spring sediments show instead more uniform characteristics, although with significant differences in the classes between $\varphi = 3.5$ and $\varphi = 4.5$. The quarry materials, on the other hand, show two distinct groups based on grain size that reflect the origin of the powders whether produced by cutting with diamond wire (finer size, modal class $\varphi = 4.0–4.5$) or chain saws (coarser size, modal class $\varphi \leq 3.5–4.0$).

To overcome the representativeness problems linked to the representation in volume percentage and to emphasize the difference in the finer portion, GSD is plotted also as percentage in number of particles **Figures 6B,D,F**). GSD expressed as number of particles is quite uniform in quarry powder. Cave sediments show relevant differences in the finer portion ($\varphi > 8$) where active cave deposits are usually finer than the relict cave ones. Spring sediments are also quite differentiated in the finer portion ($\varphi > 7$): CT.01, PZ.01, and FR.02 samples

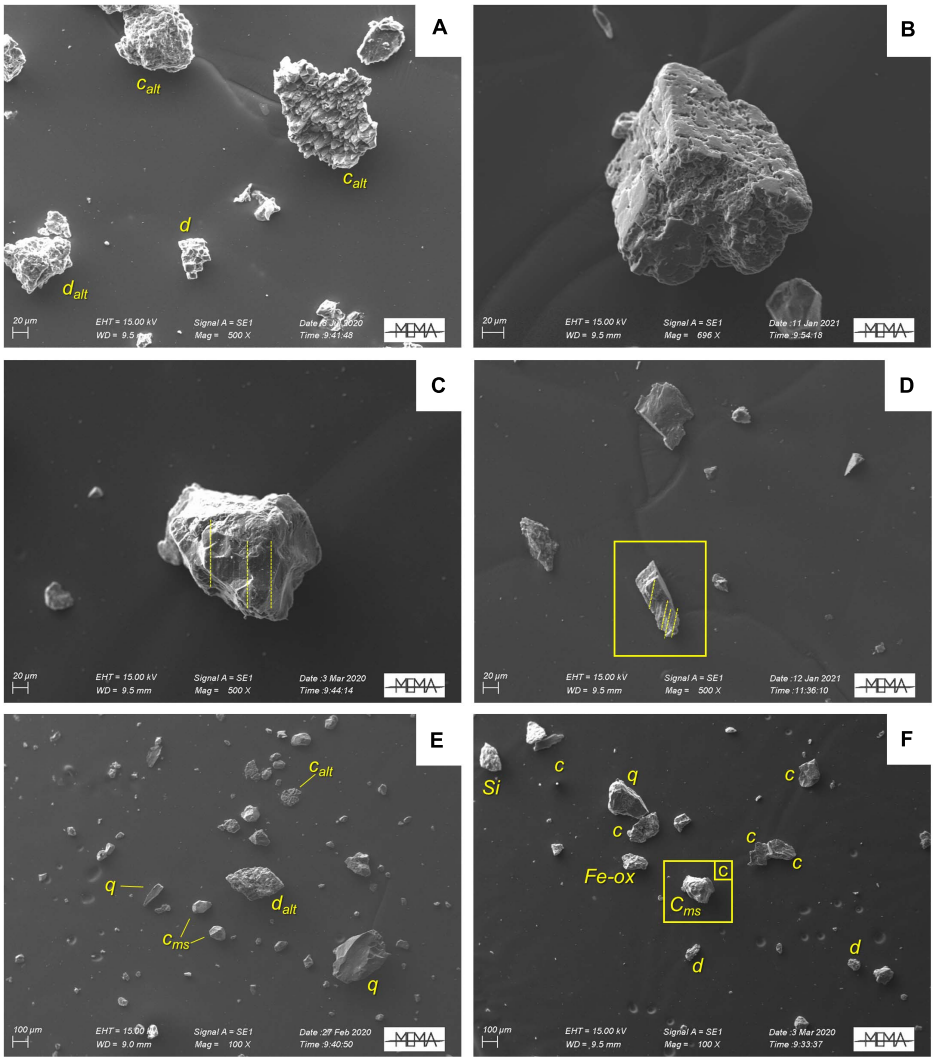

FIGURE 5 | SEM secondary-electrons pictures of natural and anthropogenic particles in different types of samples. **(A)** Naturally weathered grains of dolomite and calcite (sample AC.01). **(B)** Calcite grain with clear dissolution cavities (sample RC.01). **(C)** Magnification of a calcite grain with typical morphological features produced by chainsaw cutting (the yellow dashed lines). **(D)** Typical shape of quarry deposits: angular edges, no dissolution features, preferential fracturing along cleavage planes, chainsaw scratches (grain in the yellow box; sample TV.01). **(E)** Overview of some common features of spring sediments: angular, non-altered calcite grains, quartz with conchoidal fracture, weathered dolomite, and calcite grains (sample FR.01). **(F)** Typical features of cave samples collected in active vadose passages (VD.01): angular calcite grains, conchoidal quartz [the yellow box highlights the grain of picture **(C)**]. c, calcite; c_{ms}, anthropogenic calcite; c_{alt}, weathered calcite; d/d_{alt}, unaltered/weathered dolomite; Si, silicate; q, quartz; Fe-ox, iron-oxide.

have a modal class (φ = 7.5–8) coarser than the other samples ($\varphi \geq 8.5$).

Grain Morphometry

Analysis performed with the MGS provide also morphometrical data describing the shape (namely the shape of the projected particles outline) of each grain. The selected shape parameters (aspect ratio, circularity, convexity, and solidity) range, for all the types of samples, over a quite large interval of values, however, suggesting some important differences. Considering only the fine to coarse silt fraction, the mean values of the four selected shape parameters for the relict cave samples are comprised in the following ranges: AR = 0.64–0.75; *C* = 0.84–0.92; Cv = 0.97–0.99 and *S* = 0.94–0.98 (**Figure 7**). Their mean values for the active cave samples vary in the intervals: 0.66–0.74 for AR, 0.85–0.91 for C, 0.97–0.99 for Cv, and 0.95–0.98 for S. Karst spring samples have mean values of 0.68–0.70 for AR, 0.86–0.91 for C, 0.97–0.99 for Cv, and 0.94–0.98 for S. In the quarry samples, AR mean values range between 0.66 and 0.69, C mean values are comprised between 0.83 and 0.91, Cv is comprised in the 0.96–0.99 interval, and S mean values range between 0.93 and 0.98. Interquartile ranges are always asymmetrically distributed around the median value, with a large number of outliers that is generally smaller for the samples of marble powder. Interquartile ranges for AR are broader than those exhibited by the other parameters in all samples. Quarry samples display a slightly more dispersed

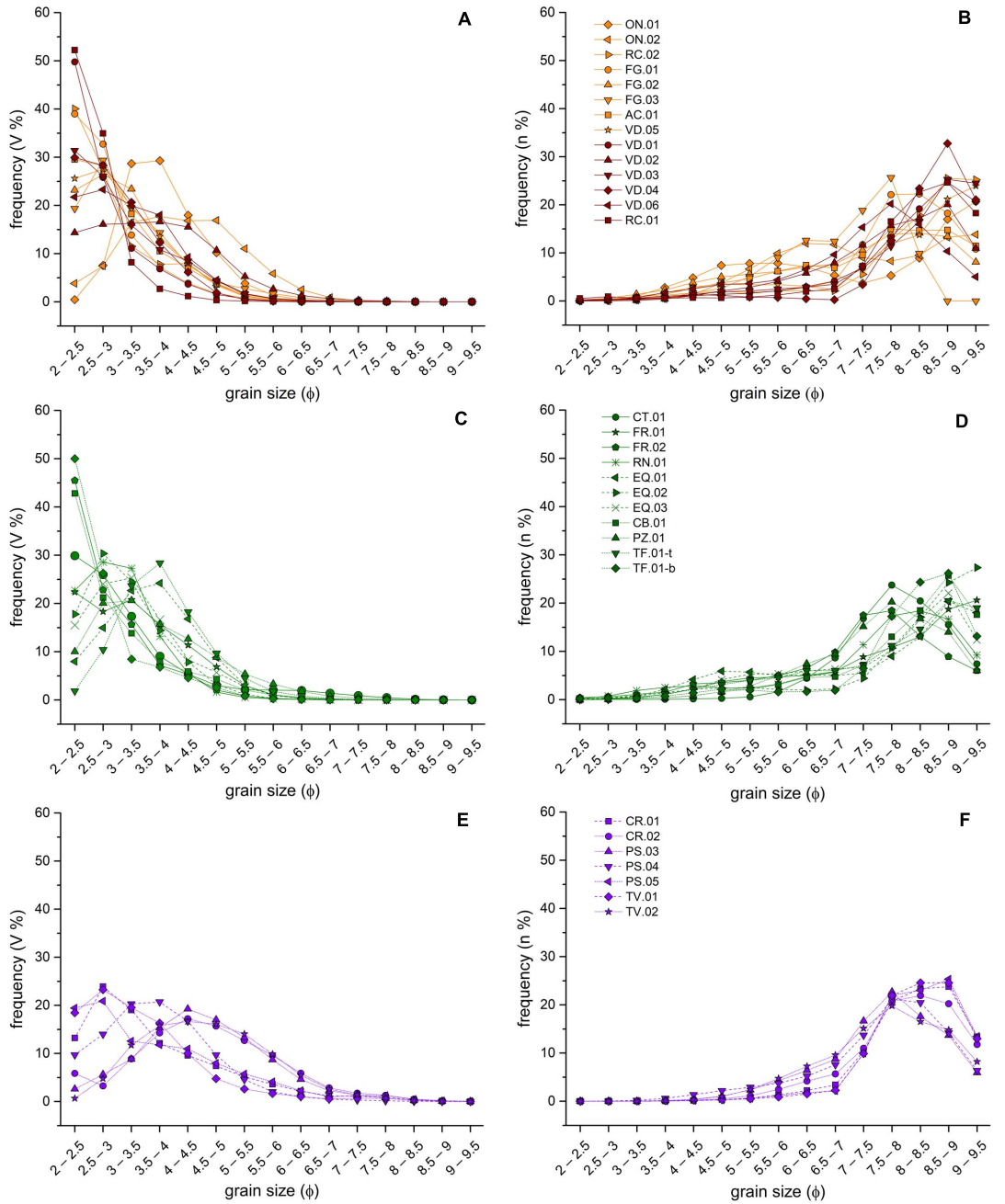

FIGURE 6 | Grain-size distributions expressed as volume percentage (V%, left column) and percentage of particles number (n%, right column), of cave sediments **(A,B)**, karst spring/cave-spring sediments **(C,D)**, and quarry marble powder **(E,F)**.

distribution of C, S, and Cv than the other types of samples, whereas AR has its higher dispersion in the cave samples.

DISCUSSION

The different types of fine clastic sediments presented in this study have textural, morphological, sedimentological, and mineralogical characteristics that depend on several factors: source area, transport mechanism, hydrodynamic conditions in the aquifer, deposition mechanisms, interplay between weathering and mechanical alteration, and, finally, supply from quarry powder. Consequently, it appears quite difficult to discriminate the role of each factor.

The abundance of carbonate sands and silt demonstrates the provenance of most of the clasts from the karst systems themselves and that the alteration processes of carbonate rocks produce solid material as well as solution load. A possible source

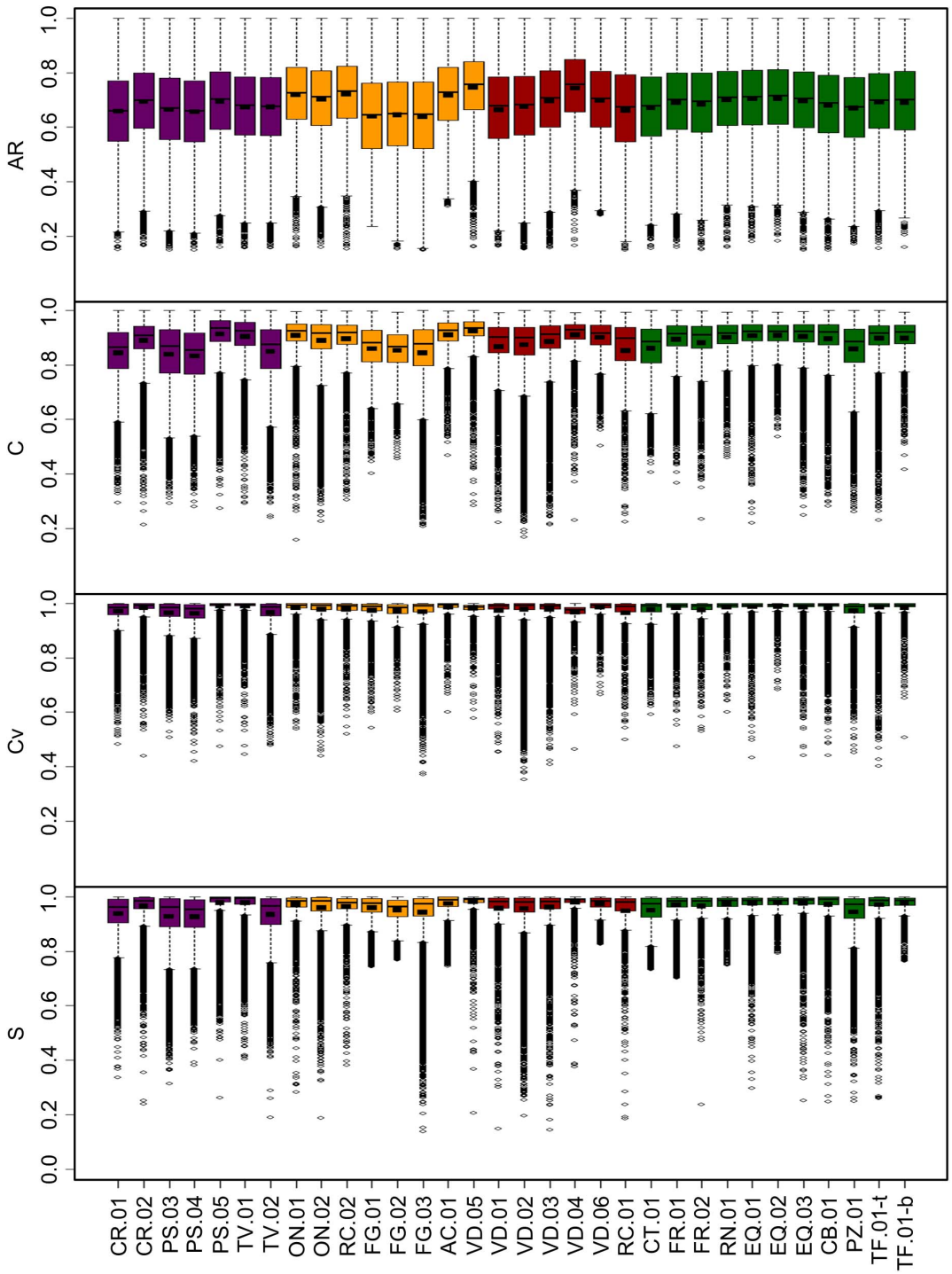

FIGURE 7 | Box-plots of aspect ratio (AR), circularity (C), convexity (Cv), and solidity (S) of the four types of samples in the fine to coarse silt size interval. Colors correspond to different types of deposits: purple, marble powder; orange, relict cave sediments; dark red, active cave sediments; green, karst spring/cave-spring sediments. Mean and median values and outliers are represented by in-box horizontal rectangles, solid segments and open circles, respectively.

of this autogenic clastic material is the incomplete dissolution of the carbonate rocks on cave walls due to chemically aggressive laminar flow and/or condensation water (Zupan Hajna, 2002, 2003). This is a selective process because it does not attack frontally the rock, but it dissolves first the contacts between grains, microstructures and crystal imperfections, weakening the mechanical cohesion of the rock, and leaving powdery, weathered surfaces. The weathered wall rock can be mechanically eroded,

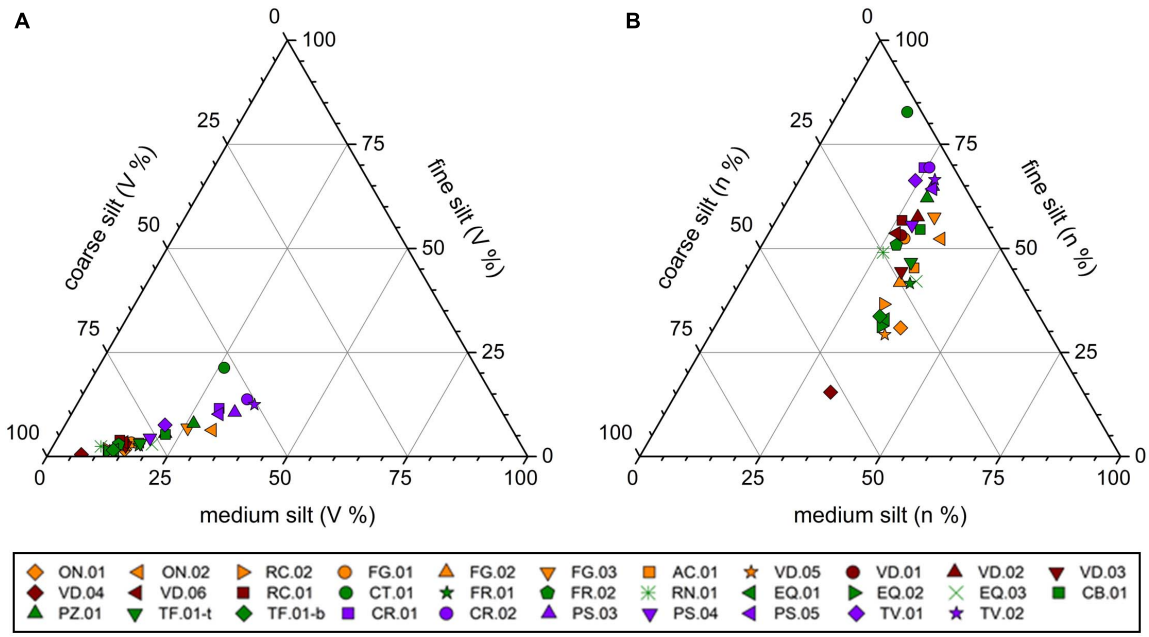

FIGURE 8 | Fine/medium/coarse silt ternary diagrams expressed as volume percentage **(A)** and number of grain percentage (**B**). Colors correspond to different types of deposits: orange, relict cave sediment; dark red, active cave sediment; green, karst spring and cave-spring; purple, quarry.

then the resulting carbonate particles can be transported through the karst network. In the AA, the occurrence of calcite grains in presently active cave and spring deposits could be mainly attributed to the contamination by the marble powders produced by the quarrying activities, which are widespread over almost the entire territory (see **Figure 1**). On the other hand, the sediment samples collected in no longer active sectors in the Corchia and Onice caves show that calcite clasts of natural origin can also be present. Dolomitic and silicate grains are instead surely due to natural weathering processes, as the lithologies that contain significant fractions of these components are not subject to excavation. The compositions of relict caves sediments vary from mostly calcitic to mostly dolomitic, demonstrating that both marbles and dolostones are subject to partial dissolution phenomena, which probably occur in the covered or semi-covered epikarst, where percolating waters have a greater dissolving power and can act for longer times. The lack of dissolution markers on the particles of anthropogenic origin, on the other hand, demonstrates that the waters that flow in the karst systems, both in vadose and phreatic conditions, have a low dissolving power, as there is no reason to think that the particles of natural origin have a longer residence time in the aquifer than those of anthropic origin.

In general, the silt fraction (φ = 4–8, i.e., from 0.0625 to 0.0039 mm) results as the most discriminant gran size fraction between the different sediment categories, when considering the portion finer than fine sand, probably because it depends more on the clast provenance (weathering of the host rock or anthropogenic sources) and it is more sensitive to the transport/deposition dynamic selection than the finer fraction, which is easily transported as suspended load. For all these reasons, we investigated in detail the silt portion of sediments comparing as relative percentages the three following fractions: 0.0625 to 0.0312 mm (coarse silt), 0.0312 to 0.0156 mm (medium silt), and 0.0156 to 0.0078 mm (fine silt). Very fine silt (0.0078–0.0039 mm) was excluded from diagrams because it is more subject to be transported away as suspended load and hardly deposited either in cave or karst spring environments (Herman et al., 2012).

The ternary diagram with the three considered silt fractions expressed as volume percentage (**Figure 8A**) reveals an alignment of the samples along a trend that goes from the coarse silt vertex toward a mean composition consisting of about 50% coarse silt, 35% medium silt, and 15% fine silt, which corresponds to the powder produced by diamond wire cutting. The active cave sediments are found exclusively close to the coarse silt vertex, whereas quarry samples are on the other extreme of the trend, confirming their finer composition. Relict cave and spring sediments are more distributed along the trend but are generally coarser than the quarry samples. A less defined trend is observed also in the silt ternary diagram with the proportions expressed as percentage of particles number (**Figure 8B**). In this latter case all the sediments are distributed from 50% of coarse silt to 75–80% of fine silt. Moreover, the quarry samples are clustered over the finest fraction. The CT.01 spring sample stands out in both diagrams and it appears to be finer than the quarry samples produced by the diamond sawing. This spring was recognized to be heavily affected by marble slurry inputs that result in episodes of strong turbidity increases (Drysdale et al., 2001). Furthermore, this sample, unlike the others, comes from the decantation tank of the capture settlement and it is therefore probable that also the finest part of the sediment could have been deposited here, while

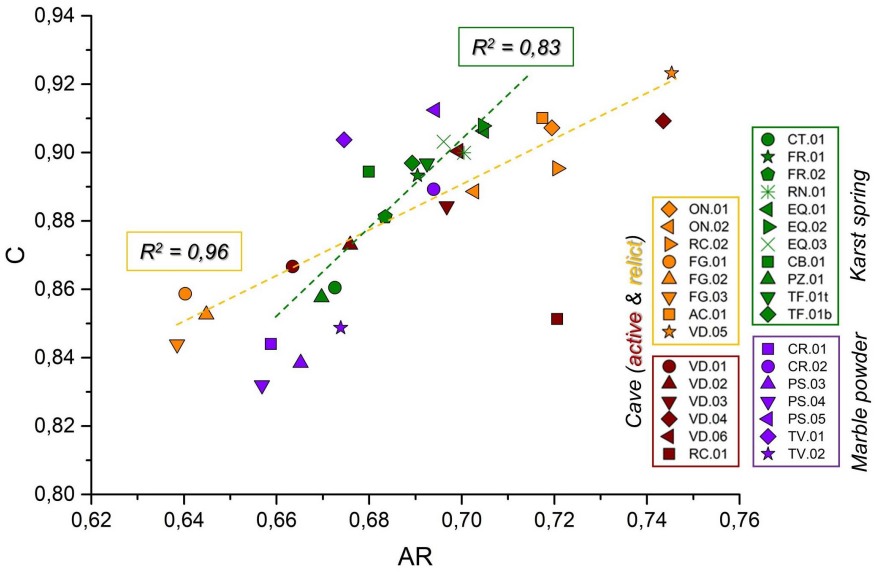

FIGURE 9 | Scatter plot of aspect ratio (AR) and circularity (C) mean values for each sample presented in this study. The orange and the green dashed lines represent the linear correlation of the two variables for relict cave and spring samples, respectively.

coarse silt may have been partially deposited during the transport through the aquifer in phreatic conditions.

Cave sediments have a higher percentage of coarse silt, probably because they have experienced transport in vadose conditions only, and the finer materials cannot be normally deposited in such conditions. Spring sediments, which have undergone also transport in phreatic conditions, are more distributed according to the different transport/deposition conditions they have experienced and to the structure of the phreatic zone of each system. In general, the samples collected in the spring with a greater flow rate (FR and EQ samples) have a higher percentage of coarse silt, while those of the smaller springs have a higher percentage of medium and fine silt. In some cases (CT.01, PZ.01, CB.01) the greater presence of medium/fine silt is certainly due to the occurrence of variable quantities of marble slurry coming from the quarries, also recognized during micro-morphological observations with SEM.

Morphometric comparison based on MSG analysis revealed some peculiar characteristics among sediments of different types: generally, cave samples show a greater variability in the distributions of shape parameters than those of spring samples. This is evident especially looking at aspect ratio and circularity distributions and secondarily at solidity (see **Figure 7**). This variability is probably due to the different deposition conditions that can occur in vadose streamways, which are characterized by a succession of pools, steps, and tight channels, where the flow velocity varies greatly. The very high number of outliers for the different shape parameters of sediments could reflect the heterogeneous composition of the natural sediments, although dominated by carbonate clasts. On the other hand, Cv and S of quarry samples have a larger interquartile range respect to those of natural sediments, suggesting more complex morphologies possibly related to the absence of a transport-related shape modifications. Plotting the mean values of the aspect ratio against the mean circularity for each sample in a scatter diagram, a rough linear relationship occurs (**Figure 9**). This is partially expected because more elongated particles (lower AR) are usually far from having a regular shape (higher values of circularity). However, it is noteworthy to observe that two trends can be distinguished, one for relict cave sediments and one for spring samples. Active cave samples fall midway between these two trends whereas quarry samples are distributed around the spring samples trend. This means that, increasing AR, the circularity increases a little faster in spring samples and quarry material respect to relict cave sediments. This could be due to the occurrence in relict cave sediments of altered clasts with a less regular perimeter. Rough surfaces should determine a particle perimeter longer than that of the particle equivalent circle, resulting in lower values of circularity. Naturally weathered calcite and dolomite particles show in fact micro-morphologies (e.g., V-V shapes) that could increase the difference between the real particle perimeter and its equivalent circle, whereas spring samples and marble powder particles have angular but more regular surfaces, reducing the difference between the two perimeters. On the contrary, AR is not sensitive to the roughness of the perimeter. In other words, it is possible that these two trends are related to the different flow conditions that spring and cave sediments experienced, and, regarding the marble powder, to its different origin. The morphological similarities between the spring and the marble powder samples could be also partially related to the fact that the quarry material can infiltrate into the karst systems and ultimately reach the karst springs, mixing with natural sediment particles.

Figure 10 summarizes the position within a karst system of the types of samples collected and their characteristics (presented with box-plots of the mean values for each parameter). The comparison of the different sediment types permits to make some

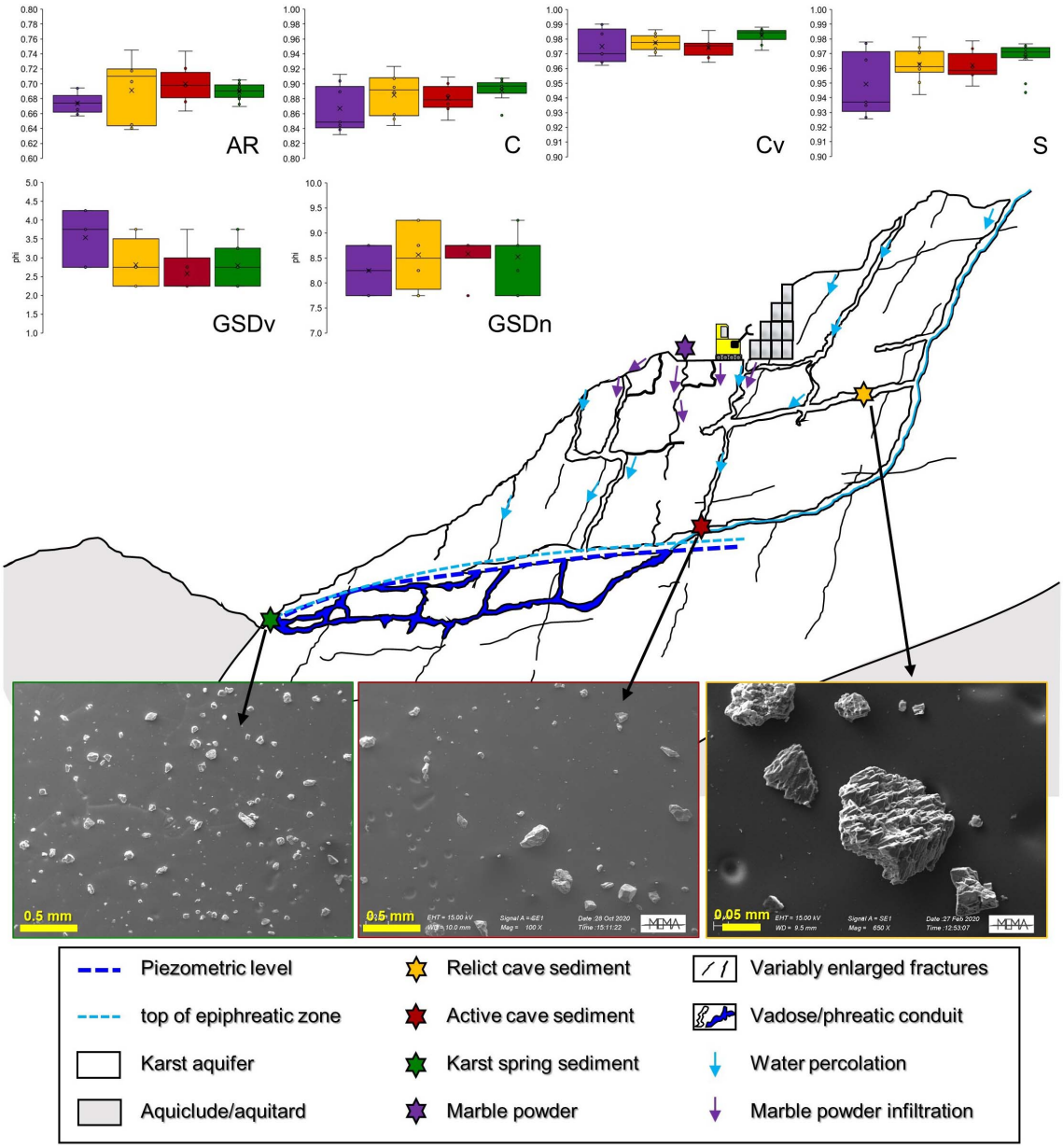

FIGURE 10 | Schematic representation of the fine clastic sediments found in the Apuan Alps karst. The box-plots report the distributions of the mean values of each shape parameter (AR, C, Cv, and S) and the modal classes of the GSDs (GSDv = v% and GSDn = n%) for each sediment group (orange, relict cave sediment; dark red, active cave sediment; green, karst spring and cave-spring; purple, quarry). The bottom SEM-SE pictures show the general morphological characteristics of each cave deposit: regular and homogeneous grains of spring-type deposits (left), less regular and more variable grains of active cave deposits (center), and solutional features typical of relict cave deposits (right).

general assessments about the transport and deposition dynamics in the AA karst systems, although the ranges of variability for the sedimentological, morphological, and mineralogical features of the deposits somewhat overlap. Overall, it can be said that the AA karst systems are not particularly granulometric-selective, at least when dealing with materials in the dimensional range investigated in this study. This observation is probably related to the overall flow organization in the AA karst systems: these aquifers are characterized by well-developed vadose and epiphreatic flow systems that determine fast and impulsive responses to precipitation, with extremely variable flowrates (Doveri et al., 2019). Phreatic flow is concentrated in a few enlarged conduits that are probably able to transport silt to fine sands sediments without significant size selection. Marble powder exhibits the finest GSD (v%) but once it infiltrates in the aquifers, its size is only partially discriminant between natural and anthropogenic-contaminated sediments. This could mean that (a) its finest fraction is washed away so it cannot be found

in the karst system, and (b) its medium to coarse fraction (i.e., the silt) variably mixes with a natural sediment that is fine itself so the marble input does not cause a significant shift in the grain size, except for the springs more heavily polluted. The morphological variability of the sediments collected in the vadose zone is strongly dependent on the choice of the sampling site: the deposition in vadose conditions is extremely site-specific due local variations of flow conditions. Therefore, samples collected only a few meters apart can exhibit different characteristics. On the other hand, sediments collected at the karst springs show the most regular morphologies probably because flow in the phreatic zone determines a morphometric selection (Baba and Komar, 1981; Garzanti et al., 2008), permitting to the most regular, but not necessarily the most rounded, particles to reach the karst system outlet. Phreatic conduits have an adverse (upward) conduit gradient in the streamwise direction that produces saturated flow conditions. Consequently, there is a fluid energy threshold for sediment transport in this portion of the karst systems. This threshold controls the sediment storage in the aquifer and it is in turn dependent on the phreatic zone architecture (Husic et al., 2017). Thus, particle settling is favored between upward sections of phreatic conduits and grains with rough and irregular surfaces are hardly re-mobilized after they settle because roughness increases both the angle of repose and the viscous friction for rolling particles (Beakawi Al-Hashemi and Baghabra Al-Amoudi, 2018). These phenomena are less relevant for regular grains so that they can be transported more efficiently to the karst springs. Marble powder shows the highest variability and the lowest values in the shape factors (except for AR) because of its origin: the shape of the particles is generally angular, but it could also depend on the direction of sawing respect to the orientations of anisotropic features (cleavage) occurring in the rock massif.

CONCLUSION

The analyzed cave and spring sediments are mainly composed of calcite, dolomite and silicates in ratios that primarily depend on the nature of the rocks outcropping in the respective feeding basins and on the presence of materials coming from the quarries. The occurrence of a significant percentages of dolomite indicates that the carbonate rocks are subject to a partial dissolution that releases the individual granules making them then subject to mechanical erosion. This process is probably favored in the AA by the saccharoidal (sugar-like) structure of the metamorphosed dolostones and limestones (Cantisani et al., 2009; Gulli et al., 2015).

Calcite grains due to weathering processes have a very different surface micromorphologies from those produced by the marble sawing. The former in fact show evident traces of dissolution, while the latter have flat faces that tend to follow the calcite cleavage. Therefore, this feature is useful for the qualitative distinction between natural and anthropogenic calcite grains.

The compositional and sedimentological analyzes of cave and spring deposits collected in some karst systems of the AA have shown quite heterogeneous characteristics in each studied category. The anthropogenic component, coming from the extraction of marble, is present in very variable percentage in almost all recent sediments but it is difficult to be quantified because its mineralogical and morpho-dimensional features partly fall within the range of variability of the natural deposits. Furthermore, this implies a good transport capacity of the entire karst systems and therefore their low dimensional selective capacity. The hydrodynamic conditions in the phreatic zones may determine a morphometric selection, consequently the particles of spring deposits have more regular and homogenous shapes respect to vadose zone samples. These observations are crucial with regards to the arrangement of the phreatic zone of the AA karst systems: these aquifers are generally characterized by extensive vadose and epiphreatic flow systems, whereas phreatic flow occurs along few, highly conductive, karstic conduits. This arrangement could be responsible for the morphometric and granulometric features observed in the AA spring sediments: phreatic flow occurs with enough energy to prevent granulometric selection and good transport capacity (at least for fine materials). However, the relatively low flow velocities in the phreatic conduits limit preferentially the mobilization/re-mobilization and transport of irregular particles respect to the regular ones, accordingly to our results.

It is also evident that there is a high variability between samples collected in the same site, which depends on the local conditions in which the sedimentation occurs. This poses a sampling problem that introduces a possible bias in the characterization of the various types of deposits. On the other hand, the presence of marble powder from quarries, whose characteristics appear relatively distinctive, offers the possibility of using this material as a sort of tracer to characterize the various aquifer systems from a hydrodynamic point of view. For the continuation of the research, it is therefore necessary to associate the various sediments with the hydraulic characteristics of each groundwater systems, comparing the sedimentological investigations with the results of the hydrogeological monitoring of underground streams and karst springs.

DATA AVAILABILITY STATEMENT

The datasets presented in this article are not readily available because they will be used for other publications. Requests to access the datasets should be directed to the corresponding author.

AUTHOR CONTRIBUTIONS

AN: SEM-EDS and XRD analyses, data processing, figures drawing, and writing of the manuscript. LP: research coordination, data analysis, and writing of the manuscript. PC: research coordination, data interpretation, and manuscript revision. NB, PG, and RC: MSG analyses and data interpretation. GP: data analysis. SB: research coordination. All authors contributed to the scientific discussion of the data and agreed to the submitted version of the manuscript.

FUNDING

This research was funded by a grant of the Agenzia Regionale per la Protezione Ambientale della Toscana (ARPAT) in the framework of CAVE project (Framework agreement Rep. 381/2017).

ACKNOWLEDGMENTS

The authors would like to thank the editor and the two reviewers for their helpful comments that helped to improve the manuscript.

REFERENCES

Baba, J., and Komar, P. D. (1981). Measurements and analysis of setting velocities of natural quartz sand grains. *J. Sediment. Res.* 51, 631–640. doi: 10.2110/jsr.51.631

Beakawi Al-Hashemi, H. M., and Baghabra Al-Amoudi, O. S. (2018). A review on the angle of repose of granular materials. *Powder Technol.* 330, 397–417. doi: 10.1016/j.powtec.2018.02.003

Bella, P., Gradziński, M., Hercman, H., Leszczyński, S., and Nemec, W. (2020). Sedimentary anatomy and hydrological record of relic fluvial deposits in a karst cave conduit. *Sedimentology* 68, 425–448. doi: 10.1111/sed.12785

Blott, S. J., and Pye, K. (2012). Particle size scales and classification of sediment types based on particle size distributions: review and recommended procedures. *Sedimentology* 59, 2071–2096. doi: 10.1111/j.1365-3091.2012.01335.x

Bosch, R. F., and White, W. B. (2007). "Lithofacies and transport of clastic sediments in karstic aquifers," in *Studies of Cave Sediments*, eds I. D. Sasowsky and J. Mylroie (Dordrecht: Springer Netherlands), 1–22. doi: 10.1007/978-1-4020-5766-3_1

Cantisani, E., Fratini, F., Malesani, P., and Molli, G. (2005). Mineralogical and petrophysical characterisation of white Apuan Marble. *Per. Mineral.* 74, 117–140.

Cantisani, E., Pecchioni, E., Fratini, F., Garzonio, C. A., Malesani, P., and Molli, G. (2009). Thermal stress in the Apuan marbles: relationship between microstructure and petrophysical characteristics. *Int. J. Rock Mech. Mining Sci.* 46, 128–137. doi: 10.1016/j.ijrmms.2008.06.005

Carmignani, L., and Kligfield, R. (1990). Crustal extension in the northern Apennines: the transition from compression to extension in the Alpi Apuane Core Complex. *Tectonics* 9, 1275–1303. doi: 10.1029/tc009i006p01275

Cheetham, M. D., Keene, A. F., Bush, R. T., Sullivan, L. A., and Erskine, W. D. (2008). A comparison of grain-size analysis methods for sand-dominated fluvial sediments. *Sedimentology* 55, 1905–1913. doi: 10.1111/j.1365-3091.2008.00972.x

Conti, P., Di Pisa, A., Gattiglio, M., and Meccheri, M. (1993). "The pre-alpine basement in the Alpi Apuane (Northern Apennines, Italy)," in *Pre-Mesozoic Geology in the Alps*, eds F. Neubauer and J.F.v Raumer (Berlin: Springer), 609–621. doi: 10.1007/978-3-642-84640-3_36

Doveri, M., Piccini, L., and Menichini, M. (2019). "Hydrodynamic and Geochemical features of metamorphic carbonate aquifers and implications for water management: the apuan Alps (NW Tuscany, Italy) case study," in *The Handbook of Environmental Chemistry*, eds T. Younos, M. Schreiber, and C. Kosic Ficco (New York, NY: Springer International Publishing), 209–249. doi: 10.1007/978-3-319-77368-1_8

Drysdale, R. N., Pierotti, L., Piccini, L., and Baldacci, F. (2001). Suspended sediments in karst spring waters near Massa (Tuscany), Italy. *Environ. Geol.* 40, 1037–1050. doi: 10.1007/s002540100311

Ekmekci, M. (1990). "Impact of quarries on karst groundwater systems," in *Hydrogeological Processes in Karst Terranes*, Vol. 207, eds G. Gunay, A. I. Johnson, and W. Back (Wallingford: IAHS), 3–6.

Fairchild, I. J., and Baker, A. (2012). *Speleothem Science*. Hoboken, NJ: John Wiley & Sons, Ltd, doi: 10.1002/9781444361094

Folk, R. L., and Ward, W. C. (1957). Brazos River bar [Texas]; a study in the significance of grain size parameters. *J. Sediment. Res.* 27, 3–26. doi: 10.1306/74d70646-2b21-11d7-8648000102c1865d

Garzanti, E., Andò, S., and Vezzoli, G. (2008). Settling equivalence of detrital minerals and grain-size dependence of sediment composition. *Earth Planet. Sci. Lett.* 273, 138–151. doi: 10.1016/j.epsl.2008.06.020

González-Tello, P., Camacho, F., Vicaria, J. M., and González, P. A. (2010). Analysis of the mean diameters and particle-size distribution in powders. *Part. Part. Syst. Charact* 27, 158–164. doi: 10.1002/ppsc.200900097

Gulli, D., Pellegri, M., and Marchetti, D. (2015). "Mechanical behavior of Carrara marble rock mass related to geo-structural conditions and in-situ stress," in *Proceedings of the 15th Pan-American Conference on Soil Mechanics and Geotechnical Engineering (PCSMGE)/8th South American Congress on Rock Mechanics (SCRM), Buenos Aires, Argentina, 15–18 November 2015*, eds A. O. Sfriso, D. Manzanal, and R. J. Rocca (Amsterdam: IOS Press), 253–260.

Häuselmann, P., Plan, L., Pointner, P., and Fiebig, M. (2020). Cosmogenic nuclide dating of cave sediments in the Eastern Alps and implications for erosion rates. *IJS* 49, 107–118. doi: 10.5038/1827-806x.49.2.2303

Herman, E. K., Tancredi, J. H., Toran, L., and White, W. B. (2007). Mineralogy of suspended sediment in three karst springs. *Hydrogeol. J.* 15, 255–266. doi: 10.1007/s10040-006-0108-2

Herman, E. K., Toran, L., and White, W. B. (2012). Clastic sediment transport and storage in fluviokarst aquifers: an essential component of karst hydrogeology. *Carbonates Evaporites* 27, 211–241. doi: 10.1007/s13146-012-0112-7

Husic, A., Fox, J., Agouridis, C., Currens, J., Ford, W., and Taylor, C. (2017). Sediment carbon fate in phreatic karst (Part 1): conceptual model development. *J. Hydrol.* 549, 179–193. doi: 10.1016/j.jhydrol.2017.03.052

Isola, I., Ribolini, A., Zanchetta, G., Bini, M., Regattieri, E., Drysdale, R. N., et al. (2019). Speleothem U/Th age constraints for the Last Glacial conditions in the Apuan Alps, northwestern Italy. *Palaeogeogr. Palaeoclimatol. Palaeoecol.* 518, 62–71. doi: 10.1016/j.palaeo.2019.01.001

Karkanas, P., and Goldberg, P. (2013). "6.23 micromorphology of cave sediments," in *Treatise on Geomorphology*, eds J. Shroeder and A. Frumkin (Amsterdam: Elsevier), 286–297. doi: 10.1016/b978-0-12-374739-6.00120-2

Leibrandt, S., and Le Pennec, J.-L. (2015). Towards fast and routine analyses of volcanic ash morphometry for eruption surveillance applications. *J. Volcanol. Geoth. Res.* 297, 11–27. doi: 10.1016/j.jvolgeores.2015.03.014

Li, K. M., Zuo, L., Nardelli, V., Alves, T. M., and Lourenço, S. D. N. (2019). Morphometric signature of sediment particles reveals the source and emplacement mechanisms of submarine landslides. *Landslides* 16, 829–837. doi: 10.1007/s10346-018-01123-1

Martini, I. (2011). Cave clastic sediments and implications for speleogenesis: new insights from the Mugnano Cave (*Montagnola Senese*, Northern Apennines, Italy). *Geomorphology* 134, 452–460. doi: 10.1016/j.geomorph.2011.07.024

Piccini, L. (1998). Evolution of karst in the Apuan Alps (Italy): relationships with the morphotectonic history. *Suppl. Geografia Fisica e Dinamica Quaternaria* 3, 21–31.

Piccini, L. (2011). Speleogenesis in highly geodynamic contexts: the quaternary evolution of Monte Corchia multi-level karst system (Alpi Apuane, Italy). *Geomorphology* 134, 49–61. doi: 10.1016/j.geomorph.2011.06.005

Piccini, L., Di Lorenzo, T., Costagliola, P., and Galassi, D. M. P. (2019). Marble slurry's impact on groundwater: the case study of the Apuan Alps Karst Aquifers. *Water* 11:2462. doi: 10.3390/w11122462

Piccini, L., Drysdale, R., and Heijnis, H. (2003). Karst morphology and cave sediments as indicators of the uplift history in the Alpi Apuane (Tuscany, Italy). *Q. Int.* 10, 219–227. doi: 10.1016/s1040-6182(02)00104-0

Piccini, L., Zanchetta, G., Drysdale, R. N., Hellstrom, J., Isola, I., Fallick, A. E., et al. (2008). The environmental features of the Monte Corchia cave system (Apuan Alps, central Italy) and their effects on speleothem growth. *IJS* 37, 153–172. doi: 10.5038/1827-806x.37.3.2

Rizzo, G., D'Agostino, F., and Ercoli, L. (2008). Problems of soil and groundwater pollution in the disposal of "marble" slurries in NW Sicily. *Environ. Geol.* 55, 929–935. doi: 10.1007/s00254-007-1043-9

Sasowsky, I. D. (2007). Clastic sediments in caves – imperfect recorders of processes in Karst. *Acta Carsol.* 36, 143–149. doi: 10.3986/ac.v36i1.216

Springer, G. S. (2019). "Clastic sediments in caves," in *Encyclopedia of Caves*, eds W. White, D. Culver, and T. Pipan (Amsterdam: Elsevier), 277–284. doi: 10.1016/b978-0-12-814124-3.00031-5

Viles, H. A., and Moses, C. A. (1998). Experimental production of weathering nanomorphologies on carbonate stone. *Q. J. Eng. Geol. Hydrogeol.* 31, 347–357. doi: 10.1144/gsl.qjeg.1998.031.p4.08

White, W. B. (2007). Cave sediments and paleoclimate. *J. Cave Karst Stud.* 69, 76–93.

Winkler, T. S., van Hengstum, P. J., Horgan, M. C., Donnelly, J. P., and Reibenspies, J. H. (2016). Detrital cave sediments record Late Quaternary hydrologic and climatic variability in northwestern Florida. USA. *Sedimentary Geol.* 335, 51–65. doi: 10.1016/j.sedgeo.2016.01.022

Zupan Hajna, N. (2002). Origin of fine-grained carbonate clasts in cave sediments. *Acta Carsologica* 31, 115–137. doi: 10.3986/ac.v31i2.392

Zupan Hajna, N. (2003). "Chemical weathering of limestone and dolomites in a cave environment," in *Evolution of Karst: from Prekarst to Cessation*, ed. F. Gabrovsek (Ljubljana: ZRC), 347–356.

Zupan Hajna, N., Pruner, P., Mihevc, A., Schnabl, P., and Bosák, P. (2008). Cave Sediments from Postojnska–Planinska cave system (Slovenia): evidence of multi-phase evolution in epiphreatic zone. *Acta Carsologica* 37, 63–86. doi: 10.3986/ac.v37i1.160

Conflict of Interest: The authors declare that the research was conducted in the absence of any commercial or financial relationships that could be construed as a potential conflict of interest.

frontiers in Earth Science

BRIEF RESEARCH REPORT
published: 20 May 2021
doi: 10.3389/feart.2021.673109

Composition and Structure of Phosphate-Rich Parietal Crusts and Nodules in Monte Corchia Cave, Alpi Apuane (Central Italy)

Leonardo Piccini, Alessia Nannoni, Pilario Costagliola, Mario Paolieri and Chiara Vigiani*

Department of Earth Science, Università Degli Studi di Firenze, Florence, Italy

Cave environment allows long-term processes of rock weathering and chemical deposition that cannot occur on Earth surface directly exposed to meteoric and external biochemical agents. Apart from the common carbonate speleothems, chemical precipitation from infiltration water can also produce phosphate-rich formations usually occurring as parietal dark crusts or spheroidal nodules. Despite the potential purposes of these kind of deposits as paleoenvironmental proxies, they have been still poorly investigated by cave scientists. Monte Corchia cave (NW Tuscany, Central Italy) is one of the most studied caves in the world, particularly for paleoclimate reconstructions from calcite speleothems. Several samples of parietal formations were collected in relict phreatic and epiphreatic passages at different altitudinal levels that reflect different evolutionary stages of this large cave system. Samples were analyzed by diffractometry and SEM-EDS possibly revealing the occurrence of hydroxyapatite or fluorapatite mixed with Fe/Mn incrustations and allogenic clastic particles. Crusts often cover the entire section of relict phreatic or epiphreatic passages and can be related to precipitation during waterfilled phases. Phosphate nodules are almost entirely composed by hydroxyapatite or fluoroapatite and could be the result of long-term chemical (or bio-chemical) precipitation in air-filled environments.

Keywords: karst, cave deposit, speleothem, Apuan Alps, apatite group

OPEN ACCESS

Edited by:
Davide Tiranti, Agenzia Regionale per la Protezione Ambientale (ARPA), Italy

Reviewed by:
Fernando Gazquez, University of Almería, Spain
Ilenia M. D'Angeli, University of Bologna, Italy

****Correspondence:***
Leonardo Piccini
leonardo.piccini@unifi.it

Specialty section:
This article was submitted to Quaternary Science, Geomorphology and Paleoenvironment, a section of the journal Frontiers in Earth Science

Received: *26 February 2021*
Accepted: *23 April 2021*
Published: *20 May 2021*

Citation:
Piccini L, Nannoni A, Costagliola P, Paolieri M and Vigiani C (2021) Composition and Structure of Phosphate-Rich Parietal Crusts and Nodules in Monte Corchia Cave, Alpi Apuane (Central Italy). Front. Earth Sci. 9:673109. doi: 10.3389/feart.2021.673109

INTRODUCTION

Caves are highly conservative environments where the effects of surface processes (concerning climate, hydrology, morphology, biology, etc.) reveal themselves in depositional records that can be either clastic (alluvial deposits) or chemical (speleothems). Calcite speleothems are the most studied formation of chemical origin in caves since their capability to provide key paleo-environmental information and for the possibility to be accurately dated. Other types of cave deposits are still poorly studied, although potentially interesting as paleo-environmental proxies. Among these are gypsum crystals (Gázquez et al., 2013, 2020) and other uncommon speleothems such as Fe and Mn oxide deposits (e.g., Rossi et al., 2010; Frierdich et al., 2011).

Beyond carbonates and sulfates, phosphates are among the most frequent minerals in caves (Hill and Forti, 1997). Commonly, they are the product of chemical reactions between guano, bones or other animal residues and cave bedrock, calcite concretions or sediments (e.g., Audra et al., 2019, and references therein). Among the most frequent phosphates we can find brushite or more commonly the minerals of the apatite group (mainly hydroxyapatite or fluorapatite) and other less common phosphates, including: taranakite, ardealite, variscite, etc. (e.g., Fiore and Laviano, 1991; Onac et al., 2001). The phosphates associated with guano accumulation often form deposits of considerable thickness that have been the object of excavation to obtain fertilizers (Frank, 1998; Audra et al., 2019). However, phosphates are often found also in caves where there are no relevant deposits of guano, usually occurring in the form of thin patinas or crusts that cover the rock or cave deposits, or as small spheroidal nodules grown on the walls (Onac and Forti, 2011; Audra et al., 2019).

Very promising results were obtained also from Fe/Mn crusts deposited in water-filled cave passages (e.g., Gázquez et al., 2011). The authors linked the genesis of the crusts that coat the cave walls to the alternation between phreatic and epiphreatic conditions. Fe and Mn mobilization were related to anoxic conditions during submerged phases, whereas Fe and Mn oxidation occurred in aerobic, bacteria-mediated, conditions during epiphreatic phases. Other ferromanganese deposits were related to the switch between phreatic and vadose conditions. Therefore, flow conditions exert a pivotal role on the formation of these deposits. In such perspective, our contribution presents a preliminary investigation on another peculiar type of crusts or thin patinas covering the rock walls of inactive karst conduits of the Monte Corchia cave system in the Alpi Apuane (NW Tuscany, Italy; **Figure 1**). Various types of dark-colored parietal coatings and crusts were recognized in several relict passages of this wide karst systems (Piccini, 2011). In a previous work, Piccini et al. (2005) mentioned the presence of these deposits. Successively, a pilot study (Mantelli et al., 2015a) reported the results of chemical analyses carried out on black patinas collected in the Corchia cave. The Monte Corchia karst complex has been the subject of very detailed studies concerning speleothems and paleoclimatic records since some decades (e.g., Drysdale et al., 2004, 2009; Drysdale et al., 2020; Zanchetta et al., 2007; Piccini et al., 2008; Regattieri et al., 2014). In this research instead, attention has been focused on: (i) a particular type of crusts that cover the wall of ancient phreatic or epiphreatic passages and, (ii) some nodules found in limited sectors of relict phreatic passages. Both deposits are described from a textural and mineralogical point of view along with their possible origin and environmental meaning.

MATERIALS AND METHODS

Sampling Site

The Alpi Apuane represent a tectonic window where the Tuscan Metamorphic Units outcrop (Carmignani and Kligfield, 1990; Molli and Vaselli, 2006 and references therein). The Paleozoic basement consists mainly of phyllites and metarenites (Conti et al., 2019). The Mesozoic cover includes Triassic continental to shallow water deposits followed by Upper Triassic-Lower Jurassic carbonate platform sediments ("Grezzoni" dolostones, dolomitic marbles and marbles). The platform meta-sediments are followed by cherty meta-limestones, cherts and calcschists, phyllites, calcschists and meta-arenites from Upper Jurassic to Oligocene. The most important karst features of this area consist of several cave systems among which the Corchia cave surely is the most studied and worldwide known. The Corchia karst system (**Figure 1**) is about seventy km long and 1,185 m deep and it is at the present time one of the largest and deepest caves in Italy. The system is characterized by different levels attributed to a multiphase lowering of the base level occurred during the past 2–2.5 million years (Piccini, 2011; Isola et al., 2021).

In several sector of this cave, different kinds of dark incrustations occur on the conduit walls (**Figure 2**). In most cases, they were formed on the surface of the bedrock or on clastic deposits and they are easy to remove because they usually lay on deeply weathered rock surfaces. Thin black patinas were also observed over some speleothems, but they have not yet been sampled because they cannot be collected without damaging calcite formations and without specific coring tools. Fourteen samples were collected in 8 different sites located in the three major levels of relict horizontal passages located around 1,400, 1,150, and 870 m above the present sea level (**Figure 1**), which are considered as formed during three major evolutionary stages of this karst system (Piccini, 1998, 2011). The most common type of sample has the appearance of a crusts, usually 1–3 mm thick and from dark to light brown colored, that directly cover the bedrock (**Figures 2A-1,B-1**). Another kind of samples is represented by small (1–3 cm) spheroidal nodules hanging from the rock wall (**Figure 2C-1**). The latter are very dark in color or almost black and show a smooth and bright surface. The dark crusts are found with greater frequency in the upper and oldest sectors of the Corchia system, on rock walls of phreatic or epiphreatic conduits, or on isolated blocks. The crusts often coat typical scallops flow morphologies and are in turn covered by remnants of alluvial deposits. Their presence appears concentrated on surfaces that are always very altered and never fresh-looking. Nodules are much less frequent and are concentrated in limited sectors of the cave of different origin, often grown in niches or hollows on the walls and never exposed to direct dripping.

X-Ray Diffraction (XRD)

Five samples of coatings and one sample of a nodule were prepared for X-ray diffraction by powdering in an agate mortar and then analyzed at Centro di Servizi di Cristallografia Strutturale - Università di Firenze (CRIST) with a D8 Advance (Bruker) diffractometer operating with a Cu X-ray source, a Theta-Theta goniometer, and a flat Eulero Cradle sample holder, equipped with a Bruker LYNXEYE-XE detector. The filament current of the tube was 40 mA and the acceleration potential 40 kV. Yttrium oxide (Y_2O_3) was used as a reference material. Other patinas' samples were too thin (thickness <0.3–0.5 mm)

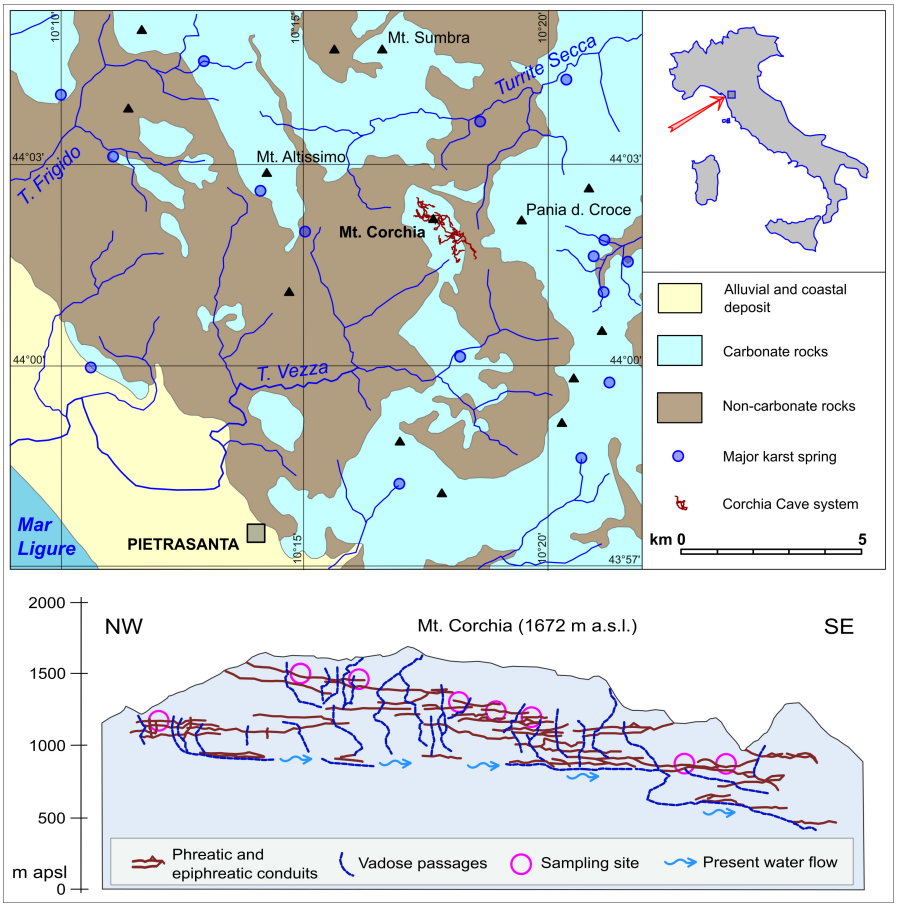

FIGURE 1 | Location map of Mt. Corchia area and schematic longitudinal profile of Corchia cave system with the position of sampling sites.

and were not analyzed because we were not able to obtain enough material for standard XRD analyses.

Scanning Electron Microscopy and Microanalysis (SEM-EDS)

Fourteen small fragments coming from all the eight sampling sites were analyzed through SEM-EDS. The fragments of crusts, nodules, and dark patinas of about 1–2 cm^2 were fixed to half inch aluminum stubs with a graphite rubber and then coated by graphite sputter. Semi-quantitative standardless microchemical analyses were performed by means of a Scanning Electron Microscope (SEM) ZEISS EVO MA15 (operating at 15 kV acceleration voltage), coupled with an Energy Dispersive Spectrometer (OXFORD INCA 250 EDS detector and software INCA 250, Oxford Instruments®) at the Centro di Microscopia Elettronica e Microanalisi (MEMA) of the Florence University. About 25-30 EDS micro-analyses were performed for each sample to chemically characterize major and minor components, for a total of about 300 punctual micro-analyses. In the crust, EDS analysis was preferably targeted to the three major components: clastic particles, matrix, and secondary incrustations. In the nodules, analysis was directed to their external surface (**Figure 2C-2**) and to cross-cut polished sections (**Figure 2C-3**).

RESULTS

The collected samples are largely attributable to three types of coatings. Eight samples are in the form of thin crusts ranging in color from light to dark brown, with a rough surface and arranged over large areas covering entire sectors of the wall or sediments in conduits of phreatic origin. These crusts are extremely friable and easily detach from the rock which appears deeply altered (de-cemented) for a few mm of thickness. Four samples appear as thin patinas with a glossy appearance and a dark brown color strongly attached to the rock. These patinas are found on the rock walls of passages that may have also undergone remodeling by epiphreatic conditions. The third kind is instead made up of nodular formations irregularly distributed in localized spots on the rock walls and ceilings of certain passages of various origins but never on recent surfaces, such as those due to collapse.

XRD analyses indicate that most of the samples are mainly composed of minerals belonging to the apatite group, but it was not possible to discriminate between hydroxyapatite

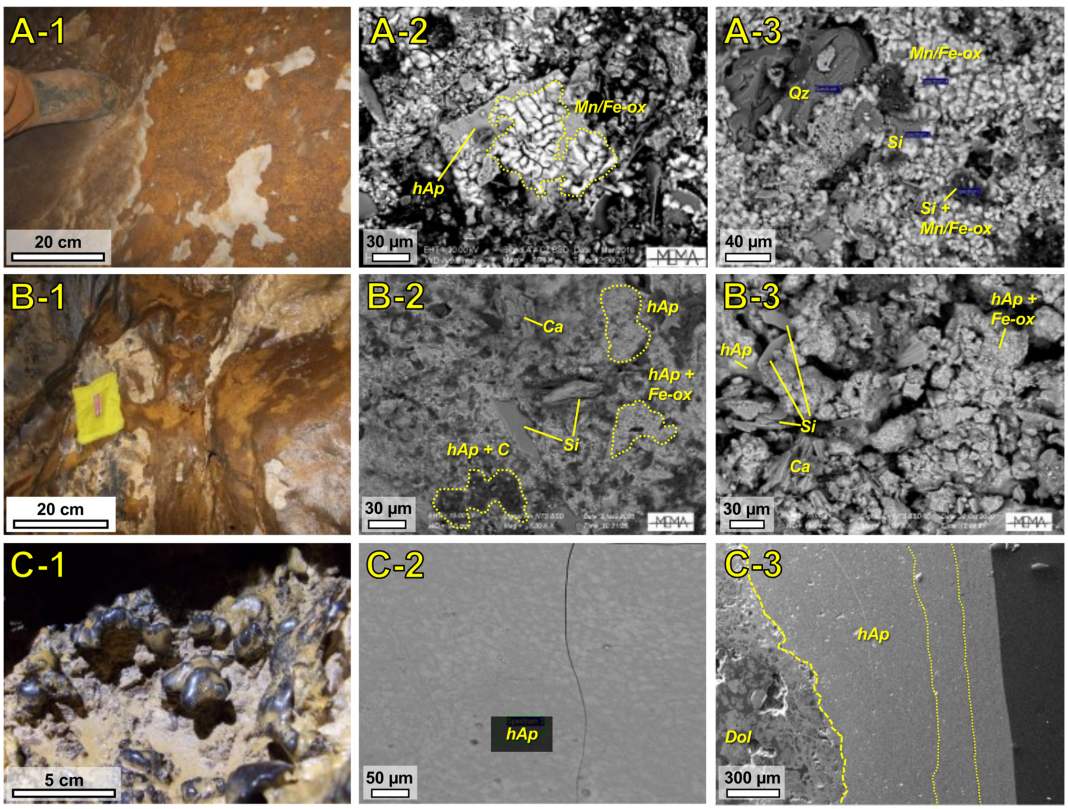

FIGURE 2 | (A-1) Brown parietal crusts on the wall of a relict phreatic passage at 1,200 m a.s.l. **(A-2,A-3)** SEM-BSE images of sample A-1 showing clasts of different nature (Qz = quartz, Si = silicate) covered by hydroxyapatite (hAp) and Fe/Mn incrustations (light areas, Mn/Fe-ox). **(B-1)** Brown parietal crusts on the wall of a relict phreatic passage at 1,400 m asl. **(B-2,B-3)** SEM-BSE images of sample B-1 showing clasts of different nature (Ca = calcite) cemented by apatite and Fe/Mn incrustations (light areas). **(C-1)** Calcium phosphate nodules on the wall of a relict phreatic passage collected in the Corchia cave at 1,200 m asl. **(C-2)** SEM-BSE images of sample C-1 showing its external regular surface consisting of hydroxyapatite. **(C-3)** Cross section of the nodule showing a regular structure roughly laminated (fine yellow dotted lines) grown on altered dolomite bedrock (yellow dashed line = bedrock/crust interface).

$[Ca_5(PO_4)_3OH]$ and fluorapatite $[Ca_5(PO_4)_3F]$. Muscovite $[KAl_2(Si_3Al)O_{10}(OH,F)_2]$ is the most abundant silicate. Traces of birnessite $[(Na,Ca,K)_x(Mn^{4+},Mn^{3+})_2O_4{\cdot}1.5(H_2O)]$ were recognized in three samples as well. One sample consists mostly of calcite $[CaCO_3]$ and/or dolomite $[CaMg(CO_3)_2]$ and secondarily of muscovite, quartz $[SiO_2]$, and a minor amount of hydroxyapatite.

SEM back scattered electrons (BSE) images shows that crusts consist of fine clastic particles cemented and often partially covered by a porous precipitation matrix. Clastic grains are rarely larger than 30 µm and are mainly composed of Si and Al, with minor amounts of K, Na and Mg. Clastic particles of calcite and Fe/Mn oxides/hydroxides (probably goethite and birnessite) are also present in some samples, although in a minor number respect to silicates. Chemical micro-analyses and morphological features suggest that the silicate grains are compatible with the phyllosilicates group and are probably made up of muscovite (**Figure 2B-3**). Matrix is easily distinguished in SEM-BSE images, since it appears of a light gray color whereas silicate clastic minerals are darker. The latter appear to be anhedral, often with an irregular shape, further evidencing their clastic nature. Matrix is generally composed of P and Ca as major constituents and often appears as an irregular layer wrapping the clastic grains (**Figure 2A-2**). P and Ca are sometimes accompanied by minor amounts of F, whereas Cl was not detected in any sample. This suggests that the phosphate minerals found in the samples are probably fluorapatite and hydroxyapatite, whereas chlorapatite is not present. Phosphatic nodules show a regular and uniform structure both on their smooth external surface (**Figure 2C-2**) and in their cross section (**Figure 2C-3**). In the crusts, apatite is usually in association with other phases, notably Fe and Mn oxides/hydroxides (with minor amounts of Al and Si, the latter being probably indicative for quartz), that locally may be more abundant forming irregular and nodular incrustations. The close textural interconnection between Mn/Fe patinas and apatite is reflected by micro analyses where Mn, Fe, P and Ca are always strictly associated as the result of the physical fine juxtaposition between these two mineralogical phases. Very dark areas in SEM-BSE images are observed as well. Micro-analyses reveal that the latter contain very low concentrations of Al, Mg, Ca, Fe whereas C (partly due to the sample graphite coating) and O are always the major constituent. This suggests that the dark areas may represents remnants of precipitated organic matter.

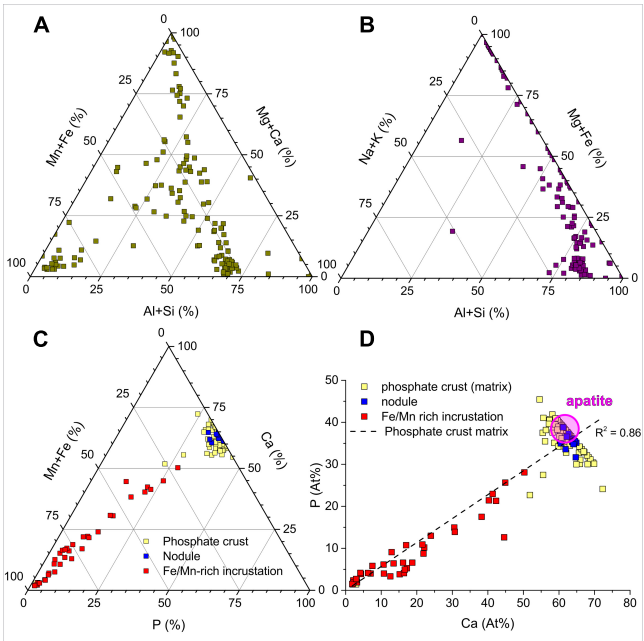

FIGURE 3 | (A) Ternary diagram showing the relative atomic% of Al + Si, Mg + Ca and Mn + Fe fractions of the clastic grains enclosed in phosphate crusts; **(B)** ternary diagram showing relative atomic% of Al + Si, Na + K and Mg + Fe fractions of the clastic grains enclosed in phosphate crusts; **(C)** ternary diagram showing the relative atomic% of P, Mg + Ca and Mn + Fe fractions of the crust's matrix; **(D)** scatter plot of Ca and P atomic% on Ca + P + Mn + Fe obtained with SEM-EDS micro-analysis of crusts' matrix: the dashed line represents the theoretical molar ratio of apatite, while pure apatite is approximately represented by the purple circle.

Figure 3 quantitatively illustrates the relative proportions of the major elements in all the micro-analyses of crusts and nodules either for their clastic (**Figures 3A,B**) or matrix (**Figure 3C**) components. **Figure 3A** clearly indicates the occurrence of three groups in the clastic component: Mn/Fe oxides/hydroxides at the left/down corner, carbonate close to the upper vertex, and silicates in the right/down area. Silicate clast are rarely clean, being often associate to a significant proportion of Mn + Fe (usually about 25%). In the midpoint sector of the diagram there is a dispersed cloud of points, which probably refers to silicate clasts coated by a patina of apatite and/or Mn/Fe oxides/hydroxides of different thickness. **Figure 3B** allows us to conclude that silicate clasts mainly consist of silicate with a low content of Na + K: this composition is well compatible with muscovite particles.

Figure 3C shows that crust matrix and nodules mainly consist of Ca-phosphate with a P/Ca proportion corresponding to the apatite group. Fe/Mn incrustations have variable contents of Ca and P, although Ca is always more abundant than P and their sum never exceed the 75% of the P + Ca + Mn + Fe. Additionally, the micro-analyses of Fe/Mn oxides/hydroxides are mostly aligned on a trend where the P/Ca ratio is still typical of apatite. Samples are clustered either close to the Mn + Fe vertex or in the area comprised between Mg + Ca = 60–85% and P = 15–30%, Mn + Fe = 0–10%. Finally, **Figure 3D** shows the P/Ca ratio of the phosphate matrix, Fe/Mn incrustations and phosphate nodules. Matrix and nodules are grouped in a restricted sector of the plot and aligned on a trend with an inverse correlation between Ca and P due to the virtual absence of Fe and Mn; in fact, P + Ca represents 95–100% of the P + Ca + Fe + Mn content. Pure hydroxyapatite samples fall near a P/Ca of 0,6 (purple circle in **Figure 3D**) whereas samples with higher P/Ca ratios could possibly represent other phosphate minerals.

DISCUSSION

The aim of this article is primarily to describe the phosphate deposits occurring in the Monte Corchia karst system, one of the most studied caves in the world from a paleoclimatic point of view. Although performed on a limited number of samples, our research indicates that the crusts and calcium phosphate nodules (i) are exclusively found in relict conduits of phreatic or epiphreatic origin, (ii) usually cover flow dissolution forms (scallops), (iii) are often associated with silicoclastic deposits of partially allogenic nature. Calcium phosphate is mainly in form of a cement incorporating very fine silicate clastic material (usually from 5 to 20 μm in diameter) and are characterized by scattered incrustations of Fe/Mn oxides/hydroxides that possibly reflect oscillations in the water level in the cave (cf., Gázquez et al., 2011). Noteworthy, no deposits of guano and no phosphates mineralization associated with present or ancient guano accumulation are known in the Corchia karst system. In addition, present seepage waters are free of dissolved phosphates (Montigiani et al., 1998; Mantelli et al., 2015b). All these elements suggest that: (i) P in the Corchia system has an ancient and allochthonous origin, (ii) it was transported into the karst system by waters coming from the surface, and (iii) that calcium

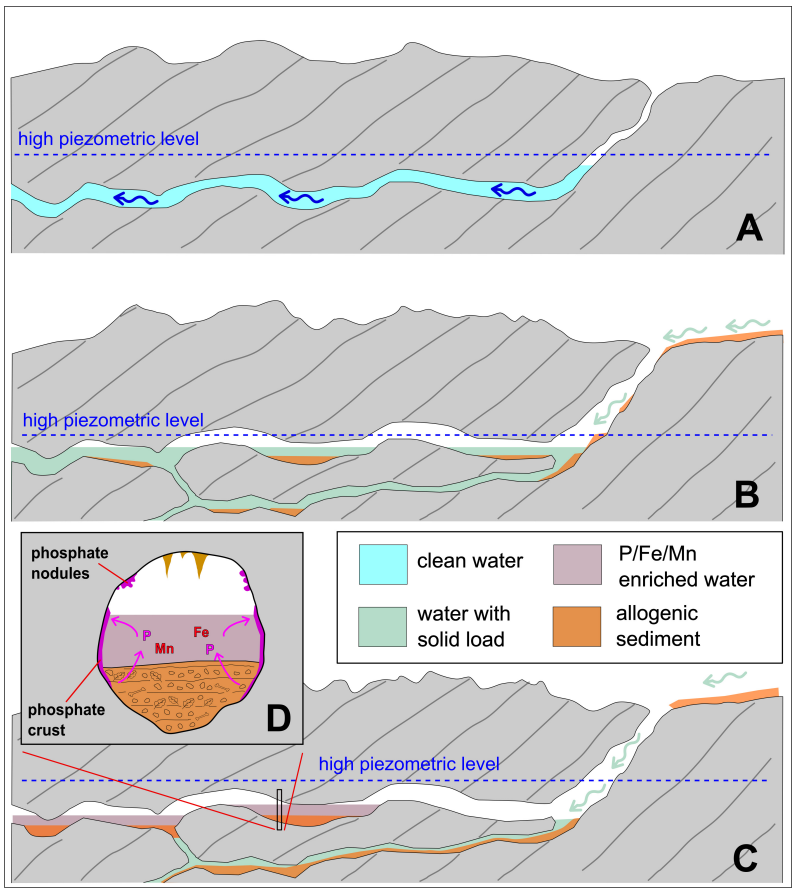

FIGURE 4 | Formation sketch of phosphate-rich crusts in the Corchia cave system. **(A)** Phreatic stage with no clastic load; **(B)** transition from phreatic to epiphreatic condition with allogenic recharge and in-filling; **(C)** Epiphreatic stage with abundant filling deposition and a reduction of hydraulic conductivity that caused flooding of relict phreatic conduits where stagnant water remains for prolonged time in contact with allogenic sediments. **(D)** P and Mn/Fe mobility from sediments to precipitation as parietal crusts.

phosphate was formed by *in situ* chemical precipitation in water-filled environments with stagnant or very slowly flowing water.

Based on these observations and on the locations in which these crusts are found, it is possible to infer an evolution sketch that can be summarized in the following phases (**Figure 4**). The formation of large dissolution conduits in phreatic regime (**Figure 4A**) was followed by a gradual transition to epiphreatic conditions with the arrival of allogenic waters and sediments, probably rich in organic matter, from the surface catchment (**Figure 4B**). This circumstance is demonstrated by the occurrence of clastic deposits containing non-metamorphic pebbles and sand in the upper level of the Corchia cave (from 1,200 up to 1,400 m asl) (Piccini, 2011; Isola et al., 2021). The development of these phreatic and epiphreatic levels is ascribed to a phase of allogenic recharge that these passages have experienced in the early stages of development and that, according to Piccini (1998, 2011), can be traced back to the early Pleistocene (up to 2.5 million years ago). Therefore, the formation of phosphate crusts may be related to phases of high flow dominated by sediment-rich water and, reasonably, with a significant content of organic matter (mainly vegetation waste), coming from a surface basin and introduced in the karst system during flood. Actually, there are several evidences of a stage when some of the upper passages of the Corchia system were almost completely filled by allogenic sediments.

Due to the introduction into the karst system of relevant quantities of sediments, conduits were partially clogged with a following reduction of their hydraulic conductivity. Consequently, occasional, or seasonal flooding of large sectors happened, following storm events or during particularly rainy periods (**Figure 4C**). This flooding stage could also be associated with a rise in the base level, possibly due to the accumulation of sediments for climatic causes into the nearby valley. During the post-flooding phases, the deposition of a thin film of silicoclastic mud occurred on conduits wall. Successively, the precipitation of calcium phosphate (mainly hydroxyapatite) cemented the mud layer, whereas Fe- and Mn-rich oxides/hydroxides finally coated the phosphate crust (**Figure 4D**). This process could be repeated several times, forming a regular coat up to 2–3 mm thick on walls and isolated blocks, until the lower passages were able to allow the discharge of major floods.

Due to the relatively low mobility of phosphate in stream water, especially those with high Ca content (e.g., Diaz et al., 1994; Filippelli, 2008; Oelkers and Valsami-Jones, 2008), we propend for phosphate ions to be transported and stored in form of vegetal organic matter associated to sediments or adsorbed onto Fe/Al oxyhydroxides, as commonly observed in lacustrine environments (Golterman, 1995, 2001; Lu et al., 2016), rather than being carried in the system as dissolved compound in flowing water. In caves, due to absence of vegetation, phosphorous precipitates as apatite instead of been absorbed by plants and algae for their life cycle.

Phosphate nodules are a more enigmatic formation and we have not still elements that could shed light on their origin. Otherwise, the lack of detrital grains, their morphology and their internal structure suggest they could be the result of a concentrical aggregation of hydroxyapatite in an aired environment due to the evaporation of phosphate-rich water parietal films on more prominent points.

CONCLUSION

In the Corchia cave system, phosphate crusts are a quite common feature of relict phreatic and epiphreatic passages, often associated with remnants of allogenic sediments. XRD and SEM-EDS analyses showed that the crusts consist of a phosphate matrix incorporating mainly silicate grains and often coated by Fe/Mn oxides/hydroxides (presumably goethite and birnessite). Texture and composition of these coatings indicate an origin in an underwater environment as the result of the precipitation of phosphates and Mn/Fe oxides/hydroxides in typical epiphreatic conditions subject to periodic flooding and with a fine solid load of predominantly silicoclastic nature. Such conditions are not compatible with the present or recent hydrologic setting, so they necessarily indicate an ancient origin. In the upper level of conduits (up to 1,400 m asl) the formation of phosphate crusts may be related to the phases dominated by allogenic recharge that these passages have experienced in the early stages of development and that can be traced back to the early Pleistocene.

Based on the present data, the Corchia's phosphate crusts do not appear as the product of in-site reactions of guano deposits with rock, as usually happens, but the result of parietal precipitation in stagnant water rich in organic matter. Differently, nodules consist almost exclusively of apatite, sometimes slightly contaminated by Mn/Fe. Their structure is compatible with a formation in aired environment through a regular deposition of concentric phosphate layers on walls asperities.

A detailed description of chemical, and possible bio-chemical, reactions and processes involving sediment, water, and bedrock, and that led to the formation of this kind of deposits, is beyond the aims of this article. Nevertheless, this represents the first detailed description of an uncommon cave phosphate deposit not directly associated with guano or other animals' remnants. Despite the difficulty to investigate the origin and the formation processes of this cave deposit, it could represent a new potential proxy for paleoenvironmental and paleoclimate records and will be possibly object of further and more sophisticate analysis in a next future.

DATA AVAILABILITY STATEMENT

The raw data supporting the conclusions of this article will be made available by the authors, without undue reservation.

AUTHOR CONTRIBUTIONS

LP: research coordination, data analysis, figures drawing, and writing of the manuscript. AN: SEM-EDS, and XRD analyses, data processing, plots drawing, and writing of the manuscript. PC: data interpretation and manuscript revision. MP and CV: SEM-EDS analyses and data interpretation. All authors contributed to the article and approved the submitted version.

FUNDING

This research has been funded by Università Degli Studi di Firenze.

ACKNOWLEDGMENTS

The authors wish to thank the Parco Regionale Alpi Apuane for sampling permission and the two reviewers whose contribute improve the quality of the manuscript.

SUPPLEMENTARY MATERIAL

The Supplementary Material for this article can be found online at: https://www.frontiersin.org/articles/10.3389/feart.2021.673109/full#supplementary-material

REFERENCES

Audra, P., De Waele, J., Bentaleb, I., Chroňáková, A., Krištůfek, V., D'angeli, I., et al. (2019). Guano-related phosphate-rich minerals in European caves. *IJS* 48, 75–105. doi: 10.5038/1827-806x.48.1.2252

Carmignani, L., and Kligfield, R. (1990). Crustal extension in the northern Apennines: the transition from compression to extension in the Alpi Apuane Core Complex. *Tectonics* 9, 1275–1303. doi: 10.1029/tc009i006p01275

Conti, P., Carmignani, L., Massa, G., Meccheri, M., Patacca, E., Scandone, P., et al. (2019). *Note Illustrative della Carta Geologica d'Italia alla scala 1:50,000 "Foglio 249—Massa Carrara"*. Italy: Servizio Geologico d'Italia.

Diaz, O. A., Reddy, K. R., and Moore, P. A. Jr. (1994). Solubility of inorganic phosphorus in stream water as influenced by pH and calcium concentration. *Water Res.* 28, 1755–1763. doi: 10.1016/0043-1354(94)90248-8

Drysdale, R., Couchoud, I., Zanchetta, G., Isola, I., Regattieri, E., Hellstrom, J., et al. (2020). Magnesium in subaqueous speleothems as a potential

palaeotemperature proxy. *Nat. Commun.* 11:5027. doi: 10.1038/s41467-020-18083-7

Drysdale, R. N., Hellstrom, J. C., Zanchetta, G., Fallick, A. E., Goñi, M. S., Couchoud, I., et al. (2009). Evidence for obliquity forcing of glacial termination II. *Science* 325, 1527–1531. doi: 10.1126/science.1170371

Drysdale, R. N., Zanchetta, G., Hellstrom, J. C., Fallick, A. E., Zhao, J. X., Isola, I., et al. (2004). Palaeoclimatic implications of the growth history and stable isotope (δ18O and δ13C) geochemistry of a Middle to Late Pleistocene stalagmite from central-western Italy. *Earth Planet. Sci. Lett.* 227, 215–229. doi: 10.1016/j.epsl.2004.09.010

Filippelli, G. M. (2008). The Global Phosphorus Cycle: past. Present, and Future. *Elements* 4, 89–95. doi: 10.2113/gselements.4.2.89

Fiore, S., and Laviano, R. (1991). Brushite, hydroxylapatite, and taranakite from Apulian caves (southern Italy): new mineralogical data. *Am. Mineral.* 76, 1722–1727.

Frank, E. F. (1998). History of the guano mining industry, Isla de Mona, Puerto Rico. *J. Caves Karst Sci.* 60, 121–125.

Frierdich, A. J., Hasenmueller, E. A., and Catalano, J. G. (2011). Composition and structure of nanocrystalline Fe and Mn oxide cave deposits: implications for trce element mobility in karst systems. *Chem. Geol.* 284, 82–96.

Gázquez, F., Bauska, T. K., Comas-Bru, L., Ghaleb, B., Calaforra, J.-M., and Hodell, D. A. (2020). The potential of gypsum speleothemes for paleoclimatology: application to the Iberian Roman humid period. *Sci. Rep.* 10:14705. doi: 10.1038/s41598-020-71679-3

Gázquez, F., Calaforra, J. M., and Forti, P. (2011). Black Mn-Fe crusts as markers of abrupt palaeoenvironmental changes in El Soplao Cave (Cantabria, Spain). *Int. J. Speleol.* 40, 163–169. doi: 10.5038/1827-806x.40.2.8

Gázquez, F., Calaforra, J.-M., Stoll, H., Sanna, L., Forti, P., Lauritzen, S.-E., et al. (2013). Isotope and trace element evolution of the Naica aquifer (Chihuahua, Mexico) over the past 60,000 yr revealed by speleothems. *Quat. Res.* 80, 510–521. doi: 10.1016/j.yqres.2013.09.004

Golterman, H. L. (1995). The role of the ironhydroxide-phosphate-sulfide system in the phosphate exchange between sediments and overlying water. *Hydrobiologia* 297, 443–454. doi: 10.1007/bf00033500

Golterman, H. L. (2001). Fractionation and bioavailability of phosphates in lacustrine sediments: a review. *Limneica* 20, 15–29.

Hill, C. A., and Forti, P. (1997). *Cave minerals of the world*. 2nd Edn, ed. A. L. Huntsville (United States: National Speleological Society).

Isola, I., Mazzarini, F., Molli, G., Piccini, L., Zanella, E., Zanchetta, G., et al. (2021). New chronological constraints from hypogean deposits for Late Pliocene to recent morphotectonic history of the Alpi Apuane (NW Tuscany, Italy). *Geosciences* 2021:65. doi: 10.3390/geosciences11020065

Lu, H., Wan, J., Li, J., Shao, H., and Wu, L. (2016). Periphytic biofilm: a buffer for phosphorus precipitation and release between sediments and water. *Chemosphere* 144, 2058–2064. doi: 10.1016/j.chemosphere.2015.10.129

Mantelli, F., Lotti, L., Montigiani, A., and Piccini, L. (2015a). Chimica delle acque del Complesso Carsico del Monte Corchia. *Acta Apuana* 11, 33–45.

Mantelli, F., Piccini, L., D'Elia, A., and Montigiani, A. (2015b). Risultati di analisi chimiche preliminari sulle patine nere nel Complesso carsico del Monte Corchia e in altre grotte italiane. *Acta Apuana* 2012, 63–72.

Molli, G., and Vaselli, L. (2006). "Structures, interference patterns, and strain regime during midcrustal deformation in the Alpi Apuane (Northern Apennines, Italy)," in *Styles of Continental Contraction*, eds S. Mazzoli and R. W. H. Butler (United States: Geological Society of America), doi: 10.1130/2006.2414(05

Montigiani, A., Lotti, L., Bianucci, P., and Manelli, F. (1998). Studio e monitoraggio dell'Antro del Corchia (Stazzema-Lucca), individuazione della sua capacità di fruizione compatibile con l'ecosistema ipogeo. *ARPAT*. 1998:37.

Oelkers, E. H., and Valsami-Jones, E. (2008). Phosphate mineral reactivity and global sustainability. *Elements* 4, 83–87. doi: 10.2113/gselements.4.2.83

Onac, B. P., and Forti, P. (2011). Minerogenetic mechanisms occurring in the cave environment: an overview. *IJS* 40, 79–98. doi: 10.5038/1827-806x.40.2.1

Onac, B. P., Mylroie, J. E., and White, W. B. (2001). Mineralogy of cave deposits on San Salvador island, Bahamas. *Carbonates Evaporites* 16, 8–16. doi: 10.1007/bf03176222

Piccini, L. (1998). Evolution of karst in the Apuan Alps (Italy): relationships with the morphotectonic history. *Suppl. Geografia Fis. Dinam. Quat.* 3, 21–31.

Piccini, L. (2011). Speleogenesis in highly geodynamic contexts: the quaternary evolution of Monte Corchia multi-level karst system (Alpi Apuane. Italy). *Geomorphology* 134, 49–61. doi: 10.1016/j.geomorph.2011.06.005

Piccini, L., Zanchetta, G., Drysdale, R., Isola, I., and Bruschi, G. (2005). Depositi fisici e chimici delle grotte delle Alpi Apuane – Atti del Convegno "Le grotte raccontano: un milione di anni di storia naturale conservato nei sistemi carsici delle Alpi Apuane", Castelnuovo Garfagnana (Lu) 11-12 dicembre 2004. *Memor. Istit. Ital. Speleol.* 18, 101–118.

Piccini, L., Zanchetta, G., Drysdale, R. N., Hellstrom, J., Isola, I., Fallick, A. E., et al. (2008). The environmental features of the Monte Corchia cave system (Apuan Alps, central Italy) and their effects on speleothem growth. *IJS* 37, 153–172. doi: 10.5038/1827-806x.37.3.2

Regattieri, E., Zanchetta, G., Drysdale, R. N., Isola, I., Hellstrom, J., and Dallai, L. (2014). Lateglacial to Holocene record (Ba, Mg, Sr) from Corchia Cave (Apuan Alps, central Italy): paleoenvironmental implications. *J. Quat. Sci.* 29, 381–392. doi: 10.1002/jqs.2712

Rossi, C., Lozano, R. P., Isanta, N., and Hellstrom, J. (2010). Manganese stromatolites in caves: el Soplao (Cantabria, Spain). *Geology* 38, 1119–1122.

Zanchetta, G., Drysdale, R. N., Hellstrom, J. C., Fallick, A. E., Isola, I., Gagan, M. K., et al. (2007). Enhanced rainfall in the Western Mediterranean during deposition of sapropel S1: stalagmite evidence from Corchia cave (Central Italy). *Quat. Sci. Rev.* 26, 279–286. doi: 10.1016/j.quascirev.2006.12.003

Conflict of Interest: The authors declare that the research was conducted in the absence of any commercial or financial relationships that could be construed as a potential conflict of interest.

frontiers in Earth Science

ORIGINAL RESEARCH
published: 28 May 2021
doi: 10.3389/feart.2021.672119

Hints on the Late Miocene Evolution of the Tonale-Adamello-Brenta Region (Alps, Italy) Based on Allochtonous Sediments From Raponzolo Cave

Francesco Sauro[1], Maria Giuditta Fellin[2], Andrea Columbu[1], Philipp Häuselmann[3], Andrea Borsato[4], Cristina Carbone[5] and Jo De Waele[1]*

[1]Department of Biological, Geological and Environmental Sciences, University of Bologna, Bologna, Italy, [2]Geological Institute, ETH Zürich, Zürich, Switzerland, [3]Swiss Institute for Speleology and Karst Studies (SISKA), La Chaux-de-Fonds, Switzerland, [4]School of Environmental and Life Sciences, University of Newcastle, Callaghan, NSW, Australia, [5]Department of Earth, Environmental and Life Sciences (DISTAV), Genoa University, Genoa, Italy

OPEN ACCESS

Edited by:
Andrea Zerboni, University of Milan, Italy

Reviewed by:
Nadja Zupan Hajna, Research Center of the Slovenian Academy of Sciences and Arts, Slovenia
Fabio Matano, National Research Council, Italy
Fabrizio Berra, University of Milan, Italy

***Correspondence:**
Andrea Columbu
andrea.columbu2@unibo.it

Specialty section:
This article was submitted to Quaternary Science, Geomorphology and Paleoenvironment, a section of the journal Frontiers in Earth Science

Received: *25 February 2021*
Accepted: *10 May 2021*
Published: *28 May 2021*

Citation:
Sauro F, Fellin MG, Columbu A, Häuselmann P, Borsato A, Carbone C and De Waele J (2021) Hints on the Late Miocene Evolution of the Tonale-Adamello-Brenta Region (Alps, Italy) Based on Allochtonous Sediments From Raponzolo Cave. Front. Earth Sci. 9:672119. doi: 10.3389/feart.2021.672119

Raponzolo is a paleo-phreatic cave explored in 2011 in the Brenta Dolomites (Trentino, Italy), at the remarkable altitude of 2,560 m a.s.l. Differently to all other caves of the area, it hosts well-cemented fine to medium sands of granitic-metamorphic composition. The composition suggests a sediment source from the Adamello and Tonale Unit, separated from the Brenta by one of the most important tectonic lineaments of the Alps (Giudicarie Line). The fine-sand sediment was sampled to determine burial time and thus a minimum age of the cave. Cosmogenic isotopes (^{26}Al and ^{10}Be) in quartz grains allowed to estimate a minimum burial age of 5.25 Ma based on the mean sediment transport time at the surface and infer original altitude of the catchment area. Detrital apatite fission-track (AFT) and U-Pb dating on zircons provide information on the source, both from a regional and altitude (exhumation) perspective. Two populations of detrital AFT ages center at 17 (–2.3 + 2.6) Ma and 23 (–3.3 + 3.9) Ma, whereas the main detrital zircon U-Pb age populations are younger than 40 Ma. These correspond to intrusive and metamorphic sources nowadays outcropping exclusively above 2,200–2,300 m a.s.l. in Northern Adamello and Tonale. The results point to a late Miocene erosion and infilling of the cave by allochtonous sediments, with important implications on the timing of cave speleogenesis, as well as the paleogeographical connection, tectonic evolution and uplift of different structural units of the Alps. The roundness and the well sorted size of the quartz grains suggest a fluvial or aeolian origin, possibly recycled by glacial activity related to cold events reported in high latitude areas of the world at 5.75 and 5.51 Ma. These glacial phases have never been documented before in the Alps. This information confirms that the valleys dividing these geological units were not yet deeply entrenched during the onset of the Messinian Salinity Crisis (5.6–5.5 Ma), allowing an efficient transport of sediments across major tectonic lineaments of the Alps. This study shows the potential of cave sediments to provide information not only on the age of speleogenesis but also on the paleogeography of a wide area of the Alps during the late Miocene.

Keywords: Al-Be isotopes, speleogenesis, paleogeography, cave sediments, AFT analysis, U-Pb zircon dating

INTRODUCTION

Understanding how the topography and physiography of the Alps evolved from the Eocene to the Miocene has been one of the main challenges in Alpine geology over the last decades (Schmid et al., 2004; Garzanti and Malusà, 2008; Schlunegger and Mosar, 2011; Campani et al., 2012; Winterberg and Willett, 2019). Paleogeographic reconstructions based on synorogenic detrital archives have resolved large-scale features of the surface evolution of the Alps (Carrapa and Di Giulio, 2001; Kuhlemann and Kempf, 2002). A detailed exhumation history of the metamorphic and igneous rocks of the Alps has been reconstructed based on a dense thermochronologic dataset (Fox et al., 2016). However, carbonate massifs as those of the Southern Alps are difficult to integrate into paleogeographic and exhumation/uplift models, lacking powerful chronological, thermal and distinct compositional markers applicable to these geological terrains. While the evolution of the Southern Alps has been studied through structural mapping and tectonic reconstruction (Doglioni and Bosellini, 1987; Castellarin and Cantelli, 2000), scarce information is available on the absolute timing of the events, uplift, erosion rates and especially paleogeographic arrangements in pre-Quaternary times (Stefani et al., 2007; Malusà et al., 2009; Potter and Szatmari 2009; Fox et al., 2016). This information gap could be fulfilled by the study of karst system, which are abundant in the Southern Alps. Kartsic caves are often characterized by the presence of well-developed paleo-phreatic levels evolving in response to surface evolution and valley entrenchment (Audra et al., 2007; Sauro et al., 2012). The arrangement of these cave levels can be correlated with the deepening of the water table due to uplift of karst massifs through time; however, constraining speleogenetic phases with absolute chronology remains challenging (Sauro et al., 2013; Columbu et al., 2015; Columbu et al., 2017; Ballesteros et al., 2019; Bella et al., 2019). The study of allochthonous sediments in ancient cave systems can be a powerful tool to better understand the paleogeographic evolution in karst areas (Stock et al., 2005b). While calcite speleothems can grow at any (usually air-filled) stage once the void is formed, and are mainly useful for paleoclimatic and paleo-environmental reconstructions (Fairchild et al., 2006), the introduction of allochthonous sediments within cave systems is often synchronous or occurs shortly after the genesis of cave passages (Häuselmann, 2007; Calvet et al., 2015), i.e., when the base level is still more or less at the same altitude of the caves themselves (Columbu et al., 2018). In this case, burial time corresponds to the approximate age of the phreatic karst network at specific water table levels (Granger et al., 2001; Häuselmann and Granger, 2005). Accordingly, cosmogenic dating on cave sediments has been successfully applied in the North-Western calcareous Alps (Häuselmann and Granger, 2005), in the Eastern Austrian Alps (Häuselmann et al., 2020), in the Southern calcareous Alps of Slovenia (Häuselmann et al., 2015) and in other karst areas of the World (Anthony and Granger, 2007; De Waele et al., 2012; Calvet et al., 2015; Granger et al., 2015; Columbu et al., 2021). Nonetheless, a set of conditions has to be satisfied to consider a cave as a potential site for sediment burial studies and to meaningfully link cave development to tectonic evolution: 1) The presence of quartz-rich terrains in the vicinity of the karst system, procuring the sediment source; 2) geological and environmental conditions able to transport these allogenic sediments from the source area to the karstified units; 3) the injection of the sediment into the phreatic or epiphreatic conduits, often developed close to the local water table. In addition, the sediment should not be re-eroded, moved and stored in younger conduits at lower levels without having been exposed at the surface again. If this later transport would happen the age obtained with cosmogenic dating could not be associated to the correct speleogenetic phase (Häuselmann et al., 2020).

The Brenta Dolomites Massif is one of the areas of the Southern Alps where information about uplift and tectonic evolution is scarce. This area is situated to the south-east of a crucial tectonic triple junction (Doglioni and Bosellini, 1987), at the intersection between the Periadriatic line and the Giudicarie South and North lines (**Figures 1**, **2**), close to the border between the Austroalpine and Southern Alps (Heberer et al., 2017).

The Brenta Dolomites Massif represents the northern area of a mainly carbonatic mountain chain region of the Southern Alps, within the Giudicarie tectonic Belt. Permian volcano-sedimentary deposits are exposed in a few outcrops in the valley entrenchment of the Giudicarie South line (between Rendena Valley and Sabion Line, **Figure 2**), but the most widespread formation in the Brenta Massif is the Upper Triassic "Dolomia Principale" (blue in **Figure 2**), a carbonate shelf succession made up of a ~1,000 m thick sequence of massive and laminated dolostones (Borsato et al., 1994; Carton and Baroni, 2017). The Brenta Massif is characterized by a well-developed karst landscape with several deep vadose vertical caves and some subterranean networks presenting paleophreatic morphologies (Conci and Galvagni, 1952; Borsato, 1991; Borsato et al., 2003; Audra et al., 2006). This makes the Brenta Massif one of the most important karst areas in the Dolomites, with a well-articulate subsurface drainage network discharging in large karst springs along its perimeter at elevations between 1,400–1,600 m a.s.l. (perched aquifers) and 400–600 m a.s.l. (base level springs) (Borsato, 2001; Borsato, 2007). The Brenta karst area is bordered by metamorphic and intrusive units. Indeed, to the north-west, the region is characterized by the metamorphic nappes of Tonale, formed by high pressure mineral assemblages (Stipp et al., 2002; Spalla et al., 2003).To the west there is the Adamello Batholith, one of the most investigated areas of the Alps (Brack 1983; Martin et al., 1993; Fellin et al., 2002). Adamello is mostly composed of igneous rocks belonging to a large batholith formed by tonalite, granodiorite and gabbro (Callegari and Brack, 2002). It is the largest intrusive body of Alpine Tertiary magmatism emplaced during the Eocene to the early Oligocene. Adamello and Brenta both exhumed from 2 to 3 km depth relatively to the modern surface since the late Miocene (Reverman et al., 2012; Heberer et al., 2017; Stalder et al., 2018). Both Adamello and Tonale are now separated from Brenta Massif by deep glacial valleys entrenched along the main tectonic lines (**Figure 1**).

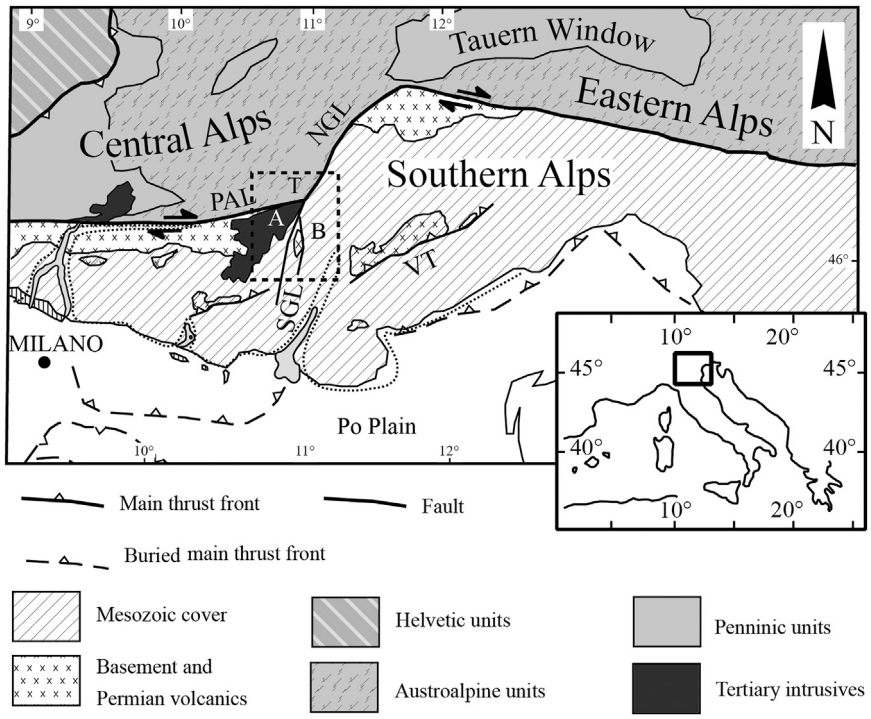

FIGURE 1 | Geographic overview of the Adamello (A), Brenta (B), Tonale (T) massifs in the frame of the Southern and Central Alps. The dotted box is approximately the area of **Figure 2**. (Modified from Reverman et al., 2012). PAL = Periadriatic Line; NGL = Northern Giudicarie Line; SGL = Southern Giudicarie Line; VT = Valsugana Thrust.

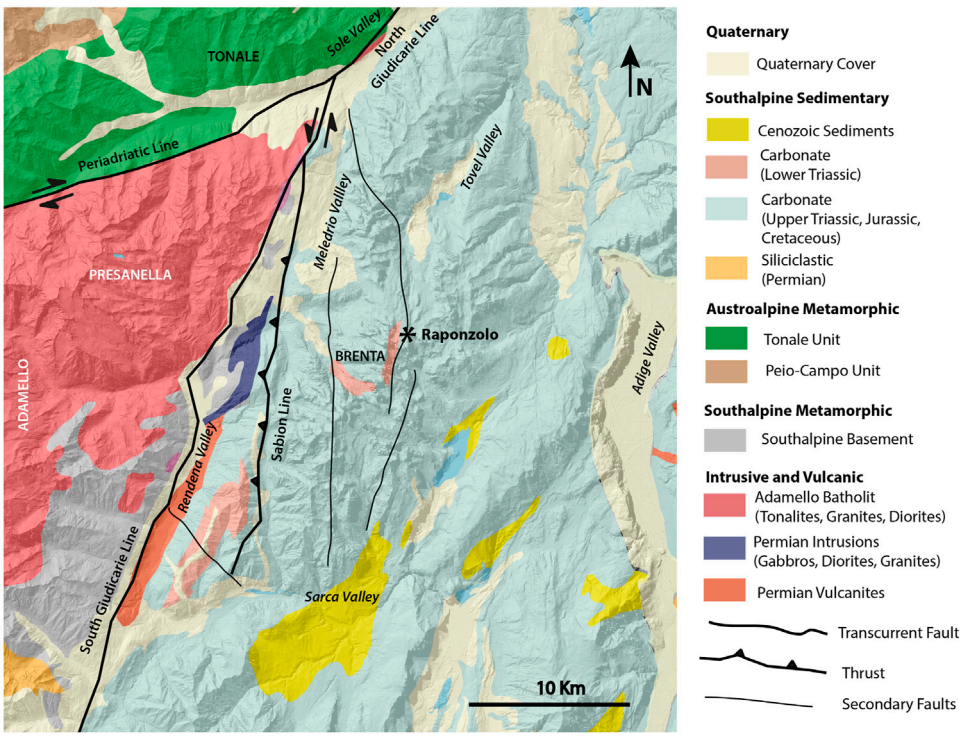

FIGURE 2 | Regional geology of the study area and location of Raponzolo Cave (simplified from Bigi and Carrozzo, 1992).

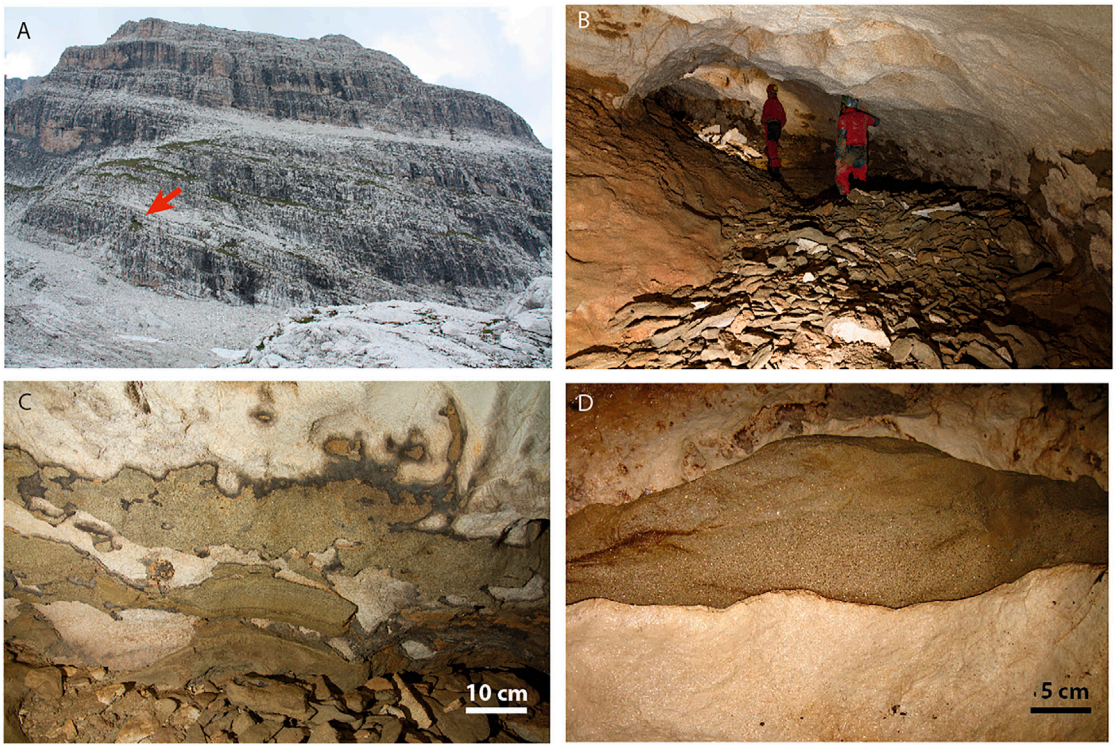

FIGURE 3 | Cave morphologies and sediment: **(A)** The entrance of the Cave is a gallery truncated by erosion on the cliffs of Cima Grosté (red arrow); **(B)** Typical paleophreatic conduit with elliptical shape and big scallops due to phreatic slow flow; **(C)** Remnants of cemented sandstone sediments on cave walls; **(D)** A sedimentary fracture infilling on the cave roof indicating that the whole gallery was originally filled and then re-excavated.

Until a few decades ago, the caves of the Brenta Massif were considered mostly related to the last glacial phases (Nicod, 1976); the discovery of extensive phreatic galleries at 2,100 m a.s.l., 1,300 m above the present-day local groundwater table (Borsato, 1991; Borsato, 2012), suggested that speleogenetic processes were indeed more ancient and complex. In fact, several U/Th dating of speleothems from the Brenta Massif as well as on the nearby Paganella mountain are in secular equilibrium for $^{238}U/^{234}U$ isotopes attesting an age older than 1 Ma (Bini et al., 1991; Borsato et al., 2003; Audra et al., 2007). However, no evidence of allochthonous cave sediments were known in the Brenta Massif until 2011, when the Gruppo Speleologico Trentino SAT Bindesi Villazzano discovered Raponzolo Cave, which represents a portion of a paleo-phreatic gallery of a presumably pre-Quaternary karst system given the high altitude occurrence (2,560 m asl). The main cave passage was partially filled with allochthonous sandy sediments mainly composed of quartz and biotite. This discovery opened the possibility of performing sediment source and burial age studies in the area for the very first time. Consequently, the study of ancient Brenta karst systems and sediments trapped within cave conduits could represent a key for understanding the evolution of this massif.

This paper shows how a detailed analysis of cave sediments can provide valuable information on the geological and speleogenetic history of a cave, providing new hints on the paleogeography and tectonic evolution of a wide region of the Alps.

AREA OF STUDY, MATERIALS AND METHODS

The Raponzolo Cave

Raponzolo Cave opens at 2,560 m asl (46°11′55.1″N, 10°54′40.7″E), on the steep eastern flank of Cima Grosté (2,898 m a.s.l.), toward the upper end of the Tovel Valley, the widest valley of the Brenta Massif (3.5 km of width, **Figure 2**). The cave is a single sub-horizontal tunnel about 180 m long, excavated in the Dolomia Principale formation. An initial W-trending ascending gallery paved with loose dolomitic sand is followed by a N-trending descending gallery partially filled with cemented medium-fine siliciclastic sand (**Figures 3**, **4**). Comparable sediments are not found anywhere else in the area. The sediments are present on the gallery floor as well as on walls and roofs, suggesting that the whole conduit was once filled (and then re-excavated). The cave presents typical phreatic morphologies with large scallops up to 0.5 m in diameter, without traces of vadose morphologies (**Figure 3B**).

The analyses targeted pristine and well cemented sediment samples from Raponzolo Cave. A multi-technique approach was used to obtain information about composition, provenance and

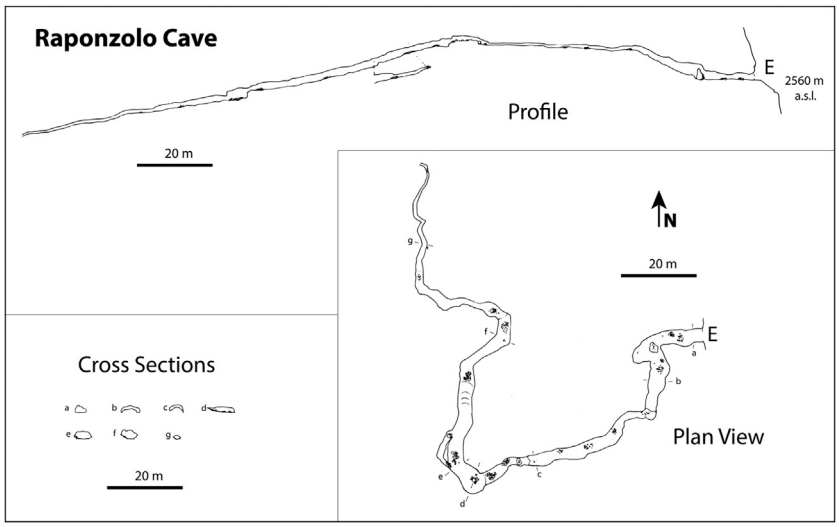

FIGURE 4 | Topographic map of Raponzolo Cave (survey GST-SAT BV).

burial time. These included: petrographic observation using an optical microscope, X-Ray Diffraction (XRD), X-Ray Fluorescence (XRF), ^{26}Al and ^{10}Be cosmogenic isotopes, Apatite Fission Track (AFT) analyses and U-Pb dating on zircons.

Petrographic Observations and Grainsize

Petrographic observations were accomplished on three thin sections (~25 μm) with a LEICA Stereomicroscope and an OLYMPUS BX-41 optical microscope. Images have been obtained using a OLYMPUS COLOR VIEW II-SET camera and processed through OLYMPUS C-VIEW II-BUND-celIB software. For grainsize measurements, 300 g of sample have been treated with a 70% acetic acid solution in order to dissolve the carbonate cement and release the insoluble fraction for grain size measurements through sieves. Pre- and post-dissolution weighing ascertained the cement/sediment ratio. Grainsize measurement utilized standard ASTM sieves 25, 40, 70, 100, 200, 230 and >230, with meshes corresponding to 0.71, 0.425, 0.212, 0.15, 0.075, 0.063 and <0.063 mm, respectively. Analyses were accomplished at Bologna University (Italy).

XRF and XRD Analysis

The sample was ground to ultrafine powders and kept 24 h at 110°C. Ten grams of sample were mixed with 2.5–5 ml of Elvacite polymer resin, dissolved in acetone. The mixture was stirred to allow acetone evaporation and Elvacite distribution. The resultant powder was placed in a penny-shaped mold and compressed with a vertical pressure of 40 MPa for 1 min. A WD-XRF Axios–Panalytical spectrometer equipped with five diffraction crystals was used for the analyses. The SuperQ software package provided by Panalytical was employed for calibration and data reduction. Calibration is based on 30 certified international standards. The precision of analyzed elemental abundances is better than ± 0.2% for SiO_2, and ± 0.1% for the other major elements except for MnO_2 and P_2O_5 that have concentration errors of approximately ± 0.02%. For trace elements, relative errors are up to 10% for concentrations of 10–100 ppm, better than 5% for higher concentrations and reaching ~50% at levels below 10 ppm. Therefore, the detection limit is approximately 5–10 ppm.

The mineralogical composition was investigated by a Philips PW3710 X-Ray diffractometer (current: 20 mA, voltage: 40 kV, range 2θ: 5–80°, step size: 0.02° 2θ, time per step: 2 s) operating at the University of Genua (Italy), which mounted a Co-anode. Acquisition and processing of data was carried out using the Philips High Score software package.

Cosmogenic Isotopes

The burial age method involves the measurement of two isotopes (^{26}Al and ^{10}Be) that are produced by cosmic radiation in quartz near the surface prior to burial. ^{26}Al and ^{10}Be accumulate at a ratio of about 6.8:1 (Balco et al., 2013) in quartz grains, with a rate of a few atoms per Gram of quartz per year. Sufficiently deep burial (more than 10 m) of such quartz-rich sediments in a cave assures shielding from further cosmic rays. After burial, the ^{26}Al and ^{10}Be concentrations in the sample are only affected by their relative decay resulting in a decrease in the ^{26}Al/^{10}Be ratio. This ratio can be used to derive a burial age (Gosse and Phillips, 2001; Granger, 2006). A prerequisite of the burial dating technique is that samples have been exposed long enough to cosmic rays and accumulated sufficient cosmogenic nuclides prior to burial. The upper limit for measurement of the ^{26}Al and ^{10}Be isotope pair is between 5 and 6 Ma depending on the accumulated cosmogenic isotopes during surface exposure (Häuselmann et al., 2020).

The isotope concentrations can also be used to infer paleo-erosion rates of the source area prior to burial of the clasts. This is accomplished by backward modeling the quantity of nuclides present prior to the burial coupled with local production rate estimates. The pre-burial ^{26}Al/^{10}Be ratio (~6.8:1) is basically not influenced by production rate and thus elevation (Nishiizumi et al., 1989; Stock et al., 2005a) and therefore burial ages remain unaffected by altitude changes in the source area.

The sediment sample was broken into smaller pieces and decarbonated using HCl; due to many accessory minerals, only

38.0062 g of pure quartz could be recovered. Quartz was sieved and the fraction between 250 and 710 μm was physically concentrated (separation by form, magnet- and reverse magnet separation and heavy liquid) and then cleaned with HF-HNO_3 to remove intergrown feldspars to obtain a clean quartz concentrate. This concentrate was dissolved and cleaned by dissolution, precipitation, and ion exchange. ^{26}Al and ^{10}Be were separated, precipitated, oxidized, and measured on an AMS (in Purdue University). Chemical blanks were also measured to subtract laboratory influence. The AMS measures the $^{10}Be/^{9}Be$ ratio and the $^{26}Al/^{27}Al$ ratio; while ^{9}Be is added artificially, ^{27}Al normally abounds in quartz-rich samples.

Apatite Fission-Track Analyses

Fission-tracks in apatite are damage zones in the crystal lattice formed during the radioactive decay of ^{238}U. At temperatures above 120°C tracks are quickly annealed, whereas at temperatures below 60°C tracks are retained. The temperature range between retention and total annealing is called the partial annealing zone (PAZ). In this range fission tracks progressively narrow and shorten as a function of time and temperature (Naeser, 1979).

Fission-track sample preparation and analysis were performed on 100 apatite grains at ETH Zurich. Mounts of grains were polished and etched in 5.5 N HNO_3 at 21°C for 20 s to reveal spontaneous tracks. Samples were irradiated with thermal neutrons in the reactor at the Radiation Center of Oregon State University with a nominal fluence of 1.2×10^{16} n/cm^2. The CN-5 dosimeter was used to measure neutron fluence. After irradiation, induced fission tracks in the external detectors, low U muscovite sheets, were exposed through etching in 40% HF at 21°C for 45 min. AFT ages were calculated using the external-detector and the ζ-calibration methods (Hurford and Green, 1983) with IUGS standards (Durango and Fish Canyon) and a value of 0.5 for the 4p/2p geometry correction factor. The analyses were subjected to the χ^2 test (Galbraith, 1981) to detect whether the data sets contained any extra-Poissonian age scatter. A χ^2 probability of 5% denotes that the age distribution contains multiple age populations. AFT age distributions can be decomposed into age populations using kernel density estimate techniques: we used Binomfit by Brandon (1996) that is most suitable to deal with AFT samples with low density of spontaneous tracks.

U-Pb Zircon Chronology

U-Pb isotope intensities from 431 laser ablation spots in 371 zircon crystals were measured by inductively coupled plasma mass-spectrometry (LA-ICPMS) at ETH Zurich. The ablation areas with a spot diameter of 20 μm were pre-selected with the aid of cathodoluminescence images in order to identify zonations and crystal defects, which were then avoided. Both the core and rim of zircons were measured in the suitable grains.

U and Pb were analyzed using a Resonetic Resolution 155 laser ablation system with a repetition rate of 5 Hz and an energy density of 2 J cm^{-2} coupled to a Thermo Element XR Sector-field ICP-MS measuring ^{202}Hg, ^{204}Pb, ^{206}Pb, ^{207}Pb, ^{208}Pb, ^{232}Th, ^{235}U, and ^{238}U intensities (Guillong et al., 2014). GJ-1 (Jackson et al., 2004) was used as primary reference material, and accuracy of the method was confirmed by four secondary standards (AUSZ7-5, OD-3, Temora2, and 91,500). Ages and ratios corrected for instrumental drift and down hole fractionation were obtained using the iolite 2.5 (Paton et al., 2010) and VizualAge software (Petrus and Kamber, 2012). No common Pb correction was applied, since contaminated signals are recognized as discordant ages in the Concordia plots, which were produced with Isoplot 4.1 (Ludwig, 2001). Error ellipses represent 2 s analytical errors of the $^{207}Pb/^{235}U$ and $^{206}Pb/^{238}U$ ratios, respectively.

RESULTS

Grainsize, Petrography and Composition

The sampled sediment from Raponzolo Cave is a fine (51.6%) to very fine (22.8%) sand with moderate mud (clay + silt) fraction (18.2%); the carbonate cement and very few carbonatic grains, before dissolution, accounted for 54.4% of the original weight (**Figure 5**). Thin section analyses have shown the presence of both monomineralic and polymineralic grains as following (**Figure 6**; abundant: widespread in all observations; common: present in all observations; rare: only few grains detected):

- Biotite (abundant) in form of elongated grains with rounded tips casually oriented within the sample.
- Quartz (abundant) mainly rounded or sub-rounded
- Plagioclase (common), mainly rounded and a few sub-angular grains, some with polysynthetic lamination
- Zircon, mainly fractured (common)
- K-Feldspar (rare)
- Amphibole, green hornblende (rare)
- Chalcedony (rare)
- Apatite (rare)
- Garnet (very rare)
- Kyanite (very rare)

In addition, a few polymineralic grains are representative of amphibolites, micaschists and gneiss. XRD analysis confirms thin section observations, although it was not able to define the specific amphibole as hornblende due to low lines at the limit of detection for these minerals. The composition of the sample obtained through XRF is reported in **Table 1**. High Ca content (~34%) is related to the carbonate cement, while Si from quartz and Al from silicates reach respectively 25 and 9% of the sediment, with a relatively high Fe content (2.4%) (related to biotite and iron hidroxides). *p* (0.1 %wt, in form of P_2O_5) and Zr (84 ppm) are due to the presence of apatites and zircons. Sub-rounded quartz grains are indication of transport by saltation and traction. Some of these grains show striking rounded morphologies, suggesting recycling through different erosion and transport phases. On the other hand, biotite is abundant and well preserved, with some rounded elongated morphologies related to limited transport by flotation (Garzanti et al., 2011).

Burial Time From Cosmogenic Isotopes

The $^{10}Be/^{9}Be$ ratio is very small (7.8×10^{-15}), but in line with the relatively low amount of pure quartz dissolved. Nonetheless, the

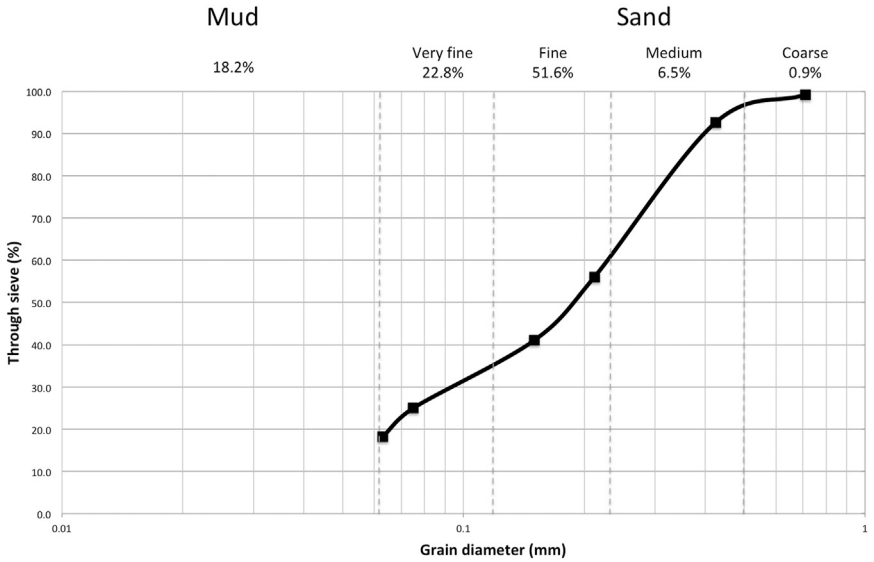

FIGURE 5 | Grainsize of the siliciclastic component of the samples: sand-size grains account for a total 81.8% while mud reached 18.2%. The siliciclastic component account for 46% of the total sample, while the total carbonate fraction (cement and few clasts) dissolved with acetic acid solution was 54% of the total sample.

error of 10% can be considered acceptable for such low values. The measurement of the procedural blanks yielded a $^{10}Be/^{9}Be$ ratio of 3.78×10^{-15} and a $^{26}Al/^{27}Al$ ratio of 6.41×10^{-15}. The blanks thus show that the measurements were good and the standards clean. All results were normalized for a ^{10}Be half-life of 1.39 Ma (Chmeleff et al., 2010; Korschinek et al., 2010). The uncertainties represent the analytical error only. The measurement of $^{26}Al/^{27}Al$ yielded a value (2.78×10^{-15}) below that of the blank (6.41×10^{-15}). Therefore, there is no detectable ^{26}Al in the sample. The combined absence of ^{26}Al and presence of ^{10}Be demonstrates that the sediment was indeed once at the surface, but that the burial time was so long that all ^{26}Al decayed because of its shorter mean half-life. Since ^{26}Al is unavailable, the exact age of the sample cannot be given, as the initial concentration of isotopes prior to burial cannot be recalculated. Nonetheless, we can infer a range of possible burial ages based on the expected mean lifetime of the sediment at the surface and isotope production rate at the altitude of the original catchment area. This hypothesis is presented in the discussion (chapter 4.2).

Paleogeographic Provenance Inferred From AFT Thermochronology and Zircon U-Pb Ages

AFT analyses (**Supplementary Table S1**) shows a distribution of dates between 4.5 ± 2.6 Ma and 56 ± 17 Ma (1σ). Two distinct populations can be identified through standard kernel density estimate techniques (Binomfit by Brandon, 1996; **Supplementary Table S2**): a minor and younger populations (P1) that includes 28% of the grains and centers at 17.6 (−2,3 + 2.6) Ma and a larger and older one (P2) that includes 72% of the grains and cetners at 23.3 Ma (−3.3 + 3.9) (**Figure 7**; **Supplementary Table S2**). The 431 U-Pb dates (**Supplementary Table S3**) show dates between 30 and >1,000 Ma old, including only two dates older than 1,000 Ma. This wide distribution consists of two main populations, a larger one (91 ± 1%) with dates centered around 35 Ma and a minor one between 270 and 600 Ma (**Figure 8**). While the first group is directly related to the emplacement of the Adamello batholith, the second is related to zircons from pre-alpine metamorphic rocks such as those of the Tonale Unit and south alpine basement, and/or to igneous zircons of the Adamello batholith with inherited cores.

DISCUSSION

Sediment Source

The petrographic composition of the sediment indicates a source situated mainly in the granitoid bodies of the Adamello Massif and in the metamorphic units of Tonale. Chalcedony is mostly related to the erosion of pseudotachylitic zones in Adamello-Presanella (Pennacchioni et al., 2006) and minor cherts eroded from the carbonatic sequence of Brenta. Metamorphic clasts (amphibolite) and minerals (especially kyanite) indicate a provenance from the Tonale Unit, which is characterized by high-P mineral suites (Davide et al., 2000).

AFT analysis provides additional indications on the source region (**Figure 9**). In the Tonale Unit, AFT dates vary between 6 and 25 Ma, and in the Adamello batholith between 8.3 and 23 Ma (Martin et al., 1998; Viola et al., 2003; Reverman et al., 2012). In both regions, AFT dates generally increase with elevation; although the AFT age-elevation relationships vary in age range and slope in different localities and in a few places they are

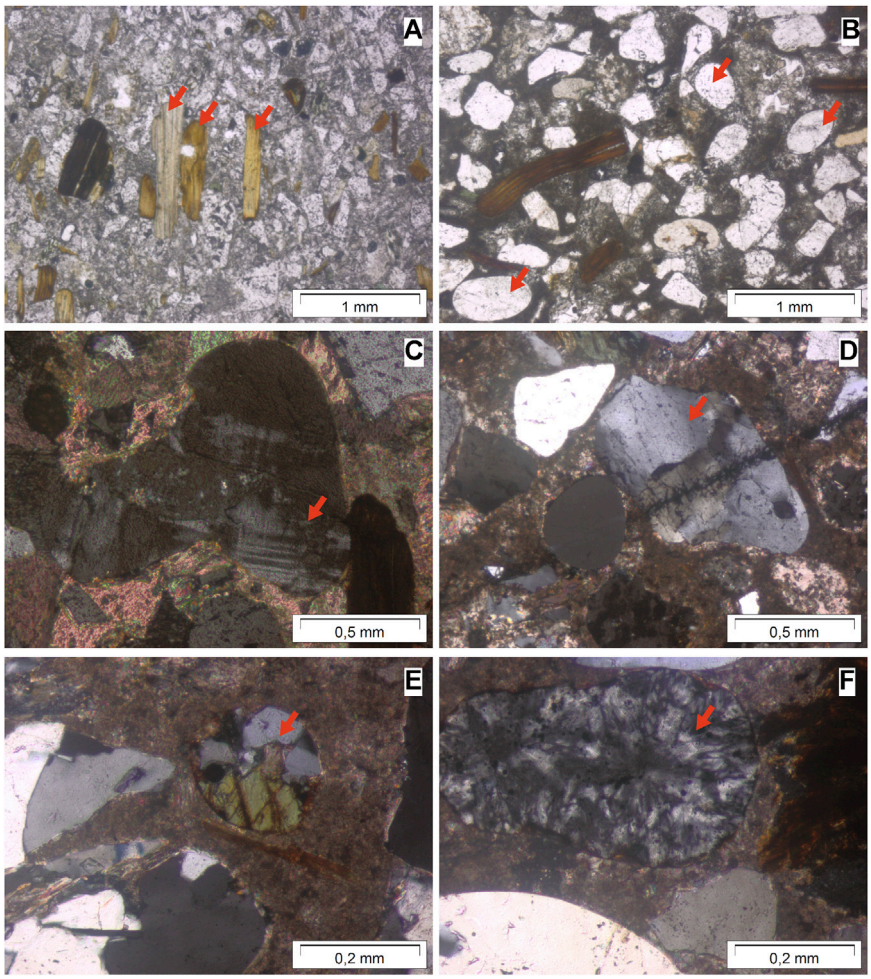

FIGURE 6 | Thin sections microphotographs [under polarizing microscope, **(A,B)** parallel polars, **(C–F)** crossed polars] showing (red arrows): **(A)** elongated biotite; **(B)** rounded to subrounded quartz; **(C)** rounded K-feldspar; **(D)** subrounded plagioclase; **(E)** a lithic grain of amphibolite (quartz + amphibole); **(F)** rounded chalcedony.

TABLE 1 | XRF results. Major elements are reported in weight percentage (%wt), Zr is reported in ppm. Other elements are considered irrelevant for this study, and thus omitted. LOI stands for loss of ignition.

Al_2O_3	CaO	Fe_2O_3	K_2O	MgO	MnO	Na_2O	P_2O_5	SiO_2	TiO_2	LOI	Zr
(wt%)	(wt%)	(wt%)	(wt%)	(wt%)	(wt%)	(wt%)	(wt%)	(wt%)	(wt%)	%	(ppm)
9.44	34.47	2.40	0.84	1.87	0.11	0.22	0.10	25.02	0.27	25.26	84

disturbed by tectonic displacements. In the sediments from Raponzolo Cave, the largest fraction (72%) of the detrital AFT dates centers at 23.3 Ma and the remaining fraction (28%) at 17.6 Ma. Thus, the largest fraction of the detrital apatites (red area in **Figure 9**) comes from the highest portions of the Tonale Unit and/or Adamello complex, at elevations above 2,300 m a.s.l, at present time. Regarding the smaller fraction at 17.6 Ma (blue area in **Figure 9**), while for Tonale the altitude range of the source region is also above the present elevation of 2,300 m a.s.l., for Adamello it is more difficult to constrain the altitude limit due to different profile distributions depending on the transect location (**Figure 9**). To solve this uncertainty, another indication is provided by zircon U-Pb ages. Zircon U-Pb ages are related to the crystallization of the magma source, which is not synchronous in all areas of the Adamello. It is thus possible to better understand which part of the batholith the sediment was eroded from if specific age groups are dominant in the cave sediment. While the older zircon age group (**Figure 9**) is related to recycling of crystals from the Permian basement and crustal rocks within the batholith (Hansmann and Oberli, 1991), the younger peak at 35 Ma indicates that the sediment source was mainly situated in the northern sectors of the Adamello batholith

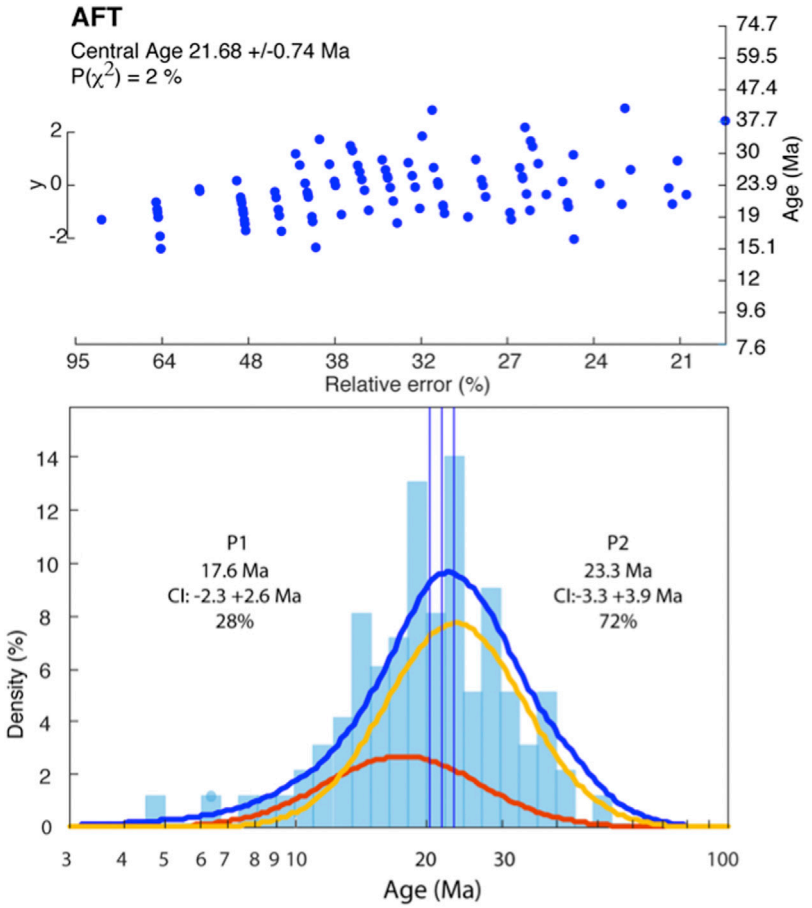

FIGURE 7 | Apatite Fission Track dating distribution in the sample. The central age of the whole population is 21.68 ± 0.74 Ma, which can be decomposed into two age populations (histogram below) using kernel density estimate techniques, showing a major peak (P2, 72%) at 23.3 Ma and a minor one (P1; 28%) at 17.6 Ma.

(Adamello North, Genova Valley, **Figures 9**, **10**), as shown by previous U-Pb, K-Ar, and Rb/Sr dating from different areas (Del Moro et al., 1983; Schaltegger et al., 2019). Very few zircons in the dataset (<10) are between 40–42 Ma indicating a negligible contribution from the southern area of the batholith (Daone, Rendena Valley; **Figures 9**, **10**; Schoene et al., 2012). This information allows to define the source region of the sediment in the northern sector of Adamello where AFT ages around 17.6 are also above 2,200–2,300 m a.s.l. at present time.

Therefore, the erosional phase producing the sediment filling Raponzolo cave occurred when the present valley network was not as deeply entrenched as today, and younger thermochronological units where not yet exposed in the source region.

Hypotheses on Age Based on Cosmogenic Nuclides

Due to the lack of ^{26}Al in the sediment, the exact age of burial cannot be calculated. However, it is possible to estimate a minimum age on the basis of the expected residence time at the surface and the cosmogenic production rate, which depends on the original altitude of the catchment area. The longer the sediment is at or near the surface (i.e., the smaller the erosion rate is), the more cosmogenic isotopes are produced. Once washed underground, these isotopes decay. If the sediment remained at the surface for a very short time, a little amount of isotopes is produced; it follows that after a comparable short burial time, the Al content would be no more measurable. The longer the sediment stayed at the surface, the more burial time is needed in order to completely deplete ^{26}Al. Therefore, in the case of the Raponzolo sediment, the main question is what a meaningful residence time at the surface could be. In order to provide a reasonable hypothesis on the residence time, we can consider the largest dataset available in the Alps: the data from Siebenhengste (Häuselmann et al., 2007). This dataset can be used as a reference for Raponzolo because of the similar settings, being Siebenhengste a karst system located within the higher ranges of the Alps (around 2000 m a.s.l.) in an area which experienced glaciations, as is the case of the Brenta Dolomites. In Siebenhengste cosmogenic dating provided erosion rates ranging from 23 to 470 m/Ma, while all but two have rates

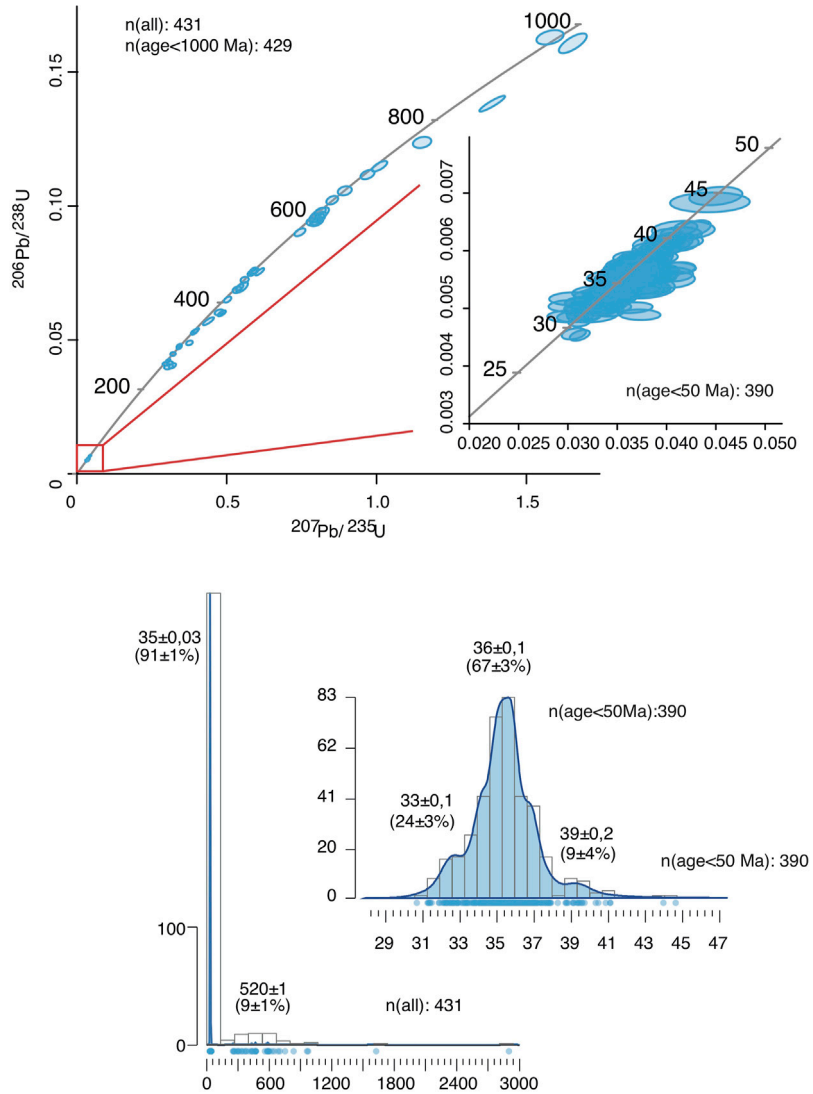

FIGURE 8 | Concordia and isochron diagrams for U-Pb dating of zircons (above). Ellipses (correlated errors) correspond to two sigma -STERR of the mean ratios. Linear regression calculations were performed with ISOPLOT-3 (Ludwig, 2001). Distribution of ages in the last 50 Ma show a peak at 36 Ma (below).

<150 m/Ma, indicating slower (pre- or interglacial) erosion. An averaged value yields 67 m/Ma, which translates into an inherited ^{10}Be amount prior to burial of 169,000 at/g. Divided by the estimated production rate in that area of 18.09 at/g/a, this gives 9,300 years residence time at the surface. The fastest, probably glacial, erosion rate gives a residence time of 1,300 years.

Since production rate is dependent on altitude, the model should also consider the approximate height of the original catchment area of the Raponzolo sediment. In order to model altitudes, production rates and erosion rates, we can use as prerequisites the available data: 1) the amount of ^{10}Be remaining in the sample measured to be 8,800 at/g; 2) no measurable ^{26}Al is present due to its complete decay. The lack of ^{26}Al can be fixed to be less than 5,000 at/g, twice the value of the blank. Considering these values, it is possible to create a model and back-calculate catchment altitudes and ages (**Supplementary Table S4**). This model shows that the fast erosion rate (surface residence time of 1,300 years) can be excluded (red ages in **Supplementary Table S4**) since it would give consistently measurable amounts of ^{26}Al (>10,000 at/g) in the sample. Therefore, we hitherto used the mean erosion rate of 67 m/Ma in the model (**Figure 10**). With this erosion rate, the model provides the minimum elevation of the catchment area (which is 1,200 m a.s.l.) and the minimum age that fulfills all prerequisites (around 5.25 Ma) (**Figure 10**). However, it is important to consider that this model output is based on the assumption that in Adamello and Brenta erosion and uplift were constant in time and space at the million-year timescale neglecting the effect of local differences as for instance fault displacement and differences in rock erodibility. This assumption is supported by

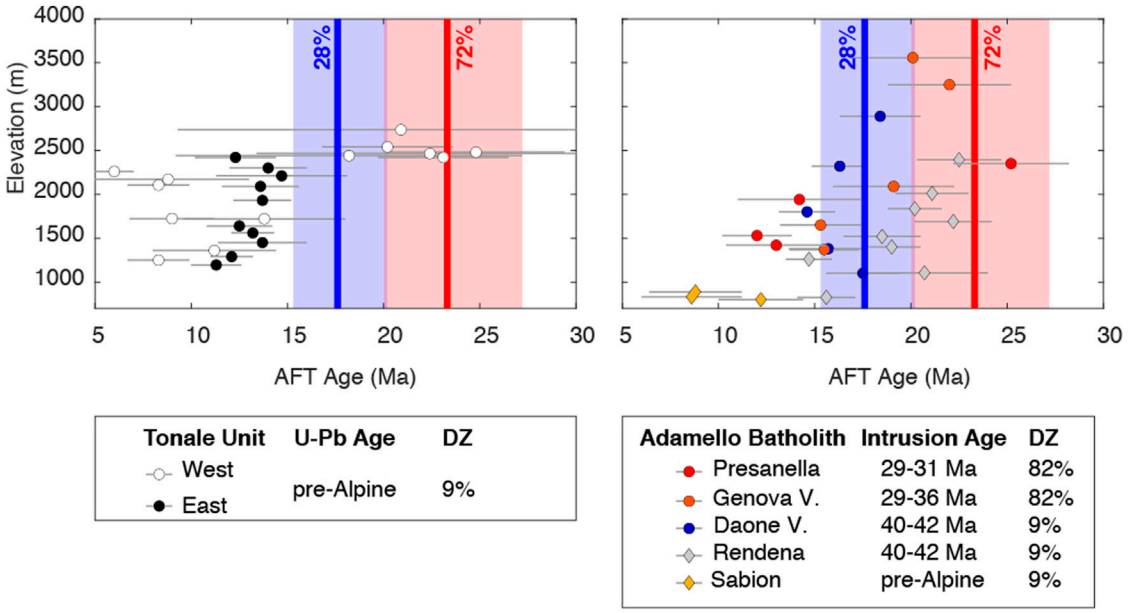

FIGURE 9 | Different AFT Age/Altitude profiles compared with the two AFT populations detected in the sediment of Raponzolo Cave (blue 17.6 Ma, red 23.3 Ma). In the lower boxes, each transect is correlated with the U-Pb age of zircons in each area. DZ shows to which percentage of ages the populations in the Raponzolo sample are associated: ages between 29 and 36 Ma (82%), ages between 40–42 (9%), pre-Alpine ages (9%). AFT profiles: Tonale from Martin et al. (1998); Presanella from Viola et al. (2001); Genova and Daone valleys from Reverman et al. (2012); Rendena from Martin et al. (1998).

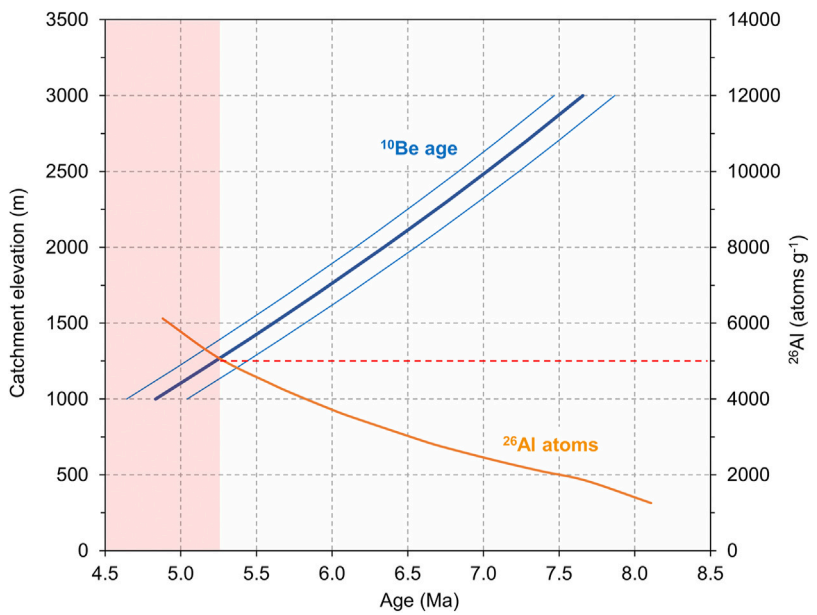

FIGURE 10 | Graph plotting the ^{10}Be burial ages as a function of the catchment elevation based on a surface sediment exposure time of 9,300 ± 930 years coupled with the calculated remaining ^{26}Al. The red dashed line at 5,000 ^{26}Al atoms/g defines the "exclusion zone" based on the absence of ^{26}Al in the sample. The line crosses the ^{10}Be age line at 5.25 Ma corresponding to a minimum catchment elevation of 1,250 m a.s.l.

thermochronologic data that in Adamello and Brenta do not resolve changes in the rate of exhumation after 4 Ma (Revermann et al., 2012) and that indicate possibly only little differential exhumation between the two massifs since 10 Ma (Heberer et al., 2017). Thus, our model points to the hypothesis that burial in the cave happened before 5.25 Ma.

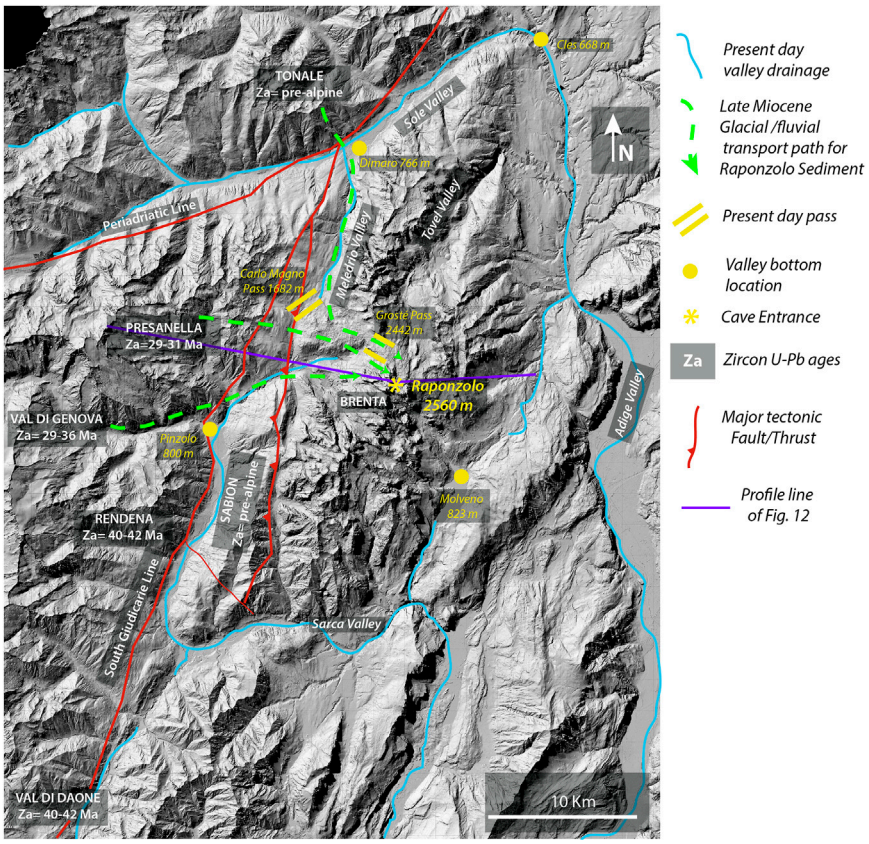

FIGURE 11 | Interpretation of sediment transport path from Adamello/Tonale toward Raponzolo Cave with the present hydrological network, major tectonic lines and U-Pb zircon ages from the different sectors.

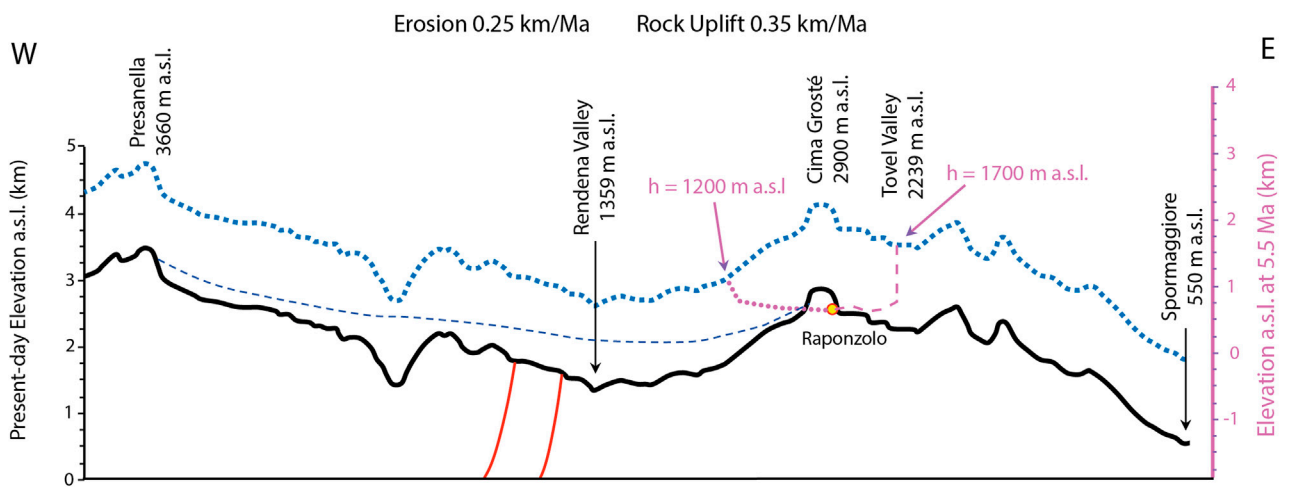

FIGURE 12 | West-east profile across the Adamello and Brenta massifs with the theoretical reconstruction of the relief at 5.5 Ma (dotted blue line). For simplicity the relief projection is based on a theoretical constant and uniform erosion rate of 0.25 km/Ma and rock uplift rate of 0.35 km/Ma, even if erosion and uplift have been surely acting with slightly different rates depending on lithologies and tectonic domains. This reconstruction is based on the assumption that nowadays valleys and prominent reliefs should have been following the footprint of the Messinian major base level drop during the Mediterranean salinity, similarly to other regions of the Alps (Garzanti and Malusà, 2008). The theoretical vertical profiles of the Raponzolo cave are represented by bold purple line (catchment in the upper Tovel valley) and dotted purple line (catchment in the Rendena valley). The dashed blue line represents the ice extent in the Rendena Valley during the Last Glacial Maximum (Trevisan, 1939).

Hints of Late Miocene Glaciations and Recycling of Fluvial Sediments

The Raponzolo Cave presents morphologies consistent with a phreatic and/or epi-phreatic origin (**Figure 3B**). The cave is probably only a fragment of an ancient karst system that has been eroded and uplifted to its present altitude (2,560 m a.s.l.). The conduits originally formed close to the water table level, which could have been situated at the level of the late Miocene valley bottom. The catchment area was situated in the northern part of the Adamello batholith up to the Tonale Unit to the north of the Periadriatic line. At present, these areas are separated from the Tovel Valley by the Rendena and Meledrio Valleys developed along the South Giudicarie Line and culminating in the Campo Carlo Magno pass at 1,682 m (**Figure 11**). Unfortunately, the irregular layering of the granitic sediments in the cave is not diagnostic of the direction of water flow during the sediment deposition, so we cannot discern if the sediment was flushed within the karst system from the Tovel valley or from the Rendena valley. These two possibilities are represented in **Figures 11**, **12**. In the profile of **Figure 12**, the present topography is projected at theoretical altitudes during the late Miocene considering, for simplicity, a constant and uniform erosion rate of 0.25 km/Ma and rock uplift rate of 0.35 km/Ma in agreement with several studies on the evolution of this alpine region (Revermann et al., 2012; Heberer et al., 2017 and references therein). This simplified assumption does not take into account differential erosion and uplift depending on lithologies and tectonic subdomains, but allows providing a general idea of the potential paleolandscape. Indeed, the Mediterranean salinity crisis and the base level dropdown during these times should have been the footprint of the present time hydrographic network in the Adamello-Brenta region, similar to what occurred in the Lepontine dome (Garzanti and Malusà, 2008). If the sediment filled the karst system entering from the Rendena Valley, the clasts of the Tonale Unit had to be transported from the Sole Valley (766 m at present-day Dimaro) uphill along the Meledrio Valley, and across Campo Carlo Magno Pass (1,682 m at present day). If the sediments had to be transported inside the Tovel valley, they would have overcome also the Grosté Pass (2,442 m at present day, **Figure 11**). From the data available and literature it is not possible to assess the hypothesis that the Meledrio or Tovel valleys were inverted at that time, allowing an efficient fluvial sediment transport from Tonale to Brenta. However, if the present topography should generally mirror the Miocene landscape, a relief inversion of these incisions after the Messinian sea level dropdown is unlikely suggesting that an uphill sediment transport from Tonale to Brenta would have been possible only by means of glaciers. The Adamello and Brenta massifs have been strongly affected by Quaternary glaciations, and during the Last Glacial Maximum, a glacial tongue from the Sole Valley filled the Meledrio Valley and surpassed the Campo Carlo Magno Pass where the reconstructed elevation of the glacier was around 2,100 m (Trevisan, 1939; Carton and Baroni, 2017). Glaciers could have used the same transport route also during more ancient glaciations and remains the best candidates for the transport of sediments of the Tonale Unit from the Sole Valley up to the Raponzolo cave entrance. This hypothesis poses an interesting dilemma because Miocene glaciations in the Alps have never been documented. Instead, sedimentary evidence of localized latest Miocene–Early Pliocene glaciations are known from Greenland (Larsen et al., 1994) to South America (Mercer and Sutter, 1982). The North Atlantic records a major cooling episode and increase in global ice volume in the period from 6.26 to 5.5 Ma that was marked by 18 glacial-to-interglacial oscillations, with the most prominent glacial phases at 5.75 and 5.51 Ma (stages TG20 and TG12; Hodell et al., 2001). These ages are within the possible range of the sediment infilling of Raponzolo being older than the minimum cosmogenic burial ages of the sediments calculated in the cosmogenic production model presented in chapter 4.2 (**Supplementary Table S4**). Also, the expected altitude of the source between 1,200 m (Rendena Valley sink, **Figure 12**) and 1700 m (Tovel Valley sink, **Figure 12**) is in agreement with the minimum altitude catchment calculated by the model.

The modest increases in global ice volume inferred from the benthic $\delta^{18}O$ signal (Hodell et al., 2001) suggest that Late Miocene glaciations were not as widespread as the Quaternary ones. In this scenario, local Alpine glaciers were probably not able to reach the Po plain and, therefore, no glacial sediments have been preserved, aside of potential local traps like caves.

A problem for this interpretation remains the roundness and well sorting of the Raponzolo sediment, which is in contrast with a glacial origin, pointing to a fluvial or aeolian transport instead. However, the first action of glacier flows is bulldozering the sediments already present at the valley bottoms (Rossato et al., 2018), which are usually rich in fluvial components. Therefore, a recycling of fluvial sediment by glacier tongues is consistent with the grain size distribution and shape, as well as with the presence of well-preserved biotite, which has not been weathered after burial (Petersen and Rasmussen, 1980; Föllmi et al., 2009). However, we cannot exclude that the most rounded quartz grains could be related to recycling of aeolian sediments, which is also consistent with an arid-cold glacial environment and with the presence of silt sized grains in the Raponzolo cave sediments (Wright, 2001).

Implications for Paleogeography and Tectonic Evolution

Cosmogenic data do not constrain a definitive age of the sediment burial, but point to a minimum age of 5.25 Ma. However, it is possible to advance additional hypotheses on the paleo-landscape during cave formation and subsequent infilling. Indeed, thermochronologic data indicate that during the late Miocene, from about 8 Ma, the Adamello batholith was exhuming rapidly to near-surface depths at about 0.65 km/Ma in response to uplift induced by tectonic activity, whereas during the Plio-Pleistocene exhumation proceeded on average at a lower rate of about 0.35 km/Ma (Reverman et al., 2012). In Brenta, on the other side of the Giudicarie line, thermochronologic data from flysch sediments on the eastern foot of the massif (Ponte Pià Formation, AFT = 9–10 Ma) indicate 3 to 2 km of rock removal since 10 Ma,

which corresponds to an average exhumation rate similar in range but possibly slightly lower than the one estimated for the Adamello massif during the late Miocene (Heberer et al., 2017). Altogether, the thermochronologic data from Adamello and Brenta, and the new data gathered from Raponzolo Cave, indicate that during the late Miocene the exhumation of the two massifs was synchronous, but the pace was possibly slightly different. This means that Adamello was possibly exhuming faster than Brenta and that this evolution may have favored a potential transfer of sediments (fluvial or glacial) from Adamello-Presanella toward Brenta. A phase of uplift and exhumation might also have favored, at the same time or shortly later, a local base-level fall; accordingly, this would be a suitable scenario for the formation of an epiphreatic cave system and its infilling. Finally, the present-day elevation of Raponzolo Cave roughly corresponds to the lower limit of its sediment source in both Adamello and Tonale as indicated by the AFT ages. This suggests that the Raponzolo sediments represent a remnant uplifted late Miocene landscape including the high elevation reaches of Tonale and Adamello, and Brenta, which was probably slightly lower in elevation as it is still today as suggested by the Ponte Pia Formation AFT ages. In this paleo-landscape, the valleys separating different geological domains (Adamello, Tonale, Brenta) were likely not as deeply entrenched as today, allowing an efficient transfer of sediment from the north-west to south-east across major tectonic lineaments, partially by fluvial systems and occasionally by glaciation events. This observation is consistent with recent studies (Winterberg et al., 2020) showing that major river valleys in inner parts of the Southern Alps (i.e., Adige Valley) were not all yet deeply carved during the Messinian sea-level drawdown.

CONCLUSION

The study of the sediments discovered in Raponzolo Cave provides new hints on the geographic, tectonic and climatic evolution of the calcareous Southern Alps in the Brenta region, and its interconnection with the Adamello crystalline bodies and the Tonale metamorphic units. Even if cosmogenic dating has not been able to define a narrow age for the sediment burial, the obtained minimum age coupled with petrographic observations, AFT ages and U-Pb on zircons provided reliable information about the sediment source and transport. Our results, combined with the known evolution of Adamello, allows inferring new clues on paleogeography of the area during the late Miocene. The data obtained thorugh the detailed analysis of the cave sediment provide the following evidences:

- The sediments were eroded from the higher (>2,200 m a.s.l) elevations of Tonale and northern Adamello-Presanella;
- The lack of ^{26}Al doesn't allow determining an exact date for the sediment burial in the cave. However, our calculation considering the remaining ^{10}Be in the sample, the mean surface exposure times of sediments in the Alps and the inferred original altitude of the source during late Miocene, points to a burial older than 5.25 Ma.

Based on these line of evidence and given the known evolution of this area of the Alps, the following hypotheses should be considered for future studies:

- The sediments were transported into Raponzolo Cave possibly by a river network or through glacial transport
- If the glacial transport would be confirmed, this could have happened during late Miocene when glaciations have been recorded in other areas of world but have been possibly overlooked in the Alps;
- At the time of sediment burial into the cave, the valley bottoms were not yet deeply entrenched allowing an efficient sediment transport from Adamello-Tonale toward Brenta.

These clues open intriguing questions that could be refined by future studies, especially if other allochtonous sediments would be identified in other caves of Brenta. For example a Miocene fluvial-glacial interconnection between different areas of the Alps (Brenta-Adamello-Tonale) suggest that the Messinian Salinity Crisis sea-level drop and related accelerated fluvial erosion may not have reached the internal most elevated region of the Southern Alps (Winterberg et al., 2020).

This is a nice case study on how a cave sediment, even from a single cave, can provide data with wide implications not only for the genesis of the cave itself but also for the complex settings and evolution of the paleo-environment of the surrounding areas. Sediments can be preserved in caves while they have been completely eroded or recycled on the surface. Therefore, the study of cave sediments in complex regions of the Alps represent a promising, still under-exploited, source of information on paleo-geography and tectonic evolution.

DATA AVAILABILITY STATEMENT

The original contributions presented in the study are included in the article/**Supplementary Material**, further inquiries can be directed to the corresponding author.

AUTHOR CONTRIBUTIONS

FS conceived the project. FS and AB carried out fieldwork. FS, MF, AC, AB wrote the draft, with contributions from PH, CC and JW. AC, MF, PH and CC accomplished lab analyses.

ACKNOWLEDGMENTS

This research was possible thanks to the logistical support of Gruppo Speleologico Trentino SAT Bindesi Villazzano especially to Walter Bronzetti and Daniele Sighel. The research was financially supported by Parco Naturale Adamello Brenta Geopark: our gratitude goes to Director Cristiano Trotte, and to Vajolet Mase and Alessia Scalfi for assistance. We are grateful

to Enrico Dinelli and Valerio Funari for XRF analysis at UNIBO, and to Marcel Guillong for LA-ICP-MS U-Pb measurements and data reduction at ETH. Finally, thanks to Giulio Viola and Paolo Garofalo (UNIBO) for the access to the optical microscope laboratory, and the three reviewers for their insightful comments.

SUPPLEMENTARY MATERIAL

The Supplementary Material for this article can be found online at: https://www.frontiersin.org/articles/10.3389/feart.2021.672119/full#supplementary-material

REFERENCES

Anthony, D. M., and Granger, D. E. (2007). A New Chronology for the Age of Appalachian Erosional Surfaces Determined by Cosmogenic Nuclides in Cave Sediments. *Earth Surf. Process. Landforms* 32, 874–887. doi:10.1002/esp.1446

Audra, P., Bini, A., Gabrovšek, F., Häuselmann, P., Hobléa, F., Jeannin, P.-Y., et al. (2007). Cave and Karst Evolution in the Alps and Their Relation to Paleoclimate and Paleotopography. *Acta Carsologica* 36, 53–67. doi:10.3986/ac.v36i1.208

Audra, P., Bini, A., Gabrovšek, F., Häuselmann, P., Hobléa, F., Jeannin, P.-Y., et al. (2006). Cave Genesis in the Alps between the Miocene and Today: a Review. *zfg* 50, 153–176. doi:10.1127/zfg/50/2006/153

Balco, G., Soreghan, G. S., Sweet, D. E., Marra, K. R., and Bierman, P. R. (2013). Cosmogenic-nuclide Burial Ages for Pleistocene Sedimentary Fill in Unaweep Canyon, Colorado, USA. *Quat. Geochronol.* 18, 149–157. doi:10.1016/j.quageo.2013.02.002

Ballesteros, D., Giralt, S., García-Sansegundo, J., and Jiménez-Sánchez, M. (2019). Quaternary regional evolution based on karst cave geomorphology in Picos de Europa (Atlantic Margin of the Iberian Peninsula). *Geomorphology* 336, 133–151. doi:10.1016/j.geomorph.2019.04.002

Bella, P., Bosák, P., Braucher, R., Pruner, P., Hercman, H., Minár, J., et al. (2019). Multi-level Domica-Baradla Cave System (Slovakia, Hungary): Middle Pliocene-Pleistocene Evolution and Implications for the Denudation Chronology of the Western Carpathians. *Geomorphology* 327, 62–79. doi:10.1016/j.geomorph.2018.10.002

Bigi, G., and Carrozzo, M. T. (1992). "Structural Model of Italy," in *Consiglio Nazionale Delle Ricerche (CNR)* (Florence: Italy), 1, 500 000.

Bini, A., Borsato, A., and Ischia, N. (1991). "Morfologia Ed Evoluzione Della Grotta Cesare Battisti (La Paganella, Trento)," in *Atti IX Convegno Regionale di Speleologia del Trentino-Alto Adige (Lavis). Natura Alpina* (Trento, Italy: Museo Tridentino di Scienze Naturali) 42, 41–77.

Borsato, A. (2001). "Characterisation of a High-Altitude alpine Karst Aquifer by Means of Temperature, Conductivity and Discharge Monitoring (Centonia spring, Brenta Dolomites, N-Italy)," in Proceedings of 7th Conference on Limestone Hydrology and Fissured Media. Editor F. Zwahlen (Besançon: France: Université de Franche-Comté), 51–54.

Borsato, A. (2007). Gli acquiferi carsici delle Dolomiti di Brenta: risorse idriche e funzionamento idrogeologico. *Memorie Istituto Italiano di Speleologia II*, 49–56.

Borsato, A. (1991). "La Grotta dello Specchio: nuova cavità del complesso carsico dei Lasteri (Gruppo di Brenta, Trentino occidentale)," in *Atti IX Convegno Regionale di Speleologia del Trentino-Alto Adige (Lavis)* (Trento: Museo Tridentino di Scienze Naturali), 42, 7–25.

Borsato, A. (2012). L'abisso Freezer ai Lasteri (Gruppo di Brenta Orientale). *XV Convegno Regionale di Speleologia Del. Trentino-alto Adige* 11, 23.

Borsato, A., Quinif, Y., Bini, A., and Dublyansky, Y. (2003). Open-system alpine Speleothems: Implications for U-Series Dating and Paleoclimate Reconstructions. *Studi Trentini di Scienze Naturali, Acta Geologica* 80, 71–83.

Borsato, A., Sartorio, D., and Frisia, S. (1994). Late Triassic-Early Liassic Stratigraphic and Diagenetic Evolution of the Margin between the Trento Platform and the Lombardy basin in the Brenta Dolomites (Italy). *Museo tridentino di scienze naturali - Acta Geologica* 69, 5–35.

Brack, P. (1983). Multiple Intrusions-Examples from the Adamello Batholith (Italy) and Their Significance on the Mechanisms of Intrusion. *Memorie della Societa Geologica Italiana* 26 (1), 145–157.

Brandon, M. T. (1996). Probability Density Plot for Fission-Track Grain-Age Samples. *Radiat. Measurements* 26, 663–676. doi:10.1016/s1350-4487(97)82880-6

Callegari, E., and Brack, P. (2002). Geological Map of the Tertiary Adamello Batholith (Northern Italy): Explanatory Notes and Legend. *Memorie di Scienze Geologiche* 54, 19–49.

Calvet, M., Gunnell, Y., Braucher, R., Hez, G., Bourlès, D., Guillou, V., et al. (2015). Cave Levels as Proxies for Measuring post-orogenic Uplift: Evidence from Cosmogenic Dating of Alluvium-Filled Caves in the French Pyrenees. *Geomorphology* 246, 617–633. doi:10.1016/j.geomorph.2015.07.013

Campani, M., Mulch, A., Kempf, O., Schlunegger, F., and Mancktelow, N. (2012). Miocene Paleotopography of the Central Alps. *Earth Planet. Sci. Lett.* 337-338, 174–185. doi:10.1016/j.epsl.2012.05.017

Carrapa, B., and Di Giulio, A. (2001). The Sedimentary Record of the Exhumation of a Granitic Intrusion into a Collisional Setting: the Lower Gonfolite Group, Southern Alps, Italy. *Sediment. Geol.* 139, 217–228. doi:10.1016/s0037-0738(00)00167-6

Carton, A., and Baroni, C. (2017). The Adamello-Presanella and Brenta Massifs, Central Alps: Contrasting High-Mountain Landscapes and Landforms, in *Landscapes and Landforms of Italy*. Editors M. Soldati and M. Marchetti (Cham: Springer Nature Switzerland), 101–112. doi:10.1007/978-3-319-26194-2_8

Castellarin, A., and Cantelli, L. (2000). Neo-Alpine Evolution of the Southern Eastern Alps. *J. Geodynamics* 30, 251–274. doi:10.1016/s0264-3707(99)00036-8

Chmeleff, J., Von Blanckenburg, F., Kossert, K., and Jakob, D. (2010). Determination of the 10Be Half-Life by Multicollector ICP-MS and Liquid Scintillation Counting. *Nucl. Instr. Methods Phys. Res. Section B: Beam Interactions Mater. Atoms* 268, 192–199. doi:10.1016/j.nimb.2009.09.012

Columbu, A., Audra, P., Gázquez, F., D'angeli, I. M., Bigot, J.-Y., Koltai, G., et al. (2021). Hypogenic Speleogenesis, Late Stage Epigenic Overprinting and Condensation-Corrosion in a Complex Cave System in Relation to Landscape Evolution (Toirano, Liguria, Italy). *Geomorphology* 376, 107561. doi:10.1016/j.geomorph.2020.107561

Columbu, A., Chiarini, V., De Waele, J., Drysdale, R., Woodhead, J., Hellstrom, J., et al. (2017). Late Quaternary Speleogenesis and Landscape Evolution in the Northern Apennine Evaporite Areas. *Earth Surf. Process. Landforms* 42, 1447–1459. doi:10.1002/esp.4099

Columbu, A., De Waele, J., Forti, P., Montagna, P., Picotti, V., Pons-Branchu, E., et al. (2015). Gypsum Caves as Indicators of Climate-Driven River Incision and Aggradation in a Rapidly Uplifting Region. *Geology* 43, 539–542. doi:10.1130/g36595.1

Columbu, A., Sauro, F., Lundberg, J., Drysdale, R., and De Waele, J. (2018). Palaeoenvironmental Changes Recorded by Speleothems of the Southern Alps (Piani Eterni, Belluno, Italy) during Four Interglacial to Glacial Climate Transitions. *Quat. Sci. Rev.* 197, 319–335. doi:10.1016/j.quascirev.2018.08.006

Conci, C., and Galvagni, A. (1952). La Grotta del Torrione di Vallesinella nel Gruppo di Brenta. *Studi Trent. Sci. Nat.*, 1–2.

Davide, G., Gosso, G., Pulcrano, E., and Iole Spalla, M. (2000). Eo-Alpine HP Metamorphism in the Permian Intrusives from the Steep belt of the central Alps (Languard-Campo Nappe and Tonale Series). *Geodinamica Acta* 13, 149–167. doi:10.1080/09853111.2000.11105370

De Waele, J., Ferrarese, F., Granger, D. E., and Sauro, F. (2012). Landscape Evolution in the Tacchi Area (central-east Sardinia, Italy) Based on Karst and Fluvial Morphology and Age of Cave Sediments. *Geografia Fisica e Dinamica Quaternaria* 35, 119–127. doi:10.4461/GFDQ.2012.35.11

Del Moro, A., Pardini, G., Quercioli, C., Villa, I., and Callegari, E. (1983). Rb/Sr and K/Ar Chronology of Adamello Granitoids, Southern Alps. *Memorie della Società Geologica Italiana* 26, 285–299.

Doglioni, C., and Bosellini, A. (1987). Eoalpine and Mesoalpine Tectonics in the Southern Alps. *Geol. Rundsch* 76, 735–754. doi:10.1007/bf01821061

Fairchild, I. J., Smith, C. L., Baker, A., Fuller, L., Spötl, C., Mattey, D., et al. (2006). Modification and Preservation of Environmental Signals in Speleothems. *Earth-Science Rev.* 75, 105–153. doi:10.1016/j.earscirev.2005.08.003

Fellin, M. G., Martin, S., and Massironi, M. (2002). Polyphase Tertiary Fault Kinematics and Quaternary Reactivation in the central-eastern Alps (Western Trentino). *J. Geodynamics* 34, 31–46. doi:10.1016/s0264-3707(01)00072-2

Föllmi, K. B., Arn, K., Hosein, R., Adatte, T., and Steinmann, P. (2009). Biogeochemical Weathering in Sedimentary Chronosequences of the Rhône and Oberaar Glaciers (Swiss Alps): Rates and Mechanisms of Biotite Weathering. *Geoderma* 151 (3-4), 270–281. doi:10.1016/j.geoderma.2009.04.012

Fox, M., Herman, F., Willett, S. D., and Schmid, S. M. (2016). The Exhumation History of the European Alps Inferred from Linear Inversion of Thermochronometric Data. *Am. J. Sci.* 316, 505–541. doi:10.2475/06.2016.01

Galbraith, R. F. (1981). On Statistical Models for Fission Track Counts. *Math. Geology.* 13, 471–478. doi:10.1007/bf01034498

Garzanti, E., Andó, S., France-Lanord, C., Censi, P., Vignola, P., Galy, V., et al. (2011). Mineralogical and Chemical Variability of Fluvial Sediments 2. Suspended-Load silt (Ganga-Brahmaputra, Bangladesh). *Earth Planet. Sci. Lett.* 302, 107–120. doi:10.1016/j.epsl.2010.11.043

Garzanti, E., and Malusà, M. G. (2008). The Oligocene Alps: Domal Unroofing and Drainage Development during Early Orogenic Growth. *Earth Planet. Sci. Lett.* 268, 487–500. doi:10.1016/j.epsl.2008.01.039

Gosse, J. C., and Phillips, F. M. (2001). Terrestrial *In Situ* Cosmogenic Nuclides: Theory and Application. *Quat. Sci. Rev.* 20, 1475–1560. doi:10.1016/s0277-3791(00)00171-2

Granger, D. E. (2006). A Review of Burial Dating Methods Using ^{26}Al and ^{10}Be. *Spec. Papers-Geological Soc. America* 415, 1–16. doi:10.1130/2006.2415(01)

Granger, D. E., Fabel, D., and Palmer, A. N. (2001). Pliocene–Pleistocene Incision of the Green River, Kentucky, Determined from Radioactive Decay of Cosmogenic 26Al and 10Be in Mammoth Cave Sediments. *Geol. Soc. America Bull.* 113, 825–836. doi:10.1130/0016-7606(2001)113<0825:ppiotg>2.0.co;2

Granger, D. E., Gibbon, R. J., Kuman, K., Clarke, R. J., Bruxelles, L., and Caffee, M. W. (2015). New Cosmogenic Burial Ages for Sterkfontein Member 2 Australopithecus and Member 5 Oldowan. *Nature* 522, 85–88. doi:10.1038/nature14268

Guillong, M., Von Quadt, A., Sakata, S., Peytcheva, I., and Bachmann, O. (2014). LA-ICP-MS Pb-U Dating of Young Zircons from the Kos-Nisyros Volcanic centre, SE Aegean Arc. *J. Anal. Spectrom.* 29, 963–970. doi:10.1039/c4ja00009a

Hansmann, W., and Oberli, F. (1991). Zircon Inheritance in an Igneous Rock Suite from the Southern Adamello Batholith (Italian Alps). *Contr. Mineral. Petrol.* 107, 501–518. doi:10.1007/bf00310684

Häuselmann, P. (2007). How to Date Nothing with Cosmogenic Nuclides. *Acta Carsologica* 36, 93–100. doi:10.3986/ac.v36i1.212

Häuselmann, P., Fiebig, M., Kubik, P. W., and Adrian, H. (2007). A First Attempt to Date the Original "Deckenschotter" of Penck and Brückner with Cosmogenic Nuclides. *Quat. Int.* 164-165, 33–42. doi:10.1016/j.quaint.2006.12.013

Häuselmann, P., and Granger, D. E. (2005). Dating of Caves by Cosmogenic Nuclides: Method, Possibilities, and the Siebenhengste Example(Switzerland). *Acta Carsologica* 34, 43–50. doi:10.3986/ac.v34i1.278

Häuselmann, P., Mihevc, A., Pruner, P., Horáček, I., Čermák, S., Hercman, H., et al. (2015). Snežna Jama (Slovenia): Interdisciplinary Dating of Cave Sediments and Implication for Landscape Evolution. *Geomorphology* 247, 10–24. doi:10.1016/j.geomorph.2014.12.034

Häuselmann, P., Plan, L., Plan, L., Pointner, P., and Fiebig, M. (2020). Cosmogenic Nuclide Dating of Cave Sediments in the Eastern Alps and Implications for Erosion Rates. *Ijs* 49, 107–118. doi:10.5038/1827-806x.49.2.2303

Heberer, B., Reverman, R. L., Fellin, M. G., Neubauer, F., Dunkl, I., Zattin, M., et al. (2017). Postcollisional Cooling History of the Eastern and Southern Alps and its Linkage to Adria Indentation. *Int. J. Earth Sci. (Geol Rundsch)* 106, 1557–1580. doi:10.1007/s00531-016-1367-3

Hodell, D. A., Curtis, J. H., Sierro, F. J., and Raymo, M. E. (2001). Correlation of Late Miocene to Early Pliocene Sequences between the Mediterranean and North Atlantic. *Paleoceanography* 16, 164–178. doi:10.1029/1999pa000487

Hurford, A. J., and Green, P. F. (1983). The Zeta Age Calibration of Fission-Track Dating. *Chem. Geology.* 41, 285–317. doi:10.1016/s0009-2541(83)80026-6

Jackson, S. E., Pearson, N. J., Griffin, W. L., and Belousova, E. A. (2004). The Application of Laser Ablation-Inductively Coupled Plasma-Mass Spectrometry to *In Situ* U-Pb Zircon Geochronology. *Chem. Geology.* 211, 47–69. doi:10.1016/j.chemgeo.2004.06.017

Korschinek, G., Bergmaier, A., Faestermann, T., Gerstmann, U. C., Knie, K., Rugel, G., et al. (2010). A New Value for the Half-Life of 10Be by Heavy-Ion Elastic Recoil Detection and Liquid Scintillation Counting. *Nucl. Instr. Methods Phys. Res. Section B: Beam Interactions Mater. Atoms* 268, 187–191. doi:10.1016/j.nimb.2009.09.020

Kuhlemann, J., and Kempf, O. (2002). Post-eocene Evolution of the North Alpine Foreland Basin and its Response to Alpine Tectonics. *Sediment. Geology.* 152, 45–78. doi:10.1016/s0037-0738(01)00285-8

Larsen, H. C., Saunders, A. D., Clift, P. D., Beget, J., Wei, W., and Spezzaferri, S. (1994). Seven Million Years of Glaciation in Greenland. *Science* 264, 952–955. doi:10.1126/science.264.5161.952

Ludwig, K. (2001). *A Geochronological Tool Kit for Microsoft Excel*. Berkeley Geochronology Center, 55. Isoplot/Ex rev. 2.49.

Malusà, M. G., Zattin, M., Andò, S., Garzanti, E., and Vezzoli, G. (2009). Focused Erosion in the Alps Constrained by Fission-Track Ages on Detrital Apatites. *Geol. Soc. Lond. Spec. Publications* 324 (1), 141–152. doi:10.1144/sp324.11

Martin, S., Bigazzi, G., Zattin, M., Viola, G., and Balestrieri, M. L. (1998). Neogene Kinematics of the Giudicarie Fault (Central-Eastern Alps, Italy): New Apatite Fission-track Data. *Terra Nova* 10, 217–221. doi:10.1046/j.1365-3121.1998.00119.x

Martin, S., Prosser, G., and Morten, L. (1993). Tectono-magmatic Evolution of Sheeted Plutonic Bodies along the north Giudicarie Line (Northern Italy). *Geol. Rundsch* 82, 51–66. doi:10.1007/bf00563270

Mercer, J. H., and Sutter, J. F. (1982). Late Miocene-Earliest Pliocene Glaciation in Southern Argentina: Implications for Global Ice-Sheet History. *Palaeogeogr. Palaeoclimatol. Palaeoecol.* 38, 185–206. doi:10.1016/0031-0182(82)90003-7

Naeser, C. W. (1979). Fission-track Dating and Geologic Annealing of Fission Tracks," in *Lectures in Isotope Geology*. Editor E. Jäger (Heidelberg: Springer), 154–169. doi:10.1007/978-3-642-67161-6_10

Nicod, J. (1976). Les Dolomites de la Brenta (Italie) Karst haut-alpin typique et le problème des cuvettes glacio-karstiques. *Z. für Geomorphologie Suppl. Band* 26, 35–57.

Nishiizumi, K., Winterer, E. L., Kohl, C. P., Klein, J., Middleton, R., Lal, D., et al. (1989). Cosmic ray Production Rates of10Be and26Al in Quartz from Glacially Polished Rocks. *J. Geophys. Res.* 94, 17907–17915. doi:10.1029/jb094ib12p17907

Paton, C., Woodhead, J. D., Hellstrom, J. C., Hergt, J. M., Greig, A., and Maas, R. (2010). Improved Laser Ablation U-Pb Zircon Geochronology through Robust Downhole Fractionation Correction. *Geochem. Geophys. Geosystems* 11, 1–36. 10.1029/2009GC002618. Art. Q0AA06.

Pennacchioni, G., Di Toro, G., Brack, P., Menegon, L., and Villa, I. M. (2006). Brittle-ductile-brittle Deformation during Cooling of Tonalite (Adamello, Southern Italian Alps). *Tectonophysics* 427, 171–197. doi:10.1016/j.tecto.2006.05.019

Petersen, L., and Rasmussen, K. (1980). Mineralogical Composition of the clay Fraction of Two Fluvio-Glacial Sediments from East Greenland. *Clay miner.* 15 (2), 135–145. doi:10.1180/claymin.1980.015.2.04

Petrus, J. A., and Kamber, B. S. (2012). VizualAge: A Novel Approach to Laser Ablation ICP-MS U-Pb Geochronology Data Reduction. *Geostandards Geoanalytical Res.* 36, 247–270. doi:10.1111/j.1751-908x.2012.00158.x

Potter, P. E., and Szatmari, P. (2009). Global Miocene Tectonics and the Modern World. *Earth-Science Rev.* 96 (4), 279–295. doi:10.1016/j.earscirev.2009.07.003

Reverman, R. L., Fellin, M. G., Herman, F., Willett, S. D., and Fitoussi, C. (2012). Climatically versus Tectonically Forced Erosion in the Alps: Thermochronometric Constraints from the Adamello Complex, Southern Alps, Italy. *Earth Planet. Sci. Lett.* 339-340, 127–138. doi:10.1016/j.epsl.2012.04.051

Rossato, S., Carraro, A., Monegato, G., Mozzi, P., and Tateo, F. (2018). Glacial Dynamics in Pre-Alpine Narrow Valleys during the Last Glacial Maximum Inferred by lowland Fluvial Records (Northeast Italy). *Earth Surf. Dynam.* 6 (3), 809–828. doi:10.5194/esurf-6-809-2018

Sauro, F., Piccini, L., Menichetti, M., Artoni, A., and Migliorini, E. (2012). Lithological and Structural Guidance on Speleogenesis in Spluga Della Preta Cave, Lessini Mountains (Veneto-Italy). *Geogr. Fis. Din. Quat.* 35, 167–176. doi:10.4461/GFDQ.2012.35.15

Sauro, F., Zampieri, D., and Filipponi, M. (2013). Development of a Deep Karst System within a Transpressional Structure of the Dolomites in north-east Italy. *Geomorphology* 184, 51–63. doi:10.1016/j.geomorph.2012.11.014

Schaltegger, U., Nowak, A., Ulianov, A., Fisher, C. M., Gerdes, A., Spikings, R., et al. (2019). Zircon Petrochronology and 40Ar/39Ar Thermochronology of the Adamello Intrusive Suite, N. Italy: Monitoring the Growth and Decay of an Incrementally Assembled Magmatic System. *J. Pet.* 60, 701–722. doi:10.1093/petrology/egz010

Schlunegger, F., and Mosar, J. (2011). The Last Erosional Stage of the Molasse Basin and the Alps. *Int. J. Earth Sci. (Geol Rundsch)* 100, 1147–1162. doi:10.1007/s00531-010-0607-1

Schmid, S. M., Fügenschuh, B., Kissling, E., and Schuster, R. (2004). Tectonic Map and Overall Architecture of the Alpine Orogen. *Eclogae Geol. Helv.* 97, 93–117. doi:10.1007/s00015-004-1113-x

Schoene, B., Schaltegger, U., Brack, P., Latkoczy, C., Stracke, A., and Günther, D. (2012). Rates of Magma Differentiation and Emplacement in a Ballooning Pluton Recorded by U-Pb TIMS-TEA, Adamello Batholith, Italy. *Earth Planet. Sci. Lett.* 355-356, 162–173. doi:10.1016/j.epsl.2012.08.019

Spalla, M., Zucali, M., Salvi, F., Gosso, G., and Gazzola, D. (2003). Tectono-metamorphic map of the Languard-Campo-Serie del Tonale nappes between upper Val Camonica and Valtellina (Central Italian Alps, Austroalpine Domain). *Memorie di Scienze Geologiche* 55, 105–118.

Stalder, N. F., Fellin, M. G., Caracciolo, L., Guillong, M., Winkler, W., Milli, S., et al. (2018). Dispersal Pathways in the Early Messinian Adriatic Foreland and Provenance of the Laga Formation (Central Apennines, Italy). *Sediment. Geology.* 375, 289–308. doi:10.1016/j.sedgeo.2017.09.016

Stefani, C., Fellin, M. G., Zattin, M., Zuffa, G. G., Dalmonte, C., Mancin, N., et al. (2007). Provenance and Paleogeographic Evolution in a Multi-Source Foreland: The Cenozoic Venetian Friulian Basin (NE Italy). *J. Sediment. Res.* 77, 867–887. doi:10.2110/jsr.2007.083

Stipp, M., Stünitz, H., Heilbronner, R., and Schmid, S. M. (2002). The Eastern Tonale Fault Zone: a 'natural Laboratory' for crystal Plastic Deformation of Quartz over a Temperature Range from 250 to 700°C. *J. Struct. Geology.* 24, 1861–1884. doi:10.1016/s0191-8141(02)00035-4

Stock, G. M., Anderson, R. S., and Finkel, R. C. (2005a). Rates of Erosion and Topographic Evolution of the Sierra Nevada, California, Inferred from cosmogenic26Al and10Be Concentrations. *Earth Surf. Process. Landforms* 30, 985–1006. doi:10.1002/esp.1258

Stock, G. M., Granger, D. E., Sasowsky, I. D., Anderson, R. S., and Finkel, R. C. (2005b). Comparison of U-Th, Paleomagnetism, and Cosmogenic Burial Methods for Dating Caves: Implications for Landscape Evolution Studies. *Earth Planet. Sci. Lett.* 236, 388–403. doi:10.1016/j.epsl.2005.04.024

Trevisan, L. (1939). *Il Gruppo di Brenta:(Trentino occidentale)*. Roma: Società Cooperativa Tipografica.

Viola, G., Mancktelow, N. S., and Seward, D. (2001). Late Oligocene-Neogene Evolution of Europe-Adria Collision: New Structural and Geochronological Evidence from the Giudicarie Fault System (Italian Eastern Alps). *Tectonics* 20, 999–1020. doi:10.1029/2001tc900021

Viola, G., Mancktelow, N. S., Seward, D., Meier, A., and Martin, S. (2003). The Pejo Fault System: an Example of Multiple Tectonic Activity in the Italian Eastern Alps. *Geol. Soc. America Bull.* 115, 515–532. doi:10.1130/0016-7606(2003)115<0515:tpfsae>2.0.co;2

Winterberg, S., Picotti, V., and Willett, S. D. (2020). Messinian or Pleistocene valley Incision within the Southern Alps. *Swiss J. Geosciences* 113, 1–14. doi:10.1186/s00015-020-00361-7

Winterberg, S., and Willett, S. D. (2019). Greater Alpine River Network Evolution, Interpretations Based on Novel Drainage Analysis. *Swiss J. Geosci.* 112, 3–22. doi:10.1007/s00015-018-0332-5

Wright, J. S. (2001). Desert" Loess versus "Glacial" Loess: Quartz silt Formation, Source Areas and Sediment Pathways in the Formation of Loess Deposits. *Geomorphology* 36 (3–4), 231–256. doi:10.1016/S0169-555X(00)00060-X

Conflict of Interest: The authors declare that the research was conducted in the absence of any commercial or financial relationships that could be construed as a potential conflict of interest.

frontiers in Earth Science

ORIGINAL RESEARCH
published: 30 June 2021
doi: 10.3389/feart.2021.672229

Changes in Cave Sedimentation Mechanisms During the Late Quaternary: An Example From the Lower Cerovačka Cave, Croatia

Tomislav Kurečić[1], Neven Bočić[2], Lara Wacha[1], Koraljka Bakrač[1], Anita Grizelj[1], Dinko Tresić Pavičić[3], Christopher Lüthgens[4], Andreja Sironić[5], Siniša Radović[6], Loris Redovniković[7] and Markus Fiebig[4]*

[1]Department of Geology, Croatian Geological Survey, Zagreb, Croatia, [2]Department of Geography, Division of Physical Geography, Faculty of Science, University of Zagreb, Zagreb, Croatia, [3]Kaducej d.o.o., Split, Croatia, [4]Institute of Applied Geology, University of Natural Resources and Life Sciences (BOKU), Vienna, Austria, [5]Laboratory for Low-level Radioactivities, Division of Experimental Physics, Ruđer Bošković Institute, Zagreb, Croatia, [6]Institute for Quaternary Palaeontology and Geology, Croatian Academy of Sciences and Arts, Zagreb, Croatia, [7]Department of Applied Geodesy, Faculty of Geodesy, University of Zagreb, Zagreb, Croatia

OPEN ACCESS

Edited by:
Aurel Perşoiu, Romanian Academy, Romania

Reviewed by:
Andrea Zerboni, University of Milan, Italy
Christos Pennos, University of Bergen, Norway

***Correspondence:**
Neven Bočić
nbocic@gmail.com

Specialty section:
This article was submitted to Quaternary Science, Geomorphology and Paleoenvironment, a section of the journal Frontiers in Earth Science

Received: 25 February 2021
Accepted: 15 June 2021
Published: 30 June 2021

Citation:
Kurečić T, Bočić N, Wacha L, Bakrač K, Grizelj A, Tresić Pavičić D, Lüthgens C, Sironić A, Radović S, Redovniković L and Fiebig M (2021) Changes in Cave Sedimentation Mechanisms During the Late Quaternary: An Example From the Lower Cerovačka Cave, Croatia. Front. Earth Sci. 9:672229. doi: 10.3389/feart.2021.672229

During archeological excavations in the Lower Cerovačka Cave (Mt. Velebit, Croatia), the test trench penetrated to a depth of 1.8 m. An undisturbed sequence of sediments was exposed. Considering that caves represent highly efficient sediment traps it was possible to recognize changes in the depositional mechanisms during the Pleistocene–Holocene period. Using the multiproxy approach, the mineralogical, petrographic, and biostratigraphic characterization of the cave sediments was performed. Facies analysis revealed several stages in the development of the clastic filling of cave channels. Allochthonous origin of the sediment was assumed. Sedimentation took place under various conditions from pronounced cold and dry climate during Pleistocene stages in the base of the profile, to humid periods with anthropogenic influence during the Holocene at the very top of the profile. Although traditionally these sediments were believed to be of a Pleistocene age, here for the first time a stratigraphic calibration of the profile has been performed based on luminescence dating of detrital cave sediments and radiometric dating of speleothems.

Keywords: cave sediments, facies analysis, provenance, numerical dating, palynofacies, *Ursus spelaeus*, Dinaric karst

INTRODUCTION

Situated in the locus typicus of the Dinaric karst (Zupan Hajna, 2019) within the NE slopes of Mt. Crnopac (SE part of the Velebit massif in Croatia) (**Figures 1A,B**), the Cerovačke Caves represent a network of subhorizontal hydrologically inactive cave channels (**Figures 2A,B**) in today's vadose zone. There are three Cerovačke caves, namely Lower, Middle and Upper Cerovačka Cave (LCC, MCC and UCC). LCC was discovered in 1913 (Malez, 1956, 1958) during the construction of the railroad. The caves have been the focus of research for many speleologists and other geoscientists ever since. Because of the scientific interest, as well as exploitation interest related to the geo-heritage and tourist potential of the cave, intensive cave surveying was conducted, combined with paleontological and archaeological excavations. That research gave insight into the rich cave history, as evidenced by

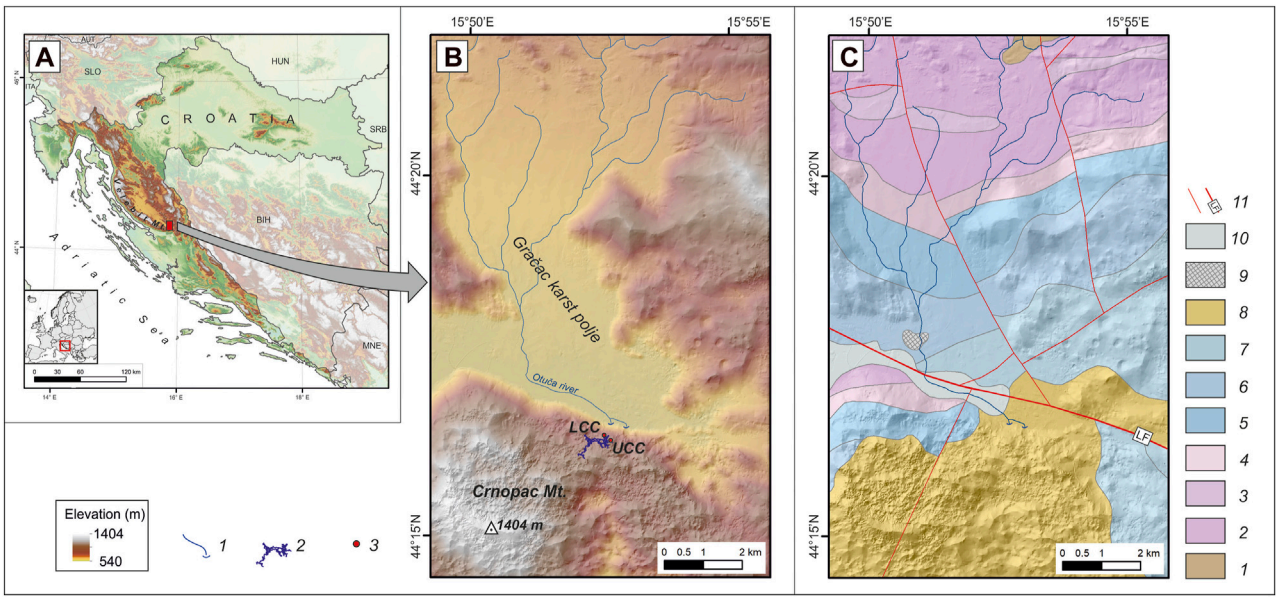

FIGURE 1 | (A) Geographic position of the Cerovačke Caves, **(B)** Elevation map of the surrounding area, legend: 1—surface streams with ponors, 2—cave chanells of Lower and Upper Cerovačka Cave, 3—entrance positions of Lower (LCC) and Upper (UCC) Cerovačka Cave, **(C)** Geological map of the surrounding area, sources: Geological map of Croatia 1:300.000 (Croatian Geological Survey, 2009), Basic geological map of Croatia 1:100.000, sheet Obrovac (Ivanović et al., 1973), Basic geological map of Croatia 1:100.000, sheet Udbina (Šušnjar et al., 1973), legend: 1—clastic rocks (C, P), 2—carbonate rocks (T_2), 3—clastic-pyroclastic rocks (T_3), 4—dolomites (T_3), 5—limestones and dolomites (J_1), 6—thick layered limestones and dolomites (J_2), 7—limestones and dolomites (J_3), 8—carbonate (Jelar) breccia (Pg, Ng), 9—alluvial deposits (Q), 10—Terra Rossa (Q), 11—faults, LF—Lika fault.

findings of large Pleistocene fossil mammals (Malez, 1960a; 1965a). Consequently, excavation campaigns resulted in the first available data of cave channel sediment infill and provenance of cave detrital sediments (e.g., Ivanović et al., 1976). First interpretations suggest that these sediments represent products of host rock weathering, deposited after the caves lost their ponor (swallow hole) function during the uplift of the mountain and lowering of the Gračac karst polje level (Malez, 1965b).

In recent years, the interest in revitalizing the tourist potential of the LCC intensified. Following requirements prescribed by the Conservation Department in Zadar (Croatia), new archaeological research in the LCC was conducted during 2019. Excavations included the area of the cave with archaeological potential, endangered by construction works along the new visitor pathway. The main archaeological excavation area was placed along the route of the new pathway, spanning 120 m from entrance. Three distinctive phases of human occupation were determined within the excavation sites of the LCC, above the geological record (Tresić Pavičić, 2020). The latest phase is attributed to the modern period, from the discovery of the cave in 1913 until today, and includes various features such as existing pathway, trenches for electrical cables and archaeological and geological test trenches from previous excavations. The medieval phase within the cave was represented by a small number of finds dated to the 13th century (Tresić Pavičić, 2020) when the cave was used sporadically, probably as a shelter. The earliest and archeologically most significant phase of human occupation represented in the excavated area, corresponds to features and finds from the Late Bronze Age period which in the area of Lika roughly corresponds to the period from the 14th to 10th century BC (Blečić-Kavur, 2014; Bakarić, 2017). The data collected suggest that the cave was used for food storage and as a temporary dwelling in specific circumstances such as extreme weather conditions during the Late Bronze Age. The archaeological remains are numerous and well documented. However, there has been a significant lack of any new geological research within the cave since the seventies.

The sediment profile (DC-SP) investigated within our research is situated within a test trench placed 120 m from the cave entrance at the end of archaeological excavation area (**Figure 2B**). Since the test trench penetrated to a depth of 1.8 m, an undisturbed sequence of sediments was exposed. At the site, the Late Bronze Age and Modern Period features were found within the investigated profile (**Figure 3A**). However, the majority of the profile represents geological strata of unknown origin and age. The aim of this study, therefore, is to determine the provenance of sediments, and the type and degree of changes in the environment during the time of deposition of clastic cave sediments within the main channel of the LCC. A multiproxy research approach was applied to the sediment including detailed sedimentological and mineralogical analysis. The lithofacies analysis of the detrital cave sediments was used to answer questions regarding the deposition mechanisms in specific conditions during the Pleistocene. Mineralogical analyzes are applied to get insight into the provenance of the cave sediments. Macropaleontological analysis was performed for a detailed determination of the excavated fossil bones as well as

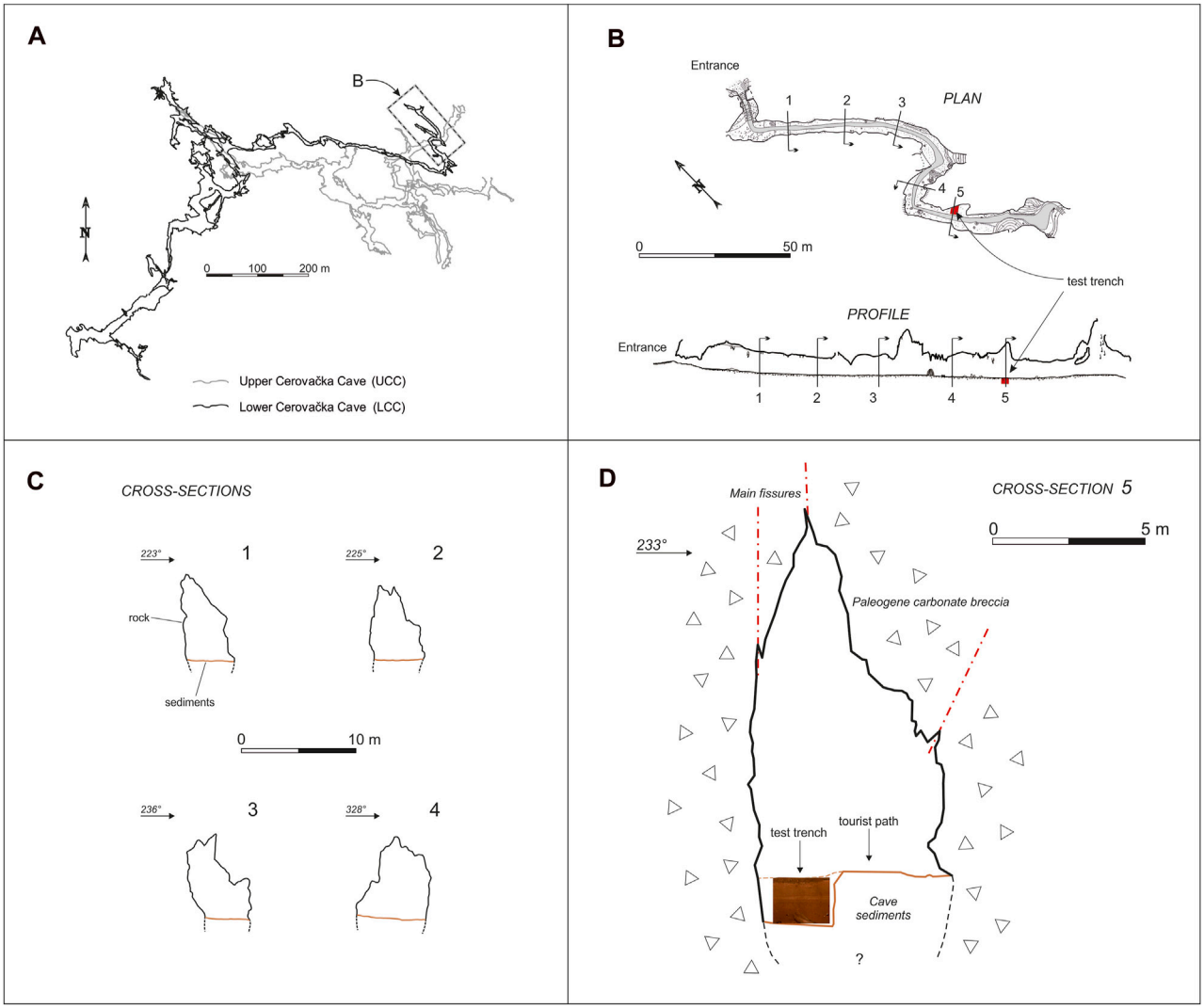

FIGURE 2 | (A) Simplified plan view of the Upper and Lower Cerovačka Cave, **(B)** plan view of the entrance part of the Lower Cerovačka Cave with the marked position of the researched test trench (cave survey according Bočić et al., 2016), **(C)** selected cross-sections (1–4), and **(D)** cross-section of the cave channel at the location of the test trench.

palynological analysis to determine the palynofacies. To establish the time frame and stratigraphic calibration of the investigated profile, luminescence dating of detrital cave sediments was performed and supported with radiometric dating of speleothems found within the sediment sequence. Furthermore, a comparison with available data on similar (spatio-temporal) sedimentary profiles will be given.

GEOLOGICAL AND GEOMORPHOLOGICAL SETTING

Velebit Mt. is a part of the Dinaric mountain system and the longest mountain range in Croatia (**Figure 1A**). Cerovačke Caves are located on the northern slope of its extreme southeastern part, Crnopac (**Figure 1B**). To the north of Crnopac lies the Gračac karst polje. In the structural-geological sense, the area of the Gračac polje forms an anticline with Paleozoic clastites in their core. Around them Mesozoic sediments spread periclinally (Sokač et al., 1976; Šušnjar et al., 1973; Ivanović et al., 1973, 1976). Triassic dolomites and clastites and Jurassic dolomites predominate at the surface. The youngest are Quaternary Terra Rossa and alluvial deposits recorded at the bottom of the polje (see **Figure 1C** for details). This lithology causes the bottom of the Gračac polje to act as a hydrogeological barrier. A surface drainage network has developed on its surface with a general drainage direction to the south. The main stream is the Otuča River, which forms a ponor zone in the southern, deepest part of the field (**Figures 1B,C**). The Otuča drainage system superficially drains an area of about 90 km^2 as well as the underground karst water that converges to the polje from the surrounding hills. The lowest point of the field is at an elevation of 544 m. South of the

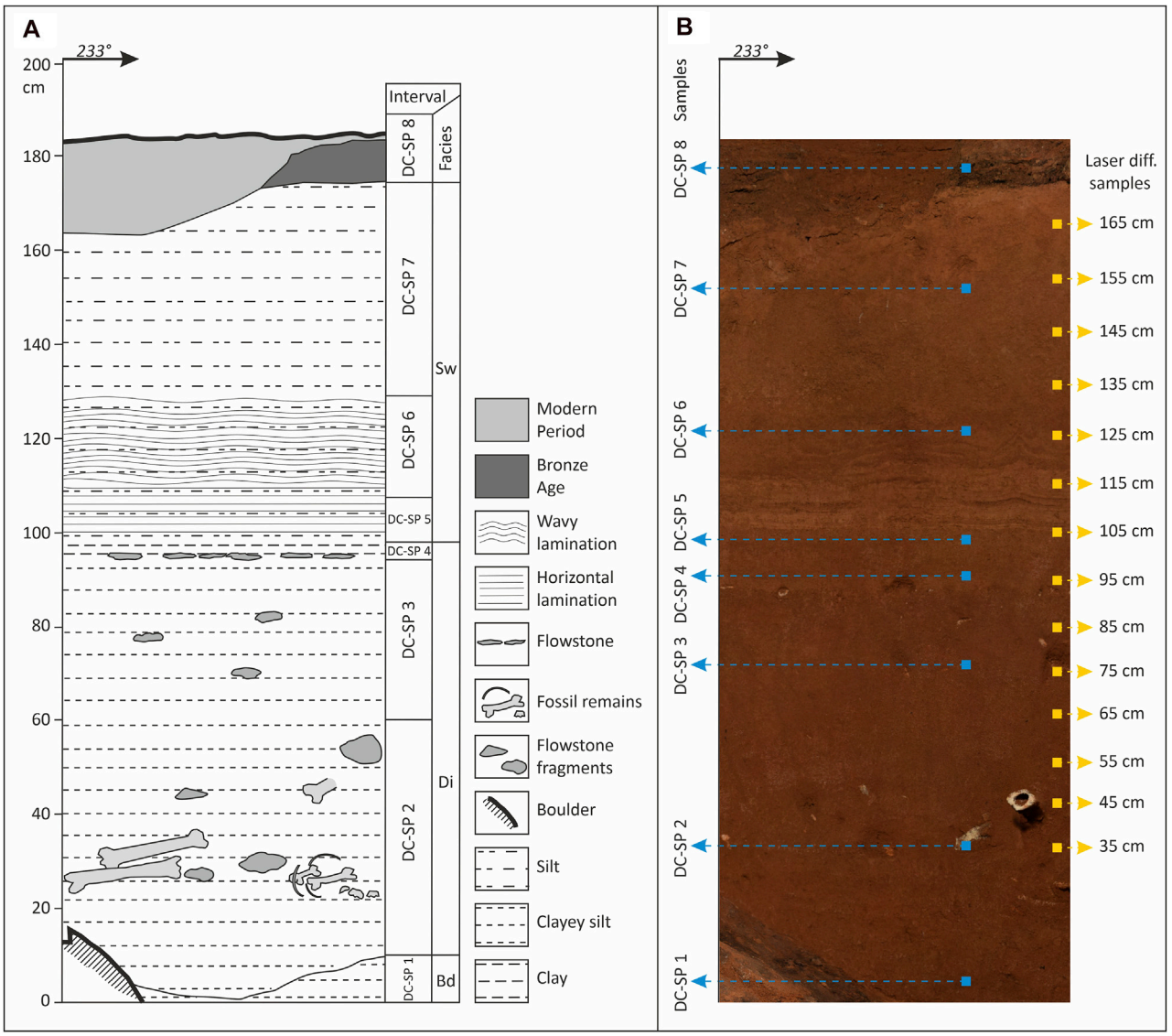

FIGURE 3 | Sedimentary log and photo of the investigated profile DC-SP within the archaeological excavation site in the Lower Cerovačka Cave **(A)** Sedimentary log with indicated main structural and lithological features, **(B)** photo of profile and indicated position of sampling spots (on the left side—bulk analysis of described intervals; on the right side—high-resolution granulometric analyses).

Gračac polje rises the Crnopac massif (1,404 m), separated by the Lika fault (**Figures 1B,C**). Crnopac is a part of the main ridge and tectonic unit Velebit. Its structure is dominated by Jurassic and Cretaceous carbonate rocks separated by paleo-relief boundaries from overlaying Paleogene carbonate breccias (Ivanović et al., 1973, 1976) known as Jelar breccia (Bahun, 1963, 1974). Areas built up of Jelar breccias like the Northern Velebit are intensively karstified, with a large number of dolines and deep caves, including Lukina jama, the deepest cave in the Dinarides (Bočić et al., 2019). Similar to the Northern Velebit, the Crnopac area is also extremely karstified. The area is characterized by large, steep, and numerous dolines whose maximum density reaches 93 dolines per km^2 (Marković et al., 2016). More than 200 caves have been explored in the area, the largest of which is the Crnopac Cave System (CCS) (Barišić, 2017), which is the longest cave in the Dinarides and 67th longest cave in the world, measuring 53.3 km in length (Caver Bob, 2021; Croatian Mountaineering Association, 2021).

Sinking waters from the Gračac polje flow underground through the Crnopac massif toward the south, to the valleys of the Krupa and Zrmanja rivers. These allogenic flows influence the formation of cave systems. Due to the uplifting of the Crnopac massif cave channels form at several levels. The speleogenesis of the Crnopac massif is also influenced by autogenous water, which has a vertical circulation through a deep unsaturated zone (Kuhta and Stroj, 2005).

This area has the climate type Cfb (temperate humid with warm summer) (Filipčić, 1998). Basic climatological

characteristics of the area are visible through the basic data of the Gračac meteorological station for the period 2004–2014: (i) the average annual air temperature is 9.9°C and the mean annual precipitation is 1,960 mm and (ii) the warmest month is July (19.9°C), but the highest mean monthly precipitation is in December (283 mm) (Czuppon et al., 2018).

All three known caves at the investigated site (UCC 4,035 m, LCC 4,048 m, MCC, 390 m long) are located in the ponor (input) zone of the Crnopac karst system above the level of the karst polje, i.e., the currently active ponors. All three caves are formed in Paleogene carbonate (Jelar) breccias (**Figures 1B,C**).

The LCC is a predominantly horizontal branchwork cave (sensu Palmer, 1991). The entrance altitude is 630 m, i.e., about 80 m higher than the active ponors at the edge of the karst polje. The cave can be morphologically divided into two parts. In the northern part, the channels run mainly in NW-SE direction, following the main fold and thrust belt direction of the External Dinarides (Tari, 2002; Schmid et al., 2008; Korbar, 2009). Here the channels are relatively narrower and rarely exceed 5 m. In the southern part of the cave, which extends toward the SW, the channels are much wider and often exceed 10 m in width (**Figure 2A**). The formation of the cave is most likely related to the function of the karst conduit of sinking waters from the Gračac karst polje. The investigated test trench is located in the main channel at a distance of about 120 m from the entrance, measures about 3 × 3 m in plan and is 1.8 m deep (**Figure 2B**).

MATERIALS AND METHODS

The cave survey was the starting point to obtain data on the morphology of the cave. The part of the cave open for visitors (about 700 m long) was surveyed at a scale of 1: 200, the rest of the cave at a scale of 1: 500. The survey was made in the UIS-5-4-BC mapping grade (Häuselmann, 2011). A standard procedure was used to determine the relative position of survey points by measuring the distance, azimuth and inclination angle. The Leica hand laser distometer and Suunto clino-compas were used. The starting point outside the cave was stabilized with a GNSS receiver. Additional data on the morphology of the investigated part of the cave were obtained by laser scanning. The first laser scanning of LCC was performed in the period from January 15 to 17, 2016. At that time, two geodetic bases were established, one in front of and the second inside of the cave. The Faro Focus3D X 330 laser scanner, the Topcon HiPer SR GNSS receiver and two total stations (TOPCON GTS 105N and Cygnus 2LS) were used for the geodetic survey of the LCC. The laser scanning was performed again on June 13th and 14th, 2019. but this time strong lighting was used and panoramic 360° photographs were collected during the scan to obtain a colored point cloud. Point clouds obtained by the photogrammetric method during archaeological research are connected to the new colored point cloud and presented within this paper as 3D supplement (**Supplementary Material S1**). Leica Cyclone 3DR software was used to visualize the obtained data and to create a characteristic profile.

Archaeological excavations were carried out with hand tools following stratigraphic principles, and standard archaeological field records were kept. A detailed catalog of methods and archaeological findings is given by Tresić Pavičić and Burmaz (2020) and Tresić Pavičić (2020). Sedimentological field data and sampling were acquired within the archaeological test trench.

For a detailed sedimentological analysis individual layers and lithofacies units were recognized below the archaeological layer (**Figure 3A**). The nomenclature for the established lithofacies units was based on Bosch and White (2004). All layers were sampled (**Figure 3B**). The grain-size of the sediment was determined on five bulk samples from each observed lithological unit using the areometric method (**Figure 3B**; Samples DC-SP 2, 3, 5, 6, 7) while high-resolution grain-size (in 10 cm resolution) was determined using the laser diffraction method. A total of 14 samples were analyzed with a Shimadzu Laser Diffraction Particle Size Analyzer SALD-2300 to determine the detailed dynamics of vertical changes in the particle size distribution (**Figure 3B**; Samples DC-SP 35–165 cm). 0.1 g of a dry representative sample was isolated for the analysis. The samples were treated with a 4% solution of tetra-sodium diphosphate decahydrate ($Na_4P_2O_7{\cdot}10H_2O$) and deionized water against coagulation and dispersed for at least 6 h on a shaker. Each measurement was repeated five times and an average value was used for the grain-size distribution. The sediment was classified according to Trefethen (1950).

To get insight in the composition of the sediment and determine the provenance of the material, the modal (heavy and light minerals) and XRPD analyses were performed. For the separation of heavy and light minerals, the 0.09–0.16 mm fraction of five samples was used (**Figure 3B**; Samples DC-SP 2, 3, 5, 6, 7). Samples were treated with 10% HCl to remove the carbonates, and washed with H_20 in an ultrasonic bath. The grains were separated using sodium polytungstate (ρ = 2.8 g cm^{-3}). Thin slides were prepared from the separated material, and the composition was determined by counting up to 300 grains per sample using a Leitz Orthoplan polarizing microscope (Mange and Maurer, 1992). Typical mineral groups were isolated and their characteristics and relative proportions in the samples were described. Due to the low content of transparent heavy minerals (THM) within the heavy mineral fraction (HMF), real percentages and statistical analysis are not shown.

The mineral composition of seven cave sediment samples and a bone fragment were determined by X-ray powder diffraction (XRPD) (**Figure 3B**; Samples DC-SP 1-bone, 1-7-sediment). The samples were grinded, sieved through a 0.063 mm sieve and the <2 μm fraction was separated using the centrifuge method (Krumm, 1994). Oriented mounts from <2 μm fraction were prepared. Oriented samples were treated with following treatments: a) air drying, b) saturation with K^+ c) saturation with Mg^{2+} d) Mg^{2+} saturation and ethylene-glycol solvation, e) K^+ saturation and ethylene-glycol solvation, f) Mg^{2+} saturation and glycerol solvation, g) K^+ saturation and DMSO solvation, h) heating more than ½ hour to 400 and 550°C, i) treating with HCl (18%, 24 h) (Weaver, 1967; Starkey et al., 1984; Moore and Reynolds, 1997) and XRD patterns were recorded. The measurements were performed using the Philips vertical

goniometer (type X`Pert) equipped with a Cu tube under the following experimental conditions: 45 kV, 40 mA, PW 3018/00 PIXcel detector, primary beam divergence 1/4°, continuous scan (step 0.02°2θ/s). The interpretation of XRPD was obtained using HIGH SCORE PLUS (2016) calculation and PDF-4 / Minerals (2020) databases. The semi-quantitative analysis was performed using the procedure described by Schultz (1964).

Palynological analyses were carried out on four samples collected from the lower and upper part of the section (**Figure 3B**; Samples DC-SP 1, 2, 7, 8). Standard palynological processing techniques were used to extract the organic matter (e.g., Moore et al., 1991; Wood et al., 1996). The samples were treated with 4% solution of tetra-sodium diphosphate decahydrate ($Na_4P_2O_7{\cdot}10H_2O$) against coagulation, cold HCl (15%) and HF (40%), removing carbonates and silica, respectively. Heavy liquid ($ZnCl_2$, ρ > 2.1 kg/l) was used to separate the organic matter from the undissolved inorganic components. The organic residue was sieved through a 10 µm mesh. For palynofacies analysis slides were mounted in glycerin and, for palynomorphs analysis in silicon oil. Microscopic analyses were performed using the Olympus BH-2 and Leica DM2500 microscope (Croatian geological survey). Photomicrographs were taken using an AmScopeTM camera adapter connected to the AmScope v.3.7 camera software and Leica MC190 HD camera connected to the Leica LAS EZ software. The palynofacies analyses were performed according to the classifications proposed by Tyson (1995) and Sebag et al. (2006). Three categories of organic matter (OM) were used: (1) phytoclasts: opaque phytoclasts (OP) and ligno-cellulosic debris (LcD), which can be preserved as cuticles and membranes (CM), transparent (TLC), altered (ALC), amorphous (AP) or gelified particles (GP), (2) Amorphous organic matter (AOM) and (3) palynomorphs. Minimum 500 particles of OM were counted per sample. Results were plotted in OM percentage abundance diagram and diagram presenting the relation between preserved/transformed phytoclasts and AOM to characterize the palaeoenvironment.

Macropaleontological analyses were performed on faunal remains collected during the research. The material was dry sieved on site using a mesh size of 6 × 6 mm, bagged and named. In the laboratory the faunal remains were washed and dried and a detailed palaeontological analysis was conducted at the Institute for Quaternary Palaeontology and Geology in Zagreb. During the anatomical and taxonomical analysis, the fossil remains were compared with the fossil and recent comparative collection stored at the Institute. This was followed by a detailed taphonomic study. All bone and teeth fragments were carefully examined with a hand lens (×10 magnification) looking for any bone modifications that could indicate butchery, gnawing, and other taphonomic traces as direct indicators of different agencies responsible for the accumulation and preservation of the skeletal material. Due to a relatively modest number of identified remains (873), taxonomic representation and element frequency were quantified using NISP (Number of Identified Specimens; Lyman, 1994).

The luminescence dating method was applied on two cave sediment samples to establish a chronological framework of the deposits (**Figure 3B**; Samples DC-SP 3 and 7). The samples were taken using stainless steel cylinders driven into the freshly cleaned sediment and sealed light tight after sampling. Additional samples for radionuclide determination were taken in the direct surroundings of the luminescence samples. During sample preparation, the ends of the cores were removed, because of potential light exposure during sampling. Since detrital cave sediments as water-lain sediments are known to be prone to incomplete bleaching (insufficient light exposure of the sediment during transport and before burial), the obtained ages are often overestimated. In luminescence dating, reliable methods for the detection and correction of the effects of incomplete bleaching are available. However, a basic restriction is that measurements have to be conducted on subsamples (aliquots) containing only small numbers of grains, ideally down to the single grain level. For that reason, single quartz and potassium-rich feldspar grains (usually between 63–300 µm) were extracted from the collected samples. Sample preparation and measurements were conducted at the Vienna Laboratory for Luminescence dating (VLL) using standard methods (Lüthgens et al., 2017; Rades et al., 2018). After sample preparation, no significant amount of coarse grains could be extracted from sample DC-SP 7 (VLL-0496-L), while a minimal number amount of coarse grains could be retrieved from sample DC-SP 3 (VLL-0495-L). All subsequent analyses could therefore only be conducted for the latter sample. In contrast to potassium-rich feldspar, it is known that only a small fraction of quartz grains (usually <10%, but frequently also down to only few percent) does emit a luminescence signal suitable for dating (e.g., Lüthgens et al., 2011). Given the very small amount of grains available for measurements and previous results showing rather low quartz luminescence sensitivity in the broader area (e.g., Zhang et al., 2018), single grain measurements on potassium-rich feldspar as the only dosimeter was the method of choice in this study.

A single grain, post infrared, infrared stimulated single aliquot regenerative dose protocol (SG $pIRIR_{225}$ SAR, e.g., Reimann et al., 2012; Garcia et al., 2019 but modified to include the pIRIR225 signal) was applied for the determination of the equivalent dose. Measurements were conducted at the VLL on a RISØ DA-20 luminescence reader system (Bøtter-Jensen et al., 2000, 2003) equipped with an infrared laser (830 nm) for stimulation of the single-grain luminescence signals, which were detected through a LOT/Oriel D410/30 interference filter. For laboratory dosing, the system is equipped with a $^{90}Sr/^{90}Y$ beta source delivering a dose of about 0.1 Gy/s. Dose recovery experiments were conducted for both luminescence signals measured in the $pIRIR_{225}$ dose protocol [stimulated at 50°C (IR_{50}) and at 225°C ($pIRIR_{225}$)]. The results showed agreement with unity within the error (rejection criteria: recycling/recuperation in percent of the natural signal/test dose error = 30/30/10%), proving the suitability of the protocol. Whenever using feldspar as a dosimeter, the effects of anomalous fading (athermal signal loss over time, Wintle 1973) must be considered. Fading experiments were conducted using the approach of Auclair et al. (2003) but modified to also include the $pIRIR_{225}$ signal.

Naturally occurring radionuclides contributing to the doserate (decay chains of ^{238}U and ^{232}Th, and ^{40}K) were measured using low-level, high-resolution gamma spectrometry on a Baltic Scientific Instruments high purity Germanium (HPGe) p-type detector (~52% efficiency) after storage of the sample of more than 4 weeks. The sample were found to be in secondary secular equilibrium. The overall doserates and age calculations were conducted using the software ADELE (Kulig, 2005).

Radiocarbon dating method was applied on a speleothem and bone found in the sediment succession. Radiocarbon dating was performed by accelerator mass spectrometry (AMS). Samples were prepared into graphite targets at the Ruđer Bošković Institute (RBI, Croatia). The bone sample of *Ursus spelaeus* (DC-SP-2, LCC, sample ID number Z-7351) was precleaned using acid-base-acid wash and collagen extraction (Longin 1971). However, the amount of collagen in the bone was below 0.1%, which indicated that the carbon in the collagen was too degraded for radiocarbon dating (Marom et al., 2013). The speleothem sample (DC-SP-4/1, LCC, ID number Z-7352) was cut, and about 200 mg of powder were scraped off the surface. The powder was hydrolyzed to CO_2 in a vacuum rig using 4% HCl. An aliquot of the obtained CO_2 was sealed in a pyrex tube for ^{13}C composition analysis on the isotope ratio mass spectrometer (IRMS). Another aliquot of the CO_2 in reaction with zinc was reduced to graphite for radiocarbon AMS analysis (Krajcar Bronić et al., 2010; Sironić et al., 2013). The sample $^{14}C/^{13}C$ ratio was measured on a 0.5 MeV AMS and $^{13}C/^{13}C$ ratio ($\delta^{13}C$) on isotope ratio mass spectrometer (IRMS), at the Center for Applied Isotope Studies, University of Georgia (CAIS, United States). $\delta^{13}C$ values are expressed in per mil relative to VPDB. Measured $^{14}C/^{13}C$ ratios were corrected for isotope fractionation using the corresponding $\delta^{13}C$ values measured by IRMS and normalized to –25‰ VPDB and presented as $F^{14}C$ and the ^{14}C age before present (BP) (Stuiver and Polach, 1977; Reimer et al., 2004). Radiocarbon age was rounded of digits in accordance with the recommendations given by Stuiver and Polach (1977). The radiocarbon age was calibrated using the OxCal v 4.2.4 software (Bronk Ramsey 2009, 2016) and IntCal20 calibration curves (Reimer et al., 2020). Speleothem radiocarbon date was presented without reservoir correction (dead carbon fraction, $DCF = 0$), with DCF of 15% which is generally used for Dinaric secondary carbonates (Horvatinčić et al., 2003), and also with DCF of 12.5% determined at the Modrič cave near the LCC location (Rudzka et al., 2012), since DCF can vary with location (Srdoč et al., 1986; Krajcar Bronić et al., 1986, 1992; Sironić et al., 2020) and time (Hua et al., 2017; Bajo et al., 2017; Therre et al., 2020). Reservoir corrections were reported according to Soulet et al. (2016):

$$DCF = \left(1 - F^{14}R_{s-atm}\right) * 100\%;$$
$$R_{S-atm} = -8033 * \mathrm{In}\left(F^{14}R_{s-atm}\right)$$

where $F^{14}R_{s\text{-}atm}$ is ratio of measured fraction ^{14}C in speleothem and fraction ^{14}C in contemporary atmosphere and $R_{S\text{-}atm}$ is reservoir offset for correction to reservoir effect (reservoir age). Reservoir age is given without rounding.

RESULTS

Cave Morphology

The entrance part of the LCC consists of a main channel and several smaller branches. Morphologically, the channel consists of three parts. The first part, 70 m long, is straight and has a Dinaric orientation (NW–SE). This is followed by two successive bends and a third straight section about 50 m long. The entire channel runs almost parallel to the hill slope at the surface. The present cave entrance is a 1.6 × 1 m door. The entrance was naturally probably much lower but it was artificially slightly modified. The main channel is 6–8 m high, although in some places it is much higher (over 15 m). The width of the channel is generally in the range of 4–7 m. The area cross-sections (**Figure 2C**) are generally 20–35 m^2 but may be larger in some places, especially where the ceiling is higher due to some fractures. The depth of the allogenic sediment in the bottom of the cave channel is not known, so the full dimensions and shapes of the cross sections are not completely known. Three sets of fractures were recorded within the channel, which significantly influence its shape and formation. The first part of the channel is dominated by a set of fractures with Dinaric orientation (~130°–310°), the middle part by a set of fractures with meridional orientation (~0°–180°), and the last part is the most influential by the set of fractures with orientation of ~100°–280°. The host-rock is not stratified, so there is no visible influence of bedding planes on the cave morphology. Numerous speleogens were recorded behind the channel walls: scallops, elongated domes, solution pockets, pendants, wall rills, etc. Flowstones appear only about 80 m from the entrance, mostly in the form of wide stalagmites and wall flowstones. Due to low temperatures in winter and occurrence of ice on the cave walls, the cryofracture weathering of flowstones is pronounced in this part. The floor in the almost entire length of the channel is built of sediment and in the upper part it is mostly covered by archaeological layer. At the site of the test trench, the channel is slightly larger. It is 12 m high, 6.6 m wide, and the cross-sectional area is about 45 m^2. This is most likely caused by the intersection of the two sets of fractures (**Figure 2D**, **Supplementary Material S1**). The genesis of the whole cave, including this entrance channel, is related to the denudation effect of the sinking waters of the Gračac karst polje. However, its mechanism is not yet completely clear. Morphological traces (cross-sectional shapes and speleogens indicating saturated conditions) of speleogenesis indicate that the channel was formed mainly under saturated conditions. Erosion traces of water flow in the vadose zone were not recorded because, if present, they are located in the lower parts of the channel covered with sediment.

Sediment Characteristics and Facies

Within the cave sediment infill found in the passage of the LCC, eight intervals were recognized and described. Based on similar lithological and structural features they were grouped into three lithofacies units and the top archaeological layer. A detailed description of the profile and the individual lithofacies units is given in **Table 1** and **Figure 3A**. According to the results of particle size analysis by the sedimentation method (shown by cumulative

TABLE 1 | Sedimentological field description of DC-SP profile in the Lower Cerovačka Cave with described intervals and lithofacies.

Sediment intervals within the profile DC-SP (cm) Lithology—short field description	Lithofacies described within the profile DC-SP
DC-SP 1 (0–10) Centimeter to decimeter blocks of limestones and broken speleothems with clayey to silty matrix	**Breakdown facies (Bd)**—within the test trench it appears in two stratigraphic horizons which are laterally interrupted. The lower boundary is not visible within the profile DC-SP. Laterally within the test trench, when visible, it is sharp and uneven. Bd facies is built of very poorly sorted angular clasts. Clasts vary in diameter from centimeter to decimeter blocks of limestones and broken speleothems with the chaotic clast supported arrangement (**Figures 1A**, **3A**). Clasts are often colored with black coatings (black coating can be seen also on the flowstone on today's surface of the cave—black coated speleothems). Matrix is clayey to silty. The Bd facies is best visible on the western and southern vertical surfaces of the excavation site, while on the eastern side it is completely absent. The upper boundary of the Bd facies is sharp and uneven. The thickness of the Bd deposits is highly variable laterally. Based on the archaeological photo documentation and field description, the maximum thickness of Bd facies reaches up to 50 cm
DC-SP 2 (10–60) clayey silt to silty clay (carbonate-free sediment) with fragments of speleothems. Numerous findings of well-preserved bones and teeth, belonging to a large vertebrate (27 cm from the bottom of the profile) **DC-SP 3 (60–95)** clayey silt, probably contains a smaller amount of the sandy component (carbonate-free sediment). Fragments of speleothems are visible in places **DC-SP 4 (95–98)** Horizontally oriented speleothem fragments - laterally discontinuous layer covered with a thin layer (3 cm) of light brown clay that disappears laterally	**Diamicton facies (Di)**—represents the filling of a depression formed on the upper surface of the Bd facies, as can be seen, form the disconformity between Bd and Di facies (**Figures 3A**, **11A**). The lower boundary of the facies is partly unclear. The impression is that the sediments of the Di facies in the transition zone intertwine with underlying Bd facies. The same sediments which built the majority of the Di facies also built a matrix of the Bd facies. Di facies is built of clayey silt with no visible gradation through the vertical profile (**Figures 4A,B**). Although on the described profile these facies appear massive, laterally, unevenly scattered speleothem (seem to be collapsed from the ceiling into the clastic sediment) and limestone fragments can be observed (**Figure 3A**) resulting in unsorted or poorly sorted sediment. There are no clearly arranged sedimentary textures, the larger clasts appear to "float" in the clayey silt. Numerous osteological remains of large vertebrates can be found on this horizon (**Figures 3A**,**B**, **11A,D**). An unnatural position of the bones is visible on the excavated part of the skeleton. This can be the result of taphonomic processes, but also a sign of re-deposition of the skeleton. The upper boundary of the Di facies represents the lateral continuation of the upper boundary of the Bd facies. It is marked with a thin dashed horizontal zone with fragments of speleothems (**Figures 3A**, **11C**) (platy habitus, perhaps a flowstone deposited on the underlying sediment)
DC-SP 5 (98–108) clayey silt (carbonate-free sediment) **DC-SP 6 (108–130)** laminated clayey to sandy silt with intercalations of mm laminae and thin layers (carbonate-free sediment) **DC-SP 7 (130–170)** Homogeneous clayey-silt to silty-clay sediment (carbonate-free sediment)	**Slackwater facies (Sw)—Facies of grayish-yellow laminated silt**: it is visible on all sides of the test trench. The lower boundary of the Sw facies is sharp and clearly marked. At the bottom, 10 cm of homogeneous silt sharply turns into an interval of horizontally laminated sediment (mm laminae) (**Figures 3A,B**). Lamination is marked by vertical alterations of the silty laminae and silty-sandy laminae. Occasionally thin layers occurred (up to 1 cm). The thickness of the laminated interval varies laterally - the laminated interval is thinnest at about 1 m from the side of the cave wall with laminae and layers dipping toward the middle of the cave channel. Therefore, lamination partly follows the inherited morphology in the underlaying homogeneous silt and it showing a channel-like form with a maximum height of up to 10 cm, but erosional discordance has not been observed. Laminae follow the shape of the "channel". Toward the top of the profile, there is a transition toward the zone with wavy lamination (probably a post-sedimentary deformation of the sediment—convolution). Small cracks with vertical displacement between layers were also observed (micro faults). The increase in the amount of sand in the laminated horizon is visible from the particle size distribution curves (samples DC-SP 105 to DC-SP 135, **Figure 4B**). The upper 40 cm of the Sw facies represent silty massive sediment with a decreased amount of sand (**Figures 4B**, **11B**) and show a finning upwards trend. The upper boundary is marked with uneven and sharp disconformity to the late Bronze age and Modern period archaeological strata (**Figure 11A**)
DC-SP 8 (170–195) archaeological strata with pottery fragments. Iapodes, late Bronze age	

granulometric curves, **Figure 4A**) it can be seen that all described intervals consist of clayey silt to silt with a small amount of very fine sand particles (<9% of sand). According to Trask's sorting coefficient (S_0), all samples show poor to very poor sorting (1.802–3.067), while the asymmetry coefficient (Sk < 1) shows that grains smaller than the median (average Md value is 0.0154) predominate in the samples. Samples DC-SP 2, 3 and 5 are classified as very poorly sorted clayey silt, while samples DC-SP 6 and 7 are classified as poorly sorted silt. Furthermore, the results of the high-resolution particle size analysis using the laser diffractometer show a decrease in the amount of the clay-sized fraction from bottom to top of the section (**Figure 4B**), the trend

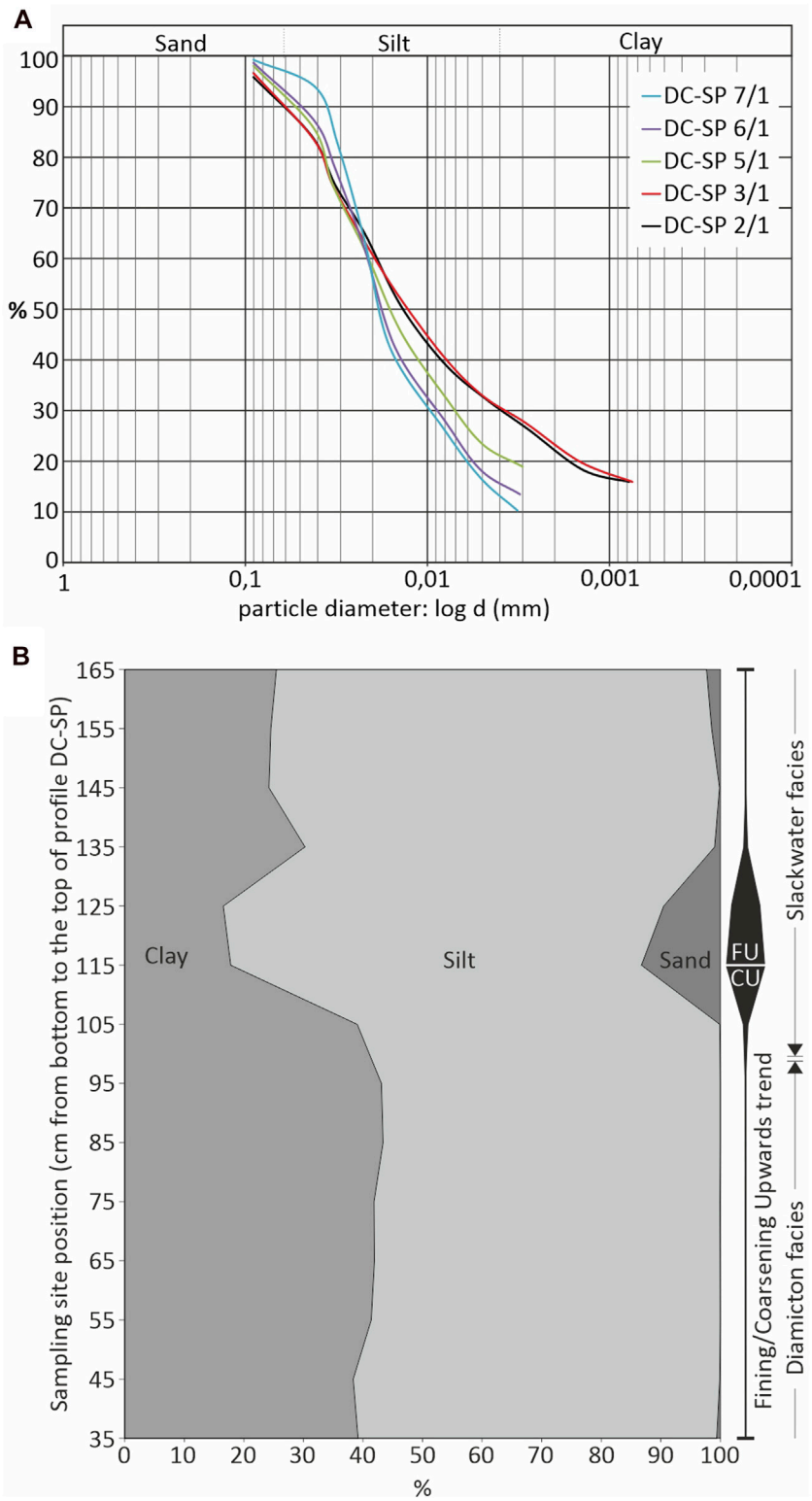

FIGURE 4 | Granulometric composition of samples from the profile DC-SP. **(A)** Granulometric analysis by sedimentation method: cumulative granulometric curves, **(B)** distribution curves of individual fractions (clay, silt, and sand) through the investigated profile.

TABLE 2 | Mineral composition of silty cave sediment from profile DC-SP in the Lower Cerovačka Cave.

Light mineral fraction composition (fraction 0.09–0.16 mm) shown in %										
Sample	**Quartz (monocrystalline)**	**Feldspars (kfs+Pl)**			**Lithic particles (chert and other)**				**Muscovite**	
DC-SP 2	92	2			6					
DC-SP 3	92	3			5				+	
DC-SP 5	88	8			4					
DC-SP 6	87	9			4					
DC-SP 7	84	8			8				+	
XRPD analysis (bulk samples) shown in %										
	Qtz	**Pl**	**14 Å**	**10 Å**	**9 Å**	**7 Å**	**Gbs**	**Hem**	**HA**	**Clays**
DC-SP 1 bone									100	
DC-SP 1	12		+	+	+				39	49
DC-SP 2	35		+	+	+	+	?	*		65
DC-SP 3	36		+	+	+	+	*	*		64
DC-SP 4/2	30	6	+	+		+	?	?		64
DC-SP 5	31	4	+	+		+	*	?		65
DC-SP 6	32	7	+	+		+	?	?		61
DC-SP 7	34	6	+	+		+		?		60
XRPD analysis (fraction < 2 μm) shown by the relative abundance										
	L.c. Vrm	**Vrm**	**Ill/Ms**	**Tlc-Prl**	**Kln**	**KlnD**	**Chl**	**Qtz**	**Chl-V**	**I-S**
DC-SP 2	*	XX	X	*	X	*	XX	–	X	*
DC-SP 3	*	XX	X	*	XX	*	X	*	X	
DC-SP 4/2	X	X	X	*	XX		X	*	X	
DC-SP 5	*	XX	X	*	XX	*	X	*	X	
DC-SP 6	*	X	X		XX	*	X	*	X	*
DC-SP 7	X	X	X		XX	*	X	*	X	*

*Data is obtained by modal analysis of Light mineral fraction (performed on fraction 0.09–0.16 mm), and by Quantitative XRPD analysis. Quantitative mineral composition of bulk samples and semi-quantitative mineral composition of the <2 μm fractionis are shown. Abbreviation codes: Qtz—quartz, Pl—plagioclase, Gbs—gibbsite, Hem—hematite, HA—hydroxylapatite, 14, 10, 9, 7 Å—type of clay minerals present in bulk sample marked with +, ?—mineral is probably present in the sample but cannot be confirmed with certainty because of low content and/or overlapping of diffraction maximums. L.c. Vrm—Low-charge vermiculite or high-charge smectite, Vrm—vermiculite, Ill/Ms—illite/muscovite, Tlc-Prl—talc-pyrophillite group, Kln = Kaolinite which does not intercalate with DMSO, KlnD—kaolinite which forms intercalation compounds with DMSO, Chl—chlorite, Chl-V—chlorite-vermiculite mixed-layerd clay mineral, I-S—illite-smectite mixed-layerd clay mineral, XXX—dominant (>50%), XX—abundant (20–50%), X—subordinate (1–20%), *—traces (<1%).*

comparable to the results of areometric particle size analysis (**Figure 4A**).

Mineralogical Composition of the Sediment

The results of the modal analysis of the sediment samples are given in **Table 2**. Within all samples the LMF predominates, represented by grains of monocrystalline quartz (84–92%) which is mostly represented by angular and slightly rounded grains of uniform and undulose extinction. In addition to this dominant group, euhedral quartz grains can be found (**Figure 5A**). Sporadic occurrences of well-rounded and spherical quartz grains were recorded, as well. The amount of rock fragments ranges from 4 to 8%. Among them, the most common are chert particles. Rare tuffitic particles were found, as well as schist rock fragments. Feldspars are represented mainly in the form of potassium feldspars, and their total amount is up to 9%. Feldspars are most often anhedral (**Figure 5B**) to subhedral. Mica (muscovite) appears only sporadically (<1%) in the form of transparent plates with a rounded outline (**Figure 5C**). The LMF is quite uniform throughout the profile (**Table 2**). A slight decrease in the number of quartz grains toward the top of the profile was observed, and in connection with that, a slight increase in the number of feldspars and lithic particles. The mineral composition of all analyzed samples is uniform. Among the HMF, the amount of opaque minerals is high, about 90%. Completely opaque black grains, often well rounded, are observed. Chromite grains, slightly reddish-brown colored, are present in all analyzed samples and in some samples pyrite (**Figure 5D**). The THM are very sparse in the samples. Among the THM, the pyroxene predominates. They appear in the form of anhedral to stubby prismatic grains, are green in color and the typical "hacksaw" terminations are often visible (**Figures 5F,G**). According to the extinction angle, they are classified in the group of clinopyroxene. The second most common translucent heavy mineral is zircon. Zircons, mainly short-prismatic or anhedral (slightly rounded) are present in all samples. Euhedral grains are rare (**Figure 5G**). Tourmaline is present in roughly the same proportion as zircon. It appears in the form of subhedral grains. It is rounded in some places. Pleochroism in brown to greenish color is visible in places. Other observed varieties belong to a group of hemimorphic grains with multicolored poles (**Figures 5E,H**). Rutile is rare but still present in all samples, appearing in rounded forms with a slightly prismatic habitus. Their color is usually reddish-brown or dark red. Garnets are rare, occur in the form of weakly rounded grains or angular grains/shards with

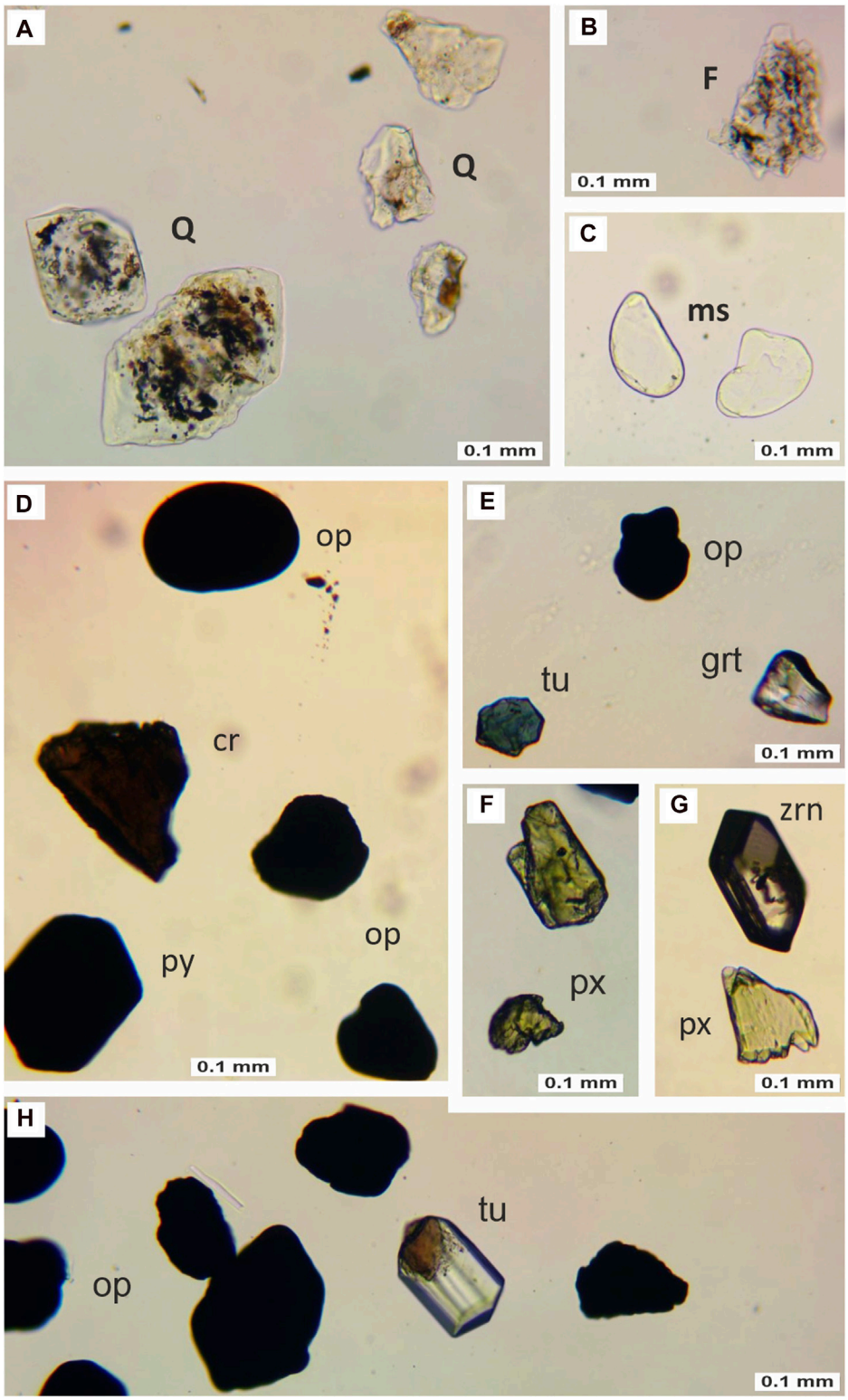

FIGURE 5 | Overview of selected mineral grains from the light and heavy mineral fraction of the DC-SP profile (photo without analyzer). **(A)** Weakly rounded allotriomorphic and hypidiomorphic quartz grains (Q) from sample DC-SP 2, **(B)** Feldspar (F) from sample DC-SP 2, **(C)** muscovite grains (ms) from sample DC-SP 7, **(D)** rounded opaque minerals (op), chromite (cr), and pyrite (py) from sample DC-SP 2, **(E)** opaque minerals (op), tourmaline (tu), and garnet (grt) from sample DC-SP 6, **(F)** pyroxenes (px) from sample DC-SP 6, **(G)** zircon (zrn), and pyroxene (px) from sample DC-SP 2, and **(H)** opaque minerals (op) and tourmaline (tu) from sample DC-SP 3.

sharp edges. Colorless garnets predominate. Slightly pink garnets are also present (**Figure 5E**). Among other THM, grains from the epidote-zoisite group rarely occur. The epidote is greenish, semi-rounded, in the form of irregular grains while mineral grains classified as zoisite/clinozoisite look fresh and show an anomalous blue interference color. Rare occurrences of biotite and greenish anhedral amphiboles are also present.

The results of the XRPD method are shown in **Table 2**. Sample DC-SP 1 is extremely heterogenous. It consists of bone fragments, and sandy silt size sediments. The analysis was performed on both parts. Sediment sample DC-SP 1 (silt), in addition to clay minerals, contains a significant amount of hydroxylapatite (HA) and quartz (**Table 2**). Quantities of fractions <2 μm were too small for clay analysis, so the analysis was performed on a fraction <0.063 mm. In that fraction quartz, vermiculite, illite/muscovite, talc-pyrophyllite, kaolinite and a small amount of chlorite are present. Bone fragment sample consists only of HA. The main mineral phases in all other analyzed samples are clay minerals and quartz (**Table 2**). Samples DC-SP 4 to DC-SP 7 contain a smaller amount of plagioclase. Some of the samples (**Table 2**) contain a very small amount of gibbsite and hematite, but due to the low content cannot be confirmed with certainty in all samples. Mineral composition of <2 μm fraction of all analyzed samples is similar. In the analyzed samples, among clay minerals, vermiculite, illite/muscovite, kaolinite, and a lesser amount of chlorite and chlorite-vermiculite regularly appear. In some samples, small quantities of low-charge vermiculite or high-charge smectite, talc-pyrophyllite, kaolinite which forms intercalation compounds with DMSO and illite-smectite are also present. Samples DC-SP 3 and DC-SP 5 probably contain secondary chlorite (the 14Å diffraction maximum disappeared after heating to 550°C).

Palynofacies

Palynofacies of all studied samples beside the oldest one (DC-SP 1) are dominated by phytoclasts. Sporomorphs occur in a small amount and therefore there is no standard palynological diagram. Instead of that, only organic matter abundance is presented in the diagram (**Figure 6**). In the oldest analyzed sample, DC-SP 1, the palynofacies is dominated by bacterial amorphous organic matter (AOM) particles (**Figure 7A**), and non-opaque phytoclasts, mostly amorphous particles, which indicate an increased input of terrigenous material. Only a few Pinaceae pollen (**Figure 7C**) and Fungi spores occur. Microscopic charcoal remains (around 100 microns in size; **Figure 7B**) point to the influence of fire (Whitlock and Larsen, 2002). Palynofacies from the sample DC-SP 2 is dominated by opaque phytoclasts, mostly corroded charcoal, while non-opaque phytoclasts decreased. Sporomorphs from conifer Pinaceae (**Figure 7D**) family as well as herbs of Asteraceae (**Figure 7D**) and Cichoriaceae family (**Figure 7E**) dominate in the same ratio (6%). They point to a cold and dry climate, probably to a glacial stage. In sample DC-SP 7 palynofacies is still dominated by the opaque phytoclasts, mostly corroded charcoal. Beside phytoclasts there are a lot of particles resembling cyanobacteria, maybe degraded cyanobacteria (**Figures 7F,G**) that lived in the cave. Palynofacies from the youngest sample DC-SP 8 is dominated by the phytoclasts, mostly non-opaque phytoclasts—brown wood and amorphous particles. Rare findings of the palynomorph *Pseudoschizaea* (**Figure 7I**), probably related to Zygnemataceae, indicate the runoff due to periods of enhanced soil erosion outside the cave (Leroy et al., 2007). The presence of spores from the genus *Glomus* suggests erosion from a forested upstream slope (van Geel, 2001), possibly due to fires, themselves evidenced by an increase in microcharcoal particles. Aquatic pollen (*Typha*) and grasses (Graminae) were also present in the similar ratio (ca. 3%). At the same time rare *Polygonum persicaria* (**Figure 7H**) points to anthropogenic influence.

Paleontological and Taphonomic Analysis

The vertebrate remains from the Pleistocene deposits of the test trench (specifically 873 fragments) were recovered at a depth of ~1.2 m, within a 30 cm thick layer (**Figure 3A**). Of these, 230 bones and teeth are identified to the genus *Ursus* (26.4%). The vertebrate remains are therefore documented and presented within **Figure 8**. Based on morphological and metrical characteristics, all bear remains from LCC are attributed to cave bear (*U. spelaeus*), making this species the only mammalian taxon identified within the analyzed faunal assemblage from Pleistocene deposits. The vast majority of the remains, however, remained taxonomically undetermined. Based on their relative size and robustness, many of these remains could also come from a cave bear. However, given the mention of rare findings of other large carnivores and herbivores in previous studies (Malez, 1965b; Paunović et al., 1999), this assumption should be considered with caution and the possibility of the existence of other taxa in this assemblage should not be ruled out. Although most of the remains could not be aged precisely, information of the relative age at death shows predominance of adult bears (81.7%), while the rest belongs to juveniles (**Figure 8**). A single bone is attributed to a fetal or newborn animal.

In order to study the body part representation of bears in the LCC, data for both cave bear and taxonomically indeterminate remains of the similar body size are combined. All major parts of the body are present (**Figure 8**) suggesting deposition of complete bear carcasses within the cave. However, a closer examination of the differential representation of different body parts revealed the following: the most abundant class are trunk elements (32.2%), closely followed by the elements of the head (teeth included; 29.1%) and feet bones (25.2%). Relative to them, larger bones of the appendicular skeleton are under-represented within the analyzed assemblage. Thus, the upper elements of the fore limbs (*scapula, humerus, radius, ulna*) and hind limbs (*pelvis, femur, tibia, fibula*) are represented by only 6.1 and 7.4%, respectively.

With the exception of a few more complete bones, the skeletal material is fragmented. Recent breaks are present but most breakages are dry and attributable to natural processes typical of cave environment (e.g., trampling by other animals, sediment pressure). Looking at the bone surface modifications the material is relatively well preserved. The average bone color varies between pale white to yellowish white. Just a few fragments display small areas of dark brownish coloration, suggesting light staining probably due to exposure to minerals in the sediment. Besides fragmentation, the most common taphonomic modification is very light weathering (fine line fractures and spalling of bone surface), while chemical etching is evidenced on several

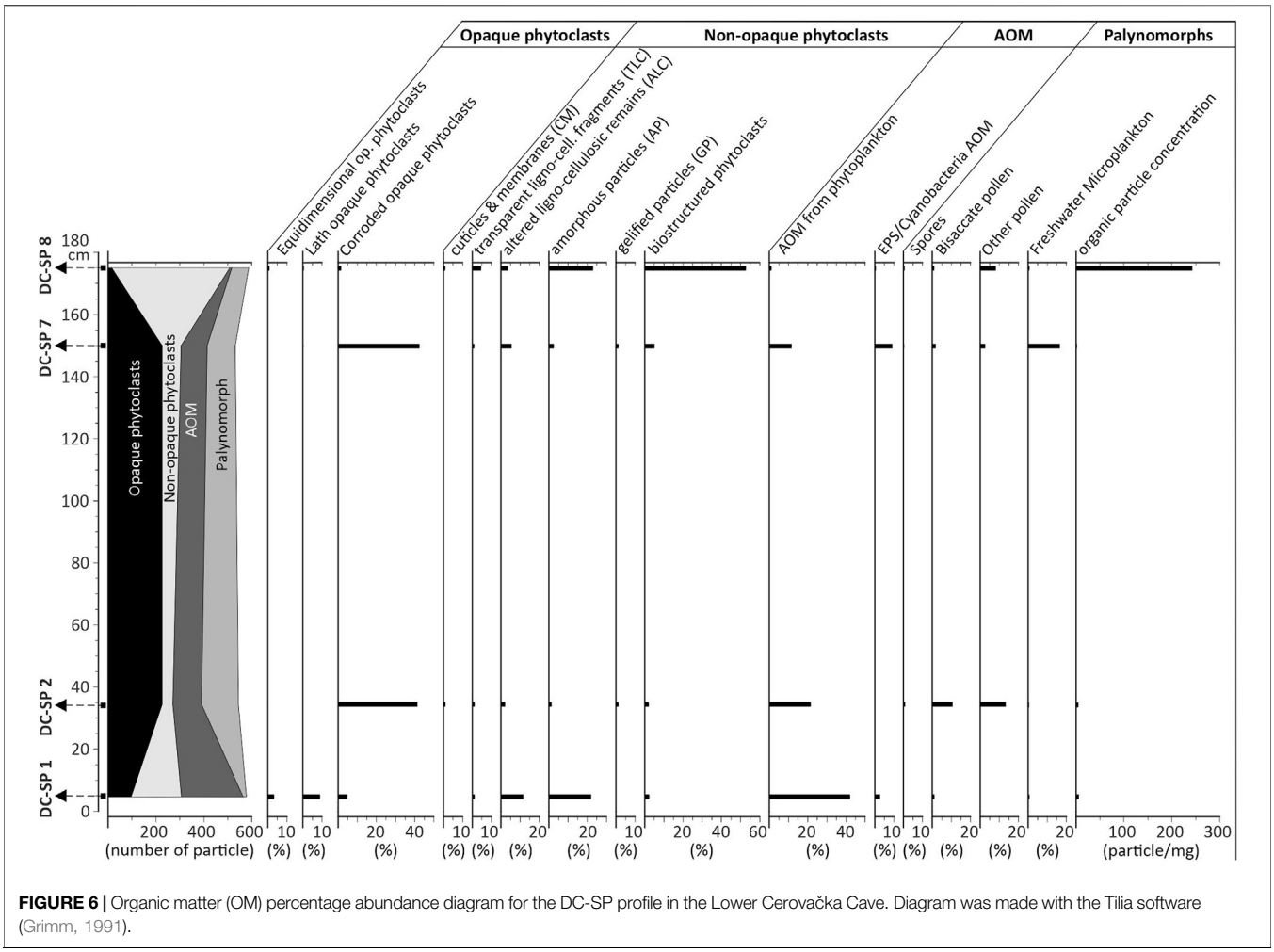

FIGURE 6 | Organic matter (OM) percentage abundance diagram for the DC-SP profile in the Lower Cerovačka Cave. Diagram was made with the Tilia software (Grimm, 1991).

fragments. In addition, only a few bones were gnawed by large carnivores (e.g., cave lion or hyena) and there is no evidence of modification by hominins.

Luminescence Dating

Using the rejection criteria determined in dose recovery experiments, 43 equivalent dose values were accepted for the IR_{50} signal, and 33 for the $pIRIR_{225}$ signal, respectively. Dose distributions for both signals are positively skewed and show overdispersion values of 56 ± 7% (IR_{50}) and 42 ± 7% ($pIRIR_{225}$), which in combination can be interpreted as an indication for incomplete bleaching being significant in the sample. Therefore, average equivalent doses for both signals were calculated using a bootstrapped three-parameter minimum age model (Galbraith et al., 1999; Cunningham and Wallinga, 2012), with $sigma_b$ of 0.3 ± 0.2 as a threshold value, based on the overdispersion values from dose recovery experiments and assigned with an uncertainty to account for the lack of a well-bleached natural reference sample. The g-values of 5.6 ± 0.8 for the IR_{50} and 0.6 ± 0.9 for the $pIRIR_{225}$ signal were obtained after fading corrections. Fading correction was conducted using the approach of Huntley and Lamothe (2001) and calculated using the R-Luminescence package of Kreutzer et al. (2012). Equivalent dose values and resulting ages as well as all luminescence results are summarized in **Table 3**.

The different characteristics of the two luminescence signals measured with the $pIRIR_{225}$ dose protocol can be used to assess the reliability of the determined ages. The IR_{50} and $pIRIR_{225}$ signals are known to exhibit different fading rates, as was confirmed by the fading measurements in this study, and different bleaching rates, with the IR_{50} signal bleaching much faster than the $pIRIR_{225}$ signal (e.g., Murray et al., 2012; Bickel et al., 2015a, 2015b). If incomplete bleaching is significant in a sample, the success of the correction of the effect of incomplete bleaching using the statistical approach of the bootstrapped MAM can be assessed by comparing the fading corrected ages for both signals. If the apparent age of the IR_{50} is significantly younger than that of the $pIRIR_{225}$ signal, incomplete bleaching was not successfully corrected for. If, however, the fading corrected ages for the two signals are in agreement within error limits, like is the case here, this is a strong argument for a successful correction of the effects of incomplete bleaching. Although fading correction was applied also for the $pIRIR_{225}$ signal for comparative reasons, the fading rate is negligible

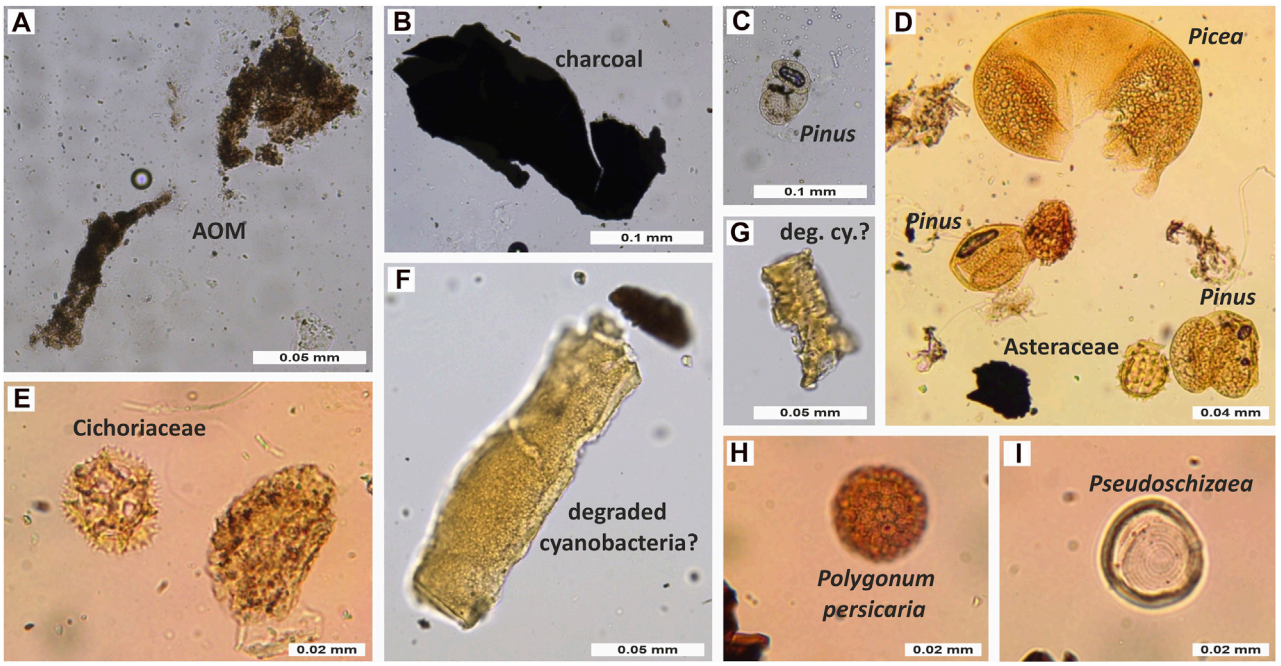

FIGURE 7 | Palynofacies from the profile DC-SP in the Lower Cerovačka Cave **(A,B)** DC-SP 1, **(C,D)** DC-SP 2, **(E,F)** DC-SP 7, and **(G,H)** DC-SP 8.

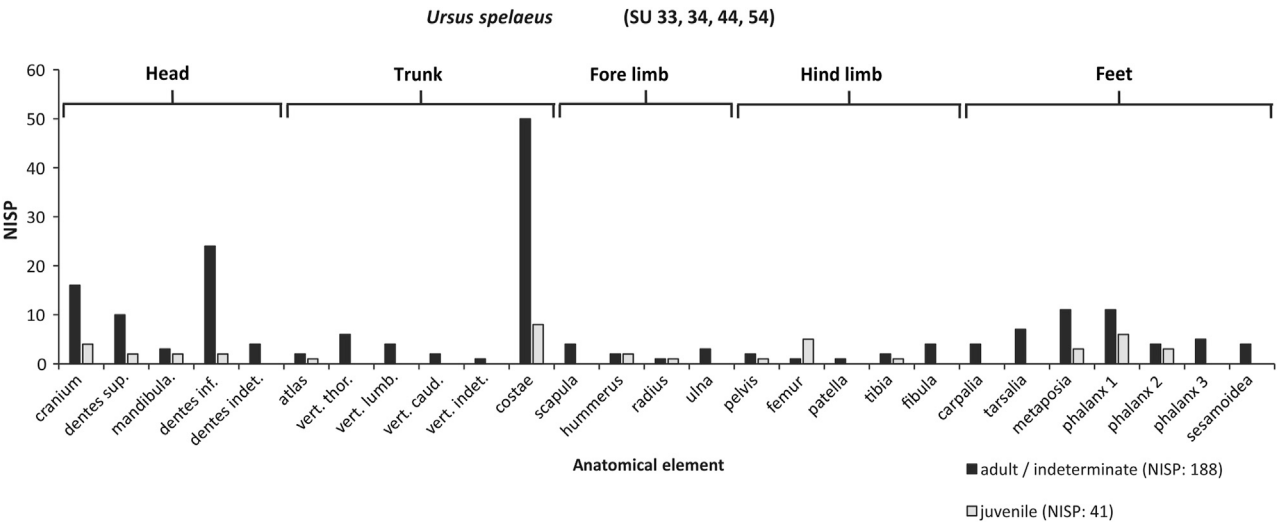

FIGURE 8 | Body part representation (NISP) of *Ursus spelaeus* at the profile DC-SP in the Lower Cerovačka Cave, presented separately for two main age categories. A single fetal/neonatal bone has been excluded.

within error and because of that the $pIRIR_{225}$ based age not corrected for fading of 53.7 ± 6.9 ka can be regarded as the most reliable depositional age for the sample (marked in bold in **Table 3**). In addition, it is important to note that the luminescence age is in stratigraphic order with the radiocarbon age obtained from a flowstone sample (Chapter 4.6.2), further corroborating the high reliability of the age determination.

Radiocarbon Dating

The speleothem sample (Z-7352, graphite number A2160 (RBI), ID number UGAMS# 49576 (CAIS)—**Figures 9A–C**) had $F^{14}C$ = 0.1148 ± 0.0006 (17,390 ± 40 BP) and $\delta^{13}C$ -5.3 ± 0.1‰. $F^{14}C$ and radiocarbon dates without and with *DCF* of 12.5 and 15%, along with their calibrated dates are presented in **Table 4**. Compared calibration curves for both 12.5 and 15% *DCF* and both for using the reservoir function in OxCal and calibrating raw ^{14}C dates are

TABLE 3 | Results from radionuclide analysis and luminescence dating of detrital cave sediments from profile DC-SP in the Lower Cerovačka Cave.

Sample lab code	Sample field code	^{238}U (Bq/kg)	^{232}Th (Bq/kg)	^{40}K (Bq/kg)	Depth below land surface (m)	Overall doserate Fs (Gy/ka)[a]	IR50 SG (n)[b]	pIRIR225 SG (n)[b]	σb[c] IR50 (%)	σb[c] pIRIR225 (%)	IR50 D_e (Gy)[d]	pIRIR225 D_e (Gy)[d]	IR50 age (ka) faded[e]	IR50 age (ka) fading corr[f]	pIRIR225 age (ka) faded[e]	pIRIR225 age (ka) fading corr[f]
VLL-0495-L	DC-SP 3	75.33 ± 5.42	94.92 ± 5.32	506.00 ± 30.36	~60 m	4.41 ± 0.48	43	33	56 ± 7	42 ± 7	136.5 ± 24.4	237.0 ± 16.3	30.9 ± 6.5	60.8 ± 20.6	**53.7 ± 6.9**	56.7 ± 8.2

[a]*Cosmic doserate determined according to Prescott and Stephan (1982) and Prescott and Hutton (1994), taking the geographical position of the sampling spot (longitude, latitude, and altitude), the depth below surface, as well as the average density of the sediment overburden into account. An uncertainty of 10% was assigned to the calculated cosmic doserate. External and internal doserate calculated using the conversion factors of Adamiec and Aitken (1998) and the ß-attenuation factors of Mejdahl (1979), including an alpha attenuation factor of 0.08 ±0.01 and an internal K content of 12.5 ±0.5% (Huntley and Baril 1997) and an estimated average water content of 30 ± 10% throughout burial time. Error was propagated to the overall doserate calculation.*

[b]*Number of grains passing all rejection criteria.*

[c]*Overdispersion calculated using the CAM (Galbraith et al., 1999).*

[d]*Calculated using the bootstrapped MAM-3 (Galbraith et al., 1999; Cunningham and Wallinga 2012).*

[e]*Calculated using the software ADELE (Kulig, 2005).*

[f]*Corrected for fading according to the method of Huntley and Lamothe (2001) using the R Luminescence package (Kreutzer et al., 2012).*

presented in **Figure 9D**. Here should be pointed out that there is a large difference between conventional radiocarbon dated (expressed as BP) and calibrated calendar dates (expressed as cal AD and cal BC) in this part of the radiocarbon calibration curve, resulting in difference of about 2,500 years between the conventional and calibrated age. The true age of material with the obtained age of 16 ka BP is therefore ~19.5 ka old (**Table 4**).

DISCUSSION

Mineral Composition and Provenance of Cave Sediments

The investigated sediments represent the clastic filling of cave channels. Earlier research assumed that the clastic filling of cave channels is an accumulation of *in situ* products of weathering of the host rock (Malez, 1965). According to mineralogical analysis presented within this paper the cave sediment is mainly allochthonous clastic detritus but a part of it is autochthonous chemogenic and collapse material. The overall mixture of cave detrital sediments depends greatly on the weathering products in the source area, transported and deposited by episodic events in different facies types (depending on flow dynamics) inside the cave (Georgiadis et al., 2019). Therefore, our results are compared to the geological units in the river Otuča catchment area (**Figures 1B,C**).

The results of the LMF and XRD analysis (**Table 2**) shows that the main components of the analyzed cave sediments are quartz and clay minerals. The sample DC-SP 1 additionally contains bone fragments and significant amounts of hydroxyapatite (HA) (**Table 2**). HA is the main constituent of mammalian bones and teeth and is often recognized within cave sediments, like e.g., in the Modrič Cave (Miko et al., 2001). Also, the relationship between the habitation of bats and HA formation in caves has been found in limestone caves worldwide (Hill and Forti, 1997). HA is usually formed as a crust that coats speleothems and bedrock substrate surfaces within or near bat habitats, while powdery forms of HA could be found under bat guano deposits (Chang et al., 2010 and references therein). Hence, it is possible that beside the tiny bone fragments in the fine-grained part of the sample DC-SP 1, a part of the HA may also have originated from the *in situ* bat guano, as indicated by the dark color of the sediment. In samples DC-SP 4 to DC-SP 7 small amount of plagioclase are also present (**Table 2**). Their preservation in the samples and the absence of gibbsite and hematite indicates that these samples were subjected to less intensive pre-burial weathering compared to samples DC-SP 2 and DC-SP 3. The clay minerals contained in the analyzed cave sediments (**Table 2**) are similar in composition to the Terra Rossa type paleosols developed on the carbonate rock in the Adriatic region (Durn et al., 2007, 2018). In the wider Mediterranean area, the mineral composition of Terra Rossa type soils and palaeosols may be very variable (Durn, 2003). This variable composition is a consequence of the polygenetic nature of Terra Rossa which can form exclusively from the insoluble residue of limestone and dolomite but much more often encompasses a range of parent materials that arrived on the carbonate terrain by different

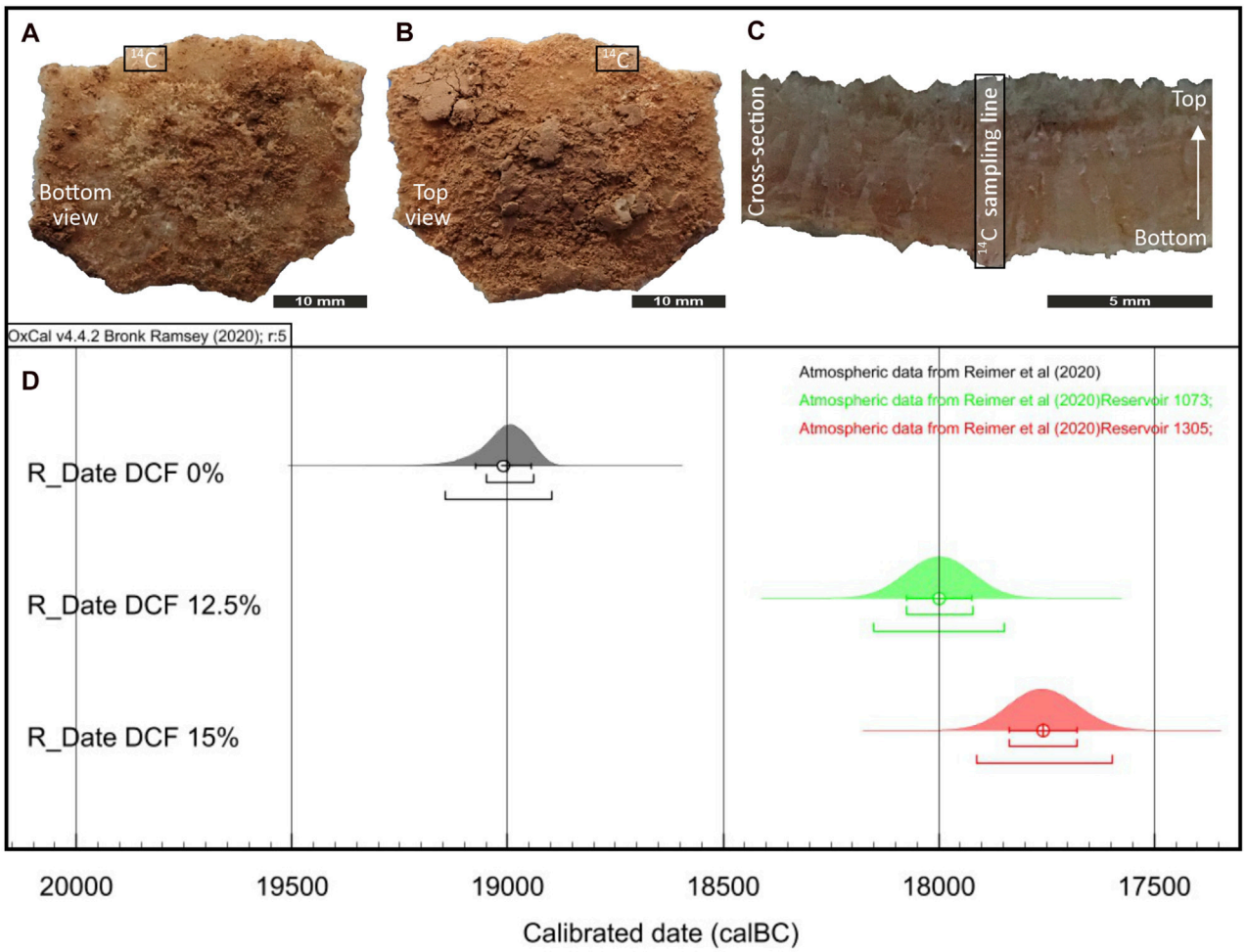

FIGURE 9 | Sampled flowstone (^{14}C) from the DC-SP profile in the Lower Cerovačka Cave **(A)** Bottom view, **(B)** top view, **(C)** cross-section with indicated sampling line, **(D)** calibration curves for ^{14}C date without *DCF* correction (in gray), and for 12.5% ("Reservoir 1,073," in green) and 15% ("Reservoir 1,305," in red) *DCF*.

TABLE 4 | F^{14}C and radiocarbon dates and calibrated dates for dead carbon fraction of 0, 12.5 and 15%, $R_{S\text{-}atm}$—reservoir offset for correction to reservoir effect using the OxCal v 4.2.4 software (Bronk Ramsey 2009, 2016).

DCF (%)	F^{14}C	$F^{14}R_{s\text{-}atm}$	^{14}C date (BP)	$R_{S\text{-}atm}$ (BP)	Calibrated date (95.4%)	
					Span	Median
0	0.1148 ± 0.0006	1	17,390 ± 40	–	19,050–18,940 cal BC	19,002 cal BC
12.5		0.875	16,315 ± 40[a]	1,073	18,189–17,811 cal BC	18,000 cal BC
15		0.85	16,080 ± 40[a]	1,305	17,949–17,562 cal BC	17,758 cal BC

[a]*Dates presented only for orientation, not used directly in the calibration curve.*

Radiocarbon dates were calibrated using IntCal20 calibration curve (Reimer et al., 2020) and calibrated date spans are given with 95.4% confidence (k = 2).

transport mechanisms (Durn, 2003). Thus, in Istrian Terra Rossa, the dominant mineral phases in the clay fraction are kaolinite, illitic material, Fe-oxides and XRD amorphous inorganic compounds, while vermiculite, low-charge-vermiculite or high-charge smectite, chlorite, mixed-layer clay minerals and quartz are present in smaller quantities (Durn, 2003). Terra Rossa soils from Western Herzegovina have a similar composition where the dominant mineral phases in the clay minerals fraction are kaolinite, Fe-oxides and XRD amorphous inorganic compounds, while vermiculite, smectite, illitic material, chlorite–vermiculite and quartz are present in a subordinate amount (Durn et al., 2014). However, even though cave sediments show similarities to Terra Rossa type soils, they cannot be classified as soils (Zupan Hajna et al., 2020). Cave

sediments reveal a good, multi-proxy record of cave and surface environmental conditions in the time of their deposition (Bosák, 2002). Therefore, the red clayey-silty sediments found in the LCC can, to some extent, be considered as redeposited Terra Rossa. Despite the similarities, cave sediments appear to have suffered less advanced stages of weathering compared to Terra Rossa. Iacoviello and Martini (2012) came to the same conclusion comparing the clay mineral composition of cave sediments and Terra Rossa soils in the karst massif of Montagnola Senese in Italy. The source area of the investigated sediment could be in the Gračac karst polje in the close vicinity of the entrance to the LCC. In the catchment area of the Otuča river (**Figure 1B**), approximately 3.5 km upstream of today's ponors close to the cave entrance, the river flows through the area covered with Terra Rossa type sediment, as can be seen from the geological map (**Figure 1C**, unit 10; Ivanović et al., 1973). Beside kaolinite, vermiculite, illite/muscovite, chlorite and mix-layered clay minerals, samples DC-SP 2 to DC-SP 6 contain minerals from the talc-pyrophillite group (**Table 2**). Talc-pyrophyllite usually occurs as a minor component in soils, which could be inherited from the parent rock, but they can also form as a result of weathering processes (Weaver, 1989). According to Velde and Meunier (2010) talc can be formed directly from pyroxenes. Other secondary minerals that can be formed from pyroxene are vermiculite, smectite, kaolinite or hematite. The analyzed samples contain a small amount of pyroxene group minerals (**Table 2**) which could have been the parent material for the talc-pyrophyllite group of minerals. Hematite is present only in traces (**Table 2**), very likely derived from the Terra Rossa. The mineral assemblage determined by the XRD within the analyzed DC-SP samples is comparable to detrital cave sediments within Dinaric karst (Bosák et al., 2012; Zupan Hajna et al., 2021), and e.g., cave sediments from northwestern Oltenia in Romania (Ghenciu, 2017). When comparing cave sediment compositions, it should be noted that the composition of these sediments depends on the clastic source rocks, and factors such as weathering and/or pedogenesis.

To answer the question about the clastic source rocks and source areas, results of LMF and HMF analysis (**Table 2**; **Figure 5**) were compared to the main lithological units in today's catchment area of the Otuča river and Gračac karst polje (**Figures 1B,C**). Underground passages of the LCC are developed in the Tertiary carbonate breccia host rock (Ivanović et al., 1973) (**Figure 1C**, unit 8), known as Jelar breccia (Bahun, 1963, 1974) which is locally composed of various lithic fragments, most commonly related to the lithological composition of underlying rocks. Therefore, the breccia is mainly composed of lithic fragments of Jurassic, Cretaceous, and younger Paleogene carbonate rocks (Ivanović et al., 1976). In the investigated sediment, it was not possible to recognize this carbonate source area, except within the clearly *in situ* formed Bd facies which contains angular boulders of the host rock (**Figure 11A**). However, in most of the sediment, the siliciclastic detritus predominates (**Table 2**) which points to the allochthonous origin of the detritus. According to the results of the HMF and LMF analysis (**Figure 5**; **Table 2**) it can be concluded that the source of the clastic detritus is connected to the wider river Otuča catchment area. Downstream from the source, river Otuča flows through the upper Carboniferous deposits (Šušnjar et al., 1973) (**Figure 1C**, unit 1), mostly clayey shales and sandstones, accompanied by conglomerates. In the composition of the clayey shales quartz, muscovite, chlorite, plagioclase, kaolinite, organic substance, and pyrite can be found. In the layered, well-sorted, and fine-grained sandstones the detritus is composed mainly of quartz, muscovite, chlorite, lithic fragments, and a small amount of plagioclase (Sokač et al., 1976). Traces of such mineral assemblages can be recognized within the composition of LMF from LCC where quartz grains prevail (84–92%), together with the occurrence of muscovite and feldspar (**Table 2**), while the presence of chlorite and kaolinite is confirmed by XRD analysis (**Table 2**). Potential source area could be found within the clastic-pyroclastic series of middle to upper Triassic (**Figure 1C**, unit 3), composed of shales, quartz-calcarenites, subgraywacke sandstones, calcilutites, breccias, and tuffitic rocks (Sokač et al., 1976). The subgraywacke shows pronounced domination of quartz, followed by chert, plagioclase, and platy minerals such as biotite, muscovite, and chlorite, all comparable with the composition of the analyzed samples (**Table 2**; **Figure 5**). Furthermore, other rocks within the clastic-pyroclastic series contain angular quartz, chert/radiolarite, and in smaller amounts fragments of older sandstones and shales, similar to the investigated samples. The predominance of pyroxenes among the THM in investigated samples points to the upper part of the middle Triassic clastic-pyroclastic series as the possible source rocks (Sokač et al., 1976). Pyroxenes, as chemically unstable detrital constituents, possibly indicate higher erosion rates of the source rocks, rapid transport, and short grain residence time in the river (Sevastjanova et al., 2012; Wacha et al., 2019). Although present, garnet grains are not the dominant phase within the composition of THM in LCC detrital sediments (Chapter 4.3, **Figure 5**) but the overall mineral assemblage is almost identical except for the absence of corundum and apatite. The apatite absence could be related to the sample preparation process and chemical dissolution. The relatively abundant well-rounded opaque grains within HMF resembles to Fe-Mn nodules, which are common in clastic cave sediments and Terra Rossa type soils and paleosols (Durn et al., 2018; unpublished data) (**Figures 5D,E,H**). Their occurrence could be related to the earlier mentioned Terra Rossa type soil in the Gračac karst polje (**Figure 1B**, Ivanović et al., 1973). To conclude, the mineral composition of the clastic detritus in which there is high proportion of quartz, followed by feldspars, muscovite, opaque minerals, biotite, chlorite, chromite, pyroxenes, zircon, rutile, garnets, epidote, zoisite/clinozoisite group minerals and chromite can indicate a diverse source area, but the one that is geographically connected to the nearby river Otuča catchment area.

Sedimentary Facies and Depositional Environments

Due to the unique characteristic of cave environments, it is sometimes difficult to interpret specific depositional conditions

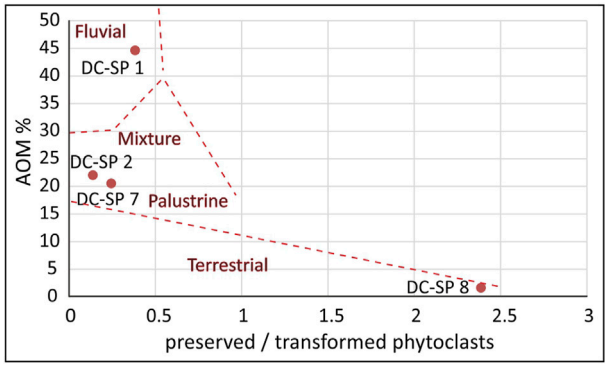

FIGURE 10 | Diagram for discrimination of depositional environments according to palynofacies analysis applied to samples from DC-SP profile in the Lower Cerovačka Cave with optical indices "AOM contents" (aquatic or microbial production) and "preserved/transformed ratio" (preservation degree of terrestrial plant debris) (according to Sebag et al., 2006).

within sequences of detrital cave deposits. Cave sediments represent the most complex terrestrial depositional environment where the law of superposition is often violated, facies are usually diachronous and re-deposition along the same cave passage is very common (White, 2007; Zupan Hajna et al., 2020 and references within). However, we were able to describe and interpret three lithofacies types within the sedimentary profile DC-SP in the LCC; the Breakdown facies (Bd), the Diamicton facies (Di) and the Slackwater facies (Sw) (**Figure 3A**; **Table 1**).

Sediments of the Bd facies are commonly formed by the gravitational collapse of the host-rock or speleothems from the ceiling of the caves. Such facies type has been described in other caves, and is considered as an autochthonous type of sediment (e.g., Bosch and White, 2004; White, 2007). The transport of material, in this case, is very short, as is confirmed by the angularity of collapsed blocks and poor sorting of the debris (**Table 1**; **Figure 11A**). Collapsed sediments are common near the cave entrances (e.g., Bočić et al., 2012; Haddad-Martim et al., 2017), although they can often be seen as big accumulations of unsorted boulders and cobbles on the floor of big chambers within caves (Fornós et al., 2014). Deposition is, besides other processes, often triggered by the cryofracturing process within cave channels during the cold periods (White, 2019). Hence, it can be assumed that sedimentation of the Bd facies in the channel of the LCC could also happen during a relatively cold period. That assumption is confirmed by palynological data which shows that the base of the investigated profile was formed during a period of cold and dry climate (see Chapter 4.4). The silty matrix within the Bd facies is the result of secondary infiltration (e.g., Martini, 2011) due to the existence of occasional and relatively insignificant water flow within the open cave channel. This is evidenced by the preserved/transformed phytoclast ratio according to Sebag et al. (2006). Even though this index was introduced by Sebag et al. (2006) for Holocene alluvial sediments, our data show a distribution of the index (**Figure 10**) which allows us to distinguish the paleoenvironment, confirming a transition from a fluvial paleoenvironment in the lower (older) part of the section (DC-SP 1—Bd facies) to a non-aquatic terrestrial paleoenvironment toward the youngest part of the section (DC-SP 8—Late Bronze Age). Such interpretation shows a good correlation with the sedimentological data. The appearance of microscopic-sized charcoal remains (**Figure 7B**) and possible traces of guano and bone remains (**Table 2**) between collapsed blocks of the Bd facies indicate that during the deposition of the Bd facies the cave channel was already fully developed and well connected to the surface in an open-air environment. Charcoal remains could indicate occurrences of wildfires in the area. Deposits of this type are formed during the vadose, air-filled stages of cave development (Hill, 1999). However, the distribution of palynofacies shown on **Figure 10** in the lower part of the section, could also be a reflection of palynomorph transport by hydrological mechanism of cave drip water into the vadose cave channel.

Coevally to the Bd facies, the sediments of the Di facies were deposited (**Figures 11A,D**), as implied by their lateral contact. The red clayey silt resembles the Terra Rossa type soils and palaeosols whose genesis within the karst has not yet been unambiguously resolved. Polygenetic, detrital, and residual origins are most commonly mentioned (Durn et al., 2007). Similar red clayey-silty sediments in caves are interpreted as a composite of detritus introduced into the cave, and the insoluble residue from the dissolution of the host rock (e.g., Iacoviello and Martini, 2012). Mostly allogenic origin of the Di sediment within LCC is confirmed by mineralogy reflecting the composition of the river Otuča drainage area (Samples DC-SP 2, 3 in **Table 2**; Chapters 4.3 and 5.1). Although the vast majority of this interval is formed by finer sediment (Samples DC-SP 2, 3; **Figure 4A**), a significant number of larger clasts and bone fragments were found within (**Figures 3A**, **11A**), could indicate depositional mechanisms by non-selective agents within cave specific environments. The aeolian contribution could also played important role in creating fine-grained sediment sequences within the cave. However, in the close vicinity of the LCC, there are no occurrences of loess on the surface (**Figure 1C**). Loess and loess-like deposits were widespread in the Adriatic region during oxygen isotope stage 3 (Wacha et al., 2018; Zhang et al., 2018). Nevertheless, aeolian sediments also play a significant role in the forming of polygenetic Terra Rossa type of soils (Durn et al., 2007) which were found in the river Otuča catchment area (**Figure 1C**, unit 9). According to paleontological data, it is necessary to mention that most probably intertwining of the depositional and biological processes resulted in today's distribution of clasts and fossil remains within the sediment. Despite the fact that all parts of the *U. spelaeus* body are represented (Chapter 4.5), there is a lack of articulated sets and high fragmentation with indications of certain movements and destruction of the faunal material within the sampled DC-SP 2 interval of Di facies (**Table 1**; **Figure 3**). In density-mediated attrition, low-density elements are quickly destructed and removed from the assemblage (Lyman, 1994), which does not explain why there are very few fragments of major limb bones. The post-depositional disturbance is possible. However, based on data on body parts representation and

fragmentation, it is possible that a larger dispersal of the skeletal material occurred even before, when bear carcasses were lying on the fossil surface of the cave. Except for a single questionable finding of cut marks (Trbojević Vukičević and Babić, 2008), no traces of butchering were previously found on cave bear bones from LCC, so it is safe to assume that hominins were not responsible for the accumulation and dispersal of cave bear bones. Since the cave has probably been used for a very long time by several generations of cave bears (Malez, 1965b), lack of articulated skeletons can be also explained as a result of trampling by other cave bears. However, high fragmentation and under-representation of major long bones may be due to scavenging activities of large carnivore predators, whose presence should not be ruled out despite the lack of corresponding taphonomic traces within the analyzed assemblage. Bears used caves as shelter and for hibernation, and were often targeted by other large carnivores, mostly hyenas, who entered deep into caves in search of them (Diedrich, 2012). To conclude, described lack of complete skeletons or articulated sets, as well as high fragmentation undoubtedly indicate certain movements and destruction of the faunal material within the sediment, although taphonomic processes could have a significant influence (Chapter 4.5). Given the chaotic arrangement of clasts and random orientation of long bones with no visible textures in the clayey silt, the facies of the red clayey silt is interpreted as Di facies (e.g., Bosch and White, 2004; White, 2007; Haddad-Martim et al., 2017). This type of sediment could be formed by high-density debris flows within the caves and by the redeposition of older clastic cave deposits. Distinguishing facies types within this type of deposits is not always unambiguous because cave sediments deposited near cave entrances are often transported by nonselective mechanisms such as slumping, creeping, and collapsing. Such processes result in the fact that they are mainly built of similar ratios of silt, clay and sand, which makes it difficult to recognize unconformities (Haddad-Martim et al., 2017). The chaotic character of the Di facies (see description in **Table 1**) and the possible redeposition of the sediments, is supported by the results of the palynological analysis which shows signs of redeposition, for example high (relative) values of phytoclasts fragments especially corroded charcoal remains (**Figure 10**). Deposition of the Di facies sediments took place during a period of a colder and drier climate (Chapter 4.4). Such occurrence of poorly sorted fossiliferous sediments coincides with the results of previous research within the LCC (e.g., Malez, 1960b). Namely, the horizon of the Di facies could be related to deposits earlier described in the caves of the nearby Gračac area as sediment composed of reddish-brown phosphate clays with numerous osteological remains of the Late Pleistocene with traces of the Upper Paleolithic culture (Malez, 1960b; Ivanović et al., 1976). Those sediments were correlated to the Last Glacial Period. Although cave bears are one of the most abundant taxon recovered from Pleistocene cave sites in Croatia (Miracle, 1991), with Cerovačke caves being one of the most important cave bear sites (Paunović et al., 1999), our paleontological data are limited by the relatively modest sample size. Therefore, *U. spelaeus* remains within the investigated sequence cannot be used as a precise stratigraphic marker. The earliest appearance of the *U. spelaeus* dates back to the end of the Middle-Late Pleistocene transition, and it became extinct in central Europe during the LGM, around 24 ka BP (Kurtén, 1958, 1968; Pacher and Stuart, 2009). Within Dinaric karst there are dated cave bear specific sites (e.g., Križna jama) with ages of cave bear thanatocenoses around 47–45 ka and >94 ka BP (Bosák et al., 2012). To establish a chronological framework of the Di facies of the LCC luminescence dating was performed. Although it is a new approach in the region, the application of luminescence dating techniques has proven to be a suitable chronometer in cave settings (e.g., Montanari et al., 2019). In general, luminescence techniques enable the determination of depositional ages of sediments by determining the point in time when quartz or potassium-rich feldspar grains were last exposed to daylight during transport before final deposition (for the basic principles of luminescence dating see Preusser et al., 2008, Rhodes 2011; Wintle 2008). According to the obtained luminescence age, the sediment directly overlying cave bear remains entered the cave environment 53.7 ± 6.9 ka ago (**Table 3**), which correlates well with oxygen isotope stage 3 (OIS3). The obtained date does not necessarily indicate the time of deposition at the investigated site but the time when the sediment entered the cave environment. It also indicates that this part of the sequence is not older than ~54 ka. The end of deposition of the Di facies is marked by a change in color from reddish to gray to yellow and the appearance of a discontinuous flowstone level (**Table 1**; **Figure 11C**). Similar it is also described in other caves of the investigated area (reddish-brown phosphate clays phase covered with flowstone—Ivanović et al., 1976).

A thin layer of laminated flowstone composed of columnar sparry calcite was determined with visible crystal growth directions (**Supplementary Material S2**). Millimeter-sized sparry calcite possibly indicate a relatively high growth rate of the flowstone. We assumed *in situ* genesis of the flowstone because platy fragments (**Figures 9A–C**) are distributed at the same horizontal level with visible distinct uneven base/nucleation plane shoving traces of the underlying silty-clayey sediment (**Supplementary Material S2**). However, due to the thin and discontinuous horizon (**Figure 3A**), an allochthonous origin is not excluded. If *in situ*, the flowstone within the sedimentary profile is an indicator of change in the cave environment since their formation implies the absence of the detrital input (Haddad-Martim et al., 2017). Flowstones could be formed from sheets of flowing water derived from fissures or major conduits (Fairchild et al., 2006) or as subaqueous flowstones fed with turbulent underground stream water (Wróblewski et al., 2017). As valuable marker horizons for dating, they were previously used in this region as source material for acquiring ^{14}C ages within caves (e.g., Bočić et al., 2012). Within this study the obtained ^{14}C age from the flowstone is supported by the $pIRIR_{225}$ dating of the sediment horizon below the flowstone.

Comparing $\delta^{13}C$ of the LCC speleothem sample (**Table 4**) of 5.3‰ to the Modrič cave speleothem (Rudzka et al., 2012) that has a mean value of −7.37‰ (2σ = 1.74‰), it could be concluded that the speleothem in the Modrič cave had a lower amount of DCF. Therefore, the most likely date for the LCC speleothem would be the OxCal Reservoir function date 17,949–17,562 cal BC

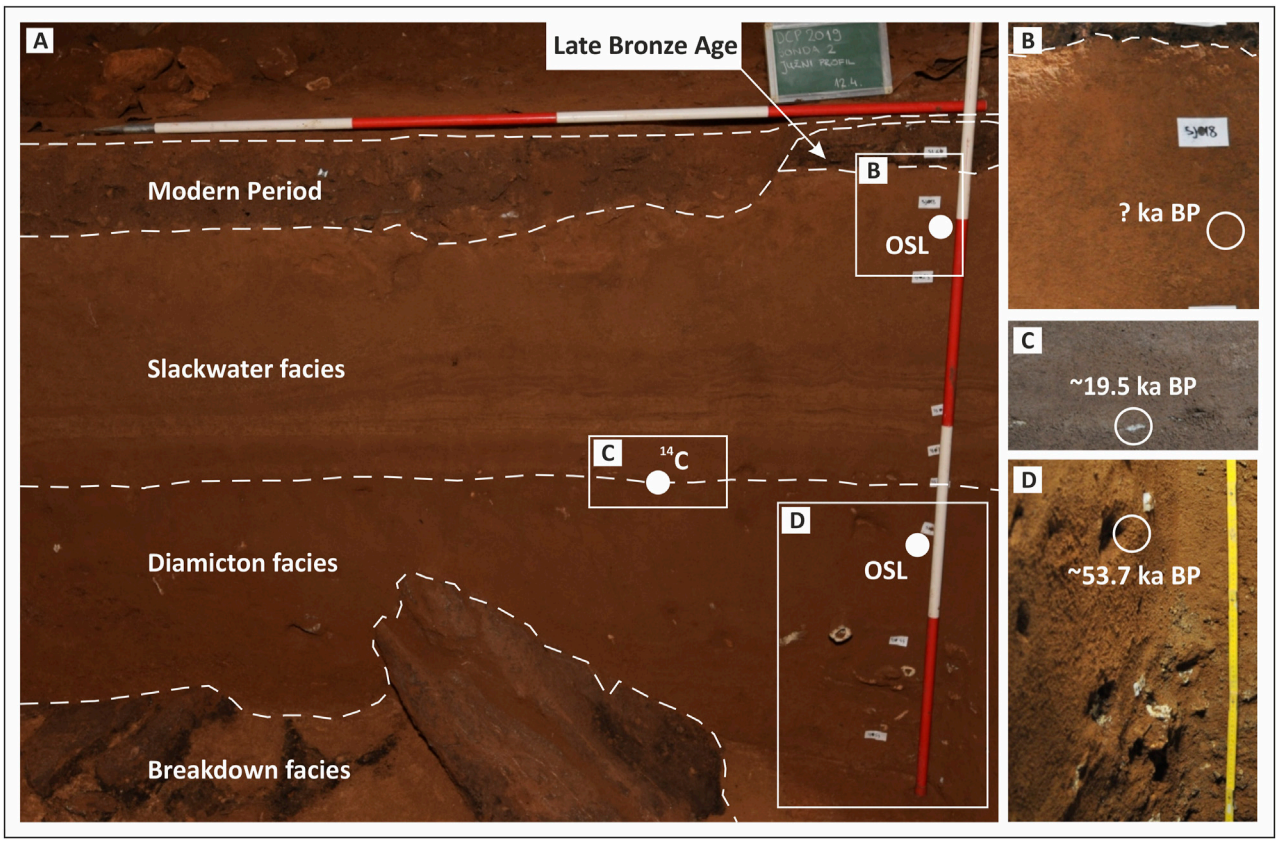

FIGURE 11 | Facies types and age on profile DC-SP in the Lower Cerovačka Cave **(A)** Facies distribution with indicated sampling spots, **(B)** detail from upper part of Slackwater facies with indicated sampling spot and luminescence age, **(C)** ^{14}C age with indicated sampling spot within flowstone fragment, **(D)** detail from diamicton facies with visible larger clasts and bone fragments of *Ursus spelaeus* with indicated sampling spot and luminescence age [authors of photographs **(A)** DTP, **(B)**–**(D)** NB].

(median 17,758 cal BC) for DCF = 15%. The formation of a relatively thin flowstone layer within the sedimentary profile in LCC, therefore, could be related to the known period-related phenomena in the border zone between the temperate Mediterranean and the periglacial/glacial parts of Europe (Surić and Juračić, 2010) when the formation of speleothems were rare or slow. Speleothem deposition ceased during the Last Glacial Maximum (LGM) in most of Europe and began again around 15 ka ago (Gascoyne, 1992; Lowe and Walker, 1997; Mihevc, 2001; Surić and Juračić, 2010). According to our data, the pronounced collapse processes and deposition of both Bd and Di facies sediments happened probably during local LGM, sometimes before ~19.5 ka from today (^{14}C age 17,949–17,562 cal BC—**Table 4**, **Figure 11C**), before postglacial warming commenced. The Dinaric mountains were glaciated during the Middle and Late Pleistocene (Hughes and Woodward, 2009). Therefore, periglacial influence on the LCC could be expected. If the flowstone is allochthonous (e.g., spallation from the ceiling), the obtained age could still be used as the oldest possible date when deposition of the upper section of the DC-SP profile commenced. Sedimentation in a calm aquatic environment therefore set on after ~19.5 ka ago, as evidenced by the sedimentary filling of the cave channel which covers the flowstone marker horizon. This phase is characterized by gray to yellow laminated silt (**Table 1**; **Figure 3A**) which can be interpreted as slackwater deposit (Sw facies) (e.g., Bosch and White, 2004; White, 2007; Iacoviello and Martini, 2012; Ballesteros et al., 2017). These fine-grained sediments (**Figure 4**) entered the cave after flood events and settled during calmer conditions with very low flow velocities (often submerged cave channels). The allogenic origin of the Sw sediment is confirmed by the mineralogy, reflecting the composition of the river Otuča drainage area (Samples DC-SP 5–7 in **Table 2**; Chapters 4.3 and 5.1). Although the detritus was transported underground by turbulent flows rich in suspended sediment, the final depositional mechanism of this sediment type is very likely related to deposition from stagnant water suspension, as evidenced by the particle size characteristics and the lamination of the sediment. This is also confirmed by the fining upwards sequence observed in the upper part of the Sw facies interval (**Figure 4B**; **Table 1**). Slight reduction of the grain size from the base to the top indicating a decrease in the hydrodynamic energy conditions of the cave, is commonly observed within the Sw facies (Fornós et al., 2014). This is also confirmed by the palynofacies analysis, results of which indicate sedimentation in a calm palustrine environment

(**Figure 10**). However, the laminated structure of the sediment in the lower part of the SW facies followed by a slight increase of the sand content (**Figures 3A**, **4B**), described as vertical alterations of silty laminae and silty-sandy laminae (**Table 1**), could also resemble sediments deposited in stagnant hydrological conditions in regions prone to glaciation. Nearby areas of southern Velebit Mt. were prone to glaciation, documented with morphological moraine features and with glacial and glacio-fluvial sediments (Nikler, 1973; Krklec et al., 2015; Marjanac and Marjanac, 2016; Velić et al., 2017). The retreat of mountain glaciers in the southern Velebit Mt. is therefore dated roughly around 20.7–22.7 ka ago (Sarıkaya et al., 2020). Even so, there is no data about glacial chronology and processes in the very close vicinity of LCC. It should be mentioned that warming and deglaciation in the inland part of the Dinarides commenced mainly after 12.5 ka BP. It can be seen from increased speleothem growth in the Dinaric karst (Horvatinčić et al., 2003). Hence, we assume that it is highly possible to recognize glacial/periglacial influence on the deposition of Sw facies. According to our data, the Sw sediments were deposited during the Late Pleistocene (starting after ~19.5 ka). In caves within glaciated regions, similar varve-like deposits are common (Ford and Williams, 2007). Even though the grain-size curves of the Sw facies (**Figure 4A**) resemble the varve-like sediments (Valen et al., 1997; Ford and Williams, 2007), the glacial-related depositional environment through the whole profile of the Sw facies sediments is ambiguous and needs further proof. Grain-size distribution curves themselves do not point to an unambiguous conclusion, it is necessary to compare them with known sediment ages to resolve the glacial-related origin of the laminae (Tischler et al., 2020).

The termination of allogenic siliciclastic sedimentation in an aquatic environment and consequently the end of the ponor function of this part of the LCC channel cannot be precisely dated within our research. Nevertheless, our data revealed a relatively young age in comparison to the known data within the wider area of the Dinaric karst where cave sediments cover the time span of the last ~5 Ma years (Zupan Hajna et al., 2020; Zupan Hajna et al., 2021). We can conclude that this pronounced sedimentary environment shift is visible in the profile DC-SP with the onset of a Holocene Late Bronze Age layer (Tresić Pavičić, 2020). As known, the cessation of allogeneic sedimentation in caves is mostly controlled by tectonics and therefore related to changes in the hydrological regimes due to the separation of cave systems from active watercourses (Zupan Hajna et al., 2020). At Postojnska Cave, the sequence follows the series of events: formation of the fault, growth of the initial conduit due to groundwater circulation through the fault, infilling of the conduit with allogenic sediment, abandonment due to regional base level lowering, and continued motion along the fault (Sasowsky et al., 2003). Locally in LCC, it could be related to the permanent neotectonic uplift of this area (Prelogović, 1975). Especially pronounced uplift along the main NW–SE faults, e.g., along the Lika fault (**Figure 1C**), was recorded during the Pliocene and Quaternary (Prelogović, 1975). Maximum uplift of the local mountains was calculated of up to 1,200 m, with vertical shifts on individual faults averaging from 300 to 500 m (Prelogović, 1975). The sedimentary profile DC-SP, and the obtained data therefore possibly reveal the sedimentation history of the youngest inactive cave level within Mt. Crnopac. The same phases in the development of allogenic cave sediments occurred earlier in the higher cave levels within the mountain. It is evidenced with similar facies types (Sw) of detrital sediments which were found within the hypsometrically highest horizontal level of the todays CCS (Talaja and Kurečić, 2017). Considering that caves and their sediments are often related to the former base level and can conserve this information for long periods (Neuhuber et al., 2021), the average offset rate of local ongoing uplift/base level drop can be roughly estimated. Considering the relative displacement value of ~80 m between today's LCC entrance (at 624 m a.s.l.), and the recent active ponor phase on the polje level we have calculated the relative displacement rate. It is based on the obtained ^{14}C age of 17,949–17,562 cal BC (before approximately 19.5 ka from today) of the flowstone strata identified within the DC-SP profile (**Table 4**). The displacement rate gives us a relatively high value up to ~0.004 m per year. The calculated result is higher and not unambiguously comparable with fault slip rates calculated in the area of External Dinarides (Kastelic and Carafa, 2012). Therefore, due to scarce data without numerous variables, we believe that the computed rate could only be used as a rough estimation and basis for further research. Even if we use the combination of absolute and relative methods in order to get an accurate and robust age estimate (Häuselman et al., 2015), the critical problems identified are lack of data regarding the timing of the cessation of the allogenic sediment input. The archeological data suggests that the LCC was used for specific purposes during the Late Bronze Age (Tresić Pavičić, 2020), such as food storage and as a temporary dwelling in specific circumstances which surely indicate already ceased sediment input. However, due to the possible large time gap between the cessation of the Sw deposition and the onset of the Late Bronze Age, we cannot use that data for accurate calculations.

CONCLUSION

The allogenic cave deposits in Croatia have been poorly explored, especially from the point of view of their origin and depositional mechanisms. Numerical dating is also absent. This is the first detailed study of detrital cave sediments with reliable luminescence age constraints in the Croatian part of the Dinaric karst region. The presented data are a significant contribution to solving the complex stratigraphy and genesis of a multilevel cave system of Mt. Crnopac and Dinaric karst. Our conclusions are as follows:

- The genesis of the LCC and its entrance channel is related to the denudation effect of the sinking waters of the Gračac karst polje, mainly under saturated conditions.
- Within the investigated sedimentary profile (DC-SP) three lithofacies types were identified: Breakdown deposits (Bd), Diamicton deposits (Di), and Slackwater deposits (Sw)

covered with an archaeological Late Bronze Age and Modern period deposits.
- The mineral composition of cave detrital sediments points to an allochthonous origin, derived from the wider Otuča river catchment area.
- The source rocks which derived the siliciclastic detritus found within the entrance channel of the LCC belong to the upper Carboniferous clastic series, middle to upper Triassic clastic-pyroclastic series, Terra Rossa type of sediments, and arguably in some extent to the insoluble remnant of the host rock.
- Sedimentary facies analysis coupled with the palynofacies analysis revealed changes in depositional events within the LCC, ranging from intensive collapse processes with fluvial influence through re-deposition by mechanisms of high density flows to the forming of stagnant water environments with laminated sediments, and finally to the terrestrial environment with pronounced human activity.
- Numerous bones of *U. spelaeus* were found, giving us a broad estimation of the stratigraphic position of the Di facies sediments spanning from the early Late Pleistocene to the Last Glacial Maximum.
- The lack of complete skeletons or even articulated sets, as well as high fragmentation, indicate movements and destruction of the faunal material as a result of taphonomic processes coupled with re-deposition within the fossiliferous interval.
- Deposition of first allochthonous detrital cave sediment sequence (Di facies) within the LCC channel commenced around or after ~54 ka ago as evidenced by luminescence dating. For the first time in Croatia, luminescence dating contributed to resolving the chronostratigraphy of clastic sedimentary sequence within the cave environment.
- The major shift in sedimentation mechanisms between collapse and redeposition processes, and deposition within stagnant water conditions commenced through the period after 19.5 ka from today up to the onset of the Late Bronze Age.
- The cessation of allogenic sedimentation within the LCC is related to the permanent neotectonic uplift of the area, especially pronounced uplift along the main NW–SE faults.

DATA AVAILABILITY STATEMENT

The original contributions presented in the study are included in the article/**Supplementary Material**, further inquiries can be directed to the corresponding author.

AUTHOR CONTRIBUTIONS

TK conceptualized, drafted and prepared the paper with the contribution of all coauthors. DP (archaeology), TK, NB, and LW (geology and sedimentology) conducted the field work and sampling. TK conducted detailed sedimentological and mineralogical analysis as well as laser diffraction particle size distribution. NB performed morphological analysis. KB performed palynological, SR macropaleontological and AG XRD analysis. CL performed luminescence dating and all related analyses and data evaluation. AS performed radiocarbon dating. DP acquired photogrammetric data. LR performed laser scanning of the cave and prepared the 3D model. MF accompanied the luminescence dating part and gave advice during lab work and elaboration of the manuscript. All authors reviewed the manuscript and approved the final version.

ACKNOWLEDGMENTS

The authors are thankful to the archaeological firm Kaducej Ltd. which conducted rescue archaeological excavation at LCC, from March to May 2019. Excavation gives us insight into geological layers, and the opportunity to sample sediments. All relevant photogrammetric data about the test trench was also provided by Kaducej Ltd. The archaeological excavation was the first part of the revitalization project: Centre of Excellence Cerovac Caves - Sustainable Management of Natural Heritage and the Karst Underground, under the direction of Public Institution Park prirode Velebit with partners Zadar County, Public Institution Natura—Jadera and Zagreb Speleological Union, co-funded by the European Regional Development Fund. The authors would also like to thank to Mirjana Drušković, Dragica Kovačić, Antun Škrtić and Damir Galović from Croatian Geological Survey for the sample preparations. This work was partially funded by the University of Zagreb within the project "Geomorphological and hydromorphological research at selected sites of the Dinaric Karst in Croatia." The research was also supported by the Croatian Geological Survey through program funding provided by the Croatian Ministry of Science and Education. The authors would like to thank the editor (Dr. Aurel Perşoiu), and the two reviewers (Dr. Andrea Zerboni, and Dr. Christos Pennos) for their comments.

SUPPLEMENTARY MATERIAL

The Supplementary Material for this article can be found online at: https://www.frontiersin.org/articles/10.3389/feart.2021.672229/full#supplementary-material

REFERENCES

Adamiec, G., and Aitken, M. (1998). Dose-rate Conversion Factors: Update. *Ancient TL*. 16, 37–50.

Auclair, M., Lamothe, M., and Huot, S. (2003). Measurement of Anomalous Fading for Feldspar IRSL Using SAR. *Radiat. Measurements*. 37, 487–492. doi:10.1016/s1350-4487(03)00018-0

Bahun, S. (1963). Geološki Odnosi Okolice Donjeg Pazarišta U Lici (Trijas I Tercijarne Jelar-Naslage) [Geological Relations of the Surroundings of Donje Pazarište in Lika - in Croatian]. - *Geološki vjesnik*. 16, 161–170.

Bahun, S. (1974). Tektonogeneza Velebita I Postanak Jelar Naslaga [Tectonogenesis of Mt. Velebit and the Origin of the Jelar Deposits - in Croatian]. *Geološki vjesnik* 27, 35–51.

Bajo, P., Borsato, A., Drysdale, R., Hua, Q., Frisia, S., Zanchetta, G., et al. (2017). Stalagmite Carbon Isotopes and Dead Carbon Proportion (DCP) in a Near-

Closed-System Situation: An Interplay between Sulphuric and Carbonic Acid Dissolution. *Geochimica et Cosmochimica Acta*. 210, 208–227. doi:10.1016/j.gca.2017.04.038

Bakarić, L. (2017). "Japodi [Iapodes]," in *In Iapodes - the Forgotten Highlanders [in Croatian]*. Editor L. Bakarić (Zagreb: Archaeological museum Zagreb), 21–60.

Barišić, T. (2017). Perspektive Spajanja Velikih Jama Crnopca [Perspectives of Connecting the Large Pits of the Mt. Crnopac - in Croatian]. *Speleolog*. 65 (1), 26–31. Available at: https://hrcak.srce.hr/204709.

Bickel, L., Lüthgens, C., Lomax, J., and Fiebig, M. (2015a). Luminescence Dating of Glaciofluvial Deposits Linked to the Penultimate Glaciation in the Eastern Alps. *Quat. Int.* 357, 110–124. doi:10.1016/j.quaint.2014.10.013

Bickel, L., Lüthgens, C., Lomax, J., and Fiebig, M. (2015b). The Timing of the Penultimate Glaciation in the Northern Alpine Foreland: New Insights from Luminescence Dating. *Proc. Geologists' Assoc.* 126, 536–550. doi:10.1016/j.pgeola.2015.08.002

Blečić-Kavur, M. (2014). Na Razmeđu Svjetova Za Prijelaza Milenija: Kasno Brončano Doba Na Kvarneru [At the Crossroads of Worlds at the Turn of the Millennia: The Late Bronze Age in the Kvarner—in Croatian]. *Musei Archaeologici Zagrabiensis Catalogi et Monographiae*. XI, 121. doi:10.1163/9789004416604_007

Bočić, N., Božić, V., Buzjak, N., Dražina, T., Knajs, R., Miculinić, K., et al. (2016). *Stručna Podloga Za Izradu Projektno-Tehničke Dokumentacije Za Unutarnje I Vanjsko Uređenje Turističke Infrastrukture S Geodetskom Snimkom U Interesnom Žarištu Projekta U Zoni C: "Gornja I Donja Cerovačka Špilja" [Expert Basis for the Preparation of Project-Technical Documentation for Internal and External Arrangement of Tourist Infrastructure with a Geodetic Survey in the Focus of the Project in Zone C: "Upper and Lower Cerovačke Caves" - in Croatian], Expert Study*. Zagreb: Speleological club Željezničar, 248.

Bočić, N., Faivre, S., Kovačić, M., and Horvatinčić, N. (2012). Cave Development under the Influence of Pleistocene Glaciation in the Dinarides—an Example from Štirovača Ice Cave (Velebit Mt., Croatia). *Z. für Geomorphologie*. 56 (4), 409–433. doi:10.1127/0372-8854/2012/0083

Bočić, N., Pahernik, M., and Faivre, S. (2019). Geomorfološka Obilježja Sjevernog Velebita [The Geomorphological Features of Northern Velebit]. *Senjski zbornik*. 46, 5–36. [in Croatian, with English Summary]. doi:10.31953/sz.46.1.1

Bosák, P. (2002). "Karst Processes from the Beginning to the End: How Can They Be Dated?," in *In: Evolution of Karst: From Prekarst to Cessation*. Editor F. Gabrovšek (Postojna–Ljubljana): Carsologica, Založba ZRC), 191–223.

Bosák, P., Pruner, P., Zupan Hajna, N., Hercman, H., Mihevc, A., and Wagner, J. (2012). Križna Jama (SW Slovenia): Numerical-And Correlated-Ages from Cave bear-bearing Sediments. *Ac.* 39 (3), 133. doi:10.3986/ac.v39i3.82

Bosch, R. F., and White, W. B. (2004). "Lithofacies and Transport of Clastic Sediments in Karstic Aquifers," in *"Lithofacies and Transport of Clastic Sediments in Karstic Aquifers" in: Studies of Cave Sediments: Physical and Chemical Records of Paleoclimate*. Editors I. D. Sasowsky and J. Mylroie (Boston: Springer), 1–22. doi:10.1007/978-1-4419-9118-8_1

Bøtter-Jensen, L., Andersen, C., Duller, G., and Murray, A. (2003). Developments in Radiation, Stimulation and Observation Facilities in Luminescence Measurements. *Radiat. Measurements* 37, 535–541. doi:10.1016/s1350-4487(03)00020-9

Bøtter-Jensen, L., Bulur, E., Duller, G., and Murray, A. (2000). Advances in Luminescence Instrument Systems. *Radiat. Measurements*. 32, 523–528. doi:10.1016/s1350-4487(00)00039-1

Bronk Ramsey, C. (2009). Bayesian Analysis of Radiocarbon Dates. *Radiocarbon*. 51 (1), 337–360. doi:10.1017/s0033822200033865

Bronk Ramsey, C. (2016). *The OxCal Program V 4.2*. Oxford: The Oxford Radiocarbon Accelerator Unit, University of Oxford. Available at: https://c14.arch.ox.ac.uk/oxcal/OxCal.html

Caver Bob (2021). *World Longest Caves Compiled by Bob Gulden*. Available at: http://www.caverbob.com/wlong.htm (Accessed February 02, 2021).

Chang, S. J., Blake, R. E., Stout, L. M., and Kim, S. J. (2010). Oxygen Isotope, Micro-textural and Molecular Evidence for the Role of Microorganisms in Formation of Hydroxylapatite in limestone Caves, South Korea. *Chem. Geology.* 276, 209–224. doi:10.1016/j.chemgeo.2010.06.007

Croatian Geological Survey (2009). *Geološka Karta Republike Hrvatske, M 1: 300.000 [Geological Map of the Republic of Croatia, M 1: 300.000—in Croatian].– Hrvatski Geološki Institut*. Zagreb: Zavod za geologiju.

Croatian Mountaineering Association (2021). *List of the Longest Caves in Croatia*. Available at: https://www.hps.hr/specijalisticke-djelatnosti/speleologija/najvece-hrvatske-spilje/ (Accessed February 02, 2021).

Cunningham, A. C., and Wallinga, J. (2012). Realizing the Potential of Fluvial Archives Using Robust OSL Chronologies. *Quat. Geochronol.* 12, 98–106. doi:10.1016/j.quageo.2012.05.007

Czuppon, G., Bočić, N., Buzjak, N., Óvári, M., and Molnár, M. (2018). Monitoring in the Barać and Lower Cerovačka Caves (Croatia) as a Basis for the Characterization of the Climatological and Hydrological Processes that Control Speleothem Formation. *Quat. Int.* 494, 52–65. doi:10.1016/j.quaint.2018.02.003

Diedrich, C. G. (2012). Cave bear Killers and Scavengers from the Last Ice Age of central Europe: Feeding Specializations in Response to the Absence of mammoth Steppe Fauna from Mountainous Regions. *Quat. Int.* 255, 59–78. doi:10.1016/j.quaint.2011.06.048

Durn, G. (2003). Terra Rossa in the Mediterranean Region: Parent Materials, Composition and Origin. *Geol. Croat.* 56 (1), 83–100. doi:10.4154/GC.2003.06

Durn, G., Aljinović, D., Crnjaković, M., and Lugović, B. (2007). "Chapter 28 Heavy and Light Mineral Fractions Indicate Polygenesis of Extensive Terra Rossa Soils in Istria, Croatia," in *"Heavy and Light mineral Fractions Indicate Polygenesis of Extensive Terra Rossa in Istria, Croatia" in: Heavy Minerals in Use*. Editors M. A. Mange and D. T. Wrigt (Amsterdam: Elsevier), 701–737. doi:10.1016/s0070-4571(07)58028-3

Durn, G., Ćorić, R., Tadej, N., Barudžija, U., Rubinić, V., and Husnjak, S. (2014). Bulk and clay mineral Composition Indicate Origin of Terra Rossa Soils in Western Herzegovina. *Geol. Cro* 67 (3), 171–183. doi:10.4154/GC.2014.13

Durn, G., Wacha, L., Bartolin, M., Rolf, C., Frechen, M., Tsukamoto, S., et al. (2018). Provenance and Formation of the Red Palaeosol and Lithified Terra Rossa-like Infillings on the Island of Susak: A High-Resolution and Chronological Approach. *Quat. Int.* 494, 105–129. doi:10.1016/j.quaint.2017.11.040

Fairchild, I. J., Smith, C. L., Baker, A., Fuller, L., Spötl, C., Mattey, D., et al. (2006). Modification and Preservation of Environmental Signals in Speleothems. *Earth-Science Rev.* 75 (1–4), 105–153. doi:10.1016/j.earscirev.2005.08.003

Filipčić, A. (1998). Klimatska Regionalizacija Hrvatske Po W. Köppenu Za Standardno Razdoblje 1961.-1990. U Odnosu Na Razdoblje 1931–1960 [Climatic Regionalization of Croatia According to W. Köppen for the Standard Period 1961-1990 in Relation to the Period 1931–1960—in Croatian, with English Summary]. *Acta Geographica Croatica* 34, 1–15.

Ford, D., and Williams, P. (2007). *Karst Hydrogeology and Geomorphology*. Chichester: John Wiley & Sons. doi:10.1002/9781118684986

Fornós, J., Ginés, J., Gràcia, F., Merino, A., Gómez-Pujol, L., and Bover, P. (2014). Cave deposits and sedimentary processes in Cova des Pas de Vallgornera (Mallorca, Western Mediterranean). *Ijs.* 43, 159–174. doi:10.5038/1827-806X.43.2.5

Galbraith, R. F., Roberts, R. G., Laslett, G. M., Yoshida, H., and Olley, J. M. (1999). Optical Dating of Single and Multiple Grains of Quartz from Jinmium Rock Shelter, Northern Australia: Part I, Experimental Design and Statistical Models. *Archaeometry*. 41, 339–364. doi:10.1111/j.1475-4754.1999.tb00987.x

García, J.-L., Maldonado, A., de Porras, M. E., Nuevo Delaunay, A., Reyes, O., Ebensperger, C. A., et al. (2019). Early Deglaciation and Paleolake History of Río Cisnes Glacier, Patagonian Ice Sheet (44°S). *Quat. Res.* 91, 194–217. doi:10.1017/qua.2018.93

Gascoyne, M. (1992). Palaeoclimate Determination from Cave Calcite Deposits. *Quat. Sci. Rev.* 11, 609–632. doi:10.1016/0277-3791(92)90074-I

Georgiadis, I., Chatzopoulou, K., Kantiranis, N., Ioakeimidis, I., and Tsirambides, A. (2019). Petrography and Provenance of Floor Sediments from the Loutra Almopias Cave (Pella, Macedonia, Greece). *Int. J. Speleology*. 48, 237–248. doi:10.5038/1827-806X.48.3.2271

Ghenciu, M. (2017). Clay Minerals in Caves from Northwestern Oltenia, Muzeul Olteniei Craiova. Oltenia. Studii Şi Comunicări. *Ştiinţele Naturii*. 33 (1), 39–47.

Grimm, E. C. (1991). *TILIA and TILIA·GRAPH Computer Programs*. Springfield: Illinois State Museum.

Haddad-Martim, P. M., Hubbe, A., Giannini, P. C. F., Auler, A. S., Piló, L. B., Hubbe, M., et al. (2017). Quaternary Depositional Facies in Cave Entrances and Their Relation to Landscape Evolution: The Example of Cuvieri Cave, Eastern Brazil. *Catena*. 157, 372–387. doi:10.1016/j.catena.2017.05.029

Häuselmann, Ph. (2011). UIS Mapping Grades. *Int. J. Speleology*. 40, IV–VI. doi:10.18273/rev.medicasuis

Häuselmann, P., Mihevc, A., Pruner, P., Horáček, I., Čermák, S., Hercman, H., et al. (2015). Snežna Jama (Slovenia): Interdisciplinary Dating of Cave Sediments and Implication for Landscape Evolution. *Geomorphology*. 247, 10–24. doi:10.1016/j.geomorph.2014.12.034

HIGH SCORE PLUS (2016). *VERSION 4.5 (4.5.0.22741)*. Netherlands: PANalytical B.V. Almeo.

Hill, C. A. (1999). Sedimentology and Paleomagnetism of Sediments, Kartchner Caverns, Arizona. *J. Cave Karst Stud.* 61, 79–83.

Hill, C. A., and Forti, P. (1997). *Cave minerals of the world (2nd ed.)*. (Huntsville, Alabama: National Speleological Society), 464.

Horvatinčić, N., Krajcar Bronić, I., and Obelić, B. (2003). Differences in the ^{14}C Age, $\delta^{13}C$ and $\delta^{18}O$ of Holocene Tufa and Speleothem in the Dinaric Karst. *Palaeogeogr. Palaeoclimatol. Palaeoecol.* 193, 139–157. doi:10.1016/S0031-0182(03)00224-4

Hua, Q., Cook, D., Fohlmeister, J., Penny, D., Bishop, P., and Buckman, S. (2017). Radiocarbon Dating of a Speleothem Record of Paleoclimate for Angkor, Cambodia. *Radiocarbon*. 59 (6), 1873–1890. doi:10.1017/RDC.2018.1310.1017/rdc.2017.115

Hughes, P. D., and Woodward, J. C. (2009). "Glacial and Periglacial Environments," in *The Physical Geography of the Mediterranean*. Editor J. C. Woodward (Oxford University Press), 353–383.

Huntley, D., and Baril, M. (1997). The K Content of the K-Feldspars Being Measured in Optical and Thermoluminescence Dating. *Ancient TL*. 15, 11–13.

Huntley, D. J., and Lamothe, M. (2001). Ubiquity of Anomalous Fading in K-Feldspars and the Measurement and Correction for it in Optical Dating. *Can. J. Earth Sci.* 38, 1093–1106. doi:10.1139/e01-013

Iacoviello, F., and Martini, I. (2012). Provenance and Geological Significance of Red Mud and Other Clastic Sediments of the Mugnano Cave (Montagnola Senese, Italy). *Ijs*. 41, 317–328. doi:10.5038/1827-806x.41.2.17

Ivanović, A., Sakač, K., Marković, S., Sokač, B., Šušnjar, M., Nikler, L., et al. (1973). *Osnovna Geološka Karta SFRJ 1:100000, List Obrovac L33-140 [Basic Geological Map in Scale of 1:100,000 - Sheet Obrovac L33-140 - in Croatian]. Institut Za Geološka Istraživanja, Zagreb (1962-1967)*. Beograd: Savezni geološki institut.

Ivanović, A., Sakač, K., Marković, S., Sokač, B., Šušnjar, M., Nikler, L., et al. (1976). *Osnovna Geološka Karta SFRJ 1:100000, Tumač Za List Obrovac L33-140 [Guide for Basic Geological Map in Scale of 1:100,000 - Sheet Obrovac L33-140 - in Croatian]. Institut Za Geološka Istraživanja (1962-1967)*. Zagreb: Savezni geološki zavod, Beograd.

Kastelic, V., and Carafa, M. M. C. (2012). Fault Slip Rates for the Active External Dinarides Thrust-and-fold belt. *Tectonics*. 31, 33–39. doi:10.1029/2011TC003022

Korbar, T. (2009). Orogenic Evolution of the External Dinarides in the NE Adriatic Region: a Model Constrained by Tectonostratigraphy of Upper Cretaceous to Paleogene Carbonates. *Earth-Science Rev.* 96 (4), 296–312. doi:10.1016/j.earscirev.2009.07.004

Krajcar Bronić, I., Horvatinčić, N., Sironić, A., Obelić, B., Barešić, J., and Felja, I. (2010). A New Graphite Preparation Line for AMS 14C Dating in the Zagreb Radiocarbon Laboratory. *Nucl. Instr. Methods Phys. Res. B*. 268, 943–946. doi:10.1016/j.nimb.2009.10.070

Krajcar Bronić, I., Horvatinčić, N., Srdoč, D., and Obelič, B. (1986). On the Initial ^{14}C Activity in Karst Aquifers with Short Mean Residence Time. *Radiocarbon*. 28, 436–440. doi:10.1017/S0033822200007566

Krajcar Bronić, I., Horvatinčić, N., Srdoč, D., and Obelič, B. (1992). Experimental Determination of the 14C Initial Activity of Calcareous Deposits. *Radiocarbon* 34, 593–601.

Kreutzer, S., Schmidt, C., Fuchs, M., Dietze, M., and Fuchs, M. (2012). Introducing an R Package for Luminescence Dating Analysis. *Ancient TL*. 30, 1–8. doi:10.1007/springerreference_77324

Krklec, K., Domínguez-Villar, D., and Perica, D. (2015). Depositional Environments and Diagenesis of a Carbonate till from a Quaternary Paleoglacier Sequence in the Southern Velebit Mountain (Croatia). *Palaeogeogr. Palaeoclimatol. Palaeoecol.* 436, 188–198. doi:10.1016/j.palaeo.2015.07.004

Krumm, S. (1994). Centrifuge, Erlangen. Available at: http://www.ccp14.ac.uk/ccp/web-mirrors/krumm/html/software/winsoft.html.

Kuhta, M., and Stroj, A. (2005). "The Speleogenesis of the Caves in Crnopac Mt. Area," in *Proceeding. 14th International Congress of Speleology*. Editor C. Petreas Athens, Greece, 46–48.

Kulig, G. (2005). *Erstellung einer Auswertesoftware zur Altersbestimmung mittels Lumineszenzverfahren unter spezieller Berücksichtigung des Einflusses radioaktiver Ungleichgewichte in der 238U-Zerfallsreihe. 35 p., B.Sc. thesis*. Freiberg: Technische Universität Bergakademie Freiberg.

Kurtén, B. (1958). Life and Death of the Pleistocene Cave Bear. *Acta Zoologica Fennica*. 95, 1–59.

Kurtén, B. (1968). *Pleistocene Mammals of Europe*. London: Weidenfeld and Nicolson. doi:10.4324/9781315126470

Leroy, S. A. G., Marret, F., Gibert, E., Chalié, F., Reyss, J.-L., and Arpe, K. (2007). River Inflow and Salinity Changes in the Caspian Sea during the Last 5500 Years. *Quat. Sci. Rev.* 26, 3359–3383. doi:10.1016/j.quascirev.2007.09.012

Longin, R. (1971). New Method of Collagen Extraction for Radiocarbon Dating. *Nature*. 230, 241–242. doi:10.1038/230241a0

Lowe, J. J., and Walker, M. J. C. (1997). *Reconstructing Quaternary Environments*. 2nd ed. London: Routledge, 468. doi:10.4324/9781315844312

Lüthgens, C., Böse, M., and Preusser, F. (2011). Age of the Pomeranian Ice-Marginal Position in Northeastern Germany Determined by Optically Stimulated Luminescence (OSL) Dating of Glaciofluvial Sediments. *Boreas* 40, 598–615. doi:10.1111/j.1502-3885.2011.00211.x

Lüthgens, C., Neuhuber, S., Grupe, S., Payer, T., Peresson, M., and Fiebig, M. (2017). Geochronological Investigations Using a Combination of Luminescence and Cosmogenic Nuclide Burial Dating of Drill Cores from the Vienna Basin. *zdgg* 168, 115–140. doi:10.1127/zdgg/2017/0081

Lyman, R. L. (1994). *Vertebrate Taphonomy*. Cambridge: Cambridge University Press. doi:10.1017/CBO9781139878302

Malez, M. (1958). Cerovačke Pećine—Najveće U Hrvatskoj [Cerovačke Caves - the Largest in Croatia - in Croatian]. *Priroda*. 45, 6.

Malez, M. (1956). Explorationes recentes des cavernes eu Croatie [Recent explorations of caves in Croatia - in French]. *Acta geologica* 1, 149.

Malez, M. (1965a). Nalazišta Fosilnih Hominida U Hrvatskoj [Fossil Hominid Sites in Croatia - in Croatian]. *Geološki vjesnik* 18, 2.

Malez, M. (1965b). *Cerovačke Pećine [Cerovačke Caves - in Croatian]*. Zagreb: Izdanja Speleološkog društva Hrvatske, 1.

Malez, M. (1960a). *Paleontološka Istraživanja I Speleološka Rekognosciranja U 1959 Godini [Paleontological Research and Speleological Reconnaissance in 1959 - in Croatian]*. Zagreb: Ljetopis JAZU, 66.

Malez, M. (1960b). Rad Na Speleološkom Istraživanju U Hrvatskoj [Work on Speleological Research in Croatia - in Croatian]. *Ljetopis JAZU*. 64, 289–307.

Mange, M. A., and Maurer, H. F. W. (1992). *Heavy Minerals in Colour*. (London: Chapman and Hall), 151.

Marjanac, T., and Marjanac, L. (2016). The Extent of Middle Pleistocene Ice Cap in the Coastal Dinaric Mountains of Croatia. *Quat. Res.* 85 (3), 445–455. doi:10.1016/j.yqres.2016.03.006

Marković, J., Bočić, N., and Pahernik, M. (2016). Prostorni Raspored I Gustoća Ponikva Jugoistočnog Velebita [Spatial Distribution and Density of Dolines in the southeastern Velebit Area - in Croatian and English]. *Geoadria*. 20/1, 1–28. doi:10.15291/geoadria.23

Marom, A., McCullagh, J. S. O., Higham, T. F. G., and Hedges, R. E. M. (2013). Hydroxyproline Dating: Experiments on the 14C Analysis of Contaminated and Low-Collagen Bones. *Radiocarbon*. 55 (2), 698–708. doi:10.1017/S0033822200057854

Martini, I. (2011). Cave Clastic Sediments and Implications for Speleogenesis: New Insights from the Mugnano Cave (Montagnola Senese, Northern Apennines, Italy). *Geomorphology*. 134 (3–4), 452–460. doi:10.1016/j.geomorph.2011.07.024

Mejdahl, V. (1979). Thermoluminescence Dating: Beta-Dose Attenuation in Quartz Grains. *Archaeometry* 21, 61–72. doi:10.1111/j.1475-4754.1979.tb00241.x

Mihevc, A. (2001). *Speleogeneza Divaškega Krasa [*The Speleogenesis Of the Divača Karst—*in Slovenian]*. Ljubljana: – Založba ZRC, 180.

Miko, S., Kuhta, M., and Kapelj, S. (2001). "Bat Guano Influence on the Geochemistry of Cave Sediments from Modrič Cave, Croatia," in *Proceeding, 13th International Congress of Speleology, 4th Speleological Congress of Latin América and Caribbean, 26th Brazilian Congress of*

Speleology. Editor M. A. Rasteiro (Brazil: SBE – Sociedade Brasileira de Espeleologia), 188–192.

Miracle, P. (1991). Carnivore Dens or Carnivore Hunts? A Review of Upper Pleistocene Mammalian Assemblages in Croatia and Slovenia. *Rad HAZU, knj.* 458, 193–219.

Montanari, A., Fiebig, M., Lomax, J., Mainiero, M., Mariani, S., and Lüthgens, C. (2019). "Luminescence Geochronology of Pleistocene Slack Water Deposits in the Frasassi Hypogenic Cave System, Italy," in *250 Million Years of Earth History in Central Italy: Celebrating 25 Years of the Geological Observatory of Coldigioco*. Editors C. Koeberl and D. Bice (New York, NY: Geological Society of America Special Paper), 542, 411–428. doi:10.1130/2019.2542(23)

Moore, D. M., and Reynolds, R. C., Jr. (1997). *X-ray Diffraction and the Identification and Analysis of clay Minerals*. Oxford: Oxford University Press, 378.

Moore, P. D., Webb, J. A., and Collinson, M. (1991). *Pollen Analysis*. second edition. London: Blackwell Sci. Publication, 216.

Murray, A. S., Thomsen, K. J., Masuda, N., Buylaert, J. P., and Jain, M. (2012). Identifying Well-Bleached Quartz Using the Different Bleaching Rates of Quartz and Feldspar Luminescence Signals. *Radiat. Measurements*. 47, 688–695. doi:10.1016/j.radmeas.2012.05.006

Neuhuber, S., Plan, L., Gier, S., Hintersberger, E., Lachner, J., Scholz, D., et al. (2021). Numerical Age Dating of Cave Sediments to Quantify Vertical Movement at the Alpine-Carpathian Transition in the Plio- and Pleistocene. *GeolCarp*. 71, 41. doi:10.31577/GeolCarp.71.6.5

Nikler, L. (1973). Novi Prilog Poznavanju Oledbe Velebita [A New Contribution to the Knowledge of the Velebit Mt. Glaciation - in Croatian]. *Geološki Vjesnik* 25, 109–112.

Pacher, M., and Stuart, A. J. (2009). Extinction Chronology and Palaeobiology of the Cave bear (*Ursus Spelaeus*). *Boreas* 38 (2), 189–206. doi:10.1111/j.1502-3885.2008.00071.x

Palmer, A. (1991). Origin and Morphology of limestone Caves. *Geol. Soc. America Bull.* 103, 1–21. doi:10.1130/0016-7606(1991)103<0001:OAMOLC>2.3.CO;2

Paunović, M., Jambrešić, G., Brajković, D., Malez, V., and Mauch Lenardić, J. (1999). Last Glacial Settlement of Croatia: Catalogue of Fossil Sites Dated to the OIS 2&3. *Acta Geologica*. 26/2, 27–70.

PDF-4/Minerals (2020). *International Centre for Diffraction Data. SN: MIND 200133-4545*. Berlin: Springer.

Prelogović, E. (1975). Neotektonska Karta SR Hrvatske [Neotectonic Map of Croatia - in Croatian]. *Geološki vjesnik* 28, 97–108.

Prescott, J. R., and Hutton, J. T. (1994). Cosmic ray Contributions to Dose Rates for Luminescence and ESR Dating: Large Depths and Long-Term Time Variations. *Radiat. Measurements*. 23, 497–500. doi:10.1016/1350-4487(94)90086-8

Prescott, J., and Stephan, L. (1982). The Contribution of Cosmic Radiation to the Environmental Dose for Thermoluminescent Dating - Latitude, Altitude and Depth Dependencies. *PACT*. 6, 17–25.

Preusser, F., Degering, D., Fuchs, M., Hilgers, A., Kadereit, A., Klasen, N., et al. (2008). Luminescence Dating: Basics, Methods and Applications. *E&g Quat. Sci. J.* 57, 95–149. doi:10.3285/eg.57.1-2.5

Rades, E. F., Fiebig, M., and Lüthgens, C. (2018). Luminescence Dating of the Rissian Type Section in Southern Germany as a Base for Correlation. *Quat. Int.* 478, 38–50. doi:10.1016/j.quaint.2016.07.055

Reimann, T., Thomsen, K. J., Jain, M., Murray, A. S., and Frechen, M. (2012). Single-grain Dating of Young Sediments Using the pIRIR Signal from Feldspar. *Quat. Geochronol.* 11, 28–41. doi:10.1016/j.quageo.2012.04.016

Reimer, P. J., Austin, W. E. N., Bard, E., Bayliss, A., Blackwell, P. G., Bronk Ramsey, C., et al. (2020). The IntCal20 Northern Hemisphere Radiocarbon Age Calibration Curve (0-55 Cal kBP). *Radiocarbon*. 62, 725–757. doi:10.1017/RDC.2020.41

Reimer, P. J., Brown, T. A., and Reimer, R. W. (2004). Discussion: Reporting and Calibration of post-bomb ^{14}C Data. *Radiocarbon*. 46 (3), 1299–1304. doi:10.1017/S0033822200033154

Rhodes, E. J. (2011). Optically Stimulated Luminescence Dating of Sediments over the Past 200,000 Years. *Annu. Rev. Earth Planet. Sci.* 39, 461–488. doi:10.1146/annurev-earth-040610-133425

Rudzka, D., McDermott, F., and Surić, M. (2012). A Late Holocene Climate Record in Stalagmites from Modrič Cave (Croatia). *J. Quat. Sci.* 27, 585–596. doi:10.1002/jqs.2550

Sarıkaya, M., Stepišnik, U., Žebre, M., Çiner, A., Yıldırım, C., Vlahović, I., et al. (2020). Last Glacial Maximum Deglaciation of the Southern Velebit Mt. (Croatia): Insights from Cosmogenic 36Cl Dating of Rujanska Kosa. *Mediterr. Geosci. Rev.* 2, 53–64. doi:10.1007/s42990-020-00030-9

Sasowsky, I. D., Šebela, S., and Harbert, W. (2003). Concurrent Tectonism and Aquifer Evolution >100,000 Years Recorded in Cave Sediments, Dinaric Karst, Slovenia. *Env Geol.* 44, 8–13. doi:10.1007/s00254-002-0727-4

Schmid, S. M., Bernoulli, D., Fügenschuh, B., Matenco, L., Schefer, S., Schuster, R., et al. (2008). The Alpine-Carpathian-Dinaridic Orogenic System: Correlation and Evolution of Tectonic Units. *Swiss J. Geosci.* 101, 139–183. doi:10.1007/s00015-008-1247-3

Schultz, L. G. (1964). *Quantitative Interpretation of Mineralogical Composition from X-ray and Chemical Data for the Pierre Shale*. New York, NY: U. S. Geological Survey Professional Paper, 391–C, 31.

Sebag, D., Di Giovanni, C., Ogier, S., Mesnage, V., Laggoun-Défarge, F., and Durand, A. (2006). Inventory of Sedimentary Organic Matter in Modern Wetland (Marais Vernier, Normandy, France) as Source-Indicative Tools to Study Holocene Alluvial Deposits (Lower Seine Valley, France). *Int. J. Coal Geology.* 67, 1–16. doi:10.1016/j.coal.2005.08.002

Sevastjanova, I., Hall, R., and Alderton, D. (2012). A Detrital Heavy mineral Viewpoint on Sediment Provenance and Tropical Weathering in SE Asia. *Sediment. Geology.* 280, 179–194. doi:10.1016/j.sedgeo.2012.03.007

Sironić, A., Krajcar Bronić, I., Horvatinčić, N., Barešić, J., Borković, D., Vurnek, M., et al. (2020). "Carbon Isotopes in Dissolved Inorganic Carbon as Tracers of Carbon Sources in Karst Waters of the Plitvice Lakes, Croatia," in *Stable Isotope Studies of the Water Cycle and Terrestrial Environments*. Editors A. Bojar, A. Pelc, and C. Lecuyer (London: Geological Society of London), 49, 19. doi:10.1144/SP507-2020-49

Sironić, A., Krajcar Bronić, I., Horvatinčić, N., Barešić, J., Obelić, B., and Felja, I. (2013). Status Report on the Zagreb Radiocarbon Laboratory—AMS and LSC Results of VIRI Intercomparison Samples. *Nucl. Instr. Methods Phys. Res. B* 294, 185–188. doi:10.1016/j.nimb.2012.01.048

Sokač, B., Šušnjar, M., Bukovac, J., and Bahun, S. (1976). *Osnovna Geološka Karta SFRJ 1:100000, Tumač Za List Udbina L33-128 [Guide for Basic Geological Map in Scale of 1:100,000 - Sheet Udbina L33-128 - in Croatian]. Institut Za Geološka Istraživanja, Zagreb (1965)*. Beograd: Savezni geološki institut, 62.

Soulet, G., Skinner, L. C., Beaupré, S. R., and Galy, V. (2016). A Note on Reporting of Reservoir 14C Disequilibria and Age Offsets. *Radiocarbon*. 58, 205–211. doi:10.1017/RDC.2015.22

Srdoč, D., Krajcar Bronic, I., Horvatincic, N., and Obelic, B. (1986). The increase of ^{14}C activity of dissolved inorganic carbon along the river course. *Radiocarbon*. 28, 515–521.

Starkey, H. C., Blackmon, P. D., and Hauff, P. L. (1984). The Routine Mineralogical Analysis of Clay-Bearing Samples. *U. S. Geol. Surv. Bull.* 1563, 31.

Stuiver, M., and Polach, H. A. (1977). Discussion Reporting of 14C Data. *Radiocarbon* 19 (3), 355–363. doi:10.1017/S0033822200003672

Surić, M., and Juračić, M. (2010). Late Pleistocene—Holocene Environmental Changes—Records from Submerged Speleothems along the Eastern Adriatic Coast (Croatia). *Geologia Croatica*. 63 (2), 155–169. doi:10.4154/gc.2010.13

Šušnjar, M., Sokač, B., Bahun, S., Bokovac, J., Nikler, L., and Ivanović, A. (1973). *Osnovna Geološka Karta SFRJ 1:100000, List Udbina L33-128 [Basic Geological Map in Scale of 1:100,000—Sheet Udbina L33-128—in Croatian]. Institut Za Geološka Istraživanja, Zagreb (1963-1965)*. Beograd: Savezni geološki institut.

Talaja, M., and Kurečić, T. (2017). Geološka I Geomorfološka Opažanja U Jami Muda Labudova [Geological and Geomorphological Observations in the Muda Labudova Pit—in Croatian]. *Speleolog*. 65 (1), 32–41. Available at: https://hrcak.srce.hr/204711.

Tari, V. (2002). "Evolution of the Northern and Western Dinarides: a Tectonostratigraphic Approach," in *"Evolution of the Northern and Western Dinarides : A Tectonostratigraphic Approach" in Continental Collision and the Tectono-Sedimentary Evolution of Forelands*. Editors G. Bertotti, K. Schulmann, and S. A. P. L. Cloetingh (Germany, Copernicus): Katlenburg-Lindau), 1, 223–236. doi:10.5194/smsps-1-223-2002

Therre, S., Fohlmeister, J., Fleitmann, D., Matter, A., Burns, S. J., Arps, J., et al. (2020). Climate-induced Speleothem Radiocarbon Variability on Socotra Island from the Last Glacial Maximum to the Younger Dryas. *Clim. Past*. 16, 409–421. doi:10.5194/cp-16-409-2020

Tischler, J., Töchterle, P., and Moseley, G. E. (2020). Characterization of Northeast Greenland Cave Sediments. *Cave Karst Sci.* 42, 100–103. doi:10.1016/0277-3791(94)90064-7

Trbojević Vukičević, T., and Babić, K. (2008). Nalazi Kostura Špiljskog Medvjeda (*Ursus Spelaeus*) Iz Cerovačkih Pećina [Finds of the Skeleton of a Cave bear (*Ursus Spelaeus*) from the Cerovac Caves - in Croatian]. *Izdanja Hrvatskog arheološkog društva* 23, 23–27. doi:10.1016/j.quaint.2014.03.046

Trefethen, J. M. (1950). Classification of Sediments. *Am. J. Sci.* 248, 55–62. doi:10.2475/ajs.248.1.55

Tresić Pavičić, D. (2020). Arheološko Istraživanje Donje Cerovačke (Turkaljeve) Špilje [Archaeological Research of the Lower Cerovačka (Turkaljeva) Cave - in Croatian]. *Subterranea Croatica* 18 (29), 60–74.

Tresić Pavičić, D., and Burmaz, J. (2019). *Izvješće O Završetku Arheoloških Istraživanja U Donjoj Cerovačkoj Špilji 2019. Godine [Report on the Completion of Archaeological Research in the Lower Cerovačka Cave in 2019 - in Croatian]*. Zagreb: Kaducej d.o.o., 137.

Tyson, R. V. (1995). *Sedimentary Organic MatterOrganic Facies and Palynofacies*. London: Chapman & Hall, 615.

Valen, V., Lauritzen, S. E., and Lovlie, R. (1997). Sedimentation in a High-Latitude Karst Cave: Sirijordgrotta, Nordland, Norway. *Norsk Geologisk Tidsskrift* 77, 233–250.

Van Geel, B. (2002). "Non-Pollen Palynomorphs,". *Terrestrial, Algal and Silicaceous Indicators*. Editors J. P. Smol, H. J. B. Birks, and W. M. Last (Dordrecht: Kluwer Academic Publishers), Vol. 3, 99–119. doi:10.1007/0-306-47668-1_6

Velde, B., and Meunier, A. (2008). *The Origin of Clay Minerals in Soils and Weathered Rocks*. Berlin Heidelberg: Springer-Verlag, 406. doi:10.1007/978-3-540-75634-7

Velić, J., Velić, I., Kljajo, D., Protrka, K., Škrabić, H., and Špoljar, Z. (2017). A Geological Overview of Glacial Accumulation and Erosional Occurrences on the Velebit and the Biokovo Mts., Croatia. *Mining-Geology-Petroleum Bull.* 32 (4), 77–96. doi:10.17794/rgn.2017.4.8

Wacha, L., Montanari, A., Lomax, J., Fiebig, M., Luthgens, C., Korbar, T., et al. (2019). "Last Glacial Maximum Giant Sand Dunes on the Island of Vis, Croatia," in *250 Million Years of Earth History in Central Italy: Celebrating 25 Years of the Geological Observatory of Coldigioc*. Editors C. Koeberl and D. M. Bice (New York, NY: Geological Society of America Special Paper), 459–470. doi:10.1130/2019.2542(26)

Wacha, L., Rolf, C., Hambach, U., Frechen, M., Galović, L., and Duchoslav, M. (2018). The Last Glacial Aeolian Record of the Island of Susak (Croatia) as Seen from a High-Resolution Grain-Size and Rock Magnetic Analysis. *Quat. Int.* 494, 211–224. doi:10.1016/j.quaint.2017.08.016

Weaver, C. E. (1967). The Distribution and Identification of Mixed-Layer Clays in Sedimentary Rocks. *Am. J. Mineral. Soc.* 41 (3-4), 202–221.

Weaver, C. E. (1989). *Clays, Muds, and Shales*. Amsterdam: Elsevier, 721.

White, E. L. (2019). in *"Chapter 21 - Breakdown" in Encyclopedia of Caves*. Editors W. B. White, D. C. Culver, and T. Pipan. Third Edition (Boston: Elsevier Academic Press), 187–194. doi:10.1016/B978-0-12-814124-3.00020-0

White, W. B. (2007). Cave Sediments and Paleoclimate. *J. cave Karst Stud.* 69 (1), 76–93. doi:10.1007/978-1-4419-9118-8_9

Whitlock, C., and Larsen, C. (2002). "Charcoal as a Fire Proxy," in *Tracking Environmental Change Using Lake Sediments. Developments in Paleoenvironmental Research*. Editors J. P. Smol, H. J. B. Birks, W. M. Last, R. S. Bradley, and K. Alverson (Dordrecht: Springer), Vol. 3, 75–97. doi:10.1007/0-306-47668-1_5

Wintle, A. G. (1973). Anomalous Fading of Thermo-Luminescence in Mineral Samples. *Nature*. 245, 143–144. doi:10.1038/245143a0

Wintle, A. G. (2008). Luminescence Dating: where it Has Been and where it Is Going. *Boreas*. 37, 471–482. doi:10.1111/j.1502-3885.2008.00059.x

Wood, G. D., Gabriel, A. M., and Lawson, J. C. (1996). *"Palynological Techniques: Processing and Microscopy" in Palynology: Principles and Applications*. Editors J. Jansonius and D. C. McGregor (New York, NY: Am. Assoc. Stratigr. Palynol. Found.), 1, 29–50.

Wróblewski, W., Gradzinski, M., Motyka, J., and Stankovic, J. (2017). Recently growing subaqueous flowstones: Occurrence, petrography, and growth conditions. *Quat. Int.* 437, 84–97. doi:10.1016/j.quaint.2016.10.006

Zhang, J., Rolf, C., Wacha, L., Tsukamoto, S., Durn, G., and Frechen, M. (2018). Luminescence Dating and Palaeomagnetic Age Constraint of a Last Glacial Loess-Palaeosol Sequence from Istria, Croatia. *Quat. Int.* 494, 19–33. doi:10.1016/j.quaint.2018.05.045

Zupan Hajna, N., Bosák, P., Pruner, P., Mihevc, A., Hercman, H., and Horáček, I. (2020). Karst Sediments in Slovenia: Plio-Quaternary Multi-Proxy Records. *Quat. Int.* 546, 4–19. doi:10.1016/j.quaint.2019.11.010

Zupan Hajna, N. (2019). "Dinaric Karst-Geography and Geology," in *"Chapter 40 - Dinaric Karst—Geography and Geology" in Encyclopedia of Caves*. Editors W. B. White, D. C. Culver, and T. Pipan. Third Edition (Boston: Elsevier Academic Press), 353–362. doi:10.1016/B978-0-12-814124-3.00039-X

Zupan Hajna, N., Mihevc, A., Bosák, P., Pruner, P., Hercman, H., Horáček, I., et al. (2021). Pliocene to Holocene Chronostratigraphy and Palaeoenvironmental Records from Cave Sediments: Račiška Pečina Section (SW Slovenia). *Quat. Int.* in press. doi:10.1016/j.quaint.2021.02.035

Conflict of Interest: Author DP, was employed by the company Kaducej d.o.o.

The remaining authors declare that the research was conducted in the absence of any commercial or financial relationships that could be construed as a potential conflict of interest.

frontiers in Earth Science

ORIGINAL RESEARCH
published: 27 August 2021
doi: 10.3389/feart.2021.642667

Morpho-Mineralogical and Bio-Geochemical Description of Cave Manganese Stromatolite-Like Patinas (Grotta del Cervo, Central Italy) and Hints on Their Paleohydrological-Driven Genesis

Simone Bernardini[1], Fabio Bellatreccia[1,2], Andrea Columbu[3], Ilaria Vaccarelli[4], Marika Pellegrini[4], Valme Jurado[5], Maddalena Del Gallo[4], Cesareo Saiz-Jimenez[5], Armida Sodo[1], Christian Millo[6], Luigi Jovane[6] and Jo De Waele[3]*

[1]Dipartimento di Scienze, Università Roma Tre, Roma, Italy, [2]Istituto Nazionale di Fisica Nucleare – Laboratori Nazionali di Frascati (INFN-LNF), Frascati (Roma), Italy, [3]Dipartimento di Scienze Biologiche, Geologiche e Ambientali, Università di Bologna, Bologna, Italy, [4]Dip. MeSVA, Sezione di Scienze Ambientali, Università dell'Aquila, L'Aquila, Italy, [5]Instituto de Recursos Naturales y Agrobiologia (IRNAS-CSIC), Sevilla, Spain, [6]Instituto Oceanográfico, Universidade de São Paulo, São Paulo, Brazil

OPEN ACCESS

Edited by:
Aurel Persoiu, Emil Racovita Institute of Speleology, Romania

Reviewed by:
Laura Rosales-Lagarde, Nevada State College, United States
Cristina Purcarea, Institute of Biology Bucharest of the Romanian Academy, Romania

***Correspondence:**
Simone Bernardini
simone.bernardini@uniroma3.it

Specialty section:
This article was submitted to Sedimentology, Stratigraphy and Diagenesis, a section of the journal Frontiers in Earth Science

Received: *16 December 2020*
Accepted: *30 July 2021*
Published: *27 August 2021*

Citation:
Bernardini S, Bellatreccia F, Columbu A, Vaccarelli I, Pellegrini M, Jurado V, Del Gallo M, Saiz-Jimenez C, Sodo A, Millo C, Jovane L and De Waele J (2021) Morpho-Mineralogical and Bio-Geochemical Description of Cave Manganese Stromatolite-Like Patinas (Grotta del Cervo, Central Italy) and Hints on Their Paleohydrological-Driven Genesis. Front. Earth Sci. 9:642667. doi: 10.3389/feart.2021.642667

Caves are dark subsurface environments with relatively constant temperatures that allow studying bio-mineralization processes and paleoenvironmental or climate changes in optimal conditions. In the extreme and oligotrophic cave environment, manganese patinas having stromatolite-like features are uncommon. Here we provide the first detailed mineralogical, geochemical, and microbiological investigation of fine-grained and poorly crystalline MnFe stromatolite-like wall patinas formed in a deep-cave environment in Italy. These mineralizations, about 3 mm thick, consist of an alternation of Mn-layers and Fe-lenses. We show that the microbial communities' composition is dominated by Mn-oxidizing bacteria, such as *Bacillus*, *Flavobacterium*, and *Pseudomonas*. Our multidisciplinary investigation, integrating data from different analytical techniques (*i.e.,* optical microscopy, SEM-EDS, μXRF, XRPD, FT-IR, Raman spectroscopy, and DNA sequencing), revealed peculiar chemical, mineralogical, and biological features: 1) A cyclical oscillation of Mn and Fe along the growth of the patinas. We propose that this oscillation represents the shift between oxic and suboxic conditions related to different phases occurring during paleo-flood events; 2) A typical spatial distribution of mineralogy and oxidation state of Mn, bacterial imprints, detrital content, and stromatolite-like morphologies along the Mn-layers. We propose that this distribution is controlled by the local hydraulic regime of the paleo-floods, which, in turn, is directly related to the morphology of the wall surface. Under less turbulent conditions, the combination of clay mineral catalysis and biological oxidation produced vernadite, a poor-crystalline phyllomanganate with a low average oxidation state of Mn, and branched columnar stromatolite-like morphologies. On the other hand, under more turbulent conditions, the sedimentation of clay minerals and microbial communities' development are both inhibited. In this local environment, a lower oxidation rate of

Mn^{2+} favored the formation of todorokite and/or ranciéite, two compounds with a high average oxidation state of Mn, and flat-laminated or columnar stromatolite-like morphologies.

Keywords: cave deposits, karst system, MnFe patinas, bio-mineralization, biogeochemical processes, paleoenvironmental changes

INTRODUCTION

Manganese oxides/hydroxides/oxyhydroxides (hereafter MnOx) are important geomaterials, widespread in terrestrial and Martian geological records, and related to hydrothermal activity, authigenesis or sedimentary/weathering processes (Roy et al., 1997; Lanza et al., 2014, 2016; Arvidson et al., 2016). In natural environments, the mineralogy and oxidation state of Mn are strongly controlled by ambient conditions (*e.g.,* pH, Eh, ionic strength, and microbial activity). MnOx crystal structures result from the linkage of MnO_6 octahedra forming channel or layered structures, in which Mn occurs under different oxidation states (*e.g.*, Mn^{2+}, Mn^{3+}, and Mn^{4+}) (Post, 1999). MnOx occur typically as poorly crystalline material and mixtures of different Mn-compounds with Fe oxides/hydroxides, silicates, and carbonates; thus, their characterization by standard methods, such as X-ray powder diffraction (XRPD), is extremely challenging and not always conclusive. For instance, X-ray patterns are characterized by broad and weak reflections of MnOx, which can be easily overlapped by the stronger reflections of the intermixed silicates and carbonates. Spectroscopic techniques, such as Fourier-Transform Infrared (FT-IR) and Raman spectroscopy, sensitive to short-range metal-oxygen arrangements, provide a valuable tool for characterizing MnOx. Raman spectroscopy, in particular, is a very powerful technique to characterize MnOx, being suitable for disordered and/or poorly crystalline materials (Bernardini et al., 2019). In some cases, all these techniques need to be used to characterize such disordered and cryptocrystalline mixtures properly. Moreover, Raman spectroscopy is useful also for the microanalysis of the oxidation state of Mn in MnOx at sub-micrometric spatial resolution (Bernardini et al., 2020a).

MnFe mineral deposits in caves are well known (Hill and Forti, 1997, and references therein). Gázquez et al. (2011) described two types of MnFe occurrences in caves: 1) MnFe minerals deposited by running water, with no weathering of the underlying substratum, and 2) deposits linked to weathering of the host rock. The latter, relatively scarce in caves, was found in Sima de la Higuera Cave (Spain) and other hypogenic caves such as Spider Cave, Lechuguilla Cave, Jewel Cave, and Wind Cave (United States). Generally, these deposits consist of MnOx associated with Fe oxides/hydroxides and detrital or authigenic minerals, such as quartz and clay minerals. They occur as black crusts or patinas coating the walls of the caves and the stream clasts, as stains on speleothems, or as black sedimentary fill deposits (Hill and Forti, 1997). Accordingly, a multimethodological approach is necessary to characterize such disordered and cryptocrystalline mixtures properly. In the last decades, several authors have investigated the mineralogy of MnOx in caves by using different analytical techniques. Northup et al. (2000) identified todorokite from the Lechuguilla and Spider Caves (New Mexico, USA) by SEM-EDS and TEM. The same result was obtained by Cunningham et al. (1995) using SEM-EDS and XRPD. Spilde et al. (2005), integrating SEM-EDS, XRF, XRPD, and TEM results, identified todorokite and lithiophorite. Carmichael et al. (2013a), combining SEM-EDS, single-crystal micro-XRD, and FT-IR data, identified buserite and todorokite in the Carter Saltpeter Cave system, Tennessee (USA). Frierdich et al. (2011) identified birnessite and buserite from the Pautler Cave, Illinois (USA) by SEM-EDS and XRPD. White et al. (2009) studied the mineralogy of Mn-coatings in 15 caves in the United States by combining SEM-EDS, XRPD, and FT-IR data. Still, the low crystallinity of MnOx, together with other impurities, prevented proper phase(s) identification by XRPD. These authors have only attempted to assign the FT-IR spectra to different phases, such as birnessite, romanèchite, ranciéite, and pyrolusite. Papier et al. (2011), even though combining SEM-EDS, XRPD, FT-IR, and Raman spectroscopy data could not obtain a conclusive phase determination of samples from the Azé Cave, Saône-et-Loire (France). Gázquez et al. (2011) identified birnessite and goethite by XRD in black MnFe crusts from speleothems of El Soplao Cave (Spain). Rossi et al. (2010), investigating the same mineralizations by XRD and FT-IR, identified hausmannite, birnessite, ranciéite, and goethite.

In many natural environments, bacteria and fungi catalyze the oxidation of Mn^{2+} and the formation of poorly crystalline $Mn^{3+/4+}$ oxides, with an average oxidation state of Mn commonly higher than 3.4 (Tebo et al., 2004). Andrejchuk and Klimchouk (2001) and Kotula et al. (2019) described MnFe sediments from Zoloushka Cave (Ukraine/Moldova), whose formation may have been mediated by heterotrophic and autotrophic bacteria (Kotula et al., 2019). Fonollá et al. (2020) described MnFe crusts from Majada del Cura Cave (Spain). They consist of Fe oxides/hydroxides (the predominant mineral is goethite), MnOx, and silicate minerals. These authors related the formation of these crusts to the subterranean river's hydrogeomorphological evolution and bacterial activity. Rossi et al. (2010) described MnOx stromatolites in El Soplao Cave (Spain). These mineralizations show well preserved fossils of Mn-oxidizing bacteria, including genera as *Hyphomicrobium*, *Pedomicrobium*, and *Caulobacter*, which underwent low diagenetic alteration thanks to the relatively high accretion rates of the MnOx stromatolites (Lozano and Rossi, 2012). Gradziński et al. (1995) described biogenic Mn flowstones from Jaskinia Czarna Cave (Poland). These mineralizations consist of amorphous MnOx and are characterized by a dome-like structure and a high Mn/Fe ratio

(~72). Northup et al. (2003) investigated MnFe deposits in Lechuguilla and Spider caves to assess which biotic factors may be involved in their formation and study the microbial community's nature thriving in the deposits. These authors identified the presence of bacteria whose closest relatives are Fe- and Mn-oxidizing/reducing bacteria, including *Hyphomicrobium, Pedomicrobium, Leptospirillum, Stenotrophomonas*, *Pantoea* genera, in addition to representative of the *Crenarchaeota* and *Euryarchaeota* archaeal phyla. However, the extent to which Fe- and Mn-oxidizing bacteria contribute to the production of MnFe deposits in these caves is still not fully understood.

In the last decades, the role of a few bacteria in the production of MnOx was investigated in detail (Villalobos et al., 2003; Tebo et al., 2005; Spiro et al., 2010). Carmichael et al. (2015) reviewed the role of Mn-oxidizing microorganisms in caves and concluded that bacteria and fungi produced MnOx minerals, which are typically dark brown to black, and poorly crystalline, with birnessite or todorokite crystal structures. These authors reported several bacterial strains, included in the genera *Flavobacterium, Bacillus, Pseudomonas, Hyphomicrobium, Pedomicrobium, Leptothrix,* and *Pantoea*, among others. In addition, based on TEM, FE-SEM, X-ray microanalysis, and FT-IR, Saiz-Jimenez et al. (2012) proved the biogenic deposition of birnessite by the fungus *Acremonium nepalense* on the clayey sediments of Lascaux Cave.

A fundamental geochemical property of Mn is its high redox sensitivity. Compared to Fe compounds, MnOx are stable only under basic pH conditions (>8), except at high Eh (>600 mV) (Hem, 1963, 1972). Therefore, the presence/absence of Fe and Mn minerals allows recognizing different redox environments (Berner, 1981). Because of the different redox-sensitive behaviour of Mn and Fe, the Mn/Fe ratio can be successfully used to reconstruct changing redox conditions, being lower ratios related to lower O_2 concentrations in the water system (Naeher et al., 2013 and references therein). Accordingly, MnFe mineralizations can be successfully used as paleo-redox indicators to reconstruct environmental and climate changes in the geological past, in cave (see Gázquez et al., 2011), oceanic (Hein et al., 2017; Benites et al., 2018; Robertson et al., 2019; Cornaggia et al., 2020), and lake environments (Naeher et al., 2013). Moreover, because of their high specific surface area (~300 m^2/g) and low point of zero charge (PZC < 3) MnOx strongly control the mobility and availability of rare earth elements and heavy metals in aqueous systems (McKenzie, 1980; Oscarson et al., 1983; Koschinsky and Halbach, 1995). Cave secondary deposits offer the opportunity to investigate past hydrological changes, at times demonstrating climate forcing (Fairchild et al., 2006). Accordingly, numerous studies have been carried from northern (Frisia et al., 2005; Zanchetta et al., 2007; Drysdale et al., 2009; Belli et al., 2013; Columbu et al., 2018; Regattieri et al., 2019) to central (Vanghi et al., 2018), southern (Columbu et al., 2020) and insular (Frisia et al., 2006; Columbu et al., 2017, 2019) Italy. Indeed, with constant temperature and absence of light, cave environments offer ideal conditions to study various topics, like paleo-environmental and climate change, the origin and evolution of life, and bio-mineralization processes, among others. However, the study of the hydrological, environmental and climate significance of speleothems other than stalagmites and flowstones in Italy is still underrepresented compared to other countries (Hill and Forti, 1997).

This work aims to provide the first mineralogical, geochemical, and microbiological investigation of fine-grained and poorly crystalline MnFe cave-wall stromatolite-like patinas from a deep-cave environment in Italy. Our multimethodological approach, integrating optical microscopy, SEM-EDS, μXRF, XRPD, FT-IR, and Raman spectroscopy results, allowed a proper phases identification, investigate the microscale spatial distribution of the different minerals, the oxidation state of Mn, microbial imprints, morphological features, and variation in the Mn/Fe ratio along the accumulation direction. A preliminary assessment of the microbial ecology was carried out through DNA sequencing of the uncultured prokaryotic community 16S rRNA gene pool. We used this large multimethodological dataset to explore the significance of MnFe-deposits as paleohydrological indicators.

GEOLOGICAL SETTING OF THE STUDY AREA

The studied samples of MnFe patinas were collected in the *Grotta del Cervo* cave (also known as *Grotta Grande dei Cervi*) (Central Italy, Carsoli, L'Aquila, see **Figure 1** and **Supplementary Figure S1**). The cave, with the nearby sinking stream *Grotta dell'Ovito di Pietrasecca* and spring *Risorgenza di Vena Cionca* (**Figure 1**), is part of the Pietrasecca karst system, which hosts one of the most typical "through caves" in the Central Apennines. In particular, the *Grotta del Cervo* cave represents the paleosink of the karst system, which is now active with the *Grotta dell'Ovito di Pietrasecca* (Agostini and Piccini, 1994). The cave entrance is located at 42°08′09.136″ N, 13°07′ 43.558″ E, at an altitude of 858 m above sea level. The cave system has an overall height difference of 107 m (+6/−113 m) and a development of 1875 m.

The Pietrasecca karst system is located in the central portion of the Carseolani Mts. (Central Apennines), about 50 km NE of Rome. This area is characterized by pre-orogenic Meso-Cenozoic shallow-water carbonates, belonging to the Latium-Abruzzi carbonate platform (limestones with rudists, and limestones with bryozoa and red algae), which are overlain by Late Miocene synorogenic deposits related to an Apennine foredeep basin (Orbulina marls, and Argilloso-arenacea Fm.) (**Figure 1**) (Cosentino et al., 1997, and references therein). This portion of the Carseolani Mts., trending from NW to SE, is bounded by a set of faults trending NE-SW (Agostini and Piccini, 1994). The caves are developed along some sets of fractures, transversally to the ridge, and they are prevalently vadose in their morphologies. They show a strong erosive activity linked to high water flow associated with high solid transport (Agostini and Piccini, 1994). Seismic activity controlled the evolution of the Pietrasecca karst system during the last 350 Ky (Postpischl et al., 1991). Earthquakes caused changes in the groundwater circulation and physicochemical conditions, which affect the color,

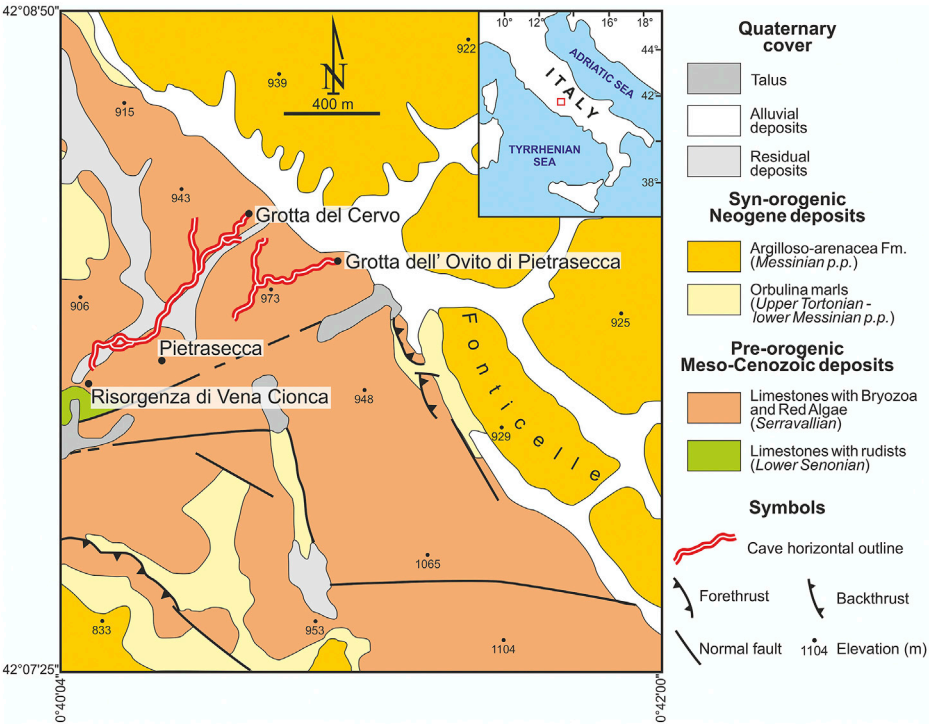

FIGURE 1 | Geological map of the study area, redrawn from Cosentino et al. (1997).

crystallinity, mineralogy, and textural features of carbonate speleothems. For instance, the last generation of carbonate speleothems in the *Grotta del Cervo* started growing after the December 1456 earthquake (the largest historical known earthquake occurred in peninsular Italy) (Postpischl et al., 1991). Black MnFe patinas are widespread in the deepest and active cave section (Forti, 1994), characterized by a strong ancient erosive activity. These patinas are occasionally submerged today by the increase of the underground river level during flooding, but only in response to periods of heavy rain. MnFe deposits can also be observed inside the *Grotta dell'Ovito di Pietrasecca,* and in general, where the hydrogeological and morphological conditions are similar to those of the deepest section of the *Grotta del Cervo*.

SAMPLE COLLECTION AND EXPERIMENTAL METHODS

Black patinas coat the walls of *Grotta del Cervo*, especially in the presence of streams and water pools. A total of six samples were collected from the patinas covering the walls of the cave, in the section of the cave named "*Fiume di Fango*", 1 km from the entrance and at an altitude of ca. 810 m asl, about 1 m above the water level (see **Supplementary Figures S1, S2**). In this area, characterized by mud on the floor, the patinas are continuous black coatings that extend from a few tens of centimeters to a few meters above the average water level. These mineralizations occur more frequently as patchy coatings on the areas sheltered from the water current by the irregularities of the walls (scallops, solution pockets, pendants, and echinoliths). In this part of the cave, the pH of water is 7.1, temperature is nearly constant throughout the year (~8 °C) with relative humidity close to saturation (97.7%). For biological analysis, five replications of the black patinas were scraped off the mud coating, and collected in sterile tubes containing RNAlater and kept in cold storage until the arrival in the laboratory, then stored at -80°C. Another sample (named GC), about 3 mm thick, consisting of black layers and brown lenses (**Figure 2**), was also collected for mineralogical and elemental characterizations (see **Supplementary Figure S2**). For this purpose, a polished cross-section (prepared by impregnating the sample with epoxy resin to maintain its integrity during the polishing operation) was used for punctual SEM-EDS, μXRF, and Raman analyses (**Figure 2**). Finally, material from a black layer (GC1) and a brown detrital lens (GC2) (see **Figure 2** for the position on the sample) was carefully extracted by hand-picking (particular care was taken to avoid getting materials from other layers) and grounded to powder for whole-rock XRPD and FT-IR analyses.

SEM analyses were carried out at the *Laboratorio Interdipartimentale di Microscopia Elettronica* (LIME), Roma Tre University, using a Zeiss Sigma 300 FE-SEM (Field-Emission Scanning Electron Microscope). The microscope is equipped with a HDBSE (High Definition Back Scatter Electron) detector and an energy dispersive (EDS) Bruker QUANTAX detector. The elemental composition was determined using an accelerating voltage of 20 kV, a filament current of 1.80 A and an aperture size of 20 μm. High-pass filtering of the SEM images collected along the growth of the

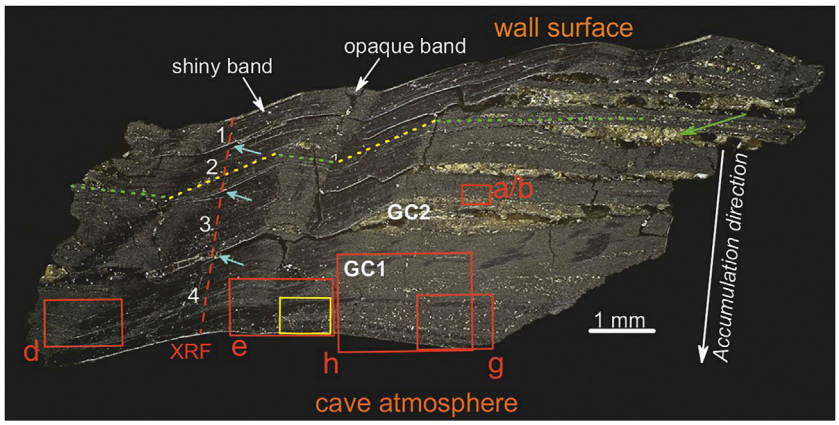

FIGURE 2 | Optical microscope image of the polished cross-section (sample GC). Red boxes indicate the areas investigated by SEM-EDS (**Figure 4**), while the yellow box indicates the position of Raman map (**Figure 7**). Red dashed line indicates the μXRF scan profile (**Figure 9**). Green and yellow dotted lines show the layer orientations (horizontal and transversal, respectively). Cyan arrows indicate discontinuous surfaces between the black layers (numbered in white). The green arrow indicates a detrital lens. GC1 and GC2 show the areas selected to extract the material for XRPD and FT-IR.

patinas was used to sharpen and count the micro-laminae (~1.5 μm thick) and laminae (~5–20 μm thick) within the sample.

X-Ray Powder Diffraction (XRPD) was performed at the *Laboratorio di Diffrazione ai Raggi X*, Department of Science, Roma Tre University, using a Scintag X1 diffractometer under CuKα1 radiation (λ = 1.54055 Å, 40 mA, 45 kV), fixed divergence slits and a Peltier-cooled Si(Li) detector (resolution < 200 eV). A divergent slit width of 2 mm and a scatter-slit width of 4 mm were employed for the incoming beam; a receiving slit width of 0.5 mm and scatter-slit width of 0.2 mm were used for the diffracted beam. Data were collected in step-scan mode in the 5–70° 2θ range, with a step size of 0.05° 2θ, and a counting time of 3 s/step.

Powder Fourier Transform Infrared Spectroscopy (FT-IR) data were collected at the *Laboratorio di Spettroscopia Infrarossa*, Department of Science, Roma Tre University, using a Nicolet iS50 FTIR spectrometer equipped with a DTGS detector and a KBr beamsplitter; the nominal resolution was 4 cm^{-1}, and 64 scans were averaged for each sample and for the background. Samples were prepared as pellets containing about 1 mg of powdered sample in 200 mg of KBr.

Raman measurements were performed at the *Laboratorio di Spettroscopia Raman*, Department of Science, Roma Tre University, at room temperature using an inVia Renishaw Raman spectrometer equipped with a diode laser (532 nm, output power 50 mW), an edge filter to select the Raman scattering avoiding the elastic contribution, a 1800 lines per mm diffraction grating and a Peltier cooled 1,024 x 256 pixel CCD detector. Samples were mounted on the manual stage of a Leica DM2700 M confocal microscope. Focusing of the laser beam and collection of Raman signals were obtained with a 50x long-working distance objective. Following Bernardini et al. (2019, 2020b) Raman spectra were collected by keeping the laser power on the sample at 1 mW, thanks to the use of neutral filters, and each accumulation time was fixed at 10 s to avoid any possible laser-induced degradation of the sample. Raman mapping was carried out on a polished cross-section, by collecting a grid of single-point spectra, at 50 × 30 μm step, for a total number of 89 points, from 200 to 900 cm^{-1}. Following Bernardini et al. (2020a) the intensity ratio between the band around 630 cm^{-1} (assigned to the ν_1 stretching mode of Mn^{4+}-octahedra) and the band around 570 cm^{-1} (assigned to the ν_1 stretching mode of Mn^{3+}-octahedra) was integrated over the scanned area to map the spatial distribution of the oxidation state of Mn. The Raman spectrometer was calibrated prior to the measurements using a Si wafer and by performing the automatic offset correction. The spectra acquisition and data analyses were accomplished using WiRE™ and Origin 9.0 software. The peak positions are estimated to be accurate to at least ±2 cm^{-1}.

Micro X-ray Fluorescence (μXRF) was performed at the XRF beamline of the Brazilian Synchrotron Light Laboratory (LNLS, Campinas, Brazil) to study the distribution of elements. Measurements were acquired at 10 keV along a 3.125 mm scan-line profile, orthogonally to the growth of the mineralization (see **Figure 2** for the location), at 25 μm step for a total number of 125 points, and count time per point of 600 ms. The softwares PyMCA 5.4.2 and Origin 9.0 were used for spectra calibration and processing, and for data elaboration, respectively.

The polished cross-section (**Figure 2**) was also investigated for the presence of microbial imprints by a Zeiss Gemini500 SEM of *Centro Microscopie* of the University of L'Aquila. Micrographs were acquired working with variable pressure and using an acceleration voltage of 10 kV and with a BSD4 detector (to detect backscattered electrons).

DNA extraction was performed two times on 0.5 g of homogeneous samples of black patinas (5 sub-samples mixed) fixed in RNA-later by a NucleoSpin® Soil kit" (Macherey Nagel, Germany). DNA extraction was performed following the manufacturer's protocol. The extracted DNA samples (named GCA and GCB) were sent to Bio-Fab Research laboratories (Italy) for purification and sequencing. The amplification of prokaryotes (bacteria and archaea) was obtained by a specific protocol of the

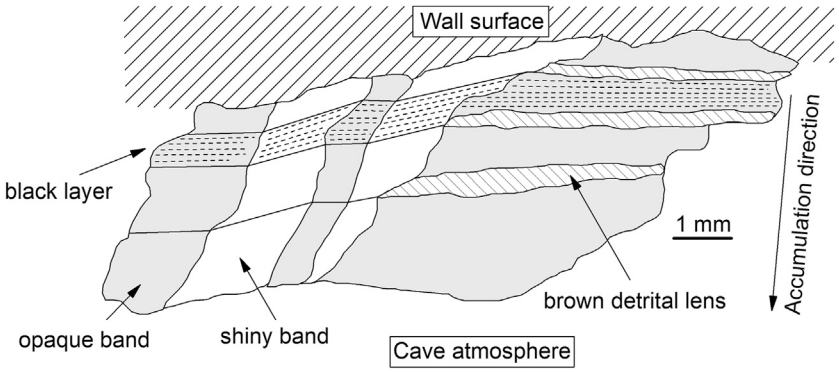

FIGURE 3 | Sketch of the sample GC showing the brown detrital lenses, black layers, and the lateral alternation of shiny (white colour) and opaque (gray) bands. The dashed lines show the orientation of the layering within the opaque and shiny bands (horizontal and transversal, respectively).

Mi-Seq Illumina platform, using primers that targeted the V3 and V4 regions of 16S rRNA – i.e. Forward Primer = 5′ TCGTCGGCAGCGTCAGATGTGTATAAGAGACAGCCTAC GGGNGGCWGCAG, Reverse Primer = 5′ GTCTCGTGGGCTCGGAGATGTGTATAAGAGACAGGACT ACHVGGGTATCTAATCC (Choi et al., 2020). A metagenomic workflow was carried out to classify microorganisms, using QIIME2 (Bolyen et al., 2019) and SILVA 132 database (https://www.arb-silva.de/); taxonomic assignments were checked through LPSN service (https://lpsn.dsmz.de). The Shannon Index (H′) and rarefaction curves were obtained by PAST 4.03 software (Hammer et al., 2001).

RESULTS

Elemental Composition and Mineralogy

A careful optical microscope study of the cross-section revealed a layered texture made of millimetric black layers and brown lenses (**Figure 2**). Brown lenses (green arrow in **Figure 2**), with a thickness of ~ 0.3 mm, are made of micrometric crystals/grains of detrital minerals, such as quartz, feldspar, and phyllosilicate-like minerals. All the brown lenses show the same horizontal orientation (green dotted line in **Figure 2**). Black layers consist of micrometric detrital crystals/grains embedded in a fine black matrix. Four layers, with an average thickness of ~ 0.7 mm, were identified (white numbers in **Figure 2**). These layers are separated by discontinuity surfaces (indicated by cyan arrows in **Figure 2**), with lateral transition into the brown detrital lenses (to the right in **Figure 2**). Moreover, "opaque" and "shiny" bands (due to the occurrence of materials with different mechanical properties, less resistance to polishing for the former), characterized by a different strata orientation were identified. The layering within the opaque bands is horizontally orientated (*i.e.,* the same orientation of the brown detrital lenses, green dotted line in **Figure 2**). Moreover, these bands are associated with detrital minerals but with a smaller size than the minerals within the brown lenses, while the layering within the shiny bands is transversely oriented (yellow dotted line in **Figure 2**). As a result, opaque and shiny bands alternate laterally following the orientation of the layers, therefore following the geometry, *i.e.,* roughness, of the wall surface (the wall surface is not perfectly plane but is irregular and carved by concave and convex forms. Accordingly, the strata of the MnOx deposit have to follow and adjust to the geometry and roughness of the rock substratum, see **Figure 2** and **Figure 3**).

SEM-EDS analyses allowed us to define further the brown lenses, the black layers, and the shiny and opaque structures inside the latter based on their elemental composition and morphologies. The brown detrital lenses mainly consist of micrometric crystals of quartz and K/Mg-rich phyllosilicate-like minerals preferentially oriented parallel to the stratification (**Figure 4A**). Other phases, such as alkali-feldspar, Fe- and Ti-oxide(s) with minor zircon, pyroxene, and olivine (the latter probably related to the weathering of volcanic rocks outcropping inside the cave, see Bertolani et al., 1994; Stoppa et al., 2002) were also identified. Fe is ubiquitously present, while Mn is scarce to absent in these Fe-rich brown detrital lenses (**Figure 4B**), and abundant in the Mn-rich black layers (**Figure 4C**). EDS data collected from the black layers show high content in Mn, Fe, Ca and a lower content in K, Ba, Mg, Al, Si, Cl, and P. SEM-EDS images confirm the presence of opaque bands (initially identified under the optical microscope, see **Figure 2** and **Figure 3**), associated with detrital minerals and voids, whereas the shiny bands contain few detrital minerals (see the Si distribution in **Figure 4D**). The lateral alternation of these bands (relative to the layer orientation) is recognizable even at micrometric scale (**Figures 4D–F**). The accumulation of detrital minerals, within the opaque bands, can lead to the formation of micrometric lenses of debris (white arrow in **Figure 4F**).

Stromatolite-like features are recognized exclusively within the Mn-rich black layers. We have distinguished three different morphotypes based on morphological and mineralogical characteristics, alternating laterally within the Mn-rich black layers (**Figures 4G,H**). In detail: 1) *branched columnar* morphotype, typical of the opaque bands characterized by voids and detrital minerals, with a convex-outward micro-lamination (**Figures 4I,J**); 2) *flat-laminated* morphotype,

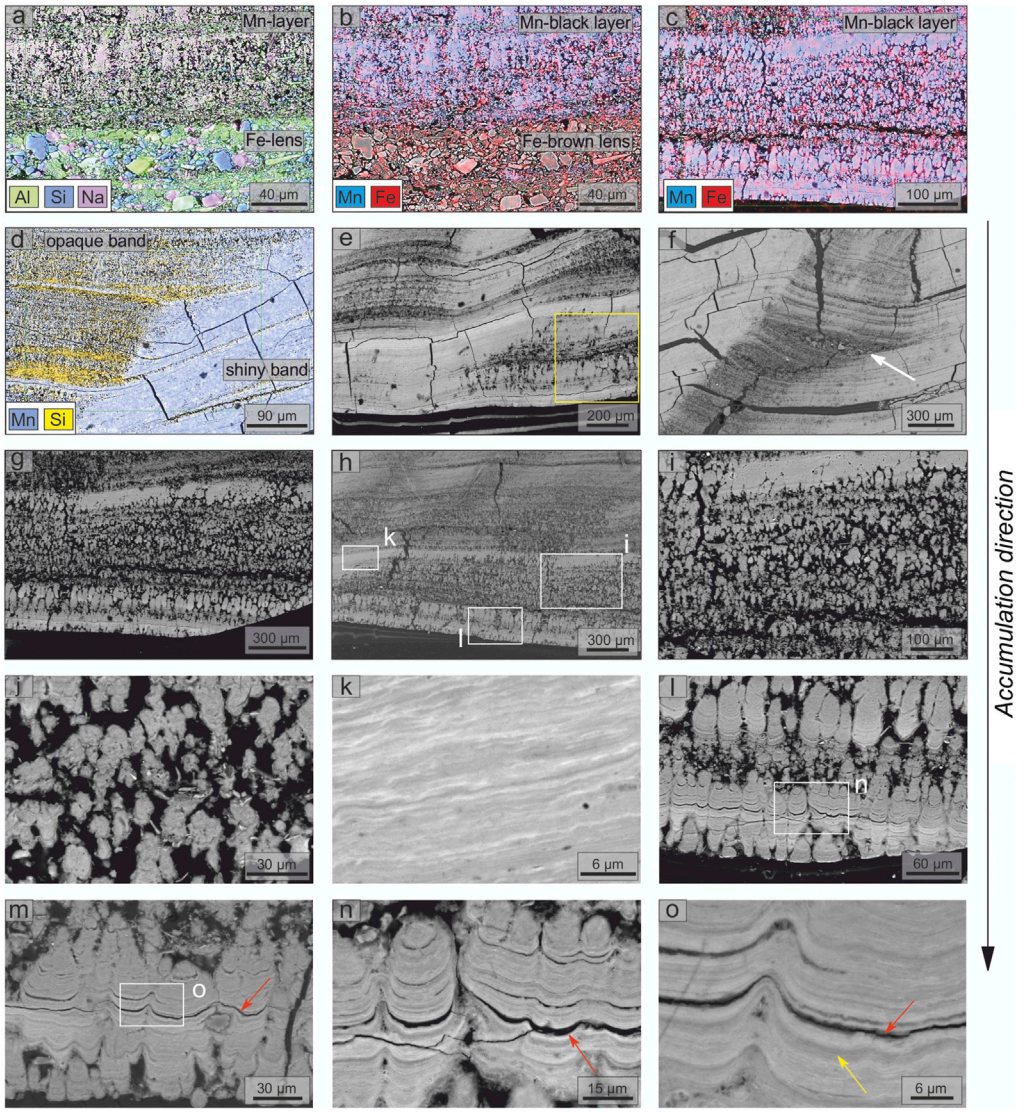

FIGURE 4 | SEM-EDS investigation of polished cross-section of the Fe-Mn patinas (sample GC): **(A, B)** EDS elemental maps (Mn, Fe, Al, Si, and Na) of the boundary between brown Fe-lens and black Mn-layer; **(C, D)** EDS elemental maps (Mn, Fe, and Si) of black Mn-layers; **(E, F)** alternation of the shiny and opaque bands, yellow box indicates the position of Raman map shown in **Figure 7**; **(G, H)** spatial distribution of the three different morphotypes identified, white boxes indicate the positions of panels **(I)**, **(K)**, and **(L)**; **(I, J)** detail of the *branched columnar* morphotype; **(K)** detail of the *flat-laminated* morphotype; **(L–O)** details of the *columnar or pseudo-columnar* morphotype (see **Figure 2** for the position on the sample). White arrow indicates a lens of debris. Red arrows indicate discontinuity between laminations. Yellow arrow shows ~1.5 µm bands.

characterized by flat and parallel micro-lamination (**Figure 4K**); and 3) *columnar or pseudo-columnar* morphotype, characterized by outward, dome-like structures (**Figures 4I–O**). Morphotypes 2) and 3) were recognized in the shiny bands only. Layering at different scales was identified throughout the sample, especially in the *flat-laminated* and *columnar or pseudo-columnar* morphotypes (**Figure 4**). Nano-laminae, with a thickness of hundreds of nanometers (**Figure 4O**), were identified. These nano-laminae form darker and lighter micro-laminae with a thickness of ~ 1.5 µm (yellow arrow in **Figure 4O**), which in turn form laminae (sometimes separated by discontinuity surfaces, red arrows in **Figures 4M–O**) with a variable thickness from 5 to 20 µm (the thicker ones are associated with detrital minerals). Nano-laminae, micro-laminae and laminae form super-laminae with a thickness of ~ 300–400 µm, which, in turn, form the four millimetric layers observed (see **Supplementary Figure S3** for details). Along the µXRF scan line profile (red dotted line in **Figure 2**), in areas belonging to the *flat-laminated* morphotype, a total of ~ 1900 micro-laminae, which form ~ 170 laminae, has been recognized.

Mineralogy of the brown detrital lenses and the black layers (GC2 and GC1 in **Figure 2**, respectively) is further elucidated through X-ray powder diffraction, FT-IR, and Raman spectroscopy.

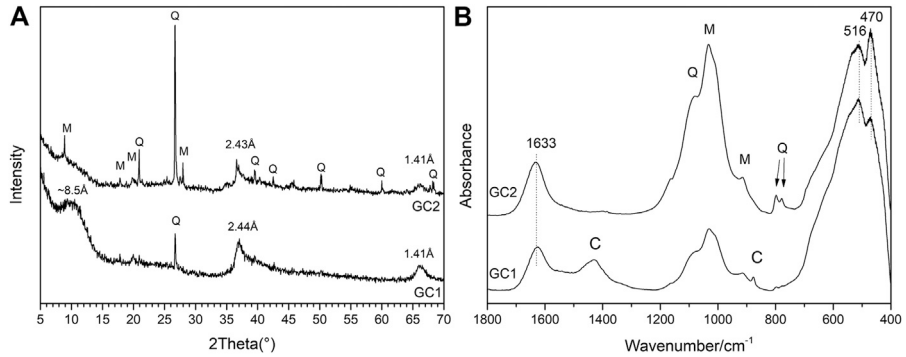

FIGURE 5 | XRPD **(A)** and FT-IR **(B)** results from the black layers (GC1) and brown layers (GC2) (**Figure 2** shows the areas selected to extract the material for the analyses). M, mica; Q, quartz, C: carbonate minerals.

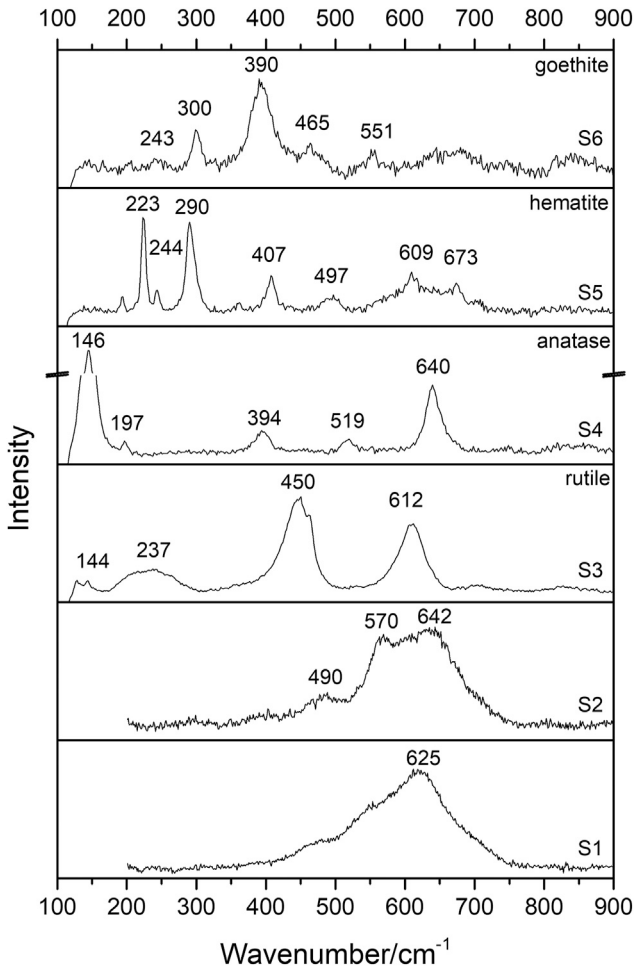

FIGURE 6 | | Raman spectra collected on black layers (spectra S1, and S2) and brown lenses (spectra S3, S4, S5, and S6). Spectra collected at λ = 532 nm.

X-ray powder diffraction data collected on the brown detrital lens (GC2 in **Figure 5A**) showed sharp Bragg peaks of quartz at *d-spacing* (Å)(I%) 4.26(20), 3.34(100), 2.28(5), 1.82(10), and mica (muscovite and/or phlogopite) at *d-spacing* (Å)(I%) 9.95(100), 4.99(30), 3.20(90). Broad peaks of poor-crystalline and/or nanocrystalline compounds were also detected. Strong peaks at 2.43 and 1.41 Å allow recognizing vernadite [$(Mn,Fe,Ca,Na)(O,OH)_2 \cdot nH_2O$], a disordered variety of

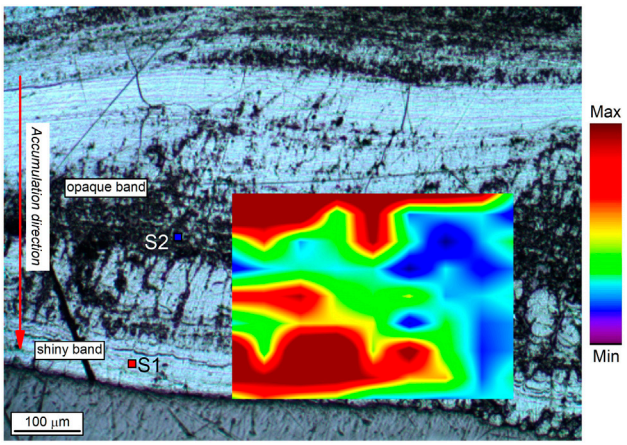

FIGURE 7 | Raman map of the oxidation state of Mn obtained by integrating the intensity ratio between the band at 630 cm^{-1} (ν_1 stretching mode of Mn^{4+}-octahedra) and the band at 570 cm^{-1} (ν_1 stretching mode of Mn^{3+}-octahedra) over the scanned area (see methods for details). Red/yellow: higher average oxidation state of Mn (todorokite and/or ranciéite in a shiny band), blue/green: lower average oxidation state of Mn (vernadite in an opaque band). S1 and S2 are the spots where Raman spectra of **Figure 6** were obtained.

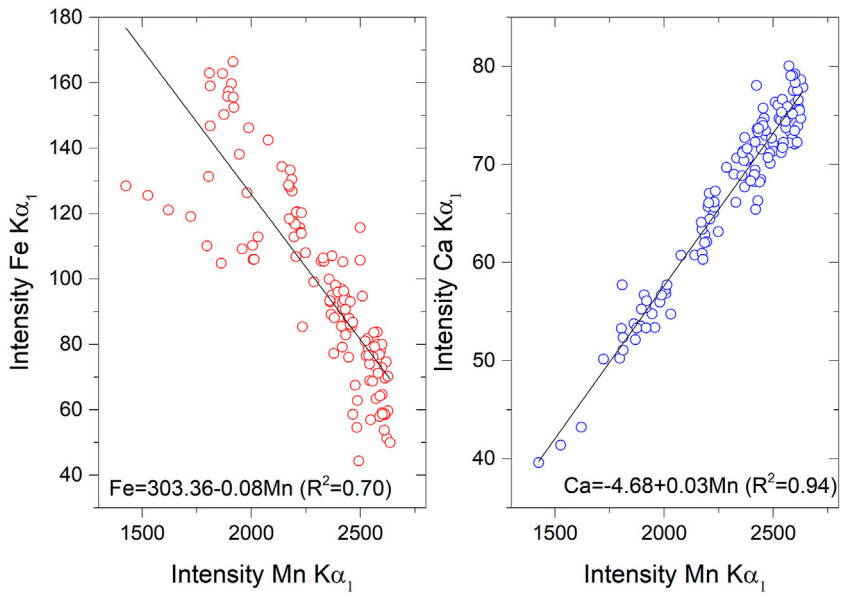

FIGURE 8 | Scatter plot of the abundances of Mn, Fe, and Ca measured along the µXRF scan profile (see **Figure 2**).

birnessite typical of crusts throughout the global ocean. Since SEM-EDS data show Mn is absent in these layers (**Figure 4B**), the presence of this Mn-phase in the sample is possibly due to the accidental collection of material from nearby layers. Diffraction data collected on the black Mn-layers (GC1 in **Figure 5A**) showed the strongest peaks of quartz and broad peaks of vernadite at 2.44 and 1.41 Å. Moreover, a very broad peak, centered around 8.5 Å, was also detected. This broad peak can be due to the 001 reflection of mica, clay minerals, and/or to the presence of poorly/nano crystalline 7Å (birnessite and ranciéite) and/or 10Å (buserite and todorokite) Mn-phases.

The same powdered samples previously used for XRPD were also investigated by FT-IR. The spectrum collected on the brown detrital lenses (GC2 in **Figure 5B**) shows strong and broad bands of silicates (*i.e.,* quartz and muscovite) around 1,000 cm^{-1}. While, the black layers (GC1 in **Figure 5B**) show weak absorptions bands of silicates and carbonates, the latter at 1,430 and 875 cm^{-1} (labelled as C in **Figure 5B**), due to the occurrence of carbonate traces not detectable by XRPD. Finally, both samples show broad and unresolved absorption bands at 470, 516, and 1,633 cm^{-1}, which point to the presence of highly disordered and/or nanocrystalline Mn-compounds. These bands can be assigned to

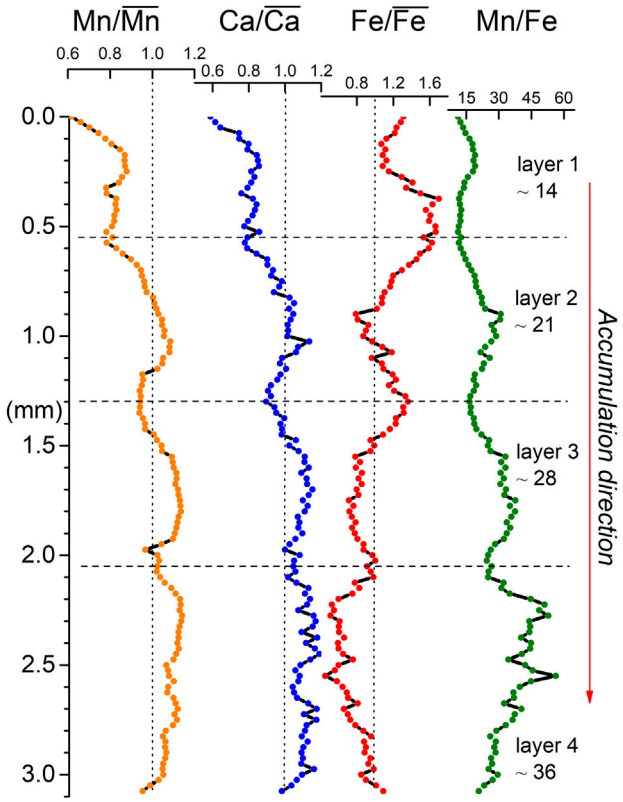

FIGURE 9 | Mn/$\overline{\text{Mn}}$, Fe/$\overline{\text{Fe}}$, Ca/$\overline{\text{Ca}}$, and Mn/Fe profiles along the growth direction of sample GC, obtained by μXRF (see **Figure 2** for the position on the sample). Horizontal dotted lines mark the boundary of each cycle (minimum Mn/Fe values) corresponding to the discontinuity surfaces between layers (cyan arrows in **Figure 2**).

several MnOx, such as birnessite, ranciéite, todorokite, and vernadite (Chukhrov et al., 1978; Potter and Rossman, 1979).

Raman spectra were collected in several points of the brown detrital lenses and the black layers to check for heterogeneities. Four different spectra were obtained from the brown detrital lenses (spectra S3 to S6 in **Figure 6**). Titanium dioxides, such as rutile (bands at 144, 237, 450 and 612 cm^{-1}, spectrum S3) and anatase (bands at 146, 197, 394, 519 and 640 cm^{-1}, spectrum S4) (Balachandran and Eror, 1982), and Fe oxides, such as hematite (bands at 223, 244, 290, 407, 497, 609 and 673 cm^{-1}, spectrum S5) and goethite (bands at 243, 300, 390, 465 and 551 cm^{-1}, spectrum S6) (de Faria and Lopes, 2007), were detected. Two different spectra were obtained from the Mn-rich black layers as follows: spectrum S1, collected on the shiny bands (*flat-laminated* and *columnar* or *pseudo-columnar* morphotypes, see **Figure 7** for the position of the spot in the sample), is characterized by a strong and broad band at ~ 625 cm^{-1} and shoulders at ~ 570 and 490 cm^{-1} (**Figure 6**). These spectral features can be assigned to ranciéite or todorokite (Bernardini et al., 2019). Moreover, also considering XRPD and FT-IR results, neither can be excluded. Spectrum S2, collected on the opaque and silicate/void-rich bands (*branched columnar* morphotype, see **Figure 7** for the position of the spot in the sample) is characterized by strong and broad bands at ~ 642 and 570 cm^{-1} and a weak band at ~ 490 cm^{-1} (**Figure 6**). According to XRPD and FT-IR results, this spectrum can be assigned to vernadite (Post et al., 2003). Bernardini et al. (2020a) calibrated a method to extract the oxidation state of Mn from the Raman spectra. Following this method, we show that Mn occurs as Mn^{4+} (recognized by the band at 625 or 642 cm^{-1}) and as Mn^{3+} (recognized by the band at 570 cm^{-1}) (see spectra S1 and S2 in **Figure 6**).

Following Bernardini et al. (2020a), the microscale spatial distribution of the Mn oxidation state at the boundary between an opaque and a shiny band was studied by Raman mapping (**Figure 7**). Opaque bands, associated with vernadite, silicate minerals, and voids (*branched columnar* morphotype), are characterized by a lower oxidation state of Mn (blue area in **Figure 7**). In contrast, shiny bands, associated with todorokite and/or ranciéite (*flat-laminated* and *columnar* morphotypes), are characterized by a higher oxidation state of Mn (red area in **Figure 7**).

XRF data were collected from the same area used to count the ~1.5 μm microlaminae and the ~10 μm laminae (*i.e.,* along a shiny band, see **Figure 2**), avoiding detrital crystals and voids. Consistently with EDS results, XRF data show high content of Mn, Fe, Ca, and smaller amounts of K, Ba, Ti, and P. Moreover, heavy metals, such as V, Ni, Zn, Cu, and As, were also detected.

A μXRF scan-line profile (see Methods and **Figure 2**) allows investigating the variations in elemental abundances along the accumulation direction of the patinas, and at the transitions between the four millimetric layers (white numbers in **Figure 2**). A positive correlation between Mn and Ca (R^2 = 0.94), suggests that the sample consists of Ca-rich MnOx. Moreover, Mn shows a negative correlation with Fe (R^2 = 0.70) (**Figure 8**).

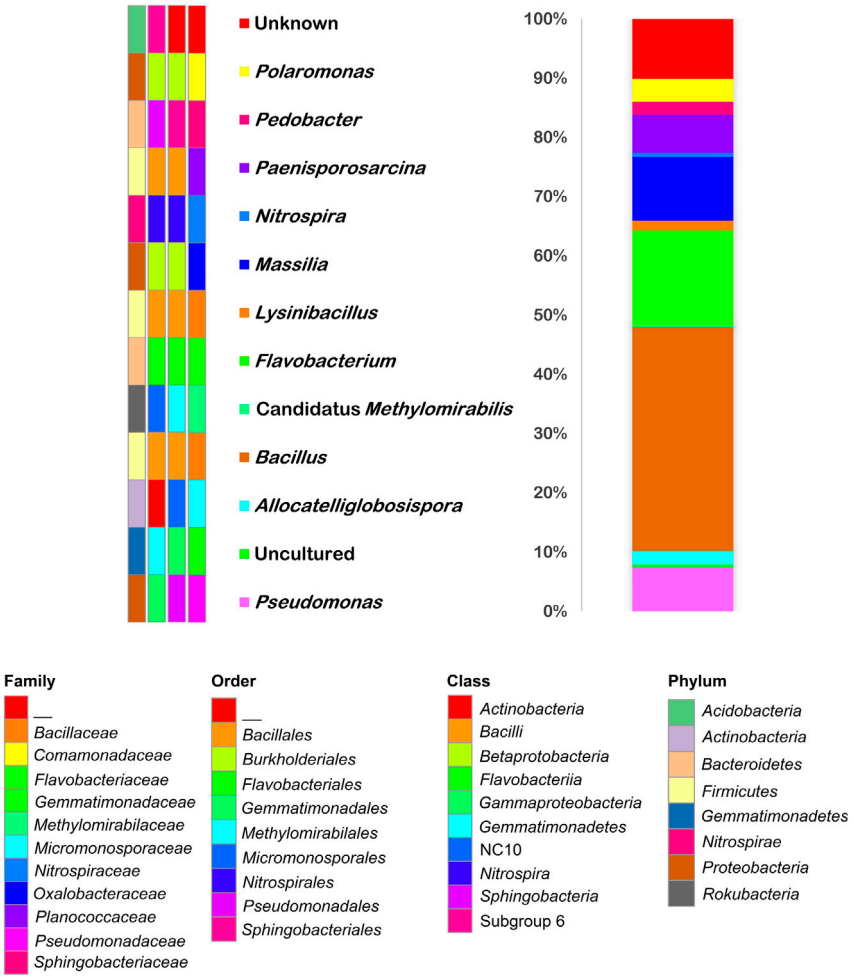

FIGURE 10 | Taxonomy barplot of microbial community composition of the Fe-Mn patina sample. The color changes in the barplot show the percentages occupied by genera (color keys on the left). Taxa assignments (P, phylum; C, class; O, order; F, family) are indicated by the color keys on the bottom.

μXRF profiles show four main oscillations for Mn, Fe, and Ca (**Figure 9**), each one related to one of the four millimetric layers. They can be recognized by Mn peaks (*i.e.,* max relative values) and Fe troughs (*i.e.,* min relative values) toward the center of the layers and Fe peaks and Mn troughs at the boundaries of the layers. The Ca pattern resembles that of Mn. Moreover, the oscillations are characterized by a trend in the Mn/Fe ratio, which increases from the older to the younger layers (i.e. from layer 1 to layer 4 in **Figure 2**). Mean Mn/Fe ratios increase from ~ 14 in cycle 1 (the oldest), to ~ 21 in cycle 2, 28 in cycle 3, and 36 in cycle 4 (the most recent). The minimum Mn/Fe values (black dotted horizontal line in **Figure 9**) are associated with the discontinuity surfaces (cyan arrows in **Figure 2**). The mean Mn/Fe ratio in the whole profile is ~ 26 (min ~ 11 and max ~ 55).

Microbiological Analysis

The Illumina sequencing results on GCA and GCB samples showed very similar profiles. Thus, we considered the combined profile for further elaborations. The single GCA and GCB samples profiles at the genus level, the quantitative reports of sequencing and metagenomic analysis, the calculated Shannon Index (H′), and diversity rarefaction curves are shown in **Supplementary Material** (**Supplementary Figure S3** and **Supplementary Table S5**). The results showed that the investigated samples have high diversity (H' > 3; GCA: 4.76 and GCB: 5.91) and that the communities are mainly composed of *Bacteria* (~99%), with a very small percentage of *Archaea* (~1%). Within the *Archaea* domain, except for the identified phylum *Bathyarchaeota* with a relative abundance of 2.4%, an unknown taxon was found. Within the *Bacteria* domain, the predominant phyla (**Supplementary Table S1**) were *Firmicutes* (36%), *Proteobacteria* (33%), and *Bacteroidetes* (13%). Another phylum with a significant relative abundance was *Actinobacteria* (7%). Less abundant phyla were *Acidobacteria, Chloroflexi*, and *Planctomycetes* (relative abundances over 2%). The distribution in classes of the different phyla (**Supplementary Table S2**) showed that the most abundant class was *Bacilli* (35%), followed by *Betaproteobacteria* and *Flavobacteria* (18 and 12%,

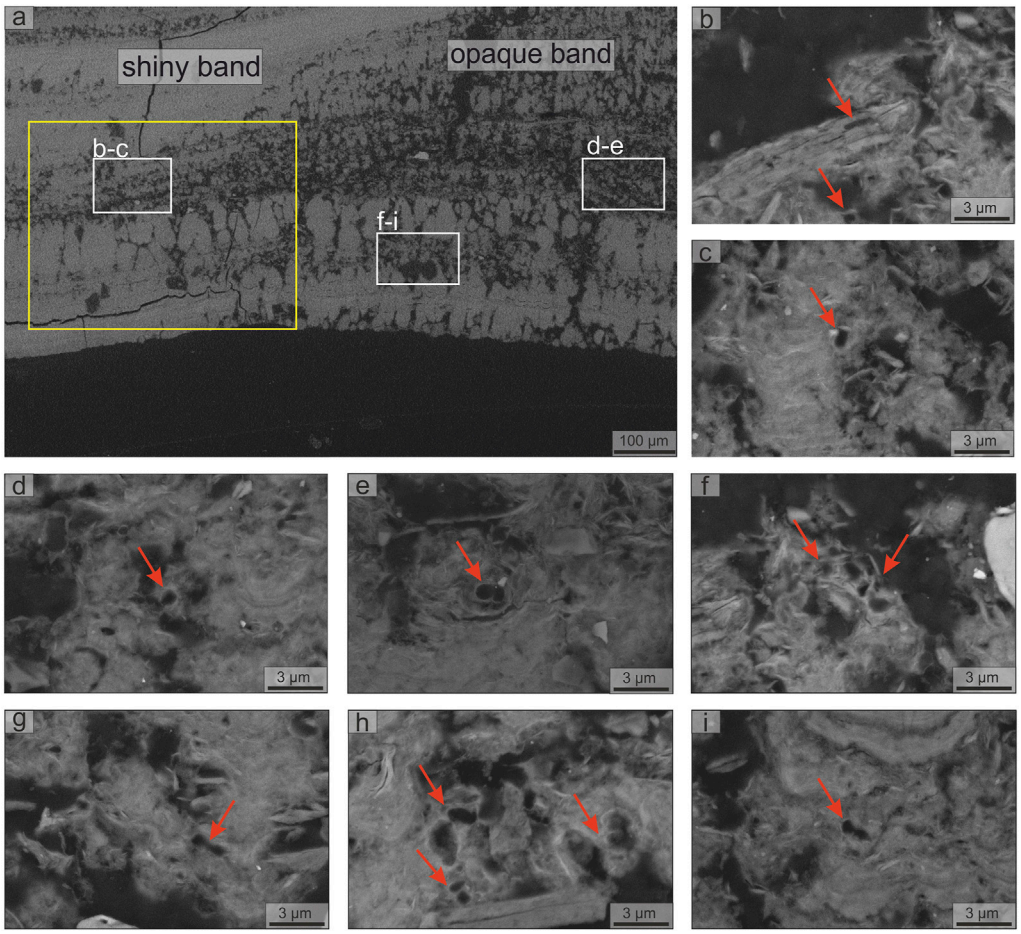

FIGURE 11 | SEM-EDS investigation of polished cross-section of the Fe-Mn patinas (sample GC): **(A)** areas of investigation, white boxes indicate the positions of other panels, yellow box indicate the position of the Raman map (**Figure 7**), **(B–I)** bacterial microbial imprint (red arrows). Putative predivisional cell stages typical of staked bacteria are showed in panels **(E)**, **(G)**, and **(I)**.

respectively). Less abundant were *Alphaproteobacteria, Gammaproteobacteria*, and *Actinobacteria* classes (relative abundances over 4%). *Bacillales, Burkholderiales*, and *Flavobacteriales* were the main orders (35%, 15%, and 12%, respectively, **Supplementary Table S3**); while, among families, *Bacillaceae* and *Flavobacteriaceae* accounted for significant percentages (28 and 12%, respectively, **Supplementary Table S4**). In **Figure 10** the results of the relative abundances obtained for the genera and their taxonomic assignments are summarized. *Bacillus* (25%) was the predominant genus, followed by unknown and uncultured genera (18 and 17%, respectively). The remaining percentage was represented by other genera with a relative abundance ≤ 10%.

SEM images collected in the area previously investigated by Raman mapping (yellow box in **Figure 11A**) revealed the presence of empty bacterial sheath imprints (**Figures 11B–I**). Some of the latter can be identified as putative predivisional cells, typical of dimorphic prosthecate bacteria (**Figures 11E,G,I**). Moreover, we found an interesting spatial distribution of these imprints. They were identified only in areas with a lower oxidation state of Mn and detrital minerals (*i.e.,* opaque bands in **Figure 11A**). On the contrary, no evidence of microbial imprints was recognized in areas with a higher oxidation state of Mn (*i.e.,* shiny bands in **Figure 11A**).

A summary of the results obtained on the black layer (shiny and opaque bands) and brown lenses in sample GC is given in **Table 1**.

DISCUSSION

Mineralogical and Microbiological Implications

Our mineralogical and elemental characterization shows that the black patinas covering the walls of the *Grotta del Cervo* consist of brown detrital Fe-rich lenses and black Mn-rich layers. The former consisting of a fine-grained mixture of quartz, mica, titanium dioxides (anatase and rutile), zircon, and Fe oxyhydroxides, such as goethite and hematite. Instead, the latter consists of few detrital minerals embedded in a fine Mn-

TABLE 1 | Distribution of the mineralogy, oxidation state of Mn, stromatolite-like structures, and bacterial imprints between the black layers (shiny and opaque bands) and brown lenses, obtained integrating SEM-EDS, XRPD, FT-IR, and Raman spectroscopy results.

Sample GC		Mn, Fe, Ca minerals	Oxidation state of Mn	Detrital minerals	Stromatolite morphotypes	Bacterial imprints
Black layers (GC1)	shiny bands	todorokite/ranciéite, carbonates	higher	quartz, mica, anatase, rutile, zircon, pyroxene, olivine	flat-laminated and columnar	absent
	opaque bands	vernadite, carbonates	lower		branched columnar	present
Brown lenses (GC2)		hematite, goethite	/		absent	absent

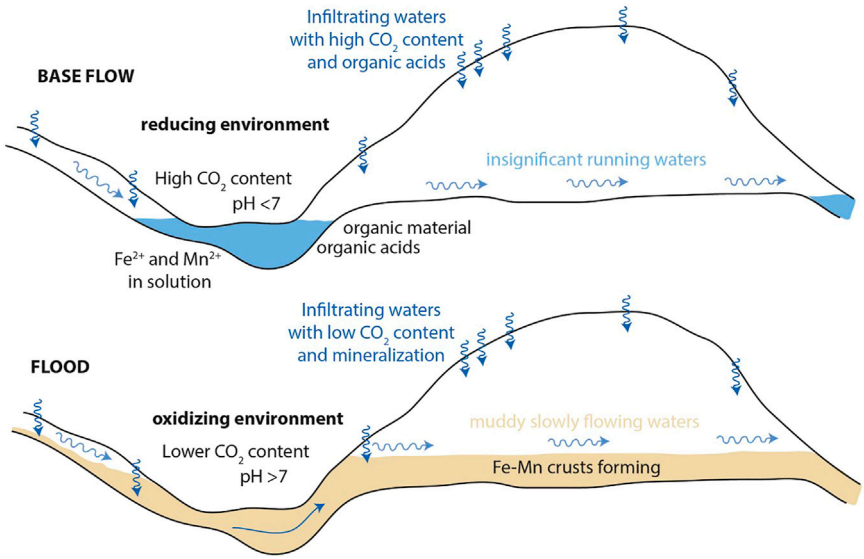

FIGURE 12 | Depositional model proposed for the MnFe patinas. During base flow hydrological conditions (upper panel), the studied karst system drains infiltrating water with no significant increase of underground water level. Patinas form during recurrent floods according to hydrological-driven changes on geochemical parameters and depositional conditions as explained within the text.

matrix. In these layers, the absence of Fe-oxides revealed by XRPD, FT-IR, and Raman spectroscopy, the negative correlation between Mn and Fe shown by μXRF data, and the necessity for balancing the entry of additional cations (such as Ca^{2+}) within the channel/interlayer sites, all suggest that Fe replaces Mn in the structure of Ca-rich MnOx. Our data show the occurrence of different MnOx, such as vernadite [$(Mn,Fe,Ca,Na)(O,OH)_2{\cdot}nH_2O$], a nano-sized or z-disordered variety of birnessite (Lee et al., 2019), and todorokite [$(Ca,Na,K)(Mn^{4+},Mn^{3+})_6O_{12}{\cdot}nH_2O$], a compound whose structure consists of triple chains of edge-sharing (Mn^{4+},Mn^{3+})O_6 octahedra linked such as to give channels with cross sections of 3x3 occupied by water molecules and large cations (Post and Bish, 1988; Post et al., 2003). Moreover, we cannot exclude the presence of ranciéite [$(Ca,Mn^{2+},K,Ba)(Mn^{4+},Mn^{3+})_4O_9{\cdot}nH_2O$], a phyllomanganate with disordered stacked layers of (Mn^{4+},Mn^{3+})O_6 octahedra, with water molecules and large cations located between the layers (Ertl et al., 2005).

An interesting aspect emerging from our microbiological investigation is the scarce contribution of *Archaea* to microbial communities. Most of the microbial communities of caves, located in different geographical regions and environmental conditions, showed an almost exclusive dominance of *Bacteria* and a negligible percentage of *Archaea* (Pasic et al., 2010; Itcus et al., 2018; Wiseschart et al., 2019; Jurado et al., 2020; Gonzalez-Pimentel et al., 2021). Only in a few cases, *Archaea* were linked to MnFe deposits, such as in Lechuguilla Cave (Northup et al., 2003).

Regarding *Bacteria*, the genera *Bacillus, Flavobacterium* and *Pseudomonas* represented almost 45% of the total relative abundance of the sample. *Bacillus* and *Pseudomonas* have been thoroughly investigated as model Mn-oxidizing bacteria (Francis and Tebo, 2002; Tebo et al., 2005; Jiang et al., 2010). Indeed, *Bacillus* spp. can remove Mn and other heavy metals due to their biosorption ability (Xu et al., 2019). The genus *Flavobacterium* was commonly detected in Mn deposits and Mn removal biofilters (Hou et al., 2020). *Flavobacterium* was also a member of the microbial communities inhabiting a birnessite-type Mn deposit in a Swedish mine (Sjöberg et al., 2018) and the Mn-oxidizing bacteria forming a biofilm in water transmission pipelines (Allward et al., 2018). Carmichael et al. (2013b) demonstrated the contribution of

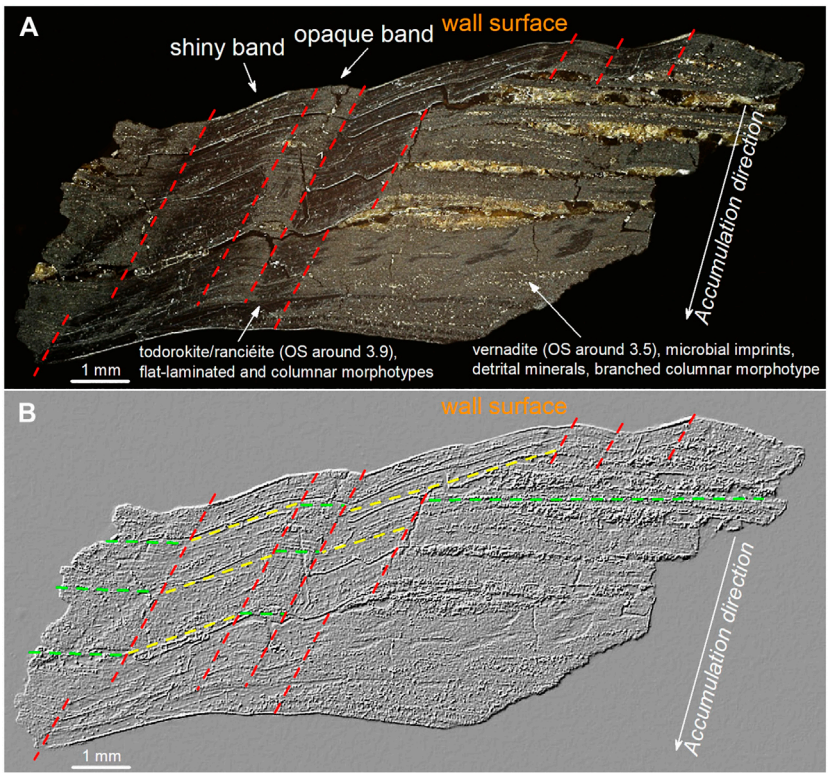

FIGURE 13 | Optical microscope image of sample GC **(A)**, and after directional filtering for linear enhancement **(B)**. These images show the distribution of shiny bands (associated whit layers transversely oriented, todorokite/ranciéite (OS ~ 3.9), and planar forms produced in a more turbulent "local" environment) and opaque bands (associated with layers horizontally oriented, vernadite (OS ~ 3.5), microbial imprints, detrital minerals, and forms produced in a less turbulent "local" environment, allowing the microbial community to stay attached to the wall surface). These bands alternate laterally, decreasing in number (from 7 to 2) along the accumulation direction of the patinas, as the surface becomes flatter. All the features point to strong control of the wall surface geometry (*i.e.,* roughness) on the spatial distribution of morphology, detrital mineral abundance, mineralogy of MnOx, and oxidation state of Mn. OS: average oxidation state of Mn.

Flavobacterium in the formation of cave MnFe deposits in the upper Tennessee River Basin by Mn(II)-biomineralizing bacteria isolation. Other less common bacteria involved in the biogeochemistry of Mn are found in the patinas of *Grotta del Cervo*. In fact, *Lysinibacillus* spp. were isolated from a Mn mining soil (Liu et al., 2013) and a Brazilian Mn mine (Barboza et al., 2015), and were able to solubilize low grade ores from a Mn deposit (Ghosh et al., 2016). Chen et al. (2019) isolated the Mn-oxidizing bacterium *Massilia* sp. from soil Mn nodules. He et al. (2008) stated that *Gemmatimonadetes* and *Nitrospirae* phyla occurred in acidic soil Mn nodules. Chaput et al. (2015) reported that microbial communities from Mn remediation systems, treating coal mine drainage, were composed of *Betaproteobacteria* mostly represented by the orders *Burkholderiales* and *Nitrosomonadales*, both of which have been found in the cave patinas.

Concerning the nature of the MnOx, *Bacillus* and *Pseudomonas* strains produced a poorly crystalline birnessite-like phyllomanganate (vernadite) that often represents the initial phase precipitated by bacteria during microbially mediated Mn^{2+} oxidation (Villalobos et al., 2003; Bargar et al., 2005). However, Feng et al. (2010) found that a strain of *Pseudomonas putida* formed nano-crystalline todorokite, and Kim et al. (2003) reported that *Leptothrix discophora* produced nanocrystalline todorokite-like manganese oxides. In this context, our microbiological data suggest that the genera identified in the samples could play a role in the Mn geochemical cycle. Moreover, our results show microbial imprints, some identified as putative predivisional cells (this fact has already been reported from other Mn deposits of *Grotta del Cervo, see* Vaccarelli et al., 2021), associated only with vernadite, suggesting a microbial origin for this highly disordered compound. In addition, bacteria of the genera *Bacillus, Flavobacterium*, *Pseudomonas*, *Lysinibacillus*, etc., appeared to be involved in calcium carbonate precipitation (Meier et al., 2017; Farrugia et al., 2019; Ortega-Villamagua et al., 2020). Most of these bacteria are ureolytic strains (Mitchell et al., 2019; Reeksting et al., 2020), although non-ureolytic precipitation was reported (Lee et al., 2017). Therefore, the bacteria identified in the manganese patinas have a high potential for biomineralization.

Hypothesis on the Hydrological Controls Driving MnFe Patina Formation

We here present a preliminary genetic model for the studied deposits (**Figure 12**), supposing that different karst hydrological

regimes lead to changes on cave geochemical environment and depositional conditions. Direct observations cannot be done during floods since the cave is inaccessible during these high flow conditions. Nevertheless, cave floods are here considered the main driver of the deposition of the patinas because of: 1) their location (*i.e.,* cave walls), 2) their morphological, sedimentological and mineralogical features, and 3) similar deposits described elsewhere (Rossi et al., 2010; Gázquez et al., 2011). Periods of intense rainfall would recharge the karst aquifer rapidly, increasing the water level up to a certain height according to the ratio between the water amount and drainage capability, as can occur in stream-passage caves (Columbu et al., 2015). During base flow hydrological conditions, the studied karst system drains infiltrating water with no significant increase of underground water level (**Figure 12**). However, floods are recurrent in this area, generally during autumn (rain events) and spring (snowmelt season). Water entrains detrital grains during floods; the mud deposits, well recognizable on the explored cave floors and walls (**Supplementary Figure S2**), witness this process. Recent mud deposits show a soft texture (*i.e.,* unconsolidated), confirming that flooding processes are still active in the *Grotta del Cervo* Cave (as reported by cavers). However, the studied patinas are consolidated, and they are found stratigraphically below the soft mud deposits (**Supplementary Figure S2**). From a geochemical perspective, the clear separation between Mn and Fe found in the sample may be due to variations in the redox conditions of the system. In fact, compared to Fe-oxides, MnOx are stable only under basic conditions (pH > 8), except at high oxidation/reduction potential (Eh > 600 mV) (Hem, 1963, 1972). In accordance, the MnFe patinas are deposited during the subaqueous period in the oxidizing environment when flood is rising, with Mn depositing first and Fe, together with detrital particles, in the later dewatered stage (when pH falls back to neutral or turns slightly acidic). When flood water retreats, slow decantation leaves the clay particles settle down slowly, covering the patinas again. The latter constitutes the unconsolidated deposits still visible in the studied cave. Thus, MnFe patinas can be considered indicators of cave paleo-flooding, with more basic conditions during the floods peaks (thus promoting an oxic geochemical environment), and less basic conditions during the flooding increases and decreases (thus promoting a sub-oxic geochemical environment). Accordingly, a cyclical shift between oxic (high Mn/Fe ratio) and suboxic (low Mn/Fe ratio) conditions, related to flood rise and retreat, may have led to the formation of Mn-layers or Fe-lenses and oscillations of the Mn/Fe ratio along the accumulation direction of the patinas. Because more recent floods did not erode patinas, it is reasonable to think that during flooding, in this part of the cave, the water rises and falls gently, without causing turbulent flow. In the rising flood period, waters can flow slowly through the cave passages, possibly only cleaning the walls from the more recent unconsolidated soft mud coatings left by previous floods.

Significance of Patinas Morphotypes

Black Mn-layers show bands, developed along the accumulation direction of the patinas, characterized by different appearance (shiny or opaque), relative orientation of the layering, mineralogy, microbial imprints, and stromatolite-like structures (**Figure 13**). In these areas three morphotypes were identified: 1) *branched columnar* morphotype (**Figures 4I,J**). This morphotype, typical of opaque bands (**Figure 13**), is associated with vernadite, microbial imprints, detrital minerals, and voids. Moreover, it occurs exclusively within layers displaying the same orientation of the Fe-lenses (green dotted lines in **Figure 13B**). While 2) *flat-laminated* morphotype (**Figure 4K**) and 3) *columnar or pseudo-columnar* morphotype (**Figures 4I–O**) are typical of the shiny bands (**Figure 13**). These latter two morphotypes are associated with todorokite and/or ranciéite, with a lower detrital mineral content, and occur exclusively within layers displaying an orientation different from that of the Fe-lenses (yellow dotted lines in **Figure 13B**). Moreover, within these morphotypes, no evidence of microbial imprints was recognized. As a result, opaque (*i.e., branched columnar* morphotype) or shiny (*i.e., flat-laminated* and *columnar or pseudo-columnar* morphotypes) bands, depending upon the orientation of the layers (*i.e.,* related to the roughness of the wall surface) and on the presence or absence of detrital minerals, alternate laterally (**Figure 13**). During the growth of the patina the surface becomes progressively flatter (compared to the wall surface), then the last layer that formed shows only two bands, one shiny on the left side and one opaque on the right side of the sample (**Figure 13**). The presence of such bands, parallel to the growth direction of the patinas, and the occurrence of different Mn species (*i.e.,* vernadite: in the opaque bands related to detrital minerals and microbial imprints; and todorokite/ranciéite: in the shiny bands free of detrital minerals and microbial imprints), within the same layers, suggests that the accessory clay minerals and microbial activity may be important factors in controlling MnOx mineralogy, further enhancing the oxidation rate of Mn^{2+} by combining surface catalysis with biological oxidation. In fact, the formation of the poorly crystalline vernadite requires very rapid oxidation of Mn^{2+}, to prevent the formation of more stable MnOx, such as todorokite (Chukhrov, 1980). Other environmental conditions (*e.g.,* pH, Eh, chemistry of the water) cannot explain either the lateral variations of the different morphotypes, or the correlation existing between the morphotypes and the detrital minerals, or even the correlation between the morphotypes and the orientation of the layering. In fact, variations of these environmental parameters would lead to an alternation of layers with different mineralogy/structures (as typically occurs in MnFe nodules and crusts on the ocean floor; see Benites et al., 2018; Marino et al., 2018), and therefore do not appear to be responsible for the recognized distribution of minerals and structures. On the contrary, this spatial distribution points to quite constant environmental conditions, during the growth of the Mn-layers, which change abruptly (toward suboxic conditions) only during the deposition of the Fe-lenses. As well known, the morphology of stromatolite-like deposits strongly depends on sedimentation, grain size of the sediments, nutrient supply, flow velocity, among others (Hickman-Lewis et al., 2019 and references therein). For instance, branching forms develop in less turbulent environments, which facilitate sedimentation; whereas planar forms are produced in more turbulent environments

characterized by lower sedimentation rate (Dupraz et al., 2006 and references therein). Moreover, hydrodynamic conditions set the spatial distribution of shear stress and oxygen availability, promoting specific microbial colonization patterns (Thomen et al., 2017). In this environment, bacteria adhered to the wall surface in low energy zones (*i.e.,* opaque bands), less susceptible to leach, where they found more stable conditions to catalyze Mn^{2+} oxidation (Nealson, 2006). This hypothesis is further supported by the identification of putative predivisional cells, which are usually associated with the attachment of cells to the substrate (Gliesche et al., 2015; Hirsch and Gebers, 2015). Accordingly, the spatial distribution of the different morphotypes points to a strong influence exerted by the geometry of the substrate surface (*i.e.,* morphology of the cave walls) on the hydraulic regime, which, in turn, controls the detrital supply and microbial colonization that trigger the formation of highly disordered vernadite, instead of todorokite and/or ranciéite. This process ultimately affects the spatial distribution of the oxidation state of Mn. Our analyses by Raman mapping (see **Figure 7**) shows that the *flat-laminated* and *columnar or pseudo-columnar* morphotypes (more turbulent local environment) are characterized by the higher average oxidation state of Mn (note that in todorokite/ranciéite Mn occurs under an average oxidation state ~ 3.8, see Chalmin et al., 2009; Post et al., 2003; McKeown and Post, 2001; Post and Bish, 1988). While the *branched columnar* morphotype (associated with a less turbulent local environment, detrital minerals, and bacterially-mediated vernadite), on the other hand, is characterized by the lower average oxidation state of Mn (note that in vernadite Mn occurs under an average oxidation state ~ 3.5, see Manceau et al., 2014).

We suggest that Mn-oxidizing bacteria catalyze the formation of vernadite, a poorly crystalline and disordered compound with high specific surface area and adsorption capacity. Moreover, XRF results show Ni, Zn, Cu, V, and As; consequently, biological activity also controls the partitioning of potentially toxic elements between solid phases and the water system in the studied area.

CONCLUSION

In this work, MnFe patinas from deep inside the *Grotta del Cervo* (Italy) were sampled to study the relationship between mineralogy and oxidation state of Mn, detrital minerals, microbial communities, and morphological features. Our data show that the microbial communities' composition is dominated by Mn^{2+}-oxidizing bacteria and related to Mn-rich environments (*i.e., Bacillus*, *Flavobacterium*, and *Pseudomonas*). Based on our data, we cannot precisely determine which bacteria were directly involved in this process. Nevertheless, this study is a starting point for the identification of bacteria involved in biomineralization processes within this cave. In such an extreme cave environment, bacterial activity catalyzes the oxidation of Mn^{2+} and Fe^{2+} to $Mn^{3+/4+}$ and Fe^{3+}, thereby controlling the partitioning of potentially toxic elements, such as Ni, Zn, Cu, V, and As, between solid phases and the aqueous system. Combining SEM-EDS, XRF, XRPD, FT-IR, and Raman spectroscopy data, we show that these patinas consist of an alternation of Fe-lenses (characterized by a fine-mixture of hematite, goethite, and detrital minerals), and Mn-layers (in which vernadite, todorokite, and/or ranciéite were identified). Moreover, we show an oscillation of Mn and Fe along the growth of the patinas. Based on these results, we hypothesize that the patinas during their growth are recording paleo-floods, alternating oxic and suboxic environments according to the different phases of the flood events, similar to what has been documented in other caves (Rossi et al., 2010; Gázquez et al., 2011). We also recognized a sub-millimetric lamination within the flood events themselves, probably pointing towards normal (seasonal) flood events, higher-than-normal floods (decadal), and a few (secular) extreme events. We thus consider these deposits as indicators of a climate condition characterized by recurrent heavy and prolonged rain periods.

Within the Mn-layers, stromatolite-like structures were identified and related to different mineralogy and oxidation state of Mn, absence/presence of microbial imprints, the abundance of detrital minerals, and layering orientation, namely 1) *branched columnar* morphotype, associated with vernadite and lower oxidation state of Mn, occur in areas rich in detrital minerals, microbial imprints, and voids, 2) *flat-laminated* and 3) *columnar* morphotypes, both associated with todorokite and/or ranciéite and higher oxidation state of Mn, occur in areas with little detrital minerals and free of microbial imprints. These three morphotypes alternate along each Mn-layer as a function of the local layer orientation. All these features suggest that the wall surface's geometry (*i.e.,* roughness) firmly controls the very local hydraulic regime and, in turn, the sedimentation of clay minerals and microbial communities development. Accordingly, in a less turbulent environment, microbial communities development and sedimentation of clays can occur. In this environment, the combination of clay surface catalysis and biological oxidation increases the oxidation rate of Mn^{2+} producing poor-crystalline vernadite, whereas in a more turbulent environment, this catalysis is not possible, and todorokite and/or ranciéite can form.

Our results show that MnFe patinas are precious tools for reconstructing past hydrogeological, mineralogical, and biological processes, particularly for areas where other indicators are lacking, as well as in exoplanetary research. For instance, MnOx have been found on the Mars ground, pointing to a more Earth-like Martian past than previously thought (Lanza et al., 2014, 2016). With this in mind, NASA, ESA/Roscosmos, and CNSA are making great efforts to reconstruct the past Martian environment and seek signs of microbial life, with the Mars 2020, ExoMars 2022, and Tianwen-1 missions, respectively. Therefore, investigating potential microbial-mediated MnOx could be of primary importance to reconstructing the past Martian redox conditions and looking for traces of past or present life.

DATA AVAILABILITY STATEMENT

The nucleotide sequences of the partial 16S rRNA gene segments determined in this study have been deposited in the NCBI database repository, BioProject: PRJNA723830 (https://www.ncbi.nlm.nih.gov/bioproject/PRJNA723830).

AUTHOR CONTRIBUTIONS

SB research coordination, SEM-EDS, XRPD, μXRF, FT-IR, and Raman spectroscopy analyses, data interpretation, writing of the manuscript with support from AC, MDG, CS-J, JDW, and corresponding author; FB scientific supervision, research coordination, manuscript revision, geological data interpretation, SEM-EDS analysis, sampling; AC data interpretation; IV sampling, microbial analysis and interpretation; MP microbial analysis and interpretation; VJ microbial data curation; MDG supervising microbiological work, resources provision; CS-J microbiological data analysis; AS Raman spectroscopy analysis; CM μXRF analysis; LJ μXRF analysis; JDW data interpretation. All the authors have contributed to the scientific discussion of the data and agreed to the submitted version of the manuscript.

ACKNOWLEDGMENTS

This research was conducted in collaboration with the Brazilian Synchrotron Light Laboratory (LNLS), an open national facility belonging to the Brazilian Centre for Research in Energy and Materials (CNPEM) under the supervision of the Brazilian Ministry of Science, Technology, and Innovations (MCTI). Douglas Galante and Carlos Alberto Perez (LNLS - XRF beamline), Priyeshu Srivastava, Mariana Benites, and Ana Martini (IOUSP) are acknowledged for the assistance during XRF measurements. We thank Anas Abbassi (Roma Tre University) for kindly providing the geological map (**Figure 1**), and Roberto Pucci for kindly producing the image shown in **Figure 2**. The Spanish project MINECO CGL 2016-75590-P with ERDF funds is gratefully acknowledged. LJ acknowledge funding from Fundação de Amparo a Pesquisa do Estado de São Paulo (FAPESP) grant 2018/17061-6.

FUNDING

Spanish project MINECO CGL 2016-75590-P with ERDF funds Fundação de Amparo a Pesquisa do Estado de São Paulo (FAPESP) grant 2018/17061-6.

SUPPLEMENTARY MATERIAL

The Supplementary Material for this article can be found online at: https://www.frontiersin.org/articles/10.3389/feart.2021.642667/full#supplementary-material

REFERENCES

Agostini, S., and Piccini, L. (1994). Aspetti geomorfologici ed evolutivi del sistema carsico di Pietrasecca (M. Carseolani - Appennino Centrale, Italia). *Ital. Speleol. Mem.* 5, 61–70

Allward, N. E., Gregory, B. S., Sotddart, A. K., and Gagnon, G. A. (2018). Potential for Manganese Biofouling in Water Transmission Lines Using Model Reactors. *Environ. Sci. Water Res. Technol.* 4, 761–772. doi:10.1039/c8ew00074c

Andrejchuk, V. N., and Klimchouk, A. B. (2001). Geomicrobiology and Redox Geochemistry of the Karstified Miocene gypsum Aquifer, Western Ukraine: The Study from Zoloushka Cave. *Geomicrobiol. J.* 18, 275–295. doi:10.1080/01490450152467796

Arvidson, R. E., Squyres, S. W., Morris, R. V., Knoll, A. H., Gellert, R., Clark, B. C., et al. (2016). High Concentrations of Manganese and Sulfur in Deposits on Murray Ridge, Endeavour Crater, Mars. *Am. Mineral.* 101, 1389–1405. doi:10.2138/am-2016-5599

Balachandran, U., and Eror, N. G. (1982). Raman Spectra of Titanium Dioxide. *J. Solid State. Chem.* 42, 276–282. doi:10.1016/0022-4596(82)90006-8

Barboza, N. R., Amorim, S. S., Santos, P. A., Reis, F. D., Cordeiro, M. M., Guerra-Sá, R., et al. (2015). Indirect Manganese Removal byStenotrophomonassp. andLysinibacillussp. Isolated from Brazilian Mine Water. *Biomed. Res. Int.* 2015, 1–14. doi:10.1155/2015/925972

Bargar, J. R., Tebo, B. M., Bergmann, U., Webb, S. M., Glatzel, P., Chiu, V. Q., et al. (2005). Biotic and Abiotic Products of Mn(II) Oxidation by Spores of the marine Bacillus sp. strain SG-1. *Am. Mineral.* 90, 143–154. doi:10.2138/am.2005.1557

Belli, R., Frisia, S., Borsato, A., Drysdale, R., Hellstrom, J., Zhao, J.-x., et al. (2013). Regional Climate Variability and Ecosystem Responses to the Last Deglaciation in the Northern Hemisphere from Stable Isotope Data and Calcite Fabrics in Two Northern Adriatic Stalagmites. *Quat. Sci. Rev.* 72, 146–158. doi:10.1016/j.quascirev.2013.04.014

Benites, M., Millo, C., Hein, J., Nath, B., Murton, B., Galante, D., et al. (2018). Integrated Geochemical and Morphological Data Provide Insights into the Genesis of Ferromanganese Nodules. *Minerals* 8, 488. doi:10.3390/min8110488

Bernardini, S., Bellatreccia, F., Casanova Municchia, A., Della Ventura, G., and Sodo, A. (2019). Raman Spectra of Natural Manganese Oxides. *J. Raman Spectrosc.* 50, 873–888. doi:10.1002/jrs.5583

Bernardini, S., Bellatreccia, F., Della Ventura, G., Ballirano, P., and Sodo, A. (2020b). Raman Spectroscopy and Laser-Induced Degradation of Groutellite and Ramsdellite, Two Cathode Materials of Technological Interest. *RSC Adv.* 10, 923–929. doi:10.1039/c9ra08662e

Bernardini, S., Bellatreccia, F., Della Ventura, G., and Sodo, A. (2020a). A Reliable Method for Determining the Oxidation State of Manganese at the Microscale in Mn Oxides via Raman Spectroscopy. *Geostand. Geoanal. Res.* 45, 223–244. doi:10.1111/ggr.12361

Berner, R. A. (1981). A New Geochemical Classification of Sedimentary Environments. *J. Sediment. Petrol.* 51, 359–365. doi:10.1306/212F7C7F-2B24-11D7-8648000102C1865D

Bertolani, M., Lugli, S., and Rossi, A. (1994). Petrographic Investigations in the Pietrasecca Cave System (L'Aquila - Central Italy). *Ist. Ital. Speleol. Mem.* 5, 71–83

Bolyen, E., Rideout, J. R., Dillon, M. R., Bokulich, N. A., Abnet, C. C., Al-Ghalith, G. A., et al. (2019). Reproducible, Interactive, Scalable and Extensible Microbiome Data Science Using QIIME 2. *Nat. Biotechnol.* 37, 852–857. doi:10.1038/s41587-019-0209-9

Carmichael, M. J., Carmichael, S. K., Santelli, C. M., Strom, A., and Bräuer, S. L. (2013b). Mn(II)-oxidizing Bacteria Are Abundant and Environmentally Relevant Members of Ferromanganese Deposits in Caves of the Upper Tennessee River Basin. *Geomicrobiol. J.* 30, 779–800. doi:10.1080/01490451.2013.769651

Carmichael, S., Carmichael, M., Strom, A., Johnson, K., Roble, L., Gao, Y., et al. (2013a). Sustained Anthropogenic Impact in Carter Saltpeter Cave, Carter County, Tennessee and the Potential Effects on Manganese Cycling. *J. Cave Karst Stud.* 75, 189–204. doi:10.4311/2012MB0267

Carmichael, S. K., Bräuer, S. L., and Engel, A. S. (2015). "Microbial Diversity and Manganese Cycling: A Review of Manganese-Oxidizing Microbial Cave Communities", *Microbial Life In Cave Systems*," in *Life in Extreme Environments* (Boston: De Gruyter), 137–160.

Chalmin, E., Farges, F., and Brown, G. E. (2009). A Pre-edge Analysis of Mn K-Edge XANES Spectra to Help Determine the Speciation of Manganese in Minerals and Glasses. *Contrib. Mineral. Petrol.* 157, 111–126. doi:10.1007/s00410-008-0323-z

Chaput, D. L., Hansel, C. M., Burgos, W. D., and Santelli, C. M. (2015). Profiling Microbial Communities in Manganese Remediation Systems Treating Coal Mine Drainage. *Appl. Environ. Microbiol.* 81, 2189–2198. doi:10.1128/AEM.03643-14

Chen, S.-C., Chiu, C.-H., Chiu, P.-T., Chen, Y.-C., Lin, Y.-H., Young, C.-C., et al. (2019). Draft Genome Sequence of Manganese-Oxidizing Bacterium

Massilia Sp. Strain Mn16-1_5, Isolated from Serpentine Soil in Taitung, Taiwan. *Microbiol. Resour. Announce* 8, e00694–19. doi:10.1128/MRA.00694-19

Choi, K., Choi, J., Lee, P. A., Roy, N., Khan, R., Lee, H. J., et al. (2020). Alteration of Bacterial Wilt Resistance in Tomato Plant by Microbiota Transplant. *Front. Plant Sci.* 11, 1186. doi:10.3389/fpls.2020.01186

Chukhrov, F. V., Gorshkov, A. I., Rudnitskaya, Y. S., Berezovskaya, V. V., and Sivtsov, A. V. (1978). On Vernadite. *Bull. Acad. Sci. USSR Ser. Geol.* 6, 5–19.

Chukhrov, F. V. (1980). On Vernadite. *Int. Geol. Rev.* 22, 58–74. doi:10.1080/00206818209466863

Columbu, A., Chiarini, V., Spötl, C., Benazzi, S., Hellstrom, J., Cheng, H., et al. (2020). Speleothem Record Attests to Stable Environmental Conditions during Neanderthal-Modern Human Turnover in Southern Italy. *Nat. Ecol. Evol.* 4, 1188–1195. doi:10.1038/s41559-020-1243-1

Columbu, A., De Waele, J., Forti, P., Montagna, P., Picotti, V., Pons-Branchu, E., et al. (2015). Gypsum Caves as Indicators of Climate-Driven River Incision and Aggradation in a Rapidly Uplifting Region. *Geology* 43, 539–542. doi:10.1130/G36595.1

Columbu, A., Drysdale, R., Capron, E., Woodhead, J., De Waele, J., Sanna, L., et al. (2017). Early Last Glacial Intra-interstadial Climate Variability Recorded in a Sardinian Speleothem. *Quat. Sci. Rev.* 169, 391–397. doi:10.1016/j.quascirev.2017.05.007

Columbu, A., Sauro, F., Lundberg, J., Drysdale, R., and De Waele, J. (2018). Palaeoenvironmental Changes Recorded by Speleothems of the Southern Alps (Piani Eterni, Belluno, Italy) during Four Interglacial to Glacial Climate Transitions. *Quat. Sci. Rev.* 197, 319–335. doi:10.1016/j.quascirev.2018.08.006

Columbu, A., Spötl, C., De Waele, J., Yu, T.-L., Shen, C.-C., and Gázquez, F. (2019). A Long Record of MIS 7 and MIS 5 Climate and Environment from a Western Mediterranean Speleothem (SW Sardinia, Italy). *Quat. Sci. Rev.* 220, 230–243. doi:10.1016/j.quascirev.2019.07.023

Cornaggia, F., Bernardini, S., Giorgioni, M., Silva, G. L. X., Nagy, A. I. M., and Jovane, L. (2020). Abyssal Oceanic Circulation and Acidification during the Middle Eocene Climatic Optimum (MECO). *Sci. Rep.* 10, 1–9. doi:10.1038/s41598-020-63525-3

Cosentino, D., Carboni, M. G., Cipollari, P., Di Bella, L., Florindo, F., Laurenzi, M. A., et al. (1997). Integrated Stratigraphy of the Tortonian/Messinian Boundary: The Pietrasecca Composite Section (Centra Appenines, Italy). *Eclogae Geol. Helv.* 90, 229–224.

Cunningham, K. I., Northup, D. E., Pollastro, R. M., Wright, W. G., and LaRock, E. J. (1995). Bacteria, Fungi and Biokarst in Lechuguilla Cave, Carlsbad Caverns National Park, New Mexico. *Environ. Geol.* 25, 2–8. doi:10.1007/BF01061824

de Faria, D. L. A., and Lopes, F. N. (2007). Heated Goethite and Natural Hematite: Can Raman Spectroscopy Be Used to Differentiate Them? *Vib. Spectrosc.* 45, 117–121. doi:10.1016/j.vibspec.2007.07.003

Drysdale, R. N., Hellstrom, J. C., Zanchetta, G., Fallick, A. E., Sanchez Goni, M. F., Couchoud, I., et al. (2009). Evidence for Obliquity Forcing of Glacial Termination II. *Science* 325, 1527–1531. doi:10.1126/science.1170371

Dupraz, C., Pattisina, R., and Verrecchia, E. P. (2006). Translation of Energy into Morphology: Simulation of Stromatolite Morphospace Using a Stochastic Model. *Sediment. Geol.* 185, 185–203. doi:10.1016/j.sedgeo.2005.12.012

Ertl, A., Pertlik, F., Prem, M., Post, J. E., Kim, S. J., Brandstä tter, F., et al. (2005). Rancieite Crystals from Friesach, Carinthia, Austria. *Eur. J. Mineral.* 17, 163–172. doi:10.1127/0935-1221/2005/0017-0163

Fairchild, I. J., Smith, C. L., Baker, A., Fuller, L., Spötl, C., Mattey, D., et al. (2006). Modification and Preservation of Environmental Signals in Speleothems. *Earth-Sci. Rev.* 75, 105–153. doi:10.1016/j.earscirev.2005.08.003

Farrugia, C., Borg, R. P., Ferrara, L., and Buhagiar, J. (2019). The Application of *Lysinibacillus Sphaericus* for Surface Treatment and Crack Healing in Mortar. *Front. Built Environ.* 5, 62. doi:10.3389/fbuil.2019.00062

Feng, X. H., Zhu, M., Ginder-Vogel, M., Ni, C., Parikh, S. J., and Sparks, D. L. (2010). Formation of Nano-Crystalline Todorokite from Biogenic Mn Oxides. *Geochim. Cosmochim. Acta* 74, 3232–3245. doi:10.1016/j.gca.2010.03.005

Fonollá, C., Sanz, E., and Menéndez-Pidal, I. (2020). Lateral Ferruginous Groundwater Transfer as the Origin of the Iron Crusts in Caves: a Case Study. *J. Cave Karst Stud.* 82, 183–197. doi:10.4311/2019ES0143

Forti, P. (1994). I fenomeni concrezionari nelle grotte del Cervo e dell'Ovito a Pietrasecca. *Ist. Ital. Speleol. Mem.* 5, 85–96.

Francis, C. A., and Tebo, B. M. (2002). Enzymatic Manganese(II) Oxidation by Metabolically Dormant Spores of Diverse Bacillus Species. *Appl. Environ. Microbiol.* 68, 874–880. doi:10.1128/AEM.68.2.874–880.200210.1128/aem.68.2.874-880.2002

Frierdich, A. J., Hasenmueller, E. A., and Catalano, J. G. (2011). Composition and Structure of Nanocrystalline Fe and Mn Oxide Cave Deposits: Implications for Trace Element Mobility in Karst Systems. *Chem. Geol.* 284, 82–96. doi:10.1016/j.chemgeo.2011.02.009

Frisia, S., Borsato, A., Mangini, A., Spötl, C., Madonia, G., and Sauro, U. (2006). Holocene Climate Variability in Sicily from a Discontinuous Stalagmite Record and the Mesolithic to Neolithic Transition. *Quat. Res.* 66, 388–400. doi:10.1016/j.yqres.2006.05.003

Frisia, S., Borsato, A., Spötl, C., Villa, I. M., and Cucchi, F. (2005). Climate Variability in the SE Alps of Italy over the Past 17 000 Years Reconstructed from a Stalagmite Record. *Boreas* 34, 445–455. doi:10.1080/03009480500231336

Gázquez, F., Calaforra, J. M., and Forti, P. (2011). Black Mn-Fe Crusts as Markers of Abrupt Palaeoenvironmental Changes in El Soplao Cave (Cantabria, Spain). *Int. J. Speleol.* 40, 163–169. doi:10.5038/1827-806X.40.2.8

Ghosh, S., Mohanty, S., Nayak, S., Sukla, L. B., and Das, A. P. (2016). Molecular Identification of Indigenous Manganese Solubilising Bacterial Biodiversity from Manganese Mining Deposits. *J. Basic Microbiol.* 56, 254–262. doi:10.1002/jobm.201500477

Gliesche, C., Fesefeldt, A., and Hirsch, P. (2015). Hyphomicrobium. *Bergey's Manual of Systematics of Archaea and Bacteria*. New York: Springer-Verlag, 1–34. doi:10.1002/9781118960608.gbm00820

Gonzalez-Pimentel, J. L., Martin-Pozas, T., Jurado, V., Miller, A. Z., Caldeira, A. T., Fernandez-Lorenzo, O., et al. (2021). Prokaryotic Communities from a Lava Tube Cave in La Palma Island (Spain) Are Involved in the Biogeochemical Cycle of Major Elements. *PeerJ* 9, e11386. doi:10.7717/peerj.11386

Gradziński, M., Banaś, M., and Uchman, A. (1995). Biogenic Origin of Manganese Flowstones from Jaskinia Czarna Cave, Tatra mts., Western Carpathians. *Ann. Soc. Geol. Pol.* 65, 19–27.

Hammer, Ø., Harper, D. A. T., and Ryan, P. D. (2001). Past: Paleontological Statistics Software Package for Education and Data Analysis. *Palaeontol. Electronica* 4, 1–9.

He, J., Zhang, L., Jin, S., Zhu, Y., and Liu, F. (2008). Bacterial Communities inside and Surrounding Soil Iron-Manganese Nodules. *Geomicrobiol. J.* 25, 14–24. doi:10.1080/01490450701829014

Hein, J. R., Konstantinova, N., Mikesell, M., Mizell, K., Fitzsimmons, J. N., Lam, P. J., et al. (2017). Arctic Deep Water Ferromanganese-Oxide Deposits Reflect the Unique Characteristics of the Arctic Ocean. *Geochem. Geophys. Geosyst.* 18, 3771–3800. doi:10.1002/2017GC007186

Hem, J. D. (1972). Chemical Factors that Influence the Availability of Iron and Manganese in Aqueous Systems. *Geol. Soc. Am. Bull.* 83, 443–450. doi:10.1130/0016-7606(1972)83[443:CFTITA]2.0.CO;2

Hem, J. D. (1963). Chemical Equilibria Affecting the Behavior of Manganese in Natural Water. *Int. Assoc. Sci. Hydrol. Bull.* 8, 30–37. doi:10.1080/02626666309493334

Hickman-Lewis, K., Gautret, P., Arbaret, L., Sorieul, S., De Wit, R., Foucher, F., et al. (2019). Mechanistic Morphogenesis of Organo-Sedimentary Structures Growing under Geochemically Stressed Conditions: Keystone to Proving the Biogenicity of Some Archaean Stromatolites? *Geosciences* 9, 359. doi:10.3390/geosciences9080359

Hill, C., and Forti, P. (1997). *Cave Minerals of the World*. Huntsville: National Speleological Society.

Hirsch, P., and Gebers, R. (2015). Pedomicrobium Aristovskaya 1961, 957 AL Emend. Gebers and Beese 1988, 305. *Bergey's Manual of Systematics of Archaea and Bacteria*. New York: Springer-Verlag, 527–538.

Hou, D., Zhang, P., Wei, D., Zhang, J., Yan, B., Cao, L., et al. (2020). Simultaneous Removal of Iron and Manganese from Acid Mine Drainage by Acclimated Bacteria. *J. Hazard. Mater.* 396, 122631. doi:10.1016/j.jhazmat.2020.122631

Itcus, C., Pascu, M. D., Lavin, P., Perşoiu, A., Iancu, L., and Purcarea, C. (2018). Bacterial and Archaeal Community Structures in Perennial Cave Ice. *Sci. Rep.* 8, 15671. doi:10.1038/s41598-018-34106-2

Jiang, S., Kim, D.-G., Kim, J.-H., and Ko, S.-O. (2010). Characterization of the Biogenic Manganese Oxides Produced by *Pseudomonas Putida* Strain MnB1. *Environ. Eng. Res.* 15, 183–190. doi:10.4491/eer.2010.15.4.183

Jurado, V., Gonzalez-Pimentel, J. L., Miller, A. Z., Hermosin, B., D'Angeli, I. M., Tognini, P., et al. (2020). Microbial Communities in Vermiculation Deposits from an Alpine Cave. *Front. Earth Sci.* 8, 586248. doi:10.3389/feart.2020.586248

Kim, H.-S., Pastén, P. A., Gaillard, J.-F., and Stair, P. C. (2003). Nanocrystalline Todorokite-like Manganese Oxide Produced by Bacterial Catalysis. *J. Am. Chem. Soc.* 125, 14284–14285. doi:10.1021/ja0375784

Koschinsky, A., and Halbach, P. (1995). Sequential Leaching of marine Ferromanganese Precipitates: Genetic Implications. *Geochim. Cosmochim. Acta* 59, 5113–5132. doi:10.1016/0016-7037(95)00358-4

Kotula, P., Andreychouk, V., Andreychouk, V., Pawlyta, J., Marynowski, L., and Jendrzejewska, I. (2019). Genesis of Iron and Manganese Sediments in Zoloushka Cave (Ukraine/Moldova) as Revealed by $\delta^{13}C$ Organic Carbon. *Int. J. Speleol.* 48, 221–235. doi:10.5038/1827-806X.48.3.2255

Lanza, N. L., Fischer, W. W., Wiens, R. C., Grotzinger, J., Ollila, A. M., Cousin, A., et al. (2014). High Manganese Concentrations in Rocks at Gale Crater, Mars. *Geophys. Res. Lett.* 41, 5755–5763. doi:10.1002/2014GL060329

Lanza, N. L., Wiens, R. C., Arvidson, R. E., Clark, B. C., Fischer, W. W., Gellert, R., et al. (2016). Oxidation of Manganese in an Ancient Aquifer, Kimberley Formation, Gale Crater, Mars. *Geophys. Res. Lett.* 43, 7398–7407. doi:10.1002/2016GL069109

Lee, S., Xu, H., Xu, W., and Sun, X. (2019). The Structure and crystal Chemistry of Vernadite in Ferromanganese Crusts. *Acta Crystallogr., Sect B: Struct. Sci., Cryst. Eng. Mater.* 4, 591–598. doi:10.1107/S2052520619006528

Lee, Y. S., Kim, H. J., and Park, W. (2017). Non-ureolytic Calcium Carbonate Precipitation by *Lysinibacillus* Sp. YS11 Isolated from the Rhizosphere of *Miscanthus Sacchariflorus*. *J. Microbiol.* 55, 440–447. doi:10.1007/s12275-017-7086-z

Liu, H., Song, Y., Chen, F., Zheng, S., and Wang, G. (2013). *Lysinibacillus Manganicus* Sp. nov., Isolated from Manganese Mining Soil. *Int. J. Syst. Evol. Microbiol.* 63, 3568–3573. doi:10.1099/ijs.0.050492-0

Lozano, R. P., and Rossi, C. (2012). Exceptional Preservation of Mn-Oxidizing Microbes in Cave Stromatolites (El Soplao, Spain). *Sediment. Geol.* 255–256, 42–55. doi:10.1016/j.sedgeo.2012.02.003

Manceau, A., Lanson, M., and Takahashi, Y. (2014). Mineralogy and crystal Chemistry of Mn, Fe, Co, Ni, and Cu in a Deep-Sea Pacific Polymetallic Nodule. *Am. Mineral.* 99, 2068–2083. doi:10.2138/am-2014-4742

Marino, E., González, F., Lunar, R., Reyes, J., Medialdea, T., Castillo-Carrión, M., et al. (2018). High-Resolution Analysis of Critical Minerals and Elements in Fe-Mn Crusts from the Canary Island Seamount Province (Atlantic Ocean). *Minerals* 8, 285. doi:10.3390/min8070285

McKenzie, R. (1980). The Adsorption of lead and Other Heavy Metals on Oxides of Manganese and Iron. *Soil Res.* 18, 61–73. doi:10.1071/sr9800061

McKeown, D. A., and Post, J. E. (2001). Characterization of Manganese Oxide Mineralogy in Rock Varnish and Dendrites Using X-ray Absorption Spectroscopy. *Am. Mineral.* 86, 701–713. doi:10.2138/am-2001-5-611

Meier, A., Kastner, A., Harries, D., Wierzbicka-Wieczorek, M., Majzlan, J., Büchel, G., et al. (2017). Calcium Carbonates: Induced Biomineralization with Controlled Macromorphology. *Biogeosciences* 14, 4867–4878. doi:10.5194/bg-14-4867-2017

Mitchell, A. C., Espinosa-Ortiz, E. J., Parks, S. L., Phillips, A. J., Cunningham, A. B., and Gerlach, R. (2019). Kinetics of Calcite Precipitation by Ureolytic Bacteria under Aerobic and Anaerobic Conditions. *Biogeosciences* 16, 2147–2161. doi:10.5194/bg-16-2147-2019

Naeher, S., Gilli, A., North, R. P., Hamann, Y., and Schubert, C. J. (2013). Tracing Bottom Water Oxygenation with Sedimentary Mn/Fe Ratios in Lake Zurich, Switzerland. *Chem. Geol.* 352, 125–133. doi:10.1016/j.chemgeo.2013.06.006

Nealson, K. H. (2006). The Manganese-Oxidizing Bacteria. *The Prokaryotes*. New York: Springer, 222–231. doi:10.1007/0-387-30745-1_11

Northup, D. E., Barns, S. M., Yu, L. E., Spilde, M. N., Schelble, R. T., Dano, K. E., et al. (2003). Diverse Microbial Communities Inhabiting Ferromanganese Deposits in Lechuguilla and Spider Caves. *Environ. Microbiol.* 5, 1071–1086. doi:10.1046/j.1462-2920.2003.00500.x

Northup, D. E., Dahm, C. N., Melim, L. A., Spilde, M. N., Crossey, L. J., Lavoie, K. H., et al. (2000). Evidence for Geomicrobiological Interactions in Guadalupe Caves. *J. Cave Karst Stud.* 62, 80–90.

Ortega-Villamagua, E., Gudiño-Gomezjurado, M., and Palma-Cando, A. (2020). Microbiologically Induced Carbonate Precipitation in the Restoration and Conservation of Cultural Heritage Materials. *Molecules* 25, 5499. doi:10.3390/molecules25235499

Oscarson, D. W., Huang, P. M., Liaw, W. K., and Hammer, U. T. (1983). Kinetics of Oxidation of Arsenite by Various Manganese Dioxides. *Soil Sci. Soc. Am. J.* 47, 644–648. doi:10.2136/sssaj1983.03615995004700040007x

Papier, S., Baele, J. M., Gillan, D., Barriquand, J., and Barriquand, L. (2011). Manganese Geomicrobiology of the Black Deposits from the Azé Cave, Saône-Et-Loire, France. *Quaternaire* 4, 297–305.

Pasić, L., Kovce, B., Sket, B., and Herzog-Velikonja, B. (2010). Diversity of Microbial Communities Colonizing the walls of a Karstic Cave in Slovenia. *FEMS Microbiol. Ecol.* 71, 50–60. doi:10.1111/j.1574-6941.2009.00789.x

Post, J. E., and Bish, D. L. (1988). Rietveld Refinement of the Todorokite Structure. *Am. Mineral.* 73, 861–869.

Post, J. E., Heaney, P. J., and Hanson, J. (2003). Synchrotron X-ray Diffraction Study of the Structure and Dehydration Behavior of Todorokite. *Am. Mineral.* 88, 142–150. doi:10.2138/am.2007.213410.2138/am-2003-0117

Post, J. E. (1999). Manganese Oxide Minerals: Crystal Structures and Economic and Environmental Significance. *Proc. Natl. Acad. Sci.* 96, 3447–3454. doi:10.1073/pnas.96.7.3447

Postpischl, D., Agostini, S., Forti, P., and Quinif, Y. (1991). Palaeoseismicity from karst sediments: the "Grotta del Cervo" cave case study (Central Italy). *Tectonophysics* 193, 33–44. doi:10.1016/0040-1951(91)90186-v

Potter, R. M., and Rossman, G. R. (1979). The Tetravalent Manganese Oxides: Identification, Hydration, and Structural Relationships by Infrared Spectroscopy. *Am. Mineral.* 64, 1199–1218.

Reeksting, B. J., Hoffmann, T. D., Tan, L., Paine, K., and Gebhard, S. (2020). In-depth Profiling of Calcite Precipitation by Environmental Bacteria Reveals Fundamental Mechanistic Differences with Relevance to Application. *Appl. Environ. Microbiol.* 86, e02739-19. doi:10.1128/AEM.02739-19

Regattieri, E., Zanchetta, G., Isola, I., Zanella, E., Drysdale, R. N., Hellstrom, J. C., et al. (2019). Holocene Critical Zone Dynamics in an Alpine Catchment Inferred from a Speleothem Multiproxy Record: Disentangling Climate and Human Influences. *Sci. Rep.* 9, 1. doi:10.1038/s41598-019-53583-7

Robertson, A. H. F., Necdet, M., Raffi, I., and Chen, G. (2019). Early Messinian Manganese Deposition in NE Cyprus Related to Cyclical Redox Changes in a Silled Hemipelagic basin Prior to the Mediterranean Salinity Crisis. *Sediment. Geol.* 385, 126–148. doi:10.1016/j.sedgeo.2019.03.009

Rossi, C., Lozano, R. P., Isanta, N., and Hellstrom, J. (2010). Manganese Stromatolites in Caves: El Soplao (Cantabria, Spain). *Geology* 38, 1119–1122. doi:10.1130/G31283.1

Roy, S., Nicholson, K., Hein, J. R., Buhn, B., and Dasgupta, S. (1997). Genetic Diversity of Manganese Deposition in the Terrestrial Geological Record, *Geol. Soc. Lond. Spec. Publications*. *Manganese Mineralization: Geochemistry and Mineralogy of Terrestrial and Marine Deposits*, 119. London: Geological Society Special Publication, 5–27. doi:10.1144/gsl.sp.1997.119.01.02

Saiz-Jimenez, C., Miller, A. Z., Martin-Sanchez, P. M., and Hernandez-Marine, M. (2012). Uncovering the Origin of the Black Stains in Lascaux Cave in France. *Environ. Microbiol.* 14, 3220–3231. doi:10.1111/1462-2920.12008

Sjöberg, S., Callac, N., Allard, B., Smittenberg, R. H., and Dupraz, C. (2018). Microbial Communities Inhabiting a Rare Earth Element Enriched Birnessite-type Manganese deposit in the Ytterby Mine, Sweden. *Geomicrobiol. J.* 35, 657–674. doi:10.1080/01490451.2018.1444690

Spilde, M. N., Northup, D. E., Boston, P. J., Schelble, R. T., Dano, K. E., Crossey, L. J., et al. (2005). Geomicrobiology of Cave Ferromanganese Deposits: a Field and Laboratory Investigation. *Geomicrobiol. J.* 22, 99–116. doi:10.1080/01490450590945889

Spiro, T. G., Bargar, J. R., Sposito, G., and Tebo, B. M. (2010). Bacteriogenic Manganese Oxides. *Acc. Chem. Res.* 43, 2–9. doi:10.1021/ar800232a

Stoppa, F., Woolley, A. R., and Cundari, A. (2002). Extension of the melilite-carbonatite province in the Apennines of Italy: the kamafugite of Grotta del Cervo, Abruzzo. *Mineral. Mag.* 66, 555–574. doi:10.1180/0026461026640049

Tebo, B. M., Bargar, J. R., Clement, B. G., Dick, G. J., Murray, K. J., Parker, D., et al. (2004). BIOGENIC MANGANESE OXIDES: Properties and Mechanisms of Formation. *Annu. Rev. Earth Planet. Sci.* 32, 287–328. doi:10.1146/annurev.earth.32.101802.120213

Tebo, B. M., Johnson, H. A., McCarthy, J. K., and Templeton, A. S. (2005). Geomicrobiology of Manganese(II) Oxidation. *Trends Microbiol.* 13, 421–428. doi:10.1016/j.tim.2005.07.009

Thomen, P., Robert, J., Monmeyran, A., Bitbol, A.-F., Douarche, C., and Henry, N. (2017). Bacterial Biofilm under Flow: First a Physical Struggle to Stay, Then a Matter of Breathing. *PLoS One* 12, e0175197. doi:10.1371/journal.pone.0175197

Vaccarelli, I., Matteucci, F., Pellegrini, M., Bellatreccia, F., and Del Gallo, M. (2021). Exploring Microbial Biosignatures in Mn-Deposits of Deep Biosphere: A Preliminary Cross-Disciplinary Approach to Investigate Geomicrobiological Interactions in a Cave in Central Italy. *Front. Earth Sci.* 9, 590257. doi:10.3389/feart.2021.590257

Vanghi, V., Borsato, A., Frisia, S., Drysdale, R., Hellstrom, J., and Bajo, P. (2018). Climate Variability on the Adriatic Seaboard during the Last Glacial Inception and MIS 5c from Frasassi Cave Stalagmite Record. *Quat. Sci. Rev.* 201, 349–361. doi:10.1016/j.quascirev.2018.10.023

Villalobos, M., Toner, B., Bargar, J., and Sposito, G. (2003). Characterization of the Manganese Oxide Produced by *Pseudomonas Putida* Strain MnB1. *Geochim. Cosmochim. Acta* 67, 2649–2662. doi:10.1016/S0016-7037(03)00217-5

White, W. B., Vito, C., and Scheetz, B. E. (2009). The Mineralogy and Trace Element Chemistry of Black Manganese Oxide Deposits from Caves. *J. Cave Karst Stud.* 71, 136–143.

Wiseschart, A., Mhuantong, W., Tangphatsornruang, S., Chantasingh, D., and Pootanakit, K. (2019). Shotgun Metagenomic Sequencing from Manao-Pee Cave, Thailand, Reveals Insight into the Microbial Community Structure and its Metabolic Potential. *BMC Microbiol.* 19, 144. doi:10.1186/s12866-019-1521-8

Xu, Z. G., Ding, Y., Huang, H. M., Wu, L., Zhao, Y. L., and Yang, G. Y. (2019). Biosorption Characteristics of Mn (II) by Bacillus Cereus Strain HM-5 Isolated from Soil Contaminated by Manganese Ore. *Pol. J. Environ. Stud.* 28, 1–10. doi:10.15244/pjoes/84838

Zanchetta, G., Drysdale, R. N., Hellstrom, J. C., Fallick, A. E., Isola, I., Gagan, M. K., et al. (2007). Enhanced Rainfall in the Western Mediterranean during Deposition of Sapropel S1: Stalagmite Evidence from Corchia Cave (Central Italy). *Quat. Sci. Rev.* 26, 279–286. doi:10.1016/j.quascirev.2006.12.003

Conflict of Interest: The authors declare that the research was conducted in the absence of any commercial or financial relationships that could be construed as a potential conflict of interest.

Publisher's Note: All claims expressed in this article are solely those of the authors and do not necessarily represent those of their affiliated organizations, or those of the publisher, the editors and the reviewers. Any product that may be evaluated in this article, or claim that may be made by its manufacturer, is not guaranteed or endorsed by the publisher.

frontiers in Earth Science

REVIEW
published: 24 January 2022
doi: 10.3389/feart.2021.720038

A Review of Ice Core Drilling in Cave Environment – Challenges, Achievements and Future Directions

Zoltan Kern[1]* *and Aurel Perşoiu*[2,3,4]*

[1]Institute for Geological and Geochemical Research, Research Centre for Astronomy and Earth Sciences, Eötvös Loránd Research Network, Budapest, Hungary, [2]Emil Racoviță Institute of Speleology, Romanian Academy, Cluj-Napoca, Romania, [3]Stable Isotope Laboratory, Ştefan cel Mare University, Suceava, Romania, [4]Romanian Institute of Science and Technology, Cluj-Napoca, Romania

Worldwide, more than 141 m of ice cores has been extracted from 20 cave ice deposits, with the drilling projects focusing mainly in Central European caves. The fact that half of the cave ice cores (3 out of 6) published in 2020 represent non-European localities, however, predicts that an increasing number of cave ice drilling projects will be carried out in the near future in other geographical areas hosting ice caves. Based on the gathered experience the most commonly encountered technical challenge of ice-core drilling problems in cave environment is englacial rocky/woody debris. The complex stratigraphy of cave ice deposits represents a crucial methodological problem. We propose an (Cave Ice Sedimentary Architecture and Deposition - CISAD) approach to take into consideration of the stratigraphic peculiarities of the investigated cave ice deposit and additional crucial meta-data before establishing the location of a drilling site best-suited to obtain the highest quality paleoenvironmental data.

Keywords: ice cave, ice core, drilling, paleoclimate, stratigraphy

OPEN ACCESS

Edited by:
Davide Tiranti,
Agenzia Regionale per la Protezione Ambientale (ARPA), Italy

Reviewed by:
Luca Paro,
Agenzia Regionale per la Protezione Ambientale (ARPA), Italy
Giandomenico Fubelli,
University of Turin, Italy

***Correspondence:**
Zoltan Kern
zoltan.kern@gmail.com
Aurel Perşoiu
aurel.persoiu@gmail.com

Specialty section:
This article was submitted to Quaternary Science, Geomorphology and Paleoenvironment, a section of the journal Frontiers in Earth Science

Received: *03 June 2021*
Accepted: *28 December 2021*
Published: *24 January 2022*

Citation:
Kern Z and Perşoiu A (2022) A Review of Ice Core Drilling in Cave Environment – Challenges, Achievements and Future Directions. Front. Earth Sci. 9:720038. doi: 10.3389/feart.2021.720038

INTRODUCTION

Ice cores recovered from glaciers have provided several of the longest, oldest and highest-resolution records of climate variability during the mid-to-late Quaternary (Jouzel, 2013). While polar and alpine glaciers have been generally targeted by such studies, the quest to understand past climate variability led to the expansion of drilling efforts towards "non-traditional" perennial ice accumulation such as ice wedges (Meyer et al., 2015; Opel et al., 2018), rock glaciers (Cecil et al., 1998; Krainer et al., 2015) and cave ice. While the first ice core from a cave ice deposit was extracted from Scărișoara Ice Cave (Romania) in 1947 (Serban et al., 1948) and thus the history of cave ice drilling activity is comparable to the semicentennial history of ice core drillings in polar (Dansgaard, 2004; Langway, 2008) and alpine (Oeschger et al., 1977) regions, the field gained more traction only in the past decade. Thus, several studies in Europe in the early 2000s (Citterio et al., 2004; Fórizs et al., 2004; Kern et al., 2004; Holmlund et al., 2005) have proved the potential of perennial ice caves to host valuable, high-resolution, long records of past environmental variability. Building on the early studies, in the 2010s, new ice cores were drilled in caves in Europe, North America and Asia (see below).

While ice core drilling campaigns in the more traditional polar and alpine environment face numerous challenges (Jouzel, 2013; Talalay, 2014; Talalay et al., 2015), cave ice drilling efforts received much less attention and their achievements and challenges have been generally restricted to the small ice caves community (Perşoiu and Lauritzen, 2018). Given the peculiar nature of ice

formation and dynamics in caves and the associated glacial, periglacial and karst-specific processes, drilling in cave glaciers and extracting continuous ice cores have proved a challenge for all teams involved. Various methods, techniques and equipment have been used with diverse degrees of success.

In this paper, we summarize the achievements and the main challenges of cave ice drilling efforts of the past 70 years and identify the best solution available considering both the peculiarities of cave ice deposits and the potential research questions that could be addressed. The article is structured as follows: in section 2, we present the main mechanisms of cave ice formation and the resulting ice bodies; section 3 is dedicated to a brief overview of the past cave ice drilling efforts and the methods used during the past 30 years and in section 4 we discuss potential approaches to maximize the results.

PERENNIAL ICE ACCUMULATION IN CAVES

Perennial ice accumulations in caves are found in most karst regions of the Northern Hemisphere, in a latitudinal band stretching between ~19 and 80 °N (Pflitsch et al., 2016; Barton et al., 2020), and from 30 m a.s.l. (above sea level) in Svalbard (Lauritzen et al., 2018) to 3,350 m a.s.l. (above sea level) on Mount Alberta, Canada (Yonge et al., 2018). The most significant processes responsible for the formation of perennial ice deposits in caves are freezing of water and snow accumulation, with glacial intrusion and hoarfrost deposition playing only minor roles (Perşoiu and Lauritzen, 2018; Kwiecien et al., 2022). Snow deposits occur at the base of near vertical entrance shafts in high-to-mid altitude mountains, forming deposits up to 80 m in thickness (Perşoiu and Onac, 2019). The reduced thickness of the snowpack does not result in pressures high enough to compact snow to ice (Langway et al., 1993). In most of the cases, the deposits consist of firn (density well below 0.83 g/cm^3) with intercalated layers of ice, formed by freezing of meltwater percolated through the snow mass. Contrary, ice formed by the freezing of water, so-called congelation ice, attains a density approaching the upper limit for ice (0.917 g/cm^3). The freezing process (Perşoiu et al., 2011) occurs as both thin films of inflowing water form successive layers of ice (floor ice) or as stagnant water freezes from top to bottom, to form a thick layer of ice trapping allochthonous sediments, *in-situ* forming cryogenic cave calcite (CCC, Žák et al., 2008) and occasional air bubbles (lake ice).

The vast majority of existing cave glaciers in caves are formed by water-freezing processes. They have formed since at least the early Holocene (Perşoiu et al., 2017; Sancho et al., 2018), experiencing periods of growth and decay, under the complex interplay of seasonally varying air temperatures and precipitation amounts (Stoffel et al., 2009; Spötl et al., 2014; Kern et al., 2018). The various climate and environmental proxies archived in these deposits (e.g., isotopologues of water and CCC, pollen, surface-derived sediments) offer a unique window in the past history of the environment and have been targeted with increased scrutiny over the past decades.

PAST CAVE ICE DRILLING PROJECTS

The first documented cave ice core was extracted from Scărişoara Ice Cave (Romania) in 1947 (Serban et al., 1948), and additional trials were performed in the 1960s (Serban et al., 1967) although these first attempts could extract only short (< 1 m) ice cores. Following these pioneer works there was a halt in the cave ice drilling projects for more than 3 decades. The next documented ice core (and the first outside Europe) was extracted from Candelaria Ice Cave (New Mexico, United States) in 1995 (Dickfoss et al., 1997). Subsequently, Europe became the hot spot of cave ice drilling activities during the first decades of the 21st century. Twenty-three drilling projects took place in 20 ice caves (**Table 1**) and the total length of the extracted ice cores is ~141 m (**Figure 1A**). First reports of cave ice drilling projects have usually been published following the biennial International Workshops on Ice Caves (IWIC). All but one cave ice drilling campaigns documented in the scientific literature were performed in the temperate mid-latitudes of the northern Hemisphere (**Figure 1B**). The only cave ice core representing a polar latitude was extracted from Svarthammarhola (Norway) (Lauritzen et al., 2005). The publication evidence shows the greatest concentration of cave ice cores in Central Europe, the Southern Alps (Italy and Slovenia) and the Western Carpathians (Romania) (**Figure 1A**). Replicated ice cores were extracted from subterranean ice deposits only in Romania and Cave 29 (New Mexico, United States) (**Table 1**).

The main objectives of these drilling projects were to reconstruct past climate variability using the isotopologues of water as climate proxies, a process initiated through the pioneering work of Serban et al. (1967) shortly after similar efforts were initiated in Greenland. These early efforts were continued in 20th century, with varying degrees of success, mostly due to difficulties in building reliable chronologies of ice accumulation (Kern, 2018). Thus, cave ice-based studies addressed the geochemistry and stable isotope geochemistry of cave ice (Kern et al., 2009; Kern et al., 2011a; Kern et al., 2011b; May et al., 2011), the dynamics of past winter (Perşoiu et al., 2017) and summer (Bădăluță et al., 2020) air temperatures, past environmental and vegetation changes (Feurdean et al., 2011; Sancho et al., 2018; Leunda et al., 2019) and the dynamics of cave ice accumulations (Stoffel et al., 2009; Perşoiu and Pazdur, 2011; Spötl et al., 2014; Kern et al., 2018). Over the past few years, several studies investigated microorganism in cave ice deposits, with specifically designed drilling strategies (Sattler et al., 2013; Itcus et al., 2018) allowing the recovery of millennia-old microbial (Mondini et al., 2019; Paun et al., 2019) and fungal (Brad et al., 2018) communities. Considering the wide geographical distribution of potential and confirmed area of cave glaciation (Mavlyudov, 2008; Mavlyudov, 2018) the current overrepresentation of Europe does not reflect the spatial distribution of the known ice caves in the World. There is great potential in cave ice science, including drilling the cave ice deposits, outside Europe as well. Interestingly, three of the six published cave ice drilling projects were carried out in non-European ice caves (Cave 29, New Mexico, United States - Onac et al., 2020, Kinderlinskaya and Askinskaya caves, Russia - Trofimova et al., 2020) in the closing year of the data collection of this review

TABLE 1 | Published cave ice drilling activities during the past 25 years.

Cave	Country	Max ice thickness (m)	Drilling technique	Max core length (m)	Reference
Eisriesenwelt	Austria	~7	electromechanical (not detailed)	7.1	May et al. (2011)
Dachstein-Mammuthöhle		~7	Manual	6.5	Kern et al. (2011a)
Hundsalm Eis- und Tropfsteinhöhle		>7	Manual	1.5	Sattler et al. (2013)
Vukusic Ice Cave	Croatia	>10	Manual	2.5	Kern et al. (2011b)
Schellenberger Eishöhle	Germany	—	not reported	8	Maggi et al. (2020)
LoLc1650	Italy	~15	SIPRE	1.20	Citterio et al. (2004)
Vasto Ice Cave		8.3	SIPRE	7.8	Colucci et al. (2016b)
Leupa Ice Cave		—	SIPRE	~1	Colucci et al. (2017)
Ledena Pecina	Montenegro	n.d.	Manual	1.99	Kern et al. (2007a)
Svarthammarhola	Norway	~20	PICO	5	Lauritzen et al. (2005)
Focul Viu Ice Cave	Romania	~20[a]	Manual	6.67	Kern et al. (2004)
			SIPRE	8.26	Maggi et al. (2008)
			modified PICO	4.87	Bădăluță et al. (2020)
Scărișoara Ice Cave		>22	PICO	22.53	Holmlund et al. (2005)
			modified PICO	25.3	Bădăluță et al. (2018)
Bortig Ice Cave		~21	Manual	2.05	Kern et al. (2007b)
Askinskaya Cave	Russia	—	manual (PI-8)	2	Trofimova et al. (2020)
Kinderlinskaya Cave		—		2	
Dobsinska Ice Cave	Slovakia	26.5	electromechanical (not detailed)	13.93	Vrana et al. (2007)
Snežna Cave	Slovenia	—	SIPRE	2	Carey et al. (2020)
Monlési Ice Cave	Switzerland	12–15	FELICS	1.7[b]	Luetscher et al. (2007)
Candelaria Ice Cave	United States	~4.5	not reported	1.88	Dickfoss et al. (1997)
Cave 29		<3	Kovacs-II corer	2	Onac et al. (2018)
			manual (Bosch)	0.59	Onac et al. (2020)

[a]*Given in Maggi et al., 2008.*
[b]*Steam drill to 8.5 m depth.*

(**Table 1**). This may suggest that cave ice drilling projects may also start in parts of the geographical distribution range of ice caves outside Europe in the near future.

With few exceptions, where the morphology of the caves and ice blocks allowed for direct access to lower (and thus older) ice layers, most of the drilling efforts were concentrated on drilling vertical boreholes through the ice. Thirteen of the 23 ice core drilling projects employed a machine operated auger and simple manual drilling device was used in eight projects (no technical details were reported for 2 cases, **Table 1**). Because several of the largest ice caves (e.g., Scărișoara Ice Cave in Romania, Dachstein-Rieseneishöhle in Austria) are managed as show caves, the installed electric wiring allowed operating a drilling device driven by an electric motor in these caves. Light-weight, portable drill systems developed by and named after the Snow, Ice and Permafrost Research Establishment (SIPRE, Rand and Mellor, 1985) and Polar Ice Coring Office (PICO, Koci and Kuivinen, 1984) were used most frequently in these cases (**Table 1**).

Complete darkness in the caves and the general remote location of ice deposits within caves challenges the use of solar powered drilling devices, so a solar-powered drilling rig (FELICS abbreviated from Fast Electromechanical Lightweight Ice Coring System, Ginot et al., 2002) was used only for one project (Monlési Ice Cave, Luetscher et al., 2007). Poor ventilation in caves further excluded the usage of on-spot generated electric energy (health risk and cave pollution impact due to stagnation of exhaust fume). In a special situation a generator was operated outside the Focul Viu Ice Cave (Maggi et al., 2008; Bădăluță et al., 2020). Thus, due to limitations in access to the caves, manual augers were usually the only available drilling option. The most frequently applied device consisted of a self-designed simple walled auger coupled to an Eijkelkamp soil auger handle and rod system. The main weaknesses of this system are that the undisturbed sampling is not assured and the relatively small diameter of these augers strongly limited the available ice amount to be recovered (Kern et al., 2007b).

CHALLENGES AND SUGGESTIONS FOR FUTURE ICE CORE DRILLING PROJECTS IN CAVES

The "best" cores recovered from cave glaciers should contain an undisturbed sequence of ice layers, with no hiatuses induced during drilling and capable to offer data that responds to multiple research questions. All these are challenged by the characteristics of the ice itself and of the ice blocks, the processes acting after deposition and the difficulties of drilling in a cold, dark and remote environment. In the following, we will discuss the main issues and propose potential solutions (or at least suggestions to be improved upon).

The main challenges encountered during drilling cave ice deposits result from the nature of the ice itself (see section 2 above). Combining the high density of the ice with the (generally) low power (electric or manual) applied to the drilling machines results in low penetration speeds. The succession of clear ice and

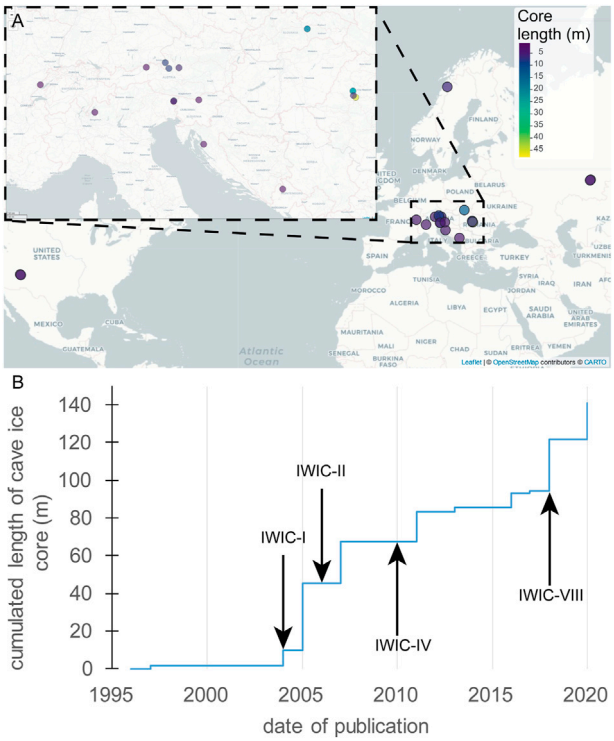

FIGURE 1 | Spatial and temporal distribution of the published cave ice cores. **(A)** Circles mark the location of cave ice deposits with reported cave ice drilling project. The colour code of the circles shows the total length of the extracted ice cores for each ice cave. The region of Central Europe is enlarged for better visibility. **(B)** Cumulated length of cave ice cores according to the date of publication of the first scientific reference. Data collection closed by December 31, 2020.

layers of impurities (containing both cryogenic cave calcite and surface-derived sediments) that build-up most of the cave ice blocks results in a sedimentary structure with very low cohesivity between the individual layers, prone to shearing, thus resulting in low-quality ice cores. Second, once formed, cave ice blocks have a dynamic that is shaped by both glacial and karstic-specific processes (Perşoiu and Lauritzen, 2018). The high plasticity of ice, combined with the usually inclined topography of the cave floor and the possible presence of breakdowns below the ice, leads to slow flow-like movement of the entire ice mass. The flow is further complicated by the uneven melting at the sole and sides of the ice blocks and the morphology of the surrounding walls, so that folds and tilting of the ice layers up to the vertical (**Figure 2**) are a common occurrence (Perşoiu and Pazdur, 2011; Spötl et al., 2014). Additionally, as most of the ice caves are located close to or well below the altitude of the 0°C isotherm, annual melting affects both the surface and sides of the ice blocks, with extreme ablation events possibly leading to the ablation of several years' worth of annual accumulation (Colucci et al., 2016a; Perşoiu et al., 2021). Ablation could affect either the entire surface of an ice block or only part of it, and also acts on time scales ranging from years to centuries.

Ice cave monitoring studies reported cave ice temperature usually in the range of -4 to 0°C (Luetscher et al., 2008; Strug et al., 2008). Attempting of core drilling in such warm ice is not recommended with the SIPRE augers (U.S. Ice Drilling Program, 2019). Drilling ice close to melting point, is extremely difficult with electromechanical drills because as the drill penetrates into warm ice, the ice particles from the cutting area melt and freeze again in a stiff mass stuck on the cutting ring face (Murariu et al., 2013) and the performance of the drill rapidly deteriorates to a point where penetration

FIGURE 2 | Example of post-depositional modifications of ice layering. **(A)** The ice wall in the Little Reserve, Scărişoara Ice Cave, Romania. Individual layers have different degrees of inclination, making cores drilled in different section of the ice block intersecting layers of different age at the same depth. Newly formed ice covers part of the old ice in the center- left (blue ice between the two cavers). **(B)** Ice layers tilted to near vertical (indicated by the red arrows) in Crna Ledenica Cave, Croatia (photo by Željko Marunčić Bospor).

TABLE 2 | The main problems and solutions in ice core drilling in cave environment.

	Problem	Cause	Solution
1	Drilling stopped and drill hole was abandoned	rock and wood in the ice	avoiding such objects visible under the ice surface, GPR survey to check major objects in deeper ice layers
2	Broken core	CCC layers creating shearing surfaces	High speed drilling
3	—	Vibrating extension rods	Modify the connections between the extension rods to make the entire pole rigid
4	Skidding of cutters on top of the ice at the bottom of the hole	Refrozen water and CCC	Screws inserted between the cutters to scratch the top of the hardened surface
5	Blocked drill in the drilling hole	Heat generated by friction melting of the ice and keeping a motionless auger at the bottom of the drill hole resulted in quick freezing of water	Removal of the auger immediately (<1 s) after engine stop (Several) reversals of the rotation direction Alcohol usage to lower the freezing temperature (and subsequent abandonment of the drill hole)
6	Ice chips at the bottom of the drill hole, machine idling on top a rotating ice mass	Warm (0 to −2°C) temperatures and broken ice chips accumulating at the bottom of the drill hole	Removal of the ice chip mass (bent spoon attached to the extension rod), varying the speed without stopping the engine, abandonment of the drill hole

stops (Talalay et al., 2015). As a practical solution it was suggested that the drillers can be forced to stop, bring back up the core barrel frequently and the drilling can be continued after cleanout the ice (Murariu et al., 2013), an approach that was successfully used in Scărişoara Ice Cave (Romania).

Clastic and organic debris are commonly observed in cave ice deposits and represent another type of difficulty seldom experienced in surface ice bodies. Clastic debris is produced by periglacial processes leading to intense weathering of the cave walls and continuous accumulation (and subsequent incorporation in ice) of pieces of limestone of varying sizes. Cave ice drilling projects frequently reported that such rocky (Luetscher et al., 2007; Vrana et al., 2007; Sattler et al., 2013; Bădăluță et al., 2020) or woody (Kern et al., 2004; 2011b) debris embedded in the ice caused problems or completely stopped the drilling effort. The coarse rocky debris can wear out the cutting edge of the auger in a relative short time, so an easily replaceable cutting teeth system can be required in the field (see section 4.1). Obviously the spots with large rocks or logs visible in a shallow depth in the transparent ice must be avoided when looking for a drilling spot (see section 4.2). However, surveying the deeper interior of the ice block can be extremely useful before the selection of the drilling spot. Ground Penetrating Radar (GPR) is capable imaging the internal structure of the ice and its basal topography (Hausmann and Behm, 2011; Colucci et al., 2014; Gómez Lende et al., 2016; Munroe, 2021). GPR survey of the ice block not only helps to avoid the sectors of the cave ice with embedded rocks but also provides information about the thickness of ice cave deposits hence finding the thickest accessible cave ice sequence.

The combination of all these factors generally leads to a complex stratigraphy of any cave ice block, making a unitary interpretation rather impossible. To address these challenges, we have developed 1) a dedicated drilling device for cave glaciers (Murariu et al., 2013) and 2) a "*Cave Ice Sedimentary architecture and deposition (CISAD)*" approach to investigating subterranean cave ice deposits. This approach has been used in several past (Perşoiu et al., 2017; Bădăluță et al., 2020) and ongoing studies in caves in Romania, Norway, Greece, Slovakia, Slovenia, Croatia etc.

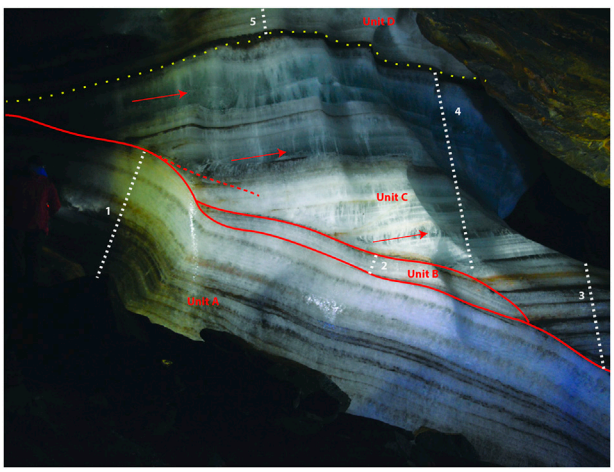

FIGURE 3 | The lower section of the ice block in Svarthammarhola, Cave, Norway. The red arrows indicate layers of clear ice, formed as ponds of water frozen from top to bottom. The red dashed line indicates the (potential) former top of Unit A. The stippled yellow line indicates a massive flooding episode. The white dashed lines (1–5) indicate the longest potential paleoclimate record. The caver on the left is ~1.80 m tall.

Cave Ice Drilling Auger

The ISER-HD[1] auger is a modified PICO electric drill (Koci and Kuivinen, 1984), build by Heavy Duties SRL (Cluj-Napoca, Romania). It consists of a core barrel with a cutting head, extension rods and a 220 V driving engine (Murariu et al., 2013). The barrel is 100 cm long and with an interior diameter of 10 cm. In addition to the original PICO device, the cutting head was fitted with four cutters made of 42CrMo4 alloy steel, with a rake (leading) angle of 30° (may vary from 30° to 45°) and a relief angle of 10° (may vary from 10° to 15°). The slightly lower angles of the main cutters were chosen to allow for slower penetration under low power in the

[1]Emil Racoviță Institute of Speleology – Heavy Duty

cave ice deposits with a density far higher than that of surface ice in mountain and polar glaciers. Additionally, the low angles allow for easier cutting through layers of CCC up to 3 cm thick and through occasional wood found in ice (Bădăluță et al., 2020). Adjustment screws were incorporated between the cutters to regulate the penetration speed. Both the screws and the cutters were fitted with screws to allow for quick replacement in the field, as the presence of CCC and allochthonous dues worn out the cutting edge. In the few cases when a thin layer of refrozen water and CCC formed an impenetrable hard surface at the bottom of the drillhole, the adjustment screws were replaced with long screws reaching below the main cutters and these were used to break-up the refrozen layer. The cutting head has two helical paths that direct the ice chips towards similarly placed helical spirals along the barrel and further inside it, through several 30 cm diameter holes. Two spring-loaded core dogs were fitted to the cutting head to hold the core after each run. The extension rods are made of aluminum alloy 6060 (Murariu et al., 2013) and the engine is a 220 V, 1.8 kW reversible engine, with a variable maximum speed of 1,300 rpm. This device was tested in two ice caves in Romania, Scărișoara Ice Cave and Focul Viu ice Cave, on several occasions between 2012 and 2016. The drilling auger has been deployed to drill both vertically and horizontally, allowing the recovery of ice core down to a depth of 25 m below surface (Bădăluță et al., 2018), using power drawn from both the national electric grid and a gasoline generator. The main problems and solution we have encountered are listed in **Table 2**.

Cave Ice Sedimentary Architecture and Deposition (CISAD) Approach

Forced by the shape of the cave passage system, cave ice deposits often have complex geometries (Gómez-Lende and Sánchez-Fernández, 2018) and dynamic processes active in ice caves regularly obscure and/or modify further the original morphology and stratigraphy of the perennial ice blocks targeted by drilling efforts. Consequently, the assumption that an ice core drilled vertically through the ice block will intersect only chronologically ordered layers is often falsified by the findings (see for example figures in Holmlund et al., 2005; Stoffel et al., 2009; Spötl et al., 2014; Lauritzen et al., 2018). These problems are mainly affecting smaller cave glaciers, whereas large ice blocks (> 30,000 m^3) are less affected, at least partly, and layers in stratigraphic order can be drilled (Maggi et al., 2008; Kern et al., 2009; Perşoiu et al., 2017; Bădăluță et al., 2020). However, even such large cave glaciers can be affected by post-depositional processes (**Figure 2**), with newly formed ice layers covering old ones (**Figure 2A**) and potential contamination of old ice with modern water and organic matter, tilting of the strata (**Figure 2B**) and successive periods of melting and accumulation resulting in a complex cut-and-fill structure (**Figure 3**). The aim of virtually all ice core drilling efforts is to obtain an undisturbed record of past environmental variability but this is hampered by the problems detailed above. To partly address this conundrum, we propose an approach that takes into account the mechanisms leading to ice formation and accumulation and those affecting the already formed ice block.

First, the processes responsible for ice formation must be understood, especially when the stable isotope composition of oxygen and hydrogen in water is the main target. Whereas snow accumulation will likely result in the successive accretion of ice layers preserving the original $\delta^{18}O$ and $\delta^{2}H$ signals of snow and thus the climatic information it holds (e.g., Belmonte Ribas et al., 2014; Munroe et al., 2018), freezing of water is accompanied by complex fractionation processes (Perşoiu et al., 2011). Ice blocks formed through this process could have layers that froze from very thin water films and these, while also affected by kinetic fractionation, will likely preserve the original $\delta^{18}O$ and $\delta^{2}H$ values, in a manner similar to ice wedges (e.g., Meyer et al., 2015). Contrary, downward freezing of stagnant pools of water will result in an ice layer with a strong $\delta^{18}O$ and $\delta^{2}H$ gradient (Perşoiu et al., 2011), with the upper (first to freeze) layer enriched in the heavy isotopes (^{18}O and ^{2}H). Consequently, drilling through such a layer will yield a stable isotope gradient, potentially be interpreted as indicating a climatic change, albeit a false one. Therefore, analyzing the stable isotope composition of ice core retrieved from cave ice deposits requires the identification of genetic layers, either in ice cores or in the field (**Figure 3**) and sampling should be done considering this layering. For example, the ice layers indicated by red arrows in **Figure 3** likely formed as shallow pools of water froze. The stable isotope composition of oxygen and hydrogen in that ice would reflect that of the original water (and thus hold a putative climatic information) only of the entire layer of ice is considered as one sample–and thus drilling should be made accordingly.

Second, the post depositional processes affecting any ice block result in often complex stratigraphy, that preserves the history of the glacier but not always that of the climate changes during its lifetime. Before drilling for a continuous record of past climate change, this stratigraphic history must be understood (Citterio et al., 2003; Stoffel et al., 2009). For example, the ice block shown in **Figure 3** (Svarthammarhola, Norway), underwent several episodes of melting, tilting and accumulation. The structure and composition of the lower layers (unit A), suggest slow freezing of shallow pools of water. Several episodes of enhanced melting with inflow of external water carrying soil and macrofossils (dark layers in the lower half of unit A) interrupted this accumulation. The upper part of unit A was likely affected by a severe melting episode, that led to the removal of part of it (**Figure 3**). On top of this truncated unit A, a new layer of ice formed–unit B. Melting at the sole of the glacier tilted the block, leading to the inclined appearance of both units A and B. Subsequently, shallow ponds formed on top of unit B and a new unit started to develop–unit C. Depending on location, this unit is between 0.5 and 4.4 m thick (see the left and right ends of unit C in **Figure 3**). The ice layers within unit C are a combination of lake ice and floor ice. A severe flooding episode likely affected the ice block (thick brown layer capping unit C) and ice accumulation resumed afterwards, with both lake and floor ice

accumulating (unit D). The consequence of these different processes is that a continuous ice core cannot be directly extracted from the sequence shown in **Figure 3**. First, the likely loss of ice due to the melting events that truncated units A, C and possibly B resulted in the loss of continuity of the record. Second, depending on the position of a potential core, the age of successive ice layers could be very different. Third, the genetically different types of ice layers visible in unit C, must be targeted differently in order to obtain meaningful stable isotope data (the strong kinetic fractionation associated with the freezing of lake water shown by the red arrows likely resulted in extremely variable $\delta^{18}O$ and $\delta^{2}H$ values). Fourth, freezing, melting, refreezing and inflow of water mixed the organic matter that could provide a chronological anchor for the entire sequence. The layers capping units A, B and C likely contain a mixture of 1) organic matter derived from the top of any of the considered units following melting, 2) material transported during the melt event and 3) material deposited when accumulation resumed. In this case, as well as in others (Perşoiu and Pazdur, 2011; Spötl et al., 2014; Kern et al., 2018; Munroe et al., 2018; Sancho et al., 2018), this sequence of events could have been separated in time by years or centuries, thus preventing the formation and preservation of a continuous sequence of climatic events. The white dashed lines numbered one to five shown in **Figure 3** suggest the potential location of drilling efforts that would maximize the length of a paleoclimate record. Obviously, vertical drilling would totally miss this, hence horizontal drilling is the only possible course of action.

In the light of the above, we propose the following approach–which we call the *Cave Ice Sedimentary Architecture and Deposition (CISAD)* approach–in establishing the location of a drilling site best-suited to obtain valuable paleoclimate data. The morphology of ice caves usually allows drilling to be performed either vertically or laterally (i.e., on a layer-by-layer approach, **Figure 2B**), depending on the results of the CISAD analyses.

1. Detailed stratigraphic investigation of the ice sequence and delimitation of genetically unitary stratigraphic units
2. Identification of the ice layer forming processes (snow accumulation, freezing of water as either floor or lake ice), uniquely important for the interpretation of stable isotope data.
3. Establishment of the chronology of ice deposition, separately for each stratigraphic unit. The most important one and also the most difficult to date are the layers separating individual units, we thus recommend avoiding them and target the layer closest to the bottom and top of the unit that contain datable material (^{14}C, ^{3}H). While this methodology will inevitably lead to the loss of continuity (but we stress that this has been already lost if unconformities are present in the sequence) and of "some" years from a potentially long record, it nevertheless is the only one that offers trustful ages.
4. Correlation of the "floating" records based on relative positions (stratigraphy-based), rather than on depth below surface (above bottom) or chronology. The later issue is especially important, as, depending on the process affecting an ice block in the past, different parts of it could preserve partly overlapping sequences, but which could be discontinuous and hence the desire to obtain continuous records might lead to erroneous results.
5. Detailed knowledge of the ice forming mechanism(s) and of those responsible for proxy incorporation in ice (e.g., stable isotopes, pollen) are mandatory.

AUTHOR CONTRIBUTIONS

ZK and AP designed the project and contributed equally to the writing of the manuscript.

FUNDING

This work was supported by a grant of the Romanian Ministry of Education and Research, CNCS - UEFISCDI, project numbers PN-III-P1-1.1-TE-2016–2210 and PN-III-P4-ID-PCE-2020–2723, within PNCDI III, awarded to AP. This study was financially supported by the EEA Grants 2014–2021 under Project EEA126 (KARSTHIVES), contract no. 3/2019.

ACKNOWLEDGMENTS

We thank the numerous friends who helped us during fieldwork (Carmen, Vlad, Christos, Yorgos, Nenad, Neven, Viorica, Stavros, Ioanna, Bospor, Tasos, Mike, Ioana, Christian, Geza, Stein-Erik, Cristina, Traian, Denisa, Corina and many others). The friendly IWIC meetings offered excellent venues to discuss problems, ideas, challenges, failures – we thank all organizers, hosts, sponsors and participants for the stimulating environment they created. This is contribution No. 77. of 2 ka Palæoclimatology Research Group.

REFERENCES

Bădăluță, C.-A., Perşoiu, A., Ionita, M., and Piotrowska, N. (2020). Stable Isotopes in Cave Ice Suggest Summer Temperatures in East-central Europe Are Linked to Atlantic Multidecadal Oscillation Variability. *Clim. Past* 16, 2445–2458. doi:10.5194/cp-16-2445-2020

Bădăluță, C. A., Perşoiu, A., Ionită, M., and Piotrowska, N. (2018). *Proceedings of the 8th International Workshop on Ice Caves*. Spain: Potes, 20.Summer Climate Changes during the Last 1000 Years as Seen in Cave Ice

Barton, H. A., Breley, G. J., Tochterle, P., and Moseley, G. E. (2020). Cryogenic Features of the Permafrost Ice Caves of Grottedal, Northeast Greenland. *Cave Karst Sci.* 47, 93–99.

Belmonte-Ribas, A., Sancho, C., Moreno, A., Lopez-Martinez, J., and Bartolome, M. (2014). Present-day Environmental Dynamics in Ice Cave A294, Central Pyrenees, Spain *Geografia Fisica & Dinamica Quaternaria* 37/2, 131–140. doi:10.4461/GFDQ.2014.37.12

Brad, T., Itcus, C., Pascu, M.-D., Perşoiu, A., Hillebrand-Voiculescu, A., Iancu, L., et al. (2018). Fungi in Perennial Ice from Scărişoara Ice Cave (Romania). *Sci. Rep.* 8, 10096. doi:10.1038/s41598-018-28401-1

Carey, A. E., Smith, D. F., Welch, S. A., Tičar, J., Zorn, M., Lipar, M., et al. (2020). Shallow Ice Core Profiles from Snežna Cave, Slovenia. *Aragonit* 25/1, 39.

Cecil, L. D., Green, J. R., Vogt, S., Michel, R., and Cottrell, G. (1998). Isotopic Composition of Ice Cores and Meltwater from Upper Fremont Glacier and Galena Creek Rock Glacier, Wyoming. *Geografiska Annaler: Ser. A, Phys. Geogr.* 80, 287–292. doi:10.1111/j.0435-3676.1998.00044.x

Citterio, M., Turri, S., Bini, A., and Maggi, V. (2004). Observed Trends in the Chemical Composition, $\delta^{18}O$ and crystal Sizes vs. Depth in the First Core from the LoLc 1650 "Abisso Sul Margine Dell'Alto Bregai" Ice Cave (Lecco, Italy). *Theor. Appl. Karstology* 17, 45–50.

Citterio, M., Turri, S., Bini, A., and Maggi, V. (2003). "Some Observtions on the Structure and Morphology of an Ice deposit in the " Abisso suI Margine Dell' Alto Bregai " Cave (Grigna Settentrionale, Italian Alps)," in Proc. VI Symposium of the UIS-GLACKIPR IntI. Commission, Ny-Alesund (Svalbard, Norway), 3-8 Sept. 2003.

Colucci, R. R., Fontana, D., and Forte, E. (2014). "Characterization of Two Permanent Ice Cave Deposits in the southeastern Alps (Italy) by Means of Ground Penetrating Radar (GPR)," in Proceedings of the Sixth International Workshop on Ice Caves, August 17-22, Idaho Falls, Idaho, USA: NCKRI Symposium 4. Editors L. Land, Z. Kern, V. Maggi, and S. Turri (Carlsbad (NM): National Cave and Karst Research Institute), 33–39.

Colucci, R. R., Fontana, D., Forte, E., Potleca, M., and Guglielmin, M. (2016a). Response of Ice Caves to Weather Extremes in the Southeastern Alps, Europe. *Geomorphology* 261, 1–11. doi:10.1016/j.geomorph.2016.02.017

Colucci, R. R., Forte, E., Maggi, V., Stenni, B., Barbante, C., Bertò, M., et al. (2016b). "The Vasto Ice Cave in the South-Eastern Alps, Europe: Preliminary Results from an Ice Core Analysis," in 7th International Workshop on Ice Caves (IWIC VII) (Postojna), 42–43.

Colucci, R. R., Luetscher, M., Forte, E., Guglielmin, M., Lanza, D., Principalle, F., et al. (2017). First alpine Evidence of *in Situ* Coarse Cryogenic Cave Carbonates (CCCcoarse) *Geografia Fisica & Dinamica Quaternaria* 40, 53–59.

Dansgaard, W. (2004). *Frozen Annals Greenland Ice Sheet Research*. Odder, Denmark: Narayana Press.

Dickfoss, P. V., Betancourt, J. L., Thompson, L. G., Turner, R. M., and Tharnstrom, S. (1997). History of Ice at Candelaria Ice Cave, New Mexico. *New Mexico Bur. Mines Mineral Resour. Bull.* 156, 91–112.

Feurdean, A., Perşoiu, A., Pazdur, A., and Onac, B. P. (2011). Evaluating the Palaeoecological Potential of Pollen Recovered from Ice in Caves: A Case Study from Scărişoara Ice Cave, Romania. *Rev. Palaeobotany Palynology* 165, 1–10. doi:10.1016/j.revpalbo.2011.01.007

Fórizs, I., Kern, Z., Nagy, B., Szántó, Zs., Palcsu, L., and Molnár, M. (2004). Environmental Isotope Study on Perennial Ice in the Focul Viu Ice Cave, Bihor Mts., Romania. *Theor. Appl. Karstology* 17, 61–69.

Ginot, P., Stampfli, F., Stampfli, D., Schwikowski, M., and Gäggeler, H. W. (2002). FELICS, a New Ice Core Drilling System for High-Altitude Glaciers. *Mem. Nat. Inst. Polar Res.* 56, 38–48.

Gómez Lende, M., Serrano, E., Bordehore, L. J., and Sandoval, S. (2016). The role of GPR techniques in determining ice cave properties: Peña Castil ice cave, Picos de Europa. *Earth Surf. Process. Landforms* 41 (15), 2177–2190. doi:10.1002/esp.3976

Gómez-Lende, M., and Sánchez-Fernández, M. (2018). Cryomorphological Topographies in the Study of Ice Caves. *Geosciences* 8, 274. doi:10.3390/geosciences8080274

Hausmann, H., and Behm, M. (2011). Imaging the Structure of Cave Ice by Ground-Penetrating Radar. *The Cryosphere* 5, 329–340. doi:10.5194/tc-5-329-2011

Holmlund, P., Onac, B. P., Hansson, M., Holmgren, K., Mörth, M., Nyman, M., et al. (2005). Assessing the Palaeoclimate Potential of Cave Glaciers: the Example of the Scărişoara Ice Cave (romania). *Geografiska Annaler: Ser. A, Phys. Geogr.* 87, 193–201. doi:10.1111/j.0435-3676.2005.00252.x

Itcus, C., Pascu, M. D., Lavin, P., Perşoiu, A., Iancu, L., and Purcarea, C. (2018). Bacterial and Archaeal Community Structures in Perennial Cave Ice. *Sci. Rep.* 8, 15671. doi:10.1038/s41598-018-34106-2

Jouzel, J. (2013). A Brief History of Ice Core Science over the Last 50 Yr. *Clim. Past* 9 (6), 2525–2547. doi:10.5194/cp-9-2525-2013

Kern, Z., Bočić, N., and Sipos, G. (2018). Radiocarbon-Dated Vegetal Remains from the Cave Ice Deposits of Velebit Mountain, Croatia. *Radiocarbon* 60, 1391–1402. doi:10.1017/RDC.2018.108

Kern, Z. (2018). "Dating Cave Ice Deposits," in *"Dating Cave Ice Deposits" in Ice Caves*. Editors A. Perşoiu and S. E. Lauritzen (Elsevier), 109–122. doi:10.1016/b978-0-12-811739-2.00005-x

Kern, Z., Fórizs, I., Kázmér, M., Nagy, B., Szántó, Zs., Gál, A., et al. (2004). Late Holocene environmental changes recorded at Gheţarul de la Focul Viu, Bihor Mts, Romania. *Theor. Appl. Karstology* 17, 51–60.

Kern, Z., Fórizs, I., Pavuza, R., Molnár, M., and Nagy, B. (2011a). Isotope Hydrological Studies of the Perennial Ice deposit of Saarhalle, Mammuthöhle, Dachstein Mts, Austria. *The Cryosphere* 5, 291–298. doi:10.5194/tc-5-291-2011

Kern, Z., Molnár, M., Perşiou, A., and Nagy, B. (2007b). "Radiochemical and Stratigraphic Analysis of Two Ice Cores from Borţig Ice Cave, Apuseni Mts, Romania," in Proceedings of the 2nd International Workshop on Ice Caves. Editor J. Zelinka (Liptovský Mikuláš), 65–69.

Kern, Z., Molnár, M., Svingor, É., Perşoiu, A., and Nagy, B. (2009). High-resolution, Well-Preserved Tritium Record in the Ice of Bortig Ice Cave, Bihor Mountains, Romania. *The Holocene* 19, 729–736. doi:10.1177/0959683609105296

Kern, Z., Surányi, G., Molnár, M., Nagy, B., and Balogh, D. (2007a). "Investigation of Natural Perennial Ice Deposits of Durmitor Mts, Montenegro," in Proceedings of the 2nd International Workshop on Ice Caves. Editor J. Zelinka (Liptovský Mikuláš), 70–73.

Kern, Z., Széles, E., Horvatinčić, N., Fórizs, I., Bočić, N., and Nagy, B. (2011b). Glaciochemical Investigations of the Ice deposit of Vukušić Ice Cave, Velebit Mountain, Croatia. *The Cryosphere* 5, 485–494. doi:10.5194/tc-5-485-2011

Koci, B. R., and Kuivinen, K. C. (1984). The PICO Lightweight Coring Auger. *J. Glaciol.* 30 (105), 244–245. doi:10.1017/s0022143000006018

Krainer, K., Bressan, D., Dietre, B., Haas, J. N., Hajdas, I., Lang, K., et al. (2015). A 10,300-Year-Old Permafrost Core from the Active Rock Glacier Lazaun, Southern Ötztal Alps (South Tyrol, Northern Italy). *Quat. Res.* 83, 324–335. doi:10.1016/j.yqres.2014.12.005

Kwiecien, O., Braun, T., Brunello, C. F., Faulkner, P., Hausmann, N., Helle, G., et al. (2022). What We Talk About When We Talk About Seasonality - A Transdisciplinary Review. *Earth-Sci. Rev.* 103843. doi:10.1016/j.earscirev.2021.103843

Langway, C. C., Jr. (2008). The History of Early Polar Ice Cores. *Cold Regions Sci. Tech.* 52 (2), 101–117. doi:10.1016/j.coldregions.2008.01.001

Langway, C. C., Shoji, H., Mitani, A., and Clausen, H. B. (1993). Transformation Process Observations of Polar Firn to Ice. *A. Glaciology.* 18, 199–202. doi:10.3189/S026030550001150210.1017/s0260305500011502

Lauritzen, S. E., Baastad, L., Bjørlien, J., Fedje, E., and Holmlund, P. (2005). "The Svarthamar Cave Research Project, Fauske, north Norway," in Proceedings of the 14th International Congress of Speleology, August 2005 (Athen-Kalamos), 1–5.

Lauritzen, S. E., Baastad, L., and Engelien, J. (2018). in *"Ice Caves in Norway, Fennoscandia and the Arctic" in Ice Caves*. Editors A. Perşoiu and S. E. Lauritzen (Elsevier), 237–262.

Leunda, M., González-Sampériz, P., Gil-Romera, G., Bartolomé, M., Belmonte-Ribas, Á., Gómez-García, D., et al. (2019). Ice Cave Reveals Environmental Forcing of Long-Term Pyrenean Tree Line Dynamics. *J. Ecol.* 107, 814–828. doi:10.1111/1365-2745.13077

Luetscher, M., Bolius, D., Schwikowski, M., Schotterer, U., and Smart, P. L. (2007). Comparison of Techniques for Dating of Subsurface Ice from Monlesi Ice Cave, Switzerland. *J. Glaciol.* 53, 374–384. doi:10.3189/002214307783258503

Luetscher, M., Lismonde, B., and Jeannin, P.-Y. (2008). Heat Exchanges in the Heterothermic Zone of a Karst System: Monlesi Cave, Swiss Jura Mountains. *J. Geophys. Res.* 113, F02025. doi:10.1029/2007JF000892

Maggi, V., Meyer, C., Leoni, B., Nava, V., Maspero, F., and Pflitsch, A. (2020). Chemical and Physical Stratigraphy of the Schellenberger Eishole Ice Core. *Aragonit* 25, 48.

Maggi, V., Turri, S., Bini, A., and Udisti, R (2008). "2500 Year of History in Focul Viu Ice Cave," in Proceedings of the 3rd International Workshop on Ice Caves. Editors O. Kadebskaya, B. R. Mavlyudov, and M. Pyatunin (Perm): Mining Institute of Ural Branch of the Russian Academy of Sciences), 11–15.

Mavlyudov, B. R. (2018). "Geography of Cave Glaciation," in *"Geography of Cave Glaciation" in Ice Caves*. Editors A. Perşoiu and S. E. Lauritzen (Elsevier), 209–220. doi:10.1016/B978-0-12-811739-2.00012-7

Mavlyudov, B. R. (2008). *Oledenenie Pesher (Caves Glaciation)*. Moscow: Institute of Geography of the Russian Academy of Science, 290. (in Russian).

May, B., Spötl, C., Wagenbach, D., Dublyansky, Y., and Liebl, J. (2011). First Investigations of an Ice Core from Eisriesenwelt Cave (Austria). *The Cryosphere* 5, 81–93. doi:10.5194/tc-5-81-2011

Meyer, H., Opel, T., Laepple, T., Dereviagin, A. Y., Hoffmann, K., and Werner, M. (2015). Long-term winter Warming Trend in the Siberian Arctic during the Mid- to Late Holocene. *Nat. Geosci* 8, 122–125. doi:10.1038/ngeo2349

Mondini, A., Donhauser, J., Itcus, C., Marin, C., Perşoiu, A., Lavin, P., et al. (2019). High-throughput Sequencing of Fungal Communities across the Perennial Ice Block of Scărişoara Ice Cave. *Ann. Glaciol.* 59, 134–146. doi:10.1017/aog.2019.6

Munroe, J. S. (2021). First Investigation of Perennial Ice in Winter Wonderland Cave, Uinta Mountains, Utah, USA. *The Cryosphere* 15, 863–881. doi:10.5194/tc-15-863-2021

Munroe, J. S., O'Keefe, S. S., and Gorin, A. L. (2018). Chronology, Stable Isotopes, and Glaciochemistry of Perennial Ice in Strickler Cavern, Idaho, USA. *GSA Bull.* 130, 175–192. doi:10.1130/b31776.1

Murariu, V., Pacurar, A., and Gyenge, Cs. (2013). New Ice Core Drilling Machine for Small Glaciers. *ACTA TECHNICA NAPOCENSIS* 56/2, 411–414.

Oeschger, H., Schotterer, U., Stauffer, B., Haeberli, W., and Röthlisberger, H. (1977). First Results from Alpine Core Drilling Projects. *Z. für Gletscherkunde Glazialgeologie* 13, 193–208.

Onac, B. P., Baumann, S. M., Parmenter, D. S., Weaver, E., and Sava, T. B. (2020). Late Holocene Droughts and Cave Ice Harvesting by Ancestral Puebloans. *Sci. Rep.* 10, 20131. doi:10.1038/s41598-020-76988-1

Onac, B. P., Parmenter, D. S., Weaver, E., Baumann, S. M., and Sava, T. B. (2018). Ice deposits in lava tubes of El Malpais National Monument, New Mexico (USA). in Proceedings of the 8th International Workshop on Ice Caves, Potes, Spain, 19.

Opel, T., Meyer, H., Wetterich, S., Laepple, T., Dereviagin, A., and Murton, J. (2018). Ice Wedges as Archives of winter Paleoclimate: A Review. *Permafrost and Periglac Process* 29, 199–209. doi:10.1002/ppp.1980

Paun, V. I., Icaza, G., Lavin, P., Marin, C., Tudorache, A., Perşoiu, A., et al. (2019). Total and Potentially Active Bacterial Communities Entrapped in a Late Glacial through Holocene Ice Core from Scarisoara Ice Cave, Romania. *Front. Microbiol.* 10, 1193. doi:10.3389/fmicb.2019.01193

Perşoiu, A., Onac, B. P., Wynn, J. G., Blaauw, M., Ionita, M., and Hansson, M. (2017). Holocene winter Climate Variability in Central and Eastern Europe. *Sci. Rep.* 7 (1), 1196. doi:10.1038/s41598-017-01397-w

A. Perşoiu and S. E. Lauritzen (Editors) (2018). *Ice Caves* (Elsevier).

Perşoiu, A., Buzjak, N., Onaca, A., Pennos, C., Sotiriadis, Y., Ionita, M., et al. (2021). Record Summer rains in 2019 Led to Massive Loss of Surface and Cave Ice in SE Europe. *The Cryosphere* 15, 2383–2399. doi:10.5194/tc-15-2383-2021

Perşoiu, A. (2018). "Ice Dynamics in Caves," in *Ice Caves*. Editors A. Perşoiu and S. E Lauritzen (Elsevier), 97–108.

Perşoiu, A., Onac, B. P., Wynn, J. G., Bojar, A.-V., and Holmgren, K. (2011). Stable Isotope Behavior during Cave Ice Formation by Water Freezing in Scărişoara Ice Cave, Romania. *J. Geophys. Res.* 116, D02111. doi:10.1029/2010JD014477

Perşoiu, A., and Onac, B. P. (2019). *"Ice in Caves" in Encyclopedia of Caves*. Academic Press, 553–558.

Perşoiu, A., and Pazdur, A. (2011). Ice Genesis and its Long-Term Mass Balance and Dynamics in Scărişoara Ice Cave, Romania. *The Cryosphere* 5, 45–53. doi:10.5194/tc-5-45-2011

Pflitsch, A., Schörghofer, N., Smith, S. M., and Holmgren, D. (2016). Massive Ice Loss from the Mauna Loa Icecave, Hawaii. *Arctic, Antarctic, Alpine Res.* 48, 33–43. doi:10.1657/AAAR0014-095

Rand, J., and Mellor, M. (1985). Ice–coring Augers for Shallow Depth Sampling. *CRREL Rep.*, 85–21.

Sancho, C., Belmonte, Á., Bartolomé, M., Moreno, A., Leunda, M., and López-Martínez, J. (2018). Middle-to-late Holocene Palaeoenvironmental Reconstruction from the A294 Ice-Cave Record (Central Pyrenees, Northern Spain). *Earth Planet. Sci. Lett.* 484, 135–144. doi:10.1016/j.epsl.2017.12.027

Sattler, B., Larch, P., Rambacher, J., and Spötl, C. (2013). Das Eis der Hundsalm Eis- und Tropfsteinhöhle als Lebensraum für mikrobielle Gemeinschaften. *Die Höhle* 64, 15–24.

Serban, M., Blaga, L., Blaga, L., Chifu, A., and Ciobotaru, T. (1967). Contribuţii la stratigrafia depozitelor de gheaţa din Gheţarul de la Scărişoara. *Lucrarile Institutului de Speologie "Emil Racovita* 6, 107–140.

Serban, M., Coman, D., and Givulesco, R. (1948). Decouvertes récentes et observations sur la glacière naturelle dite Ghearul de la Scărişoara. *Bull. Soc. Hist. Natur. Sci. Cluj X*, 174–210.

Spötl, C., Reimer, P. J., and Luetscher, M. (2014). Long-term Mass Balance of Perennial Firn and Ice in an Alpine Cave (Austria): Constraints from Radiocarbon-Dated wood Fragments. *The Holocene* 24, 165–175. doi:10.1177/0959683613515729

Stoffel, M., Luetscher, M., Bollschweiler, M., and Schlatter, F. (2009). Evidence of NAO Control on Subsurface Ice Accumulation in a 1200 Yr Old Cave-Ice Sequence, St. Livres Ice Cave, Switzerland. *Quat. Res.* 72, 16–26. doi:10.1016/j.yqres.2009.03.002

Strug, K., Perşoiu, A., and Zelinka, J. (2008). "Preliminary Results of Ice Temperature Measurements in the Dobšinská Ice Cave (Slovakia) and Scărişoara Ice Cave (Romania,"In Proceedings of the 3rd International Workshop on Ice Caves. Editors O. Kadebskaya, B. R Mavlyudov, and M. Pyatunin (Perm: Mining Institute of Ural Branch of the Russian Academy of Sciences), 16–22.

Talalay, P. G. (2014). Perspectives for Development of Ice-Core Drilling Technology: A Discussion. *Ann. Glaciol.* 55 (68), 339–350. doi:10.3189/2014AoG68A007

Talalay, P., Yang, C., Cao, P., Wang, R., Zhang, N., Fan, X., et al. (2015). Ice-core Drilling Problems and Solutions. *Cold Regions Sci. Tech.* 120, 1–20. doi:10.1016/j.coldregions.2015.08.014

Trofimova, E. V., Sokolov, Y. V., and Trofimov, A. A. (2020). Ice in Caves Askinskaya and Kinderlinskaya: Comparative Characteristic. *Bull. Russ. Geographical Soc.* 152 (2), 70–74. doi:10.31857/S086960712002007X10.17747/2311-7184-2020-3-70-74

U.S. Ice Drilling Program (2019). SIPRE Hand Auger Operations and Maintenance Manual. 1-16. Available at: https://icedrill.org/sites/default/files/8507-0011.pdf.

Vrana, K., Baker, J., Clausen, H. B., Hansen, S. B., Zelinka, J., Rufli, H. O., et al. (2007). "Continental Ice Body in Dobšiná Ice Cave (Slovakia) – Part I. – Project and Sampling Phase of Chemical and Isotopic Study," in Proceedings of the 2nd International Workshop on Ice Caves. Editor J. Zelinka (Liptovský Mikuláš), 24–28.

Yonge, C. J., Ford, D., Horne, G., Lauriol, B., and Schroeder, J. (2018). "Ice Caves in Canada," in *"Ice Caves in Canada" in Ice Caves*. Editors A. Perşoiu and S. E Lauritzen (Elsevier), 285–334. doi:10.1016/b978-0-12-811739-2.00015-2

Žák, K., Onac, B. P., and Perşoiu, A. (2008). Cryogenic Carbonates in Cave Environments: A Review. *Quat. Int.* 187, 84–96. doi:10.1016/j.quaint.2007.02.022

Conflict of Interest: The authors declare that the research was conducted in the absence of any commercial or financial relationships that could be construed as a potential conflict of interest.

Publisher's Note: All claims expressed in this article are solely those of the authors and do not necessarily represent those of their affiliated organizations, or those of the publisher, the editors and the reviewers. Any product that may be evaluated in this article, or claim that may be made by its manufacturer, is not guaranteed or endorsed by the publisher.

frontiers in Earth Science

ORIGINAL RESEARCH
published: 02 March 2022
doi: 10.3389/feart.2021.665193

Geoarchaeology and Heritage Management: Identifying and Quantifying Multi-Scalar Erosional Processes at Kisese II Rockshelter, Tanzania

Ilaria Patania[1,2], Samantha T. Porter[3], William F. Keegan[4,5], Rukia Dihogo[6], Sara Frank[6], Jason Lewis[7], Husna Mashaka[8], Julius Ogutu[9], Elena Skosey-Lalonde[4,10], Christian A. Tryon[4,11], Elizabeth M. Niespolo[12,13], Debra Colarossi[14,15] and Kathryn L. Ranhorn[16,17]*

[1]Zinman Institute of Archaeology, University of Haifa, Haifa, Israel, [2]Department of Maritime Civilization, University of Haifa, Haifa, Israel, [3]Liberal Arts Technologies and Innovation Services, University of Minnesota, Minneapolis, MN, United States, [4]Department of Anthropology, University of Connecticut, Storrs, CT, United States, [5]Heritage Consultants LLC, Newington, CT, United States, [6]History and Archaeology Department, University of Dar es Salaam, Dar es Salaam, Tanzania, [7]Department of Anthropology and Turkana Basin Institute, Stony Brook University, New York, NY, United States, [8]Department of History and Archaeology, University of Nairobi, Nairobi, Kenya, [9]Facultad geografía e historia, Universidad Complutense de Madrid, Madrid, Spain, [10]The Interdisciplinary Center for Archaeology and Evolution of Human Behaviour, Universidade do Algarve, Faro, Portugal, [11]Human Origins Program, National Museum of Natural History, Smithsonian Institution, Washington, DC, United States, [12]Department of Earth and Planetary Science, University of California-Berkeley, Berkeley, CA, United States, [13]Berkeley Geochronology Center, Berkeley, CA, United States, [14]Department of Human Evolution, Max Planck Institute for Evolutionary Anthropology, Leipzig, Germany, [15]Department of Geography and Earth Sciences, Aberystwyth University, Aberystwyth, United Kingdom, [16]School of Human Evolution and Social Change, Arizona State University, Tempe, AZ, United States, [17]Institute of Human Origins, Arizona State University, Tempe, AZ, United States

OPEN ACCESS

Edited by:
Andrea Zerboni, University of Milan, Italy

Reviewed by:
Guido Stefano Mariani, University of Cagliari, Italy
Aurel Perşoiu, Romanian Academy, Romania
Christos Pennos, University of Bergen, Norway

***Correspondence:**
Ilaria Patania
ilariapat@gmail.com

Specialty section:
This article was submitted to Sedimentology, Stratigraphy and Diagenesis, a section of the journal Frontiers in Earth Science

Received: *07 February 2021*
Accepted: *10 December 2021*
Published: *02 March 2022*

Citation:
Patania I, Porter ST, Keegan WF, Dihogo R, Frank S, Lewis J, Mashaka H, Ogutu J, Skosey-Lalonde E, Tryon CA, Niespolo EM, Colarossi D and Ranhorn KL (2022) Geoarchaeology and Heritage Management: Identifying and Quantifying Multi-Scalar Erosional Processes at Kisese II Rockshelter, Tanzania. Front. Earth Sci. 9:665193. doi: 10.3389/feart.2021.665193

Natural and anthropogenically induced soil erosion can cause serious loss of the archaeological record. Our work shows the value of multi-scalar geoarchaeological study when excavating and re-excavating rockshelters in a highly dynamic sedimentary environment where erosion is prominent. Here we present our work on Kisese II rockshelter, Tanzania, originally excavated in the 1950s and largely unpublished, that preserves an important Pleistocene-Holocene archaeological record integral to understanding the deep history of the Kondoa Rock-Art World Heritage Center. Unlike rockshelters in quiescent tectonic settings, like much of central Europe or South Africa, Kisese II exists in highly dynamic sedimentary environments associated with the active tectonics of the Great Rift Valley system exacerbated by human-induced environmental and climate change. We report on our 2017 and 2019 exploratory research that includes integrated regional-, landscape-, and site-scale geoarchaeological analyses of past and present sedimentary regimes and micromorphological analyses of the archaeological sediments. Historical records and aerial photographs document extensive changes in vegetation cover and erosional regimes since the 1920s, with drastic changes quantified between 1960 and 2019. Field survey points to an increased erosion rate between 2017 and 2019. To serve future archaeologists, heritage specialists, and local populations we combine our data in a geoarchaeological catena that includes soil, vegetation, fauna, and

anthropogenic features on the landscape. At the site, micromorphological coupled with chronological analyses demonstrate the preservation of *in situ* Pleistocene deposits. Comparison of photographs from the 1956 and 2019 excavations show a maximum sediment loss of 68 cm in 63 years or >10% of >6-m-thick sedimentary deposit. In the studied area of the rockshelter we estimate ~1 cm/yr of erosion, suggesting the ongoing removal of much of the higher archaeological sediments which, based on the coarse stratigraphic controls and chronology of the original Inskeep excavations, would suggest the loss of much of the archaeological record of the last ~4000 years. These multi-scalar data are essential for the construction of appropriate mitigation strategies and further study of the remaining stratigraphy.

Keywords: cave entrance, eastern Africa, Kondoa, micromorphology, sedimentology, archaeological stewardship

INTRODUCTION

Caves and rockshelters are important sedimentary archives for studying the deep human past because of their persistent and repeated use across the Pleistocene and Holocene for habitation, burial of the dead, as surfaces for painting or engraving, and other purposes. Excavation of these sites require an archaeological methodology attuned to reconstructing the environmental processes that formed and shaped them over millennia. We emphasize here the documentation of environmental and anthropogenic factors that may contribute to the loss of these cultural-environmental archives through erosion. We use the Kisese II rockshelter in north-central Tanzania as our case study to explore how an integrated geological and archaeological approach can document past and present sedimentary regimes to understand portions of the deep history of eastern Africa and help frame conservation approaches to preserve this record.

Climate change affects cultural heritage at all latitudes and for decades archaeologists have documented these processes (Sesana et al., 2021). In particular, erosion has been studied at sites along coastal areas as these environments are particularly sensitive to changes in sea level (e.g., Davis et al, 2020). In arctic environments archaeologists have documented accelerated loss of heritage in association with melting ice (e.g., Hollesen et al., 2018). Despite these known processes, methods to study how landscape dynamics can potentially erase records of the past are still uncommon. Geoarchaeological advances have made possible important studies on 1) how past human and natural forces impact archaeological and natural sediments (e.g., Karkanas et al., 2000; Stiner et al., 2001; Shahack-Gross et al., 2004); 2) how erosion can contribute to the creation of a complex geo-archaeological stratigraphy (e.g., Karkanas and Goldberg, 2013); and 3) how landscape erosion, sedimentation, and cave entrance and rockshelter stratigraphy can be incorporated to reconstruct the past (Karkanas et al., 2020). Our geoarchaeological study at Kisese II builds on these approaches and investigates historic and continuing impacts of changing strategies of pastoralism, farming, and land use policy changes on the archaeological record of the Kondoa region in north-central Tanzania. The results of this study can both contribute to roadmaps for future climate change responses and provide a model for integrating multiple stakeholder community perspectives in the reconstruction and study of ancient social and environmental processes.

This paper extends from a simple observation: comparison of archival photographs and present-day field observations suggest the loss of up to 60 cm of sediment by erosion at Kisese II between 1956 and 2019, a loss that likely removed most of the "Iron Age" archaeological record (beginning locally ~1 ka; Kessy 2013) at the shelter, and sediments sampling the period when much of the rock art for which the region is famous was made (Bwasiri and Smith, 2015). Combined with observations about the rapid fading and possible loss of many of the painted images since their first recording almost a hundred years ago (Temu, 2018), we are confronted with the immediate need to understand and hopefully mitigate some of these processes that are contributing to the alteration of the local sedimentary and archaeological records at Kisese II.

Our study is one of the first in Tanzania to consider historical and coeval landscape studies. We employ a multi-scalar analytical approach, from the regional to the microscopic, to understand the impact of slope-erosional and sedimentary forces on rockshelter sediments to aid excavation strategy, interpretation of sedimentology, and issues of site conservation. Scholars in general and archaeologists specifically have described the importance of ensuring practical outcomes of research (Bwasiri and Emmanuel, 2011; Mehari and Ryano, 2016; González-Ruibal et al, 2018; Schmidt, 2019) and collaborating with community stakeholders in academic research (Schmidt and Pikirayi, 2016, Douglass and Cooper, 2021). We build a critical link between archaeological research, heritage management, and climatic and environmental change in the Kondoa region. The site of Kisese II is a relevant case study as it is situated in an area notorious for high erosion, where human intervention to minimize soil impoverishment and erosion is well documented (reviewed in Lane 2010). Overall, this study will contribute to our understanding of the impact of erosion on rockshelter and cave entrance sediments in highly active erosive environments such as the one in Kondoa where archaeological sites are abundant. We hope to contribute to a way of doing archaeology in eastern Africa and elsewhere that answers the call to produce a "usable past" (Andah, 1995; Kryder-Reid, 1997; Hassan, 1999; Schmidt, 2006; Lane, 2009).

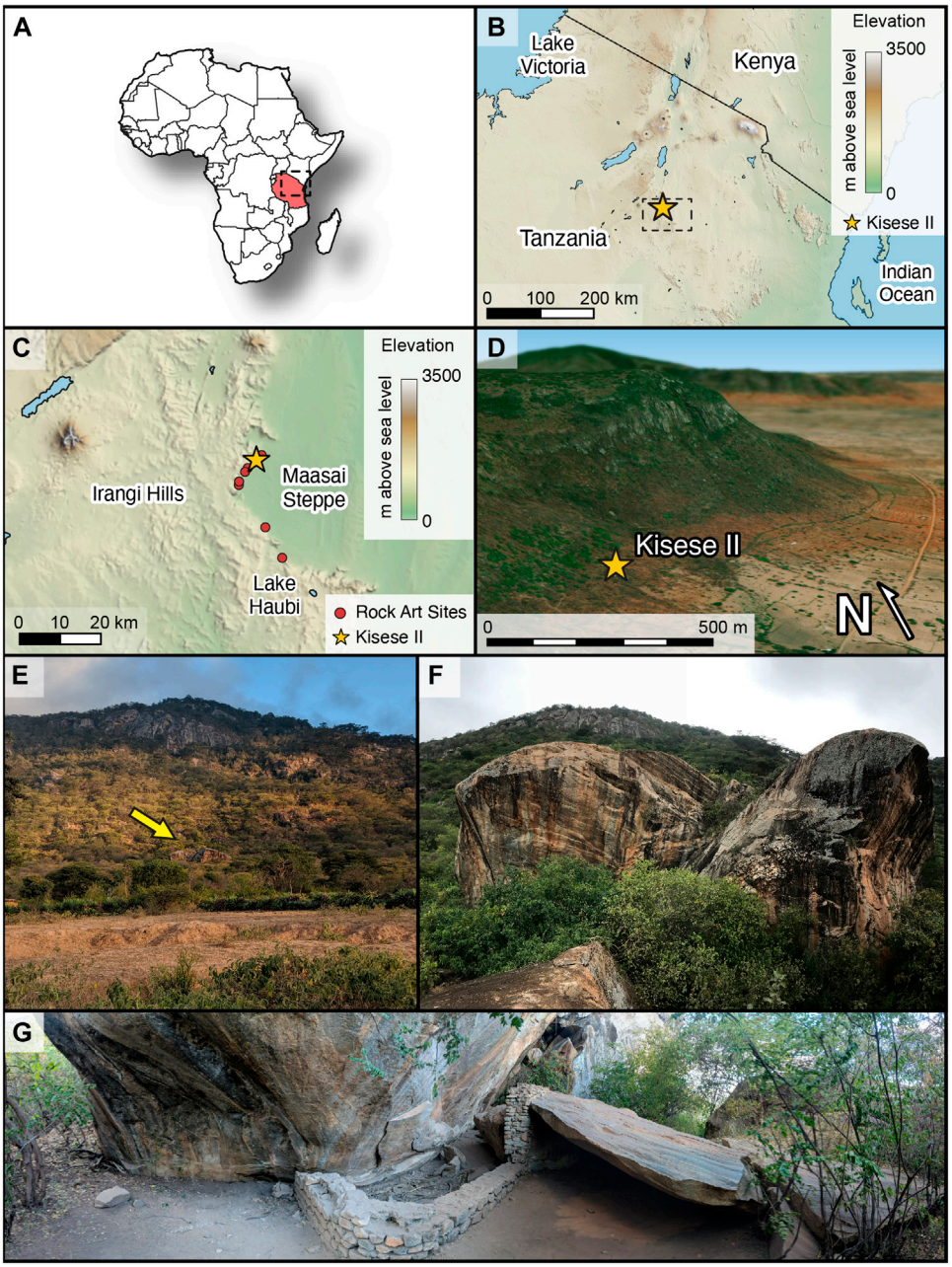

FIGURE 1 | (A) Political map of Africa with Tanzania and the area shown in **(B)** indicated by a dashed line. **(B)** Geographic location of Kisese II rockshelter (marked by the star) and the area shown in **(C)** indicated by a dashed line. **(C)** Close up of the area with the location of Kisese II and other rock art sites identified by the UNESCO World Heritage Centre (red dots). **(D)** Position of Kisese II on the slope of the Irangi Hills. View facing NE. Image generated with the BlenderGIS addon for Blender. **(E)** View of the site (indicated by an arrow) taken from the downslope facing northwest. **(F)**. Detail of the two large boulders sheltering the Kisese II site taken from the smaller front boulder and facing northwest. **(G)** Panoramic image of the archaeological site taken in 2019 showing the location of the shelter, slabs, small boulder, and modern wall.

Kisese II Site Context

The site of Kisese II lies within the Kondoa Rock Art Sites World Heritage Region in Tanzania (**Figure 1**), the richest area of preserved rock art in eastern Africa, likely made by both foragers and pastoralists (Bwasiri and Smith, 2015). Kisese II is one of the few sites in the region with a long (>6-m-thick) stratigraphic sequence that preserves a record of environmental and human behavioral change spanning portions of the Late Pleistocene and Holocene (see Masao, 1976; Ranhorn et al., in review). First excavated in 1951 by M.D. and L.S.B. Leakey, major excavations later took place in 1956 by R.R. Inskeep (summarized in Tryon et al., 2018; Tryon et al., 2019) which demonstrated the

presence of multiple human burials, thousands of ostrich eggshell beads, and a rich corpus of worked and unworked ochre, stone tools, ceramics, and fossil fauna.

Published details of the Leakey and Inskeep excavations are sparse, and our initial restudy of the site began in 2012 and focused on archival and museum-based collections from these initial excavations (e.g., Tryon et al., 2018; Niespolo et al., 2020; Laird et al., 2021). Radiocarbon dates from ostrich eggshell fragments indicate the Kisese II archaeological record spans at least the last 50,000 years (50 ka) (Tryon et al., 2018) but due to limited excavation information the extent of lateral variation in deposition and age was unknown. Excavations and field study resumed in 2017 and 2019 by the Kondoa Deep History and Heritage Project (KDHP), initiated and directed by Ranhorn in 2017. Published studies of the rock art of the Kondoa region more broadly began in the 1920s, with detailed efforts by L.S.B. Leakey (1936); Leakey (1950); Masao (1982); Leakey (1983); Bwasiri and Smith (2015).

The rockshelter is positioned on the Irangi Hills on the eastern margin of the Gregory Rift Valley (**Figures 1D,E**) and consists of a shallow (~10 m), east-facing, overhang on a large boulder about 200 m below the escarpment; one other large boulder makes up the complex while one smaller one and a fallen slab rest in front of the rockshelter (**Figures 1E–G**). The site is somewhat protected from the elements by the front boulder, with a favorable lookout point easily reached by climbing on top of the boulders where the Maasai Steppe and the eastern margins of the Irangi Hills are visible, making it a desirable place for habitation and other human activities.

The Irangi Hills mostly consist of Pre-Cambrian feldspathic gneisses and schists (Eriksson et al, 2000). Soil types change gradually downslope and are today highly eroded; the main soils listed in past studies of the Kondoa landscape include chromic luvisols, lixisols, and regosols on the upper slope, ferric lixisols in the mid-slope, and albic arenasols and gleysols (locally called mbuga soils) in the piedmont and plains of the Maasai Steppe (Payton et al., 1992).

Today, the Kondoa region has a semi-arid to tropical savanna climate with a bimodal precipitation pattern and an average of 500–800 mm mean annual precipitation with frequent high-intensity storms during rainy seasons (Lyaruu and Backeus, 1999). Reconstructions of Late Pleistocene-Holocene rainfall from materials collected at Kisese II indicate similar or drier conditions in the past (Niespolo et al., 2020). Paleoenvironmental studies at the Lake Haubi Basin, ca. 25 km NE of Kondoa, show that the history of erosion in Kondoa dates to at least 14 ka (Eriksson et al, 2000) (**Figure 1**).

METHODOLOGY

To reach a full understanding of the site and the landscape, a diachronic understanding of sedimentary processes is necessary. For this reason, we employ a multi-scalar analytical approach, from regional to landscape to microscopic, that includes a combination of bibliographic research, archival aerial photographs, landscape survey, 3D reconstruction, GIS mapping of the slope below the site and the rockshelter, total station mapping of rockshelter sediments and rock faces, and micromorphological study of the archaeological sediments.

Historical Synthesis of Regional Paleoenvironments

To contextualize our analyses we performed a regional paleoenvironmental review of published material and historical documents. This is necessary to understand the modern environmental situation and its impact on the archaeological and land resources of Kondoa. We reconstructed vegetation change, erosion, sedimentary regimes and the impacts on local inhabitants using published geological and palaeoclimatological data as well as colonial and post-independence land management policies over the last 100 years. These results are presented in the discussion section only as they are not newly produced data but are necessary for the appropriate contextualization of our data.

Landscape Reconstruction Using Aerial Imagery, GIS Analyses, and Pedestrian Survey

By landscape scale we mean the immediate vicinity (~5 km^2 radius) of the site of Kisese II for which we did comparative GIS analyses on photographs from 1960 to 2019 and two foot surveys of the slope. For 1960, we used aerial photographs DOS-49-TN-0011-0122 and DOS-49-TN-0011-0123 from flights over the area in July 1960 produced for the Directorate of Overseas Surveys (D.O.S.) from the D.O.S. archives at the National Collection of Aerial Photography (NCAP) in Scotland. The 1960 flights represent the earliest systematic aerial photography of the region (cf. McGrath, 1976; McIlwaine, 1997; Caillard, 2003), and dates to 4 years after Inskeep's excavations at Kisese II. All images used in the analysis were taken during the dry season. Modern aerial photograph data was collected from Google Maps for 2019, with the image captured on July 24, and thus all aerial imagery was taken during the dry season. Fieldwork at Kisese II in 2019 was conducted in August. Our GIS measurements of topsoil change are based on the amount of ferric lixisol (paleosol) vs. the yellow regosol exposed in 2019 in comparison to the 1960s aerial image. The total area analyzed is 20,710.1 km^2. In order to cover the landscapes of Kisese II and the surrounding area, we also analyzed a close up of the transect of Kisese II (area of 1,643.63 km^2).

Both the 2019 and 1960 aerial photographs were first converted to a common TIFF format in Adobe Photoshop. The TIFF images were combined to create a single data layer for each year, and each year's image was georegistered in ArcGIS software 10.8.1 to the datum Arc 1950 UTM Zone 36 South in a Transverse Mercator projection using the Clarke 1880 spheroid. This is the datum, projection, and spheroid used in the 1:50,000 scale topographic maps series Y742 85/4 and 104/2 prepared by the D.O.S. in 1963, which were based in part on the 1960 photographs as well as field survey. After georegistration, the image files were converted to the ERDAS IMAGINE 4.0 file

format, retaining the original image data and georegistration with minimal pixel loss and distortion. ERDAS IMAGINE file formats produce the best and most consistent results when used in IDRISI Selva software. The files were then imported into IDRISI Selva and processed using supervised classification to extract the reddish areas we identify as a ferric lixisol revealed through the erosion of the overlying yellow sandy regosol. The resulting classified areas were then converted from raster format to vector format, and the area of the exposed ferric lixisol was calculated in square meters.

We conducted pedestrian surveys of the area surrounding the site to record soils and sediments currently on the slope, document the erosional and sedimentary forces at play, and establish a base level for a multi-year study on the impact of erosion on the landscape. Survey in 2017 and 2019 was guided by 1:50,000 maps published by the Tanzania Geological Survey (quarter degree sheets 85 and 104) and used a hand-held GPS (Garmin GPSmap 62s, GPS accuracy: < 10 m, altimeter accuracy: < 3 m) to record the latitude and longitude of erosional surfaces, rills, gullies, and changes in vegetation. We documented erosive features with digital photographs to create terrestrially based 3D photogrammetric models of the slope. To contextualize these erosive features historically we used the digitized historical aerial photographs noted above. To summarize and display our results we adopt the soil catena model initially developed by Milne et al. (1936); Bushnell (1942). To create an archaeologically relevant environmental study of the area we used a general soil catena of the Irangi escarpment (Payton et al., 2019) as a roadmap to create a one localized to Kisese II, and integrated it with vegetation, fauna, and archaeological data thus constructing a geoarchaeological catena.

Excavation

At the site of Kisese II we studied erosion patterns from rainwater runoff on the sediments and contextualized them with the landscape data generated by our survey. Using archival data and digital techniques, we directly measured sediment loss at the site since major excavations occurred in 1956. These data guide field excavation to investigate the remaining stratigraphy. Micromorphological analyses were used to interpret the archaeological palimpsest(s) and reconstruct human activities and depositional and erosional history of the shelter from >50 ka to ~5 ka.

Our 2017 and 2019 excavations of 2 × 3 m and 2 × 2 m reached a maximum depth of 2.40 and 1.40 m respectively relative to the modern surface. The main goal was to identify the limits of the older excavations; for this reason we adopted the 1956 grid north and placed units adjacent to the Inskeep and Leakey trenches, with their boundary positions estimated using archival photographs. To investigate the presence and extent of previously unexcavated stratigraphy we placed a test pit, measuring 1 × 1 m for 50 cm depth, under the largest rock slab. Based on comparison with existing radiocarbon dates on materials from the 1956 excavations (Tryon et al., 2018), the recent excavations span >50–5 ka including the Last Glacial Maximum. A total station relative to a local datum was used to record all positional data including of each micromorphological sample using a handheld data collector running EDM Mobile (McPherron et al., 2005). For each initialization, the X, Y, Z coordinates of 3 points were measured on permanent datums to calculate the station's position relative to the archaeological grid. This position was then verified by taking a point on a fourth permanent datum. A maximum of 0.5 cm of combined error in the X, Y, and Z positions of this verification point was accepted for initialization.

Micromorphological Sampling

Eleven intact oriented sediment samples for micromorphological analyses were collected from excavation profiles in 2017 (for sampling techniques see Courty et al, 1989; Goldberg and Macphail, 2008). The position of the blocks on the profile was recorded with a Leica total station and mapped into the archaeological site grid within 0.5 cm error. The sediments were studied using a petrographic microscope to 1) determine the nature and organization of the components (e.g., composition, size, texture), 2) distinguish natural and cultural formation processes and 3) build a framework for interpreting the history of human occupation of the rockshelter. The blocks were processed in the Multi-User Laboratory at Harvard University Department of Anthropology. The samples were oven-dried for 7 days at 60°C, and then impregnated with mixture of 7 parts unpromoted polyester resin and 3 parts styrene catalyzed with methyl-ethyl-ketone-peroxide (MEKP; 8 ml per liter of mixture). Once dried the blocks were sliced into 50 × 75 × 10 mm chips that were sent to Spectrum Petrographics (Vancouver, WA) for mounting. The thin sections were examined using a microfilm reader, and binocular and petrographic microscopes in plane-polarized light (PPL), cross-polarized light (XPL), and oblique incidence light (OIL) at various scales from × 5 to × 200 (Courty et al, 1989). Descriptive nomenclature follows that of Stoops (2003); Courty et al. (1989).

3D Modelling

3D models of the site were created both during and after excavation using photogrammetry (structure from motion). Advances in both the affordability and quality of photogrammetry software in recent years has resulted in a proliferation of the technique in archaeology, including its use to quantify sediment volumes (Koenig et al, 2017; Emmitt et al., 2021; Nobles and Roosevelt 2021). Photographs were taken using a Sony RX100 Mark V compact digital camera. RAW images were collected for archival purposes, which were converted into JPG images for further processing. Calibrated scale bars designed for photogrammetry purchased from Cultural Heritage Imaging were included in the areas being photographed. The position of coded targets printed on these scale bars were recorded using a Leica reflectorless total station. Photographs were processed into textured 3D models as well as 2.5D digital elevation models (DEMs) using Agisoft Metashape. These models were scaled and referenced to the site grid in 3D in Agisoft Metashape. The resulting outputs allow for accurate and precise measurement of features in three dimensions outside of a field context.

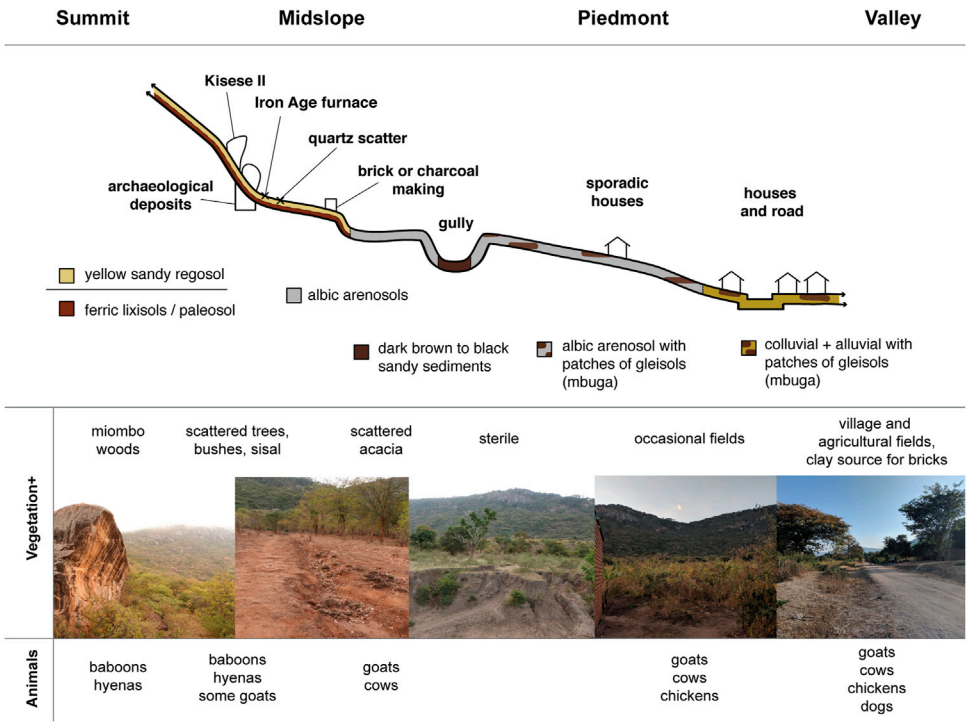

FIGURE 2 | Schematic diagram representing the transect of the slope where Kisese II is located. The elevation of the site is 1,287 ± 3 m above sea level. The diagram shows a geoarchaeological catena constructed from the results of our foot survey. To create a resource relevant to archaeological work we combined a classic soil catena with environmental features such as vegetation and fauna, and anthropogenic features such as sites and modern human presence. Follows a description of the soils we recorded on the slope (**Table 1**).

We quantified erosion at the rockshelter since 1956 by measuring the distance between the former topsoil line visible on the shelter wall and the modern topsoil height, using a scaled and georeferenced orthographic photo of the rockshelter wall with Agisoft Metashape. The photographs for this model were largely taken post-excavation when a total station was not available. In order to georeference this model, the post-excavation chunk was aligned to an already georeferenced model in Metashape using point-based alignment. The total error on the four scale bar control points for the georeferenced model was 0.0755 cm. Finally, using QGIS we then traced both the modern sediment line and weathering line and measured the distance between these two lines at 50 cm intervals.

RESULTS

Geo-Archaeological Catena of Kisese II

Our geoarchaeological catena shows a schematic diagram of local natural and anthropogenic features (**Figure 2**). Moving from the summit towards the valley the catenary sequence is shown in **Figure 2** and explained in detail in **Table 1**. (**Figures 2**, **3**); (**Figures 2**, **3**); (**Figures 3**, **4A–D**); (**Figures 4E–G**); (**Figure 4**); (**Figures 4H,J**); (**Figures 2**, **4A,J**); (**Figure 4I**); (**Figures 4A,H,J**); (**Figures 2**, **4A**)

To quantify erosion on the landscape in the past 60 years we analyzed historical and modern aerial photographs of the landscape around the site using GIS (**Figures 5**, **6**). Briefly, 1) there was a drastic change in topsoil exposure; 2) new gullies and rills formed; 3) forest cover expanded; and 4) anthropogenic agricultural features increased in number and size in the piedmont and valley. Inspection of data from the 1960 photographs reveals only trace amounts of the paleosol exposed, below the resolution of our analyses. In 2019 the area of Kisese II and its surrounding landscape was composed in total by 623.808 m^2 of lixisol, indicating a loss of topsoil of 3% in the total area analyzed over 59 years (**Figure 6C**). At a closer look the transect of the immediate landscape of Kisese II has been impacted the least, with a loss of 0.12% of topsoil loss in the total area, 2.129 m^2 of lixisol, on a total area analyzed of 1,643.630 m^2 (**Figure 5D**). The comparison of the landscape photographs also shows a drastic change in tree coverage with grassland and farmed fields being replaced by woodland on the Irangi escarpment. In the valley the fields have increased and small isolated dwellings seem to have disappeared altogether in favor of houses along the main road.

Observations on Erosion at the Site

Today, primary sedimentary processes at Kisese II appear to be a combination of colluvial input and erosion driven by slopewash processes, accelerated by dripline-mediated rainfall (**Figure 7**).

TABLE 1 | Commentary to the geoarchaeological catena (**Figure 2**) listing the recorded categories for each section of the surveyed area that was divided into 4 sections depending on its position on the landscape. We identified soils using geological maps and past geological surveys of the region. Characteristics for each soil we identified are as follows: Regosols: weakly developed soil found on unconsolidated materials. Luvisols: a well developed soil with an eluviated argic subsoil. These soils are prone to erosion when found on slopes and require terracing or other kinds of human intervention to retain stability. Albic arenosols: bleached sandy soil having sand or another coarse texture in the upper 50 cm soil layer. Gleysol (mbuga): wetland or hydric soil characterized by waterlogging by ground water unless drained.

Summit	
Stratigraphy	Yellow regosols
Vegetation	Thick Miombo woodlands dominated by Brachystegia trees, present today also immediately around the site, with roots and saplings encroaching on the southern edge of the rockshelter (**Figures 2**, **3**).
Fauna	Baboons and hyenas
Archaeology	Kisese II rockshelter; Iron smelting furnace (not part of our study).
Mid-slope	
Stratigraphy	Immediately below the boulders are patches of yellow sandy regosol, noted in the 1956 archival photographs (**Figures 2**, **3**), on top of a ferric lixisol (a paleosol) that we find throughout the slope and in the deeper stratigraphy of the valley as well as on top of the Irangi hills. On the higher portion of the midslope the regosols are almost completely eroded with removal of the paleosol underway and formation of new rills that are exposing the underlying brecciated bedrock (**Figures 3**, **4A–D**).
Vegetation	Sparsely wooded and edaphic grassland, with drier Acacia-Commiphora bushland, thicket of the Maasai Steppe east of the escarpment, and sporadic concentrations of sisal plants.
Fauna	While this area once supported large herbivore communities of zebra, buffalo, wildebeest, impala and elephant, that are now restricted to nearby Tarangire National Park, initially formed as the Tarangire Game Reserve in 1957 only a year after the major excavations at Kisese II (Lamprey, 1963, 1964; Borner, 1985), today the wildlife is scarce and includes downslope incursions of hyenas and baboons and sporadic uphill pasture of cows and goats.
Archaeology	During our survey we located several scatters of stone tools and pottery sherds (**Figures 4E–G**). These sites are contained within the yellow sandy regosols and only the furnace is sheltered by vegetation. The artifacts (quartz flakes and potsherds) could point to sites adjacent to the rockshelter, although comparison of the topography with photographs dated to the 1956 excavation suggests that these scatters could have been located inside the excavation camp, and therefore could result from material discarded during artifact washing and sorting station or a place where the team practiced knapping.
Erosive features	In 2019 erosion had completely removed the yellow sandy-silty soil in the non wooded areas washing away the artefacts and exposing a compact red clayey-silt paleosol with large rounded granitic rocks that were already surfacing through the yellow regosol in 2017 (**Figure 4**). In 2017, this paleosol was only visible on the lower part of the midslope or on the bottom of rills and profile of gullies, suggesting rapid change, as the red paleosol is now being actively eroded and washed away, the rills and the large gullies to the north and south are deepening and expanding, and new rills are forming. Today gullies as deep as 25 m cut into the lixisols and run W-E towards the valley crossing through the midslope to the piedmont (**Figures 4H,J**).
Piedmont	
Stratigraphy	Albic soils, patches of gleysols, and deposits of alluvial sediments (**Figures 2**, **4A,J**)
Vegetation	From the lower slopes to the piedmont trees are more sporadic while lines of sisal plants, mostly running N-S become more frequent.
Fauna	Because of the impoverishment of the soil the lower hillslopes are not farmed as heavily today but used primarily as pasture for cows and goats.
Archaeology	The lower hillslopes with their mosaic of albic arenasols, gleysols, gullies and badlands are not the ideal loci for *in situ* archaeological sites. The only scatter of stone tools here was found on the profile of a large gully (**Figure 4I**). It was impossible to determine whether the material was being eroded from the profile or had been deposited here by previous colluvial activity and was now being re-eroded further downslope. Although archaeological traces here are not clear we have identified historical and modern human activities in several charcoal and brick furnaces still in use or recently abandoned.
Erosive features	In addition to newly formed rills and gullies the older gullies that cross the piedmont tend to coalesce and create large badlands of dark sandy sediments (**Figures 4A,H,J**). Localized accretion was noticed at the base of the sisal plants creating lines of raised soils on the eroded landscape.
Valley	
Stratigraphy	Colluvial and alluvial sediments with patches of gleysols (**Figures 2**, **4A**).
Vegetation	Cultivated crops include various types of beans, maize, sorghum, and millet.
Fauna	Farm animals include chickens, goats, and cows
Human	Farm fields and houses start at the piedmont and become more common in the valley.
Erosive features	Although the valley is mainly a locus of accumulation, particularly heavy rain events form depressions especially by and over the one road that crosses the village and connects Machinjioni to the only water source in Disa and the two dispensaries in the area (located in Disa and Italolo).

Although screened by vegetation today, aeolian processes may well have been more active in the past. Sediment loss is particularly evident along the back wall of the shelter where differential weathering of the rock demarcates the height of the topsoil during the latest period of soil stability observed in 1956 photographs of the Inskeep excavation (**Figure 8**). We observed a maximum loss of 68 cm of sediment, equal to spits I and II from the 1956 excavations that contained Iron Age archaeological remains (**Figure 9**). We also observed formation of erosive features from splash erosion that caused sediment deflation to sheetwash and remove artifacts and sediments from the site (**Figure 7**).

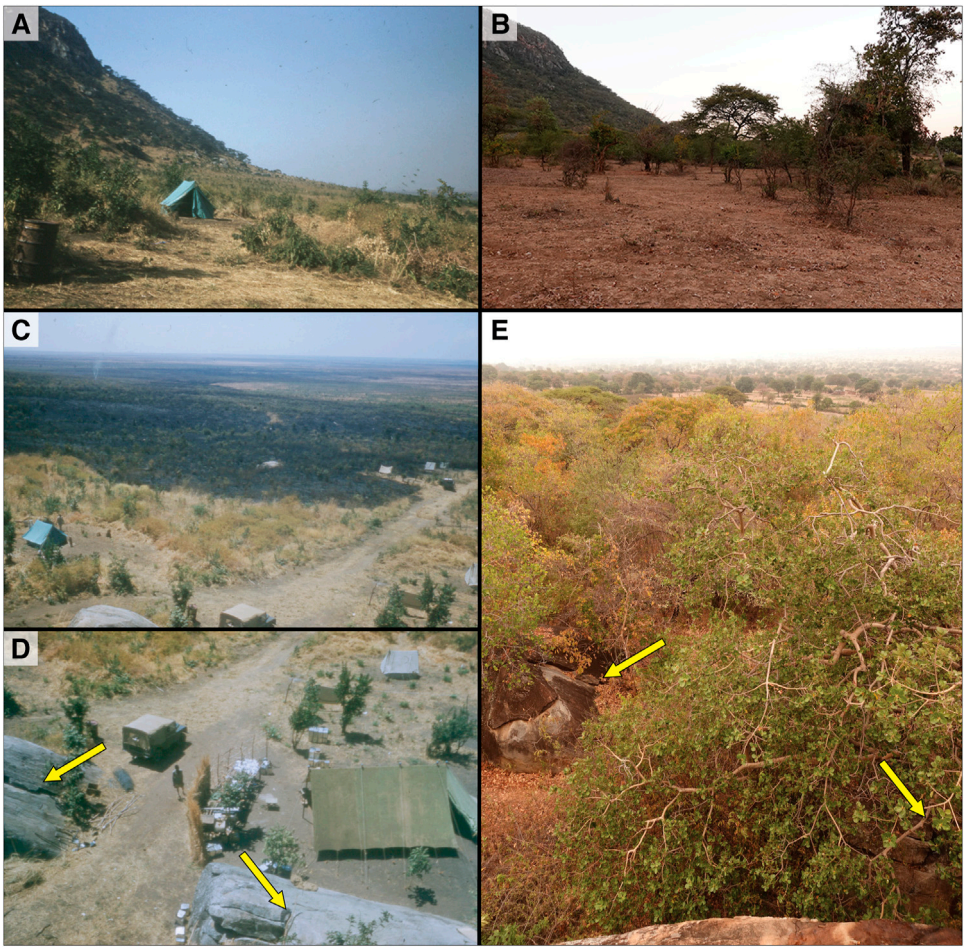

FIGURE 3 | Comparison of images taken during the 1956 Inkeep excavations **(A,C,D)** and 2019 Ranhorn excavations **(B,E)** showing changes at a landscape scale. **(A**,**B)** Photographs taken from the lowlands facing north. Note the shift from a grassland dominated vegetation to wooded, as well as the disappearance of the yellow regosol in favor of the red paleosol. **(C**–**E)** Photographs taken from the front boulder of the Kisese II facing south towards the Maasai Steppe. Arrows indicate distinctive rock features visible in the historic and modern photos. Here again the vegetation shift from savanna grassland to woods is evident as is the change in topsoil. Note the large burned patch of grass in **(C)** portraying slash and burn farming technique in use in the 1950s.

During the beginning of the 2017 rainy season, we had an opportunity to study how heavy rainfall hit the rockshelter wall and fell on the sediments (**Figure 7**). Most of the archaeological site was protected, except for the south corner where water and sediments coming from above and behind the boulder flow into the site. Because of the inward bend, most of the back wall of the rockshelter remained dry during storms with some concentrated flow that did not seem to impact the archaeological sediments. However, the curve of the back wall created a pronounced drip line that causes splash erosion on a circumscribed south-eastern portion of the sediments and in some small, circumscribed areas in the southern corner (**Figure 7**). One large piece of rockfall protects the rest of the sediments towards the center and north (**Figure 7**).

The sediments in the south outside the drip line that are not capped by the slab or the overhang are impacted by sheet erosion causing a southward dipping slope of ~20° for 15–20 m, observed also in the excavation profiles from the 1956 excavations (cf. Tryon et al., 2018). Approximately 10 m south is a steep gully of ~10 m depth that continues eastwards until the piedmont. The gully appears only as a depression in the 1956 photographs and the 1960 aerial photograph confirm the presence of an incipient erosive feature, indicating that the majority of it has been carved in the past 60 years (**Figures 5**, **8A**) in line with oral accounts from community members. Sediment and artifacts eroded from the site are in part channeled into the gully and washed down hill (**Figures 4H,I**).

Micromorphological Results

Our micromorphological study is currently restricted to samples collected in 2017 from a 2 × 3 m trench excavated to a depth of 2.40 m adjacent to the larger 1956 excavations (**Figure 10**). In a volume of 4 m^3 we recovered over 5,000 artifacts signaling a bias in recovery methods by Inskeep who reported a similar number of artifacts from 80 m^3. Our micromorphological study results suggest the presence of three distinct sedimentary groups each

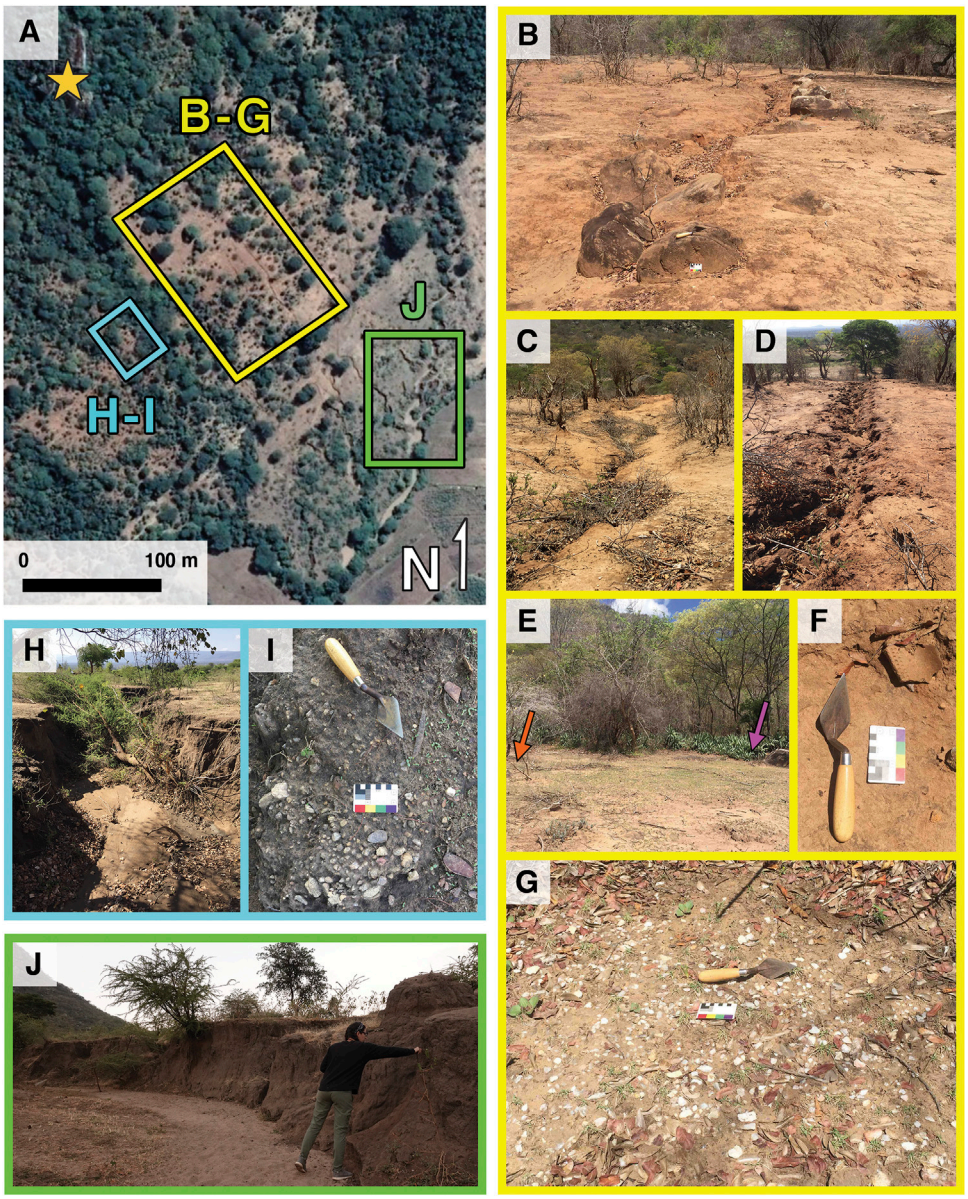

FIGURE 4 | Images of erosional features around the Kisese II site. **(A)** Satellite images of the site (ESRI World Imagery: Maxar Imagery, 2018). The location of the site is marked with a star. The three areas bounded by rectangles indicate the location of the photographs in **(B–G)**. **(B)** rill forming right below the site with small boulders, embedded in the red paleosol, being exposed by the erosion of the yellow regosol. **(C,D)** progression of erosion and rill carving between our 2017 and 2018 survey seasons. Note the complete removal of the yellow regosol and the enlargement of the rill. **(E–G)** scatters of stone tools and pottery being exposed and transported downhill. Arrows in **(E)** show the position of the scatter shown in **(G)** and a row of sisal plants to the right. As mentioned in the text sisal plants were planted as a strategy to combat slope erosion. However, they create a very limited and localized barrier to erosion as we witnessed in this case where the scatter of stone tools positioned only a few meters from it is still being impacted by colluvial activity. **(H–J)** show the more drastic effects of erosion. **(H)** shows the large gully, indicated in **Figure 2**, that starts immediately south of the site and runs downhill until the valley. Along the gully we have found scatters of stone tools, such as the one shown in **(I)**. **(J)** Area where three different gullies coalesce into a badland.

containing between 2 and 5 geological stratigraphic units for a total of 9 geoarchaeological stratigraphic aggregates, shown in **Figure 10**. Described from bottom to top these strata are:

Silty Sands With Micritic Calcite

In situ Late Pleistocene sediments. Stratigraphic aggregate SSMC is 0.94 m thick. Comparison with and partial georectification of l photograph from 1956 indicate the SSMC broadly corresponds to the middle of spit X to the bottom of spit XIV from the Inskeep excavation and thus is likely Late Pleistocene in age. The thin sections from SSMC indicate a rapidly deposited silty-sand layer with micritic calcite, rounded bone fragments, and some colluvial input (Samples 11, 10, 9, and part of 8). The lower layer (sample 11) shows no bedding and has low porosity (**Figures 11A,B**)

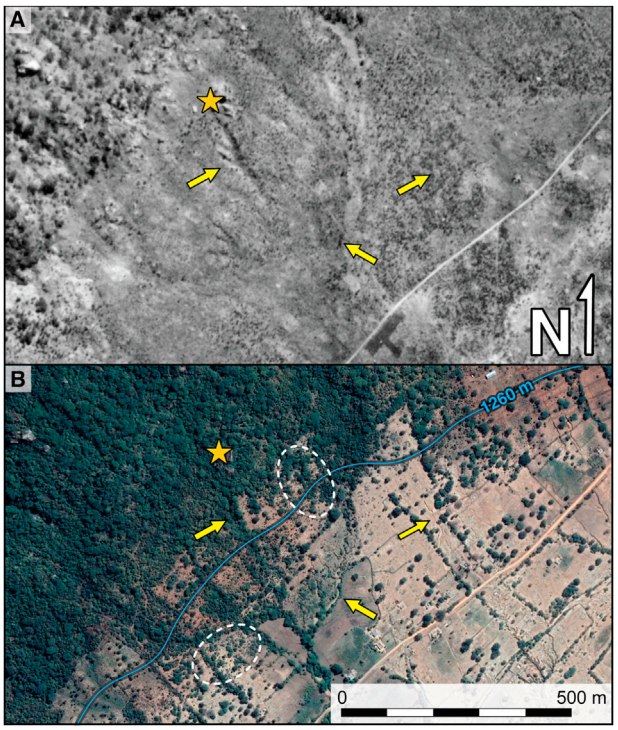

FIGURE 5 | Comparison of historic and modern aerial imagery around Kisese II. Location of the site is indicated by a star. Arrows indicate the position of modern erosional features. Although the larger gullies present today were already visible in 1960, most of the indicated erosional features were not yet present, highlighting how although erosion is a longstanding process in Kondoa it has increased significantly since 1960. Dotted white lines indicate areas demonstrating the extent of erosion of the yellow topsoil around the site, resulting in the red paleosol dominating the higher portions of the slope above the 1,260 m above sea level topographic line. Note the extent of the miombo forest slowly populating further downhill compared to the almost barren slopes in 1960. **(A)** Historic aerial photograph taken in 1960 (Directorate of Overseas Surveys archives, National Collection of Aerial Photography, Scotland, NCAP/ncap.org.uk). **(B)** Modern satellite image from ESRI World Imagery (Maxar Imagery, 2018).

indicating that it was deposited quickly, with micrite cementing the sediments (**Figure 11B** yellow arrow) and coating the heated bone inclusions (**Figure 11B** pink arrow). The layers above (samples 10 and 9) have a similar silty-sandy matrix with micrite (**Figure 11C**). However, calcite decreases moving up the section, accompanied by an increase in bone frequency (**Figures 11C,D**, pink arrows).

Humic Sands

Backfill from 1956. Sediment assigned to HS is 1.62 m thick and is only concentrated on the south portion of the excavation. Loose bioturbated humic sandy sediments (parts of samples 8 and 2 collected at the boundaries between groups) comprise much of the area excavated in 2017 (**Figure 10**). This stratigraphic aggregate is characterized by layers with sharp and straight boundaries as shown in the scan of the thin section (**Figure 11E**), suggesting an artificial cut. The sediments contain clasts of calcitic or clayey aggregates as well as pedorelicts (**Figure 11F**) that we interpret as reworked chunks of the lower and upper layers suggesting that these sediments are made of backfill of the earlier Inskeep excavation from 1956. Sample 2 in **Figure 11E** also shows the difference in porosity between the two layers, with the humic sediments being spongier and the red sediments more compact and uniform. Both these factors confirm the intrusive nature of the humic sediments. Fresh or diagenetically altered bone fragments are also present (**Figure 11F**, pink arrows) however, burned bones were not identified in the thin sections.

Colluvial Clayey Sands

Insect turbated partially-*in situ* Holocene sediments. Sediments assigned to CCS are 1.08 m thick. They broadly correspond in depth to part of spit II to spit V from the Inskeep excavation and thus are likely early Holocene in age. Periodically saturated colluvial clayey sand with a high degree of bioturbation (Samples 2–7). Sample 2 was collected from a red-brown clayey sand that in the field was identified as *in situ* Holocene deposits. This layer appeared truncated by the 1950s excavations making its stratigraphic relation with the lower *in situ* sediments unclear. Microscopic examination shows no calcite, but instead dusty red clay coatings around the quartz sand grains suggesting colluvial input. The layer lacks evidence for ash or other forms of $CaCO_3$ strengthening the probability that the calcite seen in the lower sediments was indeed original to the sediments at time of deposition and did not percolate from the upper sediments.

The rest of the upper sediments, observed in samples 3 to 7, have similar composition and inclusions as sample 2 with the addition of very few grains (~10 per slide) of olivine, a volcanic mineral. We interpreted this group as colluvial sediments as indicated by the subrounded quartz grains and the thick coating that covers each grain (**Figures 11G,H** blue arrows). Frequent redoximorphic features suggest a wetter depositional environment while a crumbly texture and open porosity pattern points to a slower rate of sedimentation relative to the lower sediments (**Figure 11G**). These layers contain abundant humic material and bioturbation passages of different ages. We hypothesize that these layers were already partially bioturbated at the time of the 1956 excavation. Because of the 1956 excavation, the loss of topsoil, and therefore the drastic change in flora and environmental conditions at the site, additional bioturbation has disturbed these sediments even further. Layers assigned to CCS lack any evidence for ash, charcoal, burned material, micrite, or animal dung. This suggests that the $CaCO_3$ observed in the lower layers was not leached out from these upper sediments and is instead restricted to the sedimentary environment of the lower sediments.

DISCUSSION

History of Landscape Processes and Environmental Change in Kondoa Region

Reconstructions by Eriksson and others (2000) that combine geology and OSL dating of colluvial and alluvial sediments trace the chronology of early Holocene erosion and show that the

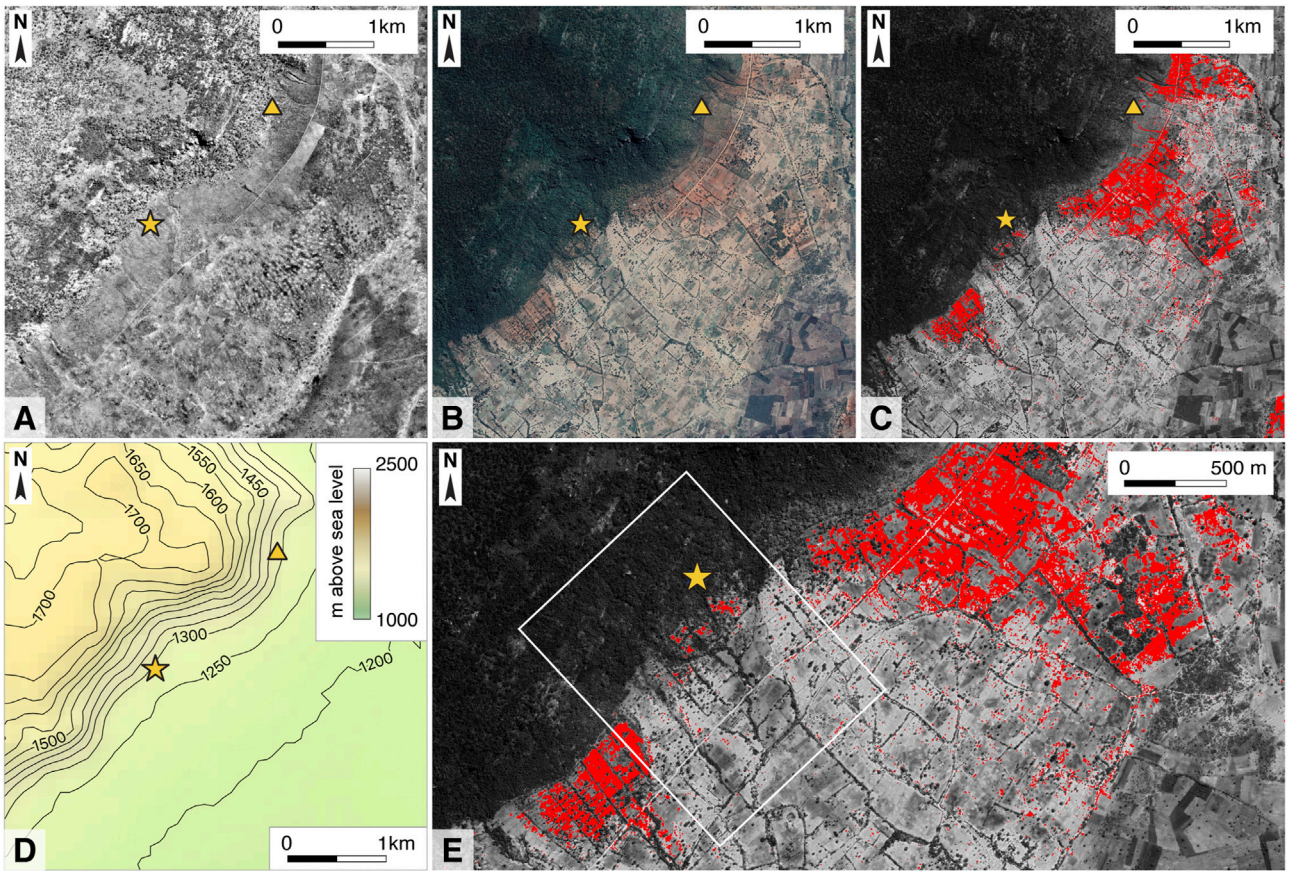

FIGURE 6 | Comparison of historic and modern aerial imagery around the wider region surrounding Kisese II. The triangle denotes the location of Kisese I, and the star denotes the location of Kisese II. Location of the site is indicated by a star. **(A)** Historic aerial photograph taken in 1960 (Directorate of Overseas Surveys archives, National Collection of Aerial Photography, Scotland, NCAP/ncap.org.uk). Note the extent of deforestation well beyond the summit of the Irangi Hills. **(B)** Modern satellite image from Google Earth. **(C)** Greyscale version of modern Google Earth imagery, with areas corresponding to exposed ferric lixisol through analysis in IDRISI Selva overlaid in red. **(D)** Topographic map of the study area. **(E)** Enlargement of **Figure 6C**. The white box corresponds to the area defined as the immediate landscape around Kisese II for the GIS analysis. It is clear that the landscape of Kisese II has been impacted the least.

Kondoa district has been characterized by a K-cycle (sensu Butler 1967) with periods of erosion and depositions punctuated by hillslope stability that allow for pedogenesis (Eriksson et al, 2000). Their published OSL dates point to an erosive episode between 14.5 and 11.4 ka when coarse colluvial material was deposited in already present depressions on the hillslopes. The terminal Pleistocene was followed by a period of stability allowing for the formation of albic-arenosols (caused by illuviation of Fe and formation of ferric nodules and ironstone). Stability seemed to last until ~900 years ago when a new more intense erosive cycle started, characterized by sheet and rill formation and the deposition of alluvial fans (Eriksson et al, 2000); more studies are needed to understand if this cycle is connected to the Medieval Warm Period (or Medieval Climate Anomaly) that in eastern Africa created drastic fluctuations between cold and warm spikes (see Lüning et al, 2017 and citations within). Approximately 600 years ago, the mid-slope ferric lixisols were exposed and eroded causing the accumulation of red colluvium and the formation of gullies (Payton et al., 1992; Eriksson et al, 2000). This Holocene erosive cycle seems to have continued until present with the growth of older gullies up to 20–25 m, erosion of older colluvium and albic arenisols, the formation of new rills and gullies in the partially bare high and mid-slope, and the formation of badlands where multiple gullies have coalesced, all features that we recognize today on the landscape surrounding Kisese II. Sediment deposition in the Lake Haubi region between 1835 and 1988, a rough proxy for erosion rates in the Irangi hills, ranges from 0.9 to 6.2 cm/year (Eriksson and Sandgren, 1999), highlighting the scale of sediment loss and redeposition in the region.

These long-term processes provide the context for more recent impacts caused by government programs to modify, control, and contain erosion. Vulnerability of rural populations and environments in Kondoa due to severe soil erosion has been at the center of governmental studies and actions since colonial times with several attempts to mitigate its effects (Kannenberg, 1900; Fosbrooke, 1951; Eriksson et al., 2000 and citations within). From 1927 to 1949 the British colonial government initiated a major program of deforestation on the lower slopes and plains. A subsequent program was launched to control the spread of tsetse

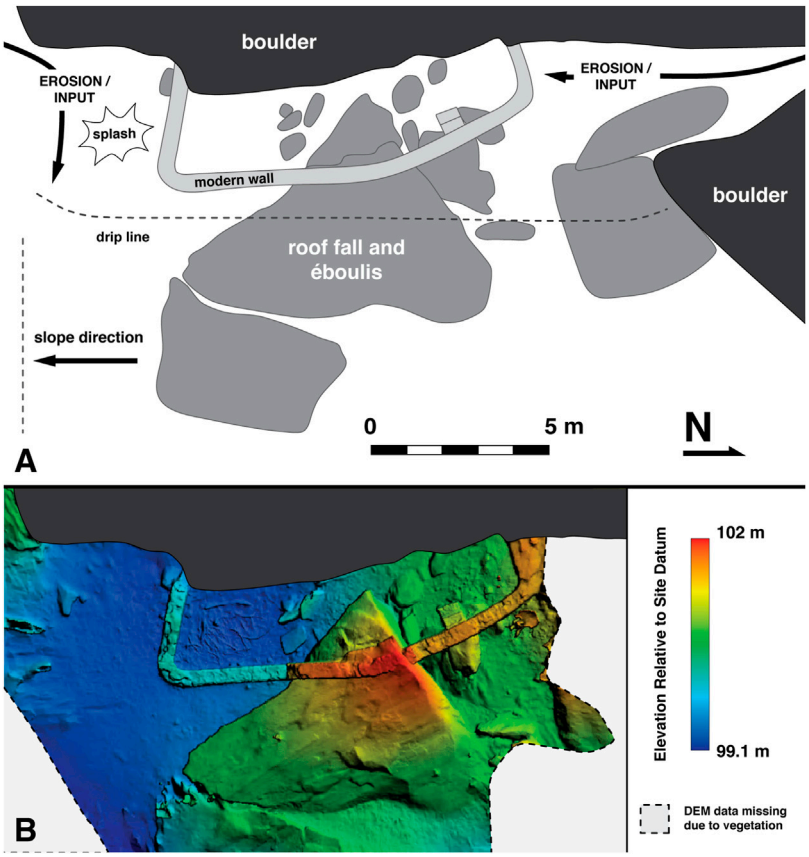

FIGURE 7 | Diagrams of the rockshelter in plan view from above. North arrow indicates grid north. **(A)** the different processes we identified: combination of erosion and sedimentation is visible especially at the S and N edges of the boulder; Splash erosion is present along the dripline and in circumscribed areas. As shown in the diagram, the majority of the sediments are protected by the rock slabs. **(B)** Digital elevation model generated from a photogrammetric model produced in Agisoft Metashape. Elevation units are relative to site datum. Note the difference in elevation between the northern and the southern portion.

flies and human trypanosomiasis or "sleeping sickness" that significantly altered local faunal communities (Swynnerton, 1936; Mugasha and Nshubemuki, 1988; Headrick, 2014).

Deforestation almost certainly exacerbated existing erosional processes, and in the last century several attempts were made to limit soil erosion and thus the loss of productive land in Kondoa (Phillips, 1930; Backéus et al., 1994; Blay et al., 2004; Lane, 2009). Although some efforts were more successful than others in slowing down erosion, in hindsight there were two main challenges with the approaches taken to limit erosion: 1) disentangling the causes of the erosion including human practices and global and local climatic shifts; 2) imposing solutions across large areas not considering local knowledge and the health and wellbeing of the population (Lane, 2009). As a result, changes were not permanent. The 1990s saw the beginning of the erosional cycle that is still in action today. Our investigations show that this new erosional cycle is caused by a combination of a lack of enforcement of regulations, an overall inefficacy of erosion mitigation strategy, and the exacerbation of localized and global climate changes. Records show that rain patterns started to drastically change in the 1990s to become increasingly more unpredictable with out-of-season high-intensity storms and droughts. Kangalawe et al. (2008) note that severe droughts struck the area of Kondoa for three consecutive years between 1994 and 1997. These were immediately followed by unusually heavy rains in 1997 and 1998. Since then, numerous erosional models have been published that assess plans to move forward (e.g., Payton et al., 1992; Eriksson et al, 2000; Mwalyosi, 2000; Madulu, 2001; Ndomba et al, 2009; Ligonja and Shrestha, 2015).

Slope Processes Between 1956 and 2019

Our landscape reconstruction adds nuance to this wider regional image of erosion and environmental change by identifying and quantifying slope processes from 1956 to 2019. GIS comparison of aerial images shows four main features that characterize landscape change at Kisese II in the past 60 years: 1) the drastic change in topsoil cover; 2) the formation of new gullies and rills; 3) forest expansion; 4) the increase of anthropogenic agricultural features in the piedmont and valley (**Figures 4–6**). Our foot survey and analyses of photographs from the 1956 excavation has demonstrated that: 1) these processes are still in place and becoming more rapid; 2) they impact the archaeological

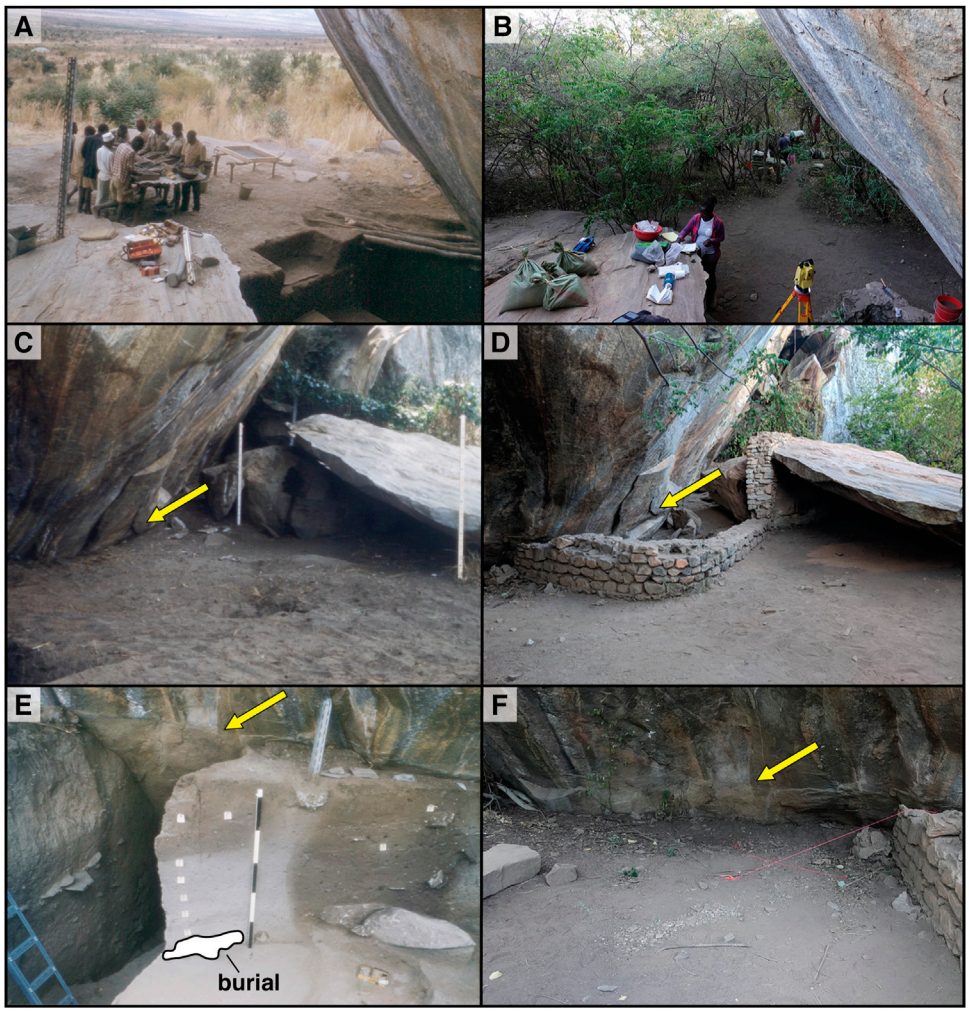

FIGURE 8 | Comparison of images taken during the 1956 Inkeep excavations (left column) and 2019 Ranhorn excavations (right column) showing changes at the site scale. **(A,B)** View of the site facing southwest towards both the historic and modern screening area and the large gully to the S of the site noted in **Figure 2**. Note the dramatic change in tree cover. **(C,D)** View of the site facing north. Yellow arrows indicate the position of the weathering line on the rock face, demonstrating the extent of sediment loss at the back wall of the shelter. **(E,F)** View of the shelter wall facing west. Yellow arrows indicate the position of the same weathering feature on the rock face, demonstrating the lateral extent of sediment erosion.

record on the landscape in different ways depending on local geomorphology.

From both archival data and our own observations we know that the soil sequence on the slope consists of yellow regosols on top of a red lixisol paleosol (**Figures 2–6**). The GIS analysis on historical and contemporary aerial views shows that, on the slope we surveyed, circumscribed to the immediate landscape of Kisese II, 2,129 m^2 of regosol coverage has been lost in the past 60 years. Our 2019 survey shows also that an erosional regime is indeed prevalent on the slope with ongoing loss of archaeological and ethnographic record (**Figures 3–6**). Scatters of stone tools recorded right below the site embedded in yellow regosol in 2017 were significantly reduced by 2019 (**Figure 4G**). Clumps of redeposited tools, probably coming from several km uphill, were found at the piedmont in the larger gully we surveyed (**Figure 4I**). Between 2017 and 2019 we also recorded an increase in numbers of eroded pottery sherds on the midslope (**Figure 4F**). Our wider GIS analysis that covered an area that includes Kisese II and Kisese I, the closest known rockshelter containing rockart, shows an even more grave situation, with 623.808 m^2 of the landscape covered by red lixysol in 2019. The extent of erosion on the Kisese I transect is such that we assume a much greater loss of archaeological record than at Kisese II. Our results show that soil erosion at Kisese II has reached a critical point, having significant impact not only on a half-century time scale but even on a yearly basis.

Erosion is also regulated by vegetation. Our study shows that tree coverage has changed the Irangi landscape several times since the beginning of the last century. As seen from our archival and bibliographic research, forced governmental deforestation started in the 1920s and its impacts were still visible in 1956. At this time the woods were sparse (**Figures 3**, **5**) and the tree line was much

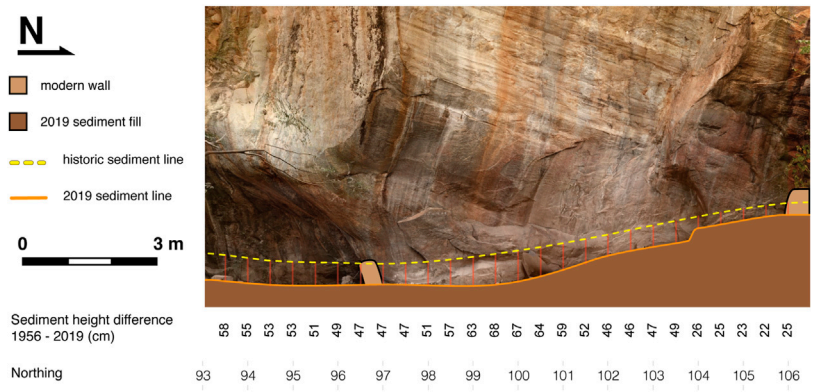

FIGURE 9 | Orthomosaic of the back wall of the shelter with outlines of modern and 1956 sediment lines, the volume outline of rock slabs, and the modern containment wall. The difference in the *Z* direction between the historic and modern sediment line is shown at positions spaced 50 cm apart along the site grid. Note the difference in elevation between the lower south portion and higher northern edge probably due to the higher impact of colluvial input versus erosion because of the slabs and the northern boulder that protect this area.

higher upslope, tens of meters above the site (**Figure 6**). While today the site is encroached by trees, in 1956 the area around the rockshelter was characterized by farmland and grassland as seen in photographs from the 1956 excavation and 1960 aerial pictures (**Figure 3**). In the 1950s slash and burn techniques were in use (**Figure 3C**) contributing to the further weakening of the ecosystem. An interesting result concerning links between vegetation and erosion concerns the sisals, xerophitic plants originally introduced by the colonial governments to serve as a biological barrier against erosion (Lane 2009) and later adopted by local farmers to signal property limits that are now abandoned due to unproductivity of the soil. We recorded lines of sisal as far uphill as a few tens of meters below the last boulder of Kisese II (**Figure 4E** pink arrow). Our observations show that in discordance with their original purpose the plants are not preventing soil erosion, instead they create localized raised sediments in a carved out landscape. The soil accretion circumscribed only around their roots has produced a localized biological barrier to colluvial sediments on their path, as such their presence can be used as an indicator of the extent of the impact of erosion on the hillslope.

One of the most visible erosional features throughout the Kondoa landscape are the deep gullies carved on the slope. Although at Kisese II some of the gullies were already present as shallow erosional features in 1956, our study shows that most gullies we see today formed between 1960 and 2019 while the ones present in 1956 and 1960 have enlarged and deepened considerably at times coalescing into badlands in the piedmont (**Figures 4A**,H,J, **5**). The erosive and rain trends are such that gullies will continue to deepen and badland areas will increase in number. Seen through the results of this study we must assume that the progressive growth of these features will impact the remaining archaeology on the landscape as well as modern anthropogenic features: homes, agricultural fields, roads etc. Comparison between the 1960 and 2019 photographs shows how the local inhabitants, at least partially guided by the erosive processes and governmental impositions mentioned here, have changed their land use patterns. We detected clear traces of farming intensification shown by the increase in plowed land in the valley, and significant anthropogenic alteration to the slope.

In the area around Kisese II our results point to a quick and drastic acceleration of the latest erosive cycle identified by Eriksson and others (2000) happening between 1960 and 2019, hundreds of years after the beginning of the cycle. Moreover, when we compare our results for the transect immediately below Kisese II, and the wider area covered in **Figure 6** it is clear that although erosion is the prevalent force in Kondoa as a whole, separate sections of the slope are impacted differently depending on their geomorphology and other environmental factors. Our study shows that the immediate landscape of Kisese II has been impacted the least. Although this might not be surprising news, it is a fact that is often ignored by archaeologists that work on this landscape.

Kisese II Erosional Regimes

Our work at the site scale has been two-fold: 1) the qualification of modern sedimentary regimes and quantification of sediment loss since 1956 and 2) understanding the archaeological stratigraphy. We were able to show that although there is sediment loss consistent with the landscape results, a more complex sedimentary regime is in place at Kisese II that also includes colluvial input. Using photographs from the 1956 excavation we confirmed that the weathering line on the wall is indeed related to past topsoil height (**Figures 8C–F**). We found a maximum loss of 68 cm, or an average of ~1 cm per year from 1956 to 2019. Our results show also a difference between the S and the N portion of the cave, with the top soil height in the N 45 cm higher than on the S (**Figure 9**). However, not all the areas of the rockshelter are impacted in the same way horizontally (**Figure 7**).

Changes in local vegetation around the site mirrors what we found for the slope. The shift from grassland to wooded, can be directly observed through comparison of photographs from 1956 to 2019 (**Figures 3**, **8**); those from the past must be inferred

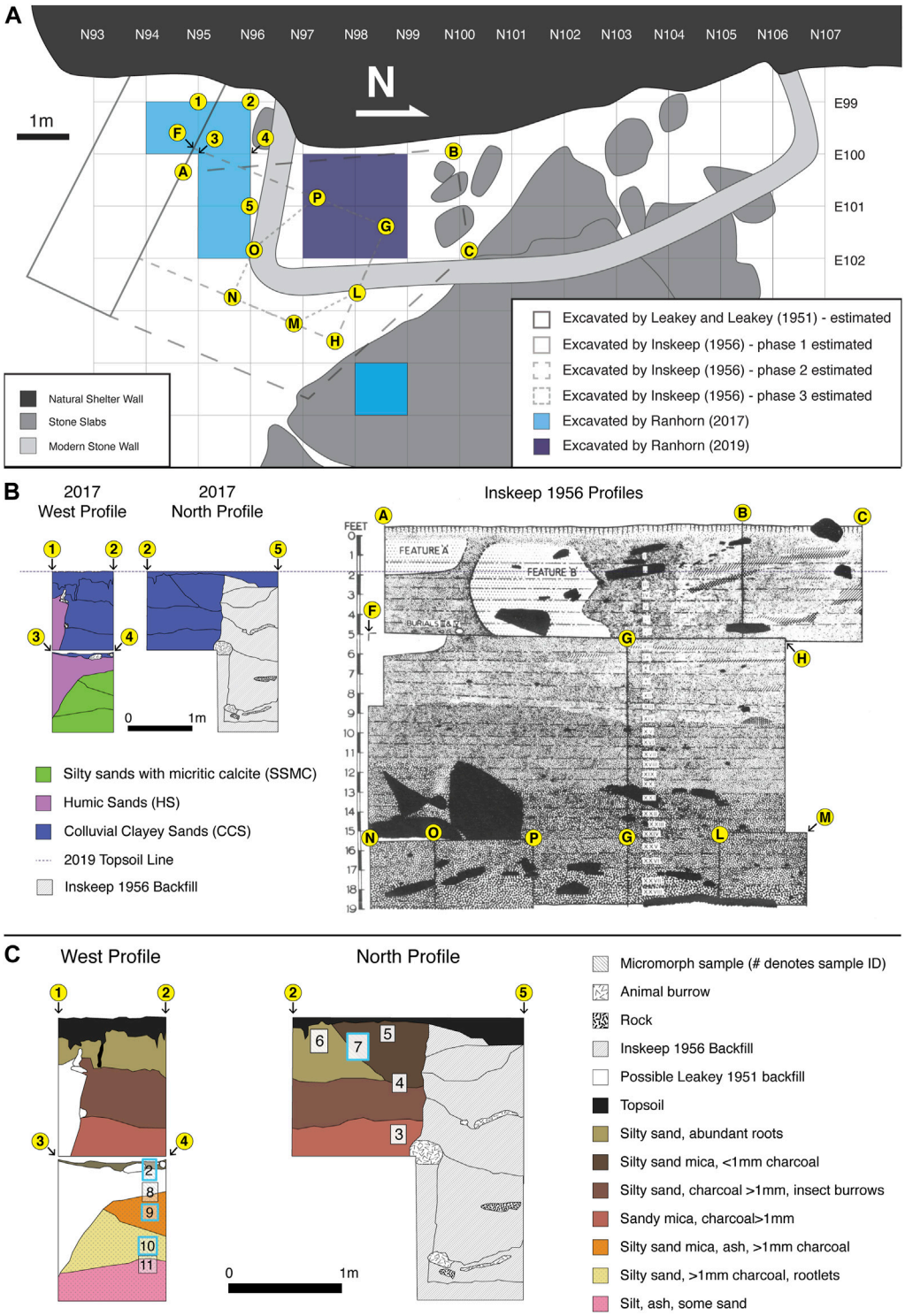

FIGURE 10 | Location and sedimentary context of the historic and modern excavations at Kisese II. The location of historic trenches was estimated using historic drawings, photographs, and the location of features as observed in modern excavations. Letters in circles (representing positions identified by Inskeep in original drawings) and numbers in circles (representing positions from the modern excavations) indicate the same locations as shown in plan and section view. **(A)**: plan view of the site. North here indicates grid north. **(B)**: Comparison of the profiles observed in the 2017 excavation correlated with Inkeep's profile. The 2017 profile shows the three sediment packs described in the text. **(C)**: Detailed profiles from the 2017 excavations showing sediment characteristics, features, and the position of micromorphology samples described in the text. Samples shown in **Figure 11** are outlined in blue.

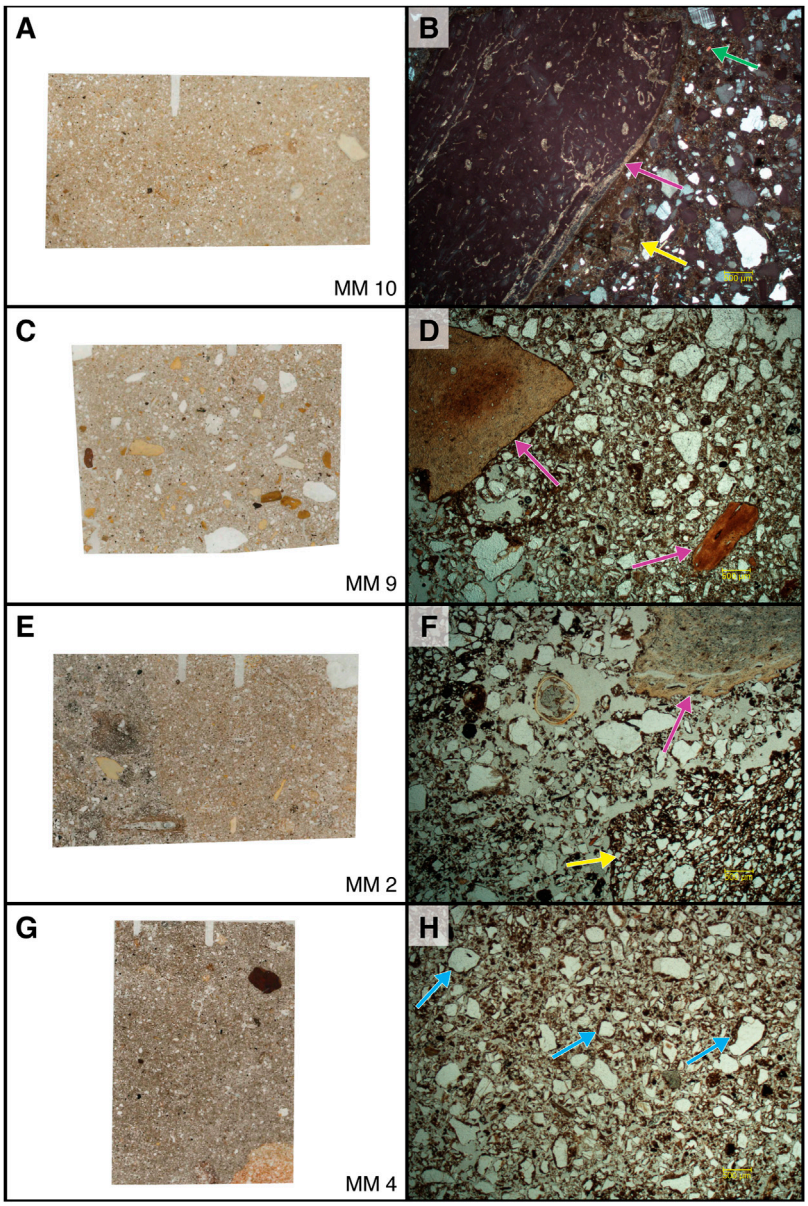

FIGURE 11 | Scans and photomicrographs of thin sections discussed in the text. Photomicrographs show the most significant features described in the text. **(A)** scan of thin sections of sample 10. Note the massive microstructure and the low quantity of bones included in the matrix. **(B)** photomicrograph of sample 10 (2x XPL) showing cemented matrix with micrite filling the space between grains (yellow arrows) and coatings on larger inclusions such as heated bones (pink arrow). Green arrow points to a grain of volcanic mineral (possibly olivine). These grains are very sporadic in the lower sediments but increase in quantity in the upper sediments. **(C)** scan of thin sections of sample 9. Note the increase in quantity of heated bones and the more open microstructure. **(D)** photomicrograph sample 9 (2x PPL) matrix containing less calcite and instead showing more redoximorphic features and a higher quantity of heated bones. However, the bones look subangular to subrounded, suggesting that they are not in primary deposition. **(E)** scan of thin sections of sample 2 containing the clayey *in situ* layer and the intrusive humic sandy layer. Note the sharp boundary between the two layers and the difference in microstructure and color between the two layers. **(F)** photomicrograph sample 2 (2x PPL) showing evidence of mixed matrix with aggregates of material from other layers (yellow arrow) and non-heated, diagenetically altered bones (pink arrow). **(G)** scan of thin section of sample 7. **(H)** photomicrograph of sample 7 (2x PPL) in the upper layer the matrix does not contain any evidence of calcite nor heated bones, moreover porosity is more spongy and open and the grains all show clay coatings (blue arrows) suggesting a fast colluvial accumulation.

indirectly. Trees encroaching the site are causing some superficial bioturbation to the remaining archaeological sediments. However, the trees are also functioning as a biological barrier against erosion, minimizing the impact of heavy rains on the area immediately outside the shelter.

The 2017 and 2019 excavation seasons were primarily aimed at locating the edge of previous excavations, and the micromorphological samples described above provide an understanding of the depositional and post-depositional sedimentary history of the last ~14 ka at the rockshelter,

including those impacts caused by previous archaeological excavations. In summary our micromorphological data show: 1) colluvial input is a major contributor to the topsoil especially in the northeastern corner of the site; 2) field observations about the boundaries of past excavations are accurate; 3) the existence of stark differences in sediment composition and arrangement between the Pleistocene and the Holocene sequences. At least two other sources of post-depositional sedimentary disturbances were noted by earlier archaeologists: Ash-lenses interpreted as hearth features and flexed human burials. Future research will investigate these and the origin of the $CaCO_3$ detected in the micromorphological analyses: since the bedrock is granitic the calcite cannot be authigenic and must have been either transported to the site or formed in place from material other than the bedrock. The micritic nature of the $CaCO_3$ suggests that it was percolated and recrystallized from a solution and the upward increase in frequency of heated bones suggests that the actual loci of the fire could be the upper layers of this group, but more samples are needed to confirm this.

Implications for People in Kondoa and Heritage

The loss of land and heritage we described here impacts not only the archaeological and geological records but most importantly the local people in very concrete ways by affecting their current and future livelihoods. Since 1960 farmers near Kisese II adapted to their fast changing environment by building terraces and using traditional farming knowledge. However the intensification of the erosional regime of the slope since the 1990s forced them to abandon the higher slopes altogether for the valley. The increased tempo of the erosion we have noticed between 2017 and 2019 will accelerate the loss of productive land, the widening of badlands, and the destruction of infrastructures having a concrete impact on the future livelihoods in Machinjioni the village in which the site is located. Crops will have to be changed to adapt production to the new impoverished environment, while transportation of goods and people will be severely impacted.

The loss of local archaeology has potentially devastating heritage effects for people living there today. For example, the loss of the record could preclude people in Machinjioni specifically and Kondoa in general from establishing new economic enterprises involving tourism and heritage management. Furthermore, erosion-induced erasure of tangible heritage may inhibit the creation and transmission of social memory. Combined, these processes create additional barriers that prevent indigenous communities from playing important roles in the development and implication of heritage management policy (Bwasiri and Bushozi, 2014).

CONCLUSION

The region of Kondoa in north-central Tanzania is famous for long-term, detailed studies of soil erosion and its impact on the local farming population (e.g., Ligonja and Shrestha, 2015). In relation to environmental changes archaeologists have long been concerned with the rapid fading of many of the painted images on the rockshelter (e.g., Temu, 2018). Our multi-scalar work combines bibliographic and field research to better understand the nature and history of the Kondoa regional dynamism to reconstruct the landscape and site sedimentary processes.

Using historical photographs and published data we reconstructed the chronology of major vegetation changes, topsoil loss, and the formation of erosional features over the past ~60 years. Archival documentation shows that since the 1930s the landscape around Kisese II has undergone three main anthropogenic shifts that altered ecosystems and exposed the landscape to more drastic impacts of climate change: 1) the forceful deforestation and removal of indigenous fauna exposed topsoil across the region and well into the mountainous terrain, 2) forceful abandonment of the previously created farm and pastureland caused disappearance of land stewardship, shortage of manure, and soil impoverishment and 3) climate change-induced intensification of rains drastically increased erosion of the already impoverished soil. Archival photographs and landscape survey shows that this regional context can be applied directly to Kisese II and the surrounding landscape.

On the landscape immediately around Kisese II we qualified erosion by interpreting our survey results within the regional data described above. We have identified: 1) the almost complete loss of yellow regosol on the mid slope and at the site; 2) the incipient erosion of the chromic lyxisol, identified as Pleistocene Paleosol and its relation to the possible loss of archaeological sites; 3) the drastic expansion of unproductive land by the rapid formation and enlargement of gullies, uncovering and eroding Pleistocene arenasols, and resulting formation of badlands.

The regional and landscape data we discuss here are invaluable to contextualize the site of Kisese II and guide archaeological work. At the site, we have recorded the topography using photogrammetry and through comparison with historical photographs and archival notes from Inskeep we have documented an erosional rate of ~1 cm/yr in the past 60 years for a total maximum loss of 68 cm. We have also identified localized erosion features such as splash erosion at the dripline and some sheet erosion outside of the sheltered area to the S and SE. Our analyses show that sediment loss at the shelter is a result of the larger regional and landscape processes described above. The loss of sediment impacts also the rock art, as comparisons with the radiocarbon chronology of the site suggest that much of the upper ~4 ka history of the shelter has been lost, an age that is the current best estimate for the age of some of the paintings at Kisese II and in the region more broadly (Masao, 1976). Using micromorphology we were able to integrate our landscape and topographic data with micro-geoarchaeological stratigraphy. We reconstructed a complex series of sedimentary forces and their interactions and our results show reason for optimism. In some instances sediment at Kisese II is protected from erosion: 1) the conformation of the boulder group and the large rock falls protect some areas of the shelter from rain activity; 2) colluvial input is also present at the cave and it mitigates sediment loss especially in the northern portion of the rockshelter, and 3) micromorphology has confirmed that the Pleistocene layers are *in situ* as are the early Holocene strata although these have suffered bioturbation

from animals and roots and any interpretation of the material coming from these must take that into account.

The loss of sedimentary and archaeological context at Kisese II and its landscape is already dramatic in itself, but in addition we have shown that context to the extant rock art at a UNESCO world heritage site is being rapidly lost. Through the analysis of the erosion at Kisese II landscape we have shown that in this environment a complete loss of context is possible. For this reason we must act quickly.

The impact of this study in particular and KDHP as a whole goes beyond the creation of scientific data. It is a step towards changing how we practice archaeology towards the creation of more practical outcomes. Natural and human induced climate change combined with at least a century of recorded agricultural and environmental policies have impacted the archaeology and sediments at the site. The integration of geological, historical, and community-based archaeological research as practiced by KDHP can be used to improve the wellbeing of local communities and aid preservation of cultural heritage to provide the local and global community with a "usable past" (sensu: Andah, 1995; Kryder-Reid, 1997; Hassan, 1999; Schmidt, 2006).

DATA AVAILABILITY STATEMENT

The original contributions presented in the study are included in the article/supplementary material, further inquiries can be directed to the corresponding author.

AUTHOR CONTRIBUTIONS

IP Conceptualization of study and article, Methodology, Investigation (excavation, survey, and sampling), Analyses, Writing-Original draft preparation, Reviewing, and Editing. SP Investigation (excavation and survey), 3D modelling, Mapping, Photography, Preparation editing and finalization of figures and graphs, Reviewing, and Editing. DR Investigation (excavation) SF Investigation (excavation), field logistics. JL Final Editing HM Investigation (excavation), field logistics. JO Investigation (excavation) ES-L Investigation (excavation, survey and sampling), Reviewing, and Editing. CT Conceptualization of article, Reviewing, and Editing. DC Reviewing, and Editing. KR Conceptualization of article, Investigation (PI), Reviewing, and Editing.

FUNDING

Funding for excavation and analyses of Kisese II was provided by Graduate Women in Science (with support from Adele Lewis, Nell Mondy, and Eloise Gerry), the American School of Prehistoric Research, and the Leakey Foundation.

ACKNOWLEDGMENTS

We thank the people of Machinjioni village who welcomed us, were open to collaborate with us, and continue to host us. We specifically want to thank Rajai, Nuhu, Paulo, Joseph, Hadija, Sofia, Eligys, Mzungu, Jida, Anna, Hamisi, Nondi, Nduju, Mariam, Amina, and Aereliana who made this work possible. We also thank the Antiquities Division at the Ministry of Natural Resources and Tourism, specifically Misana Bwire and Emmanuel Bwasiri, for their assistance in protecting the heritage around Kondoa. We thank Jennifer Charlson for permission to publish some of the photographs taken by R.R. Inskeep in 1956 that are now housed at the McDonald Institute at Cambridge University. Historical aerial photographs are reproduced with permission from the National Center for Aerial Photography (#IMSL-IR-171675). This work was permitted under COSTECH permit 2019-304-NA-2015-22. This work was possible thanks to the support of the Zinman Institute of Archaeology, the Maritime Civilization department at Haifa University, Advanced Imaging Service for Objects and Spaces at University of Minnesota Twin Cities, the Department of Anthropology at Harvard University, and the School of Human Evolution and Social Change at Arizona State University. We thank Daniel Fallu, Yitzchak Jaffe, Ruth Shahak-Gross, Michael Storozum, and Kristen Wroth for useful comments on earlier drafts of the manuscript.

REFERENCES

Agisoft (2020). *Agisoft Metashape Professional Edition*. Version 1.6.5. St. Petersburg, Russia: Agisoft LLC.

Andah, B. W. (1995). *Studying African Societies in Cultural Context*. Santa Fe, New Mexico: See Schmidt & Patterson, 149–181.

Backéus, I., Rulangaranga, Z. K., and Skoglund, J. (1994). Vegetation Changes on Formerly Overgrazed Hill Slopes in Semi-Arid Central Tanzania. *J. Appl. Veg. Sci.* 5 (3), 327–336.

Blay, D., Edouard, B., O Chamshama, S. A., and Chikamai, B. (2004). "Rehabilitation of Degraded Lands in Sub-saharan África: Lessons Learned from Selected Case Studies," in *Forestry Research Network for Sub-saharan Africa (Fornessa)* (Kumasi, Ghana: International Union of Forest Research Organizations).

Blender (2020). *Blender*. Version 2.91.0. Amsterdam, Netherlands: LTS. Available at: https://www.blender.org/download/releases/2-91/.

BlenderGIS (2020). *BlenderGIS Addon*. Version 2.2.5. Amsterdam, Netherlands: FAQ. Retrieved from https://github.com/domlysz/BlenderGIS.

Borner, M. (1985). The Increasing Isolation of Tarangire National Park. *Oryx* 19, 91–96. doi:10.1017/s0030605300019797

Bushnell, T. M. (1942). Some Aspects of the Soil Catena Concept. *Soil Sci. Soc. America, Proc.* 7, 466–476.

Butler, B. E. (1967). "Soil Periodicity in Relation to Landform Development in Southeastern Australia," in *Landform Studies from Australia and New Guinea*. Editors J. N. Jennings and J. A. Ž. Mabbutt (London: Cambridge University Press), 231–255.

Bwasiri, B., and Bushozi, M. (2011). Towards Sustainable Cultural Heritage Management in Tanzania: A Case Study of Kalenga and Mlambalasi Sites in Iringa, Southern Tanzania. *South Afr. Archaeological Bull.* 69, 136–141.

Bwasiri, E. J., and Smith, B. W. (2015). The Rock Art of Kondoa District, Tanzania. *Azania: Archaeological Res. Africa* 50, 437–459. doi:10.1080/0067270X.2015.1120436

Bwasiri, E. J., and Emmanuel, J. (2011). The Implications of the Management of Indigenous Living Heritage: The Case Study of the Mongomi Wa Kolo

Rock Paintings World Heritage Site, Central Tanzania. *South Afr. Archaeological Bull.*, 60–66.
Caillard, V. (2003). History of Mapping in Tanzania. Available at: http://web.vincentcaillard.free.fr/Images/MappingInTanzania.pdf.
Clark Labs, Clark University (2012). *IDRISI 17.0, the Selva Edition [software]*. Worcester, MA: Clark Labs, Clark University.
Courty, M. A., Goldberg, P., and Macphail, R. (1989). *Soils and Micromorphology in Archaeolog: Cambridge Manuals in Archaeology*. Cambridge: Cambridge University Press.
Davis, D. S., Seeber, K. E., and Sanger, M. C. (2020). Addressing the Problem of Disappearing Cultural Landscapes in Archaeological Research Using Multi-Scalar Survey. *The J. Isl. Coastal Archaeology* 16, 1–17. doi:10.1080/15564894.2020.1803457
Douglass, K., and Cooper, J. (2021). "Archaeology, Environmental Justice, and Climate Change on Islands of the Caribbean and Southwestern Indian Ocean," in *Proc. Natl. Acad. Sci. U.S.A.* (International Union of Forest Research Organizations) 175 (1), 8254–8262.
Emmitt, J., Pillay, P., Barrett, M., Middleton, S., Mackrell, T., Floyd, B., et al. (2021). A Comparison of Volumetric Reconstruction Methods of Archaeological Deposits Using Point-Cloud Data from Ahuahu, Aotearoa New Zealand. *Remote Sensing* 13 (19), 4015. doi:10.3390/rs13194015
Eriksson, M. G., Olley, J. M., and Payton, R. W. (2000). Soil Erosion History in Central Tanzania Based on OSL Dating of Colluvial and Alluvial Hillslope Deposits. *Geomorphology* 36, 107–128. doi:10.1016/s0169-555x(00)00054-4
Eriksson, M. G., and Sandgren, P. (1999). Mineral Magnetic Analyses of Sediment Cores Recording Recent Soil Erosion History in central Tanzania. *Palaeogeogr. Palaeoclimatol. Palaeoecol.* 152, 365–383. doi:10.1016/s0031-0182(99)00043-7
ESRI Inc (2020). *ArcGIS*. Version 10.8.1. Redlands, CA: ESRI 2011.
Fosbrooke, H. A. (1951). *The Fight to Rescue a District*. London, UK: East African Annuals, 168–170.
Goldberg, P., and Macphail, R. I. (2008). *Practical and Theoretical Geoarchaeology*. 3rd ed. Malden, MA: Blackwell Publishing Ltd.
González-Ruibal, A., González, P. A., and Criado-Boado, F. (2018). Against Reactionary Populism: towards a New Public Archaeology. *Antiquity* 92, 507–515. doi:10.15184/aqy.2017.227
Google, L. L. C. (2021). *Google Map Imagery for Tanzania*. Mountain View, California: Google LLC.
Hassan, F. A. (1999). African Archaeology: The Call of the Future. *Afr. Aff.* 98 (392), 393–406. doi:10.1093/oxfordjournals.afraf.a008046
Headrick, D. R. (2014). Sleeping Sickness Epidemics and Colonial Responses in East and Central Africa, 1900-1940. *Plos Negl. Trop. Dis.* 8, e2772. doi:10.1371/journal.pntd.0002772
Hollesen, J., Callanan, M., Dawson, T., Fenger-Nielsen, R., Friesen, T. M., Jensen, A. M., et al. (2018). Climate Change and the Deteriorating Archaeological and Environmental Archives of the Arctic. *Antiquity* 92 (363), 573–586. doi:10.15184/aqy.2018.8
Kangalawe, R. Y. M., Christiansson, C., and Östberg, W. (2008). Changing Land-Use Patterns and Farming Strategies in the Degraded Environment of the Irangi Hills, Central Tanzania. *Agric. Ecosyst. Environ.* 125, 33–47. doi:10.1016/j.agee.2007.10.008
Kannenberg, H. (1900). Reise Durch Die Hamitischen Sprachgebiete Um Kondoa. *Mittheilungen von Forschungsreisenden Und Gelehrten Aus Den Deutschen Schutzgebieten* 13, 144–172.
Karkanas, P., Bar-Yosef, O., Goldberg, P., and Weiner, S. (2000). Diagenesis in Prehistoric Caves: The Use of Minerals that Form *In Situ* to Assess the Completeness of the Archaeological Record. *J. Archaeological Sci.* 27 (10), 915–929. doi:10.1006/jasc.1999.0506
Karkanas, P., and Goldberg, P. (2013). 6.23 Micromorphology of Cave Sediments. *Treatise on Geomorphology* 6, 286–297. doi:10.1007/s00213-012-2718-910.1016/b978-0-12-374739-6.00120-2
Karkanas, P., Marean, C., Bar-Matthews, M., Jacobs, Z., Fisher, E., and Braun, K. (2020). Cave Life Histories of Non-anthropogenic Sediments Help Us Understand Associated Archaeological Contexts. *Quat. Res.* 99, 270–289. doi:10.1017/qua.2020.72
Kessy, E. T. (2013). The Transition from the Later Stone Age to Iron Age in Kondoa, Central Tanzania. *Afr. Archaeol Rev.* 30 (3), 225–252. doi:10.1007/s10437-013-9141-4
Koenig, C. W., Willis, M. D., and Black, S. L. (2017). Beyond the Square Hole. *Adv. Archaeol. Pract.* 5 (1), 54–70. doi:10.1017/aap.2016.8
Kryder-Reid, E. (1997). Making Alternative Histories: The Practice of Archaeology and History in Non-western Settings:Making Alternative Histories: The Practice of Archaeology and History in Non-western Settings. *Am. Anthropologist* 99 (3), 646–647. doi:10.1525/aa.1997.99.3.646
Laird, M. F., Sawchuk, E. A., Kwekason, A., Mabulla, A. Z. P., Ndiema, E., Tryon, C. A., et al. (2021). Human Burials at the Kisese II Rockshelter, Tanzania. *Am. J. Phys. Anthropol.* 175 (1), 187–200.
Lane, P. (2009). Environmental Narratives and the History of Soil Erosion in Kondoa District, Tanzania: An Archaeological Perspective. *Int. J. Afr. Hist. Stud.* 42 (3), 457–483.
Leakey, L. S. B. (1950). Archaeological Aspects of the Tanganyika Paintings. *Tanganyika Notes Rec.* 29, 15–19.
Leakey, L. S. B. (1936). *Stone Age Africa*. London, United Kingdom: Oxford University Press.
Leakey, M. D. (1983). *Africa's Vanishing Art: The Rock Paintings of Tanzania*. London, United Kingdom: Hamish Hamilton.
Ligonja, P. J., and Shrestha, R. P. (2015). Soil Erosion Assessment in Kondoa Eroded Area in Tanzania Using Universal Soil Loss Equation, Geographic Information Systems and Socioeconomic Approach. *Land Degrad. Develop.* 26 (4), 367–379. doi:10.1002/ldr.2215
Lüning, S., Gałka, M., and Vahrenholt, F. (2017). Warming and Cooling: The Medieval Climate Anomaly in Africa and Arabia. *Paleoceanography* 32, 1219–1235. doi:10.1002/2017PA003237
Lyaruu, H. V. M., and Backeus, I. (1999). Soil Seed Bank and Regeneration Potential on Eroded hill Slopes in the Kondoa Irangi Hills, central Tanzania. *Appl. Veg. Sci.* 2, 209–214. doi:10.2307/1478984
Madulu, N. F. (2001). Reversed Migration Trends in the Kondoa Eroded Area: Lessons for Future Conservation Activities in the Hado Project Areas, Tanzania. *Soc. Sci. Res. Rep. Ser.* 20, 1.
Masao, F. T. (1982). *The Rock Art of Kondoa and Singida: A Comparative Description*. Dar es Salaam: National Museums of Tanzania, Occasional Paper No. 5.
Masao, F. T. (1976). *The Late Stone Age and the Rock Paintings of Central Tanzania*. Vancouver, BC: Simon Fraser University. Ph.D. dissertation.
McGrath, G. (1976). *The Surveying and Mapping of British East Africa 1890-1946: Origins, Development and Coordination. Cartographica Monograph No. 18*. Toronto: University of Toronto Press.
McIlwaine, J. (1997). *Maps and Mapping of Africa: A Resource Guide*. London: Hans Zell Publishers.
McPherron, S. J. P., Dibble, H. L., and Goldberg, P. (2005). Z. *Geoarchaeology* 20 (3), 243–262. doi:10.1002/gea.20048
Mehari, A. G., and Ryano, K. P. (2016). "Maasai People and Oldupai (Olduvai) Gorge: Looking for Sustainable People-Centered Approaches and Practices," in *Community Archaeology and Heritage in Africa* (Oxfordshire, United Kingdom: Routledge), 35–59.
Milne, G., Beckley, V. A., Jones, G. H. G., Martin, W. S., Griffith, G., and Raymond, L. W. (1936). *A ProvisionalSoil Map ofEast Africa (Kenya, Uganda, Tanganyika, and Zanzibar) with Explanatory Memoir*. London: publisher not identified, 34.
Mugasha, A. G., and Nshubemuki, L. (1988). Soil Conservation in Kondoa, Tanzania: the Case of the Rangi People in the HADO Area. *For. Ecol. Manag.* 25, 159–180. doi:10.1016/0378-1127(88)90085-0
Mwalyosi, R. B. B. (2000). Vegetation Changes Following Land Reclamation in the Kondoa Eroded Area, Central Tanzania. *Afr. J. Ecol.* 38 (3), 265–268. doi:10.1046/j.1365-2028.2000.00257.x
Ndomba, P. M., Mtalo, F., and Killingtveit, A. (2009). Estimating Gully Erosion Contribution to Large Catchment Sediment Yield Rate in Tanzania. *Phys. Chem. Earth, Parts A/B/C* 34 (13–16), 741–748. doi:10.1016/j.pce.2009.06.009
Niespolo, E. M., Sharp, W. D., Tryon, C. A., Faith, J. T., Lewis, J., Ranhorn, K. L., et al. (2020). Ostrich Eggshell Stable Isotopes Record Site-Specific Paleoenvironmental Changes During the Middle to Later Stone Age Transition in Eastern Africa. *Quaternary Science Reviews* 230. doi:10.1016/j.quascirev.2019.106142
Nobles, G. R., and Roosevelt, C. H. (2021). Filling the Void in Archaeological Excavations: 2D Point Clouds to 3D Volumes. *Open Archaeology* 7 (1), 589–614. doi:10.1515/opar-2020-0149
Payton, R. W., Christiansson, C., Shishira, E. K., Yanda, P., and Eriksson, M. G. (1992). Landform, Soils and Erosion in the North-Eastern Irangi Hills, Kondoa,

Tanzania. *Geografiska Annaler: Ser. A, Phys. Geogr.* 74 (A), 65–79. doi:10.1080/04353676.1992.11880351

Phillips, J. (1930). Some Important Vegetation Communities in the Central Province of Tanganyika Territory (Formerly German East Africa): A Preliminary Account. *J. Ecol.* 18, 193–234. doi:10.2307/2256004

QGIS.org (2021). *QGIS Geographic Information System*. QGIS Association.

P. R. Schmidt and I. Pikirayi (Editors) (2016). *Community Archaeology and Heritage in Africa: Decolonizing Practice*. Routledge, 324

Schmidt, P. R. (2006). *Historical Archaeology in Africa: Representation, Social Memory, and Oral Traditions*. Vancouver, BC: Rowman Altamira.

Schmidt, P. R. (2019). *Participatory Archaeology and Heritage Studies: Perspectives from Africa*. Routledge.

Sesana, E., Gagnon, A. S., Ciantelli, C., Cassar, J., and Hughes, J. J. (2021). Climate Change Impacts on Cultural Heritage: A Literature Review. *Wires Clim. Change* 12, 1. doi:10.1002/wcc.710

Shahack-Gross, R., Berna, F., Karkanas, P., and Weiner, S. (2004). Bat Guano and Preservation of Archaeological Remains in Cave Sites. *J. Archaeological Sci.* 31 (9), 1259–1272. doi:10.1016/j.jas.2004.02.004

Stiner, M. C., Kuhn, S. L., Surovell, T. A., Goldberg, P., Meignen, L., Weiner, S., et al. (2001). Bone Preservation in Hayonim Cave (Israel): A Macroscopic and Mineralogical Study. *J. Archaeological Sci.* 28, 643–659. doi:10.1006/jasc.2000.0634

Stoops, G. (2003). *Guidelines for Analysis and Description of Soil and Regolith Thin Sections*. Madison, WI: Soil Science Society of America Inc.

Swynnerton, C. F. M. (1936). *The Tsetse Flies of East Africa: A First Study of Their Ecology, with a View to Their Control*. London: Transactions of the Royal Entomological Society of London, 1.

Temu, E. L. (2018). Rock Art Damage Reducing Facilitators of Central Tanzania Heritage: A Gateway to Tourism Promotion. *J. Popular Edu. Africa* 2 (2), 52–68.

Tryon, C. A., Ranhorn, K., and Lewis, J. E. (2019). "Excavating the Archives: The 1956 Excavations of the Late Pleistocene-Holocene Sequence at Kisese II (Tanzania)," in *Modern Human Origins and Dispersal*. Editors H. Reyes-Centeno, C. Bentz, and Y. Sahle (Tübingen: Kerns-Verlag), 215–238.

Tryon, C. A., Lewis, J. E., Ranhorn, K. L., Kwekason, A., Alex, B., Marean, M. F., et al. (2018). Middle and Later Stone Age Chronology of Kisese II Rockshelter (UNESCO World Heritage Kondoa Rock-Art Sites), Tanzania. *PLoS One* 13 (2), e0192029. doi:10.1371/journal.pone.0192029

Conflict of Interest: Author WK was employed by the company Heritage Consultants LLC.

The remaining authors declare that the research was conducted in the absence of any commercial or financial relationships that could be construed as a potential conflict of interest.

Publisher's Note: All claims expressed in this article are solely those of the authors and do not necessarily represent those of their affiliated organizations, or those of the publisher, the editors and the reviewers. Any product that may be evaluated in this article, or claim that may be made by its manufacturer, is not guaranteed or endorsed by the publisher.

Advantages of publishing in Frontiers

OPEN ACCESS
Articles are free to read for greatest visibility and readership

FAST PUBLICATION
Around 90 days from submission to decision

HIGH QUALITY PEER-REVIEW
Rigorous, collaborative, and constructive peer-review

TRANSPARENT PEER-REVIEW
Editors and reviewers acknowledged by name on published articles

Frontiers
Avenue du Tribunal-Fédéral 34
1005 Lausanne | Switzerland

Visit us: www.frontiersin.org
Contact us: frontiersin.org/about/contact

REPRODUCIBILITY OF RESEARCH
Support open data and methods to enhance research reproducibility

DIGITAL PUBLISHING
Articles designed for optimal readership across devices

FOLLOW US
@frontiersin

IMPACT METRICS
Advanced article metrics track visibility across digital media

EXTENSIVE PROMOTION
Marketing and promotion of impactful research

LOOP RESEARCH NETWORK
Our network increases your article's readership